ISSN 0915-6348

NATIONAL INSTITUTE FOR FUSION SCIENCE

Proceedings of the Second Asian Pacific Plasma Theory Conference APPTC '97

Y. Tomita, Y. Nakamura and T. Hayashi (Eds.)

(Received - July 17, 1998)

NIFS-PROC-38 Aug. 1998

RESEARCH REPORT
NIFS-PROC Series

NAGOYA, JAPAN

Proceedings of
the second Asian Pacific Plasma Theory Conference
APPTC '97

Combined with

Japan-Australia fusion theory workshop, and

US-Japan JIFT workshop on Theoretical Study for Helical Plasmas

Edited by Yukihiro Tomita,
Yuji Nakamura,
and Takaya Hayashi

September 24-26, 1997

National Institute for Fusion Science

Toki, Japan

Abstract

This issue is the proceedings of the second Asian Pacific Plasma Theory Conference (APPTC '97), which was held on September 24-26, 1997 at National Institute for Fusion Science (Toki, Japan) under the auspices of the Japan Society of Plasma Science and Nuclear Fusion Research and the National Institute for Fusion Science. A part of APPTC '97 was a joint session with Japan-Australia fusion theory workshop and US-Japan JIFT workshop on Theoretical Study for Helical Plasmas. The conference covers all plasma theory areas including magnetic confinement, inertial fusion, space plasmas, astrophysical plasmas, industrial processing plasmas, and dusty plasmas, etc.

Keywords: plasma theory, magnetic confinement, inertial fusion, space plasma, astrophysical plasma, industrial processing plasma, dusty plasma

Preface

The second Asian Pacific Plasma Theory Conference (APPTC '97) was held on September 24-26, 1997 at National Institute for Fusion Science (Toki, Japan) under the auspices of the Japan Society of Plasma Science and Nuclear Fusion Research and the National Institute for Fusion Science. A part of APPTC '97 was a joint session with Japan-Australia fusion theory workshop and US-Japan JIFT workshop on Theoretical Study for Helical Plasmas. The Conference was attended by about 115 participants from 14 countries. The program included 43 oral presentations and 40 poster presentations.

APPTC '97 was a continuation of APPTC '96 held in Korea, which covered all plasma theory areas including magnetic confinement, inertial fusion, space plasmas, astrophysical plasmas, industrial processing plasmas, and dusty plasmas, etc. The purposes of the conference are to facilitate cooperation among plasma theorists and also to induce and educate young and bright scientists in the Asia-Pacific countries where rapidly increasing research activities in plasma science and technologies have been taking place. This conference was the first international conference held at the new site of the National Institute for Fusion Science, which had moved to the Toki site from Nagoya in April, 1997. In this conference particular emphasis was placed on the pure scientific aspects of plasma physics, hoping that plasma physics would be able to emanate attractive fragrance not only to plasma scientists but also to scientists in other fields.

Tetsuya Sato
Conference Chair

Local Organizing Committee

Tetsuya Sato , National Institute for Fusion Science, Toki
Kunioki Mima , Osaka University, Osaka
Masafumi Azumi , Japan Atomic Energy Research Institute, Naka
Masahiro Wakatani , Kyoto University, Uji
Takaya Hayashi, Secretary, National Institute for Fusion Science, Toki
Yuji Nakamura, Secretary, Kyoto University, Uji

International Organizing Committee

Tetsuya Sato , National Institute for Fusion Science, Toki
Liu Chen , University of California, Irvine
Duk-In Choi , Korea Basic Science Institute, Taejeon
Gyung-Su Lee , Korea Basic Science Institute, Taejeon
Choong-Seock Chang , Korea Advanced Institute of Science and Technology, Taejeon
Sang-Hee Hong , Seoul National University, Seoul
Jae-Koo Lee , Pohang University of Science and Technology, Pohang
Lou-Chung Lee , National Cheng-Kung University, Tainan
Kwo-Ray Chu , National Tsing Hua University, Hsinchu
Xian-Tu He , Institute of Applied Physics and Computational Mathematics, Beijing
Sing Lee , Nanyang Technology University, Singapore
C. Z. Cheng , Princeton Plasma Physics Laboratory, Princeton
James W. Van Dam IFS, University of Texas at Austin, Austin
Robert L. Dewar , Australian National University, Canberra
Quankang Lu , Fudan University, Shanghai
Kunioki Mima , Osaka University, Osaka
Masafumi Azumi , Japan Atomic Energy Research Institute, Naka
Masahiro Wakatani , Kyoto University, Uji

Executive Committee

Tetsuya Sato , National Institute for Fusion Science, Toki
Duk-In Choi , Korea Basic Science Institute, Taejeon
Liu Chen , University of California, Irvine
Xian-Tu He , Institute of Applied Physics and Computational Mathematics, Beijing
Lou-Chung Lee , National Cheng-Kung University, Tainan
Kunioki Mima , Osaka University, Osaka
Masahiro Wakatani , Kyoto University, Uji

Contents

Program

Wednesday, September 24, 1997

Opening Session [Room A_3 · 401]

9:00 - 9:20 **Atsuo Iiyoshi** (Director-General, NIFS)
Tetsuya Sato (Chair of Executive Committee, NIFS)

Session 1: New Tokamak and Heliotron - Oral [Room A_3 · 401]
Chairperson: **Yuji Nakamura** (Kyoto Univ.)

9:20 - 9:50 *"Confinement Theory of LHD"* (**Masao Okamoto**, NIFS)

9:50 - 10:20 *"Current Status of the KSTAR (Korea Superconducting Tokamak Advanced Research) Project"* (**Duk-In Choi**, G. S. Lee, J. Kim, H. K. Park, and KSTAR Project Team, Korea Basic Science Institute)

10:20 - 10:40 ***< Coffee Break >***

Session 2: Magnetic Confinement - Oral [Room A_3 · 401]
Chairperson: **Chio Z. Cheng** (PPPL)

10:40 - 11:05 *"Nonlinear Dynamics of Alfvén Eigenmodes in Toroidal Plasmas"* (**Fulvio Zonca,** L. Chen, G. Hu, R. A. Santoro, E.N.E.A.)

11:05 - 11:30 *"Toroidal Plasma Response to External Fields"* (**Robin G. Storer**, Flinders University)

11:30 - 11:55 *"Toroidal Mode Structure and Related Transport in Reversed Shear Plasma"* (**Yasuaki Kishimoto**, J. Y. Kim, T. Tajima, and W. Horton, JAERI)

11:55 - 12:20 *"Rotation-Induced Local Heat Sink and Formation of Thermal Transport Barrier in Tokamaks"* (**Xiao-Ming Qiu**, Southwestern Institute of Physics)

12:20 - 13:40 ***< Lunch >*** and ***International Organizing Committee Lunch***

Session 3: Plasma Phenomena in Laboratory, Earth and Star - Oral [Room A_3 · 401]
Chairperson: **Xian-Tu He** (Institute of Applied Physics and Computational Mathematics)

13:40 - 14:05 *"Integrated Physics of Laser Produced Plasmas"* (**Hideaki Takabe**, Osaka Univ.)

14:05 - 14:30 *"Double Tearing Reconnection and the Off-Axis Sawteeth Crash"* (**Ding Li**, Institute of Plasma Physics)

14:30 - 14:55 *"Collective Scattering of Electromagnetic Waves from a Relativistic Magnetized Plasmas"* (**Lu Quankang**, Fudan University)

14:55 - 15:15 ***< Coffee Break >***

Session 4 A: Oral [Room A_3 · 401]
Chairperson: **Noriyoshi Nakajima** (NIFS)

15:15 - 15:30 *"Recent Progress of Nonlinear Simulation on the Toroidal Alfvén Eigenmode"* (**Yasushi Todo** and T. Sato, NIFS)

15:30 - 15:45 *"Effects of the Safety Factor Profile on the Ion Temperature Gradient Mode in Tokamak Plasmas"* (**Xiao-Dong Peng**, J. H. Zhang, Q. D. Gao, Southwestern Institute of Physics)

15:4 5 - 16:00 *"Lagrangian and Hamiltonian Forms of the Guiding Center Equation for Toroidal Plasmas"* (**Vitalij D. Shafranov**, Russian Research Center "Kurchatov Institute")

16:00 - 16:15 *"The Plug Potential Formation and Ion Axial Transport in a Tandem Mirror"* (**Isao Katanuma**, R. Minai, Y. Kiwamoto, Y. Tatematsu, K. Ishii, T. Saito, T. Tamano and K. Yatsu, Univ. of Tsukuba)

16:15 - 16:30 *"Nonlinear Simulation of Electromagnetic Current Diffusive Interchange Mode Turbulence"* (**Masatoshi Yagi**, S.-I. Itoh, K. Itoh, A. Fukuyama, Kyushu Univ.)

16:30 - 16:45 *"Two-Dimensional Model of Conventional Stellarator"* (**Vladimir D. Pustovitov**, Russian Research Center "Kurchatov Institute")

16:45 - 17:00 *"Virtual Reality for Plasma Physics"* (**Henry J. Gardner**, Australian National University)

Session 4 B: Oral [Room A_1 · 402]

Chairperson: **Kunioki Mima** (Osaka Univ.)

15:15 - 15:30 *"Numerical Study of Hydrodynamic Instability of Laser Implosion"* (**Atsushi Sunahara**, H. Takabe and K. Mima, Osaka Univ.)

15:30 - 15:45 *"Supersonic Solitons and Boundary-Value Problem"* (**Levan N. Tsintsadze**, K. Mima and K. Nishikawa, Osaka Univ.)

15:45 - 16:00 *"A Universal Parametrization of Chaos in Various Beam-Wave Interactions"* (**Jae-Koo Lee**, H. J. Lee, M. S. Hur, I. D. Bae and Y. Yang, Pohang Univ. of Science and Technology)

16:00 - 16:15 *"Complexity in a Three-Wave Interaction"* (**Milos M. Skoric** and T. Sato, NIFS)

16:15 - 16:30 *"Relaxation of a Two-Species Magnetofluid"* (L. C. Steinhauer and **Akio Ishida**, Niigata Univ.)

16:30 - 16:45 *"Plasma Transport due to Alfvén Waves in a Strongly Nonuniform Magnetic Field"* (**Chio Z. Cheng**, J. R. Johnson, PPPL)

16:45 - 17:00 *"Nonlinear Dynamics of Magneto-Gravity Instability in Sheared Magnetic Field"* (**Kanya Kusano**, K. Moriyama, T. Miyoshi, Hiroshima Univ.)

18:00 - 20:00 ***International Organizing Committee Meeting***

Thursday, September 25, 1997

Session 5: Tokamak and Stellarator Theory - Oral [Room A_3 · 401]

Chairperson: **Liu Chen** (University of California, Irvine)

9:00 - 9:30 *"Reduced Form of MHD Lagrangian for Ballooning Modes"* (**Robert L. Dewar**, Australian National University)

9:30 - 10:00 *"Two-Fluid and Parallel Compressibility Effects in Tokamak Plasmas"* (**Linda E. Sugiyama** and W. C. Park, MIT)

10:00 - 10:20 ***< Coffee Break >***

Session 6: Space and Solar Plasma Physics - Oral [Room A_3 · 401]
Chairperson: **George J. Morales** (UCLA)

10:20 - 10:45 *"Magnetohydrodynamic Origin of Jets from Accretion Disks"* (**Richard V. Lovelace**, Cornell University)

10:45 - 11:10 *"Pulsar Electrodynamics-Some Outstanding Problems"* (**Donald B. Melrose**, Univ. of Sydney)

11:10 - 11:35 *"Astrophysical Plasma MHD Processes Revealed by the Solar X-ray Satellite YOHKOH"* (**Yutaka Uchida**, Science Univ. of Tokyo)

11:35 - 12:00 *"Solitary Kinetic Alfvén Wave in Low Aurora"* (**De-Yu Wang**, Purple Mountain Observatory)

12:00 - 13:30 ***< Lunch >***

Session 7: Fundamental Theory - Oral [Room A_3 · 401]
Chairperson: **De-Yu Wang** (Purple Mountain Observatory)

13:30 - 13:55 *"Nonlinear Physics of Twisted Magnetic Field Lines"* (**Zensho Yoshida**, Univ. of Tokyo)

13:55 - 14:20 *"Transition from Mode Competition to Spatiotemporal Chaos in Nearly Integrable Hamiltonian System"* (**Xian-Tu He**, Institute of Applied Physics and Computational Mathematics)

14:20 - 14:45 *"On Creating Transport Barrier by Radio-Frequency Waves"* (**Sudip Sen**, R. A. Cairns, Saha Institute of Nuclear Physics, India)

14:45 - 15:10 *"Computer Simulation of Complexity in Plasmas"* (**Takaya Hayashi**, T. Sato, NIFS)

15:10 - 15:30 ***< Coffee Break >***

Session 8: Poster , 15:30 - 17:50 [Room A_3 · 401]
Chairperson: **Shigeo Kida** (NIFS)

1) *"Thermal Stability Analysis of Ignited Plasma on ELMy-H mode, L-mode and High β_p-mode"* (**Gonta Tateishi**, S.-I. Itoh, M. Yagi, K. Itoh, Kyushu Univ.)

2) *"A Non-local Model Analysis of Heat Pulse Propagation"* (**Takuya Iwasaki**, S.-I. Itoh, M. Yagi, K. Itoh, U. Stroth, Kyushu Univ.)

3) *"Diamagnetic Drift Effect on Shear Flow Generation due to Nonlinear Interchange Mode"* (**Arimichi Takayama** and M. Wakatani, Kyoto Univ.)

4) *"Resistive and Kinetic MHD Stability Studies in Tokamak Plasmas"* (**Shinji Tokuda**, T. Matsumoto, H. Naitou, T. Ozeki, Y. Ishii, M. Yamagiwa, JAERI)

5) *"Investigation Reversed Shear Equilibria in JT60U using the Pies Code"* (**S. R. Hudson**, S. Tokuda, D. A. Monticello, JAERI)

6) *"Ideal MHD Stability in Negative Shear Plasma"* (**Yasutomo Ishii**, T. Ozeki, S. Tokuda, S. Takeji, JAERI)

7) *"Gyro-Particle, Gyro-Reduced-MHD, and Hybrid Simulation of Internal Kink Modes"*
(**Hiroshi Naitou**, S. Tokuda, T. Matsumoto, H. Kozakai, Yamaguchi Univ.)

8) *"On the Generation of Alfvén Wave Current Drive in Low Aspect Ratio Tokamaks with Neoclassical Conductivity"*
(C. Bruma, **Sami Cuperman**, and K. Komoshvili, Tel-Aviv Univ.)

9) *"Calculating Pressure within Magnetic Islands"*
(**S. S. Lloyd**, Australian National University)

10) *"Kinetic Theory of Alfvénic Ion Temperature Gradient Instabilities in Toroidal Plasma"*
(**Liu Chen**, University of California, Irvine)

11) *"Modification of Shear Alfvén Spectral Gaps by Energetic Particles"*
(**James W. Van Dam**, Univ. of Texas at Austin)

12) *"Drift Surface Geometry and Trapped Particle Fraction in the H-1NF Heliac"*
(**Sean A. Dettrick**, H. J. Gardner, R. L. Dewar, Australian National University)

13) "Test Particle Simulations in a Tokamak" (**Hyoung-Bin Park**, E. G. Heo, D. I. Choi, W. Horton, Korea Advanced Institute of Science and Technology)

14) *"A Theoretical Impedance Calculation for the Solenoidal Inductively Coupled Plasma"*
(**Kwnag-Il You**, N. S. Yoon, S. M. Hwang and D. I. Choi, Korea Advanced Institute of Science and Technology and Korea Basic Science Institute)

15) *"Theoretical Study on Helicon Plasma Discharge"* (**Beyoung-Ho Park**, D. I. Choi, N. S. Yoon, Korea Advanced Institute of Science and Technology and Korea Basic Science Institute)

16) *"Excitation and Absorption of Electromagnetic Waves in Helicon Discharges by Plasma Immersed Antennas"* (**Suwon Cho**, Kyonggi Univ.)

17) *"Kinetic Simulation on Collisional Bounded Plasma"* (**Shao-Ping Zhu**, T. Sato, Y. Tomita, T. Hatori, NIFS)

18) *"Potential Structure Formed by Local Production of Negative Ions in a Magnetized Plasma"* (**Wataru Oohara**, S. Ishiguro, R. Hatakeyama, N. Sato, Tohoku Univ.)

19) *"Simulation Study of Nonlinear Alfvén Wave Propagation in a Electron-Positron Plasma"* (**Hitoshi Hojo**, Y. Kurosawa, Univ. of Tsukuba)

20) *"Plasma Turbulent Acceleration Mechanism of the Relativistic Jets in AGNs"*
(**Tong Yi** and Lirong Tian, Beijing Normal University)

21) *"X-Ray Variability and Mass Outflows in Class I Protostar"*
(**Mituru Hayashi**, K. Shibata, R. Matsumoto, JAERI)

22) *"Quantum Effects on the Motion of Charged Particles near Neutral Surface of a Magnetic Field"* (**Sergei V. Bulanov**, E. Lazzaro, J.-I. Sakai, Toyama Univ.)

23) *"Numerical Study of the Hydrodynamic Instability by ILESTA-2D"*
(**Hideo Nagatomo**, N. Ohnishi, S. Naruo, H. Takabe, K. Mima, Osaka Univ.)

24) *"Resonance with Saddle Virtual Potential and Transition to Spatio-Temporal Chaos via Crisis"* (**Kaifen He**, Beijing Normal Univ.)

25) *"Anomalous Diffusion and Multiple-Periodic Accelerator Modes in the Standard Map"* (**Yoshi-Hiko Ichikawa**, K. Hirose, T. Kamimura, Chubu Univ.)

26) *"Vortex Lattice Formation in 2D Magnetized Plasma"*
(**Mituo Kono**, Chuo Univ.)
27) *"Identification of Turbulent Vortices in Homogeneous Turbulence"*
(**Hideaki Miura**, Shigeo Kida, NIFS)
28) *"Collisionless Damping of Perpendicular Magnetosonic Pulses in a Two-Ion-Species Plasma"* (**Daiju Dogen**, M. Toida, Y. Ohsawa, Nagoya Univ.)
29) *"Production of High-Energy Electrons by Oblique Magnetosonic Shocks"*
(**Naoki Bessho**, Y. Ohsawa, Nagoya Univ.)
30) *"Acceleration of Energetic Ions by Magnetosonic Shocks"*
(**Kentaro Maruyama,** Y. Ohsawa, Nagoya Univ.)
31) *"Magnetosonic Shocks with Relativistic Propagation Speeds"*
(**Shinji Nakazawa**, Y. Ohsawa, Nagoya Univ.)
32) *"Equilibria and Stability of a Compact Torus Formed by the Spheromak Merging"*
(**Tomo-Hiko Watanabe**, T. Hayashi and T. Sato, NIFS)
33) *"Three-Dimensional Simulation Study of Spheromak Injection into Magnetized Plasmas"*
(**Yoshio Suzuki**, T.-H. Watanabe, A. Kageyama, T. Sato, T. Hayashi, NIFS)
34) *"Three Dimensional Properties of Shear Alfvén Spectrum"*
(**Noriyoshi Nakajima**, NIFS)
35) *"Simulation Study of Radial Electric Field Enhancement by ECRH in Heliotrons"*
(**Sadayoshi Murakami**, N. Nakajima, U. Gasparino and M. Okamoto, NIFS)
36) *"Averaged RMHD Equations"* (**Katsuji Ichiguchi**, NIFS)
37) *"Nonlinear Electromagnetic Gyrokinetic Equation for Magnetically Confined Plasmas with Large Flow Velocities"* (**Hideo Sugama**, W. Horton, NIFS)
38) *"Effects of Net Current on the HINT Computation"*
(**Ryutaro Kanno**, N. Nakajima, T. Hayashi and M. Okamoto, NIFS)
39) *"The Recipe for Handling Magnetic Field Properties for Desirable Stellarator Configurations"* (**Masayuki Yokoyama**, N. Nakajima, M. Okamoto, NIFS)
40) *"Simulation Study of the Structural Formation in Systems with Short-Range Interaction"*
(**Susumu Fujiwara**, T. Sato, NIFS)

18:00 - 20:00 ***Banquet: Reception Hall***

Friday, September 26, 1997

Session 9: Dusty Plasmas - Oral [Room A_3 · 401]
Chairperson: **San-Hee Hong** (Soul National Univ.)

9:00 - 9:30 *"Dust Acoustic Instabilities in a Plasma with Background of Neutrals"*
(**Predhiman K. Kaw** and R.Singh, Institute for Plasma Research)

9:30 - 10:00 *"Dynamical Behaviors of Strongly Coupled Dusty Plasmas: from Crystal to Chaos"* (**Lin I**, W. T. Juan, J. H. Chu, C. H. Chaing and J. M. Liu, National Central University)

10:00 - 10:20 ***< Coffee Break >***

Session 10: Wave Phenomena and Reconnection - Oral [Room A_3 · 401]

Chairperson: **Donald B. Melrose** (Univ. of Sydney)

10:20 - 10:45 *"Simulation Study of Magnetic Reconnection"*
(**Ritoku Horiuchi,** NIFS)

10:45 - 11:10 *"Structure of Alfvén Waves of Small Transverse Scale and Relation to Auroral Processes"* (**George J. Morales**, UCLA)

11:10 - 11:35 *"Generation of Mirror Waves, Slow-Mode Waves and Ion Cyclotron Waves in the Earth's Magnetosheath"*
(**Lou-Chuang Lee** and B.H. Wu, National Cheng Kung Univ.)

11:35 - 12:00 *"Nonlinear Magnetohydrodynamics of Weakly Ionized Plasmas"*
(**Sergei V. Bulanov**, F. Pegoraro, J. I. Sakai, Toyama Univ.)

12:00 - 13:30 ***< Lunch >***

Session 11: Process Plasmas - Oral [Room A_3 · 401]

Chairperson: **Lin I** (National Central University)

13:30 - 13:55 *"Numerical Modeling on Thermal Plasma Characteristics and Plasma-Particle Interaction in Plasma Spray Process"*
(**Sang-Hee Hong**, K. D. Kang, and B. L. Choi, Soul National University)

13:55 - 14:20 *"The Ion Sphere Model of a Dusty Plasma and The Neighbour Effect on Dust Grain Charging in a Plasma"*
(**Yan-Ping Chen**, Institute of Physics)

14:20 - 14:45 *"Non-Local Heating Theory of Inductively Coupled Plasma Discharge"*
(**Nam-Sik Yoon**, K.I. You, D.I. Choi, Korea Basic Science Institute)

14:45 - 15:10 *"Large Diameter Plasma Production by Surface Waves in Bounded Plasma"*
(**Ivan P. Ghanashev**, M. Nagatsu and H. Sugai, Nagoya Univ.)

Closing Session

15:10 - 15:20 **Liu Chen** (Co-Chair of Executive Committee)
Tetsuya Sato (Chair of Executive Committee)

15:30 - 16:30 ***Tour to LHD (Large Helical Device) and Simulation Laboratory***

Adjourn

Confinement Theory of LHD

Masao Okamoto
National Institute for Fusion Science
Toki, Gifu 509-52, Japan

Abstract

Physics considerations are presented on the plasmas of the Large Helical Device (LHD). Characteristics of LHD configurations are also reviewed. The flexibility of LHD as an experimental device is emphasized. The nonlinear poloidal viscosity is calculated for the LHD plasma and the possibility of L-H transition is considered.

Keywords

Large Helical Device, helical system, magnetic configuration, helical axis, interchange mode, ballooning mode, bootstrap current, ripple diffusion, heliotron, poloidal viscosity

§ 1 Introduction

The helical magnetic fusion confinement device or the helical system has a great advantage of a steady state operation without driving a toroidal current. Another advantage is that the helical system is free from plasma disruptions attributed to the strong toroidal current. A large heliotron called the Large Helical Device (LHD) was designed [1]. The construction of LHD was started in 1989 at the National Institute for Fusion Science (NIFS) and is now almost completed. The experiment on LHD will begin from 1998. The heliotron is a helical system with a plane magnetic axis and the experiments on heliotrons such as H-E[2], ATF[3], and CHS[4,5] have been successfully done. The LHD project is grounded on the fruitful results obtained with these heliotrons.

The purposes of the LHD project are; (1) to investigate confined plasmas extrapolatable to a fusion plasma, (2) to obtain a steady state operation with a divertor configuration, and (3) to develop fusion technologies. The LHD can have a variety of magnetic field

configurations by controlling currents in axisymmetric poloidal coils and helical coils, and thus it will be flexible as an experimental device, because MHD equilibrium and stability, particle orbit, ripple diffusion, bootstrap current, and many other physics processes depend strongly on the configuration. However, a finite beta effect alters the configuration since the Shafranov shift becomes larger in heliotrons as the plasma pressure increases. A large Shafranov shift extends the magnetic well region to stabilize interchange modes. On the other hand, it distorts magnetic surfaces to worsen the confinement of a single particle. In the heliotron configuration, a magnetic hill region inevitablly exists at the plasma periphery. This fact makes the resistive interchange mode unstable regardless of the magnetic shear. The unstable resistive interchange mode may couple with plasma transport to be stabilized. These phenomena are less sensitive to the magnetic field configuration.

In the present paper, characteristics of the LHD configurations are briefly reviewed and physics considerations are emphasized for phenomena which depend strongly on the configuration.

§ 2 Configurations

The machine parameters of LHD are chosen as follows; the major radius is R_0=*3.9* m, the poloidal and toroidal polarities of the helical coils are l=*2* and m=*10*, respectively, the maximum magnetic field is B_0=*3 T* at the first phase and B_0=*4* T at the second phase of the experiment. The LHD coil system consists of two helical coils and three pairs of axisymmetric poloidal coils. All the coils are superconductors. The two helical coils are wound on the surface of the tours, the poloidal cross-section of which is a circle around the point (R_0=*3.9* m, Z_0=0 m) with a radius of *0.95* m. The winding law of the helical coils is $\theta = m\phi/l + \alpha \sin(m\phi/l)$ with the pith modulation α=*0.1*, where θ and ϕ are poloidal and toroidal angles, respectively. In this section, possible configurations are studied for LHD [6].

Three pairs of axisymmetric poloidal coils can control the dipole component B_V, the quadruple component B_Q, and the hexapole component B_H or the flux leakage by adjusting the coil currents. By controlling the dipole or vertical field B_V, the plasma position can be shifted horizontally inward or outward. By controlling the quadruple field B_Q and the hexapole field B_H, the ellipticity and triangularity of the plasma cross-sections can be changed, respectively. Thus, the rotational transform, the magnetic well / hill region, drift surfaces, and magnetic surfaces can be controlled externally.

The structure of each helical coil of LHD consists of three current layers. The current can be flowed independently in each current layer. The radius of the current center on the poloidal cross-section of the helical coil, which is denoted by a_c can be altered by changing the combination of the current layers in which a current is flowed. Thus, the pitch of the helical coil (pitch parameter), which is given by $\gamma_c = Ma_c/(LR_0)$, can be changed. The pitch parameter γ_C has an influence on the MHD equilibrium and stability [7]. For the full operation, in which the currents are flowed in all layers to produce $B_0 = 3$T, the two helical coils are designed so that $\gamma_c = 1.25$.

The coil current in one helical coil (I_{h1}) and the current in another coil (I_{h2}) can be different ($I_{h1} \neq I_{h2}$), because the two helical coils are independent and not linked. For the normal operation ($I_{h1} = I_{h2}$, $B_0 = 3$T), the flux surfaces have a plane magnetic axis which forms a circle. However, if $I_{h1}/I_{h2} \neq 1$, the magnetic axis becomes a helix and it is possible to create a helical axis configuration, since the unbalanced currents produce the $\ell = 1$ component in the Fourier spectrum of the magnetic field strength. This configuration is different from the plane-axis heliotron, although the magnetic field strength is less than that of normal operation ($I_{h1} = I_{h2}$). It is noted that the bootstrap current decreases as I_{h1}/I_{h2} decreases and it vanishes for $I_{h1}/I_{h2} \fallingdotseq 0.4$ and reverses it's direction with the ratio less than 0.4. The helical axis excursion is comparable to the average plasma radius ($a_p \fallingdotseq 0.4$ m) with sufficient small current ratios [8].

It is thus possible to achieve a variety of magnetic configurations for LHD changing the poloidal fields, the pitch parameter γ_c and the ratio I_{h1}/I_{h2} of the two helical coil currents. For the full ($\gamma_c = 1.25$) and the normal ($I_{h1} = I_{h2}$) mode, the configuration can be optimized by controlling the vertical and quadruple components (B_V and B_Q) of axisymmetric poloidal fields. In the LHD, the magnetic axis of the vacuum field can be shifted inward by 0.3 m from the coil center ($R_0 = 3.9$ m, $Z_0 = 0$ m) by controlling the dipole field B_V. As the plasma is shifted inward, the magnetic well area becomes small to worsen the stability of Mercier mode or interchange mode [9]. On the other hand, the orbit confinement of a single particle is remarkably improved as the plasma is shifted inward, and, hence the ripple diffusion is significantly reduced. The ellipiticity can be added to the plasma cross section by controlling B_Q to elongate the plasma cross section in the horizontal or vertical direction. This shaping of the plasma cross section affects the confinement of energetic particles and MHD stabilities, although it is less effective than the plasma positioning. The remarkable effect of plasma shaping is to alter the magnitude of the bootstrap current significantly. The optimized configuration can be obtained by adjusting the

poloidal fields to compromize different dependencies. The criteria for the optimization are (a) to obtain a high beta plasma with $\langle\beta\rangle \equiv 5\%$, (b) to obtain a good confinement of energetic particles with no loss cone in the region within one-third of the plasma minor radius, and (c) to obtain a natural build-in divertor configuration with sufficient clearance between the plasma boundary and the first wall. The optimized configuration is called the standard configuration, in which the plasma position is shifted inward in the major radius direction by *0.15*m in vacuum from the coil center and the plasma cross-sections are nearly circular if toroidally averaged. However, it should be noted that the dependences of the ripple diffusion (or particle orbit) and the bootstrap current on the configuration are different and that a compromise between the two is difficult in planar axis helical systems.

Experiments on LHD will firstly be carried out for this standard configuration and secondly for various configurations around the standard one. Other interesting experiments will be done for the operation changing the pitch parameter γ_c and for the helical axis configuration.

§ 3 Characteristics of LHD plasmas

Single particle orbit and ripple diffusion

Topologies of a single particle orbit in LHD are divided into circulating particles, toroidally trapped particles, hellically trapped particles, and transition particles. Circulating particles are well confined. However, the confinement of helically trapped particles and transition particles becomes worse as the plasma beta increases, since the spectrum of the magnetic field strength becomes complicated with increasing beta. The confinement of energetic particles has been extensively calculated and it is found that the confinement is improved with inward shift of the plasma position both in vacuum field and finite beta equilibrium.

Ripple diffusions have been investigated using the DKES code [10] in the vacuum field case [11] and in the finite beta case [12]. It is shown that the ripple diffusion is greatly improved with the inward shift.

Interchange mode

For the currentless plasma, the most important MHD modes are pressure-driven modes. The Mercier criterion has been investigated in [9] for the LHD plasma changing the plasma position and the plasma beta value. For the peaked pressure profile, the plasma is slightly Mercier unstable for $\Delta_V = -0.15$m, where Δ_V is the position of the

magnetic axis in vacuum measured from the coil center. Numerical studies for stability of low-n ideal interchange modes have shown that the low-n modes may be marginally unstable with a very small growth rate near the Mercier boundary. However, such marginally unstable modes can easily be stabilized by some kinetic effects such as the finite Larmor effect. Thus, the plasma with $\Delta_V = -0.15$m can be actually stable against the low-n ideal interchange modes. If the magnetic axis is shifted in the outward direction of the major radius, the plasma becomes more stable against the interchange modes and completely stable if $\Delta_V \geqq -0.1$m. On the other hand, the plasma becomes unstable with inward shift. If $\Delta_V \leqq -0.2$m some low-n interchange modes are unstable. However, the second stability regime exists [9]. The equilibrium beta limit gradually increases with the inward shift. From a point of view of ideal MHD equilibrium and stability, the average beta limit can be expected to be 5%. In the case of a peaked pressure profile, the Shafranov shift grows larger as the beta increases extending the magnetic well region to stabilize the interchange mode. However, if the pressure profile is broad, Mercier or interchange modes are unstable over the wide range of Δ_V and there is no second stable region, although the equilibrium beta limit increases. This fact is attributed to the small Shafranov shift.

Effect of net toroidal current on interchange and kink modes

The effect of a net toroidal current on the Mercier criterion has been investigated [9]. The net toroidal current changes the poloidal magnetic field, which leads to the deformation of the profile of the rotational transform. Two cases are studied ; one is the subtractive case decreasing the rotational transform and the additive case increasing the rotational transform. In the subtractive case, the self-stabilizing effect in the magnetic shear and the magnetic well are increased by the reduction of the central rotational transform, making a stabilizing contribution to the Mercier criterion. In the standard configuration, the unstable region is eliminated completely by -50 kA net current .On the other hard, the additive current degrades the stability. Thus it is obvious that the net current affects significantly the plasma confinement in heliotrons with a magnetic shear.

The stability against the ideal current driven mode is studied in the standard configuration. Calculations are carried out with the RESORM code[13]for fixed boundary equilibria. The internal kink mode with $m=1$ is stable up to $I_p=300$ kA. When the additive current reaches 300 kA, it is found that the $m=1$ internal kink mode becomes unstable. The internal kink modes with $m \geqq 2$ are also unstable for $I_p=300$ kA. The growth rates decrease with increasing m and the modes with $m \geqq 6$ are stable. However, the LHD has

been designed so that I_p=300 kA is the maximum permissible current that the first wall would withstand if a current disruption occurrs.

Ballooning mode

The ballooning mode is another crucial pressure-driven mode in LHD. It is revealed by Nakajima [14,15] that, in a currentless equilibrium with a large Shafranov shift as in heliotrons, the high $-n$ ballooning mode can be unstable in the region with both positive and negative gradient of the rotational transform. This is because the local shear in the field line bending term can be reduced by the fact that the local enhancement of the poloidal field varies in the radial direction. Since the local curvature of the field lines depends on the label of the magnetic field line α in heliotrons, the eigenvalue ω^2 also depends on α. In the Mercier stable region (where the pressure profile is peaked, as mentioned above), the level surfaces of ω^2 of the unstable modes, which depend strongly on α, form a spheroid in the (ψ, θ_k, α) space, where ψ and θ_k are the label of the flux surface and the radial wave number. Such high $-n$ modes cannot lead to low $-n$ modes. For the broad pressure profile, the Mercier mode becomes easily unstable. In this case, the level surface of ω^2 of the unstable high-n ballooning mode is approximately a cylinder which leads to the occurrence of the unstable low-n ballooning mode as in tokamaks. As mentioned above, the Mercier modes are stable for the peaked pressure profile. Accordingly, the low $-n$ ballooning modes are also expected to be stable for the peaked pressure profile.

Bootstrap current

The bootstrap current, resulting from the valance between viscosity force and friction force, depends strongly on the magnetic configuration in helical systems. In contrast to the axisymmetric tokamak, in the non-axisymmetric system, the direction of the flow to be damped by the parallel viscosities depends on the collisionality regime of the particle species [16] . This is due to the lack of symmetry. Equilibria including the bootstrap currents are calculated iteratively using the VMEC code for the LHD plasma and assuming that electrons and ions belong to the same collisonality regime [17] . It has been shown that the magnitude of the bootstrap current is sensitive to the Shafranov shift in LHD. Effects of the vertical field, quadruple field, and the pressure profile on the bootstrap current are also investigated in this paper. The bootstrap current can be reduced by B_Q-control by approximately a factor of three.

Another important characteristic of the bootstrap current in non-axisymmetric systems is that the geometric dependence has a different form according to the collisionality regime that reflects different characteristics of particle orbits in different collisionalities.

If electrons and ions are in different collisionalities, geometric dependence are different for electrons and ions. Thus, when electrons and ions are in different collisionality regimes, the bootstrap current proportional to the redial electric field, which does not exist in axisymmetric tokamaks, exists [16] . This comes from the fact the direction of the flow damped by the parallel viscosities is dependent on the collisionally regime in the non-axisymmetric toroidal systems due to the lack of symmetry. The term proportional to the radial electric field vanishes if the three conditions of charge neutrality, momentum conservation during the collision, and axisymmetry hold.

The connection formula between each collisionality limit is constructed and the bootstrap current in LHD is estimated by solving the connection formula and the VMEC equilibrium code iteratively [18] . If electron and ion temperatures are the same, the bootstrap current amounts from 50 to 150 kA according to the plasma parameters in the standard configuration. If electrons and ions are supposed to be in different collisionality regimes, the bootstrap current is significantly reduced with an increasing radial electric field. If the radial electric field is large enough, the bootstrap current flows in the opposite direction, reducing the rotational transform [6]. Based on [16] , poloidal and toroidal plasma rotations in non-axisymmetric devices are formulated [19] . The present neoclassical theory has also been extended to the case including a momentum input source due to NBI and others [20].

Poloidal viscosity

The possibility of occurrence of the L-H transition is studied in LHD [21] based on the nonlinear incompressible poloidal viscosity for the plateau regime [22]. Fourier spectra of the magnetic field strength in the Hamada coordinates are employed for the calculation. The appearance of the local maxima of poloidal viscosity as a function of poloidal flow, which suggests an L-H transition. depends strongly on the relative amplitude between the toroidicity and helicity in the magnetic field. Effects of magnetic configuration control such as inward or outward shift of the plasma (B_V-control) and variation of the plasma cross-sections by the quadrupole field (B_Q-control) are studied on the poloidal viscosity. Finite beta effect is also investigated. The preliminary results suggets the possibility of the L-H transition in the LHD plsma. The detailed stusy is under progress.

§ 4 Summary

The LHD is a flexible apparatus for physics experiments. It offers freedom to change the axisymmetric poloidal fields, the pitch of the helical coils, and coil currents in the two

helical coils. For normal operation, the configuration has been optimized by controlling the poloidal field to obtain the standard configuration. A change in the pitch parameter of the two helical coils can after the rotational transform, magnetic well region, plasma radius, and, thus, the MHD properties. A helical axis configuration can be obtained if the currents in the two helical coils are unbalanced. It is possible that the helical excursion becomes comparable to the plasma radius and the bootstrap current can be drastically decreased until its direction is reversed.

Physics characteristics have been studied for the standard configuration. One conclusion is that the peaked pressure profile is preferable to the MHD stabilities of Mercier or interchange mode and ballooning mode. Minimizing the bootstrap current has not been included in the optimization. It is not easy to reduce the bootstrap current in the planar axis helical system. However, it has been shown that there is a possibility to reduce or even reverse the bootstrap current if electrons and ions are in different collisionality regimes. It is pointed out that a net toroidal current affects the confinement and a current drive may be needed to cancell the bootstrap current when $T_e \fallingdotseq T_i$. The nonlinear poloidal viscosity has been calculated and the possibikity of L-H transition was discussed. Physics studies on the phenomena which are less sensitive to the magnetic configuration such as resistive interchange mode and it's related transport will be reported elsewhere.

Acknowledgement

The author is grateful to the members of theory groups at the National Institute for Fusion Science for their physics considerations on the LHD plasmas. Professors A. Iiyoshi, T. Sato, M. Fujiwara, and O. Motojima are also acknowledged for their encouragement.

References

(1) A. Iiyoshi, M. Fujiwara, O. Motojima, N. Oyabu, and K. Yamazaki : *Fusion Technology* 17 (1990)169.

(2) M. Wakatani, and S. Sudo : *Plasma Phys. Controlled Fusion* 38(1996)937.

(3) J.F. Lyon, B.A. Carreras, K.K. Chipley, M.J. Cole, J.H.Harris, T.C. Jernigan, R.L.Johnson, V.E. Lynch, B.E. Nelson, J.A. Rome, J. Sheffield, P.B. Thompson : *Fusion Technology* 10 (1986)179

(4) K. Nishimura, K. Matsuoka, M. Fujiwara, K. Yamazaki, J. Todoroki, T. Kamimura, T. Amano, H. Sanuki, S. Okamura, M. Hosokawa, H. Yamada, S. Tanahashi, S. Kubo,

Y. Takita, T. Shoji, O. Kaneko, H. Iguchi, and C. Takahashi :
Fusion Technology **17** (1990)86.

(5) S. Okamura, K. Matsuoka, K. Nishimura, K. Tsumori, R. Akiyama, S. Sakakibara, H. Yamada, S. Morita, T. Morisaki, N. Nakajima, K. Tanaka, J. Xu, K. Ida, H. Iguchi, A. Lazaros, T. Ozaki, H. Arimoto, Ejiri, M. Fujiwara, H. Idei, O. Kaneko, K. Kawahata, B. T. Kawamoto, Komori, S. Kubo, O. Motojima, V.D. Pustovitov, C. Takahashi, K. Toi, and I. Yamada : *Nucl.Fusion* **35** (1995)283.

(6) M. Okamoto : *Plasma Physics Reports* **23**(1997)533 (*Fizika Plazmy* **23** (1997)579).

(7) K. Ichiguchi, O. Motojima, K. Yamazaki, N. Nakajima, M. Okamoto :
Nuclear Fusion **36** (1996)1145.

(8) K. Ichiguchi, N. Nakajima, M. Okamoto : *Nuclear Fusion* **37**(1997)1109.

(9) K. Ichiguchi, N. Nakajima, M. Okamoto, Y. Nakamura, M.Wakatani,
Nuclear Fusion **33** (1993)481.

(10) S.P. Hirshman, K.C. Shaing, W.L. van Rij, C.O. Beasley Jr., and E.C. Crume :
Phys. Fluids **29** (1986)2951.

(11) Y. Ogawa, T. Amano, N. Nakajima, K. Yamazaki, S.P. Hirshman, W.L. van Rij, and K.C. Shaing : *Nucl. Fusion* **32** (1992)119.

(12) R. Kanno, N. Nakajima, H. Sugama, M. Okamoto, and Y. Ogawa :
Effects of Finite and Radial Electric Fiels on Neoclassical transport in the Large Helical Device (to appear in Nuclear Fusion).

(13) K. Ichiguchi, Y. Nakajima, and M. Wakatani : *Nucl. Fusion* **31**(1991)2073.

(14) N. Nakajima : *Phys. Plasma* **3** (1996)4545.

(15) N. Nakajima : *Phys. Plasma* **3** (1996)4556.

(16) N. Nakajima, and M. Okamoto : *J. Phys. Soc. Jpn.* **61** (1992)833.

(17) K. Watanabe, N. Nakajima, M. Okamoto, Y. Nakamura, M. Wakatani :
Nuclear Fusion **32** (1992)1499.

(18) K. Watanabe, N. Nakajima, M. Okamoto, K. Yamazaki, Y. Nakamura, and M. Wakatani : *Nuclear Fusion* **35** (1995)335.

(19) N. Nakajima and M. Okamoto : *J. Phys. Soc. Jpn.* **60** (1991)4146.

(20) N. Nakajima and M. Okamoto : *J. Plasma Fusion Res.* **68**(1992)46.

(21) M. Yokoyama, N. Nakajima, M. Okamoto : *Research Report of The National Insitute for Fusion Science,* **NIFS-519**, November 1997.

(22) K.C. Shaing : *Physics of Fluids* **B5**(1993)3841.

Current Status of the KSTAR Project

Duk-In Choi
Korea Basic Science Institute

I. KSTAR Project Mission

The project mission of the KSTAR (Korea Superconducting Tokamak Advanced Research) project is to develop a steady-state-capable advanced superconducting tokamak to establish the scientific and technological bases for an attractive fusion reactor as a future energy source. The KSTAR Tokamak Research Objectives are 1) To extend present stability and performance boundaries of tokamak operation through active control of profiles and transport, 2) To explore methods to achieve steady state operation for tokamak fusion reactors using non-inductive current drive, and 3) To integrate optimized plasma performance and continuous operation as a step toward an attractive tokamak fusion reactor.

The design features of the KSTAR tokamak are 1) Fully superconducting magnets, 2) Long pulse operation capability, 3) Flexible pressure and current profile control, 4) Flexible plasma shape and position control, and 5) Advanced profile and control diagnostics.

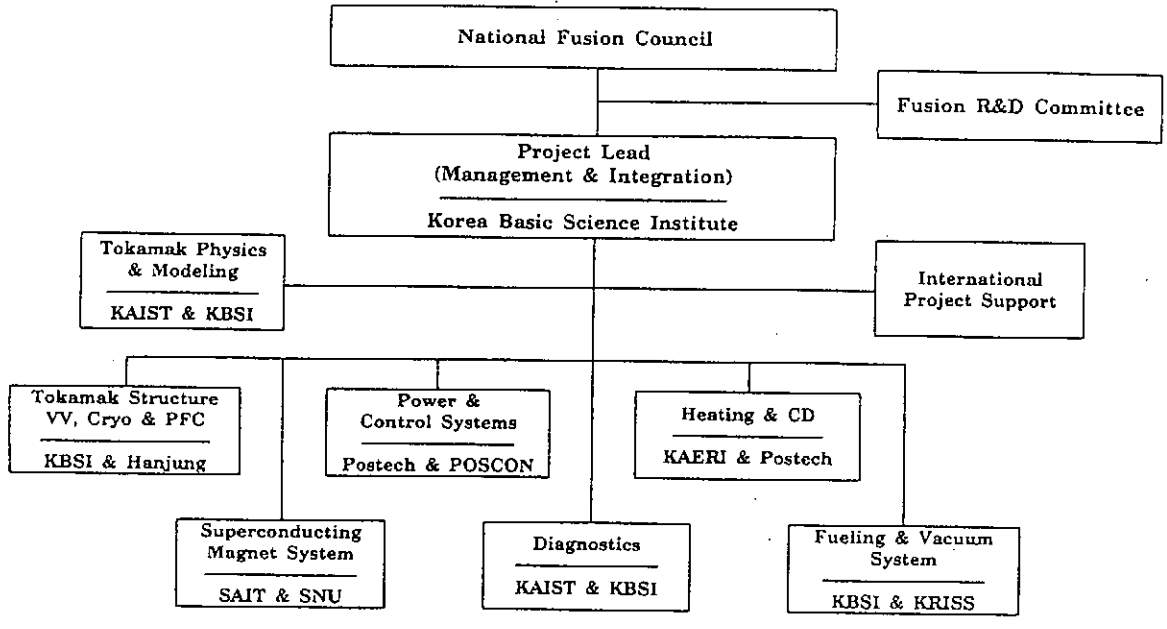

Fig.1 KSTAR Project organizational chart

The phases & milestones of the KSTAR Project are 1) Design & Construction Phase (1995 - 2002) where Conceptual Design Review Milestone (December 1997), Final Design Review Milestone (December 1998), and First Plasma Milestone (August 2002), 2) Basic Operation Phase (2002 - 2005) which includes Ohmic Discharge Baseline Operation, Basic Auxiliary Heating & Current Drive Experiment, and Advanced Diagnostics & Control

o Advanced Superconducting Tokamak R&D (HAN-Project)

(Unit : Billion Won)

Project Year / Funding Cat.	1995	1996	1997	1998~2001	Sub-Total
Government	3.0	6.1	8.0	72.9	90.0
Atomic Energy fund	-	-	4.0	21.0	25.0
KEPCO	2.0	3.0	-	-	5.0
Industries	1.5	2.0	4.0	22.5	30.0
Total	6.5	11.1	16.0	116.4	150.0

o Building and Conventional Facility Construction

(Unit : Billion Won)

Year	1997	1998	1999	2000	Total
Government	6.8	18.0	23.3	21.4	69.5

Table 1 KSTAR R&D and Construction Project Cost

Development, and 3) Advanced Mode Operation Phase (2006 - 2010) which includes High-b Experiment with Flexible Equilibrium Control, Profile Control for Confinement Improvement (J(r), P(r), etc.), Long-pulse Operation for Steady-State Issues and * Support ITER Physics Phase Issues.

		Parameters	Remarks
Major Radius,	R_0	1.8 meter	
Minor Radius,	a	0.5 meter	
Toroidal Field,	B_{T0}	3.5 Tesla	• Nb_3Sn, NbTi
Plasma Current,	I_P	2.0 MA	
Elongation,	κ	2.0	
Triangularity,	δ	0.8	• Double-null
Pulse Length		20 sec < t_{pulse} < 300 sec	• Current Drive
Heating & Current Drive		NBI	• PI, NI
		ICRH / FWCD, LHCD, ECRH	
Plasma Species		H / D	• Neutron Budget

Table 3 Korean National Fusion Project
- Advanced Superconducting Tokamak Experiment -

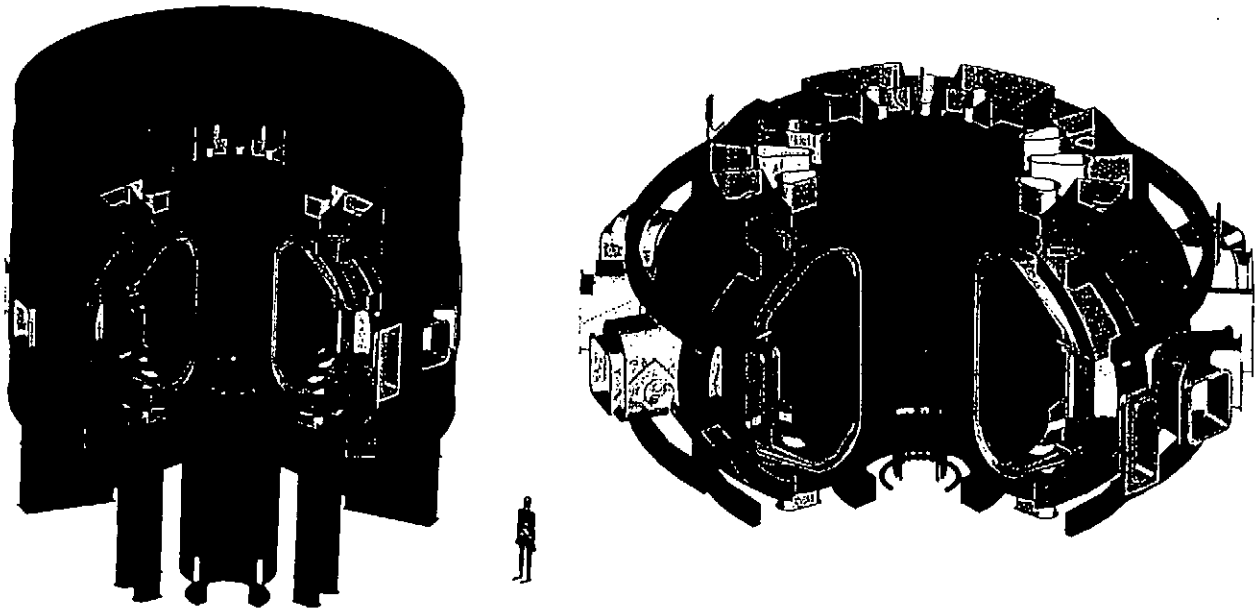

Fig. 2 KSTAR Overview

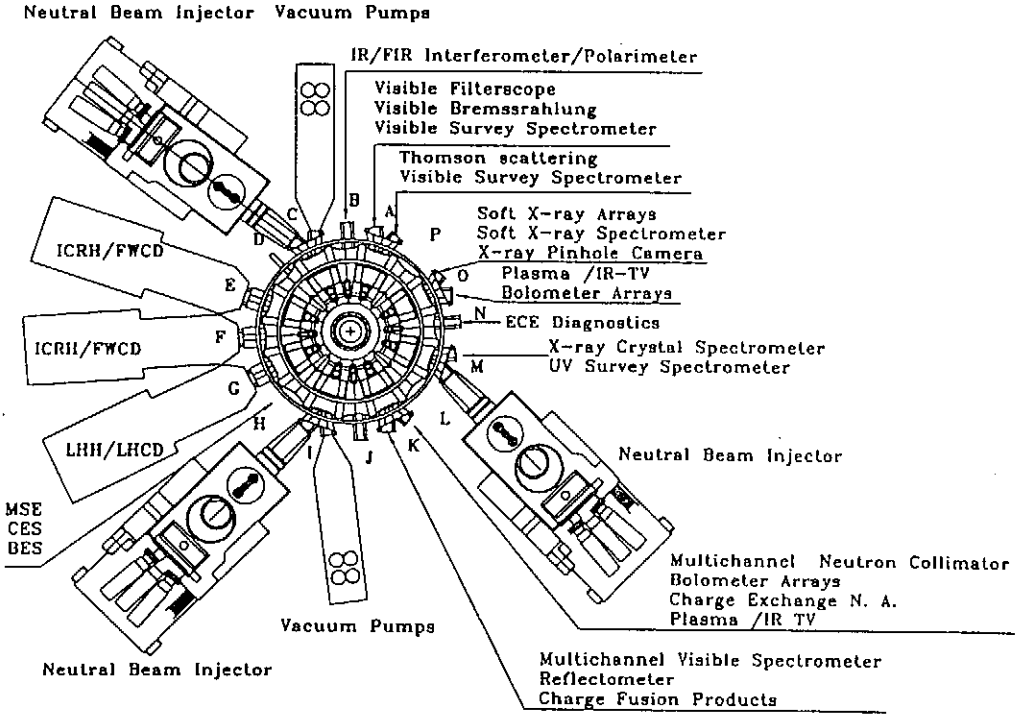

Fig. 3 KSTAR Experiment Layout

II. Issues of KSTAR

Physics design issues of the KSTAR project are as follows. 1) Magnetic Field Requirements; Two-point Ripple Criterion (16 TF Coils) and Error Field Correction Coils ("Window-pane" type), 2) Flexible Operation Boundary & Plasma Shape Control; Wide-range k and d Values (PF Coil Capability), Double-null and Single-null Configurations, Two-pairs of Fast Position Control Coils (Field-null Quality), and to Explore Feed-back Stabilization Scheme, 3) Flexible Profile Control; J(r), n(r) & P(r) Control by NBI, FWCD & LHCD, Horizontally-stacked NBI, and to Explore Local Heating & CD using

ECH/ECCD, and 4) Low Voltage Start-up Capability; ECH-assisted Start-up (possibly, LHH-assisted), and Good Field-null Quality.

The functions of KSTAR Auxiliary Heating & Current Drive Systems are 1) Plasma Heating and Current Drive, 2) Profile Control, 3) Rotation Control, and 4) Plasma Initiation, which are arranged to allow flexible current & pressure profile control.

	Baseline	Upgrade	Remarks
Neutral Beam	8 MW 1 Co	24 MW 2 Co, 1 Ctr	120 keV ~ 300 sec
ICRF/FWCD	6 MW 1 Launcher	12 MW 2 Launchers	30-80 MHz ~300 sec
LHCD	1.5 MW	4.5 MW	3.7 GHz ~ 300 sec
ECH	0.5 MW		80 GHz ECH Start-up (0.5 sec)

Table 4 KSTAR Auxiliary Heating & Current Drive Systems

To meet KSTAR Mission and Research Objective, especially, active control of Profiles and transport, and steady-state operation, KSTAR Tokamak requires 1) Advanced Profile and Control Diagnostics; Poloidal field & plasma current measurement, Spatially & temporally resolved density and temperature for each plasma species, and to Explore Diagnostic Neutral Beam for Higher Resolution MSE & CERS, and 2) Development Steady-state Capable Diagnostics & Control Techniques. To meet aggressive schedule and resource limitation, KSTAR Project requires Phase Diagnostics Implementation; Basic Diagnostics Set, Baseline Diagnostics Set I & II, and Mission-Oriented Diagnostics Set.

The Engineering Design Issues of KSTAR are 1) Superconducting Magnet Systems; ITER HP-1 based Capable-In-Conduit type Conductor, 16 TF Coils, and 8 Segmented Central Solenoid, 2) Plasma Facing Components; Initially, 20 second Full-power Capability with Upgrade Provision to 300 Second, and 3) Vacuum Vessel; Double-walled Toroidal Shell Construction with SS316LN (Borated water for Nuclear Shielding)

The KSTAR project will make critical contributions to the world fusion research and development program. It will 1) extend advanced tokamak research to high performance and steady state operation regimes, 2) contribute techniques for successful steady state physics operation of ITER, and 3) compare advanced tokamak physics results with those from superconducting stellarators and spherical tokamaks.

Successful construction and operation of KSTAR tokamak will advance Korea's scientific and technological capability in significant ways, such that 1) large scale superconducting magnet design, manufacture and operation, 2) high power neutral beam, microwave and radiofrequency technology, 3) state-of-the-art plasma diagnostics and controls, and 4) advanced computational methods.

The major milestones of the KSTAR project are that 1) Design point definition workshop (February 1997 at PPPL), 2) Physics validation review and engineering workshop (June 1997 at KBSI), 3) Tokamak systems engineering review (December 1997

at KBSI), and 4) Auxiliary systems engineering review (March 1998 at KBSI).

III. Reviews of KSTAR

The summary of findings and recommendations of the KSTAR physics validation review is as follows. The reviewers find that the KSTAR machine rightly focuses on areas which are crucial for development of fusion reactors. The reviewers also find that the KSTAR design team have incorporated state-of-the-art knowledge of plasma physics and operation to meet the goals, and that the present design of KSTAR, with 40MW of heating power and 300 sec pulse length, and with a high degree of flexibility, adequately meets its requirements. Moreover, the reviewers find that the construction of KSTAR is very timely; the knowledge of plasma physics is now mature enough to support the design of advanced tokamaks like KSTAR, and the advanced tokamak experiments in KSTAR in the middle of the next decade will contribute to filling the possible gap between the present tokamak devices and ITER, and also benefit the ITER project by exploring these operational scenarios which might well be applicable to ITER. Moreover, KSTAR long pulse experiments will further comparisons among different magnetic confinement schemes. The reviewers also find that the design of KSTAR is flexible, which is essential for experimental exploration of optimized regimes and testing of innovative concepts. The KSTAR device will be even more attractive as a result of the planned upgrades, including increases of heating power, modification of the geometry and/or materials of plasma facing components, and extension of the pulse length, ultimately approaching steady state. The reviewers expect that the advanced capability of KSTAR will assure that KSTAR will be able to significantly contribute to the world's fusion research and development for many years to come. The KSTAR project is also expected to demonstrate many areas of technology, highlighted by the full deployment of superconducting magnets, and should be an important stimulus for Korean industrial development. Furthermore, the KSTAR with its Advance Mode Operation Phase can continue to play a complementary and important role even after the start of operation of ITER. The reviewers also endorse the staffing plan as proposed by the KSTAR team as reasonable and necessary to carry out a vibrant research program.

To summarize the reviewers find that 1) The physics requirements and design for KSTAR device are sound and they adequately support the KSTAR project objectives and the program goals, and that 2) The KSTAR device provides a very important vehicle for innovative plasma physics research that will enhance the state of the art and that is directly in support of tokamak fusion reactor development.

Nonlinear Dynamics of Alfvén Eigenmodes in Toroidal Plasmas

F.Zonca*, L. Chen, G. Hu and R.A. Santoro†

Department of Physics and Astronomy,
University of California, Irvine, CA 92717-4575

1. Introduction

The non-linear saturation of Toroidal Alfvén Eigenmodes (TAE) due to mode-mode coupling is investigated both analytically and numerically. It is demonstrated that, as the mode amplitude increases, a *fine structure* density modulation associated with the *short scales* excited in the nonlinear TAE mode structure causes enhanced energy dissipation which eventually leads to mode saturation.

The nonlinear equations for the time evolution of TAE modes are derived and an analytical estimate of the saturated mode amplitude is given. Analytical predictions are compared with the results of numerical computations, showing exact agreement for the scaling of the saturated mode amplitude with $b_s = k_\vartheta^2 \rho_s^2$ and the inverse aspect ratio $\epsilon = a/R_o$. Here, k_ϑ is the poloidal wave vector, $\rho_s^2 = c^2 m_i (T_e + T_i)/(e^2 B^2)$ and $a(R_o)$ is the minor(major) radius of the torus. The magnitude of the numerically obtained saturated fluctuation levels assuming finite dissipation is shown to be systematically smaller than that predicted analytically for a non-dissipative system.

The relevance of the above discussed mechanism for non-linear saturation of TAE modes is discussed and comparisons are made with models proposed in other recent non-linear studies.

2. Non-linear TAE equations

Consider a low-β ($\beta = O(a^2/R_o^2)$) toroidal plasma, where $\beta = 8\pi P/B^2$ is the ratio between thermal plasma pressure, P, and magnetic energy density, $B^2/8\pi$. It is well known that the vorticity equation describing the dynamic evolution of a shear Alfvén wave may be written as:

$$v_A^2 B \frac{\partial}{\partial \ell} \frac{\nabla_\perp^2}{B} \frac{\partial}{\partial \ell} \delta\phi - \frac{\partial^2}{\partial t^2} \nabla_\perp \cdot \left(1 + \frac{\delta n_s}{n} \right) \nabla_\perp \delta\phi = 0 \ . \tag{1}$$

Here, $v_A = B/\sqrt{4\pi n m_i}$ is the Alfvén speed, B the equilibrium magnetic field, n the equilibrium particle density, $\partial/\partial\ell = \mathbf{B}/B \cdot \nabla$ and $\perp$ indicates the direction perpendicular to $\mathbf{B}$. Furthermore, quantities with a prefix δ indicate fluctuating fields; e.g., $\delta\phi$ is the

*Associazione EURATOM-ENEA sulla Fusione, C.P. 65, 00044 Frascati, Rome, Italy
†Naval Research Laboratory, Washington, D.C.

fluctuation in the scalar potential. Note that the ballooning-interchange term [1] has been neglected in Eq. (1), consistently with the assumption of a low-β plasma equilibrium.

The term $\delta n_s/n$ in Eq. (1) accounts for low frequency, *short* (radial) scale non-linear density fluctuations. These arise from the beating of the two degenerate counter - propagating shear Alfvén waves, whose linear superposition is responsible of the formation of the toroidicity induced frequency gap in the shear Alfvén continuous spectrum and of the existence of the TAE mode [2]. In fact, as it is well known, at radial positions with safety factor $q = (2m+1)/2n$, a TAE mode is a standing wave resulting from the linear superposition of two shear Alfvén waves with toroidal mode number n and poloidal mode numbers m and $m+1$ [2]. From the beating of these high frequency waves with $\omega \simeq \omega_A/2 = v_A/2qR_o$ a low frequency non-linear perturbation is generated, which obeys to the force balance equation:

$$nm_i \frac{d}{dt}\delta \mathbf{v}_s = -\nabla \cdot \underline{\underline{\delta \mathbf{P}_s}} + \left[\frac{\delta \mathbf{J}_h \times \delta \mathbf{B}_h^*}{c} + c.c.\right] , \tag{2}$$

where $\underline{\underline{\delta \mathbf{P}_s}}$ is the low frequency pressure tensor, whereas the subscript s and h respectively stay for "slow" and "high frequency". Equation (2) is greatly simplified when we take the weak-instability (adiabatic) limit $|\partial_t \delta n_s| \ll |(c_S/qR_o)\delta n_s|$, $c_S^2 = (T_e + T_i)/m_i$ being the sound speed. Assuming an isothermal process along with quasineutrality in addition to the slow sound wave approximation, we have

$$\frac{\delta n_s}{n} = -\frac{c^2}{4\pi n(T_e+T_i)\omega_o^2}\left|\nabla_\perp \frac{\partial}{\partial \ell}\delta\phi_h\right|^2 . \tag{3}$$

Here, use has been made of the ideal MHD parallel Ohm's law which, for a TAE of frequency ω_o reads $\delta A_\parallel = -i(c/\omega_o)\partial_t \delta\phi$.

In the following, we will use the ballooning mode representation [1] for the fluctuating field $\delta\phi$, i.e.

$$\delta\phi_h = \left(\frac{T_e+T_i}{e}\right) e^{-in\xi} \sum_m e^{im\vartheta}\Phi(nq-m) = \left(\frac{T_e+T_i}{e}\right) e^{-in\xi+im_o\vartheta} \sum_j e^{ij\vartheta}\Phi(z-j) , \tag{4}$$

where ξ and ϑ are toroidal and poloidal angles, respectively, and the new "radial coordinate" $z = nq - m_o$ has been defined, with $m = m_o + j$ and m_o playing the role of a central poloidal mode number. Furthermore, note that in Eq. (4) the field $\Phi(z)$ is dimension-less. In the high-n limit, the local linear mode structure of a TAE mode is given by the toroidal coupling of the m_o with the $m_o \pm 1$ modes at $q = (2m_o \pm 1)/2n$. The global mode structure is then obtained as a superposition of local linear modes with a given radial envelope [3]. In the present analysis we discuss how the non-linear density modulation in Eq. (1) alters the local linear TAE mode structure, eventually leading to mode saturation. In the z space, Eq. (1) can be written as:

$$\mathcal{L}_z\Phi(z) + \partial_i^2 \mathrm{NL}(\Phi) = 0 . \tag{5}$$

Here, $\hat{t} = \omega_A t$ and $\mathcal{L}_z$ is the linear operator

$$\mathcal{L}_z \Phi(z) = \left[z\hat{\nabla}_\perp^2 z + \partial_{\hat{t}}^2 \hat{\nabla}_\perp^2 \right] \Phi(z) + \epsilon_o \partial_{\hat{t}}^2 \hat{\nabla}_\perp^2 \left[\Phi(z+1) + \Phi(z-1) \right] , \tag{6}$$

where $\epsilon_o = 2(r/a + \Delta')$ and $\hat{\nabla}_\perp = (r/nq)\nabla_\perp$; i.e., $\hat{\nabla}_\perp = i\mathbf{e}_\vartheta + \mathbf{e}_\mathbf{r} s\partial_z$, with $s = rq'/q$ and $\mathbf{e}_\mathbf{r}$, $\mathbf{e}_\vartheta$ being the unit vectors along r and ϑ. The non-linear term is given by

$$\mathrm{NL}(\Phi) = \hat{\nabla}_\perp \cdot \left[n_+(z)\hat{\nabla}_\perp \Phi(z+1) + n_-(z)\hat{\nabla}_\perp \Phi(z-1) \right] , \tag{7}$$

with the definitions

$$n_\pm(z) = -4b_s \hat{\nabla}_\perp z\Phi(z) \cdot \hat{\nabla}_\perp (z \pm 1)\Phi^*(z \pm 1) . \tag{8}$$

Introducing the Fourier conjugate representation for $\Phi(z)$, i.e.,

$$\phi(\theta, \hat{t}) = (2\pi)^{-1/2} \int_{-\infty}^{\infty} \Phi(z, \hat{t}) e^{-i\theta z} dz ,$$

Eq. (5) becomes

$$\left[\partial_\theta^2 - \partial_{\hat{t}}^2 (1 + 2\epsilon_o \cos\theta) - s^2/(1 + s^2\theta^2)^2 \right] \psi(\theta, \hat{t}) - \frac{1}{4\sqrt{1 + s^2\theta^2}} \mathrm{FT}\left[\mathrm{NL}(\Phi) \right] = 0 . \tag{9}$$

Here, $\psi(\theta, \hat{t}) \equiv \phi(\theta, \hat{t})\sqrt{1 + s^2\theta^2}$ and FT$[h(z)]$ symbolically indicates the Fourier Transform $(1/\sqrt{2\pi}) \int e^{-i\theta z} h(z) dz$. Equation (9) is the starting point of our analytical and numerical investigations.

3. Non-linear dispersion relation and mode saturation

In the linear phase, TAE modes are characterized by two-scale structures both in time and θ [2, 3]; i.e., we may assume

$$\begin{aligned} \psi(\theta, \hat{t}) &= e^{-i\hat{t}/2} \left[A(\theta_1, \tau)\cos(\theta_o/2) + B(\theta_1, \tau)\sin(\theta_o/2) \right] = \\ &\quad e^{-i\hat{t}/2} \left[E(\theta_1, \tau) e^{i\theta_o/2} + F(\theta_1, \tau) e^{-i\theta_o/2} \right] , \end{aligned} \tag{10}$$

with $\partial_{\theta_1} \approx \partial_\tau \approx \epsilon_o$, $E = (A - iB)/2$ and $F = (A + iB)/2$. When Eq. (10) is substituted into Eq. (9), it is possible to show [4, 5] that the following coupled equations are obtained for A and B

$$\begin{aligned} (i\partial_\tau + \epsilon_o/4)\, A + \partial_{\theta_1} B + (n_+ F + n_- E)/4 &= 0 , \\ (i\partial_\tau - \epsilon_o/4)\, B - \partial_{\theta_1} A + i\,(n_+ F - n_- E)/4 &= 0 , \end{aligned} \tag{11}$$

with $n_+ F = n_+(-1/2 + i\partial_{\theta_1})F$ and $n_- E = n_-(1/2 + i\partial_{\theta_1})E$. Equation (11) accounts for the large θ behavior of TAE modes, which corresponds to the mode structure on short radial scales. Thus, Eq. (11) describes the formation of toroidal frequency gap in the shear Alfvén continuous spectrum as well as the effect of *short scale* non-linear density modulations on the mode structure. The matching to the $|\theta| = O(1)$ ideal region

TAE mode structure is most easily obtained introducing the Laplace transform $\hat{A}(\nu,\tau) = (1/\sqrt{2\pi})/\int_0^\infty A(\theta_1,\tau)e^{i\theta_1\nu}d\theta_1$ and analogously for $\hat{B}(\nu,\tau)$. Equation (11) then becomes

$$\begin{aligned}(i\partial_\tau + \epsilon_o/4)\,\hat{A} - i\nu\hat{B} + (1/4)N(\nu)\hat{A} &= B_o/\sqrt{2\pi}\ ,\\ (i\partial_\tau - \epsilon_o/4)\,\hat{B} + i\nu\hat{A} - (1/4)N(\nu)\hat{B} &= -A_o/\sqrt{2\pi}\ ,\end{aligned} \tag{12}$$

where $N(\nu) = -b_s(a_i^2 - b_r^2)$, $\hat{A} = a_r + ia_i$, $\hat{B} = b_r + ib_i$, $A_o = (2/\sqrt{2\pi})\int_{-\infty}^{\infty} a_r d\nu$ and $B_o = (2/\sqrt{2\pi})\int_{-\infty}^{\infty} b_r d\nu$. The matching to the ideal region is then obtained as [6]

$$\begin{aligned}B_o/A_o &= \delta T_f(s)\ ,\\ \delta T_f(s) &= \int_{-\infty}^{\infty}\left[|\partial_\theta\psi_I|^2 + s^2|\psi_I|^2/(1+s^2\theta^2)^2\right]d\theta\ ,\end{aligned} \tag{13}$$

where ψ_I indicates the ideal region (linear) solution [6].

Assuming that a non-linear saturated state is eventually reached, a time dependence in the form $\approx \exp(-i\epsilon_o\Lambda\tau/4)$ may be assumed for $\hat{A}$ and $\hat{B}$. Note that, here, $\Lambda = \pm 1$ indicates the upper(lower) accumulation point of the linear shear Alfvén continuum. Equations (12) can then be put in the normalized form

$$\begin{aligned}(\Lambda+1)\,I - \zeta R - (I^2 - R^2)I &= 0\ ,\\ (\Lambda-1)\,R - \zeta I + (I^2 - R^2)R &= -\bar{A}\ ,\ ,\end{aligned} \tag{14}$$

where $\zeta = 4\nu/\epsilon_o$, $I = (b_s/\epsilon_o)^{1/2}a_i$, $R = (b_s/\epsilon_o)^{1/2}b_r$ and $\bar{A} = (4/\sqrt{2\pi})(b_s/\epsilon_o^3)^{1/2}A_o$. In terms of normalized fields, Eqs. (13) can then be put in the form of the following non-linear dispersion relation

$$\int_{-\infty}^{\infty} R(\zeta|\Lambda,\bar{A})d\zeta = \pi\delta T_f(s)\bar{A}\ , \tag{15}$$

which obviously yields $\Lambda = \Lambda_{NL}(\bar{A}|\delta T_f)$.

Non-linear saturation occurs due to the appearance of singularities in the mode structure above a critical mode amplitude, $\bar{A}_c$, as discussed in Ref. [7]. At saturation, the solution of Eq. (9) at $\theta = 0$ is expected to be $\psi_c(\theta=0) = A_{oc} = (\sqrt{2\pi}/4)(\epsilon_o^3/b_s)^{1/2}\bar{A}_c$, i.e. to exhibit a $(\epsilon_o^3/b_s)^{1/2}$ scaling. The analytical expression for $\bar{A}_c$ parameterized with Λ can be shown to be given by

$$\bar{A}_c = \frac{4}{3}\left[1 - \Lambda + \left(\Lambda^2+\Lambda+1\right)^{1/2}\right]\left[\frac{\Lambda-1}{6} + \frac{(\Lambda^2+\Lambda+1)^{1/2}}{3}\right]^{1/2}\ ;\quad \Lambda < 1$$

$$\bar{A}_c = \frac{2(\Lambda-1)^{3/2}}{3\sqrt{3}}\ ;\quad \Lambda \geq 1\ . \tag{16}$$

Clearly, the actual value of $\bar{A}_c$ is obtained by self-consistent solution of the non-linear dispersion relation, $\Lambda = \Lambda_{NL}(\bar{A}_c|\delta T_f)$, together with Eq. (16).

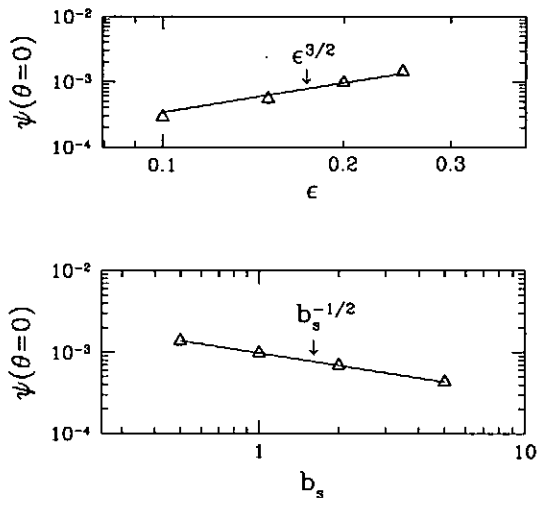

Figure 1: Scaling of the saturated mode amplitude $\psi_c(\theta = 0)$.

4. Numerical results and Discussions

In the following, we discuss the results of the numerical solution of Eq. (9). Assuming $s = 1$ as a fixed parameter, Fig. 1 shows the scaling of the mode amplitude $\psi_c(\theta = 0)$ in the non-linear saturate state. It is evident that both $\epsilon_o^{3/2}$ with $b_s = 1$ and $b_s^{-1/2}$ with $\epsilon_o = 0.2$ scalings discussed in the previous section are well reproduced. A constant mode drive of $\gamma/\omega_A = 2.0 \times 10^{-3}$ is assumed here, which makes it possible for the mode to grow from the linear phase to the non-linear saturated state. A comparison between mode structures in θ space in the linear regime (top) and non-linear saturated phase (bottom) can be observed in Fig. 2. Here, the local plasma parameters are set to $\epsilon_o = 0.2$, $s = 1.0$ and $b_s = 1.0$. The much more extended non-linear mode structure in the θ coordinate indicates the formation of a *fine* radial mode structure associated to the non-linear density modulation of Eq. (3).

The non-linear excitation of *short* scale length mode structures contributes to enhance wave energy dissipation and is responsible of the mode saturation. However, we know from the previous section that saturation can be reached even in the absence of physical dissipation due to the occurrence of a singularity in the mode structure when a *critical* amplitude is reached. For the present simulation parameters, $\epsilon_o = 0.2$, $s = 1.0$ and $b_s = 1.0$, the dissipation-less saturated amplitude obtained from Eqs. (15) and (16) is $\psi_c(\theta = 0) = A_{oc} = 5.32 \times 10^{-3}$, i.e. larger than the $\psi_c(\theta = 0) = 1.0 \times 10^{-3}$ obtained from the numerical simulation with finite dissipation. Numerical investigations are still in progress to show that the saturation level obtained numerically for decreasing dissipation indeed approaches the *ideal* limit predicted by Eqs. (15) and (16).

The mode saturated amplitude in terms of magnetic fluctuation level is given by

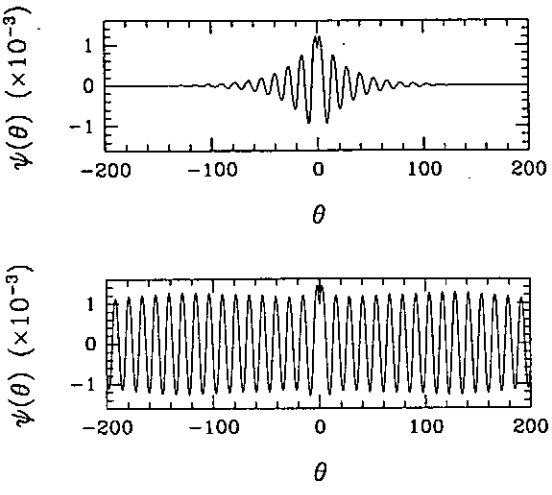

Figure 2: Linear and non-linear mode structures in θ space.

$(\delta B_r/B) \approx (c_S/v_A) b_s^{1/2} \psi_c \approx \beta^{1/2} \epsilon_o^{3/2}$. This saturation level is comparable with that obtained in previous investigations; e.g., the saturation due to $\delta\mathbf{E} \times \delta\mathbf{B}^*$ [7], $(\delta B_r/B) \approx \epsilon_o^{5/2}/(nq)$; that due to *ion Compton scattering*, $(\delta B_r/B) \approx \epsilon_o^2(\gamma/\omega)^{1/2}$ [8]; that due to *pressure caviton* effect, $(\delta B_r/B) \approx \epsilon_o^2/(nq)^{1/2}$, and *sheared flow* effect $(\delta B_r/B) \approx \epsilon_o^3/(nq)(\omega_{ci}/\omega_A)^{1/2}$ [5]. Another possible comparison is with the saturation level due to particle non-linear dynamics; e.g., *wave trapping* [9], $(\delta B_r/B) \approx \epsilon_o(a/\rho_\alpha)(\gamma/\omega)^2$ in the isolated resonance case, where ρ_α is the energetic particle Larmor radius, or stochastic diffusion in the high-n multiple resonance case. However, detailed comparisons still require further investigations in order to determine which processes would be the most relevant in a reactor.

References

[1] Connor J W, Hastie R J and Taylor J B, Phys. Rev. Lett. **40** 396 (1978)

[2] Chen C Z, Chen L and Chance M S, Ann. Phys. **161** 21 (1985)

[3] Zonca F and Chen L, Phys. Fluids B **5** 3668 (1993)

[4] Santoro R A and Chen L, Bull. Am. Phys. Soc. **40** 1682 (1995)

[5] Hu G and Chen L, Bull. Am. Phys. Soc. **41** 1397 (1996)

[6] Chen L, Phys. Plasmas **1** 1519 (1994)

[7] Zonca F, Romanelli F, Vlad G and Kar C, Phys. Rev. Lett. **74** 698 (1995)

[8] Hahm T S and Chen L, Phys. Rev. Lett. **74** 266 (1995)

[9] Berk H L and Breizman B N, Phys Fluids B **2** 2246 (1990)

TOROIDAL PLASMA RESPONSE TO EXTERNAL FIELDS

R. G. STORER

DEPARTMENT OF PHYSICS, FLINDERS UNIVERSITY,
GPO BOX 2100, ADELAIDE 5001, SOUTH AUSTRALIA

Toroidal plasmas respond to external driving fields in a way which is determined by the coupling of these fields to the spectrum of the plasma. We have extended the toroidal resistive magnetohydrodynamic spectral code, SPECTOR, to include the effects of external fields on tokamak-like plasmas. The code is capable of determining both the stable and unstable modes and also the response to helical applied fields with arbitary mode structure. Resistivity changes the continuous regions of the ideal MHD spectrum into a set of discrete eigenvalues lying along lines in the complex frequency plane with a spacing which is related to the inverse of the square root of the magnetic Reynolds number. Results are presented which relate the spectral distribution to the plasma response as a function of frequency.

1 Introduction

Any linear system, which has a spectrum of normal modes and which is coupled to an external driver, reacts in a way which is related to a linear combination of the normal modes. For simple systems the frequencies of the normal modes can be identified readily by this process, particularly in the case where the spectral frequencies are well separated. The usual phenomenon of resonance response causes the normal mode whose frequency is closest to the driving frequency to become dominant. With ideal systems (no dissipation) the spectral points lie on the real axis on the complex frequency plane and the response becomes singular as the driving frequency approaches the spectral value. In practice, dissipation is present and the resonant response is finite. This is associated with the fact that the spectrum of the dissipative system lies below (or above) the real frequency axis and cannot coincide with the real driving frequency.

Things are much more complicated when the spectrum is dense and the response becomes dominated by contibutions from a large number of normal modes. Such is the situation of a cylindrical plasma column, and even more so for a toroidal plasma. The physical situation that we consider is that of a plasma being driven by externally imposed fields and we model that situation by using the resistive MHD equations. We assume that the driving fields are sufficiently weak so that the equations can be linearised. The inclusion of resistivity will provide a dissipative mechanism which changes the character of the normal mode spectrum from an ideal continuous, real (but singular) spectrum to a discrete, but dense, spectrum which lies along characteristic lines in the lower half of the complex frequency plane (Ryu and Grimm [1, 2]; Dewar and Davies [3, 4]; Kerner *et al* [5] - [7]; Lortz and Spies [8]; Storer [9]; Schellhase [10]; Storer and Schellhase [11] and Schellhase and Storer [12]). The spacing of the spectral points along the lines is proportional to $\eta^{1/2}$, and η (the normalised resistivity) is small for high temperature plasmas, so at any particular driving frequency we could expect a contribution from a large number of modes. Studies

of this type have been carried out for a cylindrical plasma column by Poedts, Kerner and Goosens [13] with particular emphasis on the excitation of Alfvén waves.

The rationale for these studies is twofold. Firstly, the resonant absorption of power from external coils may heat the plasma. This possibility has been studied theoretically and experimentally for some time. Secondly, measurement of the plasma reponse to external fields may be related directly or indirectly to key aspects of the properties of the plasma and hence act as a diagnostic tool. We will concentrate on the later aspect in this paper. In either case, we need to develop an understanding of the relationship between the plasma response, the spectral properties of the plasma and the plasma configuration. This will be done by carefully increasing the complexity of the plasma model. Inclusion of toroidicity leads to coupling of the poloidal modes and a significant change to the spectral mode structure. Unfortunately this increase in complexity may obscure the diagnostic information and make it difficult to use the plasma reponse function to dtermine the plasma properties.

2 MHD equations

The toroidal resistive MHD code SPECTOR (Schellhase [10]; Storer and Schellhase [11] and Schellhase and Storer [12]) has been developed to find the complete (stable and unstable) spectrum of a tokamak-like plasma. This code solves the linearised resistive equations for compressible MHD, which lead to

$$\frac{\partial\left(\nabla\times\nabla\times\mathbf{u}\right)}{\partial t}=\nabla\times\left[\left(\nabla\times\mathbf{B}\right)\times\left(\nabla\times\mathbf{a}\right)+\left(\nabla\times\nabla\times\mathbf{a}\right)\times\mathbf{B}\right],$$

$$\begin{aligned}\frac{\partial\left(\nabla^2 w\right)}{\partial t} = & -\nabla^2 p+\nabla\cdot\left[\left(\nabla\times\mathbf{B}\right)\times\left(\nabla\times\mathbf{a}\right)\right]\\ & +\nabla\cdot\left[\left(\nabla\times\nabla\times\mathbf{a}\right)\times\mathbf{B}\right],\end{aligned}$$

$$\frac{\partial\mathbf{a}}{\partial t} = \left(\nabla\times\mathbf{u}+\nabla w\right)\times\mathbf{B}-\eta\left(\nabla\times\nabla\times\mathbf{a}\right)+\nabla f,$$

$$\frac{\partial p}{\partial t}=-\left(\nabla\times\mathbf{u}+\nabla w\right)\cdot\nabla P-\Gamma P\nabla^2 w,$$

where η can either be a constant or non-constant function. Here the variables are expressed in terms of $\mathbf{u}$ and w, which are the perturbed vector and scalar potentials of the velocity vector $\mathbf{v}$ (i.e. $\mathbf{v}=\nabla\times\mathbf{u}+\nabla w$) , $\mathbf{a}$, which is the perturbed magnetic vector potential and p, the perturbed pressure. The equilibrium magnetic field is $\mathbf{B}$, the equilibrium pressure is P and Γ is the ratio of specific heats. The first two of the above equations are obtained by taking the curl and divergence of the equation of motion and the third equation by

integrating Ampère's law, which leads to an arbitrary gauge function f. As explained in [10] this is chosen to be $\mathbf{B}\cdot\mathbf{u}+h(\psi)\frac{\partial a_\psi}{\partial\psi}$ where the ψ is a 'radial' coordinate whose constant surfaces coincide with the poloidal flux surfaces.
The units have been chosen so that the time scale is the toroidal Alfvén transit time,

$$\tau_A=\frac{a\sqrt{\mu_0\rho}}{B_0},$$

where a, the plasma radius, and B_0, the magnitude of the equilibrium toroidal field at the magnetic axis, are used as length and magnetic field scales.
SPECTOR performs a poloidal Fourier decomposition of these equations and takes all variables to be proportional to $\exp(-in\phi-i\omega t)$ where n is the toroidal mode number. A finite difference analysis of the equations leads to a matrix eigenvalue equation of the form

$$-i\omega\mathcal{R}\tilde{u}=\mathcal{P}\tilde{u},$$

where $\mathcal{R}$ and $\mathcal{P}$ are block-tridiagonal matrices of order $10MN\times 10MN$, where $M=m_{max}-m_{min}+1$ (number of poloidal modes), and N denotes the number of radial mesh points employed. This equation involves the eigenfunction (column vector) $\tilde{u}$ constructed from the components:

$$\tilde{u}^{\dagger}_{m,j}=\left(a_{\psi m,j}a_{\theta m,j}a_{\phi m,j}u_{\psi m,j}u_{\theta m,j}u_{\phi m,j}w_{m,j}p_{m,j}\right),$$

The index m is used to label the various poloidal modes and j labels the radial mesh points.
We have modified SPECTOR to model the interaction with external influences (magnetic fields, due to external coils, or pressure perturbations) by resetting the equations to the form

$$\left(\mathcal{P}+i\omega\mathcal{R}\right)\tilde{u}=\tilde{d},$$

where the vector $\tilde{d}$ is a driving term on the boundary of the plasma with a constant real frequency ω. By adjusting the non-zero terms in $\tilde{d}$ one can drive the plasma via e.g. the magnetic field perturbation or the pressure perturbation for various poloidal modes.

3 Results

The spectrum for a large aspect ratio (cylindrical) plasma column with a non-constant current lies along a series of lines in the complex frequency plane which form a Y-shape, with the tail of the 'Y' curving towards the negative real axis (Ryu and Grimm [1, 2]; Dewar and Davies [3, 4]; Kerner *et al* [5] - [7]; Storer and Schellhase [11] and Schellhase and Storer [12]). This shape is associated with a particular poloidal mode number and the top of the 'Y' points towards the values

$$\omega_A(\psi)=\frac{\kappa}{nq(\psi)}|m-nq(\psi)|.$$

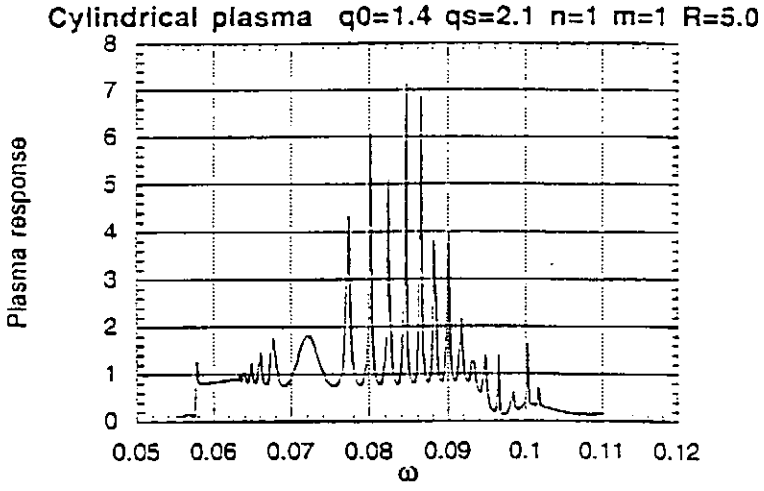

Figure 1

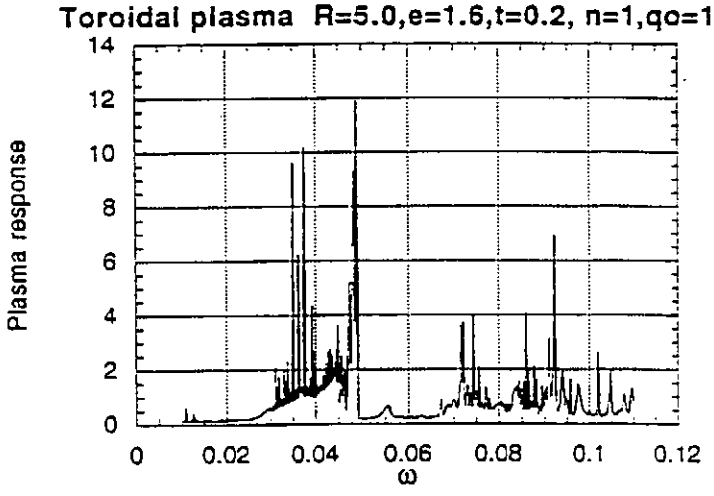

Figure 2

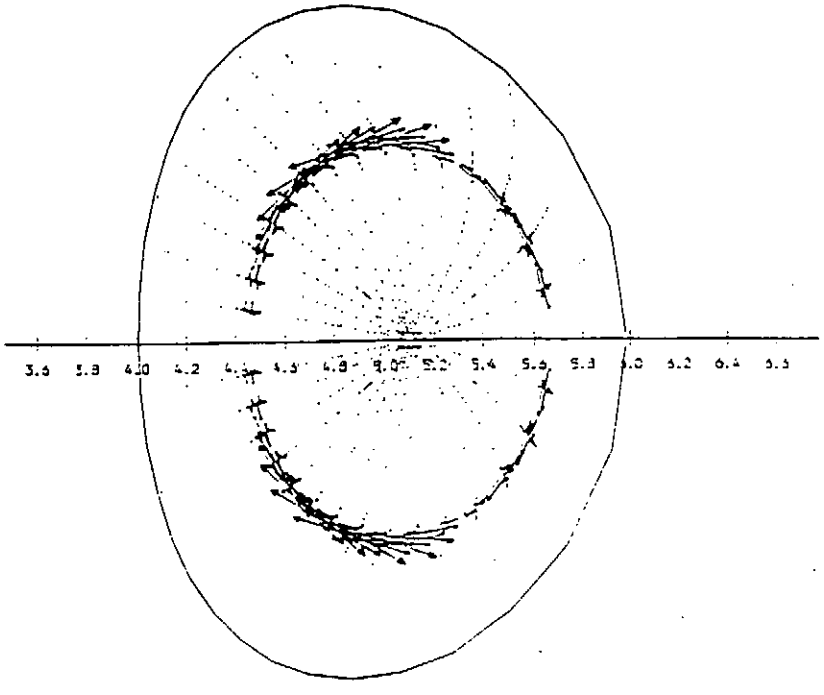

Figure 3

with ψ being a normalised flux coordinate which takes on the values 0 at the magnetic axis and 1 at the plasma edge, ($\kappa = \frac{na}{R}$.) These are the endpoints of the ideal Alfvén continuum. The ideal continua corresponding to various poloidal modes may or may not overlap, depending on the values of the safety factor at the magnetic axis and the edge. We would expect that the response of a resistive plasma, as a function of the frequency of the applied field will be dominated by the modes whose spectral values are nearest the real axis. Thus the response of the plasma will have two peaks associated with the endpoints of the ideal continuum, but with a shape which is influenced by the other modes.
To give a simple illustration, we consider a cylindrical resistive plasma equilibrium with shear, so that the safety factor at the magnetic axis is $q_0 = 1.4$ and at the edge $q_s = 2.1$ and $\kappa = 0.2$. This gives, for the m=1 poloidal modes, $\omega_0 = 0.057$ and $\omega_s = 0.104$ as the end points of the Alfvén continuum. The response of the plasma, to an $m = 1, n = 1$ helical applied magnetic field, as a function of ω is given in figure 1. This correlates with the resistive spectrum and, as expected, is large between the end points of the Alfvén continuum. Even though the normal modes are global functions of the radius, the response functions are peaked very strongly about the resonant surface associated with the applied frequency. Even with this simple model the response function is complicated. It is perhaps not surprising, therefore, that for a more realistic toroidal model the response becomes very complex and difficult to interpret in terms of the plasma parameters. Figure 2 shows the response of a toroidal plasma, again with $q_0 \approx 1.4$ and $\kappa \approx 0.2$ but with ellipticity = 1.6 and triangularity = 0.2. This case has strong poloidal coupling, with substantial $m = 2$ components in the vicinity of $\omega = 0.04$. Again the response field is strongly peaked about the resonant surface, as is illustrated by Figure 3. Unfortunately, the aim of using these response functions as diagnostic indicators has not been advanced by these calculations, but their complexity seems to be primarily associated with the complexity of the resistive spectrum.

Acknowledgements

The author acknowledges the work of Dr Anthony Schellhase in the development of the code SPECTOR. This work was supported by the Australian Research Grants Scheme, AINSE and the Australian National University Supercomputing Facility.

References

[1] Ryu,C.M. (1983) *Ph.D Dissertation*, Princeton University.

[2] Ryu,C.M. and Grimm,R.C. (1984) *J.Plasma Physics.* **32**, 207

[3] Dewar,R.L., and Davies,B. (1984) *J. Plasma Physics* **32**, 443

[4] Davies,B. (1984) *Phys. Lett.* **100A**, 3

[5] Kerner,W., and Lerbinger,K. (1986). *Phys. Fluids* **29**, 9

[6] Pao,Y.P. and Kerner,W. (1984) *Phys. Fluids* **28**. 287

[7] Kerner,W., Lerbinger,K., Gruber,R., and Tsunematsu, T. (1985) *Com. Phys. Comm.* **36**, 225

[8] Lortz,D., and Spies,G.O. (1984) *Phys. Lett.* **101A**, 7

[9] Storer,R.G. (1983) *Plasma Physics* **25**,1279

[10] Schellhase A.R. (1994) *Ph.D. Dissertation*, The Flinders University of South Australia.

[11] Storer,R.G. and Schellhase,A.R.(1995) *Physica Scripta* **T60**, 57

[12] Schellhase,A.R. and Storer,R.G. (1996) *J. Comp. Phys.* **123**, 15

[13] Poedts,S., Kerner,W. and Goosens,M. (1989) *J. Plasma Phys.* **42**, 27

Double Tearing Reconnection and the Off-Axis Sawteeth Crash

Ding Li[1]

Institute of Plasma Physics, Chinese Academy of Sciences, Hefei 230031, P. R. China

A theoretical model is developed for the onset of the off-axis sawteeth crash observed in TFTR reversed magnetic shear experiments. The dispersion relation of the double tearing mode is obtained from the solution structure of the ideal external kink equation. The onset of "annular crash" is due to the fast reconnection of the hot and cold islands, triggered by the interaction of both branches of the double tearing mode. The onset of "core crash" is mainly due to the coalescence between the hot islands, triggered by the explosive growth of the inner branch and the rapid expansion of the hot islands.

I. Introduction

The double tearing instability has been observed in the initial or skin phase of a tokamak discharge since two decades ago.[1] The stability and evolution of the double tearing mode were analyzed respectively for the skin and hollow current profiles.[2,3] Recently, the high confinement regime has been observed in the reversed magnetic shear (RMS) plasma with nonmonotonic q profile in several tokamaks.[4] Therefore, the study of the double tearing mode becomes a very important issue for achieving the advanced tokamak operation. The off-axis sawteeth activity and double tearing reconnections were observed in TFTR[5] (Tokamak Fusion Test Reactor) RMS experiments. One of the major remaining questions is the destabilization mechanism of the double tearing mode.

It is well known that the instability criterion for tearing modes is $\Delta' > 0$. The dispersion relation can be obtained by asymptotic matching between the interior and exterior regions, namely, $\Delta' = \Delta(\omega)$. Recently, analytic expressions of Δ' and instability criterion have been derived in the large aspect ratio and low-β limits for $m \geq 2$ single tearing mode.[6]

The aim of the present paper is to develop a theoretical model for onset of the off-axis sawteeth crashes. The dispersion relation of the double tearing mode is derived based on the solution structure of the ideal external kink equation in Sec. II. The off-axis sawteeth crash is analyzed in Sec. III by considering a trigger of the $m/n = 2/1$ double tearing reconnections. Finally, the conclusion and discussion are addressed in Sec. IV.

II. Dispersion Relation of Double Tearing Mode

In the large aspect ratio and low-β limits, the MHD equation is reduced to

[1] Present address: Department of Modern Physics, University of Science and Technology of China, Hefei 230027, P. R. China

$$\frac{\partial \psi}{\partial t} + \mathbf{v} \cdot \nabla \psi = \eta J \tag{1}$$

$$\frac{\partial U}{\partial t} + \mathbf{v} \cdot \nabla U = -S^2 \hat{z} \cdot \nabla \psi \times \nabla J \tag{2}$$

where $J = \nabla^2 \psi$ is a parallel current density, $U = \nabla^2 \varphi$ is a vorticity, ψ is a flux function, and φ is a stream function. In the outer region away from the resistive layer, Eqs. (1) and (2) can be reduced to the dimensionless form of the ideal kink external equation as

$$\frac{d^2\psi}{dr^2} + \frac{1}{r}\frac{d\psi}{dr} - \frac{m^2}{r^2}\psi - \frac{q(r_s)}{r}\frac{q(r)dJ/dr}{q(r)-q(r_s)}\psi = 0 \tag{3}$$

where the safety factor $q(r)$ is a nonmonotonic function. Suppose Eq. (3) has two linearly independent solutions $y_1(r)$ and $y_2(r)$ which satisfy the continuity condition at $r = r_s$ and the boundary conditions $\psi(0) = \psi(r_w) = 0$, here r_w is the location of a conductive wall. Then, one obtains the general solution

$$\psi(r) = \begin{cases} \psi(r_1) f(r,0) / f(r_1,0) & 0 < r < r_1 \\ \psi(r_1) f(r,r_2) / f(r_1,r_2) + \psi(r_2) f(r,r_1) / f(r_2,r_1) & r_1 < r < r_2 \\ \psi(r_2) f(r,r_w) / f(r_2,r_w) & r_2 < r < 1 \end{cases} \tag{4}$$

by denoting $f(x,u) = y_1(x)y_2(u) - y_1(u)y_2(x)$, $f'(x,u) = \partial f(x,u)/\partial x$. Consequently, the relation between Δ for the double tearing mode and $\Delta'^{(0)}$ for the single tearing mode is resulted as following:

$$(\Delta_1' - \Delta_1'^{(0)} - A_{12})(\Delta_2' - \Delta_2'^{(0)} - A_{21}) - A_{22} = 0 \tag{5}$$

where $\Delta_j'^{(0)} = \left.\frac{f'(r_j,u)}{f(r_j,u)}\right|_0^{r_w}$, $A_{12} = \left.\frac{f'(r_1,u)}{f(r_1,u)}\right|_{r_2}^{r_w}$, $A_{21} = \left.\frac{f'(r_2,u)}{f(r_2,u)}\right|_0^{r_1}$, $A_{22} = \frac{f'(r_1,r_1)f'(r_2,r_2)}{[f(r_2,r_1)]^2}$.

After $\Delta(\omega)$ is constructed from the solution of the tearing mode equation within the resistive layers at $r = r_j$, the dispersion relation for the double tearing mode can be obtained by inserting the relation of asymptotic matching $\Delta' = \Delta(\omega)$ into Eq. (5).

However, it is very difficult to obtain analytically the solutions $y_1(r)$ and $y_2(r)$ since there are two singularities in Eq. (3). A simple way is to solve Eq. (3) separately in the intervals [0, r_2] and [r_1, r_w], and redefine $\Delta'^{(0)}$ so that Eq. (5) becomes

$$(\Delta_1' - \Delta_1'^{(0)})(\Delta_2' - \Delta_2'^{(0)}) - A_{22} = 0 \tag{6}$$

where $\Delta_1'^{(0)} = \left.\frac{f'(r_1,u)}{f(r_1,u)}\right|_0^{r_w}$, $\Delta_2'^{(0)} = \left.\frac{f'(r_2,u)}{f(r_2,u)}\right|_{r_1}^{r_w}$. For simplicity, $\Delta'^{(0)}$ can be expressed as[6]

$$\Delta_j'^{(0)} = -\frac{\pi\lambda_j}{r_j}\cot\left[\pi\left(\sqrt{m^2+\lambda_j} - m\right)\right] \tag{7}$$

without considering the effect of the boundary condition and the coupling term A_{22} may be roughly estimated by

$$A_{22} = 4m^2 r_1^{m-1} / [r_2^{m+1} Y_1^{(o)}(1) Y_1^{(i)}(1)] \tag{8}$$

where the notations are same as in Ref. 6.

III. Onset of Off-Axis Sawteeth Crashes

Assume that the nonmonotonic q profile has a form similar to that in Ref. 3 as follows

$$q(r) = q(0)\alpha(1 + hr^{2p})^{1+1/p} / (\alpha + hr^{2p}) \tag{9}$$

where $q(0)$, α, h, and p are free parameters. The q profile is a nonmonotonic function if $\alpha < p/(p+1)$ and reaches the minimum value $q_m = q(0)\alpha(1+p)^{1+1/p}(1-\alpha)^{1/p} / p$ as $r_m = \{[p-(1+p)\alpha]/p\}^{1/2p}$. Introducing the relation $\psi_0^{*\prime}(r) = (m/n)\psi_0'(r) - r$, one has the helical flux function as

$$\psi_0^*(r) = \frac{1}{2}(1-r^2) - \frac{m}{2n\alpha q(0)}\left[\frac{1}{h}\ln\frac{1+h}{1+hr^2} - \frac{(1-\alpha)(1-r^2)}{(1+h)(1+hr^2)}\right]. \tag{10}$$

It is easy to prove that $\psi_0^*(r)$ has a minimum at $r = r_1$ and a maximum at $r = r_2$ because $\psi_0^{*\prime}(r) = 0$ is just equivalent to $q(r_j) = m/n$.

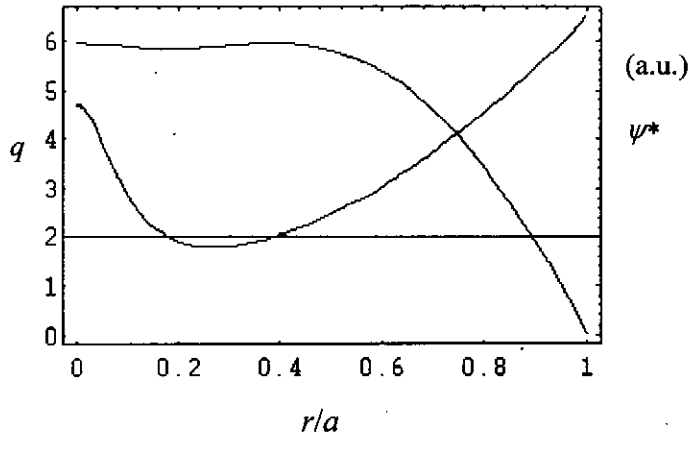

Fig. 1. The q profile and helical flux function for $q(1) = 6.5$, $q(0) = 4.7$, $q_m = 1.8$ and $p = 1$.

In the TFTR experiments, the "annular crash" occurs as $q(0)$ increases to a high value among 4 ~ 5 while the minimum of q profile, q_m, decreases to below 2. One can observe that the two rational surfaces r_1 and r_2 are close each other from the q profile plotted in Fig. 1. When $q(1) = 6.5$, $q(0) = 4.7$, $q_m = 1.8$ and $p = 1$, one has $r_1 = 0.18$, $r_2 = 0.38$, $\Delta_1'^{(0)} = -20.58$, $\Delta_2'^{(0)} = 75.24$, and $A_{22} = 967.46$ so that it is easy to obtain $\Delta_1(\omega) = -29.79$, and $\Delta_2(\omega) = 84.45$ by using Eq. (6). This indicates that the double tearing mode is strongly

unstable and becomes even more unstable due to the interaction between the two branches. This corresponds to the helical flux function plotted in Fig. 1 which has $\psi_0^*(0) \geq \psi_0^*(r_2)$ similar to the second case in Ref. 3. It is interesting to notice that the minimum of $\psi_0^*(r)$ just corresponds to the stable branch at $r = r_1$ while the maximum of $\psi_0^*(r)$ just corresponds to the unstable branch at $r = r_2$. The bulging of the hot and cold islands gives rise to current sheet formation and fast reconnection between the two singular surfaces. Such complete reconnection leads to the "annular crash". It is similar to the result of the numerical simulations,[7, 3] which are the application of Kadomtsev model[8] to the double tearing reconnections. A new equilibrium will be reached as the helical flux function (as well as q profile) is flat in the reconnection region.

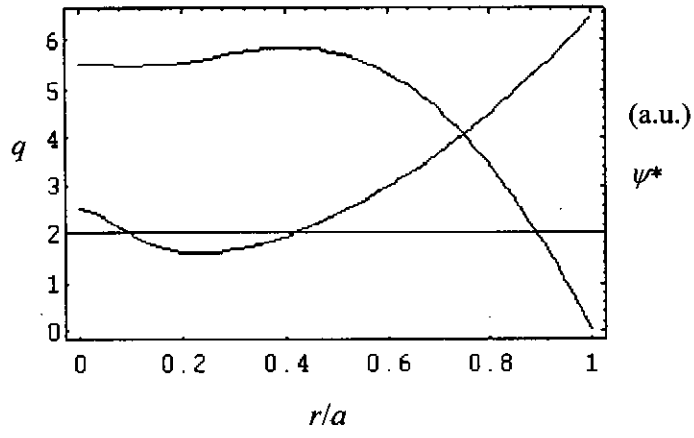

Fig. 2. The q profile and helical flux function for $q(1) = 6.5$, $q_m = 1.6$, $q(0) = 2.5$, and $p = 1$.

When $q(0)$ decreases rapidly toward to 2 while $q_{\min}$ decreases slightly, the "core crash" occurs in the TFTR experiments. In such case, the two rational surfaces r_1 and r_2 are well separated which can be seen from the q profile plotted in Fig. 2. Similarly, one can calculate $r_1 = 0.10$, $r_2 = 0.41$, $\Delta_1'^{(0)} = 47.72$, $\Delta_2'^{(0)} = 11.27$ and $A_{22} = 46.34$ as $q(1) = 6.5$, $q_m = 1.6$, $q(0) = 2.5$, and $p = 1$. It is also easy to obtain $\Delta_1(\omega) = 48.95$, and $\Delta_2(\omega) = 10.04$. The two branches of the double tearing mode are unstable but the interaction between them is quite weak. This corresponds to the helical flux function plotted in Fig. 2 which has $\psi_0^*(0) \leq \psi_0^*(r_2)$ but different from the first case in Ref. 3. As $q(0)$ decreases to 2.2, one would have $r_1 = 0.07$, $r_2 = 0.41$, $\Delta_1'^{(0)} = 142.71$, $\Delta_2'^{(0)} = 11.96$ and $A_{22} = 30.34$ so that $\Delta_1(\omega) = 142.94$ and $\Delta_2(\omega) = 11.74$. It is shown in Fig. 3 that the $\Delta_1'^{(0)}$ increases as well as $\Delta_2'^{(0)}$ while A_{22} decreases as $q(0)$ decreases. Therefore, the interaction of the two branchesis even weaker so that $\Delta(\omega)$ is almost same as $\Delta'^{(0)}$.

Obviously, the interaction of the two branches could not be the main reason to trigger the onset of the "core crash". On one hand, the linear growth of inner branch increases explosively as r_1 approaching to plasma core because $\Delta' \propto f(m,\lambda)/r_1$ becomes very large.[6] Suppose that the constant-ψ approximation is still valid in the linear and quasilinear phases since the island width can not be wider than $2r_1$. The time scale in the linear phase is

$\tau_R^{3/5}\tau_A^{2/5}\Lambda^{-4/5} \sim 60$–$.100\mu$ sec for TFTR experiment parameters, here $\Lambda = \Delta'/\overline{\Delta}' \sim 10-100$ is defined as an enhancement factor of Δ and $\overline{\Delta}'$ is a normal Δ value of the single tearing mode with monotonic q profile.

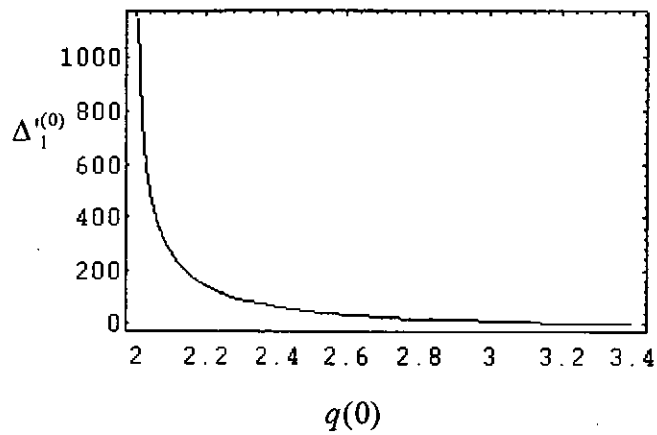

Fig. 3. The $\Delta_1'^{(0)}$ of $m/n = 2/1$ mode increases as $q(0)$ decreases for $q(1) = 6.5$, $q_m = 1.6$, and $p = 1$.

In such case, the qausilinear modification of the magnetic field becomes dominant comparing with the qausilinear current effect since the inner branch in the linear phase is strongly unstable. The well-known Rutherford behavior should be implemented as[9]

$$\left(\frac{\partial\psi}{\partial t}\right)^2 + \frac{1}{\pi^{1/2}C_0}\eta\Delta'^2\,\psi\frac{\partial\psi}{\partial t} = \frac{2^{1/2}}{C_0^2}\frac{\hat{s}_0}{q_0}\eta^2\Delta'^2\,\psi\,. \tag{11}$$

Therefore, the island width is expressed as

$$w(t) \propto \left[\frac{\psi(t)}{\hat{s}_0 - (C_0 q_0/\sqrt{2\pi}\eta)\partial\psi/\partial t}\right]^{1/2}. \tag{12}$$

When the quasilinear modification of the magnetic shear is almost equal to the equilibrium shear, the hot islands expand rapidly as the total shear is approaching to zero around $r = r_1$. The time scale in the quasilinear phase is $\tau_R\Lambda^{-1} \sim 1-10$msec for TFTR experiment parameters which is much faster than the Rutherford nonlinear time scale $\tau_R \sim 100m$sec.

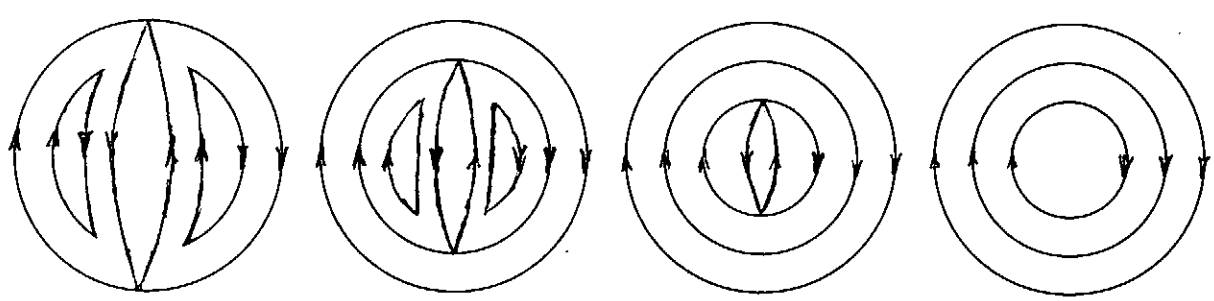

Fig. 4 Schematic drawing of the reconnection process

On the other hand, the attractive force between parallel currents induced by the hot islands accelerates the reconnection triggered by the explosive growth of the inner branch and the rapid expansion of the hot islands which are close each other. A fast reconnection in the plasma core due to coalescence between the hot islands leads to the "core crash". In the plasma core, the resistivity is quite small so that the Sweet-Parker scaling law may be suitable.[10] The time scale for the fast reconnection is $\tau_R^{1/2}\tau_A^{1/2}\Lambda^{-1} \sim 10-100\mu\sec$, which agrees with the experiment crash time. The reconnection process is shown in Fig. 4.

III. Conclusion and Discussion

In summary, the relation between Δ for the double tearing mode and $\Delta'^{(0)}$ for single tearing mode is resulted from the solution structure of the ideal external kink equation. The dispersion relation of the double tearing mode is obtained with help of the asymptotic matching condition and the analytic expression of $\Delta'^{(0)}$. The onset of "annular crash" is due to the fast reconnection of the hot and cold islands, triggered by the interaction of both branches of the double tearing mode for which Kadomtsev model can be applied to explain. The onset of "core crash" is mainly due to the coalescence between the hot islands, in which the fast reconnection is triggered by the explosive growth of the inner branch and the rapid expansion of the hot islands.

Acknowledgments

It is my pleasure to thank Dr. A. Rogister (IPP/FZ), and Dr. Z. Chang (PPPL) for valuable discussions, and Prof. Y. X. Wan (IPP/CAS) and Prof. C. X. Yu (USTC) for constant encouragement. This work is supported by the National Science Fund for Distinguished Young Scholars of China under Grant No. 19515513.

Reference

[1] T. H. Stix, Phys. Rev. Lett. **36**, 521 (1976).
[2] H. P. Furth, P. H. Rutherford, H. Selberg, Phys. Fluids, **16**, 1054 (1973).
[3] B. Carreras, H. R. Hicks, and B. V. Waddell, Nucl. Fusion, **19**, 1423 (1979).
[4] For example, F. M. Levinton et al., Phys. Rev. Lett. **75**, 4417 (1995).
[5] Z. Chang et al., Phys. Rev. Lett. **77**, 3553 (1996).
[6] D. Li, "*Instability criterion of tearing mode for arbitrary magnetic shear configuration*", submitted to Phys. Plasmas, (1997).
[7] R. B. White et al., Phys. Fluids **20**, 800 (1977).
[8] B. B. Kadomtsev, Sov. J. Plasma Phys. 1, 389 (1975).
[9] D. Li, Phys. Plasmas **2**, 3275 (1995).
[10] D. Biskamp, *Nonlinear Magnetohydrodynamics* (Cambridge Univ. Press, Cambridge), p156, (1993).

COLLECTIVE SCATTREING OF ELECTROMAGNETIC WAVES FROM A RELATIVISTIC MAGNETIZED PLASMA

Lu Quankang
Department of Physics, Fudan University
Shanghai 200433, P. R. China

also Institute of Physics and Institute of Theoretical Physics,
Chinese Academy of Sciences
Beijing 100080, P. R. China

Abstract

Recently, laser and microwave scattering has become one of the important diagnostic means for plasma. Laser and microwave correlative scattering spectrum is determined by particle-density fluctuations in a weak turbulent plasma.

In a relativistic plasma, on the basis of complete electromagnetic-interaction between particles, a general expression for particle density fluctuations and spectrums of laser and microwave scattering from a magnetized plasma are derived.

The laser and microwave scattering spectrums provide informations on electron density and temperature, ion temperature, resonance and nonresonance effects.

1. Introduction

Recently, laser and microwave scatterings have become important diagnostic means for plasma. Incoherent electromagnetic wave scattreing spectrum is determined by the particle-density fluctuations in a weak turbulent plasma. The scattering spectrum has previously been calculated with respect to Coulomb-interaction between charged particles in a non-relativistic plasma.

In a relativistic plasma, on the basis of complete electromagnetic-interaction between particles, a general expression for particle density fluctuations and spectrums of electromagnetic wave scattering from a magnetized plasma are derived in this paper.

The Laser scattering spectrum provides the information on the electron density and temperature, the ion temperature, and the direction of an applied magnetic field. As a diagnostic technique, laser scattering has advantages of providing excellent spatial and temporal resolution but causing a slight disturbance to a plasma system.

Bowles[1], Salpeter[2], Dougherty and Farlay[3] studied the scattering from the ionosphere with radar waves. They calculated separately with their own method for the scattering spectrum. Based on BBGKY theory, Rostoker[4] developed a fluctuation theory and calculated scattering spectrums of a magnetized plasma by means of a test particle model. However, the above-mentioned calculations involved only Coulomb interactions between charged particles in a non-relativistic plasma[5].

Lu[6] developed a relativistic correlative kinetic plasma theory. Based on this theory, a relativistic test particle pattern is established. In the relativistic case, induced electromagnetic

interactions between charged particles should be considered. In the description of a electromagnetic system, the mathematical calculation process is rather complex[7,8].

On the basis of Lu's work, this paper develops a relativistic bare particle Green function pattern. A closed set of equations of Green functions to first order in the plasma parameter g ($=1/n\lambda_0^3$, here n is the electron density and λ_D is the Debye length) are obtained. Solving the closed set of Green function equations, we obtain the space and time correlation functions of density fluctuations. Then, the dynamic form factor $S(\vec{k}, w)$ is calculated, where w and $\vec{k}$ is the differential frequency and differential wave vector between a scattering wave and an incident wave respectively.

Finally, we obtain an analytic expression for the scattering spectrum of a magnitized plasma.

2. Equations of Green Functions

Let $f_{\alpha 0}$ express the relativistic momentum distribution function of particle α in an uniform plasma.

The equation of Green function δf_α is expressed as

$$\frac{\partial \delta f_\alpha}{\partial t}+\vec{u}\cdot\nabla_x\delta f_\alpha+q_\alpha[\vec{E}+\frac{1}{c}\vec{u}\times(\vec{B}+\vec{B}_0)]\cdot\nabla_p\delta f_\alpha$$

$$+\frac{q_\alpha}{c}\vec{u}\times(\vec{B}+\vec{B}^0)\cdot\nabla_p f_{\alpha 0}=0, \quad (1)$$

where q_α is the electric charge of particle α, c is the velocity of light in vacuum, $\vec{u}$ is the velocity and $\vec{p}$ is the momentum of a particle.

The self-consistent electiric field $\vec{E}$ and magnetic field $\vec{B}$ are governed by Maxwell's equations

$$\nabla_x\times\vec{E}=-\frac{1}{c}\frac{\partial\vec{B}}{\partial t} \quad (2)$$

$$\nabla_x \times \vec{B} = \frac{1}{c}\frac{\partial \vec{E}}{\partial t} + \frac{4\pi}{c}\vec{j} + \frac{4\pi}{c} q_T \vec{u}' \delta[\vec{X} - \vec{X}'(t)] \qquad (3)$$

$$\nabla_x \cdot \vec{E} = 4\pi\rho + 4\pi q_T \delta[\vec{u} - \vec{u}'(t)] \qquad (4)$$

$$\nabla_x \cdot \vec{B} = 0 \qquad (5)$$

Where

$$\rho = \sum_a n_a q_a \int f_a \vec{dp}, \quad \vec{j} = \sum_a n_a q_a \int f_a \vec{u} \vec{dp} \qquad (6)$$

are the charged densities and the current densities, $\vec{X}'$, $\vec{u}'$ are the coordinate and velocity of a test particle q_T at time t. The equation of a test particle is

$$\frac{d\vec{X}'}{dt} = \vec{u}'$$
$$\frac{\vec{du}'}{dt} = \frac{q_T}{c}(\vec{u}' \times \vec{B}_0). \qquad (7)$$

It is proved that up to the order of g, in equation (7), only the external magnetic field should be considered. Eqs. (1)—(7) form a closed set of equations and will serve as basis for the treatment of fluctuations and scattering in a relativistic plasma to order of g.

In comparison of Eqs. (1)—(7) with the test particle model given in Ref. [5], it is clear that we have used Maxwell equations with the effect of a test particle (i. e. the source particle of a Green function) instead of Poission equation. Besides, we have used relativistic equations instead of non-relativistic equations. It implies the complete relativistic and full electromagnetic interactions (including Coulomb and induced electric and magnetic interactions, i. e. the interaction forces between particles are dependent on time explicitly). Eqs. (1)—(7) contain more detailed informations about plasma. This is our new model.

3. Fluctuations in Electron density

Considering a relativistic plasma in an external magnetic field $\vec{B}_0=B_0\vec{e}_3$, we choose the coordinate system shown in Fig. 1.

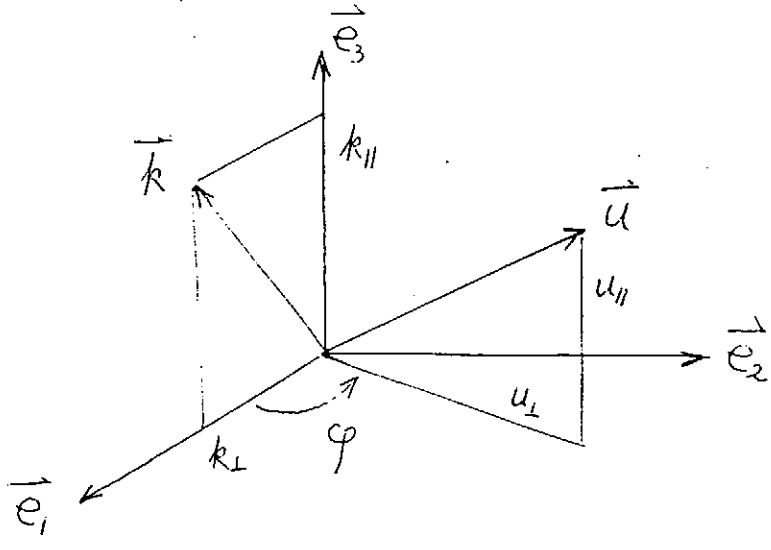

Fig. 1. Coordinate system

The orbit of a bare source particle at time t is

$$\vec{X}'(t)=\vec{X}'_0+a'_T[\cos(\Omega'_T t+\beta)-\cos\beta']\vec{e}_1$$
$$+a'_T[\sin(\Omega'_T t+\beta')-\sin\beta']\vec{e}_2+u'_{\parallel} t\,\vec{e}_3, \qquad (8)$$

$$\vec{u}_T(t)=-u'_{\perp}\sin(\Omega'_T t+\beta')\vec{e}_1$$
$$+u'_{\perp}\cos(\Omega'_T t+\beta')\vec{e}_2+u'_{\parallel}\vec{e}_3 \qquad (9)$$

Here

$$\Omega'_T=\frac{q_T B_0}{m_T c\gamma'},\quad a'_T=\frac{u'_{\perp}}{\Omega_T},$$
$$\gamma'=(1-\frac{u'^2}{c^2})^{-1/2} \qquad (10)$$

are the cyclotron frequency, radius and Lorentz factor; q_T, m_T, $(u'_{\perp},u'_{\parallel})$, β' are the charge, the rest mass, the initial velocity and the initial phase of the bare source particle of a Green function respectively.

We take the Fourier-Laplace transformation of Eqs. (1)—(6) to obtain

$$(-i\omega+i\vec{k}\cdot\vec{u})\delta f_\alpha(\vec{k},\omega,\vec{p})$$

$$+q_\alpha(\vec{E}+\frac{1}{c}\vec{u}\times\vec{B})\cdot\frac{\partial f_{\alpha 0}(\vec{p})}{\partial\vec{p}}-\Omega_\alpha\frac{\partial\delta f_\alpha(\vec{k},\omega,\vec{p})}{\partial\varphi}$$

$=0$, (Im w >0). (11)

$$\vec{k}\times\vec{E}=\frac{\omega}{c}\vec{B} \qquad (12)$$

$$i\vec{k}\times\vec{B}=-\frac{i\omega}{c}\vec{E}+\frac{4\pi}{c}\Sigma_\alpha n_\alpha q_\alpha\int\vec{u}\,\delta f_\alpha(\vec{k},\omega,\vec{p})\,d\vec{p}+\frac{4\pi}{c}\vec{j}_T(\vec{k},\omega),$$

(13)

$$\vec{j}_T=q_T\exp\{-i[\vec{k}\cdot\vec{X}_0-k_\perp a'_\perp\cos\beta']\}$$

$$\cdot\sum_{m=-\infty}^{\infty}(-i)^m e^{-im\beta'}u'_\perp\left(\frac{m}{k_\perp a'_T}\right)\frac{J_m\vec{e}_1+iu'_\perp J'_m\vec{e}_2+u_\parallel J_m\vec{e}_3}{-i\omega+i\vec{k}\cdot\vec{u}'+in\Omega'_T}, \quad (14)$$

Where $J_m=J_m(k_\perp a'_T)$ and J'_m are the Bessel functions and their derivatives.

Without loss of generality, we assume that the vector $\vec{k}$ lies in the XZ—plane. For the case of a spatially uniform plasma, the distribution function is most generally in the form $f_{\alpha 0}=f_{\alpha 0}(u_\perp^2,u_\parallel)$, From the above equations, we find.

$$\delta f_\alpha(\vec{k},\omega,\vec{p})=-iq_\alpha e^{ik_\perp a_\alpha\sin\varphi}\cdot\sum_{n=-\infty}^{\infty}\frac{\vec{A}_n^\alpha\cdot\vec{E}}{\omega-k_\parallel u_\parallel-n\Omega_\alpha}e^{in\varphi}, \qquad (15)$$

where

$$A_n^\alpha=A_{nx}^\alpha\vec{e}_1+A_{ny}^\alpha\vec{e}_2+A_{nz}^\alpha\vec{e}_3 \qquad (16)$$

and

$$\begin{cases} A^{\alpha}_{nx}=\left[\dfrac{k_{\parallel}u_{\perp}}{\omega}\dfrac{\partial f_{\alpha 0}}{\partial p_{\parallel}}+\left(1-\dfrac{k_{\parallel}u_{\parallel}}{\omega}\right)\dfrac{\partial f_{\alpha 0}}{\partial p_{\perp}}\right]\left(\dfrac{n}{k_{\perp}a_{\alpha}}\right)J_n(k_{\perp}a_{\alpha}), \\ A^{\alpha}_{ny}=\left[\dfrac{k_{\parallel}u_{\perp}}{\omega}\dfrac{\partial f_{\alpha 0}}{\partial p_{\parallel}}+\left(1-\dfrac{k_{\parallel}u_{\parallel}}{\omega}\right)\dfrac{\partial f_{\alpha 0}}{\partial p_{\perp}}\right]iJ'_n(k_{\perp}a_{\alpha}), \\ A^{\alpha}_{nz}=\left[\left(1-\dfrac{n\Omega_{\alpha}}{\omega}\right)\dfrac{\partial f_{\alpha 0}}{\partial p_{\parallel}}+\dfrac{n\Omega_{\alpha}}{\omega}\dfrac{u_{\parallel}}{u_{\perp}}\dfrac{\partial f_{\alpha 0}}{\partial p_{\perp}}\right]J_n(k_{\perp}a_{\alpha}). \end{cases} \tag{17}$$

Substituting these expressions into Eq. (13) and eliminating the vector $\vec{B}$, we obtain an equation for $\vec{E}$

$$\vec{D}\cdot\vec{E}=-\frac{4\pi i}{\omega}\vec{j}_T, \tag{18}$$

we introduce here the dielectric tensor of a plasma

$$\vec{D}=\left(\frac{1-k^2c^2}{\omega^2}\right)\vec{I}+\frac{c^2}{\omega^2}\vec{k}\vec{k}+\frac{4\pi i}{\omega}\sigma, \tag{19}$$

where

$$\sigma=-i\Sigma n_{\alpha}q_{\alpha}^2\int\vec{dp}\sum_{n=-\infty}^{\infty}\frac{\vec{S}_n}{\omega-k_{\parallel}u_{\parallel}-n\Omega_{\alpha}}, \tag{20}$$

and

$$\vec{S}_n=\begin{pmatrix} u_{\perp}\left(\dfrac{n}{k_1a_{\alpha}}\right)^2J_n^2\cup & iu_{\perp}\cup\left(\dfrac{n}{k_{\perp}a_{\alpha}}\right)J_nJ'_n & u_{\perp}\left(\dfrac{n}{k_{\perp}a_{\alpha}}\right)J_n^2W \\ -iu_{\perp}\left(\dfrac{n}{k_1a_{\alpha}}\right)J_nJ'_n\cup & u_{\perp}J_n'^2\cup & -iu_{\perp}J_nJ'_nW \\ u_{\parallel}\left(\dfrac{n}{k_{\perp}a_{\alpha}}\right)J_n^2\cup & iu_{\parallel}J_nJ'_n\cup & u_{\parallel}J_n^2W \end{pmatrix} \tag{21}$$

and define functions

$$\begin{aligned} \cup&=\left[\frac{k_{\parallel}u_{\perp}}{\omega}\frac{\partial f_{\alpha 0}}{\partial p_{\parallel}}+\left(1-\frac{k_{\parallel}u_{\parallel}}{\omega}\right)\frac{\partial f_{\alpha 0}}{\partial p_{\perp}}\right], \\ W&=\left[\left(1-\frac{n\Omega_{\alpha}}{\omega}\right)\frac{\partial f_{\alpha 0}}{\partial p_{\parallel}}+\frac{n\Omega_{\alpha}}{\omega}\frac{u_{\parallel}}{u_{\perp}}\frac{\partial f_{\alpha 0}}{\partial p_{\perp}}\right] \end{aligned} \tag{22}$$

From eq. (18), we find

$$\vec{E}=-\frac{i4\pi}{\omega}\vec{D}^{-1}\vec{j}_T, \tag{23}$$

where $\vec{D}^{-1}$ is the inverse tensor of $\vec{D}$.

Substituting Eq. (23) into Eq. (16), we obtain the distribution functions by inverting the Fourier-Laplace transform

$$\delta f_\alpha(\vec{x},\vec{p},t)=f_{\alpha 0}(\vec{p})-\frac{4\pi q_T q_\alpha}{m_\alpha}\int e^{i\vec{k}\cdot\vec{x}}\frac{d\vec{k}}{(2\pi)^3}\exp\left[ik_\perp a_\alpha\sin\varphi\right]$$

$$\cdot\exp\left\{-i[\vec{k}\cdot\vec{x}'_0-k_\perp a'_\perp\cos\beta']\right\}\sum_{n=-\infty}^{\infty}\sum_{m=-\infty}^{\infty}$$

$$\frac{e^{-in\varphi}e^{-im\beta'}(-i)^m e^{-i[\vec{k}\cdot\vec{u}']_m^T}}{[\vec{k}\cdot\vec{u}']_m^T([\vec{k}\cdot\vec{u}']_m^T-[\vec{k}\cdot\vec{u}]_n^\alpha)}\cdot\vec{A}_n^\alpha\cdot\vec{D}^{-1}\cdot\vec{I}_m^T. \qquad (24)$$

Here we introduce the notations

$$[\vec{k}\cdot\vec{u}']_m^T=k_\parallel u'_\parallel+m\Omega'_T,[\vec{k}\cdot\vec{u}]_n^\alpha=k_\parallel u_\parallel+n\Omega_\alpha \qquad (25)$$

and

$$\vec{I}_m^T=\begin{pmatrix}u'_\perp(\frac{m}{k_\perp a'_T})J_m\\ iu'_\perp J'_m\\ u'_\parallel J_m\end{pmatrix} \qquad (26)$$

Finally, we obtain a general expression for the fluctuations in electron desity caused by a bare source particle

$$\tilde{n}_{ee}=\exp\{-i[\vec{k}\cdot\vec{x}'_0-k_\perp a'_e\cos\beta']\}\cdot\sum_{m=-\infty}^{\infty}(-i)^m e^{-im\beta'}(2\pi)$$

$$\cdot\delta(\omega-[\vec{k}\cdot\vec{u}']_m^e)\cdot\{J_m(k_\perp\alpha'_e)-\omega_{pe}^2 m_e\sum_{n=-\infty}^{\infty}\int d\vec{p}$$

$$\frac{J_n(k_\perp a_e)\vec{A}_n\cdot\vec{D}^{-1}\cdot\vec{I}_M^T}{\omega(\omega-[\vec{k}\cdot\vec{u}]_m^e)}\}, \qquad (27)$$

$$\tilde{n}_{ei}=\exp\{-i[\vec{k}\cdot\vec{x}'_0-k_\perp a'_i\cos\beta']\}\cdot\sum_{m=-\infty}^{\infty}(-i)^m e^{-im\beta'}(2\pi)$$

$$\cdot\delta(\omega-[\vec{k}\cdot\vec{u}']_m^i)\cdot Z\cdot\{\omega_{pe}^2 m_e\sum_{n=-\infty}^{\infty}\frac{J_n(k_\perp a_e)\vec{A}_n^e\cdot\vec{D}^{-1}\cdot\vec{I}_M^T}{\omega(\omega-[\vec{k}\cdot\vec{u}]_n^e)}\} \qquad (28)$$

where $\tilde{n}_{ee}$, $\tilde{n}_{ei}$ are the electron density fluctuations caused by a bare source electron and a bare source ion respectively.

Eqs. (27) and (28) manifest the picture of a Green function of bare source particle model. The first term of Eq. (27) is the

contribution from a "bare electron" . The second term of Eq. (27) and the right-hand side of Eq. (26) represent the contributions from those electrons shielding a bare electron and a bare ion, i. e. the shielding cloud of a bare source particle.

4. Scattering Spectrum

The scattering spectrum is normally written in terms of electron density fluctuations

$$S(\vec{k},\omega)=\frac{1}{TV}<|\tilde{n}_e(\vec{k},\omega)|^2>,\ \begin{matrix}T\to\infty,\\ V\to\infty,\end{matrix} \qquad (29)$$

where T is the average time, V is the scattering volume, and $<>$ represents the ensemble average.

Substituting Eqs. (27) and (28) into Eq. (29) and taking the ensemble average, we obtain the scattering spectrum for a magnetized plasma

$$\begin{aligned}S(\vec{k},\omega)=&2\pi\sum_{m=-\infty}^{\infty}\int d\vec{p}'\, f_{eo}(\vec{p}')\delta(\omega-[\vec{k}\cdot\vec{u}']_m^e)\\ &\cdot|J_m(k_\perp a'_e)+P_m^e(\vec{k},\omega,\vec{p}')|^2\\ &+2\pi Z\sum_{m=-\infty}^{\infty}\int d\vec{p}'\, f_{io}(\vec{p}')\delta(\omega-[\vec{k}\cdot\vec{u}']_m^i)|P_m^i(\vec{k},\omega,\vec{p}')|^2 \qquad (30)\end{aligned}$$

with

$$\begin{aligned}P_m^e(\vec{k},\omega,\vec{p}')&=\omega_{pe}^2 m_e\sum_{n=-\infty}^{\infty}\int d\vec{p}\frac{J_n(k_\perp a_e)\vec{A}_n^e\cdot\vec{D}^{-1}\cdot\vec{I}_M^T}{\omega(\omega-[\vec{k}\cdot\vec{u}]_n^e)},\\ P_m^i(\vec{k},\omega,\vec{p}')&=\omega_{pe}^2\sum_{m=-\infty}^{\infty}\int d\vec{p}\frac{J_n(k_\perp a_e)\vec{A}_n^e\cdot\vec{D}^{-1}\cdot\vec{I}_M^T}{\omega(\omega-[\vec{k}\cdot\vec{u}]_n^e)}, \qquad (31)\end{aligned}$$

Therefore, we have obtained a complete analytic expression of the scattering spectrum for a magnetized relativistic plasma.

Acknowledgement: This work was supported by the Association for Plasma Studies of China (APSC) and Exchange Programme of Asia-African Association for Plasma Training (AAAPT) and ICF

Studies of 863-416 Programme and a Grant of NNSFC.

References

[1] Bowles, K. L. , Phys. Rev Let. , 1(1958), 452.

[2] Salpeter, E. E. , ibid. , 120(1960), 1528.

[3] Dougherty, J. P. and Farley, D. T. , Proc. Roy, Soc. , 259 (1960),79.

[4] Rostoker, N. , Nuclear Fusion, 1(1961), 101.

[5] Rostoker, N. and Rosenbluth, M. N. , Phys, Fluids, 5 (1962), 776.

[6] Lu Q. K. Chinese Phys. Let. 10(1993) sup. 69.

[7] Ichimaru, S. , Ann. Phys. , Paris, 20(1962),78.

[8] Sheffield, I. , Plasma Scattering of Electromagnetic Radiation, Academic Press, New York, 1975.

Recent Progress of Nonlinear Simulation on the Toroidal Alfvén Eigenmode

Yasushi Todo and Tetsuya Sato

Theory and Computer Simulation Center
National Institute for Fusion Science
Oroshi-cho, Toki, Gifu 509-5292, Japan

ABSTRACT

Linear and nonlinear particle-magnetohydrodynamic (MHD) simulation codes are developed to study interactions between energetic ions and MHD modes. Energetic alpha particles with a slowing-down distribution are considered and the behavior of $n=2$ toroidal Alfven eigenmodes (TAE modes) is investigated with the parameters pertinent to the present large tokamaks. The linear simulation reveals the resonance condition between alpha particles and TAE mode. In the nonlinear simulation two $n=2$ TAE modes are destabilized and alpha particle losses induced by these TAE modes take place. Counter-passing particles are lost when they cross the passing-trapped boundary as a result of the interaction with the TAE modes. They are the major part of lost particles, but trapped particles are also lost appreciably.

I. INTRODUCTION

Successful confinement of energetic alpha particles is required for self-sustained operation of fusion reactors. The alpha particles born from D-T reactions are supposed to destabilize the toroidal Alfven eigenmode (TAE mode) [1]. Nonlinear behaviors of the TAE mode and alpha particles are one of the major uncertainties for fusion reactor physics. Mechanisms of alpha-particle losses induced by a single TAE mode are investigated by a Monte-Carlo simulation in Ref. 2. They found that crossing the passing-trapped boundary is a dominant process of the alpha particle loss induced by a single mode. They also found that the fraction of lost particles depends on the amplitude of the TAE mode. Thus, nonlinear evolutions of TAE mode and alpha particles must be known for designing a fusion reactor.

Recently, theoretical and computational studies have shown that wave-trapping of resonant particles works as a saturation mechanism of a single TAE mode[3-6]. It is, however, not clear that the wave-trapping works as the dominant saturation mechanism when a large number of TAE modes are destabilized. For larger tokamaks such as the ITER high-n TAE modes are predicted to be most dangerous [7, 8]. With a relevant q profile a large number of TAE modes can be destabilized simultaneously. In such cases resonance-overlap is predicted to take place [9] and wave-trapping will be prevented by other modes. Therefore, MHD nonlinearities yet survive as potential candidates for saturation mechanism of TAE modes [10, 11].

This gives us a sufficient motivation to do a nonperturbative simulation with full nonlinear MHD equations. We developed linear and nonlinear particle-MHD simulation codes. We employ a kinetic-MHD hybrid model [12, 5] where plasma is divided into two parts, i.e., alpha particles and background plasma. The particle simulation method is used for the alpha particle component. The background plasma is described by an MHD fluid model, and the MHD equations are solved by a finite difference method. In this paper, we describe the results of linear and nonlinear particle-MHD simulations. We demonstrate that the two codes are useful tools for solving the alpha-TAE dynamics.

Compared with previous works [4, 5], the present work has an advantage that a more realistic alpha particle distribution is considered. Linear [13] and nonlinear [14, 15] δf methods enable us to use a slowing-down distribution which is isotropic in the velocity space. Realistic alpha particle distribution is really indispensable to the study of alpha particle losses.

First, we carry out a linear simulation to analyze the TAE mode structure and the resonance condition. Resonance condition is important to understand alpha particle losses

in the nonlinear simulation. Then, nonlinear simulations are carried out for two cases where the initial alpha particle pressure is changed. Alpha particle losses induced by TAE modes are investigated.

In the remainder of this paper, results of linear particle-MHD simulation are described in section 2. Resonance condition of alpha particles with TAE mode is investigated. Section 3 is for the results of nonlinear particle-MHD simulation. Summary is given in section 4. Plasma model and numerical method are described in Ref. 13 and Ref. 16.

II. LINEAR SIMULATION

The initial condition is an MHD equilibrium where the total plasma beta is 4% at the magnetic axis and its volume-average $<\beta_\alpha>$ is 0.88%. The initial alpha particle distribution is the slowing-down distribution which is isotropic in the velocity space with the maximum energy of 3.5 MeV. Particles are distributed from 0.1 MeV to 3.5 MeV. The magnetic field at the magnetic axis is 5T, the number density of the background plasma is $10^{20}m^{-3}$, the minor radius is 0.9m, and the aspect ratio is 3. With these parameters velocity of an alpha particle with energy of 1 MeV is equal to the Alfven velocity. The cylindrical coordinate system (R, φ, z) is used. The simulation region is $2a < R < 4a$, $-a < z < a$ where a is the minor radius. The magnetic axis locates at $R = R_0 = 3.20a$, $z=0$. The q-profile is shown in Fig. 1 with the poloidal harmonics of the most unstable $n=2$ TAE mode which is discussed in the next section.

This linear simulation technique has an advantage against the nonlinear δf technique in that it is less demanding in CPU time and memory. The number of used particles is 2.6×10^5 in the linear simulation, which is much less than 4.0×10^6 in the nonlinear simulation. Used grid numbers for the poloidal plane are (65, 65). The volume average beta of alpha particles for this linear simulation is 0.44%.

The linear simulation gives the fastest growing mode for each toroidal mode number. For $n=2$ mode, we find that the $n=2$ TAE mode which consists mainly of $m=2$ and $m=3$ components has the largest growth rate. In Fig. 1 shown are radial profiles of the dominant poloidal harmonics for this $n=2$ TAE mode. The real frequency ω_0 is $0.36\omega_A$ which is lower by $0.04\omega_A$ than the gap-center

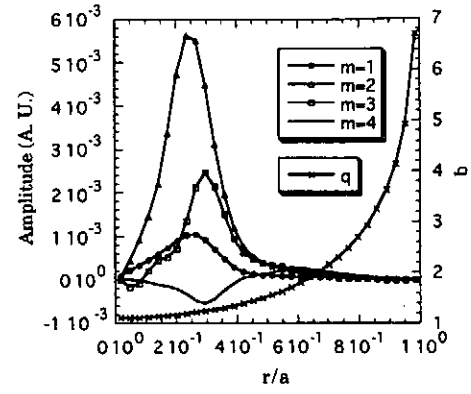

Fig. 1. Radial profiles of the dominant poloidal harmonics of the electrostatic potential for the most unstable $n=2$ TAE mode.

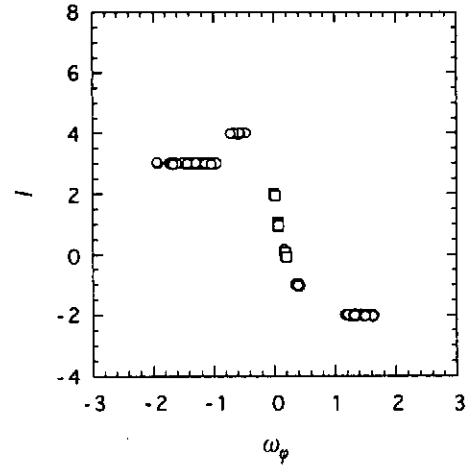

Fig. 2. Resonance condition of alpha particles to the most unstable $n=2$ TAE mode for top 2000 particles. Circles denote passing particles and squares denote trapped particles.

at $q=5/4$.

We can also investigate the resonance condition of alpha particles with the TAE mode. We expect that the resonance condition is given by,

$$\omega_0 - n\omega_\varphi - l\omega_\theta = 0\,, \qquad (1)$$

or

$$l = (\omega_0 - n\omega_\varphi)/\omega_\theta\,, \qquad (2)$$

where ω_θ, ω_φ, and l are the poloidal, toroidal frequency of each particle, and an arbitrary integer.

In order to investigate whether Eq. (2) is actually satisfied or not, we examine the poloidal and toroidal frequency of each particle. Particles are put in the order of the energy-transfer to the TAE mode. We pick up top 2000 particles which covers 67% of the total energy-transfer and calculate l according to Eq. (2). The results are shown in

Fig. 2. It can be seen that these strongly resonating particles have the values of l actually close to integers. We should notice that not only passing particles but also trapped particles are resonating with the TAE mode. This is an important point for the particle losses discussed in the next section. The energy transfer from trapped particles accounts for 37% of the total energy transfer.

III. NONLINEAR SIMULATION

Nonlinear simulations have been carried out for two initial alpha pressures, 0.33% and 0.66%. We use a finite difference method of fourth order accuracy in space and time for MHD variables with (65, 16, 65) grid points for (R, φ, z) coordinates, respectively. The simulation domain in the toroidal direction is $0<\varphi<\pi$ since we focus on the $n=2$ TAE modes.

Time evolutions of amplitude of the $(m=2, n=2)$ component of δB_r at $r=0.25a$ magnetic surface is shown in Fig. 3. For $<\beta_\alpha>=0.66\%$ the amplitude shows an oscillatory behavior after $t=400\ \omega_A^{-1}$. Frequencies of $(m=2, n=2)$ component for two cases are analyzed. In both cases one peak locates at $\omega=0.36\omega_A$ which indicates that the TAE mode which is investigated with the linear simulation is destabilized in both cases. In addition to it, another mode is excited at $\omega=0.22\omega_A$ for $<\beta_\alpha>=0.66\%$. This frequency is lower by $\omega=0.06\omega_A$ than the gap-center of $(m=3, n=2)$ and $(m=4, n=2)$ modes at $q=7/4$. The oscillation of the amplitude in Fig. 3 is a beat between these two modes.

From poloidal harmonics of the simulation result at $t=890\omega_A^{-1}$ those at $t=198\omega_A^{-1}$ are subtracted. The residual poloidal harmonics are shown in Fig. 4. These dominant harmonics are $m=3$ and $m=4$ which peak around $q=7/4$ surface. These poloidal harmonics and the frequency mentioned above strongly suggest that the new mode is another $n=2$ TAE mode. It is interesting to note that such coexistence of multiple TAE modes with the same toroidal mode number will be popular for high toroidal mode numbers, since TAE modes spatially peak close to each other.

In these two cases saturation mechanism is the wave-particle trapping. In Fig. 5 shown is time evolution of the ratio of half energy transfer rate to energy of $n=2$ MHD modes.

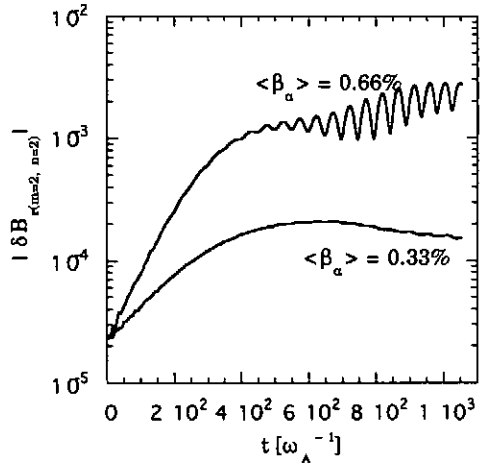

Fig. 3. Time evolution of $(m=2, n=2)$ component of δB_r on $r=0.25a$ magnetic surface for $<\beta_\alpha>=0.33\%$ and 0.66%.

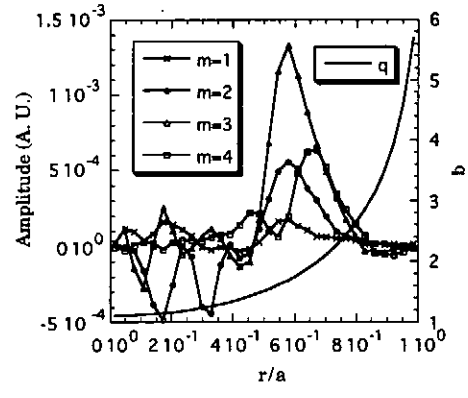

Fig. 4. Radial profiles of the dominant poloidal harmonics of the electrostatic potential for the second unstable $n=2$ TAE mode.

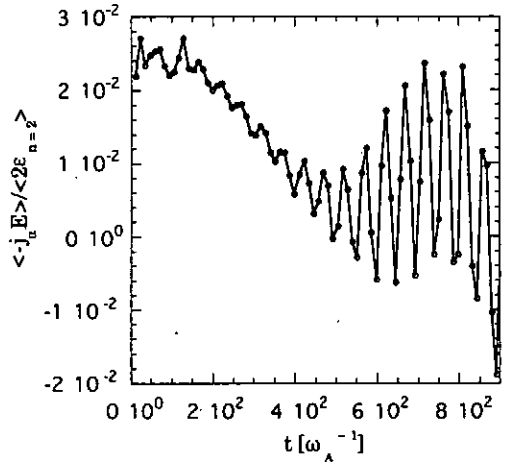

Fig. 5. Time evolution of the ratio of half energy transfer rate to energy of $n=2$ MHD modes for $<\beta_\alpha>= 0.66\%$.

We can see that decrease in the energy transfer leads to saturation of TAE instability in both cases. Though for $<\beta_\alpha>=0.66\%$ the ratio behaves in a complicated manner with two TAE modes in Fig. 5, as well as for $<\beta_\alpha>=0.33\%$ decrease in the ratio leads to entire saturation. In addition to the energy transfer rate, we confirmed the spatial flattening in alpha particle density which reduces the free energy source of the instability.

TAE-induced alpha particle losses took place in nonlinear simulation. The number ratio of lost particles to total alpha particles for $<\beta_\alpha>=0.33\%$, and 0.66% are 1.4×10^{-5} and 1.2×10^{-2}, respectively. The saturation level differs from each other by one order of magnitude. The number of lost particles, however, differs by three orders of magnitude.

Distribution of TAE-induced lost-particles for $<\beta_\alpha>=0.66\%$ in the initial minor radius and pitch angle is shown in Fig. 6. Lost particles can be classified into three types; 1) counter-passing particles which cross the passing-trapped boundary just before the encounter to the wall, 2) trapped particles, 3) passing particles other than the first type. Percentage of each type to the total number of lost particles is 63%, 26%, and 11%, respectively. Lost particles locate around the passing-trapped boundary in the phase space. It is clear that the main loss mechanism is counter-passing particles' crossing the passing-trapped boundary in the phase space. It is consistent with the results of test particle simulation in Ref. 2. It must be noted, however, that the trapped particles near this boundary are also lost in addition to the counter-passing particles. This is reasonable from the linear simulation result that trapped particles also resonate with the TAE mode.

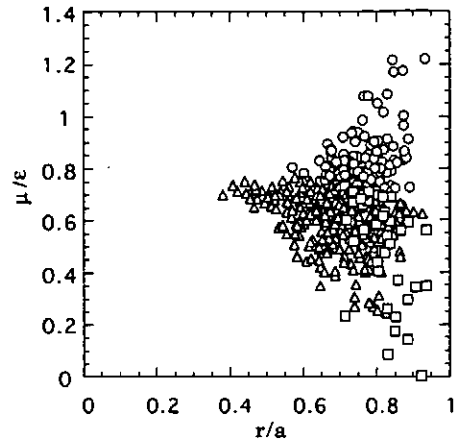

Fig. 6. Initial distribution of lost alpha particles in the $(r, \mu/\varepsilon)$ plane, where μ and ε are magnetic moment and energy. Triangles denote counter-passing particles which cross the passing-trapped boundary. Circles and squares denote trapped particles and the other passing particles, respectively.

IV. SUMMARY

In this paper we proposed new linear and nonlinear particle-MHD simulation codes and demonstrated that they are useful tools for study of linear and nonlinear TAE dynamics such as mode structure, resonance condition, and alpha particle losses. Resonance condition of alpha particles with the TAE mode is studied with linear simulation. Resonance condition $\omega_0 - n\omega_\varphi - l\omega_\theta = 0$ (l: integer) is satisfied for strongly resonating particles. Weakly resonating particles fill gaps between strongly resonating particles in the ω_φ - l plane. Not only passing particles but also trapped particles resonate with TAE mode.

Nonlinear simulations are carried out for $<\beta_\alpha>$ of 0.33% and 0.66%. An $n=2$ TAE mode whose dominant poloidal harmonics are $m=2$ and $m=3$ is destabilized in both cases. For $<\beta_\alpha>=0.66\%$ another $n=2$ TAE mode whose dominant poloidal harmonics are $m=3$ and $m=4$ is destabilized in addition to the most unstable mode. Such coexistence of multiple TAE modes with the same toroidal mode number will be popular for high toroidal mode numbers, since each TAE mode peaks close to one another. It is expected that the resonance-overlap will take place when many TAE modes are destabilized. If the resonance-overlap takes place, the wave-trapping will not work as the dominant saturation mechanism. We believe that saturation level and saturation mechanism should be studied with nonlinear MHD equations. The nonlinear particle-MHD simulation code presented in this paper is a useful tool for future studies on multiple TAE modes.

Alpha particles are lost by TAE modes in the nonlinear simulation. Distribution of the lost particles in the initial phase space is analyzed. Counter-passing particles are the major part of lost particles. They cross the passing-trapped boundary as a result of the

interaction with the TAE modes, and become trapped particles on fat banana orbits which are eventually connected to the boundary. Trapped particles are also lost. It is consistent with the results of linear simulation that trapped particles also resonate with TAE mode.

ACKNOWLEDGMENTS

The authors would like to express their thanks to all members of the Complexity Simulation Group for useful discussions. Numerical computations are performed at the Advanced Computing System for Complexity Simulation of National Institute for Fusion Science. This work is partially supported by Grants-in-Aid of the Ministry of Education, Science and Culture (No. 07832024, No. 07858057, and No. 09878090).

REFERENCES

[1] C. Z. Cheng and M. S. Chance, Phys. Fluids **29**, 3659 (1986).
[2] D. J. Sigmar, C. T. Hsu, R. White, and C. Z. Cheng, Phys. Fluids **B4**, 1506 (1992).
[3] B. N. Breizman, H. L. Berk, and H. Ye, Phys. Fluids **B5**, 3217 (1993).
[4] G. Y. Fu, and W. Park, Phys. Rev. Lett. **74**, 1594 (1995).
[5] Y. Todo, T. Sato, K. Watanabe, T. H. Watanabe, and R. Horiuchi, Phys. Plasmas **2**, 2711 (1995).
[6] Y. Wu, R. B. White, Y. Chen, and M. N. Rosenbluth, Phys. Plasmas **2**, 4555 (1995).
[7] C. Z. Cheng, R. V. Budny, L. Chen, M. S. Chu, D. S. Darrow, E. D. Fredrickson, G. Y. Fu, T. S. Hahm, C. T. Hsu, E. Mazzucato, H. E. Mynick, R. Nazikian, W. Park, N. Pomphrey, D. J. Sigmar, R. B. White, Y. Wu, S. J. Zweben, in *Plasma Physics and Controlled Nuclear Fusion Research* 1994 (IAEA, Vienna, 1996), Vol. III, p.373.
[8] J. Candy and M. N. Rosenbluth, Nucl. Fusion **35**, 1069 (1995).
[9] H. L. Berk, B. N. Breizman, and M. Pekker, Phys. Plasmas **2**, 3007 (1995).
[10] D. A. Spong, B. A. Carreras, and C. L. Hedrick, Phys. Plasmas **1**, 1503 (1994).
[11] F. Zonca, F. Romanelli, G. Vlad and C. Kar, Phys. Rev. Lett. **74**, 698 (1995).
[12] W. Park, S. Parker, H. Biglari, M. Chance, L. Chen, C. Z. Cheng, T. S. Hahm, W. W. Lee, R. Kulsrud, D. Monticello, L. Sugiyama, and R. White, Phys. Fluids **B4**, 2033 (1992).
[13] Y. Todo and T. Sato, *submitted to* J. Comput. Phys.
[14] A. M. Dimits and W. W. Lee, J. Comput. Phys. **107**, 309 (1993).
[15] S. E. Parker and W. W. Lee, Phys. Fluids **B5**, 77 (1993).
[16] Y. Todo, T. Sato, and the Complexity Simulation Group, in *Fusion Energy Conference* 1996 (IAEA, Vienna, 1997), *in press*.

Effects of the Safety Factor Profile on the Ion Temperature Gradient Mode in Tokamak Plasmas

Xiaodong Peng, Jinghua Zhang, Qingdi Gao

(Southwestern Institute of Physics, Chengdu 610041, P.O.Box 432, China)

Recently, it has been discovered that the profile of safety factor plays an important role in plasmas confinement in tokamak[1, 2]. One characteristic of the enhanced confinement with reversed magnetic shear(ERS mode) is that the profile of safety factor is a nonmonotonic function. Usually, the safety factor is only approximated by a linear function in dealing with plasma instabilities[3, 4]. So, it is necessary that we investigate the instability in the presence of nonmonotonic safety factor.

The drift-like instability driven by the ion temperature gradient(ITG) is currently the most plausible candidate for explaining the anomalous ion energy transport in tokamak plasmas. Numerous studies on this mode have been carried out theoretically and experimentally in the last decade. But most of these investigations have been confined to plasmas with monotonic safety factor. In this paper, we will study the effects of safety factor profile on ITG mode. On DIII-D tokamak, the high toroidal velocity shear was observed in the region where the confinement is improved[3]. So, the effects of the toroidal velocity must be taken into account.

The instabilities driven by ITG in the presence of the parallel velocity are described by the ion continuity equation, ion parallel velocity evolution equation, and ion pressure evolution equation, respectively[4]. In cylindrical geometry, the linearized equations are

$$\frac{\partial}{\partial t}(1-\nabla_{\perp}^2)\phi+v_D\left[1+\left(\frac{1+\eta_i}{\tau}\right)\nabla_{\perp}^2\right]\frac{\partial}{r\partial\theta}\phi+\nabla_{\parallel}v_{\parallel}=0, \tag{1}$$

$$\frac{\partial}{\partial t}v_{\parallel}+v_*\frac{\partial}{r\partial\theta}\phi=-\nabla_{\parallel}\phi-\nabla_{\parallel}p, \tag{2}$$

$$\frac{\partial}{\partial t}p+v_D\left(\frac{1+\eta_i}{\tau}\right)\frac{\partial}{r\partial\theta}\phi=-\frac{\Gamma}{\tau}\nabla_{\parallel}v_{\parallel}, \tag{3}$$

where $v_*=-(T_e/eBc_s)dv_{\parallel 0}/dx$, $v_D=-(T_e/eB)d\ln n_0/dx$, $\tau=T_e/T_i$, $\eta_i=d\ln T_i/d\ln n_0$, and ϕ, $v_{\parallel}$, and p are, respectively, normalized by T_e/e, c_s,and n_0T_e, and spatial scales are normalized by ρ_s. Here, Γ is the ratio of parallel specific heat. The other symbols have their usual meanings. The perturbation quantities are assumed to be of the form

$$f(x,\theta,\zeta,t)=\sum_k f_k(x)\exp[-i\omega t+i(m\theta-n\zeta)], \tag{4}$$

where θ and ζ are poloidal and toroidal angles, respectively. k represents the poloidal and toroidal number (m,n). The radial coordinate $x=r-r_s$, with such that the safety factor $q(r_s)=m/n$. Then, we obtain the parallel gradient operator of a perturbation quantity as

$$\nabla_{\parallel}=iB^{-1}\left(m\frac{B_\theta}{r}-n\frac{B_\zeta}{R}\right)=ik_y\frac{r}{Rq(r_s)}\left(\frac{q(r_s)}{q(r)}-1\right), \tag{5}$$

where $k_y=m/r$. Usually, the safety factor is a monotonic function of radial coordinate x, i.e., we only need the value of magnetic shear. In order to include the nonmonotonic effects, the safety factor must be expanded as

$$q(r)=q(r_s)+q'(r_s)x+q''(r_s)x^2/2+\cdots. \tag{6}$$

Especially, in the case of low magnetic shear, i.e., $q'(r_s)\approx 0$, the second order term of x must been taken into account. So, we obtain the operator

$$\nabla_{\parallel}\approx -ik_y\frac{r}{Rq(r_s)}\left[\frac{q'(r_s)}{q(r_s)}x+\left(\frac{q''(r_s)}{2q(r_s)}-\frac{q'^2(r_s)}{q^2(r_s)}\right)x^2\right]. \tag{7}$$

Employing the Eqs. (1), (2), (3), (4), and (7), we obtain the following eigen-equation

$$\frac{d^2}{dx^2}\phi_k + V(x,\omega)\phi_k = 0, \tag{8}$$

where the "potential" function is given by

$$V(x,\hat{\omega}) = -k_y^2 + \frac{1-\hat{\omega}}{\hat{\omega}+K} + \frac{\hat{k}_\parallel'^2(r_s)x^2}{\hat{\omega}^2 - (\Gamma/\tau)\hat{k}_\parallel'^2(r_s)x^2} + \frac{\hat{\omega}_*\hat{\omega}[\hat{k}_\parallel'(r_s)x + \hat{k}_\parallel''(r_s)x^2/2]}{(\hat{\omega}+K)[\hat{\omega}^2 - (\Gamma/\tau)\hat{k}_\parallel'^2(r_s)x^2]}, \tag{9}$$

with

$$\hat{k}_\parallel'(r_s) = -\frac{rq'(r_s)}{v_D Rq^2(r_s)}, \qquad \hat{k}_\parallel''(r_s) = -\frac{r}{v_D Rq^2(r_s)}\left(q''(r_s) - \frac{2q'^2(r_s)}{q(r_s)}\right), \qquad \hat{\omega} = \omega/k_y v_D,$$

$\hat{\omega}_* = \omega_*/k_y v_D$, $K = (1+\eta_i)/\tau$.

Using WKB method, Equation (8) can be solved numerically. Figure 1 shows the mode growth rate as function of $\hat{k}_\parallel''(r_s)$. We can see that the mode is stable in the region of much lower $\hat{k}_\parallel''(r_s)$. Meanwhile, we may see also that if the shear of parallel velocity increases the region of stability will be widen.

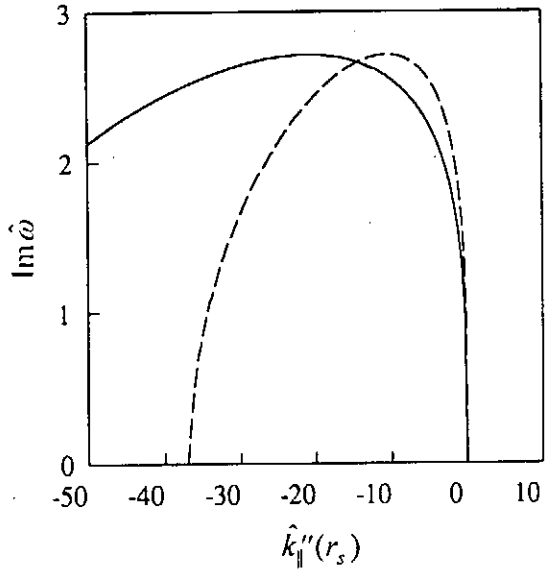

Fig.1. Mode growth rate as function of $\hat{k}_\parallel''(r_s)$ for i) $\hat{\omega}_* = 4$ (solid line), and ii) $\hat{\omega}_* = 8$. The other parameter are $k_y^2 = 0.01$, $\hat{k}_\parallel' = 0$, $\tau = 1$, $\eta_i = 3$, and $\Gamma = 0$.

Figure 2 is another curve of mode growth rate. This figure indicates that the role of $\hat{k}_\parallel'(r_s)$ is increasing the mode instability. The calculation also indicates that the mode of high radial mode number is stable.

From the properties of mode growth rate shown by Figure (1) and (2), we can explain the ERS phenomenon observed in the DIII-D tokamak experiment qualitatively. In the region of negative magnetic shear, there exists a much higher parallel velocity shear($\hat{\omega}_* >> 0$). So if

only $q''(r_s) >> 2q'^2(r_s)/q(r_s)$, that is $\hat{k}_{\parallel}''(r_s) << 0$, the ITG mode is stable. The anomalous ion energy transport is suppressed in this region. But in the region of positive magnetic shear, the parallel velocity shear is much lower. The ITG mode is usually unstable in this region. So, the enhanced confinement is observed in the region of negative magnetic shear.

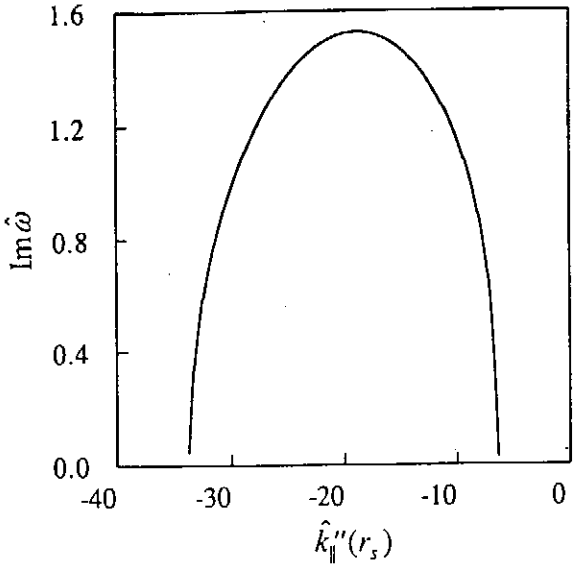

Fig.2. Mode growth rate as function of $\hat{k}_{\parallel}''(r_s)$ for $\hat{\omega}_* = 8$, $k_y^2 = 0.01$, $\hat{k}_{\parallel}' = 10$, $\tau = 1$, $\eta_i = 3$, and $\Gamma = 0.01$.

In a conclusion, we have studied the effects of the safety factor profile on the ITG mode in tokamak plasmas. The results show that the coupling of the profile of safety factor with the parallel velocity shear modifies the shape of potential function of mode equation. And this can make the ITG mode stabilize. In the region of negative magnetic shear and high parallel velocity shear, the enhanced confinement have been explained qualitatively.

This work is supported by the Nuclear Science Foundation of China under Grant No.J94c03031.

[1] F.M.Levinton *et al.*, *Phys. Rev. Lett.* **75**, 4417(1995)

[2] E.J.Strait *et al.*, *Phys. Rev. Lett.* **75**, 4421(1995)

[3] J.Q.Dong *et al.*, *Phys. Plasmas* **3**,3065(1996)

[4] N.Mattor *et al.*, *Phys. Fluids* **31**, 1180(1988)

The plug potential formation and ion axial transport in a tandem mirror

I.Katanuma, R.Minai, Y.Kiwamoto, Y.Tatematsu, K.Ishii, T.Saito, T.Tamano and K.Yatsu
Plasma Research Center, University of Tsukuba
Ibaraki 305, Japan

The plug potential is formed experimentally even without high energy sloshing ion population in the end-mirror cells of a tandem mirror. It is shown theoretically that the plug potential can be formed in the present experimental conditions by using the plausible distribution functions of ion and electron and a little of ionization source. In this paper the required ionization source is estimated for the continuous potential profile around the plug as a first topic.
The axial transport is investigated by Monte-Carlo simulation as a second topic. The ion end-loss spectrum is used to estimate the height of plug potential and ion temperature in the tandem mirror experiments. The Monte-Carlo simulation reveals that the ion temperature measured from ion end-loss spectrum deviates from the field ion temperature.

The original scenario of the plug potential formation requires the high energy sloshing ions as well as the populations of electrostatically trapped warm electrons and magnetically trapped high energy electrons. The present tandem mirror experiments, however, form the plug potential without the population of sloshing ions.

We have proposed the mechanism of the plug potential formation in a tandem mirror.[1-3] That is, the plug potential is formed by the charge neutrality condition of ions, some of which come from the central cell and others are trapped magnetically in the thermal barrier region and a little of ionized ions, and electrons, some of which come from the central cell and the remains are trapped electrostatically in the plug region.

At the point of the potential maximum, there are ion flows coming from the central cell and the barrier. On the other hand the electrons are prevented by the potential from escaping to the end-wall. The situation around the plug region, therefore, is the same as that of sheath potential formation, which leads to the discontinuity of potential profile.

The magnitude of the calculated potential jump at the plug is rather smaller than that of the sheath potential typically formed in front of the absorbed conducting wall. The existence of ions reflected at the outer mirror throat makes the potential jump lower. Because the discontinuity of the electrostatic potential at the plug is considered to be unrealistic, we seek the condition that the jump of potential does not appear.

We have introduced the distribution function of ions, which come from end-wall toward the central cell, in order that the distribution function is continuous across the line $\varepsilon = \mu B_p + e\phi_p$ in the velocity space, where ε, μ are energy, magnetic moment, and B_p, ϕ_p are the heights of magnetic field and potential at the plug. This distribution function makes the potential continuous around the plug region.[3]

We, therefore, have concluded that the small amount of ions which are born around the plug region plays an important role in the formation of the plug potential without discontinuity. This distribution function, which is assumed as that of ionized ions, however, is not realistic because these ions have a high perpendicular energy, which is almost the same as that of passing ions, around plug. We, therefore, adopt the Emmert source[4] as an ionization source, which is considered to be a plausible source term in the sheath potential formation.

$$S_i(z,\varepsilon,\mu) = <\sigma v> n_e n_0 \frac{m_i^2}{4\pi T_{ni}^2} v_\parallel(z,\varepsilon,\mu) \times \exp\left\{-\frac{\varepsilon - e\phi(z)}{T_{ni}}\right\} . \quad (1)$$

Here $<\sigma v>$ is the ionization rate coefficient, n_e, n_0 are the densities of the electrons and neutral atoms, respectively, T_{ni} is the temperature of neutral atoms. The variable $v_\parallel$ is the velocity along magnetic field line which is given in term of ε and μ to be $v_\parallel(z,\varepsilon,\mu) = (2\{\varepsilon - \mu B(z) - e\phi(z)\}/m_i)^{1/2}$.

The ion distribution function of ionized ions is obtained by the source term (1),

$$\begin{aligned} f_{ioni}(\varepsilon,\mu) = &\int_{z_p}^{z} \mathrm{d}z_0 \frac{S_i(z_0,\varepsilon,\mu<\mu_x)}{v_\parallel(z_0,\varepsilon,\mu)} \\ &+ \int_{z_{turn}(\varepsilon,\mu)}^{z} \mathrm{d}z_0 \frac{S_i(z_0,\varepsilon,\mu\geq\mu_x)}{v_\parallel(z_0,\varepsilon,\mu)} \\ &+ \int_{z}^{z_m} \mathrm{d}z_0 \frac{S_i(z_0,\varepsilon,\mu\geq\mu_x)}{v_\parallel(z_0,\varepsilon,\mu)} \\ &+ \int_{z}^{z_{turn}(\varepsilon,\mu)} \mathrm{d}z_0 \frac{S_i(z_0,\varepsilon,\mu<\mu_x)}{v_\parallel(z_0,\varepsilon,\mu)} , \end{aligned} \quad (2)$$

where z_{turn} and μ_x satisfy, respectively,

$$\varepsilon = \mu B(z_{turn}) + e\phi(z_{turn}) , \quad \mu_x = \frac{e\phi(z) - e\phi(z_0)}{B(z_0) - B(z)} . \quad (3)$$

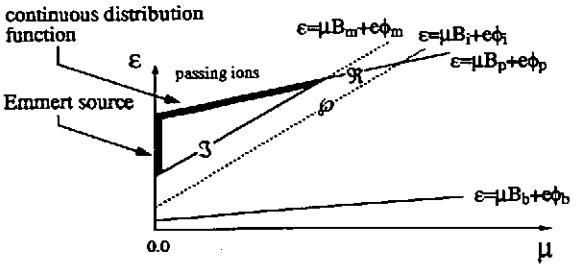

Figure 1: Diagram of ion velocity space.

Here z_0 is the axial coordinate where ions are born.

The distribution function f_{ioni} is localized the dark painted region where is pointed by an arrow, in the velocity space in Fig.1. So the ion distribution is discontinuous across the line $\varepsilon = \mu B_p + e\phi_p$. The ion and electron distribution functions in the other region are given, respectively,

$$f_i = n_{ic}\left(\frac{m_i}{2\pi T_i}\right)^{3/2} \exp\left\{-\frac{\varepsilon - e\phi_i}{T_i}\right\}, \quad (4)$$

in the region $v_\parallel \geq 0$ and $\varepsilon \geq \mu B_i + e\phi_i$ and $\varepsilon \geq \mu B_p + e\phi_p$, and

$$f_i = n_{ic}\left(\frac{m_i}{2\pi T_i}\right)^{3/2} \exp\left\{\frac{\varepsilon - e\phi_i - \alpha_i \mu B_i}{(\alpha_i - 1)T_i}\right\}, \quad (5)$$

in the region $\varepsilon < \mu B_i + e\phi_i$ and $\varepsilon \geq \mu B_p + e\phi_p$. The distribution function of Yushmanov trapped ion between $z_p \leq z \leq z_m$ is

$$f_i = n_{ip}\left(\frac{m_i}{2\pi T_i}\right)^{3/2} \exp\left\{\frac{\varepsilon - e\phi_p - \alpha_x \mu B_p}{(\alpha_x - 1)T_i}\right\}, \quad (6)$$

where $n_{ip} \equiv n_{ic}\exp\{-(\phi_p - e\phi_i)/T_i\}$. Here suffixes i, m, p represent the quantity at inner mirror throat, outer mirror throat and plug, respectively.

The electron distribution function f_e is assumed to be

$$f_e = n_{eb}\left(\frac{m_e}{2\pi T_e}\right)^{3/2} \exp\left\{-\frac{\varepsilon + e\phi_b}{T_e}\right\}, \quad (7)$$

in the region $\varepsilon \geq \mu B_b - e\phi_b$, and

$$f_e = n_{eb}\left(\frac{m_e}{2\pi T_e}\right)^{3/2} \exp\left\{-\frac{\varepsilon + e\phi_b - \alpha_e \mu B_b}{(1 - \alpha_e)T_e}\right\}, \quad (8)$$

in the region $\varepsilon < \mu B_b - e\phi_b$, where $n_{eb} \equiv n_{ic}\exp\{e(\phi_b - \phi_i)/T_e\}$, and the suffix b represents the quantity at the thermal barrier region. Here the electron distribution function (7) and (8) is applied in the region $z_b \leq z \leq z_m$ in Fig.1. The electrons are assumed to be Maxwellian in a part which comes from the central cell. The fundamental electron cyclotron resonance heating (ω_{ce}ECRH) is assumed to be applied at the point $B/B_b = 2$, so that the electrons trapped in the plug potential are assumed to be non-Maxwellian distribution in (8).

The parameters α_i, α_x and α_e describe the degree to which trapped-particle phase space is filled. This type of distribution function is a simplest distribution function which has the effect of non-Maxwellian distribution but is analytically integrable in velocity space.

Figure 2 shows the axial potential profiles calculated on the assumption of charge neutrality condition by using the ion and electron distribution functions. The plug is assumed to be located at the axial position $B_p/B_b = 2$. The magnetic field axial profile is adopted that of GAMMA10 end-mirror cell. The magnitude of the potential $z = z_m$ must be given in advance in order to determine the potential profile. So the different potential profiles in Fig.2 correspond to the different boundary conditions of ϕ at $z = z_m$. The continuous potential is found to exist only in the range of ϕ_m given in Fig.2 in the calculation, where ϕ_m is the ϕ at $z = z_m$. For example, when the magnitude of $e\phi_m/T_i$ is larger than 1.9 or is smaller than 1.3, the continuous potential is not determined in Fig.2. It is seen that $d\phi/dz = 0$ at $z = z_p$, where the maximum of potential exists.

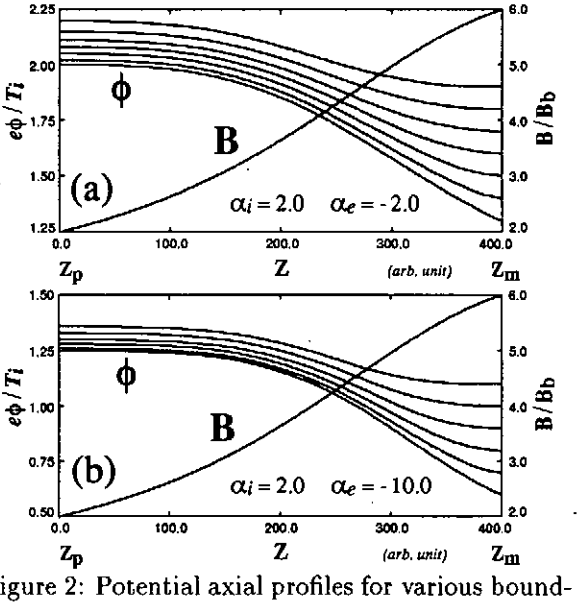

Figure 2: Potential axial profiles for various boundary condition of ϕ_m

In Fig.2 the distribution function f_{ioni} in (2) resulting from ionization is taken into account. If there is no ionization around plug the potential jump (sheath potential) appears at $z = z_p$. We have assumed $T_{ni}/T_i = 0.01$ in the calculation. The density of ionized ions is extremely smaller than that of the passing and trapped ions so that the density profile does not change due to the inclusion of the effects of ionization. The height of the potential de-

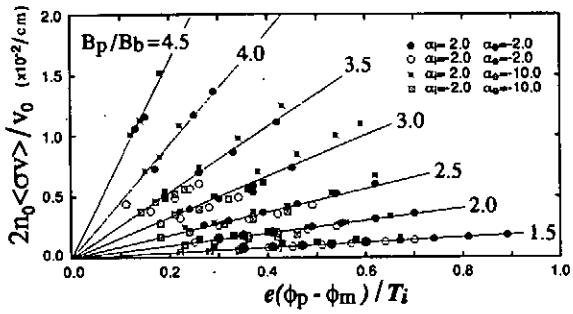

Figure 3: Required ionization rate for various α_i, α_e and B_p/B_b. Here $v_0 = (2T_{ni}/m_i)^{1/2}$.

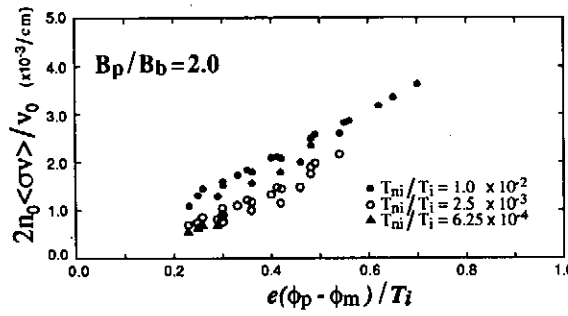

Figure 4: Required ionization rate for various α_i, α_e in the case of $B_p/B_b = 2$

pends on the coefficients of α_i and α_e as well as the magnitude of ϕ.

The required ionization rate for the formation of the continuous potential profile is shown in Fig.3 for various B_p/B_b. As is seen in the figure the ionization rate is almost proportional to the quantity $e(\phi_p - \phi_m)/T_i$, but is independent of the coefficients α_i, α_e. The magnitudes of B_p and ϕ_p are, of course, a function of α_i and α_e, so that the required ionization rate should be a function of α_i and α_e. The results in Fig.3 indicate that the required ionization rate is a function of $e(\phi_p(\alpha_i, \alpha_e) - \phi_m)/T_i$ and $B_p(\alpha_i, \alpha_e)/B_b$. When the plug locates at higher magnetic field, i.e., larger B_p/B_b, the larger ionization is required to avoid the sheath potential formation. This is due to that the potential profile around plug is flatter for the lower B_p/B_b.

Figure 4 shows that the required ionization rate in the case of $B_p/B_b = 2$. The different temperatures of neutral atoms T_{ni}/T_i are plotted in the figure. The lower temperature T_{ni} requires the lower ionization rate for the continuous potential profile.

Now we estimate the required ionization rate in the GAMMA10 tandem mirror. As seen in Fig.4 the condition $2n_0 < \sigma v > /v_0 \gtrsim 10^{-3}/\mathrm{cm}$ should be satisfied for the continuous potential formation around plug in the case of $B_p/B_b = 2$. That is, $n_0 < \sigma v >$ should be larger than $1.2 \times 10^3/sec$ with the assumption of $T_{ni} = 3\mathrm{eV}$ of Hydrogen atoms. Defining the ionization time $\tau_{ioni} \equiv 1/(n_0 < \sigma v >)$, we obtain the condition $\tau_{ioni} \lesssim 8.3 \times 10^{-4}$sec for the continuous potential formation.

In summary of first topic it is found that the plug potential can be formed in ion and electron distribution functions in a wide range of anisotropy. Emmert source was adopted as an ionization term. The ionization time $\tau_{ioni} \lesssim 1.0 \times 10^{-3}$sec is necessary for the potential to be continuous across the plug, i.e., to be formed without sheath potential formation. The required value of τ_{ioni}, however, is much shorter than that expected in GAMMA10. The different mechanism playing the role of ionized ions, therefore, should be suggested. The ion distribution function in dark painted region in Fig.1, which is shown by arrow with comment of "continuous distribution function", is expected to be supplied, for example, by the oscillation of the plug potential.

As a second topic, we present the ion axial transport in the GAMMA10 tandem mirror. The ion end-loss spectrum is an important information in order to determine the height of plug potential and ion temperature in the central cell. We carried out the Monte-Carlo simulation in the square well types of magnetic mirror and potential axial profiles.[5)]

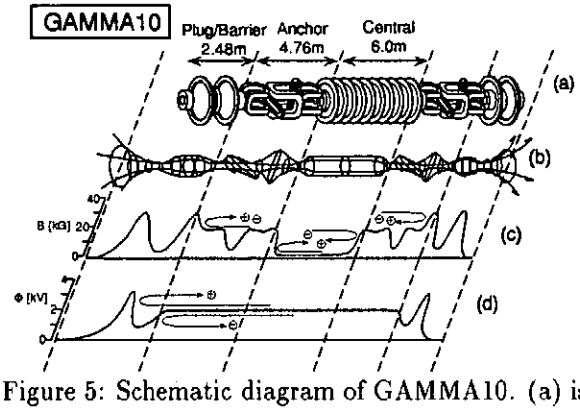

Figure 5: Schematic diagram of GAMMA10. (a) is the bird's eye view of GAMMA10 coil system, (b) is the magnetic flux tube, (c) is the axial profile of the magnetic field and (d) is the expected axial profile of electrostatic potential.

In this paper we carry out the simulation in the geometry of GAMMA10 tandem mirror, schematic diagram of which is shown in Fig.5. Basic equations used in the code are

$$\begin{aligned}
\frac{d\psi}{dt} &= -\left(c\frac{\partial\phi}{\partial\theta} + \frac{c}{e}\kappa_\theta\,(2\varepsilon - \mu B - 2e\phi)\right)\,, \\
\frac{d\theta}{dt} &= c\frac{\partial\phi}{\partial\psi} + \frac{c}{e}\kappa_\psi\,(2\varepsilon - \mu B - 2e\phi)\,, \\
\frac{dz}{dt} &= \pm\sqrt{2(\varepsilon - \mu B - e\phi)/m_i}\,, \\
\boldsymbol{B} &= \nabla\psi \times \nabla\theta\,. \qquad (9)
\end{aligned}$$

Here the flux coordinates (ψ, θ, z) are adopted. The axial transport is one dimensional problems so that

the motion in the direction ψ and θ is neglected in this problem.

The effects of coulomb collision are included by the Monte-Carlo methods.[6] The plug potential is assumed to be located at the axial point of $B_p/B_b = 2$ in the end-mirror cells of GAMMA10.

As is seen in Fig.5 the GAMMA10 tandem mirror has a complicated axial magnetic field profile. On the other hand the theoretical effort at the axial confinement time is limited to the square well magnetic and potential profiles. The first problem, therefore, is to make clear the axial confinement time of GAMMA10.

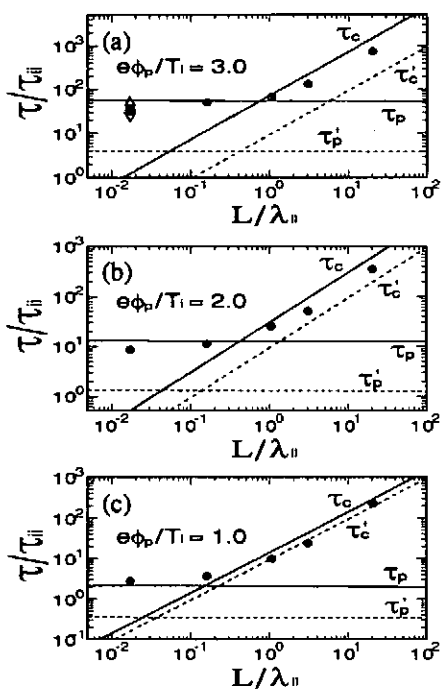

Figure 6: Confinement times obtained by the simulation (solid circles). Here L is the axial length of GAMMA10 and $\lambda_{\|}$ is the ion mean free path. The time τ_{ii} is the ion pitch angle scattering time.

The simulation results, denoted by the solid circles and the symbols ∇ and $\triangle$, are shown in Fig.6. Here τ_p are τ_c are the Pastukhov confinement time[7,8] and collisional confinement time,[9] respectively. The mirror ratio R required in calculating τ_p is chosen to be the ratio B_p/B_c, where B_c is the magnitude of magnetic field at the central cell midplane in GAMMA10. The dashed line τ_p' is the axial confinement time[8] with the assumption that the magnetic field is constant in the axial direction and plug potential exists at both ends of the magnetic mirror field. The dashed line τ_c' is the collisional confinement time[9] in the case of single loss-cone, where loss cone is described by the relation $\varepsilon \geq \mu B_p + e\phi_p$.

The symbol ∇ in Fig.6(a) is the simulation result in the magnetic field profile where magnetic field inside the inner mirror throat in the GAMMA10 magnetic field is assumed to be constant as the same as that of maximum magnetic field in the central cell of GAMMA10. The symbol $\triangle$ is the case that magnetic field is the same as that of minimum magnetic field, i.e. B_c, in the central cell of GAMMA10.

The simulation results agree well with the theoretical results shown by solid lines τ_p and τ_c in Fig.6. The simulation result in the GAMMA10 magnetic field profile denoted by solid circles comes just between the symbols $\triangle$ and ∇. The axial confinement of GAMMA10, therefore, is approximated well by the theoretically obtained confinement times τ_p with the mirror ratio being B_p/B_c and τ_c. The complicated magnetic field profile shown in Fig.5, therefore, does not have an effect on the axial confinement so much.

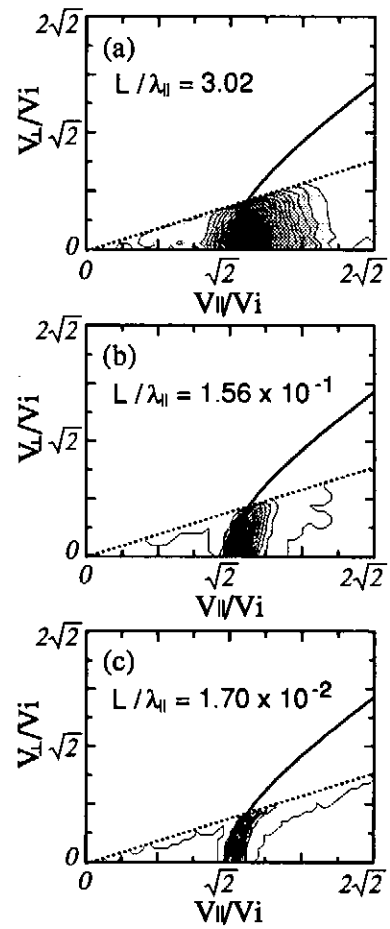

Figure 7: Contour plots of distribution function of end-loss ions. Here $e\phi_p/T_i = 2$ and $v_i \equiv (2T_i/m_i)^{1/2}$.

The distribution functions of end-loss ions are displayed in Fig.7. The loss-cone is surround by the separatrixes of magnetically trapped region (dashed straight line, $\varepsilon = \mu B_m$) and electrostatically trapped region (solid hyperbolic line, $\varepsilon = \mu B_p + e\phi_p$). Figure 8 is the ion end-loss spectrum,

which is obtained by integrating the distribution function of ion end-loss on variable μ. When $L/\lambda_{\parallel}$ is larger than unity the distribution function of end-loss ions have a large tail in the lower energy region than the energy of $e\phi_p$, where ions slow down by collision with ions and electrons during the travel from plug to outer mirror throat in Figs.7(a) and 8(a). The loss cone region is filled with the Maxwellian ions in the case of $L/\lambda_{\parallel} > 1$, so that the end-loss spectrum almost coincides to the end-loss spectrum calculated by Maxwellian ions (solid line in Fig.8).

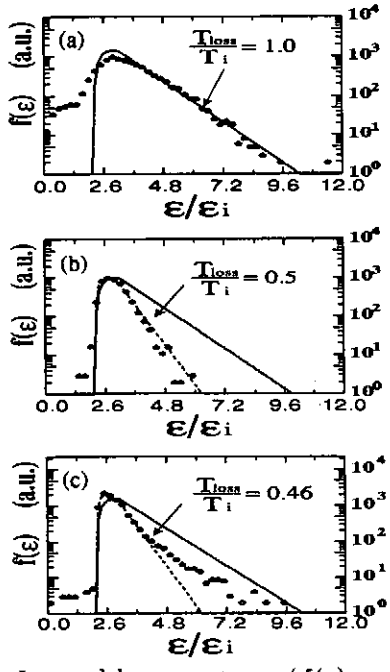

Figure 8: Ion end-loss spectrum ($f(\varepsilon)$ vs. ε). The solid circles are the results of Monte-Carlo simulation. Here $e\phi_p/T_i = 2$ and $\varepsilon_i \equiv e\phi_p$. (a) is the case of $L/\lambda_{\parallel} = 3.02$, (b) is $L/\lambda_{\parallel} = 1.56 \times 10^{-1}$ and (c) is $L/\lambda_{\parallel} = 1.70 \times 10^{-2}$.

In the case that $L/\lambda_{\parallel}$ is smaller than unity the ion end-loss spectrum deviated from the Maxwellian as seen in Figs.7 and 8. The ion end-loss spectrum have two tails in Fig.8(c), because some of ions are lost through the separatrix $\varepsilon = \mu B_p + e\phi_p$ (solid parabolic line in Fig.7) by energy relaxation and others are lost through the separatrix $\varepsilon = \mu B_p$ (solid straight line in Fig.7) by pitch angle scattering, which is clearer in Fig.7(c).

The temperature measured from the ion end-loss spectrum of the tail in the low energy side is lower than the field temperature of ions in Fig.8. Figure 9 plots the temperature measured from ion end-loss spectrum (effective temperature). When $L/\lambda \geq 1$, the effective temperature is almost the same as the field ion temperature. On the other hand the effective temperature becomes lower than the field temperature with lower L/λ in Fig.9.

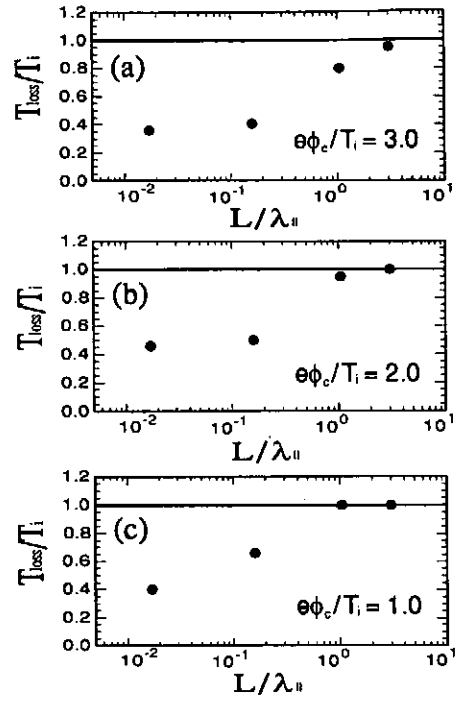

Figure 9: Effective temperature (solid circles measured from ion end-loss spectrum.

In summary of second topics the Monte-Carlo simulation was carried out in the GAMMA10 geometry. The axial confinement time of GAMMA10 is approximated well by the Pastukhov confinement time τ_p with the mirror ratio being B_p/B_c and the collisional τ_c with the loss-cone surrounded by the two separatrixes shown in Fig.7. The ion end-loss spectrum has two tails and the effective temperature is not the same as the field temperature.

References

[1] I.Katanuma, Y.Kiwamoto, Y.Tatematsu, K.Ishii, T.Saito, K.Yatsu, T.Tamano, Phys. Plasmas **3**, 2218 (1996).

[2] T.Saito, I.Katanuma, et.al., in Fusion Energy Conference 1996, (Oct.17-11, 1996, Montréal, Canada) IAEA-CN-64/C2-6.

[3] I.Katanuma, Y.Kiwamoto, Y.Tatematsu, K.Ishii, T.Saito, K.Yatsu, T.Tamano, Phys. Plasmas **4**, 2532 (1997).

[4] G.A.Emmert, R.M.Wieland, A.T.Mense, J.N.Davidson, Phys. Fluids **23**, 803 (1980).

[5] R.Minai, I.Katanuma, T.Tamano, J. Phys. Soc. Jpn. **66**, 2051 (1997).

[6] I.Katanuma, Y.Kiwamoto, M.Ichimura, T.Saito, S.Miyoshi, Phys. Fluids B **2**, 994 (1990).

[7] V.P.Pastsukhov, Nucl. Fusion **14**, 3 (1974).

[8] R.H.Cohen, M.E.Rensink, T.A.Cutler, A.A.Mirin, Nucl. Fusion **18**, 1229 (1978).

[9] T.D.Rognlien, T.A.Cutler, Nucl. Fusion **20**, 1003 (1980).

Nonlinear Simulation of Electromagnetic Current Diffusive Interchange Mode Turbulence

M. Yagi, S.-I. Itoh, K. Itoh*, A. Fukuyama†
Research Institute for Applied Mechanics, Kyushu University 87, Kasuga 816, Japan
*National Institute for Fusion Science, Nagoya 464-01, Japan
†Faculty of Engineering, Okayama Univeristy, Okayama 700, Japan

I. Introduction

The anomalous transport in toroidal plasmas has been investigated extensively. It is pointed out that the nonlinear instability is important in driving the microturbulence[1], i.e., the self-sustained plasma turbulence. This concept is explained as follows; when the electron motion along the magnetic field line is resisted by the background turbulence, it gives rise to the effective resistivity and enhances the level of the turbulence. The nonlinear simulation of the electrostatic current diffusive interchange mode(CDIM) in the two dimensional sheared slab geometry has been performed as an example. The occurrence of the nonlinear instability and the self-sustainment of the plasma turbulence were confirmed by this simulation[2]. On the other hand, the electromagnetic turbulence is sustained in the high pressure limit. The possibility of the self-organization with more variety has been pointed out[3]. It is important to study the electromagnetic turbulence based on the nonlinear simulation.

In this paper, the model equation for the electrostatic CDIM turbulence[2] is extended for both electrostatic and electromagnetic turbulence. (1) Not only $\boldsymbol{E}\times\boldsymbol{B}$ convective nonlinearity but also the electromagnetic nonlinearity which is related to the parallel flow are incorporated into the model equation. (2) The electron and ion pressure evolution equations are solved separately, making it possible to distinguish the electron and ion thermal diffusivities. The two dimensional nonlinear simulation of the electromagnetic CDIM is performed based on the extended fluid model.

This paper is organized as follows. The model equation is explained in section II. The result of simulation is shown in section III. The conclusion and discussion are given in section IV.

II. Model Equations

We start with the four fields reduced set of equations in sheared magnetic field with a bad averaged magnetic curvature. Two dimensional sheared slab geometry (x,y) is used with the box size L_x and L_y. The pressure gradient is taken in the x-direction. The main magnetic field $B_0$is in the z-direction and the sheared magnetic field is in the y-direction $B_y = B_0 x/L_s$, where L_s is the shear length. We study the two dimensional electromagnetic turbulence of the form $\tilde{\phi}(x,y,t) = \sum_{k_y} \phi(x, k_y) \exp(ik_y y + i\omega t)$ with $k_y = 2\pi m / L_y$, where m is the mode number. Hereafter, we abbreviate as $\phi(x, k_y) = \phi$ for simplicity. Basic set of equations for the electrostatic potential ϕ, the z-component of the vector potential A, the fluctuating electron pressure p_e, and the fluctuating ion pressure p_i are given in a normalized form[2] as

$$\frac{\partial}{\partial t} U + [\phi, U] + [A, W] = -\nabla_{//}\nabla_{\perp}^2 A - ik_y \alpha_e p_e - ik_y \alpha_i p_i + \mu_{\perp}\nabla_{\perp}^2 U$$

$$\frac{\partial}{\partial t} W + [\phi, W] - \xi_e [A, W] + K_e [A, p_e] = -\nabla_{//}\phi + K_e \nabla_{//} p_e - ik_y K_e A + \lambda_{\perp}\nabla_{\perp}^2 W + \lambda_{//}\nabla_{//}^2 W$$

$$\frac{\partial}{\partial t} p_e + [\phi, p_e] = -i k_y (1 - H_e)\phi - i k_y C_e p_e - F_e \nabla_{//}\nabla_{\perp}^2 A + \chi_{\perp e}\nabla_{\perp}^2 p_e + \chi_{//e}\nabla_{//}^2 p_e$$

$$\frac{\partial}{\partial t} p_i + [\phi, p_i] = -i k_y (1 - H_i)\phi - i k_y C_i p_i + \chi_{\perp i}\nabla_{\perp}^2 p_i + \chi_{//i}\nabla_{//}^2 p_i$$

with $U = \nabla_{\perp}^2 \phi$ and $W = -\nabla_{\perp}^2 A + A$. Here $[A,B]$ is the Poisson's bracket in Fourier space defined by

$$[A,B] = \sum_{k_y = k_y' + k_y''} \left(\frac{\partial A_{k_y'}}{\partial x} i k_y'' B_{k_y''} - i k_y' A_{k_y'} \frac{\partial B_{k_y''}}{\partial x} \right).$$

The non-dimensional parameters are given by $\alpha_{e,i} = -q^2 R\, d\beta_{e,i}/dx$, $\beta_{e,i} = 8\pi p_{e,i}/B_0^2$, $K_e = \alpha_e \sqrt{m_i / m_e}\,/(2q)$, $C_{e,i} = (5/3) L_{pe,pi} \alpha_{e,i} \sqrt{m_i / m_e}\,/(qR)$, $F_e = (5/3) L_{pe} \sqrt{m_i / m_e}\,/(qR)$, $L_{pe,pi}^{-1} = -dln\, p_{e,i}/dx$ and $\xi_e = v_{//e0} / v_A$. To derive these equations, we assume that the sound wave is decoupled from this mode ($\tilde{v}_{//i} = 0$) and that ϕ_0, $v_{//e0}$, $v_{//i0}$ are constant in space. If the nonlinear term $v_{//e0}\nabla_{//} v_{//e}$ which is proportional to ξ_e is renormalized, it formally reduces to the Rechester and Rosenbulth type formula[4] in the limit $v_{//e0} \to v_{the}$, where v_{the} is the electron thermal velocity. If we set $\xi_e = 0$, $\lambda_{//} = 0$, $\chi_{//e,i} = 0$, $K_{e,i} = 0$, $C_{e,i} = 0$, $F_e = 0$, $\alpha_e = \alpha_i$, $\chi_{\perp e} = \chi_{\perp i}$ and neglect the term $\partial A/\partial t$ and $[\phi, A]$ in Ohm's law, then this model reduces to the previous electrostatic model[2]. The boundary conditions $\nabla_{\perp}^2\phi(\pm L_x/2) = 0$, $\phi(\pm L_x/2) = 0$, $A(\pm L_x/2) = 0$, $p_{e,i}(\pm L_x/2) = 0$ are used for the x-direction and the periodic boundary condition is used for the y-direction.

The power spectrum of the fluctuating energy is evaluated for each k_y-Fourier component by $W_{\nabla_{\perp}\phi} = \left\langle \left| \nabla_{\perp}\phi \right|^2 \right\rangle /2$, $W_j = \left\langle \left| \nabla_{\perp}^2 A \right|^2 \right\rangle /2$, $W_{\nabla_{\perp}A} = \left\langle \left| \nabla_{\perp} A \right|^2 \right\rangle /2$, $W_{p_e} = \left\langle \left| p_e \right|^2 \right\rangle /2$, $W_{p_i} = \left\langle \left| p_i \right|^2 \right\rangle /2$ where $\langle \cdots \rangle$ indicates the space average of the x-direction $\langle \cdots \rangle = \int_{-L_x/2}^{L_x/2} \cdots dx/L_x$. The fluctuating energy is expressed by $E_{\nabla_{\perp}\phi} = \sum_{k_y} W_{\nabla_{\perp}\phi}$, $E_j = \sum_{k_y} W_j$, $E_{\nabla_{\perp}A} = \sum_{k_y} W_{\nabla_{\perp}A}$, $E_{p_e} = \sum_{k_y} W_{p_e}$, $E_{p_i} = \sum_{k_y} W_{p_i}$.

III. Simulation Results

In this section, we discuss the results of nonlinear simulation. The parameters are chosen as $L_x = 120$, $L_y = 6.4 \times 2\pi$, $\alpha_e = \alpha_i = 0.25$, $s = 0.5$, $\mu = \lambda_{\perp} = \chi_{\perp e} = \chi_{\perp i} = 0.2$, $\lambda_{//} = \chi_{//e} = \chi_{//i} = 0.5$, $K_e = 1$, $H_{e,i} = 0.2$, $C_{e,i} = 2$, $F_e = 2$ and 64 Fourier modes are used .

Figure 1 shows the linear growth rate versus the wavenumber. The maximum growth rate is given by the longest wavelength mode. The growth rate is negative for the wavenumber

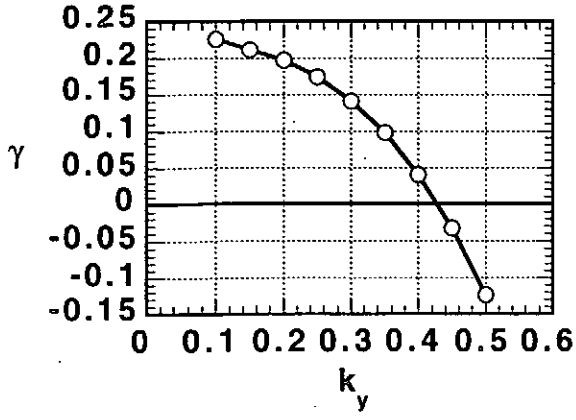

Fig.1 The linear growth rate versus the wavenumber.

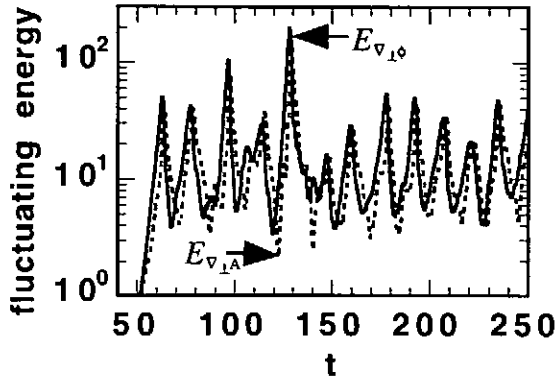

Fig.2 The time evolution of the fluctuating electrostatic and electromagnetic energy.

$k_y > 0.42$ for these parameters. This is due to the stabilization effect of the parallel thermal conductivities on the short wavelength mode. On the other hand, the drift term in Ohm's law which is proportional to K_e destabilizes the short wavelength mode. In this case, the former effect overcomes the latter effect. Comparing it with the previous model[2], it is found that the induction term $\frac{\partial A}{\partial t}$ enhances the linear growth rate and makes the maximum growth rate shift to the long wavelength mode.

Figure 2 shows the time evolution of the fluctuating electrostatic energy $E_{\nabla_\perp \phi}$ (the thick line) and electromagnetic one $E_{\nabla_\perp A}$ (the dotted line), respectively. In the early phase ($t < 45$), these evolve according to the linear growth rate ($\gamma \sim 0.2$). The inverse cascade takes place at the time $t \sim 60 - 70$ and the transit dip is observed in these cases. The oscillation of the fluctuating energy occurs in the saturation phase, and does not dump away and continues to oscillate. It should be noted that in the previous model, the transit dip was observed but the oscillation relaxed and saturated state was realized. The fluctuation amplitudes are almost same for $E_{\nabla_\perp \phi}$ and $E_{\nabla_\perp A}$. However, in the nonlinear phase($t > 45$), the retarded response of magnetic energy $E_{\nabla_\perp A}$ is observed.

Figure 3 shows the time evolution of the fluctuating electron pressure energy E_{p_e} (the thick line) and ion pressure one E_{p_i} (the dotted line), respectively. The both energies have the peak values at the same time except $t = 110$ where only the fluctuating ion pressure energy has a peak value. The time averaged electron pressure energy is estimated and presented in terms of the mean and standard deviation: *mean* ≈ 36.85 , *standard deviation* ≈ 47.90 . Due to the large standard deviation associated with the oscillatory behavior, a clear conclusion is not drawn out for the nonlinear saturation level. However, the mean value of the saturation level is found to be about 10 times larger than that in the electrostatic case.

Figure 4 shows the power spectrum of fluctuating electron and ion pressure energy in the oscillatory phase. The black circle represents the power spectrum of the fluctuating electron pressure energy at $t = 70$ (which corresponds to the minimum value of the fluctuating electron pressure energy in Fig.3) and the black square represents that at $t = 80$ (which corresponds to the maximum value). Similarly, the circle shows the power spectrum of the

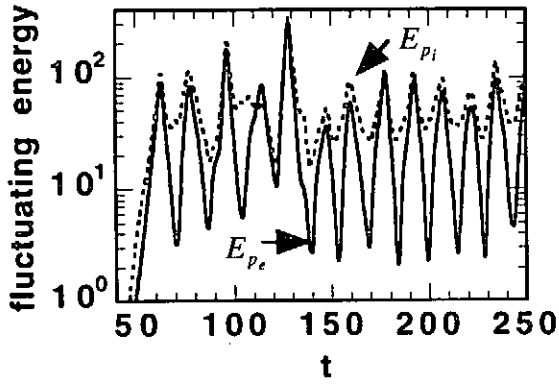

Fig.3 The time evolution of the fluctuating electron and ion pressure energy.

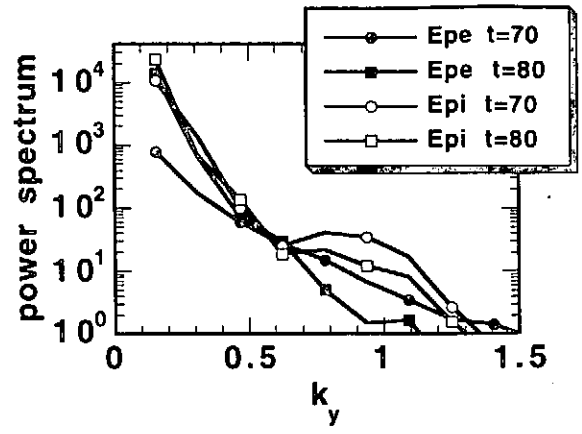

Fig.4 The power spectrum of the fluctuating electron and ion pressure energy.

fluctuating ion pressure energy at $t = 70$ and the square shows that at $t = 80$. It is found that the power spectrum of the fluctuating electron pressure energy of the longest wavelength mode changes it's value about one order. On the other hand the corresponding power spectrum of ion's changes about a factor in these time intervals. This difference reflects the absolute value of oscillation amplitude seen in Fig.3. The behavior of the modes in the middle range wavenumber ($k_y \sim 0.5$) seems to be similar for both cases. In the presence of $\frac{\partial A}{\partial t}$ term, the long wavelength region has a maximum linear growth rate as in shown in Fig.1. In addition to it, the inverse cascade more effectively takes place in the long wavelength region, and overcomes the normal cascade due to the nonlinearities. Therefore if there is no sink in the long wavelength region, the saturation level could be determined by the system size of the y-direction. The detailed analysis of the power spectrum shows that the different temporal evolutions of the low-k_y part and of the high-k_y part of the fluctuating energy. We found that the oscillatory period of the energy level in the low-k_y part is doubled compared to that in high-k_y part[5].

Figure 5 shows the contour plot of electron and ion pressures at $t = 100$ in x-y space. In our normalization the total pressure is calculated by the equation $p_{e,i}(x,y) = -(x - L_x/2) + \tilde{p}_{e,i}(x,y)$ where $-L_x/2 < x < L_x/2$ and $0 < y < L_y$. The $x = 0$ surface corresponds to the mode rational surface. The convective flow pattern is observed at the interface. The convective motion itself is different from each other in electron and ion pressure. It is found that the electrostatic components of electron and ion heat flux are comparable in these parameters and the convection is dominated by the $\boldsymbol{E} \times \boldsymbol{B}$ motion.

IV. Summary and Discussion

In this paper, the model equation for the electrostatic current diffusive interchange mode turbulence is extended for the electromagnetic one. The two dimensional nonlinear simulation of the electromagnetic current diffusive interchange mode is performed on the extended fluid model. In the linear calculations, we found that the term $\frac{\partial A}{\partial t}$ in Ohm's law enhances the linear growth rate and the maximum growth rate is shifted to the long wavelength mode. In the nonlinear simulation, the transition between linear and nonlinear instability is

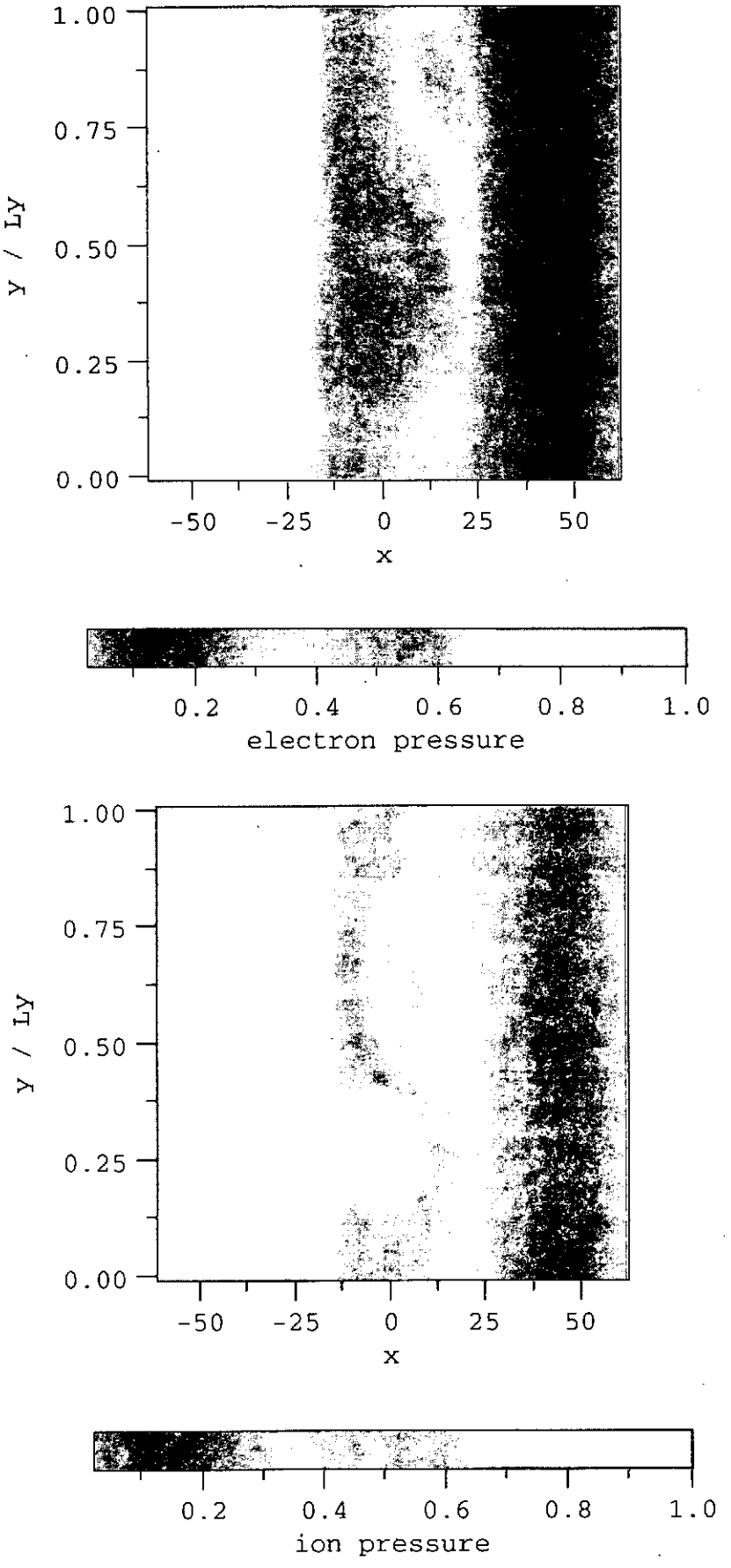

Fig.5 The electron and ion pressure contours at t=100.

observed at the early phase of the energy development. In full nonlinear stage, the relaxation oscillation of the fluctuating energy is observed. The period and the amplitude of the oscillation are governed by the longest wavelength mode. The strong inverse cascade is observed which overcomes the normal cascade due to the electromagnetic nonlinearity. The energy transfer dominantly occurs in the long wavelength region in the spectrum rather than in the short wavelength region.

Higher saturation level is observed in the electromagnetic simulation. However, it is not clearly identified whether the electromagnetic nonlinearity is the cause of the higher saturation level. This is partly because the effect of induction induces the global eigenfunction in the long wavelength region, which has the maximum growth rate. The energy tends to concentrate to the long wavelength region. As the result, the saturation level is strongly affected by the system size of the y-direction. The time evolutions of the fluctuating electrostatic and electromagnetic energies are compared. The amplitudes of these energies are almost the same. However the retarded response of the electromagnetic energy to the electrostatic energy is observed. This retarded response is also observed in the heat flux[5]. The electromagnetic component of the heat flux follows to the electrostatic one. The time evolution of fluctuating electron and ion pressure energies is also compared. The peak time of the fluctuating energy agrees with each other (except the peak at $t = 110$, where only the fluctuating ion energy has a peak). The temporal oscillation amplitude of the electron pressure energy is larger than that of ions. The power spectrum of the fluctuating electron pressure energy of the longest wavelength mode changes it's value about one order. On the other hand the corresponding power spectrum of ions changes about a factor in one period of the oscillations. The pressure contour is investigated. It is found that the convective size is similar for electrons and ions, although the motion is different. For the future work, we should analyze whether the coupling to the sound wave creates the sink in the long wavelength region. If it is not so, an inclusion of the global effect or the global simulation may be necessary.

Acknowledgements

This work is partly supported by the Grant-in-Aid for Scientific Research of Ministry of Education, Science, Sport and Culture, Japan, by the REIMEI Research Resources of Japan Atomic Energy Research Institute, and by collaboration programme of Advanced Fusion Research Center of Kyushu University.

References

[1] K. Itoh, S.-I. Itoh, A. Fukuyama, M. Yagi and M. Azumi, Plasma Phys. Control. Fusion **35** 543 (1993).
[2] M. Yagi, S.-I. Itoh, K. Itoh, A. Fukuyama and M. Azumi, Phys. Plasmas **2** 4140 (1995).
[3] S.-I. Itoh, K. Itoh, A. Fukuyama and M. Yagi, Plasma Phys. Control. Fusion **38** 527 (1996).
[4] A. B. Rechester and M. N. Rosenbulth, Phys. Rev. Lett. **40** 38(1978).
[5] M. Yagi et al., submitted to Plasma Phys. Control. Fusion.

TWO-DIMENSIONAL MODEL OF CONVENTIONAL STELLARATOR

Pustovitov V.D.

Russian Research Centre "Kurchatov Institute", Moscow, Russia

MHD theory of conventional stellarators was originally founded on the basis of so-called stellarator expansion [1]. Later in early 80s several groups developed new methods and extended the theory to the wider scope of problems. But one thing remained basically the same in all quite different approaches: the expansion which was used to reduce the equilibrium equations

$$\nabla p = [\mathbf{j} \times \mathbf{B}], \qquad (1)$$

$$\mathrm{div}\ \mathbf{B} = 0, \quad \mathbf{j} = \mathrm{rot}\ \mathbf{B}. \qquad (2)$$

Here p is the plasma pressure, $\mathbf{j}$ is the current density, $\mathbf{B}$ is the magnetic field induction.

There were other common features: expansion was always used from the very beginning; four (or even more) parameters were assumed to be small. All this made the derivations rather complicated, all expressions approximate. In addition, it was impossible to restore known exact results in the limit of axial symmetry.

These evident shortcomings gave the ground to the mistrust shown sometimes to 2D models of a stellarator. And theory itself confessed that it would not claim on the better attitude: when good agreement of 2D and full 3D models was demonstrated [2], it was commented [3] as being "much better ... than one has any right to expect".

Nevertheless, 2D models were always quite reliable, beyond expectations of those who adhere to 3D equilibrium codes. One might ask whether it was accidental or not.

Numerical comparisons [4-7], showing good agreement of 2D and 3D equilibrium models, are convincing, but particular examples. The confidence to the model depends on the assumptions and derivation procedure. Fortunately, it can be simplified and refined significantly, as shown below, and approximations can be introduced step by step, in contrast to all previous approaches.

First of all, it must be stressed that Maxwell equations (2) are "reduced" to 2D equations without any approximation. Indeed, Maxwell equations are linear and can be naturally decomposed on two parts

$$\mathrm{div}\ \bar{\mathbf{B}} = 0\,, \quad \bar{\mathbf{j}} = \mathrm{rot}\ \bar{\mathbf{B}}\,, \tag{3a}$$

$$\mathrm{div}\ \tilde{\mathbf{B}} = 0\,, \quad \tilde{\mathbf{j}} = \mathrm{rot}\ \tilde{\mathbf{B}}\,, \tag{3b}$$

when magnetic field is represented as

$$\mathbf{B} = \bar{\mathbf{B}} + \tilde{\mathbf{B}}\,. \tag{4}$$

Here $\bar{\mathbf{B}}$ is the axisymmetric and $\tilde{\mathbf{B}}$ is the helical component of $\mathbf{B}$.

There is no need to introduce simplifying assumptions at the next step also. Equation $\mathrm{div}\bar{\mathbf{B}} = 0$ is satisfied by

$$\bar{\mathbf{B}} = \left[\, \nabla(rA_t) \times \nabla\zeta \,\right] + \frac{F}{2\pi}\nabla\zeta \tag{5}$$

with A_t and F depending on r and z only (r, ζ, z are ordinary cylindrical coordinates). Then toroidal component of $\bar{\mathbf{j}} = \mathrm{rot}\bar{\mathbf{B}}$ gives

$$\bar{j}_\zeta = -\,r\ div\ \frac{\nabla(rA_t)}{r^2}\,. \tag{6}$$

These trivial straightforward operations within Maxwell equations give the result, which must be considered as the most important intermediate equation. For tokamaks Eq. (6) turns into the Grad-Shafranov equation, when $\bar{j}_\zeta$ is

expressed through plasma pressure and poloidal current. Just the same, Eq. (6) is the precursor of the desired result for stellarators. If it is understood, the rest of calculations must be oriented on getting $\bar{j}_\zeta$ as accurate as possible.

Equilibrium current density j must be found from the force balance equation (1) supplemented by div$\mathbf{j} = 0$. In all approaches the expansion technique was used to solve div$\mathbf{j} = 0$ with given $\mathbf{j}_\perp$, and it was the central and most complicated part of calculations. But again we can postpone the expansion: it is not necessary to apply it for solving the equation because we can write out its exact solution:

$$\mathbf{j}\left[1 - \frac{p}{\langle \mathbf{B}^2 \rangle}\right] = \alpha_0 \mathbf{B} - \frac{1}{\langle \mathbf{B}^2 \rangle} \text{rot } p(\mathbf{B} - \nabla f_H) . \quad (7)$$

Here brackets $\langle ... \rangle$ denote the usual volume averaging between neighboring flux surfaces,

$$\alpha_0 \equiv \frac{\langle \mathbf{j}\cdot\mathbf{B} \rangle}{\langle \mathbf{B}^2 \rangle} , \quad (8)$$

and f_H is the function satisfying the equation

$$\mathbf{B}\cdot\nabla f_H = \mathbf{B}^2 - \langle \mathbf{B}^2 \rangle . \quad (9)$$

This equation is much simpler than div$\mathbf{j} = 0$, which is identically satisfied by (7) provided

$$\mathbf{B}\cdot\nabla p = 0 . \quad (10)$$

The latter is the last unused consequence of Eq. (1).

It must be realized that Eq. (1) is replaced now by (7), (9) and (10). Another important fact is that all expressions written above are exact. The need in approximation appears later, when we try to get $\bar{j}_\zeta$ from (7).

At the beginning we have to solve Eqs (9) and (10), which belong to the class of magnetic differential equations (MDE)

$$\mathbf{B}\cdot\nabla x = y . \quad (11)$$

For stellarator both functions x and y look like $\bar{x} + \tilde{x}$, and MDE (11) is equivalent to the pair of equations

$$\bar{\mathbf{B}}\cdot\nabla\bar{x} + \langle \tilde{\mathbf{B}}\cdot\nabla\tilde{x} \rangle_\zeta = \bar{y} , \tag{12a}$$

$$\bar{\mathbf{B}}\cdot\nabla\tilde{x} + \tilde{\mathbf{B}}\cdot\nabla\bar{x} = \tilde{y} , \tag{12b}$$

where $\bar{f}$ and $\langle f \rangle_\zeta$ denote the same: averaging over ζ at fixed r and z.

In conventional stellarators the poloidal field $\mathbf{B}_p$ can be much weaker than helical field. That is the reason why $\tilde{\mathbf{B}}\cdot\nabla\tilde{x}$ must be retained in Eq. (12a). However, $\tilde{\mathbf{B}}\cdot\nabla\tilde{x}$ is disregarded in the last equation, which is allowed when $|\tilde{\mathbf{B}}| \ll |\bar{\mathbf{B}}|$.

This is the first approximation. In fact, we accept stronger restrictions

$$|\tilde{\mathbf{B}}| \ll B_t , \qquad \mu \ll m , \tag{13}$$

where B_t is the toroidal field, μ is the rotational transform, and m is the number of helical periods. Under these assumptions one gets from (12b)

$$\tilde{x} = -\,\delta\mathbf{r}\cdot\nabla\bar{x} + \frac{r}{B_t}\hat{\tilde{y}} , \tag{14}$$

where notation of [8] is used:

$$\delta\mathbf{r} = \frac{r}{B_t}\hat{\tilde{\mathbf{B}}}_p , \qquad \hat{\tilde{f}} = \int \tilde{f}\, d\zeta .$$

With given $\tilde{x}$ Eq. (12a) can be easily transformed into

$$(\bar{\mathbf{B}} + \mathbf{B}^*)\cdot\nabla\bar{x} = \bar{y} - \langle \tilde{\mathbf{B}}\cdot\nabla(\frac{r}{B_t}\hat{\tilde{y}}) \rangle_\zeta , \tag{15}$$

where

$$\mathbf{B}^* \equiv \frac{1}{2\pi}\left[\nabla\psi_V \times \nabla\zeta \right] \tag{16}$$

is the "effective" poloidal field, and

$$\psi_V \equiv \frac{\pi r^2}{B_t} \left\langle \left[\tilde{\mathbf{B}} \times \hat{\tilde{\mathbf{B}}} \right] \cdot \frac{\nabla\zeta}{|\nabla\zeta|} \right\rangle_\zeta = \frac{2\pi r^2}{B_t} \left\langle \tilde{B}_z \hat{\tilde{B}}_r \right\rangle_\zeta . \quad (17)$$

To get (15) from (12a), one needs to find $\langle \tilde{\mathbf{B}} \cdot \nabla \tilde{x} \rangle_\zeta$. This value is calculated exactly. Just use (14) and the identity

$$\left\langle \tilde{\mathbf{B}} \cdot \nabla (\delta\mathbf{r} \cdot \nabla \bar{f}) \right\rangle_\zeta = - \mathbf{B}^* \cdot \nabla \bar{f} . \quad (18)$$

Procedure described by (11)-(18) allows to express f_H in (7) through the magnetic field. Let us note that only two small parameters (13) have been introduced to reduce MDE (11) to 2D equation (15). Neither aspect ratio, nor β (ratio of kinetic and magnetic pressures) were restricted.

Assumption $\beta \ll 1$ is natural for stellarators. It can help in two ways. First, at $\beta \ll 1$ there is no need to solve Eqs (3b). Second, rhs of Eq. (9) is simplified, and we get

$$\bar{j}_\zeta = \frac{FF'(\psi)}{2\pi r} + 2\pi r \frac{dp}{d\psi} \left[1 + \frac{\langle \tilde{\mathbf{B}}^2 \rangle_\zeta + \mathbf{B}_p \cdot \mathbf{B}^*}{\langle \mathbf{B}^2 \rangle} \right] . \quad (19)$$

Here $p = p(\psi)$, $F = F(\psi)$, and

$$\psi = 2\pi r A_t + \psi_V , \quad (20)$$

which is the consequence of (10). With these two relations Eq. (6) becomes

$$\mathrm{div} \frac{\nabla(\psi - \psi_V)}{r^2} = - 4\pi^2 p'(\psi)(1 + \Omega^0) - \frac{FF'(\psi)}{r^2} . \quad (21)$$

Here Ω^0 stays for a small term from (19).

As we could see, this 2D equation is mathematically accurate. Small inaccuracy is introduced when approximate expressions for ψ_V and Ω^0 are substituted into (21). In any case the structure of the equation is absolutely correct, which can guarantee any desired accuracy, if ψ_V and Ω^0 can be properly found.

Originally stellarator expansion was based on the assumption that the lowest order configuration was a uniform axial magnetic field [1], and toroidicity was introduced as a small perturbation. With a tendency to reduce aspect ratio to 7 in ATF and to 5 in CHS, traditional large aspect ratio expansion became, from a theoretical point of view, a weak point of the method.

In fact, the role and danger of the inverse aspect ratio expansion were overestimated. As shown above, instead of a uniform field [1], a toroidal field can be considered as the lowest order configuration. Surprisingly, it does not complicate the derivation, if it goes through (6). And the gain is essential: no restriction on toroidicity results in the correct structure of the final equation.

Final equation (21) is the direct consequence of Maxwell equations. Therefore, there is nothing artificial or restrictive in the two-dimensional model of stellarator, when it is introduced and treated in a correct way. Reliability of such models was empirically proved, but honest theoreticians prudently pointed out the lack of justification [6]: "two-dimensional equilibrium models have been shown to be more useful than had been expected". We tried to show that there is a solid foundation for optimistic expectations.

References

[1] J.M. Greene and J.L. Johnson, Phys. Fluids **4**, 875 (1961).
[2] B.A. Carreras et al., Phys. Fluids **26**, 3569 (1983).
[3] G. Rewoldt and J.L. Johnson, Nucl. Fusion **24**, 733 (1984).
[4] F. Herrnegger, P. Merkel and J.L. Johnson, J. Comp. Phys. **66**, 445 (1986).
[5] B.A. Carreras et al., Nucl. Fusion **28**, 1195 (1988).
[6] Y. Nakamura, K. Ichiguchi, M. Wakatani and J.L. Johnson, J. Phys. Soc. Jpn **58**, 3157 (1989).
[7] Y. Nakamura et al., Fusion Technology **19**, 217 (1991).
[8] V.D. Pustovitov, J. Plasma Fus. Res. **70**, 943 (1994).

A Universal Parameterization of Chaos in Various Beam-Wave Interactions

Jae Koo Lee, Hae June Lee, Min Sup Hur, InDeog Bae, and Yi Yang
Department of Physics, Pohang University of Science and Technology, Pohang 790-784, S. Korea

The comprehensive parameter space of self-oscillation and its period-doubling route to chaos are shown for a bounded collisionless beam-plasma system. In this parameterization, it is helpful to use a potentially universal parameter in close analogy with free-electron-laser chaos. A common parameter, which is related to the velocity slippage and the ratio of bounce to oscillation frequencies, is shown to have similar significance for different physical systems. This single parameter replaces the dependences on many input parameters, thus suitable for a simplifying and diagnostic measure of nonlinear dynamical and chaotic phenomena for various systems of particle-wave interactions. The results of independent kinetic-simulations verify those of nonlinear fluid-simulations. Other standard routes to chaos via intermittent or quasiperiodic oscillations are also shown for the undriven plasma systems. Some correlation of linear characteristics to nonlinear phenomena was noted.

The self-oscillation in an undriven physical system and its standard routes to chaos are the subject of intense studies for plasma systems [1] and for free-electron-laser (FEL) systems [2–7]. The previous plasma studies were mostly experimental [8,9], reporting the observation of various nonlinear dynamical and chaotic oscillations in such plasma systems. The overall parameter window including all such oscillations is particularly needed for designing the parameters of future studies, experimental or theoretical.

Despite its usefulness, an analytic theory has a limited success for complex nonlinear phenomena. Fluid and kinetic simulations are thus employed for this comprehensive picture. The physical model for the simulation is that of the extended Pierce diode system [10], where an electron beam of velocity u, density n, and plasma frequency ω_p is injected to a collisionless plasma-diode system of length L with the applied DC voltage V_a. The quasineutral ions constitute an immobile background. In this extended system, there are new parameters such as normalized applied voltage and the ion to electron density ratio The past simulations showed the significance of the Pierce parameter [11] $\alpha = \omega_p L/u$, the ion-electron ratio [10,12] $\eta = n_i/n$, and the applied voltage [13] $\phi = eV_a/mu^2$.

In the present work, phase diagrams are found in terms of these control input-parameters for the self-excited periodic and chaotic oscillations of a bounded plasma system [14]. The significance and usefulness of the common quantitative diagnostic measure are shown for two different physical systems, free-electron-laser and bounded plasma-diode systems. Various self-oscillating and chaotic phenomena for the plasma chaos are classified using a common parameter in close analogy with the FEL chaos [2–5]. The parameter μ, reflecting the slippage and the ratio of bounce frequency to nonlinear oscillation frequency, has similar significance for two different physical systems of FEL and extended Pierce diode. This single parameter can be used as a quantitative and diagnostic measure of various nonlinear dynamical and chaotic phenomena for many physical systems. The results of our independent kinetic-simulations verify closely those of our nonlinear fluid-simulations.

For the numerical methods we have employed two different methods, nonlinear fluid and kinetic simulations which showed similar results. The model equations for the nonlinear fluid simulations are:

$$\frac{\partial n}{\partial t} + \frac{\partial}{\partial x}(nu) = 0, \tag{1}$$

$$\frac{\partial u}{\partial t} + u\frac{\partial u}{\partial x} = \frac{e}{m}\frac{\partial V}{\partial x}, \tag{2}$$

$$\frac{\partial^2 V}{\partial x^2} = \frac{e}{\epsilon_0}(n - n_i), \tag{3}$$

where V is the plasma potential, e is the electric charge, m is the electron mass, ϵ_0 is the vacuum permittivity, and n_i is background ion density. The boundary conditions are: the velocities and the densities of electrons at the cathode are u_0 and n_0 , and the voltages are zero and V_a at the cathode and anode, respectively. The equations are discretized by the finite difference method using a standard upwind differencing scheme. Time step $\omega_p \Delta t = 0.01$ and mesh size $\omega_p \Delta x/u_0 = 0.01$ are used. The code first calculates an inhomogeneous equilibrium for the given input parameters, and observes the growth of a small perturbation about the equilibrium. On a dedicated Pentium-Pro/200 with LINUX, a typical simulation takes less than 1 hour. The kinetic simulation has been carried out by using PDP-1 [15] which has been used for a simulation study of inhomogeneous beam-plasma interaction [16]. The applications to plasma chaos have been shown in [17]. A change in the code to give the initial velocity perturbation was necessary.

The self-oscillation, period-doubled, and period-quadrupled oscillations from the nonlinear fluid simulation of the plasma system are shown in Fig. 1, for $\alpha = 2.88\pi$, $\eta = 1$.

The overall parameter window in terms of control input-variables for various nonlinear dynamical phenomena leading to chaos is useful and illuminating for the comparison with other experiments and simulations. These parameter regimes, shown in Fig. 2, are the results of nonlinear fluid simulations extended to three-parameter space involving α, ϕ, and η. The regions for stable focus (thus no-oscillation), self-oscillation, period-doubling, chaos, and unstable region [11] are marked SF, $1P$, $2P$, C, and U, in Fig. 2 (a), respectively. At fixed ϕ and η, the reduction of α reveals the occurrence of single-frequency limit-cycle-oscillation which becomes period-doubled oscillations and then period-quadrupled, etc. with further reduction in α. These are in agreement with the previous results [11]. At fixed α and η, the increase in ϕ reveals the occurrence of single-frequency limit-cycle-oscillation as in Fig. 1 (a), which becomes period-doubled as in Fig 1 (b), and then period-quadrupled as in Fig 1 (c), and finally chaotic. The dependence on η as in Ref. [12] is also reproduced in Fig. 2 (a). The new results noted in Fig. 2 (a) are that the increase in α at a constant ϕ can also reveal the similar phenomena as shown in Fig. 2 (a) at large values of α. The saturating characteristics (the sine-like curves) of these boundary-lines for various $1P$ to $2P$ to $4P$ and ultimately to chaotic oscillations show a dependence on η and strong correlation with the linear growth rates (and not with linear oscillation frequencies) as in Fig. 2 (b).

The phase diagram for various nonlinear dynamical phenomena can be classified in terms of the parameter μ similar to one used in describing the free-electron-laser (FEL) chaos [2–5], In studying the FEL chaos, an empirical parameter μ was introduced as in [2,3]

$$\mu \equiv \frac{L_s}{L_{syn}} = N_w \lambda \left[\frac{2\pi c(c-u_0)}{\omega_b u_0}\right]^{-1}, \qquad (4)$$

where $L_s(\equiv N_w\lambda)$ is slippage length (the effective interaction length between electrons and wave) with the number of wiggler periods N_w and the radiation wavelength λ, L_{syn} is synchrotron slippage distance, c is the speed of light, u_0 is the average axial velocity of electron beam, and $\omega_b = \sqrt{ekE/m}$ is the syncrotron bounce frequency with wave number k and electric field intensity E. For the beam-plasma case,

$$\mu \equiv \frac{L_{int}}{L_{syn}} = \frac{\pi}{k}\left[\frac{2\pi v_\phi(u_0-v_\phi)}{\omega_b u_0}\right]^{-1} = \frac{\omega_b/\omega_r}{2(1-v_\phi/u_0)}, \qquad (5)$$

where $L_{int}(\equiv \pi/k)$ is the effective interaction length and $v_\phi = \omega_r/k$ is the phase velocity of the wave with oscillation frequency ω_r.

The regimes where various oscillations such as $1P$, $2P$, $4P$, and chaos appear are indicated in Fig. 3 with specific μ's. The large values of μ exceeding approximately 2 are associated with the chaotic oscillations. The transitions of the FEL chaos [3] from SF to $1P$, to $2P$, then to C occur at $\mu \sim 0.8$, 1.7, and 2.0, which compare with the plasma case at $\mu \sim 1.05$, 1.8, and 2.0. The dependence of these transition μ-values on the input parameters such as α, ϕ, and η is weak as seen from the weak horizontal slopes in Fig. 3. The utility of a single parameter μ as a diagnostic measure of various types of nonlinear phenomena leading to chaos is pronounced especially when the physical systems have complex dependences on many input parameters.

These nonlinear dynamical and chaotic phenomena for the beam-plasma are analogous to the case of FEL. The phase diagram of our FEL work [Fig. 12 of [2]] in terms of the input-parameters resembles the modest α-regimes for the plasma of Fig. 2 (a). The μ-classification for the FEL chaos [Fig. 1 of [3]], is qualitatively similar to that for the plasma chaos in Fig. 3. The intermittent chaos and the quasiperiodic oscillations are also observed in our plasma systems. Their characteristics and the fine structure similar to Fig. 1 of Ref. [3] are the subject of further detailed study.

The Feigenbaum constants δ [21] for these period-doubling sequences up to $16P$ for several typical cases of our fluid simulations are calculated. These are 4.8308 and 4.6429 for $\phi = 0$, $\eta = 1$; 4.7586 and 4.8333 for $\phi = 0.05$, $\eta = 1$; 4.9714 and 4.6667 for $\phi = 0$, $\eta = 1.05$ which are close to the universal value 4.6692. The return map using reduced (from partial differential to ordinary differential) equations has been used for the period-doubling route to chaos of FEL [22] but not yet for the plasma chaos.

Bonifacio [18] was the first to point out the similarity of the bounded FEL and the bounded plasma equations along with the importance of the slippage. He demonstrated FEL-like equations for a plasma system which have not been used for the study of the self-oscillation and chaos. The significance of the slippage (which is an equilibrium or linear quantity) in determining the nonlinear amplitude has also been recognized for a homogeneous beam-plasma instability [19] and for an FEL system [20]. The contribution to μ of the slippage along with the other factor [the ratio of bounce to nonlinear oscillation frequencies in Eq. 5] has been found important for the FEL chaos [2–5]. The present study identifies the similarity of the importance of μ both for the FEL and the beam-plasma systems.

It is also interesting to note that the linear characteristics such as the growth rates and the oscillation frequencies are correlated to the nonlinear phenomena. This was observed in Fig. 2 (b), where the strong linear growth-rates are associated with the chaos regime, either at small α or at large α for a constant ϕ. The oscillation frequencies at the linear and nonlinear stages determine the wave phase-velocities, thus the slippages, which affect the parameter μ.

The results of nonlinear fluid simulations as shown in Figs. 2 and 3 are verified in Fig. 4 by our independent kinetic results using the PDP-1 code [15]. The results from two entirely different origins agree very well despite

the slight differences in the simulation conditions, most notably in the variation of η during the calculations and the initial equilibria.

The self-oscillations in undriven (with no external a.c. driver-frequency) plasma systems are observed in many parallel-plate thermionic (with an electron beam injected from the cathode) discharges [8], electron-cyclotron-resonance plasma discharge [23], and rf plasmas [24]. Once excited, these self-oscillations follow one of the standard routes to chaos via period-doubling, intermittency, or quasiperiodic oscillation. Some of these are shown in the present paper for the parallel-plate beam-plasma collisionless discharge. Despite the differences in the plasma-formation mechanism of these various discharges, most discharges have some forms of interactions between energetic beam and collective wave, which become nonlinearly important at large wave-amplitudes. The proposed diagnostic parameter μ contains the nonlinear wave-amplitude resulting from the particle-wave interaction and the velocity slippage between particle and wave. The chaos of driven systems [9] can also be classified using μ in a similar fashion to the undriven plasma system in the present study. The collisional effects are of significance as examined in [25] and are the subject of our future study, whose preliminary results show the hysteresis and the anode-glow-mode to temperature-limited-mode transition [1,26] as well as new features. The suggested parameter μ can also be used in quantifying the plasma chaos for various chaos-control [27].

In summary, the major results are shown in Fig. 2 (a) for the phase diagrams in terms of the control input-parameters for the period-doubling route to chaos of the beam-plasma system as well as in Fig. 3 in terms of potentially universal diagnostic parameter μ in close analogy with the FEL chaos. The parameter μ, reflecting the ratio of the interaction to the synchrotron slippage lengths, has similar significance for different physical systems of FEL and plasma. The dependence on this single parameter represents the multiple dependences on many input parameters, the latter of which vary from system to system. It can thus be used as a simplifying, quantitative, and diagnostic measure of various nonlinear dynamical and chaotic phenomena for many different physical systems. The results of our independent kinetic-simulations verify closely those of the nonlinear fluid-simulations. A correlation of linear characteristics to nonlinear phenomena was noted.

Helpful suggestions from Dr. Yi Yang, I.D. Bae, Dr. Y.B. Kim, Dr. H.S. Uhm, Professors A.J. Lichtenberg, S.H. Kim, T.H. Chung, and M. Yoon, are gratefully acknowledged. This work was supported in part by the Basic Science Research Institute Program, the Korea Ministry of Education (BSRI-96 and 97-2439) and POSTECH/BSRI Special Fund.

[1] F. Greiner, T. Klinger, H. Klostermann, and A. Piel, Phys. Rev. Lett. **70**, 3071 (1993); F. Greiner, T. Klinger, and A. Piel, Phys. Plasmas **2**, 1810 (1995).
[2] S.J. Hahn and J.K. Lee, Phys. Rev. E, 2162 (1993).
[3] S.J. Hahn, J.K. Lee, E.H. Park, and T.H. Chung, Nucl. Instr. Meth. A **341**, 200 (1994).
[4] E.H. Park, J.K. Lee, and T.H. Chung, Nucl. Instr. Meth. A **358**, 448 (1995); S.J. Hahn and J.K. Lee, Nucl. Instr. Meth. A **331**, 390 (1993); Phys. Lett. A **176**, 339 (1993).
[5] G.M.H. Knippels *et al.*, Phys. Rev. Lett. **75**, 1755 (1995); Phys. Rev. E **53**, 2778 (1996).
[6] D.A. Jaroszynski *et al.*, Phys. Rev. Lett. **71**, 3798 (1993).
[7] Y. Sentoku *et al.*, Nucl. Instr. Meth. A **358**, 463 (1995).
[8] T. Braun, *et al.*, Phys. Rev. Lett. **59**, 613 (1987).
[9] P.Y. Cheung, *et al.*, Phys. Rev. Lett. **61**, 1360 (1988).
[10] S. Kuhn, Phys. Fluids **27**, 1834 (1984); J.R. Pierce, J. Appl. Phys. **15**, 721 (1944).
[11] B.B. Godfrey, Phys. Fluids **30**, 1553 (1987); W.S. Lawson, Phys. Fluids B **1**, 1483 (1989).
[12] X. Chen and P. Linsay, IEEE Trans. Plasma Sci. **24**, 1005 (1996).
[13] M. Bohm and S. Torven, Phys. Rev. Lett. **66**, 604 (1991); S. Kuhn, and M. Hörhager, J. Appl. Phys. **60**, 1952 (1986).
[14] H.J. Lee, J.K. Lee, *et al.*, Mode Transition and Nonlinear Dynamics in the Beam-Injected Plasma, IEEE ICOPS, San Diego (May 19-22, 1997).
[15] J.P. Verboncoeur, M.V. Alves, V. Vahedi, and C.K. Birdsall, J. Comp. Phys. **104**, 321 (1993).
[16] H. Gunell, J.P. Verboncoeur, N. Brenning, and S. Torven, Phys. Rev. Lett. **77**, 5059 (1996).
[17] T.H. Chung, H.J. Yoon, T.S. Kim, and J.K. Lee, J. Phys. D **29**, 1014 (1996); T.H. Chung, H.J. Yoon, and J.K. Lee, J. Appl. Phys. **78**, 6441 (1995).
[18] R. Bonifacio, *et al.*, Phys. Rev. Lett. **69**, 3177 (1992).
[19] J.K. Lee and S.J. Hahn, IEEE Trans. Plasma Sci. **19**, 52 (1991); J.K. Lee and C.K. Birdsall, Phys. Fluids **22**, 1315 (1979).
[20] C.W. Roberson and P. Sprangle, Phys. Fluids B **1**, 3 (1989); Eq. (35).
[21] M. J. Feigenbaum, J. Stat. Phys. **19**, 25 (1978), and **20**, 669 (1979).
[22] T.M. Antonsen, in *Nonlinear Dynamics and Particle Acceleration* (Tsukuba, Japan 1990), edited by Y.H. Ichikawa and T. Tajima, AIP Conf. Proc. No. 230, (AIP, New York, 1991), p. 106.
[23] P.W. Lee, *et al.*, Appl. Phys. Lett. **69**, 2024 (1996).
[24] N. Kwon, *et al.*, Phys. Rev. A, **54**, 1459 (1996); J. Du, C. Chiang, and Lin I, Phys. Rev. E **54**, 1829 (1996).
[25] J. Frey and C.K. Birdsall, J. Appl. Phys. **36**, 2692 (1965).
[26] C.A. Capeau, *et al.*, Phys. Plasmas **2**, 4650 (1995).
[27] W.X. Ding, *et al.*, Phys. Rev. Lett. **72**, 96 (1994).

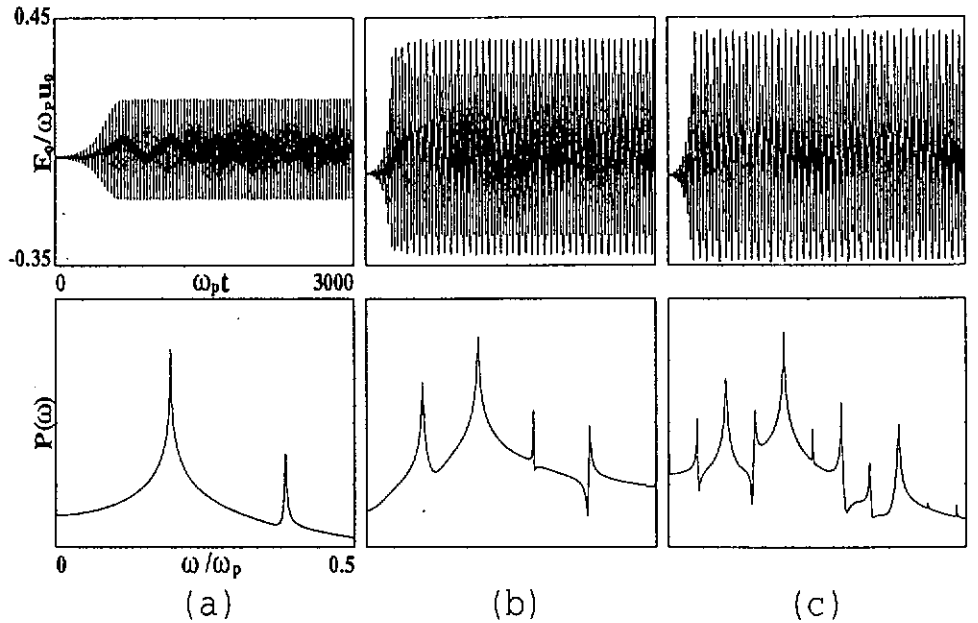

FIG. 1. Self-oscillation, period-doubled, and period-quadrupled oscillations with $\eta = 1$, $\alpha = 2.88\pi$, and (a) $\phi = 0$ (b) $\phi = 0.025$ (c) $\phi = 0.0285$.

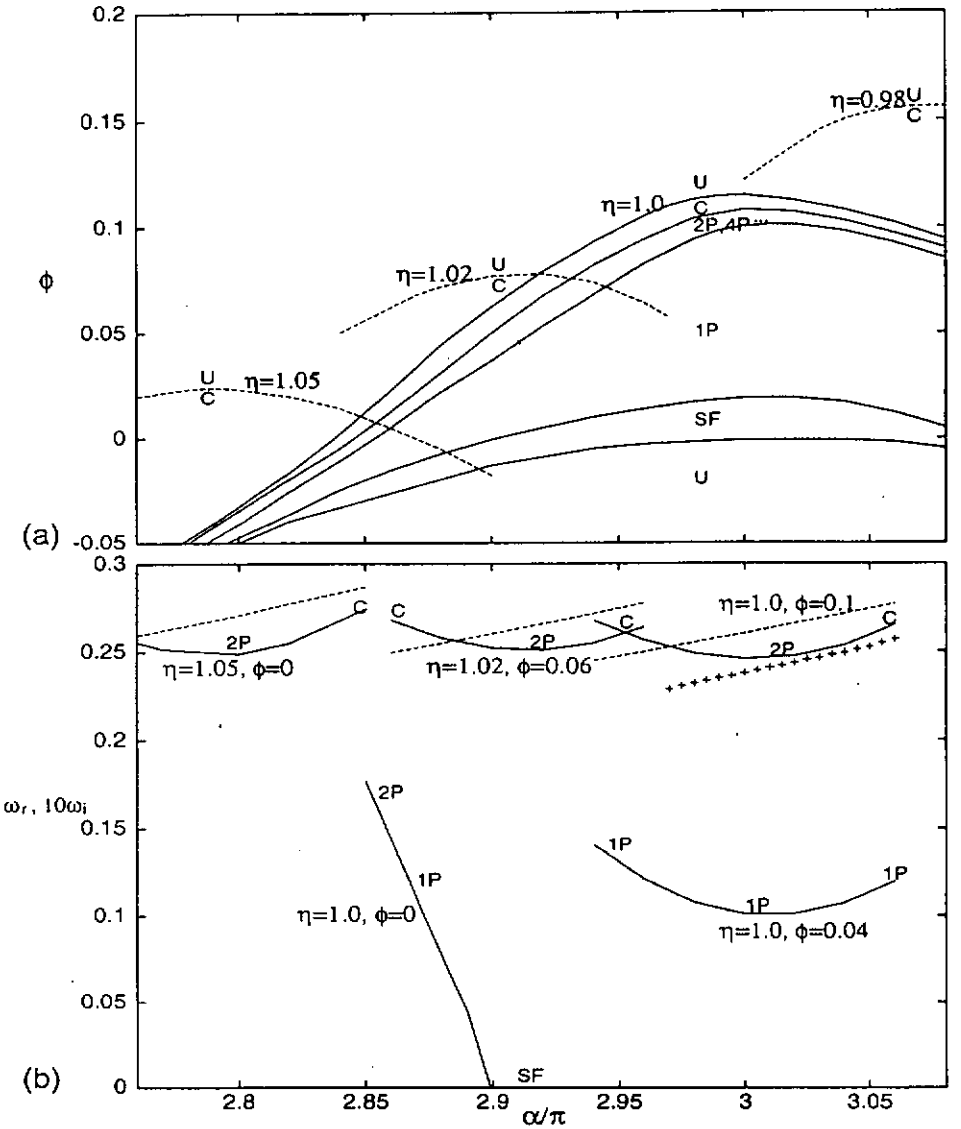

FIG. 2. The calculations on the extended Pierce system with the fluid model. (a) Phase diagrams of input parameters. The regions for spiral focus, self-oscillation, period-doubling, chaos, and unstable region are marked SF, $1P$, $2P$, C, and U. (b) Linear growth rate (solid line), oscillation frequency (dashed line), and nonlinear oscillation frequency (crosses) for varying values of η and ϕ.

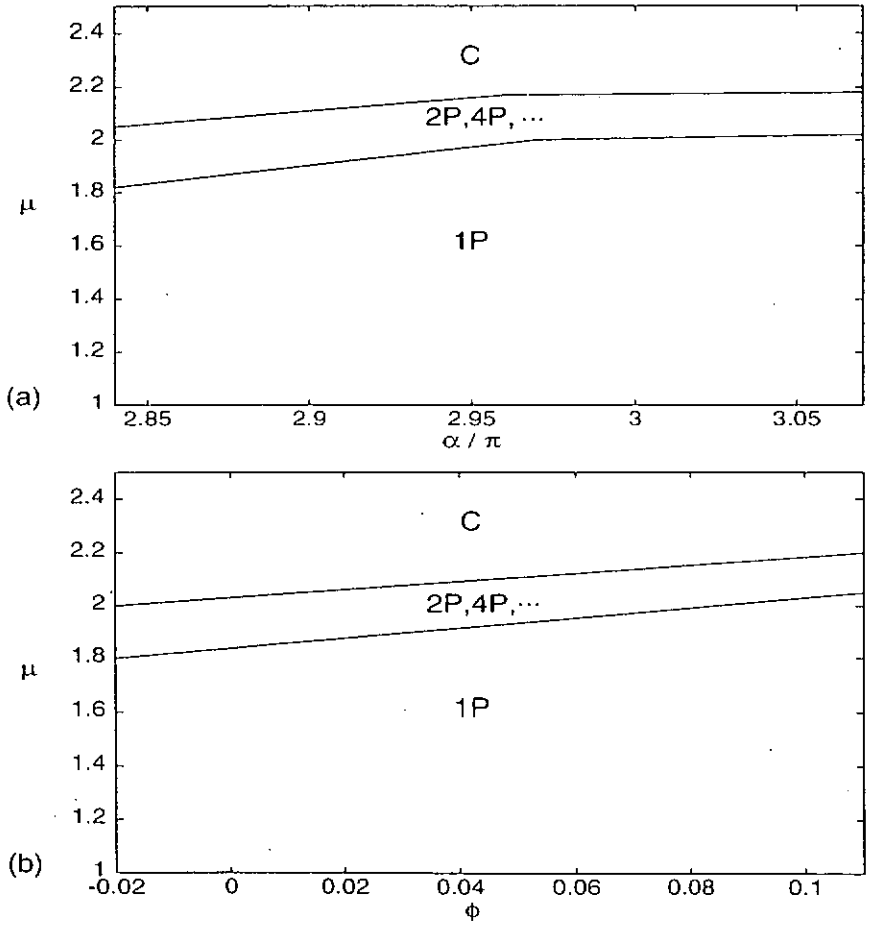

FIG. 3. Phase diagram by the fluid simulations in terms of the deterministic parameter μ vs (a) α and (b) ϕ with $\eta = 1$.

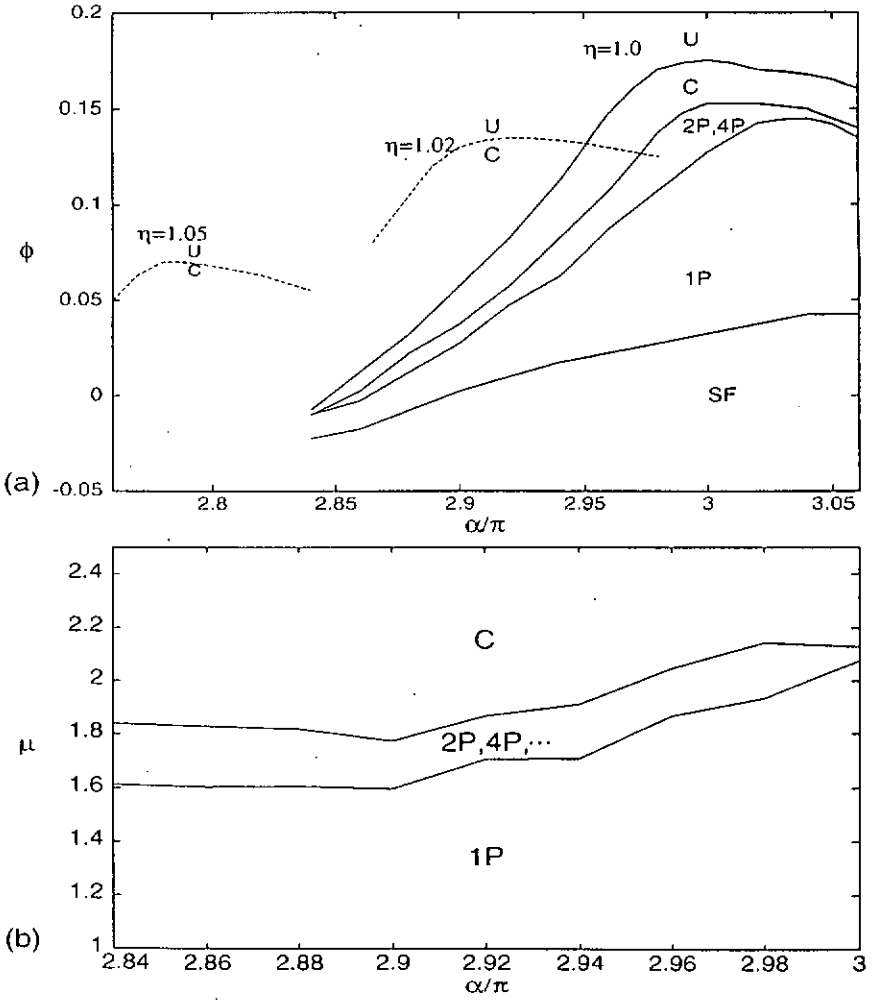

FIG. 4. Phase diagram by the kinetic simulations in terms of (a) the input parameters and (b) μ.

Reduced form of MHD Lagrangian for ballooning modes

R.L. Dewar

Research School of Physical Sciences and Engineering,

The Australian National University, Canberra ACT 0200

Abstract

The derivation of the short-perpendicular-scale-length approximate reduction of the ideal magnetohydrodynamic Lagrangian is reviewed.

1 Introduction

The three-dimensional Wentzel-Brillouin-Kramers (WKB) formalism for ballooning modes breaks down due to the formation of singular solutions signalled by the escape of ray paths to infinity in four-dimensional phase space, or the existence of attracting fixed points in the reduced three-dimensional phase that can be used in ideal MHD [1]. Thus we need to go back to first principles to investigate the nature of these singular solutions. In order to simplify the algebra it is desirable to find a reduced description for flute-like (finite $k_\parallel$, large $k_\perp$) modes *before* making the eikonal ansatz used in WKB theory.

To this end we derive a reduced form of the ideal magnetohydrodynamic Lagrangian, involving only a single scalar field similar to the energy principle given in the pioneering paper of Furth, Killeen, Rosenbluth and Coppi (FKRC) [2]. We also give the fully compressible, two field generalization of this form.

Assuming the equilibrium magnetic field lines all lie within nested invariant magnetic surfaces we label them with the enclosed poloidal flux $2\pi\psi$. Introducing poloidal and toroidal angles θ and ζ, we write the equilibrium magnetic field as $\mathbf{B} = \nabla\zeta\times\nabla\psi +$

$q\nabla\psi\times\nabla\theta$, where $q(\psi)$ is the safety factor (inverse of the rotational transform, ι). The equilibrium condition is $\nabla p = \mathbf{j}\times\mathbf{B}$, where $\mathbf{j} = \nabla\times\mathbf{B}/\mu_0$ is the equilibrium current and $p(\psi)$ is the equilibrium pressure, with μ_0 being the permeability of free space (SI units). We also define the quantities $\sigma \equiv \mathbf{j}\cdot\mathbf{B}/B^2$, proportional to the parallel component of the current, and $\boldsymbol{\kappa} \equiv \mathbf{e}_{\|}\cdot\nabla\mathbf{e}_{\|}$, the curvature of the magnetic field lines.

Using $\nabla\times\mathbf{B} = \mu_0\mathbf{j}$ and the equilibrium relation Eq. (1), we can prove the useful identity [3] relating the field-line curvature to the perpendicular component of the gradient of the total (field plus kinetic) pressure

$$\boldsymbol{\kappa} = \frac{\nabla_\perp(B^2 + 2\mu_0 p)}{2B^2} , \tag{1}$$

where subscript $\perp$ on any vector $\mathbf{f}$ denotes its projection $\mathsf{P}_\perp\cdot\mathbf{f}$ onto the plane locally perpendicular to $\mathbf{B}$, $\mathsf{P}_\perp$ being the *perpendicular projection operator*

$$\mathsf{I} - \mathbf{e}_{\|}\mathbf{e}_{\|} . \tag{2}$$

Decomposing, $\mathbf{j} \equiv \sigma\mathbf{B} + \mathbf{j}_\perp$, and using $\nabla\cdot\mathbf{j} = 0$ we see that $\mathbf{B}\cdot\nabla\sigma = -\nabla\cdot\mathbf{j}_\perp$. From the equilibrium condition, it is easily seen that $\mathbf{j}_\perp = \mathbf{B}\times\nabla p/B^2$, which is called the *diamagnetic current*. Taking its divergence and using Eq. (1) gives an identity relating the parallel current to the geodesic curvature $\mathbf{B}\cdot\nabla\sigma = 2\boldsymbol{\kappa}\cdot\mathbf{B}\times\nabla p/B^2$.

2 Lagrangian

The ideal MHD equations for a linearized displacement $\boldsymbol{\xi}$ with time dependence cos or $\sin\omega t$ are the Euler–Lagrange equations that extremize the time-averaged Lagrangian

$$L = \omega^2 K - \delta W , \tag{3}$$

where $\omega^2 K$ is the kinetic energy and δW is the potential energy of the plasma. As this variational principle can also be arrived at by minimizing δW under the normalization constraint K = const, ω^2 then being a Lagrange multiplier, the choice of K is often referred to as the "normalization".

2.1 Kinetic energy models

The kinetic energy factor K is defined by

$$K = \tfrac{1}{2}\int_\Omega d^3x\ \boldsymbol{\xi}\cdot\boldsymbol{\rho}_{\mathbf{M}}\cdot\boldsymbol{\xi}\ , \tag{4}$$

where Ω is the region occupied by the plasma. Here we have allowed for the use of a model kinetic energy with an anisotropic inertia by use of a dyadic mass density, $\boldsymbol{\rho}_{\mathbf{M}}$.

In this section we consider two choices for K:

1. **Physical normalization**

   Here we use an isotropic density

   $$\boldsymbol{\rho}_{\mathbf{M}} = \rho(\psi)\mathsf{I}\ ; \tag{5}$$

2. **Incompressible physical model**

   If we take

   $$\boldsymbol{\rho}_{\mathbf{M}} = \rho(\psi)\left(\frac{\nabla\psi\nabla\psi}{|\nabla\psi|^2} + \frac{\nabla\psi\times\mathbf{B}\,\nabla\psi\times\mathbf{B}}{|\nabla\psi|^2|\mathbf{B}|^2}\right) \tag{6}$$

   we have a compromise choice that is physical in the plane perpendicular to $\mathbf{B}$, but which annihilates the parallel component of $\boldsymbol{\xi}$ from K, so $\nabla\cdot\boldsymbol{\xi}$ vanishes identically (see Sec. 4.1).

2.2 Potential energy

For the potential energy in a plasma enclosed by a perfectly conducting wall we use the form due to Furth *et al.* [2], as given in full generality by Greene and Johnson [3]

$$\begin{aligned}\delta W \;=\; \tfrac{1}{2}\int_\Omega d^3x \Bigg[&\frac{\mathbf{Q}_\perp^2}{\mu_0} + \frac{(\mathbf{Q}\cdot\mathbf{B} - \mu_0\boldsymbol{\xi}\cdot\nabla p)^2}{\mu_0 B^2} + \gamma p(\nabla\cdot\boldsymbol{\xi})^2 \\ &- \sigma\boldsymbol{\xi}_\perp\times\mathbf{B}\cdot\mathbf{Q}_\perp - 2\boldsymbol{\xi}_\perp\cdot\boldsymbol{\kappa}\,\boldsymbol{\xi}_\perp\cdot\nabla p\Bigg]\ ,\end{aligned} \tag{7}$$

where $\mathbf{Q} \equiv \nabla\times(\boldsymbol{\xi}\times\mathbf{B})$ is the perturbation in the magnetic field.

3 Representation of $\boldsymbol{\xi}$ and Q

We shall denote our formal asymptotic expansion parameter by ϵ and adopt the following scalings as $\epsilon \to 0$:

$$L \sim k_{\|} = O(1)\,, \tag{8}$$

$$k_{\perp} = O(\epsilon^{-1})\,, \tag{9}$$

$$\mathbf{B} \sim \xi_{\perp} \sim \xi_{\|} = O(1)\,. \tag{10}$$

The motion perpendicular to $\mathbf{B}$ is dominated by the Alfvén branch and is primarily transverse to $\mathbf{k}$, but the slow magnetosonic wave provides a small longitudinal component. Thus we are led to the representation

$$\boldsymbol{\xi}_{\perp} = \frac{\mathbf{B}\times\boldsymbol{\nabla}\varphi}{B^2} - [\boldsymbol{\nabla}_{\perp}\chi]\,, \tag{11}$$

where $\varphi = O(\epsilon)$ is a stream function for the perpendicular displacement and $\chi = O(\epsilon^2)$ is a potential to provide the small longitudinal part.

In this section we indicate that terms are $O(\epsilon)$ by enclosing them in square brackets. Thus, in Eq. (11), the first term is $O(1)$ but the second is $O(\epsilon)$.

Since the curl of a gradient vanishes identically, the divergence

$$\boldsymbol{\nabla}\cdot\boldsymbol{\xi}_{\perp} = \boldsymbol{\nabla}\times\left(\frac{\mathbf{B}}{B^2}\right)\cdot\boldsymbol{\nabla}\varphi - \boldsymbol{\nabla}\cdot\boldsymbol{\nabla}_{\perp}\chi \tag{12}$$

is $O(1)$. Also, $\boldsymbol{\nabla}\cdot(\xi_{\|}\mathbf{e}_{\|}) \equiv \mathbf{B}\cdot\boldsymbol{\nabla}(\xi_{\|}/B) = O(1)$, by Eq. (8). Thus $\boldsymbol{\nabla}\cdot\boldsymbol{\xi} = O(1)$ also.

In order to calculate the magnetic field perturbation $\mathbf{Q} \equiv \boldsymbol{\nabla}\times(\boldsymbol{\xi}\times\mathbf{B})$, first note from Eq. (11) that

$$\boldsymbol{\xi}\times\mathbf{B} = \boldsymbol{\nabla}_{\perp}\varphi + [\mathbf{B}\times\boldsymbol{\nabla}_{\perp}\chi]\,. \tag{13}$$

Thus

$$\begin{aligned}\mathbf{Q} &= \boldsymbol{\nabla}\times(\boldsymbol{\nabla}_{\perp}\varphi) + \mathbf{B}\boldsymbol{\nabla}\cdot\boldsymbol{\nabla}_{\perp}\chi \\ &\quad + [\boldsymbol{\nabla}_{\perp}\chi\cdot\boldsymbol{\nabla}\mathbf{B} - \mathbf{B}\cdot\boldsymbol{\nabla}\boldsymbol{\nabla}_{\perp}\chi]\,.\end{aligned} \tag{14}$$

4 Reduction of the Lagrangian

Using the above results we find, to leading order in ϵ,

$$2\delta W^{(0)} = \int_{\Omega} d^3x \left\{ \frac{B^2}{\mu_0}\left|\boldsymbol{\nabla}_{\perp}\left(\frac{\mathbf{B}\cdot\boldsymbol{\nabla}\varphi}{B^2}\right)\right|^2 + \frac{|B^2\boldsymbol{\nabla}\cdot\boldsymbol{\xi}_{\perp} + 2\boldsymbol{\kappa}\times\mathbf{B}\cdot\boldsymbol{\nabla}_{\perp}\varphi|^2}{\mu_0 B^2}\right.$$

$$+\gamma p\left|\boldsymbol{\nabla}\cdot\boldsymbol{\xi}_\perp+\mathbf{B}\cdot\boldsymbol{\nabla}\left(\frac{\xi_\parallel}{B}\right)\right|^2$$
$$-\frac{(\boldsymbol{\kappa}\times\mathbf{B}\cdot\boldsymbol{\nabla}_\perp\varphi^*)(\boldsymbol{\nabla}p\times\mathbf{B}\cdot\boldsymbol{\nabla}_\perp\varphi)}{B^4}$$
$$\left.-\frac{(\boldsymbol{\nabla}p\times\mathbf{B}\cdot\boldsymbol{\nabla}_\perp\varphi^*)(\boldsymbol{\kappa}\times\mathbf{B}\cdot\boldsymbol{\nabla}_\perp\varphi)}{B^4}\right\}, \tag{15}$$

and

$$2K^{(0)}=\int_\Omega d^3x\,\left(\frac{\mathbf{B}\times\boldsymbol{\nabla}_\perp\varphi^*}{B^2}+\xi_\parallel^*\mathbf{e}_\parallel\right)\cdot\boldsymbol{\rho}_\mathbf{M}\cdot\left(\frac{\mathbf{B}\times\boldsymbol{\nabla}_\perp\varphi}{B^2}+\xi_\parallel\mathbf{e}_\parallel\right), \tag{16}$$

where the superscript (0) denotes the part that is $O(\epsilon^0)$ and we have used a "complexified" bilinear form in order to make sure the self adjointness is explicit.

4.1 One-field, incompressible models

If we use the a kinetic energy model, such as 2 in Sec. 2.1, in which the parallel component of $\boldsymbol{\xi}$ does not appear, then the kinetic energy norm reduces to

$$2K^{(0)}=\int_\Omega d^3x\,\frac{\mathbf{B}\times\boldsymbol{\nabla}_\perp\varphi^*\cdot\boldsymbol{\rho}_\mathbf{M}\cdot\mathbf{B}\times\boldsymbol{\nabla}_\perp\varphi}{B^4}. \tag{17}$$

By extremizing with respect to $\xi_\parallel$ and χ it can be shown that both the kinetic and field-line compression terms drop out of Eq. (15), so we are left with a potential energy involving the single field φ

$$2\delta W^{(0)}=\int_\Omega d^3x\left\{\frac{B^2}{\mu_0}\left|\boldsymbol{\nabla}_\perp\left(\frac{\mathbf{B}\cdot\boldsymbol{\nabla}\varphi}{B^2}\right)\right|^2-\frac{(\boldsymbol{\nabla}p\times\mathbf{B}\cdot\boldsymbol{\nabla}_\perp\varphi^*)(\boldsymbol{\kappa}\times\mathbf{B}\cdot\boldsymbol{\nabla}_\perp\varphi)}{B^4}\right.$$
$$\left.-\frac{(\boldsymbol{\kappa}\times\mathbf{B}\cdot\boldsymbol{\nabla}_\perp\varphi^*)(\boldsymbol{\nabla}p\times\mathbf{B}\cdot\boldsymbol{\nabla}_\perp\varphi)}{B^4}\right\}. \tag{18}$$

The wave equation, obtained from Eq. (18) by extremizing the Lagrangian with respect to φ^*, is

$$\mathbf{B}\cdot\boldsymbol{\nabla}\left\{\frac{1}{B^2}\boldsymbol{\nabla}\cdot\left[\frac{B^2}{\mu_0}\mathsf{P}_\perp\cdot\boldsymbol{\nabla}\left(\frac{\mathbf{B}\cdot\boldsymbol{\nabla}\varphi}{B^2}\right)\right]\right\}+\boldsymbol{\nabla}\cdot\left(\frac{\boldsymbol{\nabla}p\times\mathbf{B}\,\boldsymbol{\kappa}\times\mathbf{B}\cdot\boldsymbol{\nabla}\varphi}{B^4}\right)$$
$$+\boldsymbol{\nabla}\cdot\left(\frac{\boldsymbol{\kappa}\times\mathbf{B}\,\boldsymbol{\nabla}p\times\mathbf{B}\cdot\boldsymbol{\nabla}\varphi}{B^4}\right)+\omega^2\boldsymbol{\nabla}\cdot\left(\frac{\rho}{B^2}\mathsf{P}_\perp\cdot\boldsymbol{\nabla}\varphi\right)=0. \tag{19}$$

4.2 Two-field, compressible model

For model 1 of Sec. 2.1, the kinetic energy norm is

$$2K^{(0)}=\int_\Omega d^3x\,\rho(\psi)\left[\frac{|\boldsymbol{\nabla}_\perp\varphi|^2}{B^2}+\left|\xi_\parallel\right|^2\right]. \tag{20}$$

We vary $\nabla\cdot\boldsymbol{\xi}_\perp^*$, obtaining from Eq. (15) the Euler–Lagrange equation

$$\left(\frac{B^2}{\mu_0}+\gamma p\right)\nabla\cdot\boldsymbol{\xi}_\perp = -\frac{2\boldsymbol{\kappa}\times\mathbf{B}\cdot\nabla_\perp\varphi}{\mu_0} - \gamma p\mathbf{B}\cdot\nabla\left(\frac{\xi_\parallel}{B}\right) . \tag{21}$$

Using this to eliminate $\nabla\cdot\boldsymbol{\xi}_\perp$ from $\delta W^{(0)}$ we obtain from Eq. (15)

$$\begin{aligned} 2\delta W^{(0)} \;=\; \int_\Omega d^3x \Bigg\{ & \frac{B^2}{\mu_0}\left|\nabla_\perp\left(\frac{\mathbf{B}\cdot\nabla\varphi}{B^2}\right)\right|^2 \\ & + \frac{\gamma p B^2}{(B^2+\mu_0\gamma p)}\left|\mathbf{B}\cdot\nabla\left(\frac{\xi_\parallel}{B}\right) - \frac{2\boldsymbol{\kappa}\times\mathbf{B}\cdot\nabla_\perp\varphi}{B^2}\right|^2 \\ & - \frac{(\nabla p\times\mathbf{B}\cdot\nabla_\perp\varphi^*)(\boldsymbol{\kappa}\times\mathbf{B}\cdot\nabla_\perp\varphi)}{B^4} \\ & - \frac{(\boldsymbol{\kappa}\times\mathbf{B}\cdot\nabla_\perp\varphi^*)(\nabla p\times\mathbf{B}\cdot\nabla_\perp\varphi)}{B^4}\Bigg\} . \end{aligned} \tag{22}$$

Acknowledgments

The author wishes to thank Mr J. L. V. Lewandowski for raising some of the issues addressed in this brief review, Drs J. M. Greene and J. L. Johnson for their comments on a draft manuscript, and Dr Z. Yoshida for useful discussions. He also takes pleasure in acknowledging the kind hospitality of Professor A. Iiyoshi during his visit to the National Institute for Fusion Science, Nagoya where the full paper (to be published in J. Plasma & Fusion Res.) on which this is based was written.

References

[1] R. L. Dewar and A. H. Glasser, Phys. Fluids **26**, 3038 (1983).

[2] H. P. Furth, J. Killeen, M. N. Rosenbluth, and B. Coppi, in *Plasma Physics and Controlled Nuclear Fusion Research* (IAEA, Vienna, 1966), Vol. 1, pp. 103–126.

[3] J. M. Greene and J. L. Johnson, Plasma Phys. **10**, 729 (1968).

Two-Fluid and Parallel Compressibility Effects in Tokamak Plasmas

Linda E. Sugiyama
Research Laboratory of Electronics
Massachusetts Institute of Technology, Cambridge MA 02139-4307 U.S.A.
Wonchull Park
Princeton Plasma Physics Laboratory
Princeton University, Princeton N.J. 08543 U.S.A.

The MHD, or single fluid, model for a plasma has long been known to provide a surprisingly good description of much of the observed nonlinear dynamics of confined plasmas, considering its simple nature compared to the complexity of the real system. On the other hand, some of the supposed agreement arises from the lack of the detailed measurements that are needed to distinguish MHD from more sophisticated models that incorporate slower time scale processes. At present, a number of factors combine to make models beyond MHD of practical interest. Computational considerations still favor fluid rather than particle models for description of the full plasma, and suggest an approach that starts from a set of fluid-like equations that extends MHD to slower time scales and more accurate parallel dynamics.

This paper summarizes a set of two-fluid equations for toroidal (tokamak) geometry that has been developed and tested as the MH3D-T code [1] and some results from the model. The electrons and ions are described as separate fluids. The code and its original MHD version, MH3D [2], are the first numerical, initial value models in toroidal geometry that include the full 3D (fluid) compressibility and electromagnetic effects. Previous nonlinear MHD codes for toroidal geometry have, in practice, neglected the plasma density evolution, on the grounds that MHD plasmas are only weakly compressible and that the background density variation is weaker than the temperature variation. Analytically, the common use of toroidal plasma models based on aspect ratio expansion, such as reduced MHD, has reinforced this impression, since this ordering reduces plasma compressibility effects.

For two-fluid plasmas, the density evolution cannot be neglected in principle, since it provides the basic driving energy for the diamagnetic drifts of the electrons and ions perpendicular to the magnetic field. It also strongly influences the parallel dynamics, in combination with the parallel thermal conductivity. The true parallel plasma dynamics are driven by additional kinetic processes that are not included in the fluid picture, but the basic fluid effects remain and should be understood first.

The two-fluid code is part of a larger project, the M3D, or Multi-Level 3D project [3] for toroidal plasmas. Its goal is to develop a comprehensive suite of simulation models that cover a range of physics from simple to complex, starting from the fluid and progressing toward kinetic models. In addition to the new physics that it describes beyond MHD, the present two-fluid code provides a good base for adding additional, non-fluid effects in a fully electromagnetic and toroidal model. The use of gyrokinetic particle simulation to

provide an improved closure for the ion fluid, combined with an electron fluid, is currently under development.

Two-Fluid Equations

The two-fluid equations for toroidal (tokamak) geometry that comprise the MH3D-T code [1] are based on the drift ordering [4], which has been generalized to arbitrary perturbation size. This ordering contains time scales slower than MHD ($\partial/\partial t \sim \delta v_{th}$, where δ is a small parameter and v_{th} is the ion thermal velocity), while retaining validity beyond the strictly collisional regime, but it is not rigorous nonlinearly. Electrons and ions are treated as separate fluids. The model includes the ion gyroviscous force, the Hall terms and electron pressure gradient in Ohm's law, and equations for the electron and ion temperature evolution, with parallel and perpendicular thermal conductivities. As a first approximation, the electrons are treated as massless and the pressures assumed to be isotropic.

The fluid velocities can be written exactly in terms of the generalized diamagnetic velocities as $\mathbf{v}_i = \mathbf{v} + \mathbf{v}_{di}$ and $\mathbf{v}_e = \mathbf{v} + \mathbf{v}_{*e} - \mathbf{J}_{||}/en_e$, where $\mathbf{v}_{*j} \equiv \mathbf{B} \times \nabla p_j/(q_j n_j B^2)$. The perpendicular ($\perp \mathbf{B}$) component of $\mathbf{v}$ is the guiding center velocity of the electrons and ions in the perpendicular direction. The generalized ion 'diamagnetic' velocity $\mathbf{v}_{di} \equiv \mathbf{J}_\perp/(en_e) + \mathbf{v}_{*e}$ contains the polarization drift.

In terms of $\mathbf{v}$, the two-fluid equations can be written in rationalized units as

$$\frac{\partial \mathbf{v}}{\partial t} + (\mathbf{v}\cdot\nabla)\mathbf{v} = -(\mathbf{v}_{di}\cdot\nabla)\mathbf{v}_\perp + \frac{\mathbf{J}\times\mathbf{B}}{\rho} - \frac{\nabla p}{\rho} + \mu\nabla_\perp^2\mathbf{v} + \frac{\mathcal{V}_{gv}}{\rho} - \frac{\nabla\cdot\mathbf{\Pi}_{i||}}{\rho} \quad (1)$$

$$\frac{\partial \mathbf{B}}{\partial t} = -\nabla\times\mathbf{E} \quad (2)$$

$$\mathbf{E} = -\mathbf{v}\times\mathbf{B} + \eta\mathbf{J}^* - \frac{\nabla_{||}p_e}{en} - \frac{\nabla\cdot\mathbf{\Pi}_{e||}}{en}, \quad (3)$$

where $\mathbf{J}^* = \mathbf{J} + (3/2)en\mathbf{v}_{*Te}$. Here ρ is the plasma mass and $\mathcal{V}_{gv}$ represents the parallel vorticity-related part of the ion gyroviscous force $\nabla\cdot\mathbf{\Pi}_i^{gv}$, $\mathcal{V}_{gv} = -[(\nabla_\perp + 2\hat{\mathbf{b}}\nabla_{||})X + (p_i/\Omega_{ci})(\hat{\mathbf{b}}\times\nabla_\perp)\nabla_{||}\mathbf{v}_{i||}]$ with $X \equiv -(p_i/2\Omega_{ci})\,\hat{\mathbf{b}}\cdot\nabla\times\mathbf{v}_{i\perp}$. The continuity and temperature equations ($p_j = n_j T_j$, $n_e = n_i \equiv n$) are, with $\nabla\cdot\mathbf{J} = 0$,

$$\frac{\partial n}{\partial t} + \nabla\cdot(n\mathbf{v}_e) = 0 \quad (4)$$

$$\frac{\partial T_j}{\partial t} + \mathbf{v}_j\cdot\nabla T_j = -\hat{\Gamma}_j T_j\nabla\cdot\mathbf{v}_j + \nabla\cdot n\kappa_{\perp j}\nabla_\perp T_j + \nabla\cdot n\kappa_{||j}\nabla_{||}T_j - \hat{\Gamma}_j\nabla\cdot(T_j\mathbf{v}_{*Tj}), \quad (5)$$

for electrons and ions $j = e, i$, where $\hat{\Gamma}_j = \Gamma_j - 1$, Γ_j being the ratio of specific heats, and $\mathbf{v}_{*Tj}$ is the diamagnetic drift based on the temperature gradient. The neoclassical, collisional parallel viscous forces $\nabla\cdot\mathbf{\Pi}_{j||}$, that extend the fluid model into the long parallel mean free path regime [5] are currently being tested. Writing the equations in terms of $\mathbf{v}$ introduces a few approximations in the model equations and in particular in the form chosen for the ion gyroviscous stress tensor, discussed in [1]. These should be minor for the results described here.

Parallel Compressibility

Tests of the two-fluid model showed a number of unexpected effects due to the newly introduced parallel dynamics; they are equally important in MHD.

The continuity equation introduces the possibility of sound wave propagation along the magnetic field whenever the steady state condition $\nabla \cdot n\mathbf{v}_i$ is not satisfied. This propagation condition differs from that given by the pressure equation in the absence of density evolution, whenever there is a difference between the temperature and density equilibration along the magnetic field lines (e.g., different $\kappa_{||}$'s) or when the equilibrium density and temperature profiles are not simply related (e.g., by adiabaticity, $p \propto n^{\Gamma}$). A confined plasma typically encompasses both these differences. Usually the electron, and possibly the ion, temperature experiences faster parallel smoothing than the density, due to collisions, waves, or the thermal streaming of the electrons, while the density smoothing is mediated by sound waves. The parallel dynamics have much stronger effects in a torus than in a cylinder, due to the poloidal asymmetry of the flux surfaces, which also influences the poloidal plasma rotation and thereby the parallel flows through various forms of 'magnetic pumping' [6]. The plasma equilibrium profiles are also driven to deviate from a simple relation $p(n)$ relation by the different effective perpendicular conductivities and sources/sinks for the temperature and density.

The numerical results clearly illustrate the effects of the density evolution and the parallel thermal conductivity. For linear modes, the density evolution can be stabilizing or destabilizing. The strong stabilizing effect of the density equation on the 1/1 resistive mode in a torus with $R/a = 3$ has been shown for strongly and weakly ideal MHD unstable modes [9] [8]. A factor of 2 stabilization was seen for the resistive modes with weaker growth rates. The effect on the mode in a cylinder is also stabilizing, but much smaller.

The competition between the parallel thermal conductivity (stabilizing) and the density evolution (destabilizing) for a resistive ballooning MHD 3/2 mode in a torus with $R/a = 3$ and magnetic Reynold's number $S = 10^4$ is shown in Figure 1. The equilibrium density and temperature profiles are strongly peaked and the safety factor q varies from 1.1 at the magnetic axis to 5 at the edge. For the mode, the perturbed pressure and velocity stream function u contours (where $\mathbf{v} = \epsilon R \nabla u \times \hat{\phi} + \nabla_{\perp}\chi + v_{\phi}\hat{\phi}$) appear similar for the case with no density evolution ($\partial n/\partial t = 0$) and $\kappa_{||} = 0$ and for the case with density evolution and relatively strong $\kappa_{||}$. The latter is shown in (a). The growth rate for the $\partial n/\partial t = 0$, $\kappa_{||} = 0$ case is $\gamma = 0.029$ in inverse Alfvén times $\tau_A = a/v_A$, $v_A \equiv (a/R)B_o/(4\pi n m_i)^{1/2}$. Turning on $\kappa_{||}$ decouples perturbations on adjoining magnetic surfaces and stabilizes the mode, $\gamma < 0$, shown in (b). Turning on the density evolution from this state returns to the growing mode (a), but the growth rate is reduced by 1/3, to $\gamma = 0.010$.

Nonlinearly, the parallel dynamics described by the density equation also introduces important differences in the development of magnetic islands [1]. When the density evolves, the results show that both MHD and two-fluid islands can couple much more easily to islands of different toroidal mode number n as the original island grows than with a fixed density. The difference in relative island sizes between two-fluid and MHD with the same density equation were much smaller than those between an evolving or fixed density. The two-fluid islands of different mode number were somewhat more strongly coupled than in MHD when the density evolution was included, and they also had different relative phases and poloidal rotations. In the example, a 2/1 island was grown nonlinearly for a given amount of time, starting from the same initial size. With the density variation, it triggered large 3/2 and 4/3 islands, as well as the other $n = 1$ islands (3/1, 4/1, 5/1, etc.) expected from the usual toroidal mode coupling ($q_o > 1$). With an unvarying density, the companion $n = 1$ islands developed in the same amount of time, while the $n \neq 1$ islands remained very small.

Plasma Rotation

In a cylinder, plasma rotation in the poloidal direction is not strongly constrained in the steady state, due to the poloidal symmetry of the flux surfaces. A torus, however, resists poloidal rotation of the plasma, while the toroidal rotation is constrained to have the form $v_\phi = R\Omega(\psi)$. In addition to previously studied mechanisms for magnetic pumping, which require dissipation, such as an effective viscosity, to remove the rotational energy as a plasma fluid element is compressed and uncompressed in a poloidal circuit [6], the numerical simulation shows that the fluid parallel dynamics in a torus can also damp the ion poloidal rotation into toroidal motion and electromagnetic changes, even when the dissipation is small. These effects operate on both fast flows and flows on the order of the diamagnetic velocities.

For subsonic poloidal flows, $M_p \simeq v_\theta/(v_s r/Rq) < 1$, where v_s is the sound speed, poloidal motion can be converted into toroidal motion through changes in the radial electric field E_ψ over a relatively fast time scale, equivalent to several sound-wave transit times around the torus, when the parallel thermal conductivity $\kappa_\parallel$ is relatively large. The magnitude of the effect depends on $\kappa_\parallel$. Since the density steady state $\nabla \cdot n\mathbf{v} \neq 0$, the poloidal velocity v_θ oscillates on a fast scale and the oscillations experience a slow outward radial propagation for a longer time. The results support the analytic expectation that the equilibrium ion poloidal velocity is zero when the parallel viscosity and ion gyroviscous stress tensor are included [7].

In the case of a very large applied poloidal rotation, above a critical velocity with poloidal Mach number $M_p \gtrsim 1$, a much stronger effect can be generated [8]. The end result is a new MHD equilibrium with an apparent internal 'transport barrier,' a localized region of steepened temperature gradient around a certain radius, but it is not a transport process. Given a poloidal rotation source strong enough to drive a radial strong shear in the toroidal velocity, a new MHD equilibrium can be established, with a region of steepened temperature gradient just inside a very low order rational surface, while the poloidal velocity is greatly reduced inside this surface. This requires density evolution and a $\kappa_\parallel$ large enough to keep $T \simeq T(\psi)$ roughly constant on a flux surface. It is a nondiffusive, axisymmetric process, where the magnetic flux surfaces shift in response to the toroidal velocity shear, due to conservation of the toroidal canonical momentum. Since the accompanying velocity oscillations propagate radially outward, the initial region of sharp toroidal velocity shear may also propagate outward until it reaches a low order rational surface, on which the field lines close on themselves in the fewest circuits around the torus (e.g., $q = 2$, when $q > 1$). The radial shape of the driving poloidal velocity is not important, since similar effects were triggered with velocities that increased toward the plasma edge and those that reached a maximum at mid-radius.

Two-Fluid Effects

Two-fluid effects can also have important stabilizing or destabilizing effects on mode stability. The most straightforward depend on the diamagnetic drifts of the electrons and ions and is described by the ratio of ω_{*j}/γ_o, where γ_o is the growth rate without two-fluid effects. For reconnecting modes, the ion ω_{*i} is generally stabilizing, while the electron ω_{*e} has a more complex effect, since it causes a complex radial shearing of the electron motion (i.e., the current) in the reconnection layer. In addition, the sound speed gyroradius $\rho_s = v_s/\Omega_{ci}$ is always destabilizing. The two-fluid code demonstrates the stabilizing effect of ω_{*i} on the 1/1 resistive mode in a cylinder and also the general physical mechanism

of ω_{*i}-stabilization for reconnecting modes of all m [1], shown in Fig. 2. For the 1/1 resistive mode, the electron drift ω_{*e} is destabilizing. The ion ω_{*i} stabilizes the mode by causing the plasma mass inflow into the reconnection layer from $r < r_1$ to rotate poloidally relative to the reconnection X-point in the ω_{*e} direction. This results from the growth and gradual dominance of the perturbed $\tilde{v}_{*ir}$ part of the radial ion fluid velocity as ω_{*i} increases. When $\omega_{*e} = 0$, the rotation angle reaches approximately $\pi/2$ near $\omega_{*i}/\gamma_o \simeq 2$, the point where the mode reaches the maximum stabilization, i.e., the inflow is almost exactly out of phase with the reconnection (Fig. 2b). If $\omega_{*e} \neq 0$, the perturbed current J_z in the reconnection layer also shears poloidally, and the relative inflow rotation angle and stabilization effect are reduced. The poloidal direction of the velocity component $\tilde{v}_{*ir}$ is always exactly out of phase with the X-point, and has the same stabilizing effect at all m, for both cylinder and torus.

Another two-fluid diamagnetic effect is the splitting of the TAE (toroidal Alfvén eigenmode) frequency. The usual MHD TAE mode is degenerate, since two modes propagate exactly opposite to each other along the magnetic field lines at the same frequency, $\omega^2 = \omega_{MHD}^2$, $\omega_{MHD} = k_\| v_A$. When an ion diamagnetic drift exists, the modes separate, with the dispersion relation $\omega(\omega - \omega_{*i}) = \omega_{MHD}^2$. This has been demonstrated using MH3D-T, for a decaying mode [1]. Such modes can be excited by externally driven waves and have been seen on JT-60U and JET.

Two-fluid effects on nonlinear magnetic island evolution have been discussed under parallel compressibility, above.

Acknowledgments
Work supported by the U.S. Department of Energy and by the Ministry of Education, Science, Sports, and Culture (Monbusho), Japan.

References

[1] L. E. Sugiyama and W. Park, M.I.T. Research Laboratory of Electronics Report PTP-96/2 (1997).

[2] W. Park, S. Parker, H. Bigliari, M. Chance, L. Chen, C.Z. Cheng, T.S. Hahm, W.W. Lee, R. Kulsrud, D. Monticello, L. Sugiyama, R. White, *Phys. Fluids B* **4** 2033 (1992); W. Park and D.A. Monticello, *Nucl. Fusion* **30** 2413 (1990).

[3] W. Park, G.Y. Fu, H.R. Strauss, L.E. Sugiyama, in *Proc. Int'l. Wkshp on Nonlinear and Extended MHD 1997*, Madison WI, Univ. Wisconsin-Madison Report (1997).

[4] R.D. Hazeltine and J.D. Meiss, *Phys. Rep.* **121** 1 (1985).

[5] S.P. Hirshman and D. Sigmar, *Nucl. Fusion* **21** 1079 (1981); J.D. Callen and K.C. Shaing, *Phys. Fluids* **28** 1845 (1985).

[6] J.M. Berger, W.A. Newcomb, J.M. Dawson, E.A. Frieman, R.M. Kulsrud, A. Lenard, *Phys. Fluids* **1** 301 (1958); T.H. Stix, *Phys. Rev. Lett.* **16** 1260 (1973); A.B. Hassam and R. Kulsrud, *Phys. Fluids* **21** 2271 (1978).

[7] E. Bowers and N.K. Winsor, *Phys. Fluids* **14** 2203 (1971).

[8] L.E. Sugiyama, in *Proc. Int'l. Wkshp on Extended and Nonlinear MHD 1997*, Madison WI, Univ. Wisconsin-Madison NE Report (1997).

[9] B. Coppi, et al., in *16th Int'l. Conf. on Fusion Energy, 1996, Montreal*, (IAEA, Vienna,1997), paper F1-CN-64/D2-1.

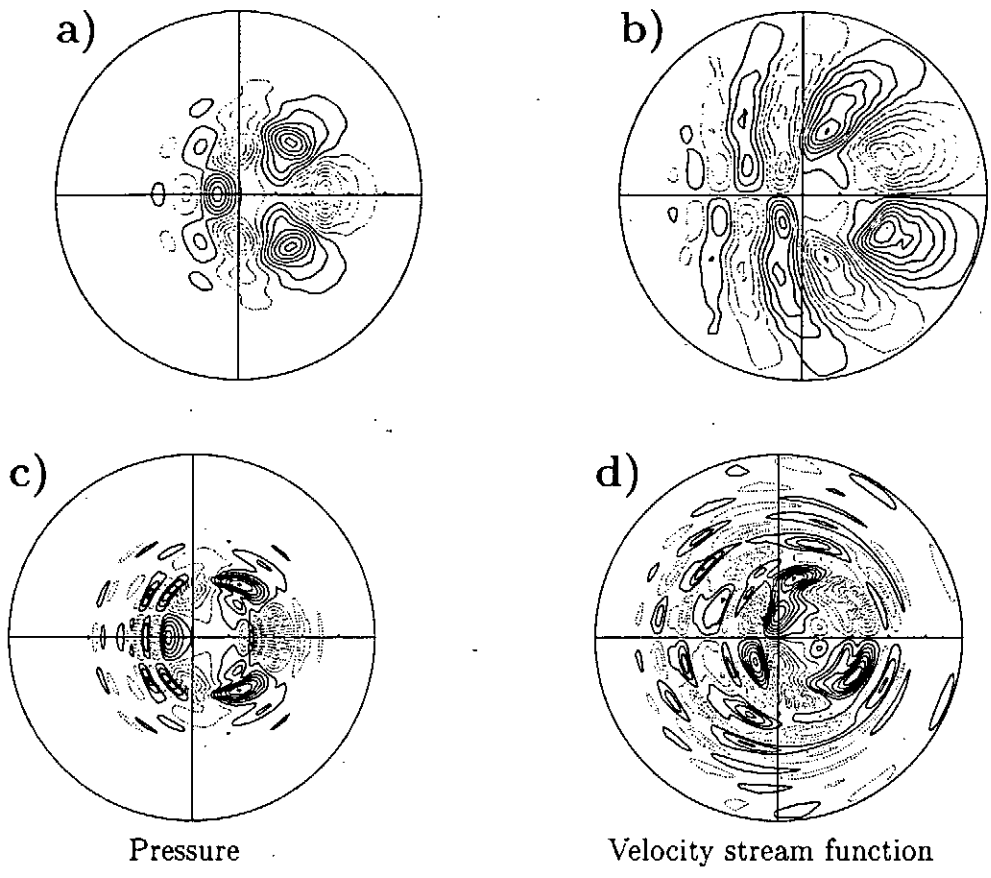

Figure 1. a) and b) Contours for resistive MHD 3/2 mode in a torus with strong $\kappa_{\|}$ and density evolution, $\gamma = 0.01$. The case with $\kappa_{\|} \simeq 0$ and $\partial n/\partial t = 0$ has similar contours, but larger $\gamma = 0.029$. c) and d) Case with large $\kappa_{\|}$ and $\partial n/\partial t = 0$ is stable, $\gamma < 0$.

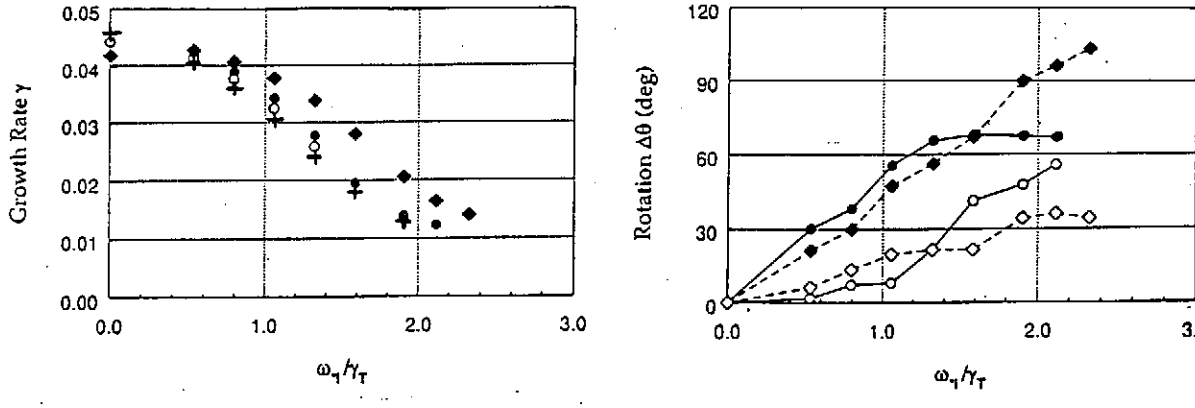

Figure 2. a) Growth rates for 1/1 resistive mode in a cylinder, showing the stabilizing effect of ω_{*i}, compared to the analytic dispersion relation (+) for $\omega_{*e} = -\omega_{*i}$ (open circles with $\kappa_{\|} = 0$ and solid circles with $\kappa_{\|} \neq 0$). The case $\omega_{*e} = 0$ is shown by diamonds. b) Relative poloidal rotation of direction of radial plasma inflow into reconnection layer from $r < r_1$, compared to the location of the reconnection X-point (ω_{*e}-direction). The ion fluid flow v_{ir} is given by the solid circles and diamonds, while the common flow v_r is given by the open symbols.

MAGNETOHYDRODYNAMIC ORIGIN OF JETS FROM ACCRETION DISKS

R.V.E. Lovelace
Department of Astronomy, Cornell University, Ithaca, NY 14853

M.M. Romanova
Space Research Institute, Profsoyuznaya 84/32, Moscow 117810, Russia; and Department of Astronomy, Cornell University, Ithaca, NY 14853

1. Introduction

A review is made of magnetohydrodynamic (MHD) theory and simulations of outflows from accretion disks for different distributions of magnetic field threading the disk. In one limit of a relatively weak, initially diverging magnetic field, both thermal and magnetic pressure gradients act to drive matter to an outflow, while a toroidal magnetic field develops which strongly collimates the outflow. The collimation greatly reduces the field divergence and the mass outflow rate decreases after an initial peak. In a second limit of a strong magnetic field, the initial field configuration was taken with the field strength on the disk decreasing outwards to small values so that collimation was reduced. As a result, a family of stationary solutions was discovered where matter is driven mainly by the strong magnetic pressure gradient force. The collimation in this case depends on the pressure of an external medium. These flows are qualitatively similar to the analytic solutions for magnetically driven outflows.[1] The problem of the opening of a closed field line configuration linking a magnetized star and an accretion disk is also discussed.

Many compact astrophysical objects emit powerful, highly-collimated, oppositely directed jets. Included are the radio jets of active galaxies, quasars (Bridle and Eilek[2]), and old compact stars in binaries (Mirabel and Rodriguez[3]), and emission line jets in young stellar objects (Mundt;[4] Bührke, Mundt, and Ray[5]). An example of the latter is shown in Figure 1.

A broad spectrum of ideas and models have been put forward to explain astrophysical jets (see reviews by Begelman, Blandford, and Rees;[6] Bisnovatyi-Kogan[7]). The matter is thought to go to the jet from the inner region of an accretion disk surrounding the compact object - a star or black hole. The disk matter must then be accelerated to a velocity higher that the escape velocity from the central object. Further, the jet matter should have sufficient momentum to propagate through surrounding inter-stellar or intra-galactic matter out to large distances. However, the main physics questions regarding the jets are *not* answered: 1. What is the main driving force pushing matter into the jet? 2. What determines the mass flow rate in the jet $\dot{M}_j$, and what faction is this of the accretion rate? **3.** What physics determines the asymptotic speed or Lorentz factor of the bulk flow? 4. What determines the collimation of the jet and at what distance from the central object does the jet become collimated? 5. What is the acceleration mechanism of leptons to Lorentz factors $\sim 10^2 - 10^3$ in the radio jets?

Here, we focus on jet formation mechanisms in which an ordered magnetic field has an essential role. Electrodynamic models for the origin of narrow jets were developed as an outgrowth of the Goldreich-Julian[8] aligned pulsar model (Lovelace;[9] Blandford;[10] Lovelace et al.;[11] Gisler et al.;[12] Wang et al.[13]). In these models the rotation of a Keplerian accretion disk twists a poloidal field threading the disk, and this results in outflows out of the disk which carry angular momentum (in the twist of the field) and energy (in the Poynting flux) away from the disk, thereby facilitating the accretion of matter. The basic mechanism is related to that involved in the braking of stellar rotation by magnetic stellar winds (Weber and Davis;[14] Mestel[15]).

Recent theoretical work on the formation of jets has focused on magnetohydrodynamic (MHD) models of jet formation from accretion disks and stars. A strong case for magnetic or MHD driving of the jets of protostellar systems emerges since the temperature of the inner regions of these systems is insufficient to permit driving by thermal or radiation pressure (see, for example, Königl and Ruden[16]). Most of these investigations have been analytical or semi-analytical, and part of this has been an outgrowth from the self-similar model of Blandford and Payne[17] (for example, Pudritz and Norman;[18] Königl;[19] Pelletier and Pudritz;[20] Contopoulos and Lovelace[21]). The outflows in this model are often referred to as "centrifugally driven" owing to the driving force close to the

disk: If the poloidal magnetic field lines diverge from the disk surface (making an angle with the z-axis of more than 30°), then the sum of the gravitational and centrifugal forces is in the $+z$ direction for an MHD fluid particle which initially tends to maintain a constant angular rotation rate. The self-similar models are unsatisfactory in the respect that they must be cutoff at small cylindrical radii, $r \leq r_{min}(z)$. This is the most important region of the jet flow. Observations of optical stellar jets (Mundt[4]) reveal jet velocities $\sim 200 - 400$ km/s, which are comparable to the Keplerian disk velocity close to the star's surface. This suggests that the jets originate from the inner region of the disk close to the star (see, for example, Shu et al.;[22] and Pringle[23]).

A general treatment of stationary axisymmetric MHD flows leads to the generalized Grad-Shafranov equation which is a second order, nonlinear partial differential equation for the flux function $\Psi(r,z) = rA_\phi(r,z)$, where A_ϕ is the toroidal component of the vector potential (Zehrfeld and Green;[24] Heinemann and Olbert;[25] Aly;[26] Sakurai;[27] Lovelace et al.;[28] Camenzind;[29] Tsinganos et al.[30]). This equation represents an extension of the work of Grad and Rubin[31] and Shafranov[32] on plasma equilibria to include the plasma flow using the theory of Chandrasekhar,[33] Woltjer,[34] and Mestel.[35]

An approximate method for deriving stationary jet flow solutions of the Grad-Shafranov equation has been independently developed by Koupelis and Van Horn[36] and Lovelace et al.[1,37,38] The method involves averaging the different physical variables over the z = constant cross-section of the jet, and it gives rise to a set of ordinary nonlinear differential equations referred to as "envelope equations." These equations give the jet's axial flow velocity, radius, rotation rate, and poloidal and toroidal field components as a function of axial distance from the disk. This method captures the main physics of the Grad-Shafranov equation, the slow and fast magnetosonic points and the Alfvén singularity. The envelope equations can be evaluated using "shooting methods" to pass through the critical points. The slow critical point is found to be located close to the disk surface.[1] At this point the magnetic force $-\partial(B_\phi^2/8\pi)/\partial z$ is crucial in driving the flow outward and for this reason the flows were referred to as *"magnetically driven."* [1] The gradient of B_ϕ^2 is related to the divergence of the poloidal field lines so that this driving mechanism is related to that of the above-mentioned centrifugal winds.

The analytical work on jet formation involves major simplifications and approximations. This motivates studies of the formation of centrifugally and/or magnetically driven jets by numerical 2D and 3D MHD simulations.

Simulation studies of jet flows have focused on three main regions: 1. The *far jet* region where the studies assume that the jet enters the region with supersonic (or super fast magnetosonic) speed. 2. The *near jet* region where the matter enters with subsonic (or sub slow magnetosonic) speed and exits with supersonic speed. This is the jet formation region. 3. The *disk* region includes the problem of the Balbus-Hawley[39] and other instabilities (Kaisig et al.[40]) and the resulting 3D magnetohydrodynamic (MHD) turbulence. There is of course a strong physical coupling between the disk and near jet region. Of particular interest is the back reaction of an MHD jet on the accretion rate (Lovelace et al.[41,42]).

Many detailed hydro and magneto-hydrodynamic simulation studies have been done for the far jet region (see, for example, for non-relativistic flows, Clarke et al.;[43] Hardee and Clarke;[44] for relativistic hydro, Duncan and Hughes;[45] Gomez et al.;[46] and for relativistic MHD, van Putten[47]). Less attention has been given to the MHD simulation of the near jet region (Uchida and Shibata;[48] Shibata and Uchida;[49] Bell;[50] Ustyugova et al.;[51] Koldoba et al.;[52] Meier et al.;[53] Ouyed and Pudritz.[54]) A few simulations address the coupled problem of the disk and near jet regions (Uchida and Shibata;[48] Shibata and Uchida;[49] Stone and Norman;[54] Stone and Norman;[55] Bell and Lucek;[56] Matsumoto and Shibata;[57] Miller and Stone;[55] Miller and Stone[58]).

Here, we review recent results on non-relativistic MHD simulations of the formation of jets. In Sec. 2, we discuss general considerations of MHD jet formation. In Sec. 3, we first discuss simulations of MHD jet formation which leads in one limit (Sec. 3.1) to non-stationary jet formation, and in a second limit (Sec. 3.2) to stationary jet formation. Section 4 gives conclusions from this work.

2. Basics of MHD Outflows from Disks

The main forces which are thought to drive matter to outflows from a rotating disk are thermal and magnetic pressure gradients, and the centrifugal force. The main opposing force is the gravity of the central object. Here, we do not consider radiatively driven outflows (see Phinney[59]). We consider a system consisting of a gravitating center

(a star or black hole) and an accretion disk. We suppose that accretion disk is threaded by an ordered magnetic field and concentrate attention on the influence of the ordered magnetic field. Accreting matter of the disk carries magnetic field flux inward thus generating a B_r component of the magnetic field as sketched in Figure 2. On the other hand, rotation of the disk acts to generate a toroidal component of the field B_ϕ (< 0 if $B_z > 0$).

An accretion disk with a sufficiently inclined magnetic field (θ in Figure 2 sufficiently large) can generate outflows as a result of the centrifugal force (Blandford and Payne;[17] Pudritz and Norman;[18] Königl and Ruden[16]) or as a result of the magnetic pressure gradient force (appproximately $-\nabla_z B_\phi^2/(8\pi)$) (Lovelace et al.;[1] Koupelis and Van Horn[36]). In spite of the enormous difference in scales between stellar jets (lengths $\sim$ 1pc) and extragalactic jets (lengths $\sim 1 - 10^3$ kpc), the physics of the matter outflow from the disk may be similar. This depends on the ratio of energy densities at the base of the outflow at the inner radius of the disk denoted r_i. Thus, the main parameters are

$$\varepsilon_{th} = (c_s/v_K)_i^2 \ , \qquad \varepsilon_B = (v_A/v_K)_i^2 \ , \tag{1}$$

where v_K is Keplerian velocity, c_s the sound speed, v_A the Alfvén speed, and the i subscript indicates evaluation at $r = r_i$ on the disk surface. For ε_B of order unity, the outflow is magnetically driven, whereas for ε_{th} of order unity, the flow is thermally driven.

As mentioned above, processes in the disk are coupled to the outflows (see also Falcke, Malkan, and Biermann[57]). But it is difficult to simulate both regions simultaneously because the time scales of the accretion and outflow are in general very different. The accretion is much slower. On the other hand the processes in the disk involve small scale instabilities (Balbus and Hawley[39]) and therefore require high spatial resolution. Stone and Norman[55] attempted to simultaneously simulate the internal MHD dynamics of a disk and MHD dynamics of outflows. This proved impractical because essentially all of the spatial resolution was needed for treating the unstable dynamics of the disk. Simulation of the internal MHD disk dynamics has led several groups to the problem of simulating 3D MHD turbulence in a sheared flow (for example, Hawley, Gammie, and Balbus;[61] Brandenburg et al.[62]). This is a much larger project than that of understanding MHD outflows. At the same time it is widely thought, and observations of cataclysmic variables support the view, that the disk turbulence - including MHD turbulence - can be modeled approximately using the Shakura and Sunyaev[63] alpha viscosity model (Eardley and Lightman;[64] Coroniti[65]). In contrast with the internal disk dynamics, there is theoretical and simulation evidence that the outflows can be treated using axisymmetric (2D) MHD (Blandford and Payne;[17] Lovelace et al.;[1] Ustyugova et al.[51]). Here, we consider outflows from a disk represented as a boundary condition (see also Meier et al.;[53] Ouyed and Pudritz[54]). This corresponds to the outflows from a disk with accretion speed small compared with the Keplerian speed.

3. Numerical Simulations of MHD Outflows

In order to test the analytical models of stationary magnetically or centrifugally driven jets, we performed numerical simulations of MHD outflows from a disk treated as a boundary condition. The disk was threaded initially by a poloidal magnetic field inclined to the disk. We investigated two configurations of the magnetic field. The first configuration was a superposition of virtual monopoles located on the $z-$axis under the disk, and the second was a tapered virtual monopole also located under the disk.

3.1 Non-Stationary Outflows

The initial field configuration was a superposition of monopoles chosen so that the magnetic field was significantly inclined to the disk ($\theta > 30^\circ$) over most of the disk surface. Matter of the corona was initially in thermal equilibrium with the gravitating center. At $t = 0$ we started to rotate the disk with Keplerian velocity and at the same time to push matter from the disk with a small poloidal velocity equal to a fraction of the slow magnetosonic velocity ($v_p = \alpha v_{sm}$, with $\alpha = 0.1 - 0.9$). For the simulations presented here, $\varepsilon_B = 0.03$, and $\varepsilon_{th} = 0.9$. Matter, coming from the disk had the same temperature as matter in the corona. Thus, we generated outflows with relatively high temperature and low magnetic field (see details in Ustyugova et al.;[51] Koldoba et al.[52]).

We found that matter outflowing from the disk is accelerated as a result of both thermal and magnetic pressure gradients, and that the outflow collimates very rapidly (after several rotation periods of the inner radius of the

disk) as a result of the pinching force of the toroidal magnetic field. The behavior of the outflows is shown in Figure 3. The maximum of the outflow from the disk was found to coincide with the maximum of the toroidal magnetic field. Analysis of the forces (Koldoba et al.[52]) shows that the main forces in the $z-$direction are thermal and gravitational forces, which compensate each other, whereas the magnetic force, in spite of its small initial value, determines the acceleration of matter. The results shown in Figure 3 used the complete system of ideal non-relativistic MHD equations assuming axisymmetry but taking into account all three components of velocity and magnetic field (Ustyugova et al.[51]). The boundary conditions on the walls and on the top of the cylinder were taken as free boundary conditions for all scalar quantities and components of vector quantities.

Analysis of the fluxes of mass, energy, and angular momentum through a horizontal surface, say, $z = 0.5z_{max}$ shows that initally the fluxes grow as a result of the initial magnetic field twist formation due to the rotation of the disk. This twist of the field forms first at the inner radius of the disk where the disk rotation is fastest. Later the twist develops at larger radii. The matter flux grows and later decreases to a relatively small value. The velocity of matter on top of the region is twice the escape velocity during the maximum of the outflow, but becomes less than the escape velocity later when the mass flux decreases. Thus, this simulation is an example of a temporary outburst of matter to a jet. One objective in this study was to investigate outflows for an inclined magnetic field. However, the field rapidly becomes collimated - not inclined - as a result of the pinching by the toroidal magnetic field. The case described in the next subsection was chosen so as to diminish the collimating effect of the toroidal magnetic field.

3.2 Stationary Outflows

This simulation differed from the previous one in several respects (see Romanova et al.[66]). Firstly, we considered a different configuration of the initial poloidal magnetic field, namely, we took $B_p = B_M/(1 + \eta \tan^2\theta)$, where B_M is the monopole magnetic field, θ is an angle between the magnetic field line and the $z-$axis, and $\eta = $ const. (typically, $1 - 10$). This field is close to a monopole in the inner part of the disk and near the $z-$axis, and it goes to zero in the outer part of the disk. We chose this configuration in order to decrease the collimating affect of the toroidal magnetic field. A weak poloidal magnetic field will give rise to a weak toroidal magnetic field in the outer regions of the flow (see Lovelace et al.[1]), and this will decrease the collimation.

Secondly, we considered outflows at different values of ε_B including the case of strong magnetic fields with $\varepsilon_B = 1$, and different temperatures ε_{th}. In contrast with the previous case, we supposed that the entropy is constant everywhere so that the energy equation is not needed. This was done taking into account that we are interested mainly in the stong magnetic field case where the thermal pressure is small compared with magnetic pressure.

After about 40 rotation periods, we found stationary outflows as shown in Figure 4. Matter from the disk goes through the slow magnetosonic, Alfvén, and fast magnetosonic surfaces. The fluxes of mass, energy, and angular momentum through a horizontal surface, say, $z = 0.5z_{max}$ grow and after about 40 rotation periods of the inner disk they approach steady values. It is of interest to note that in many simulation runs the energy flow due to the electromagnetic fields is larger than that carried by the matter.

In the stationary limit, the field lines leaving the disk are strongly inclined away from the jet axis with the angle $\theta \sim 70 - 75^o$. Within the computational region the collimation is weak. However, collimation can occur at larger distances owing to the pressure of an external medium (Lovelace et al.[1]). Analysis of the forces along poloidal magnetic field lines shows that in most of the region (excluding the region with small θ) the main driving force is the magnetic pressure gradient, approximately $-\nabla B_\phi^2/(8\pi)$. Thus, these solutions are in essential accord with the magnetically driven outflows of Lovelace et al.[1]

This type of field configuration may arise under conditions where the magnetic field threading the disk has different polarities at different disk radii (say, positive for r_1 to r_2, and negative for r_2 to r_3, etc.). Such polarity variations are expected for example in AGN disks for a **B** field random over large scales accreted from the interstellar medium or a large scale ($\Delta r/r \sim 1$) random field due to a disk dynamo (see Lovelace, Newman, and Romanova[42]).

At the radii in the disk where the poloidal field changes signs, the magnetic collimation is small. The polarity reversals in the disk will produce jets which at large distances have polarity reversals of **B** as a function of z. In the vicinity of the field reversals, collisionless reconnection may be an important particle acceleration mechanism (see Romanova and Lovelace[67]).

We have recently studied the evolution of general configurations where a **B** field of different signs threads different radii of a differentially rotating accretion disk (Romanova et al.;[68] see also Matsumoto and Shibata;[57] and Hayashi, Shibata, and Matsumoto[69]). The differential rotation of the foot-points of **B** field loops at different radii on the disk surface is found to cause a twisting of the coronal magnetic field, an increase in the coronal magnetic energy, and an opening of the loops in the region where the magnetic pressure is larger than the matter pressure ($\beta \lesssim 1$). In the region where $\beta \gtrsim 1$, the loops may be only partially opened. Current layers form in the narrow regions which separate oppositely directed magnetic field. Reconnection occurs in these layers as a result of the small numerical magnetic diffusivity of the code which we determine. In contrast with the case of the solar coronal magnetic field, the combination of magnetic and centrifugal forces leads to significant matter outflow from the disk surface. The faster rotation of the inner part of the disk gives a stronger outflow from this part of the disk. The outfow accelerates with increasing distance from the disk up to velocities in excess of the escape speed. The outflows show some collimation within the computational region and have a large power output mainly in the form of a Poynting flux. Thus these outflows are pertinent to the origin of astrophysical jets. The model and processes observed are relevant to the coronae of accretion disks around stellar mass objects, including pre-main sequence stars, compact stars, and black holes, as well as the coronae of disks around massive black holes in active galactic nuclei. Opening of magnetic field loops may lead to transient and/or steady outflows, while reconnection events may be responsible for X-ray flares in such objects (see also Matsumoto and Shibata;[57] and Hayashi et al.[69]).

4. Conclusions

The simulation results discussed here support the idea that MHD processes lead the formation of jets near the inner edges of accretion disks, and that the jets have asymptotic speeds of the order of the maximum Keplerian velocity of the disk. In contrast, observed VLBI jets in quasars and active galaxies point to bulk Lorentz factors of order 10 - much larger than the disk Lorentz factor. This may be a result of the relativistic dynamics not included here, but more likely it reflects the fact that these jets are in a different regime - possibly the Poynting flux regime discussed by Lovelace et al.[11] - and/or that the jets involve energy extraction from a rotating black hole (Blandford and Znajek[70]).

Acknowledgments

This work was supported in part by NSF grant AST-9320068 and NASA grant NAGW 2293. Also, the research described here was made possible in part by Award No. RP1-173 of the U.S. Civilian Research & Development Foundation for the Independent States of the Former Soviet Union (CRDF).

References

1. Lovelace, R.V.E., Berk, H.L., & Contopoulos, J. 1991, ApJ, 379, 696
2. Bridle, A.H., & Eilek, J.A. (eds) 1984, Physics of Energy Transport in Extragalactic Radio Sources, Greenbank: NRAO
3. Mirabel, I.F., & Rodriguez, L.F. 1994 Nature, 371, 46
4. Mundt, R. 1985, in Protostars and Planets II, D.C. Black and M.S. Mathews, Univ. of Arizona Press, Tucson, 414
5. Bührke, T., Mundt, R., & Ray, T.P. 1988, A&A, 99
6. Begelman, M.C., Blandford, R.D., & Rees, M.J. 1984, Rev. Mod. Phys., 56, 255
7. Bisnovatyi-Kogan, G.S. 1993, in Stellar Jets and Bipolar Outflows, L. Errico & A.A. Vittone, Dordrecht: Kluwer, 369
8. Goldreich, P., & Julian, W. 1969, ApJ, 157, 869
9. Lovelace, R.V.E. 1976, Nature, 262, 649
10. Blandford, R.D. 1976, MNRAS, 1976, 465
11. Lovelace, R.V.E., Wang, J.C.L., & Sulkanen, M.E. 1987, ApJ, 315, 504
12. Gisler, G., Lovelace, R.V.E., & Norman, M.L. 1989, ApJ, 342, 135
13. Wang, J.C.L., Lovelace, R.V.E., & Sulkanen, M.E. 1990, ApJ, 353, 38
14. Weber, E.J., & Davis, L. Jr. 1967, ApJ, 148, 217
15. Mestel, L. 1968, MNRAS, 138, 359
16. Königl, A., & Ruden, S.P. 1993, E.H. Levy and J. Lunine, Tucson: Univ. of Arizona Press, 641
17. Blandford, R.D., & Payne, D.G. 1982, MNRAS, 199, 883
18. Pudritz, R.E., & Norman, C.A. 1986, ApJ, 301, 571
19. Königl, A. 1989, ApJ, 342, 208
20. Pelletier, G., & Pudritz, R.E. 1992, ApJ, 394, 117
21. Contopoulos, J., & Lovelace, R.V.E. 1994, ApJ, 429, 139
22. Shu, F.H., Lizano, S., Ruden, S.P., & Najita, J. 1988, ApJ, 328, L19
23. Pringle, J.E., 1989, MNRAS, 236, 107
24. Zehrfeld, H.P., & Green, B.J. 1972, Nucl. Fusion, 12, 569
25. Heinemann, M., & Olbert, S. 1978, J. Geophys. Res., 83, 2457
26. Aly, J.J. 1986, in Magnetospheric Phenomena in Astrophysics, AIP Conference Proceedings No. 144, R.I. Epstein & W.C. Feldman, eds., Am. Inst. of Physics, New York, p. 45
27. Sakurai, T. 1987, PASJ, 39, 821
28. Lovelace, R.V.E., Mehanian, C., Mobarry, C.M., & Sulkanen, M.E. 1986, ApJ Suppl., 62, 1
29. Camenzind, M. 1987, Acta Astron., 184, 341
30. Tsinganos, K., Sauty, C., Surlantzis, G., Trussoni, E., & Contopoulos, J. 1996; in Solar and Astrophysical Magnetohydrodynamic Flows, K.C. Tsinganos, ed. (Kluwer Acad. Pub. Dordrecht), p. 427
31. Grad, H., & Rubin, H. 1958, in Proc. Internat. Atomic Energy Agency Conf., IAEA, Geneva, 31, p. 190

32. Shafranov, V.D. 1966, Rev. of Plasma Phys., 2, 103

33. Chandrasekhar, S. 1956, ApJ, 124, 232

34. Woltjer, L. 1959, ApJ, 130, 405

35. Mestel, L. 1961, MNRAS, 122, 473

36. Koupelis, T., & Van Horn, H.M. 1989, ApJ, 342, 146

37. Lovelace, R.V.E., Mobarry, C.M., & Contopoulos, J. 1989, in *Accretion Disks and Magnetic Fields in Astrophysics,* ed. G. Belvedere (Dordrecht: Kluwer), 71

38. Lovelace, R.V.E., Romanova, M.M.,& Contopoulos, J. 1993, ApJ, 403, 158

39. Balbus, S.A., & Hawley, J.F. 1991, ApJ, 376, 214

40. Kaisig, M., Tajima, T., & Lovelace, R.V.E. 1992, ApJ, 386, 83

41. Lovelace, R.V.E., Romanova, M.M., & Newman, W.I. 1994, ApJ, 437, 136

42. Lovelace, R.V.E., Newman, W.I., & Romanova, M.M., 1997, ApJ, 424, 628

43. Clarke, D.A., Norman, M.L., & Burns, J.O. 1986. ApJ, 311, L63

44. Hardee, P.E., & Clarke, D.A. 1992, ApJ, 400, L9

45. Duncan, G.C., & Hughes, P.A. 1994, ApJ, 436, L119

46. Gomez, J.L., Marti, J.M., Marscher, A.P., Ibanez, J.M., Marcaide, J.M. 1995, ApJ, 449, L19

47. van Putten, M.H.P.M. 1993, ApJ, 408, L21

48. Uchida,Y, & Shibata, K. 1985, PASJ, 37, 515

49. Shibata, K., & Uchida, Y. 1986, PASJ, 38, 631

50. Bell, A.R. 1994. Phys. Plasmas, 1, 1643

51. Ustyugova, G.V., Koldoba, A.V., Romanova, M.M., Chechetkin, V.M., & Lovelace, R.V.E. 1995, ApJ, 439, L39

52. Koldoba, A.V., Ustyugova, G.V., Romanova, M.M., Chechetkin, V.M., & Lovelace, R.V.E. 1995, Ap&SS, 232, 241

53. Meier, D.L., Edgington, S., Godon, P., Payne, D.G., & Lind, K.R. 1997, Nature, 388, 350

54. Oyed, R. & Pudritz, R.E. 1997, ApJ, 482, 712

55. Stone, J.M., & Norman, M.L. 1994, ApJ, 433, 746

56. Bell, A.R., & Lucek, S.G. 1995, MNRAS, 277, 1327

57. Matsumoto, R. & Shibata, K. 1997, in ASP Conf. Proc. *Accretion Phenomena and Related Outflows*, eds., G. Bicknell, L. Ferraria, & D. Wickramasinhe (San Francisco: ASP), p. 443

58. Miller, K.A., & Stone, J.M. 1997, preprint

59. Phinney, E.S. 1987, in Superluminal Radio Sources, J.A. Zensus, & T.J. Pearson, Cambridge: Cambridge Univ. Press, 301

60. Falcke, H., Malkan, M.A., & Biermann, P.L. 1995, A&A, 298, 375

61. Hawley, J.F., Gammie, C.F., & Balbus, S.A. 1995, ApJ, 440, 742

62. Brandenburg, A., Nordlund, A., Stein, R.F., & Torkelson, U. 1995, ApJ, 446, 741

63. Shakura, N.I., & Sunyaev, R.A. 1973, A&A, 24, 337

64. Eardley, D.M. & Lightman, A.P. 1975. ApJ, 200, 187

65. Coroniti, E.V. 1981, ApJ, 244, 587

66. Romanova, M.M., Ustyugova, G.V., Koldoba, A.V., Chechetkin, V.M., & Lovelace, R.V.E. 1997, ApJ, 482, 708

67. Romanova, M.M., & Lovelace, R.V.E. 1992, A&A, 262, 26

68. Romanova, M.M., Ustyugova, G.V., Koldoba, A.V., Chechetkin, V.M., & Lovelace, R.V.E. 1997, ApJ, accepted

69. Hayashi, M.R., Shibata, K., & Matsumoto, R. 1996, ApJ, 468, L37

70. Blandford, R.D., & Znajek, R.L. 1977, MNRAS, 179, 433

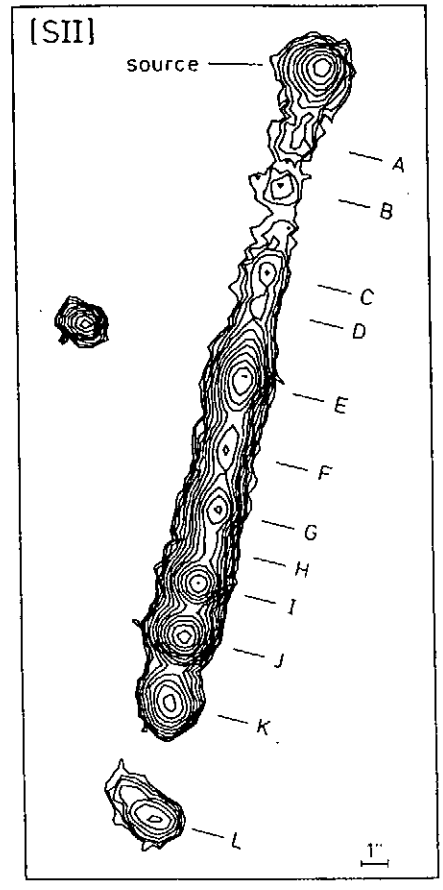

Figure 1. SII line intensity contour plot for the protostellar jet in the object HH 34 adapted from figure 2 of Bührke, Mundt, and Ray.[5] The letters denote different regions of enhanced emission.

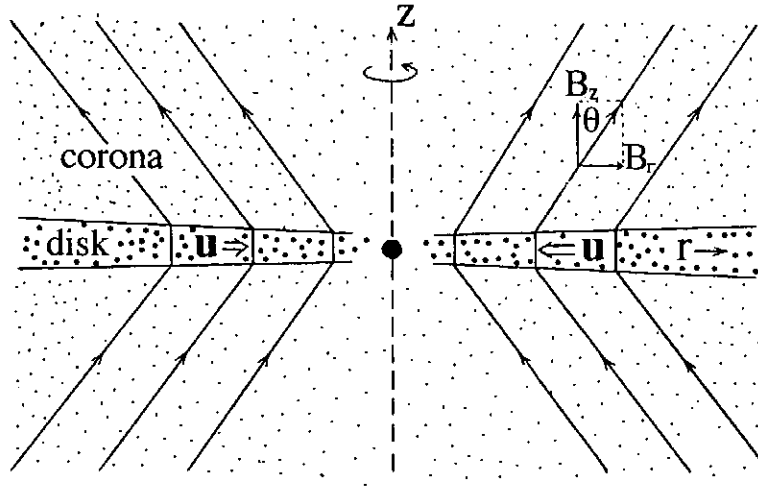

Figure 2. Sketch of a magnetized accretion disk with corona.

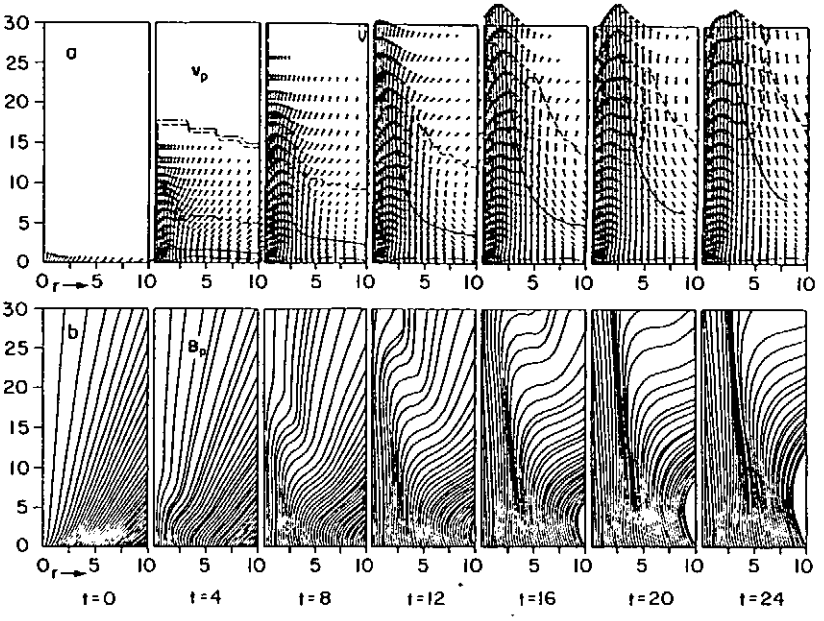

Figure 3. Outflow for a superposition of monopoles. a - poloidal velocities of the flow; b - poloidal magnetic field B_p at times $t = 0,\ 4,\ 8$, etc., where time t is measured in units of t_i which is the period of rotation of the inner radius of the disk (r_i). Only one quadrant of the flow is shown. The long dashed line (a) represents the slow magnetosonic surface; the short dashed line is the Alfvén surface; and the dashed line on top of the region is the fast magnetosonic surface. At the top of the region the flow exceeds the escape velocity.

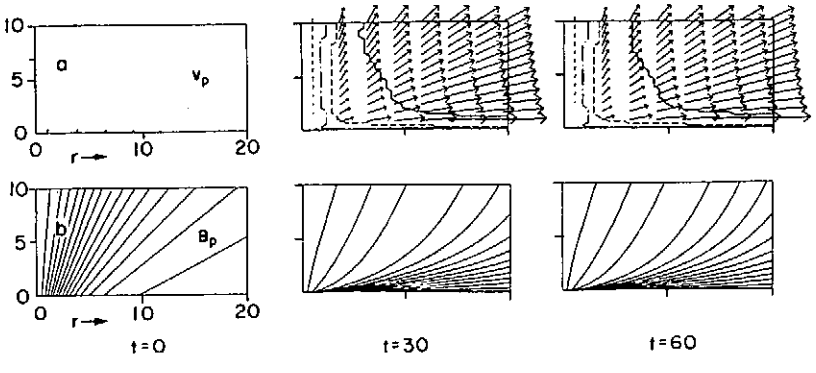

Figure 4. Outflow in the case of a tapered monopole field for $\varepsilon_B = 0.81$, $\varepsilon_{th} = 0.25$, $\eta = 2$ at time $t = 100t_i$, when a stationary flow is well established, where t_i is the period of rotation at the inner radius of the disk (r_i). The solid lines are flux lines and show the poloidal magnetic field. The arrows are the poloidal velocities. The long dashed line is the slow magnetosonic surface; the dashed line is the Alfvén surface; and the short dashed line is the fast magnetosonic surface. At the outer part of the region the flow exceeds the escape velocity.

Pulsar Electrodynamics – Some Outstanding Problems

D.B. Melrose
Research Centre for Theoretical Astrophysics
School of Physics, University of Sydney

October 10, 1997

Abstract

The "standard model" for pulsar electrodynamics is summarized. The properties of natural wave modes in the plasma rest frame in the region above the pair production front are discussed. This plasma is one dimensional and extremely strongly magnetized with a relativistic spread in energies. The break down of MHD in the pulsar wind is also discussed.

1 Introduction

The electrodynamics of pulsars in the "standard model" incorporates a number of different physical processes (see the reviews by Michel 1982; Beskin, Gurevich & Istomin 1986; Mestel 1993; Shibata 1996): large parallel electric fields ($E_{\|}$) in the polar cap regions and in "outer gaps"; acceleration of "primary" particles to extremely relativistic energies (Lorentz factors $\Gamma \sim 10^7$) by these $E_{\|}$ fields; emission of gamma rays by the primary particles; decay of the gamma rays into relativistic "secondary" pairs in a pair production front (PPF); the loss of perpendicular momentum due to gyromagnetic emission resulting in a one-dimensional pair plasma in the PPF and beyond; the screening of $E_{\|}$ by these pairs in the PPF; and, the outflow of the pairs beyond the light cylinder to form a pulsar wind which has a relativistic flow speed and a relativistic spread of particle energies. Most of these processes are well understood in principle but their application to pulsars is subject to various uncertainties. For most pulsars the only observational data available are from the radio emission, which involves only a tiny fraction of the inferred power output in the relativistic particles, and hence it may be a relatively poor diagnostic of the electrodynamics processes involved.

In this paper, after a review of the important features of the electrodynamics in the standard model, I discuss two specific plasma problems which arise in any variant of the standard model. The first problem concerns the properties of the natural wave modes of the one-dimensional relativistic pair plasma. Generation of these waves somewhere above the PPF is required to account for the observed radio emission, and the wave properties are needed to discuss both the generation of the radio emission and its propagation through the overlying plasma regions (e.g., Melrose 1995, 1996). The second problem concerns the properties of the wind. All theories of the wind rely on some form of MHD theory, but simple arguments imply that MHD theory must break down within the wind zone.

The implications of this break down cannot be neglected, but it may be that the changes required can be incorporated by slightly modifying the MHD wind models.

2 The "standard model"

Pulsars (PSRs) are rotating neutron stars (NSs). They fall into two categories: "ordinary" PSRs which are created in supernova explosions and "millisecond" PSRs (MSPs) which are very old NSs spun-up in binary systems. The parameters of NSs are radius $R_* \sim 10\,\mathrm{km}$ and mass strongly concentrated around $M \sim 1.4 M_\odot$. For ordinary PSRs, the range of rotational frequencies, $\Omega = 2\pi/P$ is typically $\sim 1\text{–}10\,\mathrm{s}^{-1}$, and the range of magnetic fields is $B \sim 10^{8\pm1}\,\mathrm{T}$. For MSPs the ranges the frequencies are higher, $\Omega \sim 10^3\,\mathrm{s}^{-1}$, and the magnetic fields lower, $B \sim 10^{5\pm1}\,\mathrm{T}$. An important parameter is the radius of the light cylinder, $r_{\rm lc} = c/\Omega = 5 \cdot 10^3\, R_*\,(T/1\,\mathrm{s})$.

A "vacuum" model for a pulsar, that is, a magnet rotating in vacuo, is clearly wrong in detail, but nevertheless is the basis for the estimate of the magnetic field. The power radiated in magnetic dipole radiation is

$$\mathcal{P} = \frac{2\pi\Omega^4 B_*^2 R_*^6 \sin^2\chi}{3\mu_0 c^3}, \tag{1}$$

where B_* is the magnetic field at the north magnetic pole and χ is the angle between the rotation and magnetic axes. The power (1) is equated to the rate of rotational energy loss,

$$\mathcal{P} = -I\Omega\dot{\Omega} = \frac{I(2\pi)^2\dot{P}}{P^3} \tag{2}$$

to find $B_* \propto (P\dot{P})^{1/2}$, which is the basis for observational estimates of B_*. The vacuum model also implies a quadrupolar surface charge on the NS, with potential

$$\Phi = -\frac{\Omega B_* R_*^5}{3r^3} P_2(\cos\theta). \tag{3}$$

The associated electric field has a component

$$E_{\|} = \frac{\mathbf{E}\cdot\mathbf{B}}{B} = \frac{2\Omega B_* R_*^5}{r^4} \frac{\cos^3\theta}{(3\cos^2\theta - 1)^{1/2}} \tag{4}$$

along the magnetic field, and this field is thought strong enough to rip charges off the surface of the star, undermining the vacuum assumption.

Before proceeding to discuss the role of a charge magnetosphere, it is relevant to define the "polar caps" on the surface of the NS as the regions magnetically connected to the light cylinder and beyond. The equation $r = r_0 \sin^2\theta$ for a dipolar field line in polar coordinates implies that the polar cap extends to angles $\theta < \theta_{\rm pc}$ from the poles, with

$$\theta_{\rm pc} = \left(\frac{\Omega R_*}{c}\right)^{1/2}. \tag{5}$$

The potential drop available across a polar cap is

$$\Delta\Phi \sim \frac{\Omega^2 R_*^3 B_*}{c} \sim 10^{13} \left(\frac{B_*}{10^8\,\mathrm{T}}\right) \left(\frac{P}{1\,\mathrm{s}}\right)^{-2} \mathrm{V}. \tag{6}$$

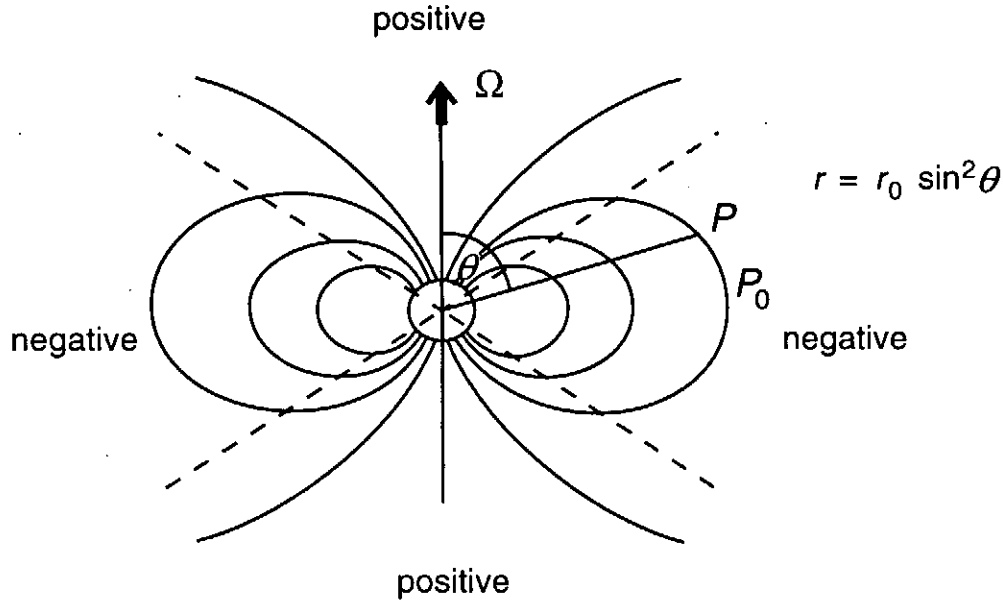

Figure 1: The corotation charge density has the same sign over the polar caps and the opposite sign in the equatorial regions: the separation between the two signs is illustrated by the dashed lines in the case of an aligned rotator.

Now suppose that there is an ample supply of plasma. Then perfect conductivity implies

$$\mathbf{E} + \mathbf{v} \times \mathbf{B} = 0; \quad \mathbf{v} = \mathbf{\Omega} \times \mathbf{x}, \tag{7}$$

and the divergence of this corotational electric field implies the Goldreich-Julian (GJ) density

$$n_{\rm GJ} = \frac{\varepsilon_0 \nabla \cdot \mathbf{E}}{e} = -\frac{\varepsilon_0 \mathbf{\Omega} \cdot \mathbf{B}}{e} = (7 \times 10^{17}\,{\rm m}^{-3}) \left(\frac{B}{10^8\,{\rm T}}\right) \left(\frac{T}{0.1\,{\rm s}}\right)^{-1} \cos\theta. \tag{8}$$

Note that $n_{\rm GJ}$ has same sign at both poles, and the opposite signs in the equatorial regions, as illustrated in Figure 1. For field lines originating from the polar cap, the charge density $en_{\rm GJ} \propto B\cos\theta$ and the current density, $J = nec$ (once the particles become relativistic) are incompatible with $n = n_{\rm GJ}$ in the absence of other sources of charge than the stellar surface. As a result an $E_{||}$ builds up, and leads to acceleration of "primary" particles to very high energies. The details of this acceleration are model dependent, but the acceleration of particles to very high energies occurs in all models.

Plasma escapes freely from polar cap. Assuming a current density $J \sim n_{\rm GJ}ec$, the total current is $I \sim J\pi(R\theta_{\rm pc})^2 \sim \varepsilon_0\Omega^2 R_*^3 B_*$. The power may be estimated from $\mathcal{P} = I\Delta\Phi$, which gives $\mathcal{P} \sim \Omega^4 B_*^2 R_*^6/\mu_0 c^3$. Apart from a factor of order unity, this is the same as the magnetic dipole value given by (1), thereby justifying its in estimating $B_* \propto (T\dot{T})^{1/2}$.

The large $E_{||}$ accelerates primary particles to Lorentz factor $\Gamma \sim e\Phi/Mc^2$. A primary particle radiates γ rays due to curvature emission, with a power per particle

$$\mathcal{P}_{\rm c} = \frac{2r_0 mc^3}{3R_{\rm c}^2}\,\Gamma^4, \qquad \varepsilon_\gamma \sim \frac{2\hbar c}{R_{\rm c}}\,\Gamma^3 \tag{9}$$

where ε_γ corresponds to the peak of what is a relatively broad spectrum of γ rays. The primaries emit γ rays nearly parallel to $\mathbf{B}$ field lines, and as they propagate, the γ rays de-

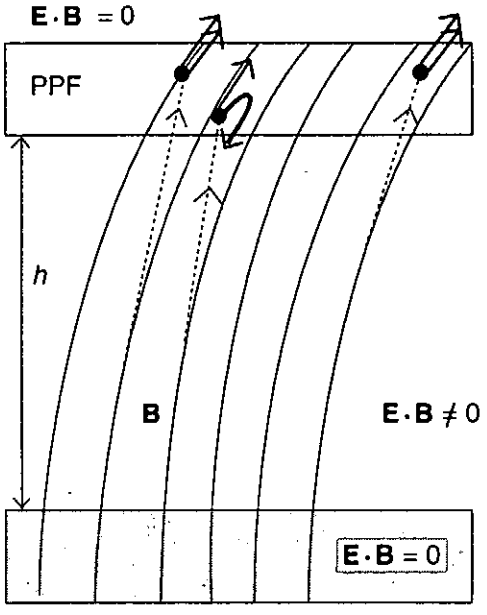

Figure 2: In the region below the pair production front (PPF) primary particles are accelerated and emit gamma rays which decay into secondary pairs in the PPF.

viate from **B**-lines (the angle ψ between them increases). The γ rays decay into secondary pairs, due to the process $\gamma + B \rightarrow e^- + e^+ + B$, provided the threshold $\varepsilon_\gamma \sin\psi > 2mc^2$ is exceeded.

The resulting production of "secondary" pairs occurs in a pair production front (PPF). These secondaries shield out $E_{||}$ above the PPF, as illustrated schematically in Figure 2. The ratio of the number of secondaries to primaries is referred to as the multiplicity factor, M, with $n_{\rm pair} = M n_{\rm GJ}$. For example,

$$n_{\rm pair} \sim \frac{\mathcal{P}_{\rm c}}{\varepsilon_\gamma}\frac{L}{c}, \tag{10}$$

with L = the height pair creation continues, leads to an estimate of M, but the actual value is model dependent, with $M = 10^2$–10^6 for the various models.

3 Wave properties in the secondary pair plasma

The pair plasma in the region above the PPF is of particular interest because it is the region from which the radio emission probably originates. The superstrong field $B \gtrsim 10^8$ T implies a cyclotron frequency $\omega \ll \Omega_e = eB/m$. It also implies that the particles radiate away their perpendicular energy in a very short time, $\approx 2 \times 10^{-17}\Gamma$ s, so that the plasma is one dimensional, with $p_\perp = 0$ for all particles.

The resulting plasma is highly relativistic, $\Gamma_0 = \langle\Gamma_\pm\rangle \sim 10^2$–$10^3$, with an intrinsically relativistic spread in energy, corresponding to $\langle(\Gamma_\pm - \langle\Gamma_\pm\rangle)^2\rangle \sim \Gamma_0^2$. The non-zero charge and current densities imply that the plasma is gyrotropic (a pair plasma with identical electron and positron distributions is nongyrotropic), but the gyrotropy is weak, and of order $1/M$, provided the multiplicity is large. As a consequence, the difference in the rest frames of the electrons and positrons may be neglected to a first approximation, provided

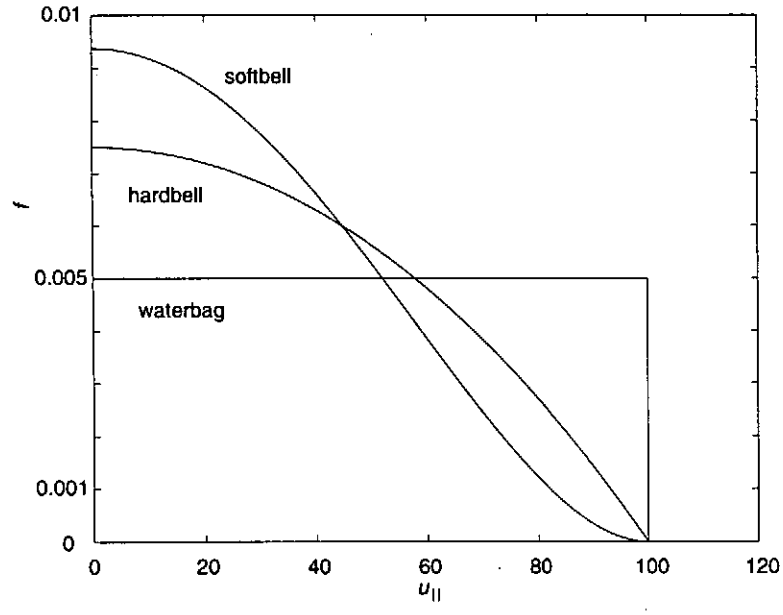

Figure 3: The distribution function, f, is shown for the waterbag, hard bell and soft bell as a function of $u_{||} = (v_{||}/c)/[1 + (v_{||}/c)^2]^{1/2}$, with maximum energy corresponding to $\Gamma = 1/[1 + (v_{||}/c)^2]^{1/2} = 100$.

that M is much larger than the mean Lorentz factors of the particles. This allows us to define a rest frame, $\langle \Gamma v_{||} \rangle = 0$, for the plasma, and to ignore the differences between the distributions of electrons and positrons to a first approximation.

In order to discuss the properties of waves in such a plasma, it is necessary to assume a specific form for the distribution function of the particles. Three idealized distributions are illustrated in Figure 3: the waterbag, hard bell, soft bell distributions. Only the waterbag distribution has been considered previously in this context (Arons & Barnard 1986), but this distribution can lead to misleading conclusions. In particular it cannot be used to discuss Landau damping, because this depends on the derivative of the distribution function which is artificially made to be zero for the waterbag distribution, except at the cutoff where it is infinite. This also leads to associated misleading features in the dispersion. The hard bell distribution only partly overcomes this difficulty, and the soft bell distribution is the simplest case where the derivative is continuous. Another case which avoids these technical difficulties is the relativistic thermal distribution which has all its derivatives continuous.

The wave properties in plasma rest frame are relatively simple (Gedalin, Melrose & Gruman 1997), as illustrated in Figure 4. There are three distinct modes. The magnetosonic (t or X) mode has a dispersion relation

$$\omega_t^2 = k^2 v_A^2 (1 - \Delta\lambda \cos^2\theta), \qquad v_A = \frac{1}{(1 + \Delta\langle\Gamma\rangle)^{1/2}}, \quad \Delta = \frac{2\omega_p^2}{\Omega_e^2}, \quad \lambda = \langle \Gamma v_{||}^2 \rangle, \qquad (11)$$

with electric vector $\mathbf{E} \parallel \mathrm{k}\times\mathbf{B}$. The L-O mode has a cutoff frequency at $\omega_c = \omega_p(2\langle\Gamma^{-3}\rangle)^{1/2}$, $\omega_p^2 = ne^2/\varepsilon_0 m$. The Alfvén ($A$) mode has a maximum frequency $\omega_{\max}$, which is sensitive to the form of the distribution function. (This maximum is absent in the waterbag and hard bell distributions and evidently requires that the second derivative of the distribution function be continuous.) Both the t and A modes become "firehose unstable" for $\Delta\lambda \gtrsim 1$.

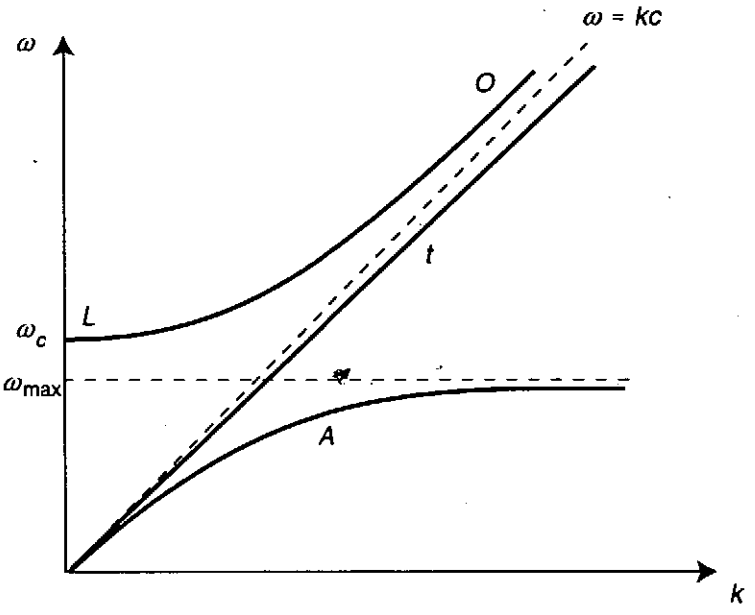

Figure 4: The dispersion relations are illustrated schematically for the three modes in a highly magnetized, intrinsically highly relativistic, one dimensional pair plasma in the rest frame of the plasma.

There is no Landau damping damping or Cerenkov emission of either the t mode (due to $E_{\|} = 0$) or of the L-O mode (due to $\omega > kc$). Hence the only waves that can be generated by a streaming instability are those in the A mode. (The nonzero charge and current densities, that is the gyrotropy in this context, allow some Landau damping of t mode due to an elliptical component to the polarization, but this is a small effect for $M \gg 1$.) This is a severe restriction on models for the radio emission based on streaming instabilities.

4 The wind zone

The wind zone in a pulsar extends from around the light cylinder to a termination shock. In the case of the Crab Nebula the termination shock is at $r_{\rm shock} \sim 2 \cdot 10^9 r_{\rm lc} \sim 0.1\,{\rm pc}$. The energy flux flux in the wind can be separated into electromagnetic and kinetic energy (KE) fluxes, determined by the ratio

$$\sigma = \frac{\text{Poynting flux}}{\text{KE flux}}. \tag{12}$$

One necessarily has $\sigma \gtrsim 1$ at light cylinder. In the wind zone an MHD model suggests Poynting flux $\propto B^2$, with $B \sim B_\phi \propto 1/r$, and a KE flux $\propto n\Gamma$, with $n \propto 1/r^2$ and $\Gamma =$ constant. This implies σ independent of r in wind. However, a detailed model requires $\sigma \sim 3 \cdot 10^{-3}$ at $r_{\rm shock}$ (Kennel & Coroniti 1984). This raises the important question as to how Poynting flux converted to KE flux (Coroniti 1990).

It is also relevant to ask whether the use of MHD is valid. MHD can break down in two different ways in this context (Melatos & Melrose 1996, hereafter MM). One is the assumption that the Ohm's law may be approximated by $\mathbf{E} + \mathbf{U} \times \mathbf{B} = 0$, where $\mathbf{U}$ is the

fluid velocity, and the generalized Ohm's law contains various terms on the RHS of this equation that must be smaller than the terms retained in order for MHD to be valid. The other is that MHD implies a conduction current density, J_c, and the maximum current that can be supplied by plasma with a given density is $J_{max} = nec$; MHD breaks down for $J_c > J_{max}$.

By starting from a (cold) two-fluid model for the electrons and positrons, and rewriting the fluid densities and velocities in terms of the fluid density and velocity and the charge and current densities, MM estimated the conditions under which the other terms in the resulting Ohm's law may be neglected. They found

$$\mathbf{E} + \mathbf{U} \times \mathbf{B} = \frac{m}{e^2}\frac{\partial}{\partial t}\left(\frac{\Gamma \mathbf{J}}{n}\right) + \frac{m}{e^2}\mathbf{U} \cdot \nabla\left(\frac{\Gamma \mathbf{J}}{n}\right) + \frac{m}{e^2}\mathbf{J} \cdot \nabla(\Gamma \mathbf{U}). \tag{13}$$

Then assuming $d/dt \rightarrow 1/T$, $\nabla \rightarrow 1/L$, the condition for the terms on the RHS to be negligible reduces to

$$\frac{\Gamma}{\omega_p^2 T^2}\frac{JT}{\varepsilon_0 E} \ll \min\left(1, \frac{L}{TU}, \frac{TU}{L}\right). \tag{14}$$

Estimates suggest that MHD breaks down at $r = r_{MHD} \sim 10^{-4} r_{shock}$ for the Crab pulsar (MM). The requirement on the current also breaks down at about the same radius. This implies *charge starvation* in the wind. Additional physics is needed to discuss the properties of the wind in the region where MHD breaks down and charge-starvation occurs. MM speculated that the electromagnetic field in the wind becomes similar to transverse waves in underdense plasmas, for which the dispersion relation is

$$n^2 = 1 - \frac{\omega_p^2}{\omega^2(1+\nu^2)^{1/2}}, \qquad \nu = \frac{eE}{mc\omega}, \tag{15}$$

and noted that efficient acceleration of test particles occurs in the fields of such a wave. This model implies $\sigma = 2\omega_p^2/\omega^2$, and a specific model for the Crab pulsar plausibly results in $\sigma \sim 3 \cdot 10^{-3}$ at $r = r_{shock}$, as required in the model of Kennel & Coroniti (1984).

5 Conclusions

The main points made is this paper are

1). In the region where the radio emission is thought to be generated, there are three natural wave modes of relevance: the magnetosonic or X mode, the Langmuir-O mode and the Alfvén mode. Only the Alfvén mode can be generated effectively through a streaming instability.

2). MHD theory breaks down in the pulsar wind. It is suggested that the properties of the electromagnetic fields are analogous to transverse waves in an underdense plasma and that the waves are slowly damped through acceleration of particles, leading to a transfer of Poynting flux to kinetic energy flux in the wind.

References

Arons, J., & Barnard, J.J. 1986, *Astrophys. J.* **302**, 120.

Beskin, V.S., Gurevich, A.V., & Istomin, Ya.N. 1986, *Sov. Phys. Usp.* **29**, 946.

Coroniti, F.V. 1990, *Astrophys. J.* **349**, 538.

Gedalin, M., Melrose, D.B., & Gruman, E. 1997, *Phys. Rev. E* (submitted).

Kennel, C.F., & Coroniti, F.V. 1984, *Astrophys. J.* **283**, 694.

Melrose, D.B. 1995, *J. Astrophys. Astron.* **16**, 137.

Melrose, D.B. 1996, in Johnston, S., Walker, M.A., & Bailes, M., (eds) *Pulsars: Problems and Progress*, Astronomical Society of the Pacific Conference Series, Volume 105, p. 139.

Melatos, A., & Melrose, D.B. 1996, *Mon. Not. R. Astron. Soc.* **279**, 1168.

Mestel, L. 1993, in Blandford, R.D., Hewish, A., & Mestel, L., (eds) *Pulsars as Physics Laboratories*, Oxford University Press, p. 93.

Michel, F.C. 1982, *Rev. Mod. Phys.* **54**, 1.

Shibata, S. 1996, in Johnston, S., Walker, M.A., & Bailes, M., (eds) *Pulsars: Problems and Progress*, Astronomical Society of the Pacific Conference Series, Volume 105, p. 409.

ASTROPHYSICAL PLASMA MHD PROCESSES REVEALED BY THE SOLAR X-RAY SATELLITE "YOHKOH"

Yutaka UCHIDA

Physics Department, Science University of Tokyo, Tokyo

Abstract. We describe in this paper some of the new findings about solar plasma dynamical processes derived by the Solar X-ray Satellite "Yohkoh". These new findings require considerable revisions of our previous pictures on what are occurring in those dynamical processes, and therefore in the much more violent activities producing superhot and high energy phenomena on active stars and accretion disks in astrophysical objects for which those dynamical activities on the Sun have in some cases been taken as their prototypes.

1. Introduction

Some of the results of the recent observations of the prototypes of the astrophysical magnetodynamical phenomena occurring on the Sun derived by the Solar X-ray Satellite Yohkoh will be reviewed here. The Satellite Yohkoh is constructed and launched by ISAS (Institute of Space and Astronautical Science) in collaboration with US and UK scientists supported by NASA and SERC. It has been very successful, and has given many new findings about the active plasma dynamical phenomena occurring on the Sun. These will affect our views on astrophysical violent phenomena for which these solar counterparts have been the prototypes.

2. New Findings about the Coronal Phenomena

The wide dynamic range Soft X-ray Telescope has made the observation of the fainter corona together with bright active region phenomena possible, so that the relation of the coronal phenomena to the phenomena in the active regions can be clarified.

As seen in Fig. 1, the corona seen in X-rays is found to be quite full of structures, some varying in time. The corona is not an atmosphere of the usual sense (continuous and stratified), but consisted of highly inhomogeneous plasma, trapped in the aggregates of loops, with obvious voids (coronal holes), as well as condensations with higher density and higher temperature plasma (active region corona), according to the inhomogeneous and anisotropic distribution in the magnetic field. In other words, the corona is a highly electromagnetic entity.

A tiny change in the strong field active regions was found to cause a rather drastic changes in the surrounding corona, and the effect eventually influences the structure several hundred-thousand km away, anisotropically along partic-

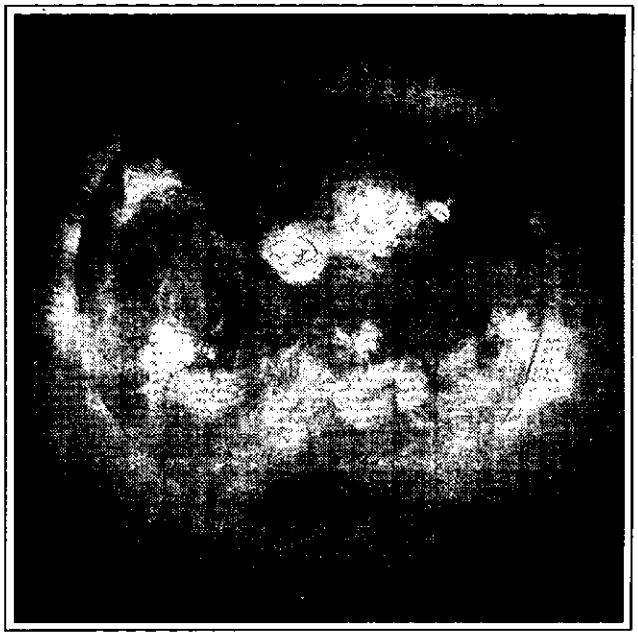

Figure 1. A soft X-ray image of the Sun on Nov 11, 1991 as an example. In this image taken near the solar activity maximum, the corona with coronal holes, active region corona, a large arcade formation in the north, a jet, and so on, are seen.

ular structures selectively, indicating some particular generic or evolutionary relations existing between them.

3. New Findings about Active Region Behavior

Active region corona has been considered to be high temperature, high density plasma tied down by the strong magnetic field of the sunspot groups in which some more or less steady mechanism of the extra heating is in operation there. In actuality, Yohkoh observation revealed that there are frequent injections of *already heated* mass from below into closed loops within the active regions (Shimizu et al. 1992). Furthermore, the material and the magnetic flux tubes in an active region expand away almost continually (Uchida et al. 1992) from the outer part as the hot mass (and probably the helicity) is injected into the inner region as the transient brightenings. This "expansion of active region corona" is a new type mass loss from the Sun, different from the Parker's thermal expansion wind along the field line, because this is likely to be due to magnetic driving.

4. New Findings about the Physics of Flares

Solar flares are sudden releases of large amount of energy in active regions. A larger scale, fainter versions are also seen outside active regions, and called X-ray arcade formations. The storing of energy may occur when the motion of the footpoints in the high $\beta(= p_{gas}/p_{mag})$ photosphere forces the field in the corona to be distorted into a stressed form. A superhot plasma region, together with high energy particles, is created when some process is allowed to occur with fast release of magnetic energy from the stressed magnetic field in Alfven-transit time, much faster than the energy loss times.

4.1. New Findings about the Initial Dynamic Phase of Loop Flares

Loop flares are generally much smaller in size but known to produce higher energy emission compared with arcade-forming flares that are greater in size and in the total energy, but softer in the spectra. The high time cadence observation by Yohkoh has revealed that in a loop flare the footpoints of the loop brighten first, and then the bright regions move up to the loop top in less than half a minute, and after bouncing back and forth, the bright knot eventually settles down in the loop top region. During this, the shape of the loop shows a distortion. The bright blob settles down at the loop top gains brightness by a factor of ten to its brightness maximum, and eventually fades away in twenty minutes or so. Previous observations with low cadence caught only this last stationary stage by missing the dynamical first 1-2 minutes, and the source was described as a stationary small source suggestive of loop shape, without any motion, probably referring to the loop top source.

Most of the previous models of loop flares dealt only with the response of the chromospheric gas either (a) to the bombardment by high energy particles, or (b) heat conduction, provided from the top of the loop and come down along the *fixed* magnetic loop. The initial dynamical (magnetodynamical) behavior of the bright blobs and the distortion of the loop shape are the new findings, revealing highly dynamical initial phase behavior. Those will provide the initial physics that was lacking in previous models, and may explain the production of superhot plasma and acceleration of high energy particles through the magnetodynamical processes (Uchida et al. 1997b).

4.2. New Findings about the Global Model of Arcade Flarings

The relaxation of the stored stress in larger scale arcade flarings is somewhat different. In such a situation, the presence of a neutral point (or an array of neutral points) in the configuration can facilitate the liberation of the magnetic stress energy stored. Magnetic reconnections, in which the magnetic flux tubes with magnetic stress can be transferred to other regions of lower stress, can play an essential role in allowing the accumulated magnetic stress energy in the system to be converted into kinetic energy, and into thermal energy in shocks. In such a stress-reducing reconfiguration, the total liberated energy through such dynamical reconfiguration can be larger than the deposition of the energy into heat in the localized reconnection site itself.

Recent observations by Yohkoh have revealed, among others, essential new information about the "global model" (what are such stress-reducing configura-

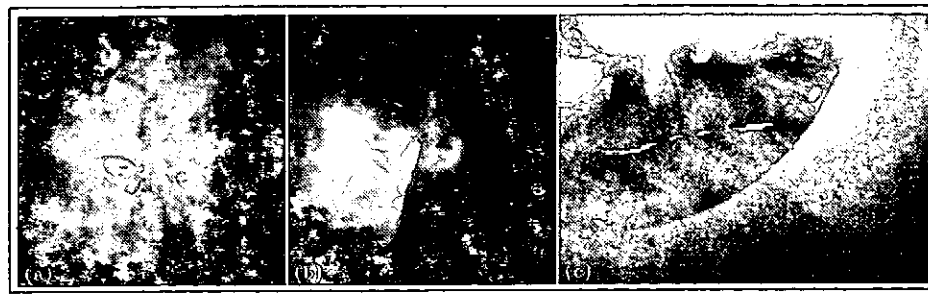

Figure 2. Evidence for quadrupolarity of the magnetic source. (a) Presence of high connections from the flare core of the Feb 21, 1992 arcade flare. (b) The same of the Dec 2, 1991 arcade flare. (c) The pre-event coronal structure with overlapped dual arcades in the pre-event structure of the Giant Cusp event of Jan 25,1992, all showing that the magnetic field involved is not a (dipped) simple bipolar arcade.

tions) for the arcade flaring processes (Tsuneta et al. 1992). Detailed analyses of the observations of the still faint pre-event coronal structures of arcade flares and high latitude X-ray arcade formation events have revealed for the first time that there exist structures like the high connections from the top of the flare core back to the photosphere on both sides (Uchida 1996)(Fig 2(a),(b)), or that the pre-event corona before high latitude arcade formations is "overlapped dual arcades" (Uchida et al. 1997)(Fig 2(c)). Those strongly suggest that the dipped bipolar connection picture that the "classical model" was based upon may not be valid. The small brightening feature along the axis of the dark tunnel below the cusped arcade is not explicable by the "classical model" either.

The situation of the arcade formation can be considered as "quadruple arrays" of magnetic sources *in a coarse sense*, explaining the observed "overlapped dual arcades" as the separatric surface in the quadruple source model (Uchida 1997b).

The so-called "classical model" by Sturrock (1966) and others, has a scenario that the simply-connected magnetic arcade supporting the dark filament at their dipped-tops is opened up by the eruption of the dark filament, and a magnetic neutral point (or an array of neutral points along the arcade) *is created* between the legs of the pulled out arcade. The reclosing of the opened-up arcade through magnetic reconnection is thought to liberate the difference in the energies of the opened and reclosed fields, and produces a flare. Uchida (1980) noted that this model has a difficulty in energy that the energy of the dark filament rise should have a kinetic energy greater than the flare energy itself.

Uchida et al. (1980, 1996,1997) advanced a model with quadruple magnetic sources in the photosphere. In this model, there exist an array of neutral points from the beginning in the field components $B_\perp$, perpendicular to the central polarity-reversal line in the middle of the arrays of +, −, +, − sources. The longitudinal field $B_\parallel$ dominating in this neutral sheet of $B_\perp$ suspends the dark filament gas in the form of a thin vertical partition, separating the squeezed

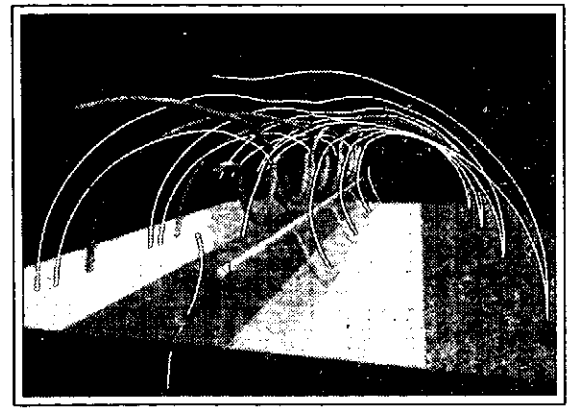

Figure 3. Pre-event coronal magnetic field in the quadruple magnetic source model. Dark filament is a thin partition type structure with $B_{\parallel}$ and neutral sheet in it. In this case, the neutral sheet splits into two, and the magnetic field in the dark filament is helical, as sometimes seen in eruptive prominences.

antiparallel vertical part of $B_{\perp}$. The gravity acting on the dark filament mass stabilizes this.

It is seen in Fig 4 (Hirose et al.1997) that the partition type dark filament is initially in equilibrium, separatingthe oppositely- directed vertical part of $B_{\perp}$, but, after the dark filament together with $B_{\parallel}$ is squeezed out, the antiparallel vertical parts of $B_{\perp}$ are pressed into a direct contact, and the reconnection can start.

The reconnection occurring there after the evacuation of the separating dark filament produces the main part of flare, heated cusped region just like the observed cusps in arcade flares at the limb, *but here*, having the upper connections connecting back the top of the heated cusp to the photosphere on both sides just as observed in Fig. 1(a),(b) (Uchida 1996). There is also a feature pressed down (S-shaped structure if seen from above), explaining the observed brightening feature at the axis of the dark tunnel. There is no counterpart for these in the classical model.

The part of the rising flux tubes will further be accelerated by the magnetic buoyancy, rolling down the slope of the magnetic potential outwards (melon-seed effect). This mechanism is the reverse of the process of pushing a magnetic blob into a stronger field region. Certain amount of work done is needed to push the blob in against the magnetic potential gradient. The reverse of that operating here can be the last and the greatest contribution to the energy and mass to produce CME (coronal mass ejection)'s.

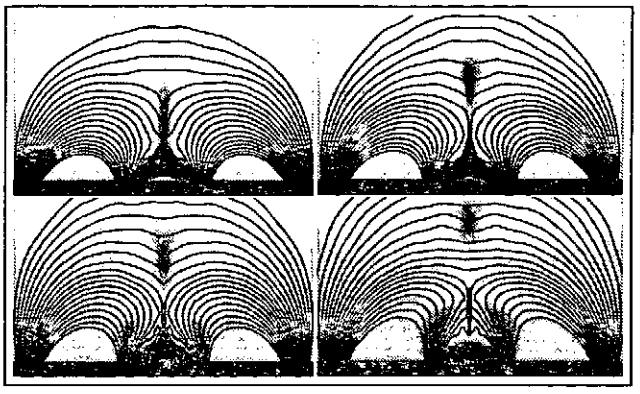

Figure 4. Dynamic simulation of dark filament eruption in quadruple source model (Hirose et al.1997). The dark filament in a thin partition form is squeezed out both up and down, and reconnection can start. As the reconnection starts, the dark filament *is accelerated* by being pushed up by the upwelling flux tubes across the separatric surface.

5. Conclusion

New information obtained by Yohkoh reviewed very briefly here is only a part of what were revealed by Yohkoh, but those already drastically influenced the previous views described in the textbooks for the last two-three decades. Further analyses of the Yohkoh data will add more to our knowledge of activities on the stars.

I acknowkedge heartily the Yohkoh Team members, Japanese, US, and UK, without whose efforts in preparing excellent hardware and software and in providing perfect operations of the satellite for more than 5 years, those results have not been obtainable.

References

Hirose,S., Cable,S.B., Uemura,S., and Uchida,Y., 1997, in preparation.

Sturrock, P.A., 1966, *Nature*, **221**, 695.

Tsuneta, S., Hara,H., Shimizu,T., Acton,L.W., Strong,K.T., Hudson,H., and Ogawara,Y., 1992, *Publ. Astron. Soc. Japan*, **44**, L63-L69.

Uchida, Y., 1980, in *Skylab Workshop, Solar Flares*, ed. P.A. Sturrock (University of Colorado Press), p67, and p110,

Uchida, Y., 1996, *Adv. Space Res.*, **17**, (4/5)19-28

Uchida, Y., Fujisaki, K., Morita,S., Torii,M., Hirose,S., and Cable, S.B., 1997a, submitted to *Publ. Astron. Soc. Japan.*

Solitary Kinetic Alfvén Waves in Low Aurora

D. Y. Wang, G. L. Huang, D. J. Wu
Purple Mountain Observatory, Nanjing, 210008, China

C.-G. Fälthammar
Alfvén Lab. Royal Institute of Technology, Stockholm, 10044, Sweden

abstract Solitary kinetic Alfvén waves (SKAW) in the case of $\beta << \frac{m_e}{m_i}$ have been studied from the observation events of Freja satellite and theory in detail. We find that (a) an analytical solution of finite-amplitude SKAW is presented. It is found that the exact analytical solution of SKAWs have a wider structure and much stronger perturbed fields than the KdV solitary with same parameters. These results have been preliminarily identified by Freja observation in low aurora. (b) The Poisson equation correction of SKAW has been considered, this correction is only important for the situation of $K_x \to 0$. (c) We suggest a dipole Alfvén vortex model to explain not only single dip or hump density solitary structures; but also composite structures of a dip and a hump solitary, observed in Freja.

1. Introduction

Several events with a strong electric field spikes ($\triangle E \sim 200mV/m$) and a density solitary structure ($\frac{dn}{n} > 10\%$) have been observed by Freja satellite in the low auroral region ($\sim 400km$), (Louran, et al., 1994; Volwerk, et al., 1996; Huang, Wang et al., 1996). These low frequency ($< 20Hz$) electromagnetic spike events with a depressive solitary density structure were interpreted as a solitary kinetic Alfvén wave,(SKAW hereafter) in the condition of $\beta << \frac{m_e}{m_i}$, (Shukla, Rahman and Sharma, 1982; Kalita and Kalita, 1986; Wang, Huang, Fälthammar et al., 1996).

However, a few observational phenomena have not been well understood. These phenomena are (1) The equation of SKAW has been simplified to KdV equation in the small-amplitude approximation, but the observation amplitude of solitary may be up to $\frac{dn}{n} \sim 70\%$. It is required to study the finite-amplitude SKAW. (2) The Sagdeev potential of SKAW will approach to infinite, as the $K_x \to 0$, K_x is the perpendicular wave number of SKAW. This puzzle should be solved. (3) We not only observe several events with a depressive density solitary structures, which are expected by SKAW model in the case of $\beta << \frac{m_e}{m_i}$; but also find some events with a hump density solitary, or with a composite structure of dip and hump solitary. (Wu, et al, 1996). These problems will be discussed in the following sections.

2. An Analytical Solution of Finite Amplitude SKAW

It is well known that the nonlinear KAW equation in the case of $\beta << \frac{m_e}{m_i}$ in the wave moving frame $\eta = K_x x + K_z z - Mt$, can be written as

$$\frac{1}{2}(\frac{dN}{d\eta})^2 + K(N, M^2, K_z) = 0 \tag{1}$$

where M is Alfvén Mach number. $K(N, M, K_z)$ is called Sagdeev potential. K_z is the wave number parallel to ambient magnetic field.

$$K(N, M^2, K_z) = -\frac{1+Q}{QK_x^2(3-N_m)}(N_m - N)(1-N)^3N^2 \tag{2}$$

where $Q = \frac{m_e}{m_i}$, $N = 1 - n$, and $N_m = (M^2 - K_z^2)/(M^2 - K_z^2/3)$ is an amplitude of density soltary. This equation can be simplified to KdV equation in the small-amplitude N_m approximation.(Kalita and Kalita, 1986). We find that this equation has an analytical solution, it is

$$N = N_m \frac{1 - tanh^2 Y}{1 - N_m tanh^2 Y} \tag{3}$$

$$Y = \Delta^{-1} \mid \eta \mid - \frac{N_m}{1 - N_m} (\frac{1 - N/N_m}{1 - N})^{\frac{1}{2}} \tag{4}$$

The main differences of analytical solution and solution of KdV equation are (1) The width of soliton of analytical solution is much larger than the width of KdV equation in the finite- amplitude N. as shown in Fig. 1. (2) The perturbed magnetic and electric field of analytical solution is much larger than the fields of KdV equation in the finite-amplitude N . (Wu, Wang, Fälthammar, 1995). A statistical relation between the amplitude and the width of SKAW, observed from Freja satellite, has been obtained, as shown in Fig.2 (Wu, Wang and Huang, 1996). The result show that the width of soliton is not always inversely proportional to the amplitude of solitary in the finite-amplitude region. It is well consistent with the expectation from analytical solution of SKAW.

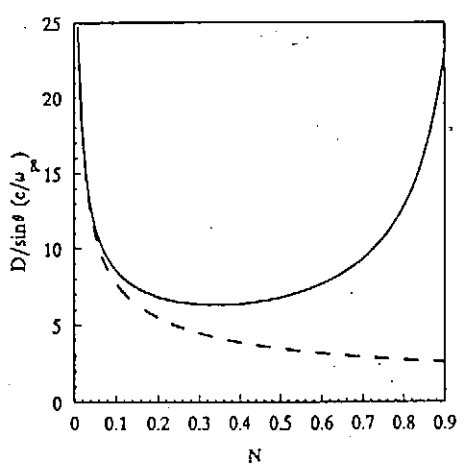

FIG. 1. The SKAW's width $D/\sin\theta$ (in the unit of c/ω_{pe}) versus the amplitude N_m, and the broken represents the width of the KdV soliton.

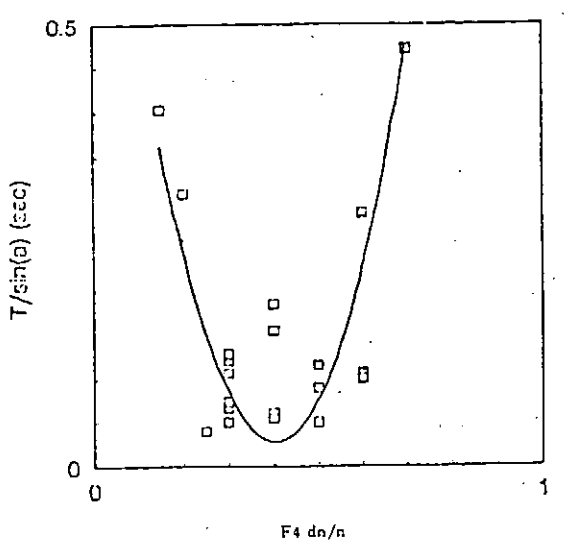

Fig. 2 Distribution of width of SKAWs observed by Freja spacecraft

3. The SKAW with Poisson Equation Correction

It is readily to find that the Sagdeev potential will approach infinite in equation (2), as $K_x \to 0$. We have further studied this puzzle problem using SKAW equation with Poisson equation correction. In this case, the Sagdeev potential can be written as

$$K_e(n_e, M^2, K_z) = -\frac{n_e^6 K_z^2}{2Q}[\frac{S}{G} - \frac{2R}{\sqrt{K_z^2 G}} + \frac{1}{GM^2}(S + 2R\sqrt{\frac{k_z^2}{G}} - 2\frac{1-n_e}{n_e}) + \frac{1}{K_z^2}(\frac{1-n_e}{n_e})^2] \tag{5}$$

$$S = \ln \frac{k_x^2 + G n_e^{-2}}{k_x^2 + G} \tag{6}$$

$$R = tan^{-1}\sqrt{\frac{G}{K_x^2 n_e^2}} - tan^{-1}\sqrt{\frac{G}{K_x^2}} \tag{7}$$

where $G = v_A^2/c^2$. It is readily to find that $\mathbf{K_e(n_e, M^2, K_z) \neq 0}$, as $\mathbf{k_x \to 0}$. However, the Poisson equation correction is only important for the $K_x^2 < G$. (Wang, Huang, Fälthammar, et al., 1996)

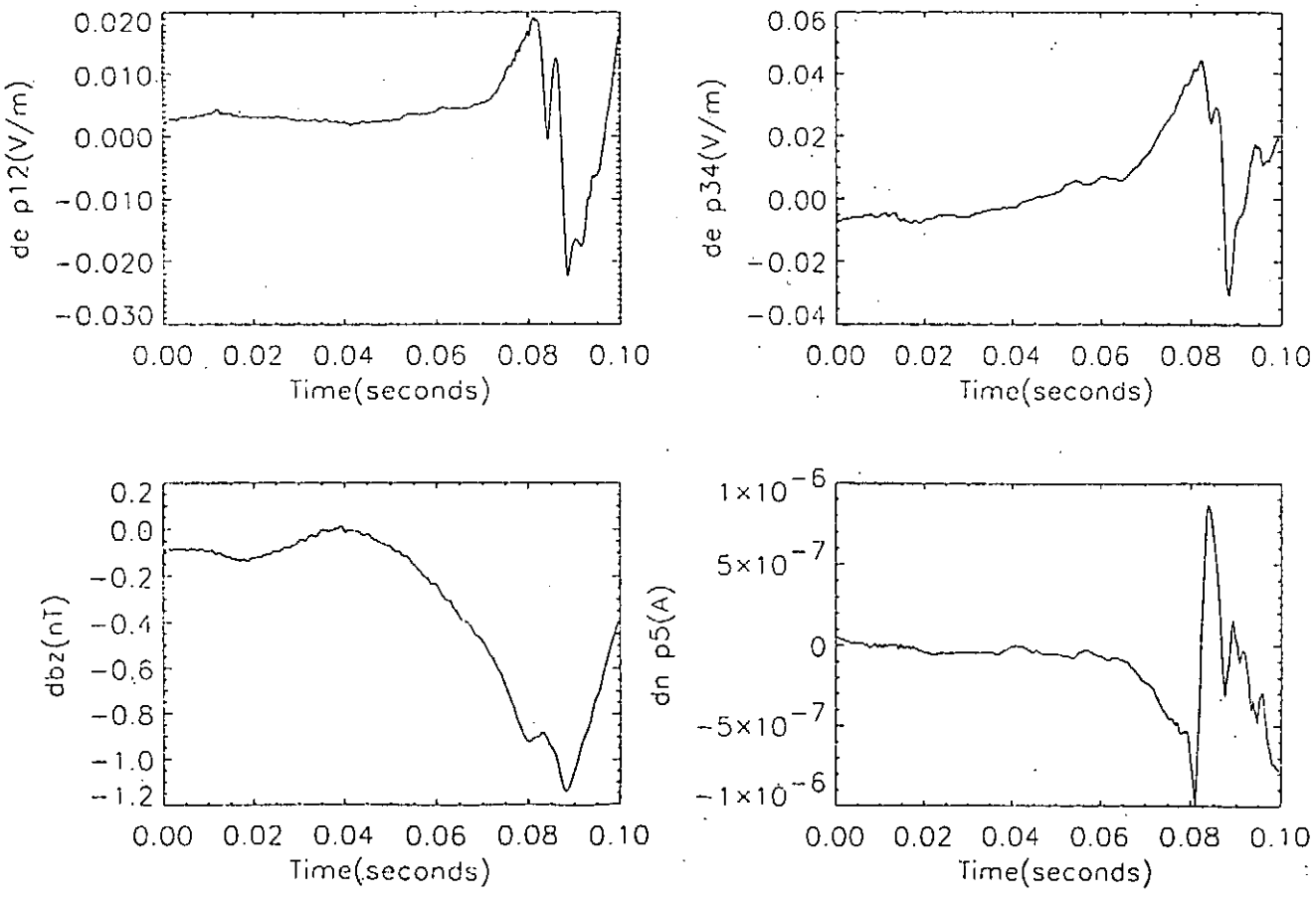

Fig.3 A composite structure event of a dip and a hump solitary, observed by Freja in low aurora.

4. Two-dimensional SKAW and Dipole Vortex Structures

We analyzed the strong density flutuations ($\mid dn/n \mid > 10\%$) associated with the SKAW events observed by Freja satellite, and found an interesting phenomenon. We not only observe some events with a dip or a hump density solitary and also find some events with a composite structure of dip and hump solitaries, as shown in Fig.3. Obviously, such kinds of hump solitary and composite structure of dip and hump solitaries cannot be explained by the SKAW model of $\beta << \frac{m_e}{m_i}$. On the other hand, as above discussion, SKAW is along the wave moving line, it is an one-dimensional SKAW model. This model can be expanded to two-dimension in the plane perpendicular to the ambient magnetic field, if the electric and polarization drift, as well as inhomogeneous space plasma are taken into account. It is a two-dimensional SKAW or Alfvén vortex, (Hasegawa and Mima, 1978). We suggest a simplified dipole Alfvén vortex model to establish a connection between the two-dimensional SKAW and the observational results from Freja.

It is assumed that the inhomogeneous background plasma density n_0 vary slowly in the x direction, and the local density solitary travels in the y direction. Assuming the charge neutral and taking Boltzmann distribution in the local potential field Φ. One has

$$n_0(x) = n_0(1 + x/L)exp(\frac{\Phi}{\Phi_0}) \qquad \mid x/L \mid << 1 \tag{8}$$

$$\mathbf{E} = - \bigtriangledown_\perp \Phi(x, y) \tag{9}$$

We can obtain a nonlinear electrostatic Hasegawa and Mima equation concerning Φ in the travelling wave frame $\eta = y - ut$

$$[\Phi - ub_0 x, \quad \bigtriangledown_\perp^2 \Phi - (\omega_{ci} B_0/\Phi_0)\Phi - (\omega_{ci} B_0/L)x] = 0 \tag{10}$$

where $[a, b] = \partial_x a \partial_\eta b - \partial_\eta a \partial_x b$ is a Poisson bracket. An analytic dipole solution of $\phi(r)$ can be written approximately as (Stenflo, 1986; Wu, Huang, Wang, 1996)

$$\phi(r) = \begin{cases} uB_0 r_0 K_1(k_0 r)/K_1(K_0 r_0), & \text{for } r > r_0; \\ uB_0 r_0[(1 + k_0^2/k_1^2)r/r_0 - (k_0^2/k_1^2)J_1(k_1 r)/J_(k_1 r_0)], & \text{for } r < r_0. \end{cases} \tag{11}$$

The results have been shown in Fig.4. We also studied the electromagnetic model of two-dimensional SKAW. (Wu, Wang, and Huang; 1997). The results show that the three kinds of solitary density structures and perturbed electric field are similar to the electrostatic model.

These Alfvén dipole vortex model have been compared to the observation of Freja. We find that (1) Two-dimensional dipole SKAWs have three kinds of solitary structure, it included dip, hump solitary and dipole vortex structure, which depends on the track of satellite crossing dipole Alfvén vortex. The width of dipole vortex structure is longer than the width of dip and hump solitary structure. These charaters are consistent with the observation of Freja in low aurora. (2) The perturbed electric field equal to zero at the peak (or bottom) of hump (or dip) solitary, but the perturbed electric field should be maximum or minimum at the center point of dipole vortex density structure. The maximum value of perturbed electric field in dipole vortex is often larger than the perturbed electric field of dip and hump solitary structures. (3) Using the parameters in low aurora, the propagation velocity of two-dimensional dipole SKAWs can be calculated. It is found that propagation velocity $u \sim 0.3km/s$, which is much smaller than the Freja satellite velocity $\sim 6.7km/s$. The two-dimensional dipole SKAW is stable during the satellite crossing time.

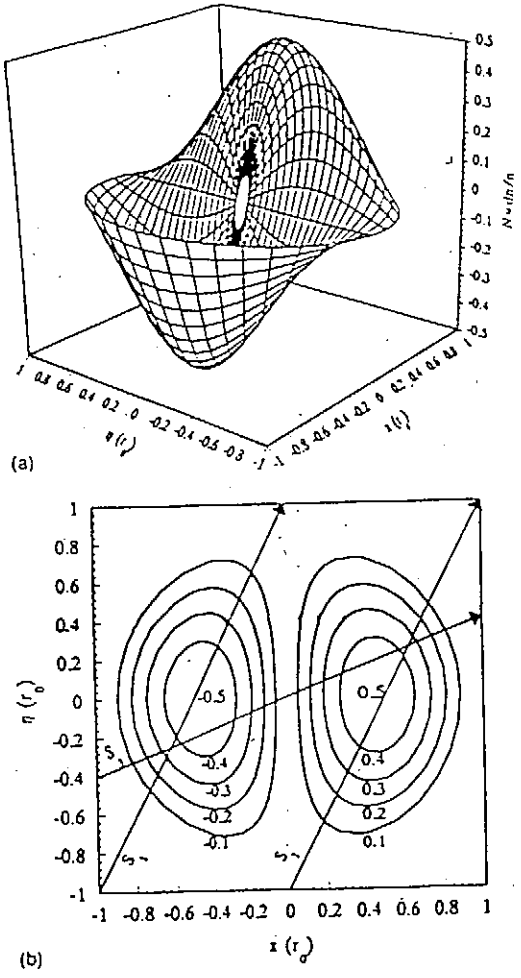

FIG. 4 An example for three kinds of density solitons (i.e., dip, hump, and dipole) observed in a dipole vortex structure. (a) The whole picture of two-dimensional density distribution; (b) constant density lines and three different cases of the satellite crossing the dipole vortex, where S_1, S_2, and S_3 are three different loci of the satellite; (c) the dip, hump, and dipole density solitons observed, respectively, by the satellite at S_1, S_2, and S_3, where the density N is enlarged by a factor of 4.

5. Conclusing Remarks

(1) We adopt a simplified dipole Alfén vortex model to explain three kinds solitary structures, observed by Freja in low aurora. Although prelimary comparison seems to be satisfied. However, it is required to improve this theoretical model, for example, small-amplitude approximation, the boundary condition of the model. On the other hand, it needs to find more observation events of Alfvén vortex in space physics, which included monopole and multipole Alfvén vortex structures.

(2) It should further study the problems of the SKAW and Alfvén vortex growth, and its evolution. It also needs to investigate the interaction between SKAW and particles and other waves. These are important plasma processes in the auroral region.

(3) It must point out that the investigation of SKAW are still restricted satellite observational condition. For example, the propagation direction of waves are not enough to be determined by four components of electric and magnetic fields, measured by F4 detectors in Freja satellite. In general, the measurement of only one satellite cannot distinglish a spatial structure and a time structure. This difficulty can be solved by Cluster satellites.

References

Hasegawa, A. and Mima, K.: 1976, *Phys. Rev. Lett.*, **37**, 267.

Hasegawa, A. and Mima, K.: 1978, *Phys. Fluids*, **21**, 87.

Huang, G.L., Wang, D.Y., Wu,D.J., de Féraudy, H., Le Quéau, D., Volwerk, M. and Holback,B.: 1997, *J. Geophys. Res.*, **102**, 7217.

Louarn, P., Wahlund, J.E., Chust, T., de Féraudy, H. and Roux, A.: 1994, *Geophys. Rev. Lett.*, **21**, 1847.

Kalita, M.K. and Kalita, B.C.: 1986, *J. Plasma Phys.*, **28**, 125.

Shukla, P.K., Rahman, H.D. and Sharma, R.P.: 1982, *J. Plasma Phys.* **28**, 125.

Stenflo, J.: 1986, *Phys. Fluids*, **30** , 3297.

Vorlwerk,M., Louran,P., Chust, T. de Féraudy, H. and Roux, A.: 1996, *J.Geophys. Res.*, **101**, 13335.

Wang, D.Y., Huang, G.L., Le Quéau, and Chen, Y.P.: 1996, *Chinese J. Space Sci.*, **16**, 17.

Wang, D.Y., Huang, G.L., Fälthammar, C.-G. Lindqvist, P.A., Blomberg, L. and Song, L.T.: 1996, *Astrophys. and Space Sci.* **240**, 175.

Wu, D.J., Wang, D.Y. and Fälthammar, C.-G.: 1995, *Phys. Plasmas*, **2**, 4476.

Wu, D.J., Huang, G.L. and Wang, D.Y.: 1996, *Phys. Rev. Lett.* **77**, 4346.

Wu, D.J., Wang, D.Y. and Huang, G.L.: 1997, *Phys. Plasmas* **4**, 611.

Yu, M.Y. and Shukla, P.K.: 1978, *Phys. Fluids* **21**, 1457.

Nonlinear Physics of Twisted Magnetic Field Lines

ZENSHO YOSHIDA
Department of Quantum Engineering, University of Tokyo,
Hongo, Tokyo 113, Japan

ABSTRACT: Twisted magnetic field lines appear commonly in many different plasma systems, such as magnetic ropes created through interactions between the magnetosphere and the solar wind, magnetic clouds in the solar wind, solar corona, galactic jets, accretion discs, as well as fusion plasma devices. In this paper, we study the topological characterization of twisted magnetic fields, nonlinear effect induced by the Lorentz back reaction, length-scale bounds, and statistical distributions.

1. INTRODUCTION

The nonlinear magnetohydrodynamics (MHD) involves a variety of complex phenomena. It is impossible to construct nontrivial theory by direct analyses of the basic equations. To elucidate a specific phenomenon, we must apply a reduction of the model with appealing to scale separations, singular perturbations, coarse-graining (averaging), etc.

In this paper, we discuss a slow motion (or a steady state) of a low-pressure magnetized plasma. In more specific terms, we consider the following singular limit. The general MHD equations read, in the standard normalized units,

$$\partial_t \boldsymbol{v} = -(\boldsymbol{v}\cdot\nabla)\boldsymbol{v} + \epsilon_A^{-2}(\nabla\times\boldsymbol{B})\times\boldsymbol{B} - \beta\nabla p + \epsilon_R\Delta\boldsymbol{v}, \quad \nabla\cdot\boldsymbol{v} = 0, \tag{1}$$

$$\partial_t \boldsymbol{B} = \nabla\times(\boldsymbol{v}\times\boldsymbol{B}) - \epsilon_L\nabla\times(\nabla\times\boldsymbol{B}). \tag{2}$$

Unknown variables are the magnetic field $\boldsymbol{B}$, the flow velocity $\boldsymbol{v}$ and the pressure p. The Alfvén number ϵ_A, Lundquist number ϵ_L^{-1}, Reynolds number ϵ_R^{-1}, and the beta ratio β are nondimensional positive parameters. The incompressibility condition ($\nabla\cdot\boldsymbol{v}=0$) may be replaced by an evolution equation for the pressure p in a more sophisticated model.

This system of nonlinear parabolic equations (1)–(2) is a close cousin of the Navier-Stokes system describing neutral fluids (see [1, 2] and papers cited therein). The MHD system includes coupling between the magnetic field and the flow velocity through the nonlinear induction effect and its reciprocal Lorentz force, which adds a considerable complexity to the usual Navier-Stokes system. Surprisingly, however, we observe a more regular and ordered behavior in some MHD systems. Such phenomena are highlighted by a singular perturbation of $\epsilon_A^2 \to 0$, with fixing the time-scale, in the momentum-balance equation (1). This limit is amenable to slow motion of a strongly magnetized low β plasma. The determining equation becomes the force-free condition $(\nabla\times\boldsymbol{B})\times\boldsymbol{B}=0$, which is equivalent to the Beltrami condition

$$\nabla\times\boldsymbol{B} = \lambda\boldsymbol{B}. \tag{3}$$

Here λ is a scalar function. By the solenoidal condition ($\nabla\cdot\boldsymbol{B}=0$) and identity $\nabla\cdot(\nabla\times\boldsymbol{B})=0$, taking the divergence of the both sides of (3) yields

$$\boldsymbol{B}\cdot\nabla\lambda = 0. \tag{4}$$

Since (4) means that the function λ should be constant along the streamline (field line) of $\boldsymbol{B}$, analysis of the system of equations (3)–(4) requires integration of the streamline equation

$$\frac{d}{ds}\boldsymbol{x} = \boldsymbol{B}(\boldsymbol{x}). \tag{5}$$

The solenoidal condition ($\nabla \cdot \boldsymbol{B} = 0$) parallels Liouville's theorem for the Hamiltonian flow, and hence one can formulate (5) in a canonical form [3]. For a general three-dimensional $\boldsymbol{B}$, the solution of (5) exhibits chaos. Hence, the general analysis of the system (3)–(4) includes an essential mathematical difficulty. Two special cases, however, can be studied rigorously. One is the case where $\boldsymbol{B}$ has an ignorable coordinate (two-dimensional). Then, (5) becomes integrable, and the system (3)–(4) reduces into a nonlinear elliptic equation [4, 5]. The three-dimensional problem involves the non-integrable streamline problem (5), however, it is decoupled from the Beltrami problem (3)–(4), if we assume a constant λ that make (4) trivial.

2. CONSTANT-LAMBDA BELTRAMI FIELD

The constant-λ condition for the Beltrami field is a strong ansatz based on the following physical reasons. The streamline equation (5) in a three-dimensional magnetic field is generally non-integrable, and hence, we may assume that streamlines (magnetic field-lines) are embedded densely in a volume. Since (4) demands that λ is constant along each field line, it is natural to assume a constant λ over such a volume. The theory of energy relaxation also derives the constant-λ condition. Woltjer [6] pointed out the importance of the magnetic helicity

$$K = \frac{1}{2}\int_{\Omega} \boldsymbol{A} \cdot \boldsymbol{B} d\boldsymbol{x}.$$

Here $\nabla \times \boldsymbol{A} = \boldsymbol{B}$, Ω is the entire volume of the plasma and $d\boldsymbol{x}$ is the volume element. The viscous dissipation does not change the helicity K, while the magnetic energy diminishes toward a "ground state". The magnetic field self-organized through this energy relaxation is characterized by a minimizer of the magnetic energy $W = \int_{\Omega} B^2 dx/2$ subject to a given helicity. This variational principle reads as $\delta(W - \lambda K) = 0$, where λ is the Lagrange multiplier. The formal Euler-Lagrange equation, under appropriate boundary conditions, is identical to (3). Taylor [7] formulated an equivalent variational principle, however, his model is based on a different hypothesis to justify the preferential conservation of the helicity. The energy dissipation proceeds faster than the change of the helicity, if the resistive dissipation is dominated by spatially concentrated fluctuation currents (see also Hasegawa [8]). Both effects, the viscous dissipation, resulting in ion heating, and the resistive dissipation, resulting in electron heating, were compared for a specific relaxation process [9].

There are many different observations suggesting the creation of constant-λ force-free fields in astrophysical, space and laboratory plasmas. Magnetic flux tubes (flux ropes), in which field lines are twisted, are produced through interactions between the magnetosphere and interplanetary magnetic fields [10]. In a laboratory plasma, detailed measurements of magnetic fields showed that the field produced after self-organization through turbulence is closely approximated by a solution of (3) [7]. Galactic jets are also considered to have similar configurations of magnetic fields [11].

The Beltrami field plays an essential role in the so-called "dynamo theory". To understand the rapid generation of magnetic fields in astrophysical systems, we have to invoke a "fast dynamo action" that has a growth rate of the magnetic energy independent of the resistivity (see [12] and papers cited therein). In a highly conductive plasma the evolution of the magnetic field $\boldsymbol{B}$ obeys Faraday's law (2) with $\epsilon_L \to 0$. A plasma flow $\boldsymbol{v}$ with chaotic streamlines (maps with positive Lyapunov exponents), which may have a large length-scale, bring about complex mixing of magnetic flux, and the length-scale of the inhomogeneity cascades toward a small scale, resulting in amplification of the magnetic field. If the length-scale reduces down to the dissipative range, and the resistive damping becomes comparable to the induction effect, then the magnetic field energy turns to diminish. In this classical picture of the kinematic dynamo, the magnetic field energy accumulates into small scale fluctuations, and the life-time of the amplified magnetic field is limited by the time-scale of the cascade process. To obtain a larger length-scale and a longer life-time of amplified magnetic fields, an appropriate

limitation for the scale reduction should occur. The nonlinear effect of the amplified magnetic fields, that is the Lorentz back-reaction, plays an essential role in this "post-kinematic phase". Here we assume that the plasma achieves a quasi-steady state through the energy relaxation process. Then, the momentum balance equation reduces into (3), and the flow $\boldsymbol{v}$ must be chosen in such a way that $\boldsymbol{B}$ satisfies (3) implicitly. The parameter λ characterizes the length-scales of $\boldsymbol{B}$. Hence, the condition (3) imposes a bound for the length-scale of the field, if the magnitude of λ is restricted by some reason. This bound avoids scale reduction down to the resistive regime, and extends the life-time of the amplified magnetic field.

Through the kinematic dynamo process, the current ($\propto \nabla \times \boldsymbol{B}$) tends to concentrate in small volumes, which may be disconnected. When the sectional length-scale of such a volume becomes small enough, the Lorentz force dominates ($\epsilon_A^2 \ll 1$). Let Ω to be such a "clump" of the magnetic field. Its length-scale is denoted by ℓ_c. This Ω may have a complex topology. We want to find a constant-λ Beltrami field in Ω. If the parameter λ can be chosen such that $|\lambda| \leq \lambda_c = O(\ell_c^{-1})$, then equilibration of the clump into such a Beltrami field results in a lower bound for the length-scale [13]. Here we solve the Beltrami condition (3) for a given helicity and an "external magnetic field". The external component of $\boldsymbol{B}$ is defined by decomposing $\boldsymbol{B} = \boldsymbol{B}_\Sigma + \boldsymbol{h}$, where $\nabla \times \boldsymbol{h} = 0$ and $\nabla \cdot \boldsymbol{h} = 0$. This $\boldsymbol{h}$, which represents the magnetic field rooted outside Ω, is assumed to be a given function. Its complement $\boldsymbol{B}_\Sigma$ is the unknown variable. We define the gauge-invariant helicity by

$$\mathcal{K} = \int_\Omega \boldsymbol{A} \cdot \boldsymbol{B}_\Sigma dx \tag{6}$$

We prove the existence of a solution with $|\lambda| \leq \lambda_c = O(\ell_c^{-1})$ for every $\boldsymbol{h} \neq 0$ and $\mathcal{K}$ in the next section (Theorem3). The nonvanishing $\boldsymbol{h}$ plays the role of symmetry breaking.

3. EXISTENCE THEOREM AND COMPLETENESS THEOREM

The constant-λ Beltrami condition (3) is regarded as an eigenvalue problem with respect to the curl operator. Interestingly, the topology of the domain plays an essential role in this eigenvalue problem.

To study the spectrum the curl derivatives, we need the fundamental theory of vector function spaces. Let Ω ($\subset \boldsymbol{R}^3$) be a bounded domain with a smooth boundary $\partial\Omega = \cup_{i=1}^n \Gamma_i$ (Γ_i is a connected surface). We consider cuts of the domain Ω. Let $\Sigma_1, \cdots, \Sigma_m$ ($m \geq 0$) be cuts such that $\Sigma_i \cap \Sigma_j = \emptyset$ ($i \neq j$), and such that $\Omega \setminus (\cup_{i=1}^m \Sigma_i)$ becomes a simply connected domain. The number m of such cuts is the first Betti number of Ω. When $m > 0$, we define the flux through each cut by

$$\Phi_{\Sigma_i}(\boldsymbol{u}) = \int_{\Sigma_i} \boldsymbol{n} \cdot \boldsymbol{u} ds \qquad (i = 1, 2, \cdots, m),$$

where $\boldsymbol{n}$ is the unit normal vector on Σ_i with an appropriate orientation. By Gauss's formula, $\Phi_{\Sigma_i}(\boldsymbol{u})$ is independent of the place of the cut Σ_i, if $\nabla \cdot \boldsymbol{u} = 0$ in Ω and $\boldsymbol{n} \cdot \boldsymbol{u} = 0$ on $\partial\Omega$.

We denote $L^2(\Omega)$ the Lebesgue space of square-integrable (complex) vector fields in Ω, which is endowed with the standard innerproduct $(\boldsymbol{a}, \boldsymbol{b})$. We define the following subspaces of $L^2(\Omega)$;

$$\begin{aligned} L^2_\Sigma(\Omega) &= \{\boldsymbol{w};\ \nabla \cdot \boldsymbol{w} = 0 \text{ in } \Omega,\ \boldsymbol{n} \cdot \boldsymbol{w} = 0 \text{ on } \partial\Omega,\ \Phi_{\Sigma_i}(\boldsymbol{w}) = 0\ (i = 1, \cdots, m)\}, \\ L^2_H(\Omega) &= \{\boldsymbol{h};\ \nabla \cdot \boldsymbol{h} = 0, \nabla \times \boldsymbol{h} = 0 \text{ in } \Omega,\ \boldsymbol{n} \cdot \boldsymbol{h} = 0 \text{ on } \partial\Omega\}, \\ L^2_g(\Omega) &= \{\nabla\phi\}. \end{aligned}$$

We have an orthogonal decomposition [14]

$$L^2(\Omega) = L^2_\Sigma(\Omega) \oplus L^2_H(\Omega) \oplus L^2_g(\Omega).$$

The space of solenoidal vector fields with vanishing normal component on $\partial\Omega$ is

$$L^2_\sigma(\Omega) = L^2_\Sigma(\Omega) \oplus L^2_H(\Omega).$$

The subspace $L^2_H(\Omega)$ corresponds to the cohomology class, whose member is a harmonic vector field and $\dim L^2_H(\Omega) = m$ (the first Betti number of Ω). When Ω is simply connected, then $m = 0$ and $L^2_H(\Omega) = \emptyset$. We have the following theorems [15].

Theorem 1 *Let $\Omega \subset \boldsymbol{R}^3$ be a smoothly bounded domain. We define a curl operator S in the Hilbert space $L^2_\Sigma(\Omega)$ by*

$$S\boldsymbol{u} = \nabla \times \boldsymbol{u}, \quad D(S) = \{\boldsymbol{u} \in L^2_\Sigma(\Omega)\ ;\ \nabla \times \boldsymbol{u} \in L^2_\Sigma(\Omega)\}.$$

Then S is a self-adjoint operator. The spectrum of S consists of only point spectra $\sigma_p(S)$, which is a discrete set of real numbers.

Theorem 2 *In $L^2_\sigma(\Omega)$ we define a curl operator $\tilde{S}$ by*

$$\tilde{S} = \nabla \times \boldsymbol{u}, \quad D(\tilde{S}) = \{\boldsymbol{u} \in L^2_\sigma(\Omega)\ ;\ \nabla \times \boldsymbol{u} \in L^2_\sigma(\Omega)\}.$$

(i) When $\dim L^2_H(\Omega) = 0$, i.e. if Ω is simply connected, then $\tilde{S} \equiv S$, and hence, the spectrum $\sigma(\tilde{S}) = \sigma_p(\tilde{S})$.

(ii) When $\dim L^2_H(\Omega) > 0$, i.e. if Ω is multiply connected, then $\tilde{S}$ is an extension of S. The spectrum $\sigma(\tilde{S})$ consists of only spectra $\sigma_p(\tilde{S})$, and $\sigma_p(\tilde{S}) = \mathbf{C}$. Hence, for every $\lambda \in \mathbf{C}$,

$$(\tilde{S} - \lambda)\boldsymbol{u} = 0 \tag{7}$$

has a nontrivial solution.

Theorem 2 proves the general existence of the constant-λ Beltrami function for every $\lambda \in \mathbf{C}$, if Ω is multiply connected. In the next theorem, we solve the constant-λ Beltrami equation (3) for a given helicity $\mathcal{K}$ and harmonic field $\boldsymbol{h} \in L^2_H(\Omega)$. Now λ is an unknown variable. This problem is related with the magnetic clump discussed in Sec. 2.

We assume that Ω is multiply connected. Let $\{\varphi_j\}$ be the complete set of the eigenfunctions of the self-adjoint curl operator S (Theorem 1). The corresponding eigenvalues are numbered as

$$\cdots \le \mu_{-2} \le \mu_{-1} < 0 < \mu_1 \le \mu_2 \le \cdots. \tag{8}$$

For every $\boldsymbol{B} \in L^2_\sigma(\Omega)$, we have an orthogonal-sum expansion

$$\boldsymbol{B}(\boldsymbol{x}, t) = \sum_j c_j(t)\varphi_j(\boldsymbol{x}) + \boldsymbol{h}(\boldsymbol{x}, t), \tag{9}$$

where $\boldsymbol{h} \in L^2_H(\Omega)$. The harmonic field $\boldsymbol{h}$ is a given function, which plays an important role of "symmetry breaking" in the following discussion. The first summation in the right-hand side of (9) is denoted by $\boldsymbol{B}_\Sigma$. The energy of $\boldsymbol{B}$ is given by

$$W = \frac{1}{2}\sum_j c_j^2 + \frac{1}{2}\|\boldsymbol{h}\|^2. \tag{10}$$

There exists $\boldsymbol{g}$ such that $\boldsymbol{h} = \nabla \times \boldsymbol{g}$. The vector potential of $\boldsymbol{B}$ is given by

$$\boldsymbol{A} = \sum_j \frac{c_j}{\mu_j}\varphi_j + \boldsymbol{g}. \tag{11}$$

Denoting $D_j = (\varphi_j, g)$, the gauge invariant helicity (6) becomes

$$\mathcal{K} = \frac{1}{2}(A, B_\Sigma) = \frac{1}{2}\sum_j (\frac{c_j^2}{\mu_j} + D_j c_j). \tag{12}$$

For given $\mathcal{K}$ and h, we can solve (3) by the variational principle $\delta(W - \lambda\mathcal{K}) = 0$, and obtain

$$c_j = \frac{\lambda\mu_j}{2(\mu_j - \lambda)} D_j \quad (\forall j). \tag{13}$$

The energy and the helicity become

$$W = \sum_j \frac{\lambda^2\mu_j^2}{8(\mu_j - \lambda)^2} D_j^2 + \frac{1}{2}\|h\|^2, \qquad \mathcal{K} = \sum_j \frac{\lambda\mu_j(2\mu_j - \lambda)}{8(\mu_j - \lambda)^2} D_j^2. \tag{14}$$

We can show that $\mathcal{K}$ is a monotone function of λ in the range of $\mu_{-1} < \lambda < \mu_1$ (see definition (8)), if $D_j \neq 0$ $(\exists j)$, viz., if we have a "symmetry breaking" $h \neq 0$. For every $\kappa \in \mathbf{R}$, the equation $\mathcal{K}(\lambda) = \kappa$ has a unique solution in this range of λ. Now we have the following theorem.

Theorem 3 *Let Ω $(\subset \mathbf{R}^3)$ be a multiply connected bounded domain. Assume that h $(\in L^2_H(\Omega))$ is finite. For every κ $(\in \mathbf{R})$, the Beltrami condition (3) has a unique solution B such that its helicity $\mathcal{K} = \kappa$, and λ such that $\mu_{-1} < \lambda < \mu_1$.*

4. STATISTICAL EQUILIBRIUM

Using the phenomenological variational principle $\delta(W - \lambda\mathcal{K}) = 0$ (Sec. 2), we develop a statistical mechanical model that reproduces the constant-λ Beltrami field at the "zero *temperature* limit". A finite *temperature* (in the sense of MHD fluctuation) equilibrium includes fluctuations. The statistical theory predicts the spectra of macroscopic physical quantities such as the energy, helicity, etc.

A key step is to find an invariant measure of the temporal evolution equation. It corresponds to Liouville's theorem in the Hamiltonian dynamics. Montgomery *et al.* [16] used the "Chandrasekhar-Kendall functions", which are the eigenfunctions of the curl in a cylindrical geometry [17], to expand the solenoidal vector fields B and v, and defined an infinite-dimensional phase space spanned by the expansion coefficients. The formal Lebesgue measure is shown to be invariant against the nonlinear ideal $(\epsilon_R, \epsilon_L \to \infty)$ dynamics. The completeness theorem of the eigenfunctions (Theorem 1) gave a mathematical justification of the expansion, and generalized the Hilbert-space approach for an arbitrary geometry. An important development in recent work [18] is the treatment of the harmonic magnetic field, which brings about a symmetry breaking associated with a topological constraint. When we consider a multiply connected domain, the harmonic magnetic fields, which are rooted outside the domain, are represented by the cohomology class. If we impose the ideal conducting boundary conditions, these harmonic fields are invariant. The rest orthogonal complement spans the dynamical phase space. The invariant harmonic component plays the role of an externally applied symmetry breaking. Interestingly, this term yields "power-law spectra" of the energy, helicity and helicity fluctuation. It is easy to verify the following proposition.

Proposition 1 (Invariant Measure) *Let $v(x,t)$ be a smooth vector field in Ω. Suppose that $B(x,t)$ obeys*

$$\partial_t B = \nabla \times (v \times B) \quad \text{in } \Omega, \tag{15}$$

$$n \times (v \times B) = 0 \quad \text{on } \partial\Omega. \tag{16}$$

Using the eigenfunctions of the curl operator φ_j and the harmonic field h_ℓ, we write $B(x,t)$ in the form of (9). Then, $dC = \prod_j dc_j$ is an invariant measure.

The ansatz of the variational principle $\delta(W - \lambda\mathcal{K}) = 0$ suggests that two additive quantities W and $\mathcal{K}$ are the relevant state variables that characterize the statistical equilibrium. The possible ensemble consistent with this variational principle is the Boltzmann distribution

$$P(W,\mathcal{K}) \propto \exp[-\beta(W - \lambda\mathcal{K})] \tag{17}$$

where β is interpreted as an inverse temperature of the magnetic field. The helicity and the energy of each mode is $(c_j^2/\mu_j + D_j c_j)/2$ and $c_j^2/2$, respectively. The Boltzmann distribution for the amplitude c_j is

$$P_j \propto \exp\left[-\frac{\beta}{2}\left(c_j^2 - \frac{\lambda}{\mu_j}c_j^2 - \lambda D_j c_j\right)\right]. \tag{18}$$

The ensemble averages of W and $\mathcal{K}$ over the phase space become

$$\langle W\rangle = \sum_j \left[\frac{\mu_j}{2\beta(\mu_j - \lambda)} + \frac{\lambda^2\mu_j^2}{8(\mu_j - \lambda)^2}D_j^2\right], \tag{19}$$

$$\langle \mathcal{K}\rangle = \sum_j \left[\frac{1}{2\beta(\mu_j - \lambda)} + \frac{\lambda\mu_j(2\mu_j - \lambda)}{8(\mu_j - \lambda)^2}D_j^2\right]. \tag{20}$$

These results are compared with (14). The first term of the right-hand side of (19) and that of (20) are the contributions of the fluctuations. In (19), the energy of the harmonic field, which is constant here, is omitted. This classical statistical model suffers from the Rayleigh-Jeans catastrophe, viz., when we pass the limit of the infinite summation over the all modes, the fluctuation terms diverge. To avoid this divergence, we can appeal to the Bose-Einstein statistics with second-quantizing the mode amplitude c_j and defining bosons MHD fluctuations [18].

REFERENCES

1. LADYZHENSKAYA O. A. & SOLONNIKOV V. A., *J. Soviet Math.* **8**, 384-422 (1977).
2. YOSHIDA Z. & GIGA Y., *J. Math. Phys.* **24**, 2860-2864 (1983).
3. YOSHIDA Z., *Phys. Plasmas* **1**, 208-209 (1994).
4. GRAD, H. & RUBIN, H., in *Second United Nation Conference on the Peaceful Uses of Atomic Energy*, Vol. 31, pp. 190-197. IAEA, Geneva (1958).
5. YOSHIDA Z., in *Current Topics in the Physics of Fluids*, Vol. 1, pp. 155-178. Council of Scientific Information, Trivandrum (1994).
6. WOLTJER L., *Proc. Natl. Acad. Sci. U.S.A.* **44**, 489-491 (1958).
7. TAYLOR J. B., *Phys. Rev. Lett.* **33**, 1139-1141 (1974).
8. HASEGAWA A., *Adv. Phys.* **34**, 1-42 (1985).
9. YOSHIDA Z., *Nucl. Fusion* **31**, 386-390 (1991); YOSHIDA Z. & HASEGAWA A., *Phys. Fluids B* **4**, 3013-3015 (1992).
10. RUSSEL C. T., in *Magnetic Reconnection in Space and Laboratory Plasmas*, (Ed. E. W. Hones), pp. 124-138. American Geophysics Union, Washington DC (1984).
11. KÖNIGL A. & CHOUDHURI A. R., *Astrophys. J.* **289**, 173-187 (1985).
12. VAINSHTEIN S. I., SAGDEEV R. Z., ROSNER R. & KIM E.-K., *Phys. Rev. E* **53**, 4729-4744 (1996).
13. YOSHIDA Z., *Phys. Rev. Lett.* **77**, 2722-2725 (1996).
14. TEMAM R., *Navier-Stokes Equations*, North-Holland, Amsterdam (1984).
15. YOSHIDA Z. & GIGA Y., *Math. Z.* **204**, 235-245 (1990).
16. MONTGOMERY D., TURNER L. & VAHALA G., *Phys. Fluids* **21**, 757-764 (1978).
17. CHANDRASEKHAR S. & KENDALL P. C., *Astrophys. J.* **126**, 457-460 (1957).
18. ITO N. & YOSHIDA Z., *Phys. Rev. E* **53**, 5200-5206 (1996).

On Creating Transport Barrier by Radio-Frequency Waves

S. Sen[1,2], R. A. Cairns[3], B. Dasgupta[4] and G. Pantis[5]

1 Max Planck Institute for Plasmaphysics, EURATOM Association, 85748 Garching, Germany

2 Department of Physics, Flinders University of South Australia, GPO Box 2100, Adelaide 5001, Australia

3 School of Mathematical and Computational Sciences, University of St Andrews, St Andrews, Fife, KY16 9SS, UK

4 Saha Institute for Nuclear Physics, AF/1 Bidhannagar, Calcutta 700064, India

5 Department of Physics, University of Ioannina, Ioannina, Greece

ABSTRACT: The use of radio frequency (RF) waves in the range of Alfven frequency is shown to stabilise the drift-ballooning modes in the tokamak if the radial profile of the RF field energy is properly chosen. Stabilisation is achieved by the ponderomotive force arising due to the radial gradient in the RF field energy. The estimate of the RF power required for this stabilisation is found to be rather modest and hence should be easily obtained in the actual experiments. This result therefore shows that the use of the RF waves can create a transport barrier to reduce the loss of particle and energy from the plasma. The new improved mode produced by the RF is expected to have all the advantageous features of the enhanced reverse shear (ERS) modes and at the same time will, unlike the ERS plasma, be sustainable for unlimited period of time and hence should be an attractive choice for the reactor-grade self-sustaining plasma.

The economic viability of a tokamak as a leading contender for a fusion reactor crucially depends on the development of a magnetic configuration that has good confinement and stability and a large fraction of bootstrap current. Understanding and control of turbulent transport and of its underlying driving agents is therefore a prerequisite in this process. Recent discoveries of various enhanced performance operational regimes like the H-modes [1], the VH-modes [2] and the enhanced reverse shear modes (ERS-modes) [3-4] has opened up a new window for improved tokamak operation. It is usually believed that the ERS configuration can provide the characteristics desirable for a fusion reactor [5].

One of the remaining challenges for enhanced tokamak operation is the development and understanding of the basic physics involved in the process that leads to the transition to the improved confinement modes. While a sheared poloidal (toroidal) flow is found to be responsible for the H- (VH-) modes, a hollow q profile (hence normally a hollow current profile) is necessary for the ERS modes. Most tokamaks however operate with inductive current drive which in general produces a peaked current density profile at the magnetic axis because of the strong dependence of the plasma conductivity on the electron temperature. Only by noninductive current drive or transient techniques can a hollow current density profile be generated.

Recent experiments in the PRX-M indicate that if NBI heated plasma is further heated up by ion Bernstein waves (IBW) there is a significant increase in the core plasma temperature and hence in the confinement, the so-called CH-modes [6]. This raises interest in whether RF waves can be used to create the transport barrier to reduce the loss of particles and energy from the

plasma. The final run of experiments in the TFTR were originally planned to investigate this key issue. From the theoretical point of view, there is already an indication that RF waves can stabilise ballooning type MHD instabilities [7]. However, no such investigation on the effect of the RF waves to our knowledge has been carried out for the drift-type microinstabilities, stabilisation of which is essential for the formation of the transport barrier.

In this work we suggest that the transport barrier may be created by suitably launching RF waves in the Alfven range of frequencies. We demonstrate that RF waves through ponderomotive force arising due to the radial gradient in the RF field energy stabilises drift-ballooning modes, which have been identified as the likely mechanism for anomalous transport in the plasma [8, 9]. We also demonstrate that the stabilisation can be achieved for rather modest values of the RF power and hence should be easily obtained in the actual experiments. The new improved mode produced by the RF will, unlike the ERS modes, be non-transient in nature and should be sustainable for unlimited period of time. This mode thus is free from the main shortcoming of the ERS plasma and should be an attractive choice for the fusion reactor.

A nonlocal stability analysis for the collisionless drift-ballooning modes is carried out on the basis of a simple two-fluid model. We use the usual (r, θ, ξ) coordinates, corresponding to the minor radial, poloidal and toroidal directions respectly and consider the long-wavelength ($k_\theta^2 \rho_s^2 \ll 1$) drift waves for a large aspect-ratio circular tokamak. The perturbed potential can then be expressed as:

$$\phi(\vec{x}, t) \equiv \phi(\rho, \theta, \xi, t) = \phi(\rho) exp[i(n\xi - m_0\theta - \omega t)],$$

where $\rho = (r - r_0)$, r_0 is the radius of the reference mode rational surface, i.e., $m_0 = nq(r_0)$, $k_\theta = \frac{m_0}{r_0}$, and $\hat{s} = \frac{rq'}{q}$ at $r = r_0$. Here, for simplicity we will assume the ions to be cold and will ignore the electron temperature gradient. Using fluid descriptions the eigenvalue equation in the presence of RF ponderomotive force can be derived in a straightforward way [10-11]

$$[\rho_s^2(\frac{\partial^2}{\partial \rho^2} - k_\theta^2) + \frac{(\omega_e^* - \omega)}{\omega} - \frac{{\omega_e^*}^2}{\omega^2}(\frac{\epsilon_c}{k_\theta \rho_s})^2 \times$$

$$(\frac{\partial}{\partial \theta} + ik_\theta \rho \hat{s})^2 - 2\epsilon_n \frac{\omega_e^*}{\omega}(cos\theta + \frac{isin\theta}{k_\theta}\frac{\partial}{\partial \rho}) - \frac{1}{2}\frac{k_\parallel}{\omega^2}\frac{d}{d\rho}|V_{RF}(\rho)|^2 -$$

$$\frac{\rho^2 \omega_e^*}{L_*^2}]\phi = 0 \qquad (1)$$

where $\rho_s^2 = \frac{C_S^2}{\omega_{ci}^2}, C_S^2 = \frac{T_e}{m_i}, \epsilon_n = q\epsilon_c = L_n/R$, $\omega_e^*(\rho)$ the diamagnetic drift frequency and L_* the density gradient variation scale length and typically of the order of density scale length L_n. $\vec{V}_{RF}(\rho)$ is the induced oscillating fluid velocity in the presence of an external RF field. The ponderomotive contribution due to the RF field enters the force balance equation through the term $mn < (\vec{V}_{RF}.\nabla)\vec{V}_{RF}^* >$ and can be simplified to $\frac{1}{2}mn\frac{d}{d\rho}|V_{RF}|^2$ assuming that the ponderomotive forces are radially symmetric [12].

The first term in equation (1) arises from the finite Larmor radius effect and the third from the ion-sound. The fourth is the effect of toroidal coupling whereas the last term introduces the

radial variation of ω_e^* with $L_*^{-2} = (\frac{1}{\omega_e^*})(\frac{d^2\omega_e^*}{d\rho^2})$. We assume a simple general case of the variation of $\vec{V}_{RF}(\rho)$ with the radial distance such that $|V_{RF}(\rho)|^2 = \frac{|V_{RFO}|^2\rho}{L_{RF}} + \frac{|V_{RFO}|^2\rho^2}{L_{RF}^2}$, where $\frac{dV_{RF}}{d\rho} = \frac{V_{RFO}}{L_{RF}}$ and $\frac{1}{2}\frac{d^2V_{RF}}{d\rho^2} = \frac{V_{RFO}}{L_{RF}^2}$.

To reduce the 2 dimensional (2D) eigenmode problem to 1 dimensional (1D), we will apply the ballooning transformation. To determine the radial mode structure the solution of the fully two-dimensional eigenmode problem must be obtained. Within the framework of ballooning formalism, this needs solving the problem to higher order. The problem then separates into two distinctive radial length scales. To leading order the problem reduces to the usual 1D eigenmode equation (with radial variable appearing only as parameter) which determines the mode structure along the magnetic field lines. The next order equation then determines the radial mode structure. In the usual theory of high n ballooning modes [13] one maps the poloidal angle θ on to an extended coordinate χ with $-\infty < \chi < \infty$ and writes the perturbation in the form

$$\phi(\theta, x) = \sum_m e^{-im\theta} \int_{-\infty}^{\infty} e^{im\chi}\hat{\phi}(\chi, x)d\chi, \quad \text{where, } \hat{\phi} = A(x)F(\chi, x)\ exp[-ix(\chi + \chi_0)]$$

where χ_o is an arbitrary phase of the eikonal and $x = k_\theta\rho\hat{s}$. Here, $A(x)$ is assumed to vary on some scale intermediate between the equilibrium scale length and the perpendicular wavelength. Now to leading order (in $n^{-1/2}$ expansion) the ballooning equation becomes

$$[\frac{\omega_e^{*2}}{\omega^2}(\frac{\epsilon_c}{k_\theta\rho_s})^2\frac{\partial^2}{\partial\chi^2} + \frac{1}{2}\frac{1}{\omega^2 qR}\frac{d}{d\rho}|V_{RF}(\rho)|^2\frac{\partial}{\partial\chi} - (\omega_e^* - \omega)/\omega + 2\epsilon_n\frac{\omega_e^*}{\omega}(cos\chi + \hat{s}(\chi + \chi_o)sin\chi) +$$

$$(k_\theta\rho)^2(1 + \hat{s}^2(\chi + \chi_o)^2) + \frac{\rho^2\omega_e^*}{L_*^2\omega}]F = 0 \qquad (2)$$

The first derivative (with respect to χ) term can be removed by suitably changing the dependent variable (to ξ). Equation (2) then reduces to

$$[\frac{\omega_e^{*2}}{\omega^2}(\frac{\epsilon_c}{k_\theta\rho_s})^2\frac{\partial^2}{\partial\chi^2} - (\omega_e^* - \omega)/\omega + 2\epsilon_n\frac{\omega_e^*}{\omega}(cos\chi + \hat{s}(\chi + \chi_o)sin\chi) - \frac{1}{4}(\frac{1}{2}\frac{1}{\omega^2 qR}\frac{d}{d\rho}|V_{RF}(\rho)|^2)^2/\frac{\omega_e^{*2}}{\omega^2}(\frac{\epsilon_c}{k_\theta\rho_s})^2$$

$$+(k_\theta\rho)^2(1 + \hat{s}^2(\chi + \chi_o)^2) + \frac{\rho^2\omega_e^*}{L_*^2\omega}]\xi = 0 \qquad (3)$$

where,

$$\xi = Fexp[\frac{1}{4\omega^2 qR}(-\frac{|V_{RFO}|^2 x}{L_{RF}} - \frac{|V_{RFO}|^2 x^2}{2L_{RF}^2})] \qquad (4)$$

Now to explore the implication of the RF field profile on the radial structure and on the stability of the modes one needs the higher order ballooning theory. In the higher order theory χ_o is obtained from the equation $\frac{\partial\Omega}{\partial\chi_o}(x, \chi_0) = 0$ and the radial envelope function $A(x)$ satisfies

$$\frac{\partial^2\Omega}{\partial\chi_0^2}\cdot\frac{d^2A}{dx^2} + [2(\Omega - \Omega_0) - p_1 - 2p_2x^2]A = 0, \qquad (5)$$

where, $\Omega = \frac{1}{k_\theta^2 \rho_s^2 \hat{s}^2}[\frac{\omega_*^*}{\omega} - 1 - k_\theta^2 \rho_s^2]$, $\Omega_o = i\frac{\epsilon_c}{k_\theta^2 \rho_s^2 \hat{s}}$, $p_1 = \frac{1}{2}(\frac{V_{RFO}^2}{\omega^2 q R L_{RF}})^2 / \frac{\omega_*^{*2}}{\omega^2}(\frac{\epsilon_c}{k_\theta \rho_s})^2$, $p_2 = \frac{1}{k_\theta^4 \rho_s^2 \hat{s}^4}(\frac{1}{L_n^2} - (\frac{V_{RFO}^2}{C_s^2}\frac{L_n}{L_{RF}^2}\frac{1}{\rho_s k_\theta})^2)$, $x = k_\theta \rho \hat{s}$. Equation (5) is a simple Weber equation. When p_2 is positive and $\partial^2\Omega/\partial\chi_o^2 > 0$ ($\partial^2\Omega/\partial\chi_o^2 > 0$ is necessary in order that the mode be most unstable [13]), $A(x)$ is a localised Gaussian function. However, an important change is introduced by the ponderomotive contribution. Assuming $L_n \sim 3cm$, $L_{RF} \sim 1cm$ and taking $k_\theta \rho_s \sim 0.1$, we find that p_2 becomes negative for $V_{RFO}/C_s \sim 10^{-1}$ (which means that the RF power is only a small fraction of the thermal power. Note also that this is the RF power at the resonance, which is much larger than the overall average RF power). It is important to note that the length scale for the RF wave is difficult to give precisely since the intensity has a singularity in ideal MHD theory, and the actual width predicted will depend on what sort of resistive damping or finite Larmor radius effects are used to eliminate the singularity. It is also interesting to note that to consider the most unstable situation we have assumed L_n rather small, which however is expected in the region where transport barrier is formed. With p_2 negative $A(x)$ is then given by

$$A(x) = exp[-i\frac{1}{2}(\mid p_2 \mid / \mid \frac{\partial^2\Omega}{\partial\chi_0^2} \mid)^{1/2} x^2] \tag{6}$$

So, the mode envelope is now radially outgoing which is reminiscent of the equivalent slab problem [14]. The quadratic x variation of the RF field energy in the toroidal problem like the magnetic shear in the corresponding slab problem creates an *antiwell* in the radial direction (instead of the well formed by the diamagnetic frequency). The wave energy is therefore convected outward. The eigenvalue is given by

$$\Omega = \Omega_0 + \frac{p_1}{2} - i\frac{1}{2}(p_2 \mid \frac{\partial^2\Omega}{\partial\chi_0^2} \mid)^{1/2} \tag{7}$$

The negative imaginary contribution in the eigenvalue shows that the RF field profile *stabilises* toroidal drift waves which otherwise escape magnetic shear damping! The actual stability of the mode will be determined by the relative magnitude of the destabilising contribution (Ω_o) and the stabilising contribution of the third term in the RHS of equation (7). Choosing, as before, $L_n \sim 3cm, q = 3, \hat{s} \sim 1, R = 1.5m, k_\theta \rho_s \sim 0.1, \lambda_\theta \sim 1cm$, $L_\Omega[= (\frac{1}{\Omega}\frac{\partial\Omega}{\partial\chi_o})^{-1}] \sim 1radian$, and $\Omega \sim 1$, it is easy to see that the complete stabilisation of the mode is actually possible. It is interesting to note that the sign and the magnitude of the linear variation of the RF energy has no direct effect on the stability. The linear term shifts the potential, but does not alter the quadratic structure. It also shifts the centre of the mode away from the x=0 rational surface. The main stabilising effect comes from the quadratic term which forms an additional *antiwell* which pushes the wave function away from x=0, thus increasing the stabilising effect and weakening the driving term simultaneously. Also important to note that the theory assumes that the RF wave is producing an oscillating fluid velocity, so this points towards a low frequency wave. One possibility is to use the Alfven resonance, which produces highly localised intensity maxima which coincide closely with flux surface [15].

We will now discuss the effect of the ponderomotive force on the turbulent transport coefficient by using the mixing length theory, according to which the turbulent diffusivity is given by

$$\chi_k = \gamma_k \triangle_k^2$$

where γ_k is the mode growth rate and $\triangle_k$ is the mode width. We have already seen that the growth rate of the linear mode is reduced in the presence of the RF field. It is also easy to see

that the radial width of the modes related to the individual magnetic surfaces is also reduced. To see this we note that in deriving Equation (3) we have removed the first derivative (w.r. to χ) term by suitably changing the dependent variable (from F) to ξ. The relation between F and ξ is given by equation (4). So as evident from equation (4) the radial width of the individual mode is reduced due to the presence of the ponderomotive force. So, the corresponding transport is also expected to be reduced by the ponderomotive force. Coming to the global transport, at the first instant it seems difficult to reach a definitive conclusion about it. This is because, whereas the growth rate of the linear mode decreases, its global mode width [given by Equation (6)] increases. However, as has been mentioned by Sen [11] that there may be some additional processes (such as electron Landau damping and fluid resonance) determining a finite mode width rather than the outgoing wave situation which otherwise holds in this situation. Hence the corresponding global transport is also expected to be reduced in the presence of the ponderomotive force.

In summary, we have investigated the effect of the RF waves on the stability of the collisionless drift-ballooning modes, which have been identified as the key mechanism for the anomalous transport. Our full analytic stability analysis shows that RF waves in the Alfven range of frequencies can have a significant effect on the stability of the drift-ballooning modes if the radial profile of the RF field energy is properly chosen. This stabilisation is achieved through the ponderomotive force arising due to the radial gradients in the RF field energy and is different from the stabilisation mechanism due to RF-induced poloidal-shear-flow which is thought to be responsible in the case of IBW induced CH modes [6]. The estimate shows that stabilisation can be achieved for rather modest values of the RF power and should be easily obtained in the actual experiments. This result therefore shows that the use of RF waves can create a transport barrier to reduce the loss of particle and energy from plasma and as there is no time limit for how long RF power can be launched, a stationary, non-transient improved mode can be envisioned in the plasma core by this technique. This mode is expected to have all the advantageous features of the ERS plasma and at the same time will, unlike the ERS mode, be non-transient in nature and should in principle be sustainable for unlimited period of time.

Before concluding it is important to mention several simplifying assumptions that have been made which may restrict the scope of our results. Among the effects that we have not considerd here are the nonlinear contributions of the RF waves, in particular the sideband coupling contributions have been neglected. Contributions coming from these terms are however negligible for the limit considered by us $L_n > L_{RF}$ [7]. We have also assumed that the ponderomotive forces due to the RF field is radially symmetric. However, it has been pointed out by Appert et al. [15] that toroidal effects do not greatly effect the position of the Alfven resonance, so this is a reasonable assumption. Furthermore, we have neglected the modification of the equilibrium profiles in the presence of the RF waves so that our results are limited to the low RF power levels. Notwithstanding these restrictions, however, the basic stabilising mechanism from the RF ponderomotive force is quite unambiguously shown by our simple model and is not expected to be seriously modified by any of the above simplifications.

We would like to thank D. Biskamp, J. W. Connor, R. L. Dewar, D. Pfirsch and H. R. Wilson for useful discussions. Thanks are also due to the TEXTOR team in particular to G. Van Oost and R. Koch for discussions on the experimental feasibility of the theory developed in this work. S. Sen acknowledges the hospitality provided at the Max-Planck Institute for Plasma Physics, Garching and the financial support through the mobility contract No. 131-83-7 FUSC.

References

[1] F. Wagner et al., Phys. Rev. Lett., **49**, 1408 (1982)

[2] G. L. Jackson et al., Phys. Rev. Lett., **67**, 3098 (1991)

[3] F. M. Levinton et al., Phys. Rev. Lett., **75**, 4417 (1995)

[4] E. J. Strait et al., Phys. Rev. Lett., **75**, 4421 (1995)

[5] C. B. Forest et al., Phys. Rev. Lett., **77**, 3141 (1996)

[6] M. Ono et al., (IAEA-CN-60/A-3-I-7, 15th International Conference on Plasma Physics and Controlled Nuclear Fusion Research, Sivelle, Spain, 1994), IAEA, Vienna (1996)

[7] D. A. D'Ippolito et al., Phys. Rev. Lett., **58**, 2216 (1987)

[8] D. Biskamp and A. Zeiler, Phys. Rev. Lett., **74**, 706 (1995)

[9] J. F. Drake et al., Phys. Rev. Lett., **77**, 494 (1996)

[10] W. Horton et al., Phys. Fluids, **21**, 1366 (1978)

[11] S. Sen, Plasma Phys. Controlled Fus., **37**, 95 (1995)

[12] S. Sen et al., Phys. Lett. A, **157**, 411 (1991)

[13] J W Connor, R J Hastie and J B Taylor, Proc. of Royal Society A, **365**, 1 (1979)

[14] L D Pearlstein and H L Berk, Phy. Rev. Lett., **23**, 220 (1969)

[15] K. Appert et al., Nuc. Fus., **22**, 903 (1983)

Computer Simulation of Complexity in Plasmas

Takaya Hayashi, Tetsuya Sato,
and the Complexity Simulation Group

National Institute for Fusion Science,
Oroshi, Toki 509-5292, Japan
e-mail: hayashi@nifs.ac.jp

Abstract

By making a comprehensive comparative study of many self-organizing phenomena occurring in magnetohydrodynamic and kinetic plasmas, we came up with a hypothetical grand view of self-organization. This assertion is confirmed by a recent computer simulation for a broader science field, specifically, the structure formation of short polymer chains, where the nature of the interaction is completely different from that of plasmas. It is found that the formation of the global orientational order proceeds stepwise.

I. Introduction

Self-organization is a generic process in nature, which describes spontaneous formation of ordered structure. Creation of orderliness is one of the central problems in the Science of Complexity. Self-organization may be typical of the nonlinear and nonequilibrium process which evolves in an open system, and develops independently of the governing interactions of its specific components. When we turn our eyes to plasmas, such as fusion plasmas and space plasmas, plasmas are always nonuniform, and open to environments, thus they are in a nonequilibrium state. To release the free energy, therefore, the system becomes unstable. Because of its nonlinearity the evolution becomes highly complex. In some situations, plasmas reveal transition processes, which may be called self-organization. In this sense, plasma is an exemplar of a medium governed by complexity, and Plasma Physics is potentially a Physics of Complexity.

One important direction in plasma physics research is to pursue plasma as "dynamic science", rather than a "static science". From traditional studies of quiescent and steady equilibrium structures in closed isolated systems, the frontiers are expanding to consider the dynamics of open, nonequilibrium systems. Computer simulation is powerful in understanding complicated dynamics. Exploring dynamic nonlinear evolutions in open, nonequilibrium systems exposed to environments, namely, complexity, is the mission of "simulation science". At our institute (National Institute for Fusion Science), we sets up a research strategy towards its exploration by developing an innovative simulation system which is called "Grand Man-Machine Interactive System for Simulation (MISSION)". The primary purpose of this paper is to extract a

grand view of self-organization through an extensive computer simulations of plasmas.

We first hypothesize that self-organization is governed by three key elements;

① Existence of an open complex system,

② Existence of information (energy) source, and

③ Existence of entropy generation and expulsion processes.

It may be natural to consider that self-organization occurs in an open system where an information (or energy) exchange can take place with an external world. When new information is introduced into a system, the system reacts upon it. When the amount of introduced information exceeds a certain threshold, the reaction may become significant and the system may experience a sizable change in its structure or state, i.e., the onset of a structural instability. A new ordered structure will thereby be created. During this process of structural change, or, phase transition, some chaotic state will be realized in an intermediate stage and something superfluous, which may be called natural odds and ends (entropy), is to be produced. In creating a clear-cut new structure, therefore, the cleaning up, or disposal, of those odds and ends is an important function. In addition to these interactions with the external world, the most important element is the nonlinearity of the system whereby operations of creating an ordered structure are practically conducted.

With these three elements in mind, we have done numerous simulations to extract a unified scenario of how order is created. Based on results of simulations which we have executed for plasmas with various configurations and states, we came up with universal features in self-organization

(1) The temporal behavior of self-organization is highly dependent on the way of energy supply. More specifically, when activation energy (information) is continuously supplied from an external system a nonlinear system self-adaptively can experience intermittent order creation, wondering local maxima and minima of the potential energy in a rather irregular way: intermittent self-organization. In contrast, when energy is suddenly pumped up in a nonlinear system and no pumping is given thereafter, then the system relaxes stepwise into a stable ordered structure.

(2) While an order is being created, the rate of entropy production is maximized; law of maximum entropy production.

(3) Depending on whether produced entropy is expulsed from the system or not, the created order structure can be quantitatively different.

II. Intermittent self-organization

We first show cases when activation energy is continuously supplied from an external system. Let us pick up a simulation of a twisted flux tube as a first example [1]. Initially, uniform straight field lines are applied in the axial direction. The axial boundaries are not periodic but are the suppliers of a continuous energy flow. Specifically, at the boundaries a circular motion is steadily applied in a limited region at both ends with the opposite polarity to each other, so that the magnetic field lines keep twisting. The bundle of straight field lines are twisted and squeezed

toward the center in the initial phase. As the twisting proceeds, the stored tension energy of the twisted bundle of field lines is released in terms of a knot-of-tension type of instability. The instability develops in such a way that the kinked part of the flux tube collides against untwisted field lines. As a consequence, reconnection is driven to take place and relaxes toward an interconnected structure (a local minimum energy state). As the twisting goes further, the flux tube linked with distant untwisted field lines reconnects with a companion flux tube to come back to the original straight topology, i.e., grand cycle. Interestingly, it has been observed that the open nonlinear system responses in an intermittent fashion to a continuous input of energy.

A next example of intermittent self-organization is dipole field generation in a rotating sphere, like the case of the dynamo mechanism in the earth. A magnetohydrodynamic simulation is performed in a rigidly rotating spherical shell [3]. The inner spherical surface is kept to a constant high temperature and the outer surface to a constant low temperature. The convection instability develops and creates a well-organized convection structure, more specifically, paired cyclon-anticyclon columns along the rotation axis which stand side by side in a circle. When a tiny magnetic fluctuation is imposed in the system, the fluctuation develops and creates a well-organized magnetic structure, as well as the convection columns, that is, the dipole-dominant magnetic structure. This is a system that energy is continuously supplied in the form of the heat flux through the inner boundary. Interestingly, when this simulation is continued for a long time scale, intermittent phenomenon takes place. Namely, the reversal in the polarity of the dipole moment occurs, much like the well-known behavior in the geo-dynamo.

III. Stepwise relaxation

In this section, we show cases of stepwise relaxation when energy is instantaneously pumped up to a high energy state (far-from-equilibrium) in a nonlinear system. Observed in Ref. 4 is the time evolution of the magnetic structure in a typical example of a magnetohydrodynamic self-organization. The final helical structure is the self-organized one [4]. In the evolutions of the magnetic helicity and energy, it is observed that the relaxation occurs in two steps for the magnetic energy but not for the magnetic helicity. The two-step relaxation reflects the fact that there was another equilibrium (unstable) state between the given initial state and the final minimum energy state. We emphasize here that each stepwise relaxation occurs in a time scale which is quite a fast process compared with the classical diffusion time.

Shown in Fig.1 is a simulation of structural formation of polymers [5], which is executed to see the universality of the stepwise relaxation in nonlinear systems. Both bond interaction and non-bond interaction in polymer chains are modeled in this simulation. It is clearly observed that the orientationally ordered structure at low temperature is formed starting from a random configuration corresponding to a high energy state. As the curve for time evolution of an index of the orderliness in Fig.1 shows, it should be noted that the ordered structure is formed stepwise although the property of the interactive force and thus nature of nonlinearity for this system are quite different from the case of plasma.

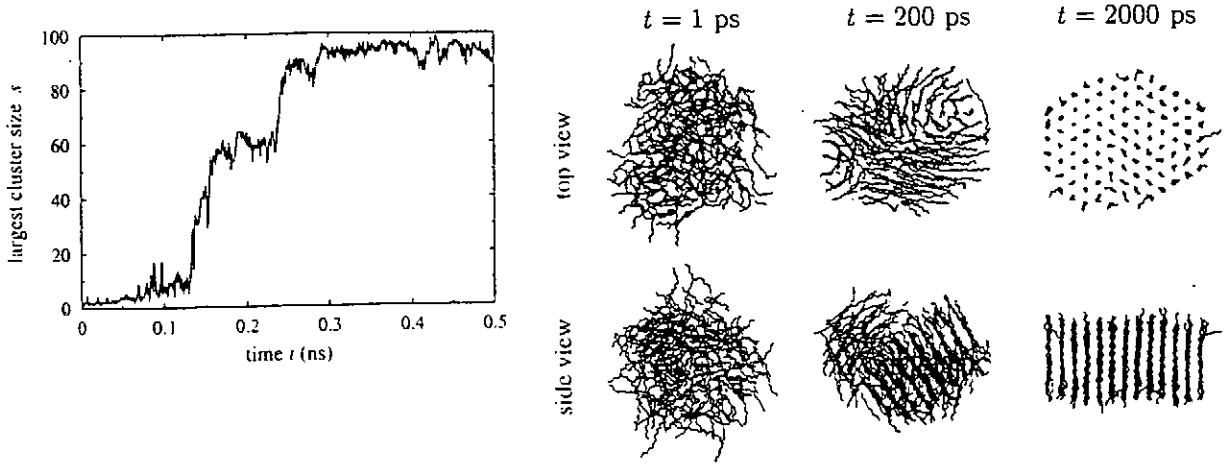

Fig. 1 Stepwise formation of orientational structure in short polymer chains.

IV. Entropy production and expulsion

In this section we examine, with particular attention, the dynamical relationship of the entropy production rate and expulsion function with creation of orderliness.

When we examine a typical example of the entropy production rate, namely, the volume-integrated ohmic heating, where intermittent self-organization takes place for the twisted flux tube stated above, one sees that the production rate repeats maximization at every sudden structural transition and minimization after transition. In the other example of the MHD self-organization stated in Sec.III where an energy (helicity) is instantaneously pumped into a system, the entropy production rate is maximized as the transition is taking place and minimized as it subsides. When the final minimum energy state is realized, the production rate almost vanishes. From these results, one can definitely confirm that whenever a new structure is being created the entropy production rate is anomalously increased, then minimized after the new structure is created.

Here, we shall attempt to look for what will happen when the produced entropy is filtered out. We take the ion acoustic double layer for this purpose [6]. What we have obtained is a remarkable and striking new self-organization phenomenon caused by filtering out the produced unnecessary entropy from the system. It is well known by particle simulation that weak ion acoustic double layer are generated in a one-dimensional collisionless plasma where electrons drift in ions. In the previous simulation, however, particles were regarded as periodic in a one-dimensional system. This periodic condition implies that the particles leaving from the downstream boundary enter into the system from the upstream boundary as they are and vice versa, no matter how seriously they are disturbed by the generation of ion acoustic double layers In other words, the disturbed information, or disorderliness, is retained in the system. A new particle simulation code is developed in which fresh particles continuously flow into the system

from each boundary in place of dirty particles leaving the system. We can thus filter out the superfluous information (entropy), when produced. The result is really striking. A giant double layer is generated. Compared with the conventional ion acoustic double layer, the potential difference of which is of the order of one electron thermal energy, the potential amplitude of this giant double layer reaches a surprisingly large level, say, larger than ten times the thermal energy. This giant double layer has a much longer lifetime than that of the normal weak ion acoustic double layer and exhibits a recurrent generation.

The implication of this simulation is that if the system contains a proper filtering function of the superfluous disorderliness, then a well-organized structure can be realized and sustained for a long period.

V. Summary: scenario of self-organization

When a system gains energy, gradually or instantaneously, from an external world, beyond a threshold (marginal) point, an instability arises. The reaction of the system is to deform its own structure so that the deposited energy is stored as much as possible. When the supplied energy far exceeds the instability threshold (a supersaturated state), the instability develops sufficiently. The nonlinearity is enormously enlarged thereby and gives rise to a large deformation of the structure. The deformation progresses in such a way that the excessively deposited energy is released along the shortest path. In order to release it in the shortest path an anomalous dissipation, or an anomalous entropy production, must take place in one way or another. Simultaneously, the structure (topology) must be drastically changed, namely, a nonlinear bifurcation must take place.

These results and others have led us to the assertion that a natural open system in a far-from-equilibrium state tends to boost itself up to a bifurcation (phase transition) point, which then gives rise to an anomalously enhanced dissipation rate, or an anomalous entropy production rate, by whatever process it may be realized, whereby a well-organized orderliness is created.

References

1. H.Amo, T.Sato, and A.Kageyama, Phys. Rev. E 51, 3838 (1995).
2. H.Kitabata, T.Hayashi, T.Sato, and the Complexity Simulation Group, Phys. Soc. Jpn. 65, 3208 (1996).
3. A.Kageyama and T.Sato, Phys. Rev. E 55, 4617 (1997).
4. R.Horiuchi and T.Sato, Phys. Rev. Lett. 55, 211 (1985).
5. S.Fujiwara and T.Sato, J. Chem. Phys. 107, 613 (1997).
6. T.Sato, H.Takamaru, and the Complexity Simulation Group, Phys. Plasmas 2, 3609 (1995).
7. T.Sato and the Complexity Simulation Group, Phys. Plasmas 3, 2135 (1996).

Thermal Stability Analysis of Ignited Plasma on ELMy-H mode, L-mode and High β_p-mode

G. Tateishi, S. -I. Itoh, M. Yagi*, K. Itoh**, and A. Fukuyama****
Interdisciplinary Graduate School of Engineering Sciences, Kyushu Univ. 39, Kasuga 816
**Research Institute for Applied Mechanics, Kyushu Univ. 87, Kasuga 816*
***National Institute for Fusion Science, Nagoya 464-01*
****Faculty of Engineering, Okayama University, Okayama 700*
Japan

I. Introduction

To understand the physics of ignited plasma is important in the design of the reactor. The ITER (International Thermonuclear Experimental Reactor) device [1], whose primal aim is to attain the self-ignition of plasma, is planned and the designing study has been continued. For a nuclear concept, the stable operational point is necessary to be searched for. There, the physics of α-particle has a key role to control of burning plasma. High energy α-particles should be used to heat up the fuel plasma to self-sustain the burning state. On the other hand, those can also be a cause of instability (so-called thermal instability, TAE-mode, Fish-bone instability, etc.). Furthermore, when α-particles are fully thermalized, they become "He-ash", which dilutes the fuels and prevents the self-ignition. In this paper, the burning performance of the ITER-like plasma is investigated, assuming the existing three confinement modes, i.e., the ELMy-H mode, the L-mode and the high β_p-mode. The stationary operational points are calculated by solving the steady state equations of the energy balance and the He particle balance. The stability analysis around the steady state solution is also performed. Considering various constraints (e.g., density limit, β limits, and divertor ash-pumping capacity), it is found that the ELMy-H mode or the L-mode seem to be a candidate for the ITER operational mode. The self-ignited high β_p-mode is difficult to be achieved in ITER-like plasma [2]. Typical operational points of these three modes are shown, and the burning performances are compared.

The organization of this paper is as follows. In Sec. II, basic model equations are introduced. In Sec. III, numerical results for the thermal stability of the ELMy-H mode, the L-mode, and the high β_p-mode are shown. Sec. IV is devoted to summary and discussion.

II. Model equations

In order to examine the ignition conditions of burning plasmas, we consider the deuterium (D) and tritium (T) mixture plasma where the α-particles (He) exist as the product of fusion reactions. Here the densities are denoted by n_j (j = D, T, He, e). The following assumptions are imposed, i.e., (1) the densities of the deuterium and tritium are equal, $n_D = n_T$ and $n_i = n_D + n_T$. (2) The volume averaged temperature T is the same value among all species. (3) α-particles are fully thermalized without escaping from the plasma.

From the condition of charge neutrality, the densities satisfy the following relations,

$$f_i = \frac{n_i}{n_e} = \frac{n_D + n_T}{n_e} = 1 - 2f_{He}, \quad (1)$$

$$f_{tot} = \frac{1}{n_e}(n_e + n_i + n_{He}) = 2 - f_{He}, \quad (2)$$

where f_{He} and f_i indicate the ratios of helium and ion densities to electron density, respectively, and f_{tot} is the total density normalized by the electron density. The energy balance equation and the particle balance equation are solved, based on a point model. The power balance equation is given as follows

$$\frac{\partial}{\partial t}\frac{3}{2}n_e f_{tot} T = \frac{1}{4}n_e^2 f_i^2 E_\alpha \langle \sigma v \rangle - \frac{3}{2\tau_E} n_e f_{tot} T - R_{br}, \quad (3)$$

where the terms in R.H.S are, from the left, the power input from slowing down of α-particles (with $E_\alpha = 3.52$ MA), the heat transport losses, and the volume power losses with bremsstrahlung, respectively. We specify the confinement modes by introducing scaling laws of the energy confinement time τ_E. For the ELMy-H mode, we employ following empirical scaling law [3],

$$\tau_E^{ELMy-H} = 0.032 I_p^{0.63} B_t^{0.34} m_i^{0.33} R^{2.52} \varepsilon^{0.33} \kappa^{0.46} P_{in}^{-0.53} n_e^{0.26} \quad [s] \quad (4)$$

where I_p is the plasma current, B_t is the toroidal magnetic field, m_i is the ion mass ratio, ε is the inverse aspect ratio, and P_{in} is the power input. For the L-mode and the high β_p-mode, we adopt a theoretically modeled one [4] defined by

$$\tau_E = f_\tau^{2.5} L I_p^2 T^{-1.5} \left(1 + \beta_p^4\right)^{0.5} \quad [s] \quad (5)$$

with $f_\tau^{2.5} L$=2.44, where f_τ is the numerical coefficient, L is the characteristic length (typically the system size), and β_p is the poloidal beta value. If the value of β_p is less than unity, this model well explains the L-mode confinement. In another limit, where the value of β_p is larger than unity, this can explain the high β_p-mode confinement. In Ref. [4], it has been shown that the current diffusive ballooning mode model can reproduce ITER89 scaling law and explain experimental results on the L-mode. Furthermore, this model can explain the formation of the transport barrier in the discharge with weak or negative shear via the bootstrap current contribution. Therefore, such an effect could reflect as the global characteristics on the burning condition through this confinement scaling law. About the radiation loss term, it is assumed that the plasma is black body for Synchrotron radiation. (It can be large at higher temperature ($T \geq 5$ (keV)) regime.) The radiation loss is dominated by the bremsstrahlung.

The particle balance of He-ash is given by

$$\frac{\partial}{\partial t} n_e f_{He} = \frac{1}{4} n_e^2 f_i^2 \langle \sigma v \rangle - \frac{1}{\tau_{He}^*} n_e f_{He}, \quad (6)$$

where τ_{He}^* is the global particle confinement time for He-ash [5]. The ratio of τ_E and τ_{He}^*, i.e., $\rho \equiv \tau_{He}^*/\tau_E$ is introduced and assumed to be constant. It means that τ_{He}^* has the same scaling

law as τ_E.

Combining Eqs. (3) and (6) with $\partial / \partial t = 0$, and using the confinement model (4) or (5), we obtain steady state solutions which satisfy ignition condition.

Next, using the steady state solutions, we calculate the linear growth rate of the thermal instability γ as follows. Linearizing Eqs. (3) and (6) with $T = T_0 + \delta T_1$ and $f_{He} = f_{He0} + \delta f_{He1}$, where δT_1 and δf_{He1} are assumed to have the growth rate as $e^{\gamma t}$, we obtain the dispersion relation as $b_0 + b_1\gamma + b_2\gamma^2 = 0$. The coefficient of each term is specified by the form of energy confinement time [2]. The solutions which satisfy $Re(\gamma) > 0$ are defined to be thermally unstable.

III. Results and analysis

In addition to the evaluations of the ignition conditions, we estimate the density limit and the β limits as operational constraints. The density limit is evaluated based on the empirical model, Greenwald limit [6] given by $n_e < n_e^G = I_p / \pi a^2$.

The critical β value, β_c, is quoted from Troyon's limit with the coefficient $g = 2.7$ [7]. The high β_p limit also restricts the operational window of the high β_p-mode. In the case of $\beta_p > R / a$, the plasma could be subject to the MHD instability [8]; the case with $\beta_p < 2.9$ is believed to be stable. The present status and expected performance of the designed ITER plasma has been reported [1]. We examine the burning performance of the core by use of the ITER-like plasma parameters ($R = 8.14$ [m], $a = 2.8$ [m], $B_t = 5.68$ [T], $\kappa = 1.6$).

III-1. The thermal stability of self ignited ELMy-H mode plasma

Substituting Eq. (4) for τ_E into Eqs. (3) and (6), the ignition condition of the ELMy-H mode is obtained. Carrying out the linear stability analysis mentioned in the previous section, the thermal stability of the solutions is investigated.

Figure 1 shows the ignition contours on $T - n_e$ plane. The case with I_p=20 MA for various values of ρ is shown. The solutions of the higher temperature region are thermally stable (solid lines), and the lower ones are unstable (dashed dotted lines). The dashed line indicates the thermal stability boundary. The lines of β_p=1, 2.9 and β_c are also plotted. The β limit is 3.39 %. In the case with I_p=20 MA, the Greenwald limit is $n_e^G = 8.0\times10^{19} m^{-3}$, which is indicated by the dotted line. The solutions below these lines (β_c, n_e^G) are considered to be stable. High performance operation is

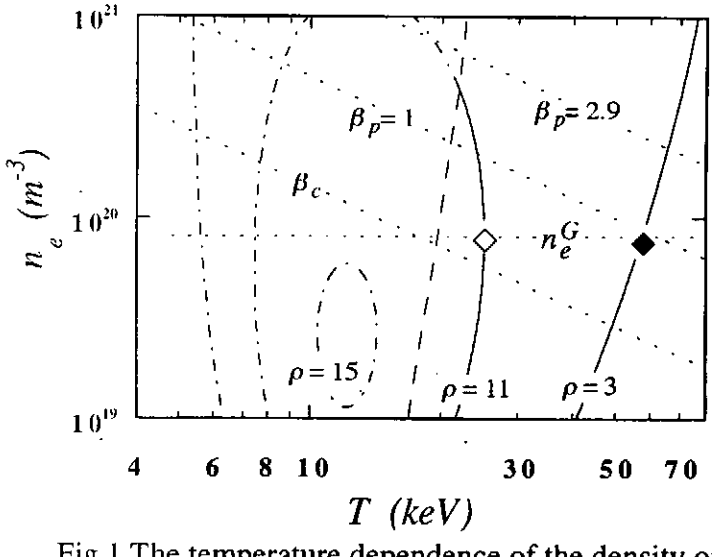

Fig.1 The temperature dependence of the density on the self ignited ELMy-H mode. The plasma current is fixed to 20 MA.

limited by β_c, however, the operations in the second stability regime could be possible therefore we expect some room for such operations. Taking the performance of He-ash pumping at the divertor into account, it is considered that the region $\rho > 10$ is realistic at present. As seen from the figure, thermally stable operations which satisfy Greenwald limit and $\rho > 10$ can be planned out. For the reference, we choose two operational points just below the density limit for $\rho = 3$ and $\rho = 11$. These are shown by ◆ and ◇, respectively.

Figure 2 re-draws the ignition contours onto the $T - P$ plane. The fusion power P is calculated according to the following formula

$$P = \frac{1}{4} n_e^2 (1 - 2f_{He})^2 \langle \sigma v \rangle E_n V, \tag{7}$$

where E_n is the energy of neutron (14.1 MeV), and V is plasma volume ($V = 2\pi^2 a^2 R$). The point marked by ◇ corresponds to that in Fig. 1 (ρ=11). The performance is given by P~0.64 GW, n_e~8.0 × 10^{19} m^{-3}, T~25 keV, f_{He}~26 %, β_p~0.4, β~5.2 % ($2\times\beta_e$, β_e: the electron beta), and the necessary confinement time is τ_E~10.4 s. If the operation is limited by Greenwald limit, it seems to be difficult to achieve high burning performance with high ρ value. The point marked by ◆ also corresponds to that in Fig. 1 (ρ=3). The performance is that P~2.0 GW, n_e~8.0 × 10^{19} m^{-3}, T~57 keV, f_{He}~15 %, β_p~0.9, β~11.4 %, and τ_E~5.7 s, in this operation. The thermal stability of this model seems to have a relatively weaker dependence on the current.

III-2. The thermal stability of self ignited L-mode, high β_p-mode plasma

Next, we examine the temperature dependence of the fusion power for both the L-mode and the high β_p-mode. We choose the parameters to distinguish the confinement mode as I_p =20 MA for the L-mode and I_p=10 MA for the high β_p-mode, respectively.

Figure 3 shows the ignition contours on $T - n_e$ plane. The case with I_p=20 MA for various values of ρ is shown. The solid line corresponds to the stable solution and the dashed dotted line to the unstable solution. The lines of β_p=1, 2.9 and β_c (=3.39 %) are also plotted. In the case with I_p=20 MA, the Greenwald limit is $n_e^G = 8.0\times10^{19}$ m^{-3}, which is indicated by the dotted line. Let us show the examples of the burning performances of the points near the density limit which are marked by ☆ and ★ in Fig. 3. The point marked by ☆ corresponds to an operation (ρ=11) which has the performance P~0.62 GW, n_e~8.0 × 10^{19} m^{-3}, T ~24 keV, f_{He}~15 %, β_p~0.4, β~4.8 %, and the necessary confinement

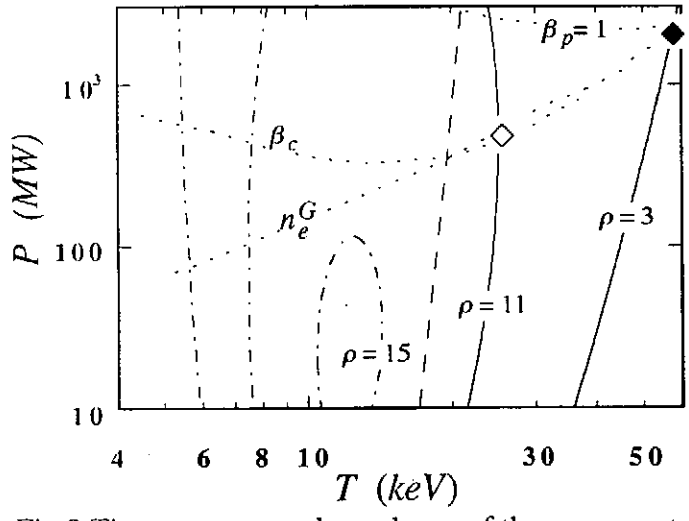

Fig.2 The temperature dependence of the power output on the self ignited ELMy-H mode. The plasma current is fixed to 20 MA.

time is τ_E~8.4 s, for a high current operation (L-mode operation). The point marked by ★ corresponds to ρ=3 case. The performance is that P~2.0 GW, n_e~8.0 × 10^{19} m^{-3}, T~42 keV, f_{He}~10 %, β_p~0.6, β~8.4 %, and τ_E~3.5 s, in this operation.

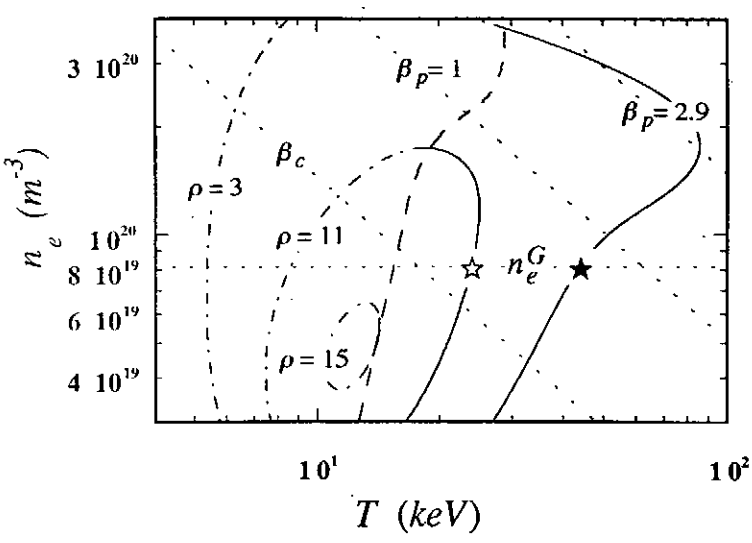

Fig.3 The temperature dependence of the density on the self ignited L-mode. The plasma current is fixed to 20 MA.

Figure 4 shows the ignition contours of the solutions on $T - n_e$ plane for the case with I_p =10 MA for various values of ρ. In the case with I_p=10 MA, the Greenwald limit is nearly equal to $n_e^G = 4.0\times10^{19} m^{-3}$ as is shown by the dotted line in Fig. 4. Here the burning performances at the operational points marked by ○ and ● in Fig. 4 are studied. The high ρ value operation (ρ=11) marked by ○ gives P ~0.77 GW, n_e~8.0 × 10^{19} m^{-3}, T~16 keV, f_{He}~10 %, β_p~1.0, β~3.2 %, and τ_E~5.4 s is necessary for I_p=10 MA. The operational point is located above the critical density n_e^G and is also thermally unstable. For the high β_p-mode operation with the high ρ value, the higher density is necessary, which may be difficult to achieve. The point marked by ● (ρ=3) has the performance for this operation P~1.7 GW, n_e~8.0 × 10^{19} m^{-3}, T~67 keV, f_{He}~18 %, β_p~4.2, β~13.4 %, and τ_E~8.0 s. The β limit is 1.69 %. The thermal stability of this model scaling is strongly affected by the total current I_p comparing with, the L and the ELMy-H mode scaling.

IV. Summary

We investigated the operational condition of the self-ignited plasma. The high β_p limit, the β limit, and the density limit are also estimated as the operational limits for the reference. We showed the typical burning performances of three different modes, evaluating the ignition conditions for different values of ρ. We choose the parameters to distinguish the mode as I_p=20 MA for the L-mode and I_p=10 MA for the high β_p-mode, respectively. The

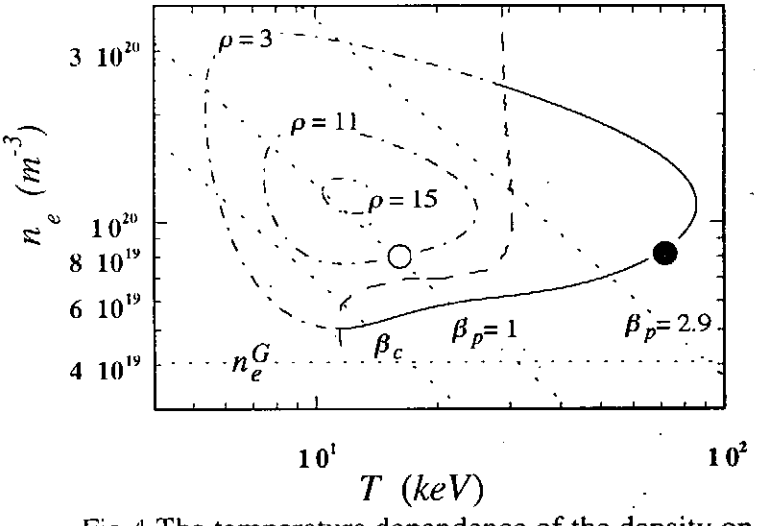

Fig.4 The temperature dependence of the density on the self ignited high β_p-mode. The plasma current is fixed to 10 MA.

achievement of the self-ignited steady state of the high β_p-mode operation is predicted to be difficult in ITER-like plasma from the view points of the Greenwald density limit, the β limit (this constraint is not so stringent, if operation in the second stability regime is possible), and the thermal instability.

Another scenario proposed for ITER is to operate at ELMy-H mode. The analysis done here shows that in the ELMy-H mode case, the thermally stable operation can be obtained even if ρ has a higher value. Near the Greenwald density limit (n_e~8.0×10^{19} m^{-3}), the burning performance are up to P~0.64 GW on the ELMy-H mode, and P~0.62 GW on the L-mode, respectively (with I_p=20 MA, and ρ=11). If a higher density operation than the Greenwald limit is possible, the ELMy-H mode seems to be a better candidate of operational mode.

We assumed that the fast α-particles can be confined perfectly and fully thermalized before they are lost from the plasma. However if the orbital loss of fast α-particle is not neglected, the effective confinement of α-particles reduces. The characteristics of the energy confinement time could be also changed in the presence of α-heating and ash-poisoning. We neglect the synchrotron radiation assuming that the plasma is black body. Analytical investigation of the synchrotron radiation in torus configuration has been carried out in Ref. [9]. In the high temperature and the low density cases, it is possible that the magnitude of the synchrotron radiation loss is comparable to that of bremsstrahlung. These problems need further analysis for the transport of the plasma, and are left for future works.

Acknowledgements

This work is partly supported by the Grant-in-Aid for Scientific Research of Ministry of Education, Science, Sport and Culture, Japan and by collaboration programme of Advanced Fusion Research Center of Kyushu University.

References

[1] ITER-JCT and Home Teams, *Plasma Phys. Control. Fusion* **37** (1995) 140.
[2] G. Tateishi, S. -I. Itoh, M. Yagi, *Plasma Phys. Control. Fusion*, to be published.
[3] F. Ryter, H mode database working group, *Nucl. Fusion* **36** (1996) 1217.
[4] A. Fukuyama, K. Itoh, M. Yagi, M. Azumi, *Plasma Phys. Control. Fusion* **37** (1995) 611.
[5] D. Reiter, G. H. Wolf, H. Kever, *Nucl. Fusion* **30** (1990) 2141.
[6] M. Greenwald, S. Ejima, M. G. Bell, S. M. Kaye, G. H. Neilson, *Nucl. Fusion* **28** (1988) 2199.
[7] F. Troyon, R. Gruber, H. Saurenmann, S. Semenzato, S. Succi, *Plasma Phys. Controlled Fusion* **26** (1984) 209.
[8] S. Ishida, Y. Koide, T. Ozeki, M. Kikuchi, S. Tsuji, H. Shirai, O. Naito, and M. Azumi, *Phys. Rev. Lett.* **68** (1992) 1531.
[9] I. Fidone, R. L. Meyer, G. Giruzzi, and G. Granata, *Phys. Fluids B* **4** (1992) 4051.

A Non-local Model Analysis of Heat Pulse Propagation

T. Iwasaki*, S.-I. Itoh**, M. Yagi**, K. Itoh+, U. Stroth++
*Interdisciplinary Graduate School of Engineering Sciences,
Kyushu University 39, Kasuga 816, Japan
**Research Institute for Applied Mechanics, Kyushu University 87, Kasuga 816, Japan
+National Institute for Fusion Science, Nagoya 464-01, Japan
++Max-Planck-Institut für Plasmaphysik, 85748, Garching , Germany

I. Introduction

The anomalous transport in a high temperature plasma has been studied for a long time, from the beginning of the fusion research. Since the electron channel in stellarators and tokamaks is clearly anomalous, it is of fundamental importance to investigate the electron heat diffusivity coefficient, χ_e and to understand the physical mechanism.

Recently, the experimental data for the transient transport of the heat pulse propagation in fusion plasmas has been accumulated [1, 2]. An observation was reported on W7-AS, that the heat flux changes faster than the change of the temperature profile, responding to the switching on-off of the central heating power [3]. The observation on the transient response has stimulated the transport modeling, e.g., the critical marginality [4] which implies the existence of a finite threshold in ∇T for the excitation of the turbulence, or the model in which the thermal conductivity is assumed to depend on the heating power [3]. Extensive study is made by use of these models, and the critical marginality model seems to be insufficient to explain various transient transport [5]. The rapid change of the plasma state and its hysteresis nature were successfully modeled by a heating-power-dependent model [3]. The foundation of this model, however, is left for future work. The development of the transport modeling remains to be an urgent problem.

In this paper, we investigate the role of the non-locality of the plasma transport in the study of the heat pulse propagation. For this purpose, a model equation is proposed, in which the non-local effect is taken into account in the heat flux. The properties of this model are investigated by performing a transport simulation. The organization of this paper is as follows: In Sec. II, the model equation is proposed and the properties of the model are explained. Using the model equation, the switching on-off experiment is simulated in Sec. III. Summary and discussions are given in Sec. IV.

II. Non-local Transport Model

In this section, we present our theoretical model and investigate its properties. To investigate the transient response of the electron temperature, let us start with the transport equation for the electron temperature,

$$\frac{\partial}{\partial t}\left(\frac{3}{2}n_e T(r,t)\right) = -\nabla\cdot q(r,t) + \Sigma Q \tag{1}$$

where n_e, $T(r,t)$, $q(r,t)$, ΣQ represent the electron density, temperature, heat flux and sources

and sinks, respectively. The boundary conditions are set to be $q(0,t) = 0$ and $T(a,t) = 0$, where a is the plasma minor radius.

The transport modeling relates the heat flux and the plasma parameters. In this article, we start from the following model, to take the non-local effect in the heat flux into account,

$$q(r,t) = -\int_0^a n_e \chi_e(T(r',t), \nabla T(r',t)) K_f(r-r') \nabla T(r',t) dr' \tag{2}$$

where χ_e is the (generalized) electron heat diffusivity which is generally the function of the temperature or temperature gradient and $K_f(r-r')$ is the kernel which includes the non-local effect. This expression suggests that the heat flux at r is influenced by the temperature gradient far from the location r. If the relation like Eq. (2) holds, then the very fast change of the heat flux is possible. The heat flux at r changes when the plasma parameter at r' is modified, without the change of the plasma parameters at r.

The basis of the model (2) is as follows. The anomalous transport is caused by the fluctuations. The property of the fluctuation at r is determined by the plasma structure within the radial correlation lengths of the fluctuations. The temperature gradient at r' could be influential on the fluctuating fields at r. Thus the heat flux at r could be dependent on the gradient at r'. When the kernel is set to be the delta function, then the heat flux is reduced to that of the local transport model, i.e., $q(r) = -n_e \chi_e \nabla T(r)$. In this study, we choose the following expression,

$$K_f(r-r') \equiv \frac{r}{r'} \cdot \left[C_{local} \delta(r-r') + C_{global} \frac{1}{\sqrt{\pi} l} \cdot \exp\left\{ -\left(\frac{r-r'}{l} \right)^2 \right\} \right] \tag{3}$$

where C_{local} and C_{global} are the numerical constants which represent the local effect and the non-local effect, l is the half width of the non-local effect and $\delta(r-r')$ is the delta function. The form (3) means that we take two classes of fluctuations, i.e., the microscopic fluctuations and the one with a long wavelength. The plasma turbulence due to nonlinear excitation [3] could generate very long correlated structures across the magnetic field. The discussion for the nonlinear theory is left for a separate article. We here only notice that the experimental study has suggested the existence of the heat flux component that has the nature of the Bohm-type diffusion [7]. Such a component is related to the long-wavelength mode [8].

The constraint of the numerical constants is imposed to be $C_{local} + C_{global} = 1$. The weighting function r/r' is introduced to impose the boundary condition, $q(0,t) = 0$. The second term in the right hand side becomes the delta function when $l \to 0$. In this limit (or when $C_{global} = 0$ holds), the heat flux is reduced to that of the local transport model. Substituting Eq. (2) and Eq. (3) into Eq. (1), we obtain

$$\frac{3}{2} n_e \frac{\partial T(r,t)}{\partial t} = C_{local} \frac{1}{r} \frac{\partial}{\partial r} \left(r n_e \chi_e \frac{\partial T(r,t)}{\partial r} \right)$$

$$+ C_{global} \frac{1}{r} \frac{\partial}{\partial r} \left(r \int_0^a \frac{1}{\sqrt{\pi} l} \exp\left\{ -\left(\frac{r-r'}{l} \right)^2 \right\} \cdot \frac{r}{r'} \cdot n_e \cdot \chi_e(T, \nabla T) \cdot \frac{\partial T(r',t)}{\partial r'} dr' \right) + \Sigma Q \tag{4}$$

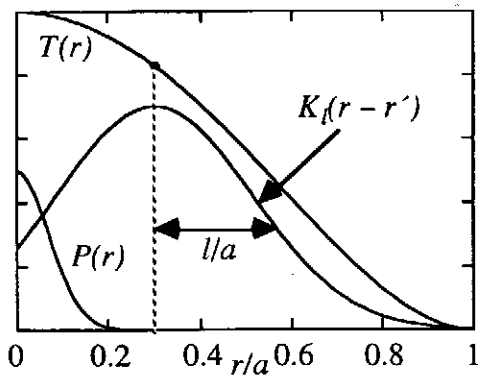

Fig. 1 Profiles of T(r), $K_l(r-r')$ and P(r) Transient response is observed at r/a = 0.3. l/a = 0.3 is assumed.

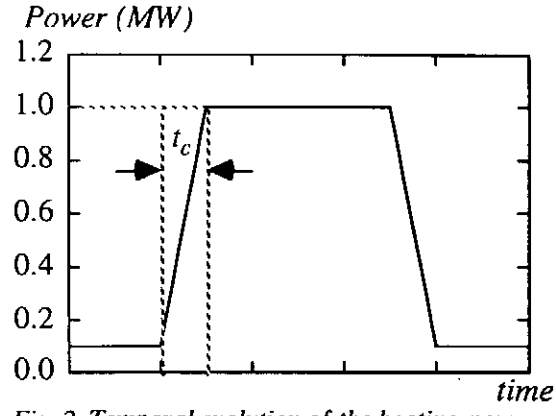

Fig. 2 Temporal evolution of the heating power The heating power changes from 0.1MW to 1MW. The change of the heating power takes place with the time period of t_c

In our study, the energy transport equation is re-formulated into the integro-differential equation from the differential equation usually used in the local transport model.

The power deposition profile is modeled in this study as,

$$P(r,t) = P_0(t) \cdot exp\left\{-100\left(\frac{r}{a}\right)^2\right\} \tag{5}$$

The power is mainly deposited in the region, $r/a \leq 0.1$. The schematic drawings of the temperature profile, the kernel profile and the power deposition profile are shown in Fig. 1, where the horizontal axis is taken as the normalized plasma radius. Figure 1 indicates that the heat flux is determined not only by the local temperature gradient but also by the global one. In other words, the heat flux at r is determined by the temperature gradient weighted by the kernel, where the Gaussian shape in the region between $r - l$ and $r + l$ is assumed. In the case of Fig. 1, the heat flux at $r/a = 0.3$, i.e., the location away from the heat deposition, is strongly influenced by the temperature profile in the heated region. The temporal evolution of the central heating power is shown in Fig. 2. The heating power changes from *0.1MW* to *1.0MW* with the rise time of t_c. Because the nature of the transient response is attributed to the fast change of the plasma state, it should be assumed to be $t_c = 0$ when we investigate the transient response. On the other hand, when $t_c \rightarrow \infty$, the change takes place as a continual change between the stationary profiles.

III. Results and Analyses of the Simulation of Non-local Model

The energy transport equation, i.e., Eq. (4), is solved under the condition given in the previous section, and the time evolution of the temperature profile is analyzed. As a first example, the electron density and heat diffusivity are assumed to be constant in this study. The possible difference in transport coefficient, which is caused by the nonlinear dependence of the transport coefficient on the gradient [1], is eliminated.

We set $t_c = 0$ to elucidate the non-local effect. We use the following plasma parameters. Major and minor radii are $R = 2.0\ m$ and $a = 0.2\ m$. The constant electron density and diffusivity

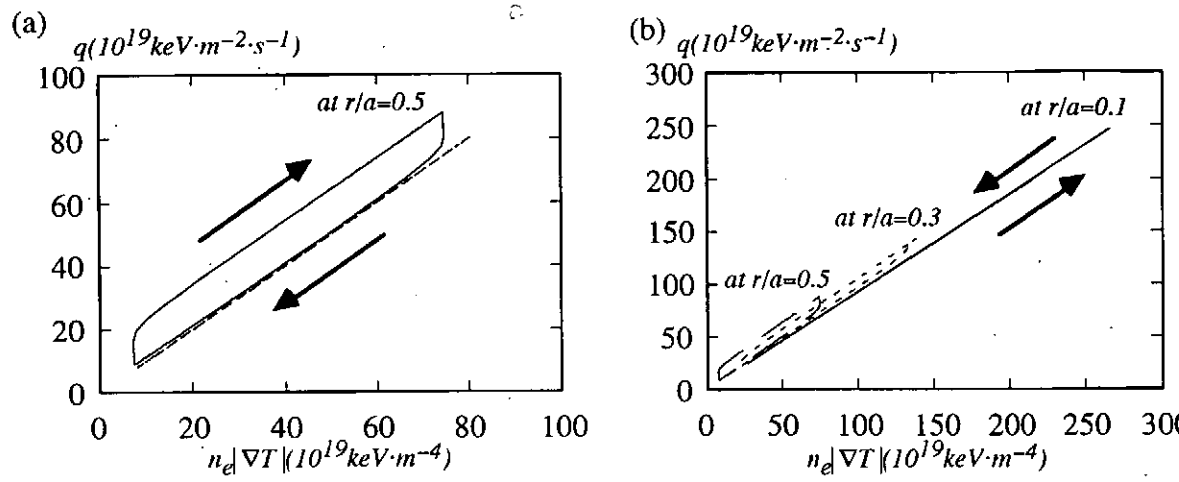

Fig. 3 The gradient – flux relation.
In both cases, we set to l/a=0.5. (a) The hysteresis is observed at r/a=0.5, which is clockwise. When l/a=0, the hysteresis disappears(dashed line). (b) The hysteresis is observed at r/a=0.1, r/a=0.3 and r/a=0.5. The hysteresis observed at r/a=0.1 where is the region heated directly is counter–clockwise.

are $n_e = 4.0 \times 10^{19}\ m^{-3}$ and $\chi_e = 1.0\ m^2 / sec.$ Then energy confinement time becomes $\tau_E \sim a^2 / \chi_e = 40\ msec.$ The value of numerical constants $C_{local} = 0.9$ and $C_{global} = 0.1$ are chosen.

Equation (4) is solved and the transient response of the temperature profile is analyzed. Figure 3 illustrates the relation between the temperature gradient and the heat flux. The vertical axis is the heat flux and the horizontal axis corresponds to the temperature gradient. A hysteresis is obtained in the gradient-flux relation. In Fig. 3 (a) the transient response is observed at $r/a = 0.5$ which is away from the region of the heat deposition. The essence of the transient response, i.e., the hysteresis in the gradient-flux relation, is reproduced by the nonlocality in the transport. In Fig. 3 (b), the transient responses are observed at $r/a=0.1$ and $r/a=0.3$ in addition to at $r/a=0.5$. The position $r/a=0.1$ is the region which is heated directly. In the local model, the heat flux is proportional to the temperature gradient because of the assumption that the electron density and diffusivity are constant. Therefore a straight line is obtained in the stationary case as is shown by the dashed line in Fig.3 (a). (This case is calculated with the parameters $\chi_e = 1.0\ m^2 / sec$, $C_{local} = 1$ and $C_{global} = 0.$) In the non-local model, the heat flux can change faster than the temperature gradient.

In the location far from the heat deposition, the temperature gradient increases slowly but the heat flux increases rapidly when the central heating power is switched on; the temperature gradient decreases slowly but the heat flux decreases rapidly when the central heating power is switched off. Therefore the hysteresis is clockwise away from the region of the heat deposition as is shown in Fig. 3 (a). The reason is explained as follows: The heat flux at the location $r/a=0.5$ is affected directly by the rapid change of the central temperature through the non-local effect when the power is switched on, but the temperature at $r/a=0.5$ is determined by the diffusion process so that its change is slow. On the other hand, in the region which is heated directly, the temperature gradient increases rapidly but the heat flux increases slowly when the central heating power is switched on and the temperature gradient decreases rapidly

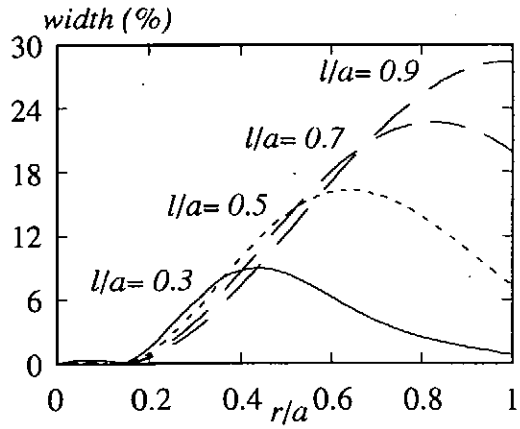

Fig. 4 The relation between the width of the hysteresis and the observed point for l/a= 0.3, 0.5, 0.7 and 0.9. r_0 is the position where the width vanishes. These curves have the peak value at $r/a \approx l/a + r_0$.

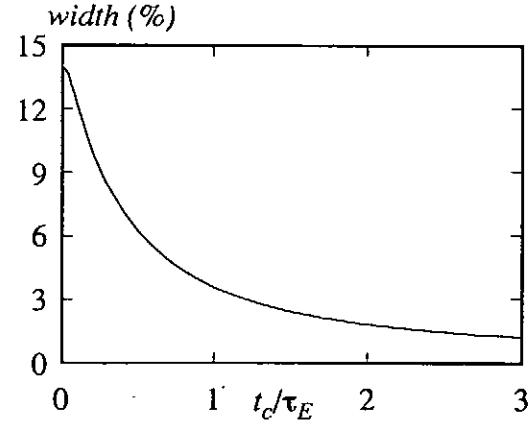

Fig. 5 The dependence of the width of the hysteresis on the switching time t_c. The width monotonically decreases with t_c.

but the heat flux decreases slowly when the central heating power is switched off, so that the hysteresis is counter-clockwise in this case. The slope of the hysteresis in Fig.3 (b) is varied depending on the observation point. This is because the steady state temperature profile is different from that in the local transport model due to the non-local effect.

Next we examine the relation between the width of the hysteresis and the observation points. The width of the hysteresis is defined by the ratio of the minor axis to the major axis by the analogy to the conic section. This relation is shown in Fig. 4 for $l/a= 0.3$, $l/a= 0.5$, $l/a= 0.7$ and $l/a= 0.9$. The vertical axis is the width of the hysteresis and the horizontal axis is the normalized plasma radius. The width of the hysteresis vanishes at $r_0 \approx 0.15$,which is comparable to the value of the half width of the central heating. The region within r_0 is the region which is heated directly, so the hysteresis is counter-clockwise. On the other hand, the hysteresis is clockwise outside of the radius r_0. These curves drawn in Fig. 4 have the peak value at $r/a \approx l/a + r_0$ ($\chi_e = const$ case). This fact indicates that if the width of the hysteresis is plotted at various position and the peak value is found in an experiment, the correlation length of the non-local effect may be determined from Fig. 4.

Finally, we examine the case of the finite switching time. It is expected that the non-locality, i.e., the hysteresis nature, becomes less noticeable with the increase of t_c. The dependence of the width of the hysteresis on t_c is shown in Fig. 5, where the vertical axis is the width of the hysteresis and the horizontal axis is the switching time of the central heating power, t_c normalized by the energy confinement time, τ_E. We can see from Fig. 5 that the width has the maximum value at $t_c = 0$ and monotonically decreases with the increase of t_c, which behaves as $1 / t_c$ for the t_c larger than the energy confinement time. In the limit $t_c \to \infty$, the width vanishes, which corresponds to the stationary case. The hysteresis is prominent when $t_c << \tau_E$.

IV. Summary and Discussion

In this paper, new expression for the heat flux, in which the non-local effect is taken into account, has been proposed. The heat flux is calculated by Eq. (2). This expression

suggests that the heat flux at r is influenced by the temperature gradient far from the location r. Such a situation is expected when the flow is influenced by a large scale convections, the scale length of which is comparable to the gradient scale length. Thus, the energy transport equation has been re-formulated into the integro-differential equation.

Solving the energy transport equation with some assumptions, i.e., the electron density and diffusivity are constant, the hysteresis has been obtained in the gradient-flux relation in the transient response. This hysteresis has not been obtained in the transport model in which the coefficient is expressed by the local plasma parameters and gradients. The findings in the experiment in W7-AS [3] has been reproduced by our non-local model theoretically. We have also investigated the dependence of the width of the hysteresis on the observation point and the switching time of the central heating power, t_c. We have obtained the following results, i) The hysteresis is clockwise at the location far from the power deposition, while it is counter-clockwise at the region heated directly. ii) The width of the hysteresis has the peak value at $r/a \approx l/a + r_0$ ($\chi_e = const$ case). This fact indicates that if the width of the hysteresis is plotted at various position and the peak value is found in an experiment, the correlation length of the non-local effect may be determined from Fig. 4. iii) The hysteresis is prominent when $t_c << \tau_E$.

In this paper, the electron density and diffusivity are assumed to be constant. Study on the radial profile of the density and the dependence of the diffusivity on temperature or temperature gradient is left for our future work.

Acknowledgments

This work is partly supported by the Grant-in-Aid for Scientific Research of Ministry of Education, Science, Sport and Culture, Japan, by collaboration programme of Advanced Fusion Research Center of Kyushu University.

References

[1] N. J. Lopes Cardozo: *Plasma Physics and Controlled Fusion* **37** (1995) 799

[2] J D Callen: presented at 24th EPS Conference (1997) *Plasma Physics and Controlled Fusion* **39** (1997) in press.

[3] U. Stroth, et. al: Plasma *Physics and Controlled Fusion* **38** (1996) 1087

[4] P. H. Rebut, et. al: *Plasma Physics and Controlled Nuclear Fusion Research* 1988 (Proc, 12th Int. Conf. Nice, 1988), Vol. 2, IAEA, Vienna (1991) 191

[5] V. Parail et al.: *Nucl. Fusion* **37** (1997) 481

[6] K. Itoh, et. al: *Plasma Physics and Controlled Fusion* **36** (1994) 279

[7] See, e.g, T. Luce et al.: *Plasma Physics and Controlled Nuclear Fusion Research* 1994 (Proc. 15th Int. Conf. Seville, 1994), Vol. 1, IAEA, Vienna (1995) 319

[8] J. W. Connor and J. B. Taylor: *Nucl. Fusion* **17** (1977) 1047

Investigation of reversed shear equilibria in JT60U using the Pies code.

S.R.Hudson[(a)], S.Tokuda[(a)] and D.A.Monticello[(b)]
(a)Fusion Plasma Theory Laboratory,
J.A.E.R.I. Naka-machi, Naka-gun, Ibaraki-ken, Japan.
email: stuart@ptl01.naka.jaeri.go.jp
(b)Princeton Plasma Physics Laboratory ,
Princeton University, New Jersey, U.S.A.

September 22, 1997

Abstract

Reversed shear equilibria in JT60U with $q_{\min} < 2$ are analyzed using the PIES code. The dependence of the island formation on the β value are investigated. Equilibria with low $q_{\min}$ values display improved confinement, but experimentally there exists a stringent limit at $q_{\min} = 2$. The PIES code calculates fully three dimensional configurations with magnetic islands and stochastic regions. Therefore we may analyze tearing modes with finite magnetic islands and determine the nature of the breakdown process as the β value increases. It is suggested that the double magnetic island chains may overlap and reconnect. A simple model field indicates that reconnection may occur if the phase of the island chains is opposite, and this is displayed by the $q = 3/2$ islands computed by PIES for JT60U. By resolving the magnetic field into an integrable plus perturbation field, the magnitude and phase of islands are determined.

1 Introduction

Experimentally, reversed shear profiles with low $q_{\min}$ enable good confinement properties. When $q_{\min} = 2$, disruptions occur which destroy the plasma. Shown in fig(3) is a typical configuration of interest. The equilibrium was constructed using the MEUDAS code, which computes solutions to the axis-symmetric Grad-Shafranov equation. This configuration is similar to experimentally important configurations. Of particular interest is the configuration with $q_{\min}$ just below $q = 2$. The behavior of these cases may give some insight into the nature of the disruptions that occur when $q_{\min} = 2$.

The PIES code [1] will take the two dimensional equilibria as input guesses for three dimensional equilibria iteration procedure. The ideal MHD equations are iterated until the magnetic field converges to a self consistent equilibria. At the double $q = 2$ rational surfaces, islands are expected to occur. It is the interaction of these islands that will be investigated using the PIES code.

It is interesting to examine the interaction of the double $q = 3/2$ islands. A similar configuration to that shown in fig(3), but with $q_{\min} < 3/2$ was computed. As the iterative procedure of PIES progresses, we see in fig 1 that islands form at the $q = 3/2$ rational surfaces. As PIES converges, these islands grow until they overlap. At this point, magnetic reconnection occurs. As a result, the safety factor profile flattens at $q = 3/2$.

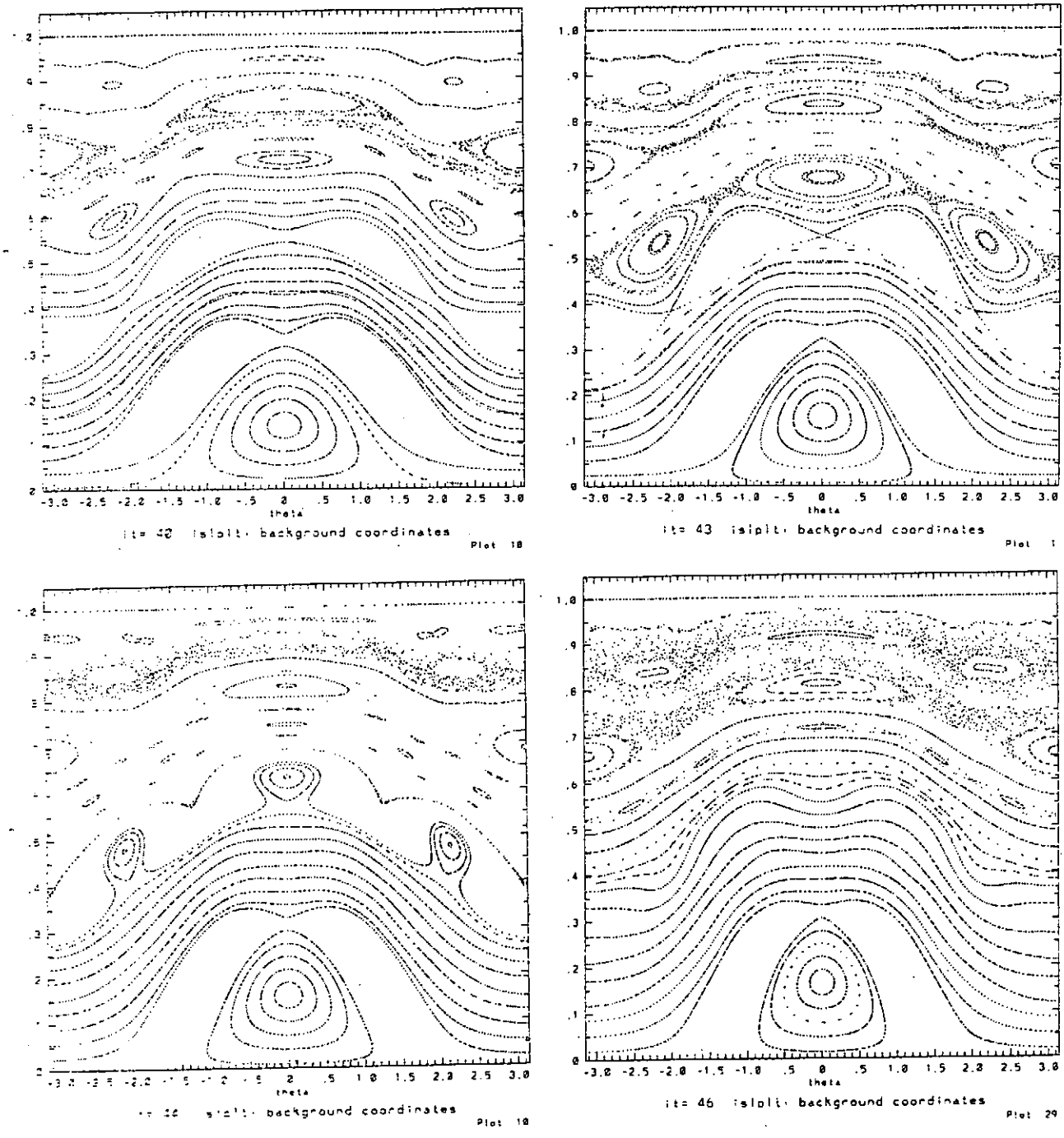

Figure 1: Reconnection of $q = 3/2$ islands in JT60U. During the iteration of Pies, the double island chains grow in size until their separatrices overlap and reconnection occurs.

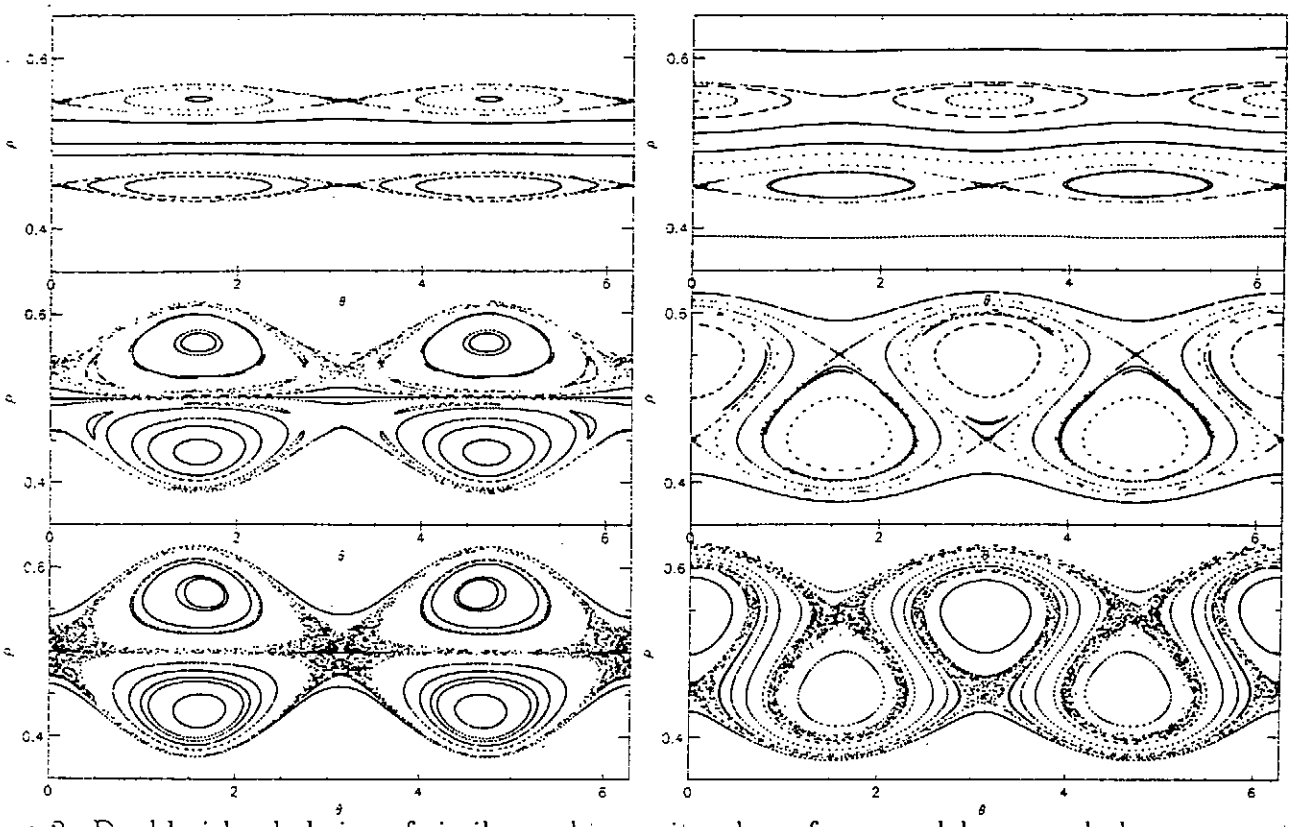

Figure 2: Double island chains of similar and opposite phase for a model reversed shear magnetic field.

It is interesting to note that the phase of the two $q = 3/2$ islands is opposite. Along the $\theta = 0$ line, the inner island chain has an X point, and the outer island chain has an O point. It is likely that this feature plays a significant role in determining whether reconnection will occur. To illustrate this, a simple model magnetic field similar to the magnetic field of the reversed shear configuration was examined. Two different perturbations, both creating double islands, were introduced. The phase of the island chains depends on the sign of the perturbation, and the sign of the underlying shear. As shown in fig 2, when the phase of the island chains is opposite, magnetic reconnection may occur. When the island chains have the same phase, magnetic reconnection does not occur.

2 Reversed shear equilibrium $q_{\min} < 2$

Four similar, configurations of reversed shear equilibrium, with varying β values, were constructed using the MEUDAS code and examined using the PIES code. Four different β values were computed, with $\beta_1 = 0.987, \beta_2 = 1.481, \beta_3 = 1.975$ and $\beta_4 = 2.965$. As β increases, the magnitude of the islands is expected to increase.

The first configuration has the lowest β value, $\beta = 0.987$. The converged Pies equilibria is shown in fig 4. The double island chains are small, but clearly observed. The phase of the island chains is the same, so perhaps reconnection would not occur. Regardless of this, as the islands are small there is no likelihood that the islands will exhibit reconnection.

The second configuration has a slightly higher β value, $\beta = 1.481$. The converged Pies equilibria is shown. This is similar to the first case, where the island chains have the same phase, but are too small for any interesting reconnection behavior to occur.

The third configuration has a larger β value, $\beta = 1.975$. The converged Pies equilibria is

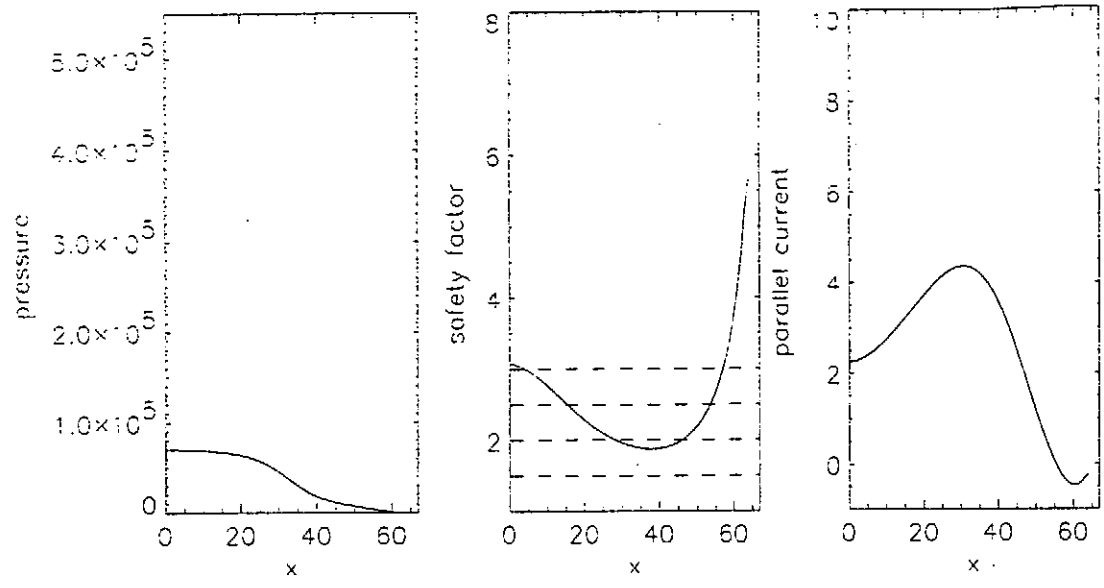

Figure 3: Two dimensional equilibria to be examined.

shown. In this case, the islands are larger and interestingly the relative phase of the island chains is opposite. In this case, if the islands grew a little more, it is possible that reconnection may occur.

The fourth configuration has the highest β value, $\beta = 2.965$. The converged Pies equilibria is shown. The islands are very large and the separatrices seem almost to overlap. The relative phase of the islands is opposite, and it is likely that reconnection may occur.

It is interesting to note that for the lower β values, the relative phase of the islands is the same, but that for the higher β values, the relative phase is opposite. The results presented here are still inconclusive and more investigation into this feature is required before any statement can yet be made. Perhaps for reversed shear equilibriums, with $q_{\min} < 2$, at low β the islands will not reconnect as the relative phase of the islands is not suitable, but that at higher β, the relative phase of the island chains becomes favorable for reconnection.

3 Decomposition of magnetic field into integrable plus perturbation

To compare the JT60U equilibria with the model magnetic field, it is convenient to write the magnetic field in the form as an integrable magnetic field plus a small perturbation. The shear of the integrable magnetic field and the magnitude of the perturbation may be used to determine the island width. The sign of the perturbation will indicate the phase of the island chain.

A suitable nearby integrable magnetic field is easily defined and constructed using the methods presented in [2]. At the heart of the method is the construction of quadratic flux minimizing surfaces [3]. A nearby integrable magnetic field is constructed with radial surfaces that pass directly through the island chains of the original non-integrable magnetic field. Another feature of the quadratic flux minimizing surfaces is that they enable a efficient method to estimate the magnitude and phase of magnetic islands, and this information may be used to find optimal configurations for stellarator magnetic fields [4].

A configuration, which is shown in fig(5) plotted in straight field line coordinates for the underlying integrable field, displays double $q = 2$ modes with opposite phase. The $(2,1)$ perturbation is also shown in fig(5)

The perturbation is the same sign on the two rational surfaces, but the shear is different

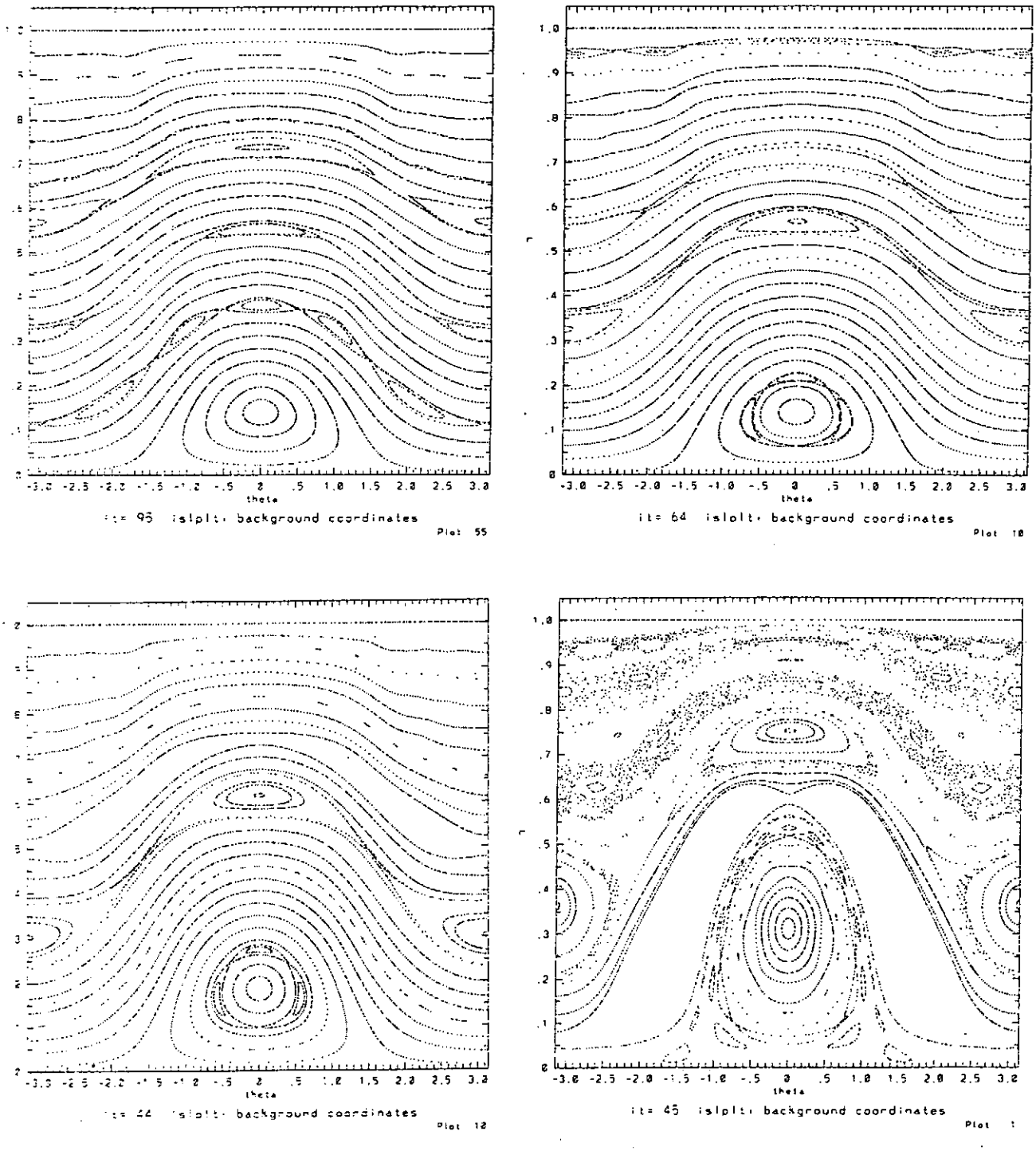

Figure 4: Poincaré plots of the four cases with $q_{\min}$ slightly under $q = 2$ with different β values. The top left has $\beta = 0.987$, the top right has $\beta = 1.481$, the bottom left has $\beta = 1.975$, and the bottom right has $\beta = 2.965$.

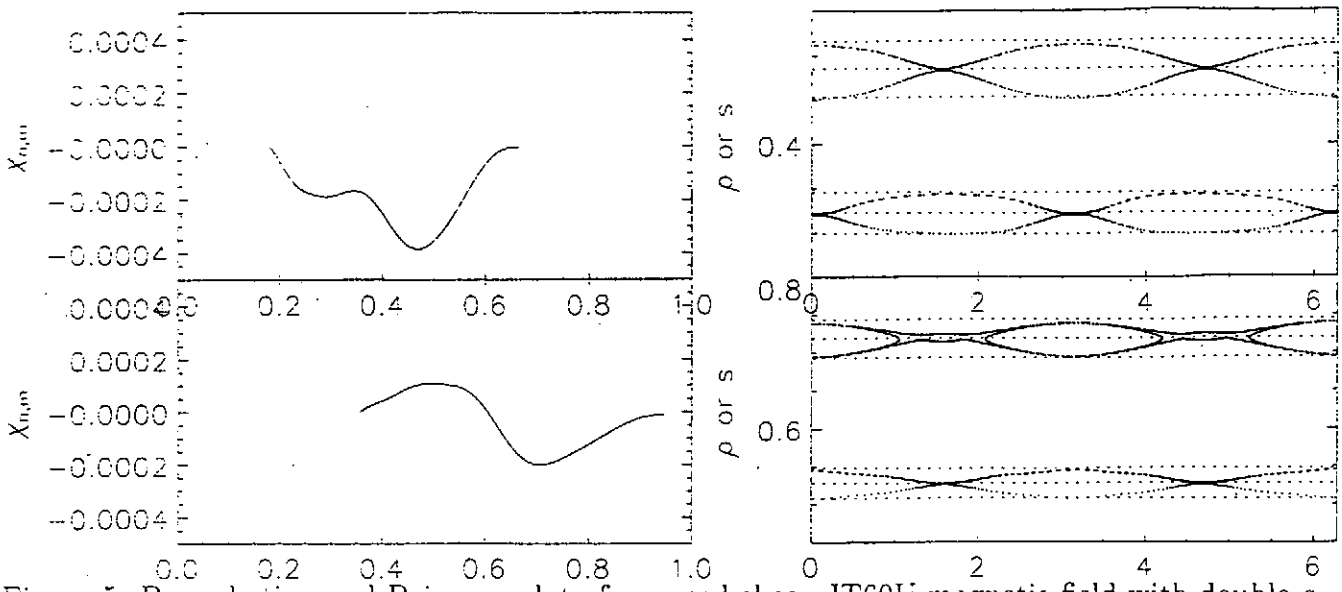

Figure 5: Perturbation and Poincare plot of reversed shear JT60U magnetic field with double $q = 2$ islands. The above left shows the $(2, 1)$ resonant perturbation, and the above right shows the resulting island chain. Below left shows the the $(2, 1)$ resonant perturbation, and the below right shows the resulting island chain.

sign, and so the island chains have opposite phase. In such a situation, the results of the model field suggest that magnetic reconnection may occur when the islands become larger.

A configuration, which is shown in fig(5) plotted in straight field line coordinates for the underlying integrable field, displays double $q = 2$ modes with opposite phase. The $(2, 1)$ perturbation is also shown in fig(5) The perturbation has different sign on the two rational surfaces, and with the shear being of different sign, the island chains have the same phase. In such a situation, the results of the model field suggest that magnetic reconnection may not occur when the islands become larger.

As both the shear of an optimal underlying magnetic field, and the resonant perturbation are provided, the island widths may be estimated and compared with the Poincaré plot. The agreement is excellent (as indicated by the dashed lines in fig 5) and confirms the accuracy of the calculation.

References

[1] A.H. Reiman and H.S. H.S.Greenside. Computation of zero β three-dimensional equilibria with magnetic islands. *Journal of Computational Physics*, 87:349, 1990.

[2] S.R. Hudson and R.L. Dewar. Construction of an integrable case close to any non-integrable toroidal magnetic field. *draft submitted to Physics Letters A*, 1997.

[3] R.L. Dewar, S.R. Hudson, and P. Price. Almost invariant manifolds for divergence free fields. *Physics Letters A*, 194:49, 1994.

[4] S.R. Hudson and R.L. Dewar. Manipulation of islands in a heliac vacuum field. *Physics Letters A*, 226:85, 1997.

Gyro-Particle, Gyro-Reduced-MHD, and Hybrid Simulation of Internal Kink Modes

Hiroshi Naitou
Department of Electrical and Electronic Engineering,
Yamaguchi University, Tokiwadai 2557, Ube 755, Japan

Shinji Tokuda, Taro Matsumoto
Department of Fusion Plasma Research,
Naka Fusion Research Establishment,
Japan Atomic Energy Research Institute, Naka, Ibaraki 311-01, Japan

Hiroshi Kozakai
Toshiba Advanced Systems Co., Kawasaki-Shi, Kanagawa 210, Japan

Abstract

The collisionless reconnection process in tokamaks due to the nonlinear development of $m = 1$ (poloidal mode number) and $n = 1$ (toroidal mode number) kinetic internal kink mode is simulated by the gyro-particle code (GYR3D), the gyro-reduced MHD code (GRM3D-2F), and the particle-fluid hybrid code (Hybrid3D). These codes are based on the nonlinear gyrokinetic Vlasov-Poisson-Ampère system and have exact energy invariances. GYR3D is a three-dimensional gyrokinetic magneto-inductive particle code with δf method. GRM3D-2F is a two-field and two-fluid model including the effects of electron inertia and the perturbed electron pressure gradients along the magnetic field. In Hybrid3D, electrons are treated as fluid, while ions are treated as particles. The results of these three codes agreed very well. We believe that the better understanding of the physics associated with the kinetic MHD phenomena in tokamaks will be achieved by executing simultaneously these codes.

1 Introduction

In the simulation study of the present-day and the next generation large tokamaks, it is crucial to treat the kinetic modification of MHD modes. There are many kinetic effects which should be included in the MHD model. Electron inertia effects, electron pressure effects along the magnetic field, finite Larmor radius effects of ions, diamagnetic effects, and effects of energetic ions like alpha particles are some examples. Development of exteded MHD simulation model, which is the kinetic extension of the conventional MHD model, and simulation study of such kinetic MHD phenomena in fusion plasmas by using massively parallel computers are one of the main subjects in the NEXT (Numerical EXperiment of Tokamak) Project in JAERI begun from 1996 [1].

There are three approaches for the simulation study of kinetic MHD phenomena. One is the (gyrokinetic) particle approach which includes the charged particle dynamics in the

self-consistent electromagnetic field. This approach is more faithful to the physics but inevitably consumes much computer resources. The second is the fluid approach which uses the moment equation of the Vlasov (or gyrokinetic Vlasov) equation. Although there is a closure problem, the fluid approach is less severe for the computer resources. The third is the hybrid approach in which electrons are treated as fluid and ions are treated as particles; we can naturally include the kinetic effects of ions while eliminating the load to follow individual electrons. We have developed gyro-particle code (GYR3D)[2, 3], gyro-reduced MHD code (GRM3D-2F)[4], and particle-fluid hybrid code (Hybrid3D)[5] based on the particle, fluid, and hybrid approaches, respectively. These three codes, which have the exact energy invariances, are based on the nonlinear gyrokinetic Vlasov-Poisson-Ampère system[6] and/or the moment equations of it.

The oultine of the paper is as follows. The brief summary of the three models are given in Sections 2-4. The simulation results of the three codes for the kinetic $m = 1$ and $n = 1$ internal kink mode, which is closely related to the fast sawtooth crash in tokamaks, are compared in Section 5. Concluding remarks and discussion are given in Section 6.

2 Gyro-Particle Model

GYR3D[2, 3] is the three-dimensional magneto-inductive gyrokinetic particle code with δf method[7] which is a quite low noise algorithm.

We assume a rectangular system with dimensions of L_x, L_y, and L_z. There is a strong and constant magnetic field (toroidal magnetic field), $\boldsymbol{B}_T = B_0\boldsymbol{b}$, where $\boldsymbol{b}$ is the unit vector in the z direction. The compressional component of the longitudinal magnetic field is neglected in the low beta approximation. The periodic boundary condition is assumed in the z direction. The system is bounded by a perfectly conducting wall in the x and y (poloidal) directions. The same assumptions are done for the gyro-reduced-MHD and hybrid models.

In the gyro-particle model, the charged particles move by the $E \times B$ drift and the parallel streaming along the magnetic field. The acceleration of particles are due to the electrostatic electric field along the magnetic field and the induced electric field. Electrons are treated in the drift kinetic approximation. We also neglect the finite gyroradius effect of ions while keeping the polarization shilding effects of ions in the Poisson equation. In the δf code, the distribution function is decomposed into the equilibrium part (f_0) and the deviated part (δf). Variable weights of particles are followed along the trajectory. Particle weights only represent the δf part; the thermal fluctuation level is considerably less than the standard gyrokinetic particle code (total f code) as long as absolute values of weights are much smaller than unity. The angular momentum, p_z, is used instead of the velocity along the magnetic field, v_z. Hence, the induced electric field does not appear explicitly in the system of equations. In the p_z formulation, the calculation of the z component of the vector potential, A_z, from the Ampère law is somewhat complicated because we cannot use v_z to calculate the current density. The poloidal magnetic field is calculated by A_z; i.e., $\boldsymbol{B}_P = \nabla \times (A_z\boldsymbol{b})$.

3 Gyro-Reduced MHD Model

The moment equations of the gyrokinetic Vlasov equations are used to derive the gyro-reduced MHD model. Because the terminology of "gyro-fluid" usually represents the gyro-Landau model[8, 9], we call our model "gyro-reduced MHD" because it is corresponding to the extention of the Strauss's reduced MHD model[10]. This model is basically the two fluid model; hence, electron inertia as well as the electron pressure gradient along the magnetic field is included in the system of equations. Although the extention to the case of the nonuniform density profile is straightforward, the equilibrium density profile is assumed to be uniform in the GRM3D-2F code[4].

The gyro-reduced MHD model comprises of the equations for the electrostatic potential ϕ and the z component of the vector potential A_z:

$$\frac{d}{dt}(\nabla_\perp^2 \phi) = -v_A^2 \, \boldsymbol{b}^* \cdot \nabla(\nabla_\perp^2 A_z) \,, \tag{1}$$

$$\frac{\partial}{\partial t} A_z = -\boldsymbol{b}^* \cdot \nabla\phi + d_e^2 \, \frac{d}{dt}(\nabla_\perp^2 A_z) + \rho_s^2 \, \boldsymbol{b}^* \cdot \nabla(\nabla_\perp^2 \phi) \,, \tag{2}$$

where $v_A = c\,\omega_{ci}/\omega_{pi}$ (c is the speed of light in vacuum, ω_{ci} and ω_{pi} are the ion cyclotron and plasma angular frequencies, respectively) is the Alfvén velocity, $d_e = c/\omega_{pe}$ (ω_{pe} is the electron plasma angular frequency) is the collisionless electron skin depth, $\rho_s = \sqrt{T_e/m_i}/\omega_{ci}$ (m_i is the ion mass, T_e is the electron temperature) is the ion Larmor radius calculated by the electron temperature, $\boldsymbol{b}^*$ is the unit vector of the magnetic field,

$$\boldsymbol{b}^* = \boldsymbol{b} + \frac{\nabla A_z \times \boldsymbol{b}}{B_0} \,, \tag{3}$$

and d/dt is the convective derivative defined by

$$\frac{d}{dt} = \frac{\partial}{\partial t} + \frac{\boldsymbol{b} \times \nabla\phi}{B_0} \cdot \nabla \,. \tag{4}$$

Eq.(1) represents the vortex equation while generalized Ohm's law in the direction parallel to the magnetic field is described by Eq.(2) which can also be expressed in the following equation,

$$\frac{\partial A_z'}{\partial t} = -\boldsymbol{b} \cdot \left\{ \nabla\phi + \frac{\nabla\phi \times \nabla A_z'}{B_0} + \rho_s^2 \left[\nabla(\nabla_\perp^2 \phi) + \frac{\nabla(\nabla_\perp^2 \phi) \times \nabla A_z}{B_0} \right] \right\} \,, \tag{5}$$

where A_z' is defined by

$$A_z' = A_z - d_e^2 \, \nabla_\perp^2 A_z \,. \tag{6}$$

In order to derive Eq.(2), we replaced the pressure term, p_e, in the electron moment equation by assuming $p_e = n_e T_e$ and $T_e =$ constant (isothermal model);

$$\nabla p_e = T_e \nabla n_e = \frac{\epsilon_0}{e} \, \frac{\omega_{pi}^2}{\omega_{ci}^2} \, \nabla(\nabla_\perp^2 \phi) \,, \tag{7}$$

where gyrokinetic Poisson equation is used in the second equality by assuming $\delta n_i = 0$ which is consistent to assume $U_i = 0$ (U_i is the ion fluid velocity parallel to the magnetic field) in the 0-th order moment equation (continuity equation) of ions.

4 Particle-Fluid Hybrid Model

In the Hybrid3D[5] code, electrons are treated as a fluid and ions are treated as gyro-particles. The equations of motion for ions are the same as those for the gyro-particle codes. Electron and ion motions are combined through the gyrokinetic Poisson equation and the Ampère equation. Here, we show only the equations for electrons. These equations are obtained by taking the moments of the gyrokinetic Vlasov equation. The continuity equation of the density, the equation of motion, and the equation for the temperature are given by the following equations.

$$\frac{dn_e}{dt} + \mathbf{b}^* \cdot \nabla(n_e U_e) = 0, \tag{8}$$

$$m_e[\frac{d}{dt}U_e + U_e \mathbf{b}^* \cdot \nabla U_e] = -\frac{1}{n_e}\mathbf{b}^* \cdot \nabla p_e + e\left(\mathbf{b}^* \cdot \nabla\phi + \frac{\partial A_z}{\partial t}\right), \tag{9}$$

$$\frac{dT_e}{dt} + U_e \mathbf{b}^* \cdot \nabla T_e + 2T_e \mathbf{b}^* \cdot \nabla U_e = 0. \tag{10}$$

Equation (9) is an inconvenient form for practical simulations because, as pointed in [6], the partial time derivative of the vector potential appears in the equation. Hence, we introduce the generalized momentum $\Gamma_e(\mathbf{x}, t)$ for the electron fluid defined by

$$\Gamma_e(\mathbf{x}, t) = m_e U_e(\mathbf{x}, t) - eA_z(\mathbf{x}, t). \tag{11}$$

The equation of motion for the electron fluid can be re-written as

$$\begin{aligned} \frac{\partial \Gamma_e}{\partial t} &= -\frac{1}{B_0}(\mathbf{b} \times \nabla\phi) \cdot \nabla(\Gamma_e + \frac{e}{m_e}A_z) \\ &- \frac{1}{m_e}(\Gamma_e + \frac{e}{m_e}A_z)\, \mathbf{b}^* \cdot \nabla(\Gamma_e + \frac{e}{m_e}A_z) \\ &- \frac{1}{n_e}\mathbf{b}^* \cdot \nabla p_e + e\mathbf{b}^* \cdot \nabla\phi, \end{aligned} \tag{12}$$

where $p_e = n_e T_e$.

Above set of equations have an energy invariance. The present version of Hybrid3D, however, assumed the isothemal condition, T_e = constant. The isothermal model, in which we do not have to solve Eq.(10), has another invariance related to the entropy conservation law[5].

5 Simulation Results

As the benchmarking problem for the three codes, the nonlinear simulation of $m = 1$ and $n = 1$ kinetic internal kink mode is selected. The collisionless magnetic reconnection is the key process which is closely related to the fast sawtooth crash in the present day large tokamaks. The system is filled with a plasma with uniform equilibrium density and temperature. The equilibrium profile of A_z is chosen to be

$$A_z(x, y) = \frac{2L_x L_y B_0}{\pi q_0 L_z} \sin\frac{\pi x}{L_x} \sin\frac{\pi y}{L_y} \tag{13}$$

where q_0 is the safety factor at the magnetic axis [10]. The q profile corresponding to the above A_z is given by

$$q(x,y) = \frac{2}{\pi} q_0 K(\sin\psi), \quad \cos\psi = \sin\frac{\pi x}{L_x}\sin\frac{\pi y}{L_y} \tag{14}$$

where K is the elliptic integral of the first kind. The q-value increases monotonically from the axis to the wall where q is infinite. The central q value (safety factor) of $q_0 = 0.85$ is selected for the equilibrium. We also fixed $d_e = 4\Delta$ and $\rho_s = \Delta$ (Δ is the grid size in the x and y directions).

The $64 \times 64 \times 32$ meshes are used for the x, y, and z directions. In GYR3D and Hybrid3D, the grid size in the z direction is stretched by the factor of 1000 from the grid size in the x and y directions. In GRM3D-2F, the aspect ratio is included in the normalization; the stretching is not necessary. For the toroidal mode numbers, the modes up to $n = 0, \pm1, \pm2, \pm3, \pm4$ were included; higher n modes are eliminated in the Fourier space to reduce the high-frequency shear Alfven waves. We used 8388608 electrons and 8388608 ions for GYR3D, while 2097152 ions are used for Hybrid3D. The simulation by GYR3D and Hybrid3D was done on the Intel Paragon XP/S15-256 which has 256 scalar processors connected with a two-dimensional mesh topology. Parallelization of GYR3D is summarized in Ref.[3]. The simulation by GRM3D-2F was executed on Fujitsu VPP500 which has 42 vector processors with a crossbar connection. The speed of the codes scales well with the number of processors.

The linear phase of the instability agrees very well for three codes. The growth rates of the order of the Alfvén time are observed; 0.44 v_A/L_z, 0.55 v_A/L_z, and 0.49 v_A/L_z for GYR3D, GRM3D-2F, and Hybrid3D, respectively. The difference of the growth rates is quite small. (The dependence of the growth rates on d_e and ρ_s is consistent with the prediction of Zakharov et. al.[11]) The width of the current layer around the $q = 1$ magnetic surface is determined by d_e, which also supports the theory of collisionless magnetic reconnection. Also the early nonlinear phase agree very well; the fast Kadomtsev type full reconnection is observed by three codes. The $E \times B$ flow due to the potential structure generated in the full reconnection phase plays the crutial role in the phenomena of post full reconnection phase (second phase); the peripheral plasma at the opposite side of the original x point comes into the central region. The configuration of $q_0 < 1$ is reformed as a results of the magnetic reconnection. This phenomenon was firstly predicted by the simulation by Biskamp et. al. [12]. In GYR3D the q_0 in the second phase is bigger than the original value of q_0, while in GRM3D-2F it is less than the original value. (The measurement of q_0 in the Hybrid code is in progress.) The difference of the electron model in the codes may explain the difference in the second phase. Further study will be needed to clarify the mechanisms which causes the difference of the three codes in the second phase.

6 Conclusions and Discussion

We have developed the gyro-particle (GYR3D), gyro-reduced-MHD (GRM3D-2F), and particle-fluid hybrid (Hybrid3D) codes. These codes are based on the formalism

of nonlinear gyrokinetic Vlasov-Poisson-Ampère system and/or the moment equations of it. Also, these codes have the energy conserving property. As the benchmarking problem, the nonlinear phenomena of the kinetic $m = 1$ and $n = 1$ internal kink mode are studied by these codes. These phenomena are closely related to the sawtooth collapse observed in present day large tokamaks. The fast full reconnection (collisionless magnetic reconnection) followed by the second phase reforming the configuration of $q_0 < 1$ has been observed by the three codes. Although there are some differences in the second phase, we believe that all of the three codes capture the basic physics of the phenomena related to the nonlinear dynamics of the kinetic internal kink modes. To develop a realistic extended MHD code, it is important to make several codes with different order of physical accuracy. Those codes should be well benchmarked for the same physical phenomena. What we have presented in this article is the first step to build the comprehensive extended MHD codes in tokamaks. The toroidal version of the Hybrid3D code is our next target in the near future.

Acknowledgements

The authors are wish to thank to Professor O. Fukumasa, Yamaguchi University, Drs. M. Azumi and T. Hirayama, JAERI and Professors T. Sato and T. Kamimura, National Institute for Fusion Science. The authors would like to express their thanks to Professor W.W. Lee, Princeton Plasma Physics Laboratory, Professors V.K. Decyk and R.D. Sydora, University of California at Los Angeles.

References

[1] S. Tokuda, J. Plasma and Fusion Science, **72** (1996) 916 [in Japanese].

[2] H. Naitou, K. Tsuda, W.W. Lee, R.D. Sydora, Phys. Plasma, **2** (1995) 4257.

[3] H. Naitou, T. Sonoda, S. Tokuda, V.K. Decyk, J. Plasma and Fusion Research, **72** (1996) 259.

[4] H. Naitou, H. Kitagawa, S. Tokuda, J. Plasma and Fusion Research, **73** (199) 174.

[5] S. Tokuda, H. Naitou, W.W. Lee, submitted for publication.

[6] T.S. Hahm, W.W. Lee, and A. Brizard, Phys. Fluids, **31** (1988) 1940.

[7] S.E. Parker, W.W. Lee, Phys. Fluids B, **5** (1993) 77.

[8] G.W. Hammett, F.W. Perkins, Phys. Rev. Lett. **64**, (1990) 3019.

[9] R.E. Waltz, R.R. Dominguez, G.W. Hammett, Phys. Fluids B **4**, (1992) 3138.

[10] H.R. Strauss, Phys. Fluids, **19** (1976) 134.

[11] L. Zakharov, B. Rogers, S. Migliuolo, Phys. Fluids B, **5** (1993) 2498.

[12] D. Biskamp and J.F. Drake, Physical Review Letters **73** (1994) 971.

On the Generation of Alfvèn Wave Current Drive in Low Aspect Ratio Tokamaks with Neoclassical Conductivity

C.Bruma, S.Cuperman and K.Komoshvili

School of Physics and Astronomy, Tel Aviv University, 69978 Tel Aviv, Israel

1. Introduction

Several low aspect ratio (spherical) tokamaks (ST's) are now in operation or under construction [1,2]. These devices would permit cost-effective and attractive embodiment of future fusion reactors: they would provide high β, good confinement and steady state operation at modest field values [3] .

Now, a steady state reactor has to be sustained by non-inductively driven currents [4]. Recently, the generation of non-inductive current driven by Alfven waves (AWCD) has been investigated theoretically within the framework of ideal ($E_{\|} = 0$) MHD [5,6] and non-ideal, resistive ($E_{\|} \neq 0$) MHD [7]; however, in all these cases, the tokamak device consisted of a cylindrical plasma with simulated toroidal effects. Rather encouraging results have been obtained.

In this work we further investigate AWCD in ST's as follows: (i) we use consistent equilibrium profiles with neoclassical conductivity corresponding to an ohmic START discharge [8]; (ii) incorporate effects due to neoclassical conductivity in the elements of the resistive MHD dielectric tensor, in the solution of the full ($E_{\|} \neq 0$) wave equation as well as in the calculation of AWCD; and (iii) carry out a systematic search for antenna parameters optimizing the AWCD.

2. Equilibrum profiles and parameters

From the numerical solution of the MHD equations with neoclassical conductivity obtained for START [8], by adequate best fit techniques, we obtain the equilibrium profiles shown in Fig.1. These results correspond to the following START-parameters: inverse aspect ratio, $\varepsilon = 0.697$; elongation of plasma boundary, 1.3; triangularity of plasma boundary, 0.3; toroidal B-field (axis), 0.4895 T; central electron temperature, $T_e(0) = 0.18$ keV; central ion temperature, $T_i(0) = 0.15$ keV; central electron density, $n(0) = 0.25\ 10^{21}\ m^{-3}$. Also, the following profiles are used: current density: $j_0(x) = j_0(0)(1-x)$; $n_e = n_i = n(0)(1-x)^{0.8}$ and $T_l(x) = T_l(0)(1-x)^{0.8}$ ($l = e, i$); here $x \equiv r/a$, a-minor radius. In this work we consider the low field side ($\theta = 0$) simulation of AWCD in START; thus, the problem reduces to a one-dimensional (radial) one, in which, however, essential toroidicity and shear effects are taken into account.

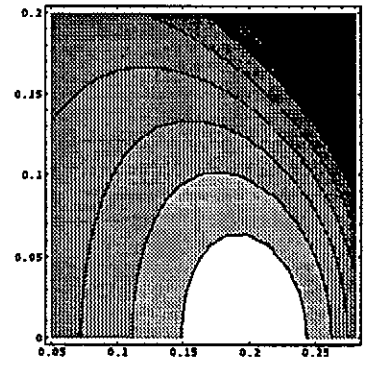

Figure 1: *START equilibrium configuration used in this work: flux surface contours $\Psi_i(R,Z) = C_i$, representing best fits to the numerical results obtained in* [8].

3. Neoclassical conductivity

We have now generalized the previously obtained expressions for current carrying, resistive plasmas [7] by incorporating effects due to neoclassical conductivity. For this, we used the neoclassical conductivity obtained in [9], namely:

$$\frac{\sigma_{nc}}{\sigma_0} = \frac{8}{3\sqrt{\pi}} \int_0^\infty dy\; y^4 e^{-y^4} \left((1 - f_t^*)\, F_s \left[1 - f_t^* \left(\nu_D^e \tau_{ee} F_s - 1 \right) \right] \right) , \tag{1}$$

where $\sigma_0 = n_e e^2 \tau_{ee}/m_e$, $\tau_{ee} = 3(4\pi\epsilon_0)^2 m_e^2 v_{th}^3 / (16\sqrt{\pi} n_e e^4 \ln\Lambda)$ and

$$\nu_D^e(y) = \left(\frac{4}{3\sqrt{\pi}} \tau_{ee} \right)^{-1} \left(\frac{\Phi(y) - G(y) + Z_{eff}}{y^3} \right) . \tag{2}$$

Φ and G are the error function and Chandrasekhar function, respectively:

$$\Phi(y) = \left(\frac{2}{\sqrt{\pi}} \right) \int_0^\infty dy\; e^{-t^2} , \qquad G(y) = \frac{\Phi(y) - y\Phi'(y)}{2y^2} \tag{3}$$

and f_t^* is the effective trapped particle fraction in the presence of collisions:

$$f_t^* = f_t \left(1 + 1.75 \nu_{ee} \left[\nu_D^e(y) \tau_{ee} \right] y^{-1} \right)^{-1} , \tag{4}$$

where f_t is the trapped particle fraction in the absence of collisions, given by the equation:

$$f_t = 1 - \frac{3}{4} \langle B^2 \rangle \int_0^{1/B_{max}} \frac{\lambda d\lambda}{\langle \sqrt{1 - \lambda B} \rangle} . \tag{5}$$

The Spitzer function, $F_s(Z_{eff}, y)$ is fitted to a polynomial and reads

$$F_s(Z_{eff}, y) = \Lambda_E(Z_{eff}) - \Lambda_T(Z_{eff}) L_1(y^2) + \frac{8}{15} \left(\frac{1}{Z_{eff}} - \Lambda_E(Z_{eff}) + \frac{3}{2} \Lambda_T(Z_{eff}) \right) L_2(y^2) \tag{6}$$

where $L_1(y^2) = (5/2) - y^2$, $L_2(y^2) = (35/8) - (7/2)y^2 + (1/2)y^4$,

$$\Lambda_E(Z_{eff}) = \frac{3.40}{Z_{eff}} \left(\frac{1.13 + Z_{eff}}{2.67 + Z_{eff}} \right) , \quad \Lambda_T(Z_{eff}) = 2.06 \left(\frac{1.38 + Z_{eff}}{3.23 + 4.68 Z_{eff} + {Z_{eff}}^2} \right) . \tag{7}$$

4. The wave equation and its solution

We solved the full (i.e., $E_\parallel \neq 0$) wave equation with the generalized resistive dielectric tensor elements mentioned above, for the case of the low field side plasma configuration represented in Fig.1, in the presence of an external, concentric wave-emitting antenna. In this, appropriate regularity (at $r = 0$) and continuity (at $r = a$) conditions were used. Details of the integration method and its accuracy are found in [7]. Illustrative solutions for the e.m. field components are shown in Figs.3-5.

5. Power absorption and current drive

The time averaged power delivered by the antenna (per unit length) equals the energy flux through the plasma surface:

$$P = -\int_{\Sigma_p} d\Sigma \; Re\left[\frac{c}{8\pi}(\boldsymbol{E}^{\star} \times \boldsymbol{B})\right] = \frac{ac}{4} Re\Big(E_{\|}^{\star} B_{\perp} - E_{\perp}^{\star} B_{\|}\Big)_{r=a} . \tag{8}$$

The locally absorbed power density is

$$p_L(r) \equiv Re(\boldsymbol{E} \cdot \boldsymbol{j}^{*})/2. \tag{9}$$

The AWCD generated in the plasma is [10],

$$j_{0z}^{RF} = j_{0z}^{HI} + j_{0z}^{MT} + j_{0z}^{PF} \tag{10}$$

where ($\eta_{\|} \equiv 1/\sigma_{\|} = m_e \nu_{ei}/1.96ne^2$)

$$j_{0z}^{HI} = \frac{B_{0z}}{2eB_0 n \eta_{\|} \omega} \left\{ \frac{B_{0\theta}}{B_0} \frac{1}{r^2} \frac{d}{dr} \left[r^2 \; Re\left(j_r^{*} \frac{E_\theta}{i} \right) \right] + \frac{B_{0z}}{B_0} \frac{1}{r} \frac{d}{dr} \left[r \; Re\left(j_r^{*} \frac{E_z}{i} \right) \right] \right\} \tag{11}$$

$$j_{0z}^{MT} = -\frac{B_{0z}}{2eB_0 n \eta_{\|} \omega} \left\{ \frac{B_{0\theta}}{B_0} \frac{m}{r} + \frac{B_{0z}}{B_0} k_z \right\} \; Re\left(\mathbf{E} \cdot \mathbf{j}^{*}\right) , \tag{12}$$

and

$$j_{0z}^{PF} = \frac{B_{0z}}{2eB_0 n \eta_{\|} \omega} \left\{ \frac{B_{0\theta}}{B_0} \frac{1}{r^2} \frac{d}{dr} \left[r^2 \; Re\left(j_r^{*} \frac{\omega j_\theta}{\omega_{pe}^2 \epsilon_0} \right) \right] + \frac{B_{0z}}{B_0} \frac{1}{r} \frac{d}{dr} \left[r \; Re\left(j_r^{*} \frac{\omega j_z}{\omega_{pe}^2 \epsilon_0} \right) \right] \right\} . \tag{13}$$

In these equations, the upperscripts HI, MT and PF indicate, respectively, contributions due to helicity injection, momentum transfer and plasma flow.

6. Results and conclusions

Inspection of the results obtained in this work reveals the following conclusions:

1. For START-like devices considered here, the neoclassical conductivity leads to a small-decrease in the intensities of the field components; correspondingly, a decrease in the current drive occurs (See Fig.2, in which, for illustration $m = 1$, $n = 4$ and $\omega = \omega_{LA}$, the lower edge of the "Alfvèn continuum").

2. There exist well defined (limited) domains in the (m, n) space corresponding to solutions of the wave equation such that a conversion layer exists in the range $0 \leq x \leq 1$; See, e.g., Fig.3 holding for the case $\omega = \omega_{LA}(m, n)$,.

3. The total AWCD is dominated by the MT-component; the maximum integrated MT-component of the AWCD is obtained for relatively small $|n|$ and $|m|$-values; in all cases, the value corresponding to the neoclassical conductivity is smaller than that corresponding to the classical one. (See Fig.4).

4. The total power absorption $P_T \equiv \int dV \; p_L$, is almost unaffected by neoclassical effects and is maximal for small n and $|m|$-values.

5. Finally, for fixed wave numbers ($m = 1$, $n = 4$, for example) the frequency spectrum of the total AWCD reveals the following behaviour: after two large peaks corresponding to

first two GAE's, the absolute value of the total AWCD current increases with the frequency $\bar{\omega} = \omega/\omega_{ci}(0)$, reaching again significant, broad peaks at $\bar{\omega}$-values about 0.5.

References

[1] Sykes, A. *et al.* 1995 *Intern. Conf. on Plasma Physics*, AIP 345.

[2] *Proc. Int. Workshop on Spherical Torus and US-Japan Workshop for Low Aspect Ratio Tokamaks*, 1996, Culham Science and Engineering Center, Abingdon, UK

[3] Peng, Y.-K.M. and Strickler, D. J. 1986 *Nucl. Fusion*, **26**, 769.

[4] Fisch, N. 1987 *Rev. Mod. Phys.*, **59**, 175.

[5] Cuperman, S., Bruma, C., Komoshvili, K. 1996 *J. Plasma Physics*, **56**, part 1, 149.

[6] Komoshvili, K., Cuperman, S. and C.Bruma. 1997 *J. Plasma Physics*, **57**, part 3, 611.

[7] Bruma, C., Cuperman, S. and Komoshvili, K. 1997 *J. Plasma Physics*, in press.

[8] Wilson, H. R., SCENE—Simulation of Self-Consistent Equilibra with Neoclassical Effects, *Fusion Theoretical and Strategic Studies Depart.* Culham Laboratory July, 1994.

[9] Hirshman, S.P. and Sigmar, D. J. 1977, *Physics of Fluids* **20**, 418.

[10] Elfimov, A. G., Petrzilka, V. and Tataronis, J. A. 1994 *Phys. Plasma*, **1**, 2882.

Captions to Figures

Fig.2. Illustrative (normalized) solutions of the full wave equation ($E_{\|} \neq 0$) for the cases of neoclassical (dashed curves) and classical (solid curves) conductivities. *Top:* (a-d) Radial profiles of ReE_N, ImE_N, ReB_N and ImB_N, respectively. *Bottom:* (e-h) Radial profiles of local power deposition and AWCD-components (i.e., plasma flow, helicity injection and momentum transfer), respectively. (Here, $m = 1,\ n = 4$).

Fig.3. (a-d) Computed "Existence Domains" corresponding to sets of (m, n) values, which, for the equilibrium state described in Fig.1, lead to conversion layers situated in the range $0 \leq x \leq 1$.

Fig.4. (m, n)-dependence of the integrated normalized total AWCD (MT+HI+PF); solid (dashed) curves correspond to the classical (neoclassical) conductivity.

Fig.5. Wave-frequency ($\bar{\omega} \equiv \omega/\omega_{ci}(0)$) — dependence of the normalized AWCD-components MT (a), HI (b), PF (c) and of the total AWCD (d). Solid (dashed) curves correspond to classical (neoclassical) conductivity; $m = 1,\ n = 4$.

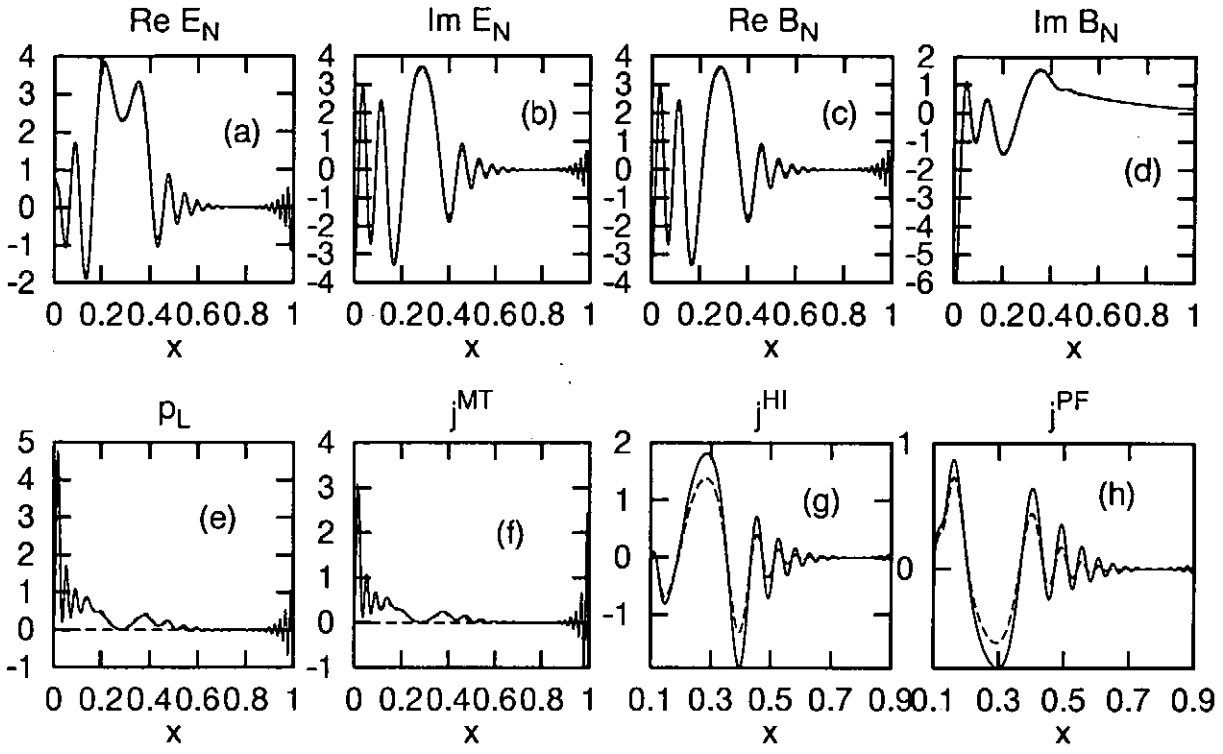

FIG.2

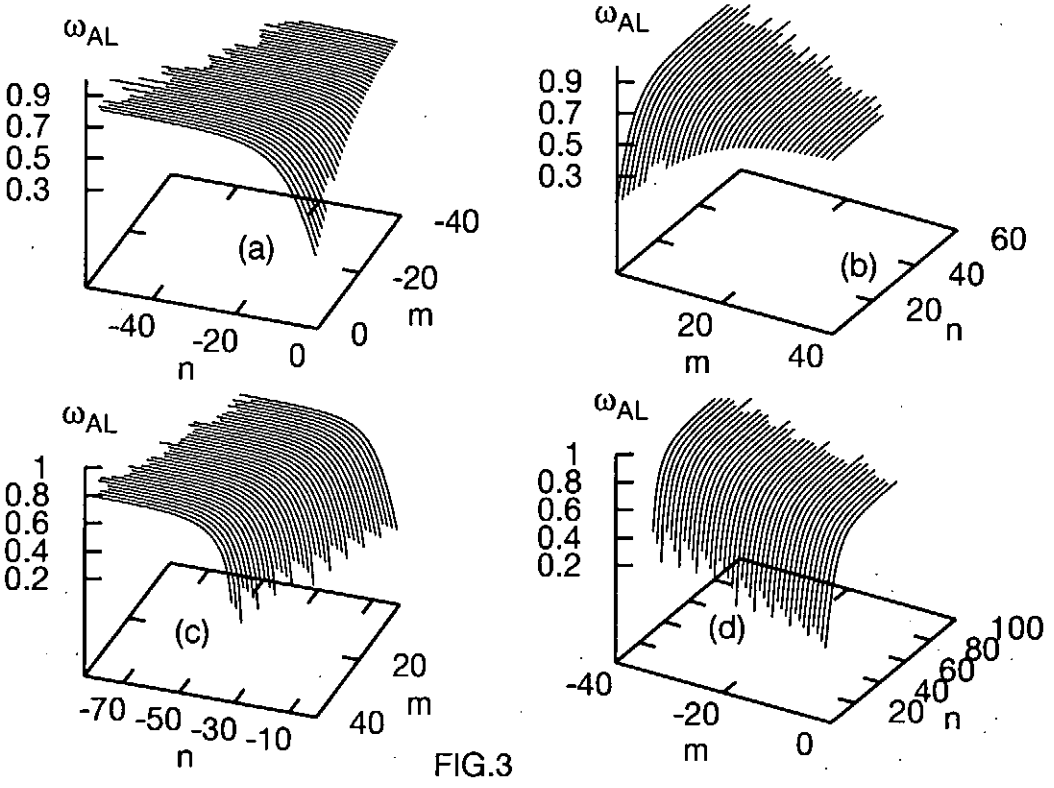

FIG.3

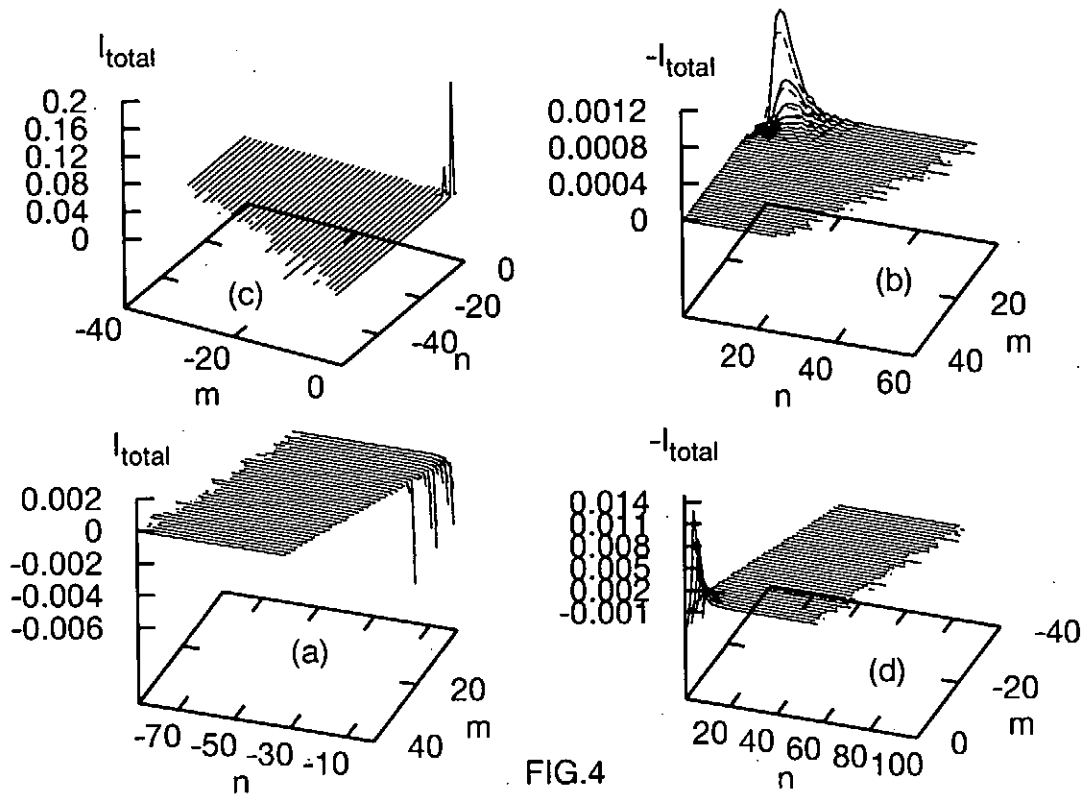
I_total
0.2
0.16
0.12
0.08
0.04
0
(c)
-40
-20
m
0
0
-20
-40
n
-I_total
0.0012
0.0008
0.0004
0
(b)
20
40
60
n
20
40
m
I_total
0.002
0
-0.002
-0.004
-0.006
(a)
-70
-50
-30
-10
n
20
40
m
-I_total
0.014
0.011
0.008
0.005
0.002
-0.001
(d)
20
40
60
80
100
n
-40
-20
0
m

FIG.4

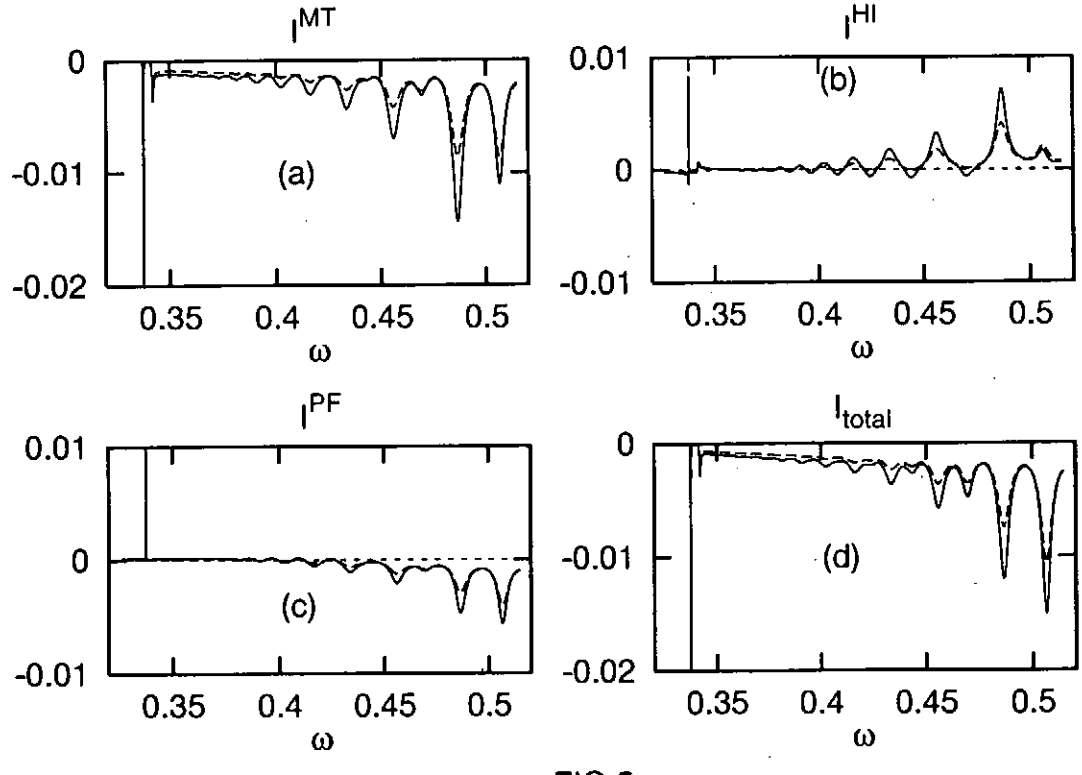
I^MT
0
-0.01
-0.02
(a)
0.35
0.4
0.45
0.5
ω
I^HI
0.01
0
-0.01
(b)
0.35
0.4
0.45
0.5
ω
I^PF
0.01
0
-0.01
(c)
0.35
0.4
0.45
0.5
ω
I_total
0
-0.01
-0.02
(d)
0.35
0.4
0.45
0.5
ω

FIG.5

Drift Surface Geometry and Trapped Particle Fractions in the H-1NF Heliac

Sean DETTRICK[†], Henry GARDNER[*] and Robert DEWAR

Theoretical Physics Department
RSPhysSE, Australian National University, ACT 0200, Australia

[†]Naka Fusion Research Establishment, Naka-machi, 311-01 Japan
[*]Department of Computer Science, Australian National University

Abstract

Drift surface geometry and the trapped particle fraction in the H-1NF heliac are investigated, using cold ion orbits to trace out the surfaces. In the absence of electric fields, the drift surfaces of the helically trapped orbits are unclosed, but when electric fields of thermal magnitude are present the helically trapped drift surfaces are effectively closed. The drift surface geometries are used to suggest an ECH heating configuration which may have improved heating efficiency.

A simple, quantitative method of classifying the geometrically different subclasses of trapped orbit is presented. It is used to show the effect of radial electric fields on the trapped particle populations.

Keywords: radial electric field, helical axis stellarator, drift orbits, ECH heating

1 Drift orbits

The H-1NF Heliac [1] is a high rotational transform, low shear, low aspect ratio device, which has multiple wells and saddles in the field strength on each flux surface, and a rich collection of subclasses of trapped orbit.

We calculate drift orbits in H-1NF using the equations of motion due to Boozer [2], in a background model magnetic field which was calculated by a vacuum run of the VMEC equilibrium code [3]. To simplify the construction of the empirical orbit class signature described below, we removed the toroidal field coil ripple ($\tilde{B}_{\rm tfc}/B_0 \sim 1.5\%$ at the plasma edge, $r = a_p$).

Figure 1 shows some drift orbits, plotted in a covering space in Boozer coordinates. The grey (white) regions in the background are where the particles drift toward (away from) the magnetic axis. The contours represent the magnetic field strength at $r = a_p/2$; the long diagonal extrema are field maxima close to the central ring conductor, while the pairs of rounded, adjacent extrema are wells in B on the outboard side of the device. The thick dashed line is a magnetic field line. Each of the orbits shown has the same kinetic energy, $\mathcal{K}_i = 100$ eV, and the average magnetic field is 1 tesla. The four orbits shown are examples of the four main types of trapped orbit in the standard configuration of H-1NF. The orbit labelled A is deeply trapped, and the B orbit is helically trapped, bouncing between the ring conductor maxima. The orbits labelled C and D are the closest analogues to the trapped particle orbits in tokamaks; they are

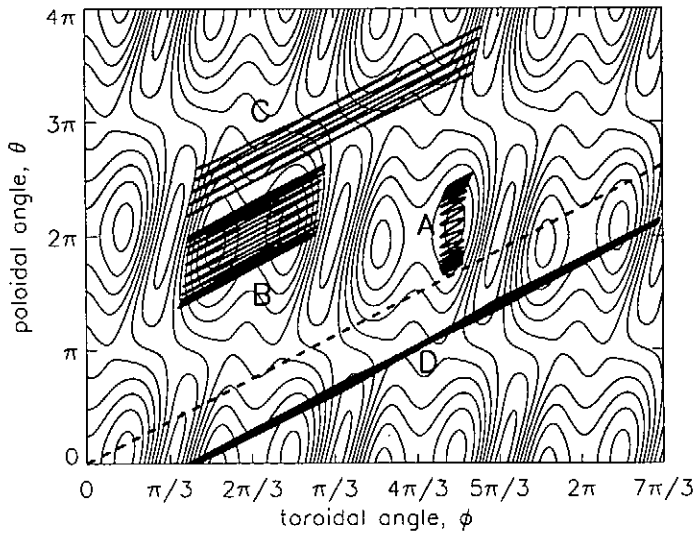

Figure 1: The position of several bounce orbits in the H-1NF magnetic field. Typical contours of $|B|$ are shown in the background. The grey regions are where the radial drift is inward, and the dashed line is a magnetic field line.

almost closed in the radial direction because they sample regions with differing signs of the radial drift.

We use each of these orbits to identify a trapping class, labelled A, B, etc, which is defined by the part of the ripple in which they are trapped. This class is an instantaneous quality, since particles with a drifting banana center commonly experience collisionless transitions between trapping states. When the $\tilde{B}_{\text{tfc}}$ component of the field is ignored, we find that the class A orbits always have one maximum in the parallel kinetic energy (one minimum in B) between bounce points. Similarly, the class B (helically trapped) orbits have two maxima in $\mathcal{K}_{\|}$ between each bounce point, and the toroidally trapped orbits also have a characteristic number of maxima, $N_{\mathcal{K}_{\|}}$ in $\mathcal{K}_{\|}$ between bounce points. The correlation between the orbit class and the associated values of $N_{\mathcal{K}_{\|}}$ is given in table 1.

Class	$N_{\mathcal{K}_{\|}}$
A	1
B	2
C	3 or 4
D	5 or 6
E	7 or 8

Table 1: Number of maxima in parallel kinetic energy per bounce section for the orbit classes.

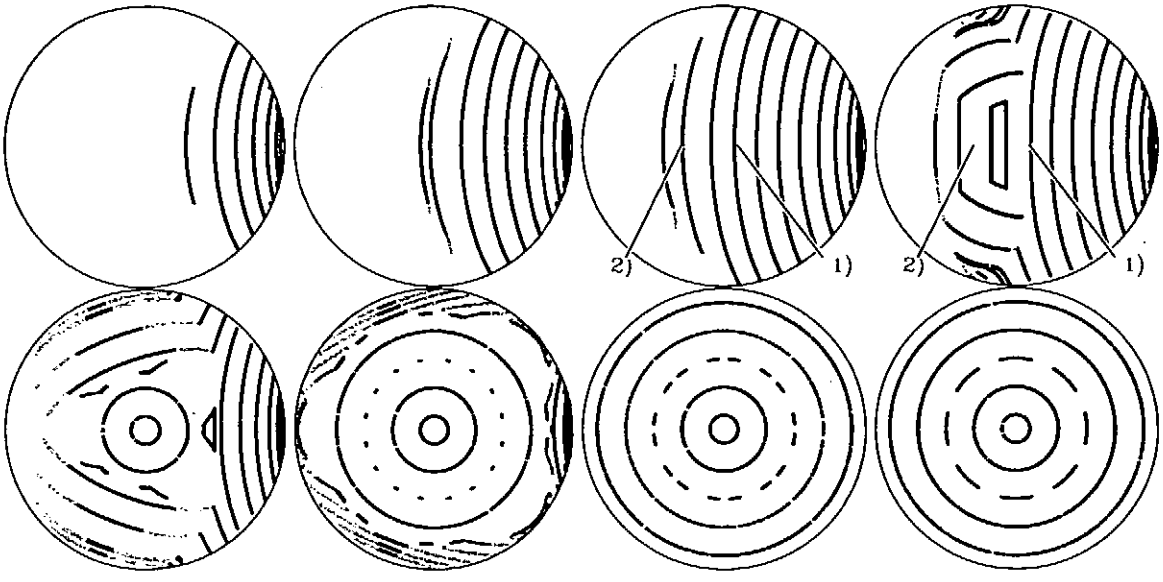

Figure 2: Phase space scan at $\phi = 0$ and with zero electric field, for the H-1NF standard configuration. In each plot, $\hat{\mu} = B_0\mu/\mathcal{E}$ is constant, taking the values $\hat{\mu} = 1.05$, 1.0, 0.95, and 0.9 (from left to right) in the top row, and $\hat{\mu} = 0.85$, 0.8, 0.75, and 0.70 in the bottom row.

2 Drift surfaces

In this paper, toroidal cross sections of drift surfaces are drawn by plotting the puncture points of cold ion orbits where they cross through the planes of constant toroidal angle, ϕ.

In Fig. 2 we plot drift surfaces in the $\phi = 0$ plane for several phase-space cross-sections specified by a normalized magnetic moment, $\hat{\mu} = \mu B_0/\mathcal{E} = 1.05$, 1.0, 0.95, 0.9, 0.85, 0.8, 0.75 and 0.70, ranging from deeply trapped ($\hat{\mu} = 1.05$) to marginally trapped ($\hat{\mu} = 0.8$) to passing ($\hat{\mu} < 0.7$). In each single graph, the total energy $\mathcal{E} = \mathcal{K}_{\|} + \mu B + eV$ of each of the particle orbits is constant, and the potential, V, is zero. In the first five of these plots, the blank regions are where the magnetic field is too strong for particles with the given values of $\hat{\mu}$ to exist. The orbits in the first three plots are helically trapped (class B orbits), which begin at the top of the figure, and move in a downward direction on the plots. The type-C toroidally trapped orbits first appear in the fourth ($\hat{\mu} = 0.9$) plot, and tend to dominate in the fifth ($\hat{\mu} = 0.85$) plot. The concentric orbits in the last four plots are passing orbits. Other types of toroidally trapped orbits (class D, E, etc) appear between the passing and the type C orbits in the $\hat{\mu} = 0.85$ and $\hat{\mu} = 0.8$ cross sections. In this magnetic configuration, there are no closed superbananas in the conventional sense, and confinement of helically trapped particles is very poor when the electric field is small.

The zero E_r results are significant in H-1NF, because experiments show that the electric field takes some time to become established, and within the first 3ms of a discharge, it may be effectively zero [4]. Also, high energy particles are less effected by the electric field, so the first four plots will closely represent the drift surfaces of electrons which have been heated by Electron Cyclotron Heating (which excites the

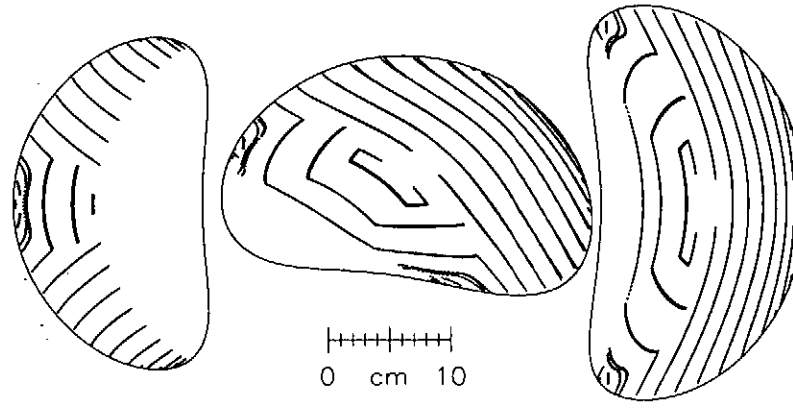

Figure 3: Toroidal cross sections of $\hat{\mu} = 0.9$ drift surfaces in real coordinates, for the standard configuration, at (left) $\phi = \pi/3$, (middle) $\phi = \pi/6$, and (right) $\phi = 0$.

perpendicular velocity, $v_\perp$). An examination of figure 2 reveals that there may be two distinct efficiency regimes for ECH heating in H-1NF. For example, by controlling the field strength and the positioning of mirrors which direct the gyrotron radiation, the ECH resonance layer could be positioned at point 1 or point 2 in figure 2. If it were at point 1, then electron pumping (of the high-$v_\perp$ electrons) would take place along the type B drift surfaces, but, if it were at point 2, then electron losses would be diminished by two processes: by "bouncing" against the magnetic hill (as in the $\hat{\mu} = 0.95$ cross section) and by collisionless detrapping into the toroidally trapped state (as in the $\hat{\mu} = 0.9$ cross section). We therefore predict improved ECH heating efficiency, when the resonant layer is positioned at point 2.

Plotting the $\hat{\mu} = 0.9$ surfaces in real coordinates, at the $\phi = 0$, $\pi/6$, $\pi/3$, and $5\pi/6$ planes (i.e. at four quarters of one field period) we arrive at Fig. 3.

3 Finite electric fields

To examine the impact of the radial electric field on the trapped particle population, we present in figure 4 the $\hat{\mu} = 0.9$ drift surfaces, in the presence of 5 electric fields specified by

$$V = V_0(0.25 - r^2/a_p^2), \tag{1}$$

and $V_0 = -1, -0.2, -0.1, 0, 0.1, 0.2$, and 1. This potential profile was chosen so that, at $r = a_p/2$, it is possible to distinguish between the effect of the electric field on the drift surface geometry (due to poloidal rotation) and the effect of electrostatic detrapping.

In the electron root ($V_0 > 0$ so $E_r > 0$), outward motion in the radial direction will be curtailed by a transition to the passing state, and inward motion is prevented by energy exclusion. In the ion root ($V_0 < 0$ so $E_r < 0$), the situation is reversed; inward radial motion is limited by transitions to the passing state, and outward radial

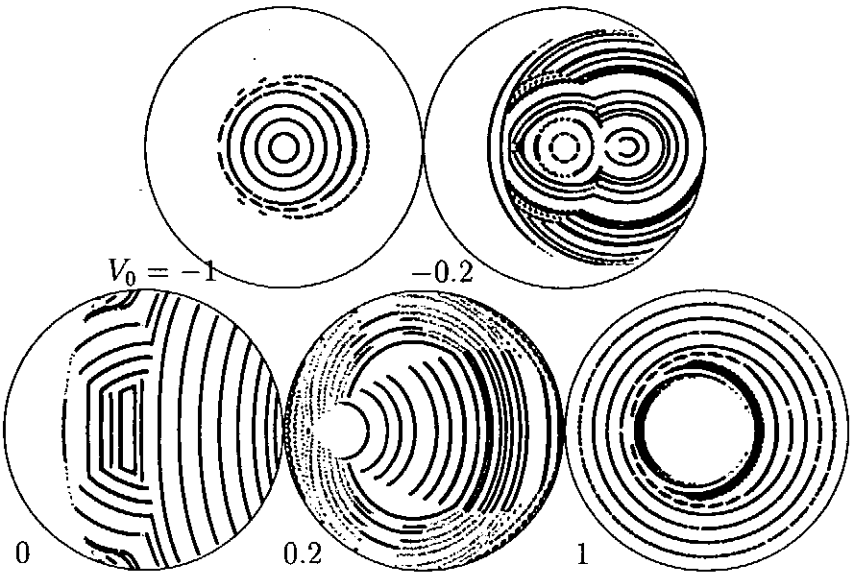

Figure 4: Electric field scan at $\phi = 0$, for the $\hat{\mu} = 0.9$ section of phase space, in the H-1NF standard configuration. The kinetic energy is the same at $a_p/2$ in each plot. Black rings concentric with the plasma radius are passing orbits. All others are trapped orbits.

motion is prevented by electrostatic confinement. This is consistent with the results of Refs. [5, 6].

4 Orbit populations

In this section we use the value of $N_{\mathcal{K}_\parallel}$ to study the trapped particle fractions due to the various orbit classes. We study the distribution of orbits on a flux surface using the assumption of an isotropic velocity distribution. For this purpose, 10^6 particle orbits were initialised uniformly through $(\theta, \phi, v_\parallel/v)$ space at half the plasma radius in the standard configuration. The orbits were propagated both forward and backward in time to their first bounce points and $N_{\mathcal{K}_\parallel}$ was recorded for each. The resulting populations, shown in figure 5, show that at $T_i = 100$ eV and $V_0 = 0$, approximately 60%, 5%, 15%, and 20% of orbits are in the passing, locally trapped (A), helically trapped (B), and toroidally trapped (C and so on) classes respectively. Therefore the total trapped particle fraction, at half the plasma radius and in the absence of electric fields, is about 40% in the H-1NF standard configuration.

The $N_{\mathcal{K}_\parallel}$ orbit classification method could be used to determine the collisionless detrapping probabilities required [7] to analytically model transport due to collisionless trapping and detrapping in the long mean free path regime. Also, while it is widely known that $\mathbf{E}_r$ improves the topology of helically trapped orbits, we have shown here that it also reduces their numbers relative to the toroidally trapped orbits.

A more detailed treatment of drift orbits in H-1NF can be found in Ref. [8].

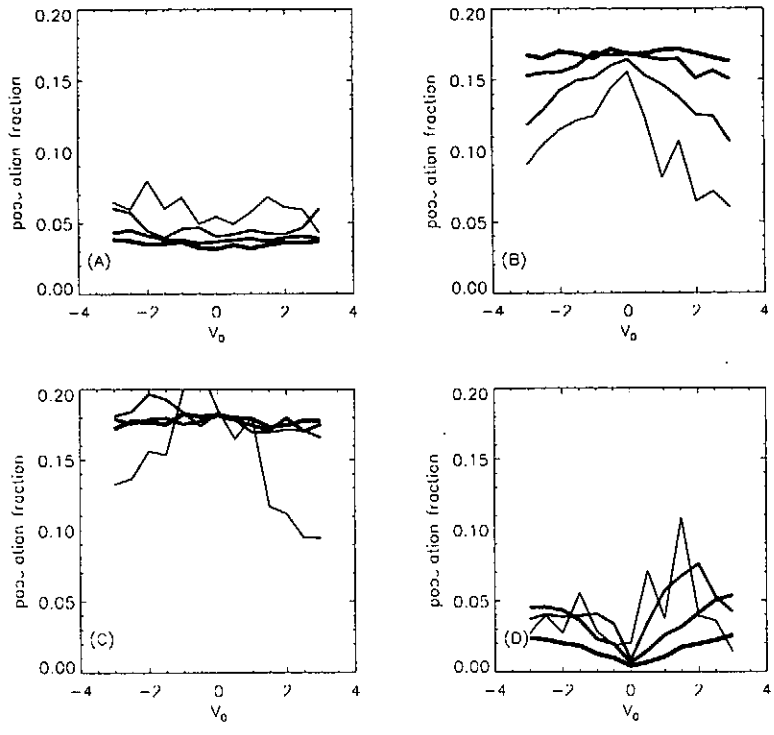

Figure 5: Fractions of the total particle population occupied by the four main classes of trapped orbit (A, B, C, and D) as a function of electric field. Four cases are shown for each orbit class, corresponding to the temperatures 1eV (thickest lines,) 10eV, 100eV, and 1000eV (thinnest lines.)

References

[1] S. M. Hamberger, B. D. Blackwell, L. E. Sharp, and D. B. Shenton, Fusion Technology **17**, 123 (1990).

[2] A. H. Boozer and G. Kuo-Petravic, Physics of Fluids **24**, 851 (1981).

[3] S. P. Hirshman and O. Betancourt, Journal of Computational Physics **96**, 99 (1991).

[4] D. Rudakov, *Magnetic configuration and plasma confinement studies in the H-1 toroidal heliac*, PhD thesis, Plasma Research Laboratory, Australian National University, 1997.

[5] J. A. Rome, Nuclear Fusion **35**, 195 (1995).

[6] J. R. Cary, C. L. Hedrick, and J. S. Tolliver, Physics of Fluids **31**, 1586 (1988).

[7] K. C. Shaing, J. A. Rome, and R. H. Fowler, Physics of Fluids **27**, 1 (1984).

[8] S. A. Dettrick, *Drift Orbits and Neoclassical Transport in the H-1NF Heliac*, PhD thesis, Theoretical Physics Dept, RSPhysSE, Australian National University, 1997.

Test Particle Simulations in a Tokamak

Hyoung-Bin Park[a], Eun-Gi Heo[c], Duk-In Choi[a,b], and Wendell Horton[d]
a Department of Physics, Korea Advanced Institute of Science and Technology, Taejon 305-701, Korea
b Korea Basic Science Institute, Taejon 305-333, Korea
c Samsung Display Devices, Suwon 442-390, Korea
d Institute for Fusion Studies, University of Texas at Austin, Austin, Texas 78712, U.S.A.

We excute test particle simulations for the motion of charged particles in toroidal magnetic confinement geometry including the Monte Carlo Coulomb collisional pitch angle scattering, model electrostatic drift wave fluctuation, and equilibrium potential. The numerically calculated microscopic diffusion coefficients for various values of collisionality ν_* in the case of no electrostatic potential agree well with the results of neoclassical theory. The diffusion coefficient increases with increasing fluctuation amplitude while the equilibrium potential diminishes the diffusion processes through both the orbit squeezing and the $\vec{E}_r \times \vec{B}$ shear flow of the poloidal velocity.

I. GUIDING CENTER EQUATIONS OF MOTION IN TOROIDAL GEOMETRY

Guiding center motion can be described with the variational principle of the general form

$$\delta \int \mathcal{L}_{g.c.}\left(Z_i, \dot{Z}_i, t\right) dt = 0 \qquad (1)$$

where $\mathcal{L}_{g.c.}$ is a guiding center Lagrangian and Z_i, $\dot{Z}_i$ $(i=1,2,\cdots,6)$ are generalized coordinates and their time derivatives in the phase space. From the Euler-Lagrange equations

$$\frac{d}{dt}\left(\frac{\partial \mathcal{L}_{g.c.}}{\partial \dot{Z}_i}\right) - \frac{\partial \mathcal{L}_{g.c.}}{\partial Z_i} = 0, \qquad (2)$$

we derive the guiding center equations of motion. The guiding center Lagrangian [2] is of the form

$$\mathcal{L}_{g.c.} = \vec{A}^* \cdot \dot{\vec{x}} + \mu\dot{\zeta} - \left(\Phi + \mu B + \frac{1}{2}\rho_\parallel^2 B^2\right), \qquad (3)$$

where $\vec{x}$ represents the guiding center position, ζ the gyrophase, and $\rho_\parallel [\equiv v_\parallel/\Omega_c]$ the parallel gyroradius. The modified vector potential $\vec{A}^*$ is defined as $\vec{A}^* = \vec{A} + \rho_\parallel \vec{B}$ and the electrostatic potential Φ is the sum of the equilibrium surface-function potential Φ_0 and the electrostatic fluctuation $\tilde{\Phi}$. All terms in Eq.(3) are normalized with the time unit $\Omega_0^{-1}[= mc/(eB_0)]$, the displacement unit R_0, and the field strength unit B_0.

The standard magnetic field model in a large aspect ratio tokamak with circular cross section is

$$\vec{B} = \frac{1}{1+\epsilon\cos\theta}\left(\hat{\phi} + \frac{\epsilon}{q}\hat{\theta}\right), \qquad (4)$$

where $\epsilon = r/R_0$ $(\epsilon \ll 1)$, q a safety factor, and (ϵ, θ, ϕ) toroidal coordinates.

With the generalized coordinates $Z_i = (\epsilon, \theta, \phi, \rho_\parallel, \zeta, \mu)$, the Euler-Lagrange equations of Eq.(2) become

$$\begin{aligned}
\dot{\epsilon} &= -G_1 F_1 - \left(G_1\frac{\partial\Phi}{\partial\theta} + G_2\frac{\partial\Phi}{\partial\phi}\right), \\
\dot{\theta} &= G_3 F_3 + G_1 F_2 + G_1\frac{\partial\Phi}{\partial\epsilon}, \\
\dot{\phi} &= G_5 F_3 + G_2 F_2 + G_2\frac{\partial\Phi}{\partial\epsilon}, \\
\dot{\rho_\parallel} &= -G_3 F_1 - \left(G_3\frac{\partial\Phi}{\partial\theta} + G_5\frac{\partial\Phi}{\partial\phi}\right),
\end{aligned} \qquad (5)$$

where

$$\begin{aligned}
F_1 &= (\mu + \rho_\parallel^2 B)B\,\tfrac{\epsilon\sin\theta}{(1+\epsilon\cos\theta)}, \\
F_2 &= -(\mu + \rho_\parallel^2 B)B \\
&\quad \cdot \left(\tfrac{\cos\theta}{(1+\epsilon\cos\theta)} - \left(1+\tfrac{\epsilon^2}{q^2}\right)^{-1}\tfrac{\epsilon}{q^2}\left(1 - \tfrac{\epsilon}{q}\tfrac{dq}{d\epsilon}\right)\right), \\
F_3 &= \rho_\parallel B^2, \\
G_1 &= \tfrac{1}{D}\tfrac{\sqrt{1-\epsilon^2}}{\epsilon}\tfrac{1}{(1+\epsilon\cos\theta)}, \\
G_2 &= -\tfrac{1}{D}\tfrac{\epsilon\sqrt{1-\epsilon^2}}{q}\tfrac{1}{(1+\epsilon\cos\theta)^2}, \\
G_3 &= \tfrac{1}{D}\tfrac{1}{q}\tfrac{1}{(1+\epsilon\cos\theta)}, \\
G_5 &= 1 - \tfrac{1}{D}\tfrac{\epsilon^2}{q^2}\tfrac{1}{(1+\epsilon\cos\theta)^2}, \\
B &= \tfrac{1}{(1+\epsilon\cos\theta)}\left(1+\tfrac{\epsilon^2}{q^2}\right)^{\frac{1}{2}}, \\
D &= \tfrac{1}{(1+\epsilon\cos\theta)^2}\left(1 - \epsilon^2\cos^2\theta + \tfrac{\epsilon^2}{q^2}\right. \\
&\quad \left. + \rho_\parallel\tfrac{\sqrt{1-\epsilon^2}}{q}\left(1 - \tfrac{\epsilon}{q}\tfrac{dq}{d\epsilon} + \tfrac{1}{(1+\epsilon\cos\theta)}\right)\right).
\end{aligned}$$

With the given function $\Phi(\epsilon, \theta, \phi) = \Phi_0 + \tilde{\Phi}$ representing the electrostatic potential, the equations of motion of Eqs.(5) describe the motion of a charged particle in tokamaks in the presence of electrostatic fluctuations such as the drift wave turbulence.

Since we are assuming a scalar pressure equilibrium, $\nabla P = \vec{J} \times \vec{B}/c$, in this paper, the pressure profile is calculated from the differential equation in Boozer's magnetic coordinates [9], [10] of

$$\frac{dP}{d\psi} = \frac{\mathcal{J}}{4\pi}\left[\left(\frac{\partial \beta_*}{\partial \varphi} - \frac{dg}{d\psi}\right) - \frac{1}{q}\left(\frac{\partial I}{\partial \psi} - \frac{\partial \beta_*}{\partial \vartheta}\right)\right], \quad (6)$$

where $\mathcal{J} = \nabla\psi \cdot (\nabla\vartheta \times \nabla\varphi)$ is the Jacobian. For the magnetic field model of Eq.(4) we write Eq.(6) in toroidal coordinates and thus obtain the differential equation for the pressure profile in toroidal coordinates related to the given q profile,

$$\frac{dP}{d\epsilon} = -\frac{\epsilon}{\sqrt{1-\epsilon^2}}\frac{1}{q^2}\left(2 - \frac{\epsilon}{q}\frac{dq}{d\epsilon}\right), \quad (7)$$

where we ignored ϵ^2 and higher order terms.

During each time step δt of integration of the equations of motion a number of Coulomb collisional small angle scatterings take place. We assume that as a result of these scatterings the magnitude of velocity is unchanged but its direction is changed. Two angle quantities α and γ describe this deflection. The angle α is chosen randomly with a uniform distribution between 0 and 2π and the distribution of γ is taken to meet with the Spitzer formula for small angle scattering [11]. From two random numbers η_1 and η_2 on [0,1] two angles of α and γ are determined as

$$\alpha = 2\pi\eta_1, \qquad \gamma = [-\nu\delta t \ln(1-\eta_2)]^{1/2}, \quad (8)$$

where ν is collision rate and $\nu\delta t \ll 1$ is required. This collision induces the following changes of the velocity variables $(\rho_\parallel, \mu)$.

$$(\rho_\parallel)_f = (\rho_\parallel)_i \cos\gamma + \sqrt{\frac{2\mu_i}{B_i}}\sin\gamma\cos\alpha,$$
$$\frac{2\mu_f}{B_f} = \left[(\rho_\parallel)_i^2 + \frac{2\mu_i}{B_i}\right]\sin^2\gamma\sin^2\alpha + \left[\sqrt{\frac{2\mu_i}{B_i}}\cos\gamma - (\rho_\parallel)_i\sin\gamma\cos\alpha\right]^2, \quad (9)$$

where subscripts $_i$ and $_f$ refer to the initial and final values, respectively.

II. TEST PARTICLE SIMULATION OF THE RADIAL TRANSPORT IN TOROIDAL GEOMETRY

In this section we investigate numerically the transport properties of ions by integrating the equations of motion in toroidal coordinates of Eqs.(5) and calculating the microscopic diffusion coefficients. We use the system parameters of TEXT, i.e., major radius $R_0 = 100cm$, minor radius $a = 26cm$, centerline field $B_0 = 3T$ and the assumed theoretical fit of the experimentally measured q profile in TEXT, $q(r) = 0.8 + 2.2\left(\frac{r}{a}\right)^2$. We also use the modeled equilibrium potential profile, $\Phi_0(r) = -T_i\left[1 - \left(\frac{r}{a}\right)^4\right]$, where T_i is ion temperature. This profile will be used in the next subsection in order to investigate the orbit squeezing effect from the equilibrium potential on radial transport.

A. Verification of the Equations of Motion

We first consider the motion of deuterium ions (D^+) in the circular toroidal equilibrium specified in section I, and verify that Eqs.(5) well describe the guiding center motion of an ion in toroidal geometry. For $\Phi = 0$ integration of the equations of motion given in Eqs.(5) results in the well known characteristic orbits for trapped particles such as the banana orbit on (r, θ) plane (the poloidal section) and the toroidal precession motion on (R, ϕ) plane (the toroidal section). [12], [13] For D^+ ions with $\lambda = 0.88$ and 1.00 we integrate the equations of motion for the cases with and without the equilibrium potential profile above, and plot the projections of their trajectories on the poloidal section in Fig.1 for comparison. As the potential is added the banana orbit of a trapped particle is shrinked : the orbit widths change from 1.655 to $1.540cm$ and from 2.334 to $2.210cm$. After a calculation following the method in the previous work of Berk and Galeev [14] and Hazeltine [7] we can expect that for the slowly varying poloidal magnetic flux and electrostatic potential the orbit is squeezed in the radial direction by $\Delta = \Delta_0/S$, where Δ and Δ_0 are the squeezed and unsqueezed orbit widths, respectively, and the squeezing factor is

$$S = \left|1 + \rho_p^2\left(\frac{\Phi''}{T_i}\right)\right| \quad (10)$$

with the poloidal gyroradius $\rho_p = (mcv_\perp)/(eB_p)$. Since $\rho_p \simeq 2.2cm$ for our system parameters, from Eq.(10) our assumed potential profile gives the squeezing factor $S \simeq 1.018$, which corresponds to the ratios of orbit widths $1.655/1.540 \simeq 1.075$ and $2.334/2.210 \simeq 1.056$ in Fig.1. The difference between Eq.(10) and the simulation results is mainly from the assumption used in deriving Eq.(10), that is, that the poloidal magnetic flux and the electrostatic potential are slowly varying in radial direction over the scale of the radial orbit width.

B. Neoclassical Diffusion

We find that the radial motion is described as a diffusion process if we correct for the effect of the radially bounded motion of trapped particles. When the running diffusion coefficient,

$$\mathcal{D}(t) = \frac{1}{2t}\frac{1}{N}\sum_{j=1}^{N}[r_j(t) - r_j(0)]^2, \qquad (11)$$

appears convergent, we regard that $\mathcal{D}(t)$ is ergodic and replace the ensemble average by its time average. We obtain the diffusion coefficient from time series of $\mathcal{D}(t)$ as

$$\bar{\mathcal{D}} = \frac{1}{T - T_0}\int_{T_0}^{T}\mathcal{D}(t)dt \qquad (12)$$

and estimate the standard deviation by

$$\delta\mathcal{D} = \left[\frac{1}{T - T_0}\int_{T_0}^{T}(\mathcal{D}(t) - \bar{\mathcal{D}})^2 dt\right]^{1/2}, \qquad (13)$$

where T_0 is the time when convergence is observed to set in.

Now varying the value of the collision rate, ν, we calculate the diffusion coefficient of Eq.(12) for case of $\Phi = 0$. We compare the computed value with the neoclassical calculation. Chang and Hinton's result [15] for concentric circular flux surfaces is

$$\begin{aligned}\mathcal{D}_{nc} &= \epsilon^{1/2}(\rho_\theta^2/\tau)K_2(\nu_*, \epsilon) \\ &= \epsilon^{1/2}(q^2/\epsilon)\nu_* K_2(\nu_*, \epsilon) \qquad [\rho_0^2\omega_b], \end{aligned} \qquad (14)$$

where $\nu_* \equiv \nu_{eff}/\omega_b$ and the dimensionless function K_2 is given as

$$K_2 = K_2^{(0)}\left(\frac{K_2^*/0.66}{1 + a_2\nu_*^{1/2} + b_2\nu_*} + \frac{(c_2^2/b_2)\nu_*\epsilon^{3/2}}{1 + c_2\nu_*\epsilon^{3/2}}F\right) \qquad (15)$$

with $K_2^{(0)} = 0.66$, $K_2^* = (0.66 + 1.88\epsilon^{1/2} - 1.54\epsilon)(1 + \frac{3}{2}\epsilon^2)$, $a_2 = 1.03$, $b_2 = 0.31$, $c_2 = 0.74$, and the Pfirsch-Schlüter factor for concentric circular flux surfaces $F = \frac{1}{2}\epsilon^{-1/2}[1 + \frac{3}{2}\epsilon^2 - (1 - \epsilon^2)^{1/2}]$. The formula (27) is a modification including the effect of finite aspect ratio to the analytic expression of the ion thermal conductivity valid for all collisionality regimes given in Ref. [8]. In Fig.2 we show the results of our simulation of the neoclassical problem for an ensemble of 512 D^+ ions. Solid line is the result from Eqs.(14) and (15), and vertical lines are simulation results. We find that the simulation is in good agreement with the neoclassical calculation of Eqs.(14) and (15) for ν_* in the range 10^{-2} to 2. To determine the dimensionless value of collisionality ν_* for the collision rate we numerically calculate the average bounce frequency for the ensemble and take it as ω_b [3]. The average bounce period is $\omega_b^{-1} = 7.24 \times 10^3 \pm 28\Omega_0^{-1}$ for our ensemble.

C. Turbulent Transport Properties

In this subsection we consider a theoretically simplified model for drift waves in toroidal geometry and investigate its effect on transport properties. Perturbed potential in tokamak can be written in the form

$$\tilde{\Phi} = \tilde{\Phi}(\theta, \rho)\exp[i(N\phi - M\theta) - i\omega t], \qquad (16)$$

where $\rho = r - r_0$ is the radial distance from the rational surface given by $M = Nq(r_0)$. With appropriate approximations, $\tilde{\Phi}(\theta, \rho)$ satisfies [16], [4]

$$\left[\frac{\partial^2}{\partial x^2} - \sigma^2\left(\frac{\partial}{\partial\theta} + ix\right)^2 - \epsilon\left(\cos\theta + is\sin\theta\frac{\partial}{\partial x}\right) - \kappa x^2 - \lambda\right]\tilde{\Phi} = 0, \qquad (17)$$

where $x = k\rho s$. Three parameters in Eq.(17) are given by

$$\sigma = \frac{\epsilon_c}{bs}, \quad \epsilon = \frac{2\epsilon_n}{bs^2}, \quad \kappa = \frac{1}{k^2 L_*^2 bs^4(1 + \tau)} \qquad (18)$$

and the eigenvalue λ is related to the mode frequency ω by

$$\lambda = \frac{\left(\frac{\omega}{\omega_*} - 1 + b(1 + \tau) - i\delta\right)}{bs^2(1 + \tau)}. \qquad (19)$$

In Eqs.(17)-(19), $k = Nq/r$, $b = k^2\rho_i^2$, and $\epsilon_n = q\epsilon_c = L_n/(R_0\tau)$, where ρ_i is the ion gyroradius, L_n is the density scale length, and $\tau = T_e/T_i$. The diamagnetic frequency $\omega_* = (kcT_e)/(eBL_n)$ is expanded about a local maximum with $L_*^{-2} = -(1/\omega_*)(d^2\omega_*/dr^2)$ and the parameter $i\delta$ represents destabilizing effect by electron Landau resonance and trapped electrons. Following the procedure of Connor and Taylor [4] we have the model for electrostatic drift wave fluctuations of

$$\tilde{\Phi}(r, \theta, \phi) = \tilde{\Phi}_0\sum_{m=-2}^{2}\exp\left[\sigma_I(x - m)^2/2\right] \cdot\cos\left[-\sigma_R(x - m)^2/2 - (m + M)\theta + N\phi - \omega t\right], \qquad (20)$$

where $\tilde{\Phi}_0$ is the mode amplitude, r_0 position of the rational surface satisfying $M = Nq(r_0)$, ω the

mode frequency, σ_R and σ_I are real and imaginary parts of σ, respectively. We choose $N = 11$ and $M = 14$, and $L_n/R_0 = 0.1$ and $\delta = 0.8$ not to contradict the assumption for Eq.(17). While in future studies we may include a spectrum of different N and M values, the complex structure of the single eigenmode is sufficient for the onset of anomalous diffusive transport.

Now we calculate the diffusivity for D^+ ions in the presence of global drift wave fluctuation of Eq.(20). In Fig.3 we show the dependences of $\bar{\mathcal{D}}$ on collisionality ν_* at fixed $\tilde{\Phi}_0$'s (e.g. $\tilde{\Phi}_0 = 4, 10$) and compare these $\bar{\mathcal{D}}$'s with those of the neoclassical cases. For given collision rate in the banana regime of $\nu_* < 1$, the diffusion coefficient increases as the electrostatic fluctuation amplitude, $\tilde{\Phi}_0$, increases. The diffusion coefficients in the presence of the electrostatic fluctuations at low collision rate are comparable to those of neoclassical diffusion at quite high collision rate, which means that electrostatic fluctuation strongly affects the motion of particles. The convergence properties of the running diffusivity, however, remain the same even with the largest $\tilde{\Phi}_0$ values used in this figure implying that the enhanced transport is a diffusion process.

In Fig.4 we present the variation of diffusion coefficient as a function of fluctuation amplitude. In this figure ν_* was fixed at 0.576. The results show that the diffusion coefficients increase approximately linearly in the regime of small fluctuation amplitude. According to the explanation in Ref. [1] where a linear variation was reported, the turbulent diffusion by drift wave fluctuations drives stochastic transport from the interaction between the particle motions characterized by $\vec{E} \times \vec{B}$ circulation frequency Ω_k and the particle bounce frequency. This Hamiltonian stochastic transport is faster than the neoclassical transport. The $\vec{E} \times \vec{B}$ circulation frequency is defined as

$$\Omega_k = ck_\perp^2 \Phi_k / B. \tag{21}$$

Also shown in Fig.4 are the diffusion coefficients in the cases that the equilibrium potential $\Phi_0(r)$ exist. We use two equilibrium potentials for this calculation to show the effect of shear in $\vec{E} \times \vec{B}$ poloidal velocity generated by equilibrium radial electric field. In the first case, $\Phi_{01}(r)$ has the radial electric field $E_r = E_0\epsilon/(1+\epsilon)$ which induces $v_p/r = cE_r/(rB_t) \sim constant$, that is, induces almost no shear in $\vec{E} \times \vec{B}$ poloidal velocity. In contrast, Φ_{02} has the electric field $E_r = E_0\epsilon exp(\epsilon)/(1+\epsilon)$, resulting in $v_p/r \sim exp(\epsilon)$. In both cases E_0 is chosen as 3×10^4 to make these electric fields comparable to that of the potential used for Fig.1. From the results of no fluctuation case($\tilde{\Phi}_0 = 0$), we can see the orbit squeezing effect is larger for Φ_{01}. However the diffusion coefficient for this low-shear case increases in a rate which is not much different to that of no equilibrium field case as fluctuation amplitude increases, which means that Φ_{01} hardly suppresses the fluctuation even for the low fluctuation level presented in the figure. The potential Φ_{02}, however, suppresses the diffusion from the fluctuations very well. It can be seen that the increase of diffusion by electrostatic fluctuation is suppressed by E_r. From the result of Ref. [6], with the factor that represents the decorelation of drift wave turbulence and plasma resulted from shear flow, the diffusion coefficient in the case that E_r exists is expressed as

$$\mathcal{D}_{(E_r \neq 0)} = \mathcal{D}_{(E_r=0)}/(1 + \Delta_{dec}), \tag{22}$$

where $\Delta_{dec} = k\Delta r v_p' \tau_c$ is the decorelation factor which represents the reduction of interaction between drift wave and plasma by shear flow, Δr is the radial excursion of ions trapped in a drift wave, and τ_c is the period of the motion. The idea that the sheared $\vec{E} \times \vec{B}$ flow results in the decrease of turbulent transport which was first proposed by Biglari et al. [5] is now verified for the global toroidal system by the reduced diffusion reported here. Our result that the equilibrium potential induces shear in poloidal velocity v_p and in turn diminishes the diffusion caused by electrostatic fluctuation can be explained by these theoretical results. The $\vec{E} \times \vec{B}$ flow of cE_r/B_t suppresses the enhanced diffusion from the drift wave electrostatic fluctuation given in Eq.(20).

III. CONCLUSIONS

We derived the guiding center equations of motion expressed in magnetic and toroidal coordinates which describe the particle motion in tokamak equilibrium in the presence of drift wave electrostatic fluctuation from the generalized variational principle. On the basis of the guiding center equations of motion the test particle problem of transport in tokamak including pitch angle scattering and electrostatic potential fluctuation function $\tilde{\Phi}(r, \theta, \phi)$ which was modeled from theoretical calculation of drift wave equation was solved. About the neoclassical problem of transport only through collisions the test particle simulation using Lorentz collision operator agrees well with the neoclassical theory. When fluctuations $\tilde{\Phi}$ exist, the diffusion coefficient of test particle simulation is larger than the result of the neoclassical problem in the whole range of $10^{-2} \leq \nu_* \leq 2$. This increase of the diffusivity indicates that drift wave electrostatic fluctuations

can account for the anomalous transport observed in tokamaks. In particular we modeled the equilibrium potential measured in the TEXT tokamak to show the effect of the radial electric field E_r. The observed suppression of the diffusivity with the two models for $E_r(r)$ is thought to be consistent with the explanations of the onset of the H-mode with increasing shear in the poloidal velocity induced by E_r. The results show that E_r diminishes the banana orbit width of a trapped particle, and especially E_r generating enough shear in $\vec{E} \times \vec{B}$ poloidal velocity suppresses the transport induced by the drift wave electrostatic fluctuations. The further study of the effect of E_r on plasma transport in tokamak edge region may provide important information about the H-mode, and thus more detailed investigation of this problem using the test particle simulations is under active study and will be reported elsewhere.

---

[1] D.-E. Kim, D.-I. Choi, W. Horton, P.N. Yushmanov, and V.V. Parail, Phys. Fluids **B2**, 547(1990).
[2] R.G. Littlejohn, J. Plasma Phys. **29**, 111(1983).
[3] E.-G. Heo, B.-H. Park, D.-I. Choi, and W. Horton, J. Korean Phys. Soc. **27**, 49(1994).
[4] J.W. Connor and J.B. Taylor, Phys. Fluids **30**, 3180(1987).
[5] H. Biglari, P.H. Diamond, and P.W. Terry, Phys. Fluids **B2**, 1(1990).
[6] J. Liu, W. Horton, and J.E. Sedlak, Phys. Fluids **30**, 467(1987).
[7] R.D. Hazeltine, Phys. Fluids **B1**, 2031(1989).
[8] F.L. Hinton and R.D. Hazeltine, Rev. Mod. Phys. **48**, 239(1976).
[9] A.H. Boozer, Phys. Fluids **24**, 1999(1981).
[10] A.H. Boozer, Phys. Fluids **25**, 1288(1983).
[11] R. Shanny, J.M. Dawson, and J.M. Greene, Phys. Fluids **7**, 1281(1967).
[12] J.A. Rome and Y-K.M. Peng, Nucl. Fusion **19**, 1193(1979).
[13] D.J. Sigmar, C.T. Hsu, R.B. White, and C.Z. Cheng, Phys. Fluids **B4**, 1506(1992).
[14] H.L. Berk and A.A. Galeev, Phys. Fluids **10**, 441(1967).
[15] C.S. Chang and F.L. Hinton, Phys. Fluids **25**, 1493(1982).
[16] W. Horton, Jr., R.D. Estes, H. Kwak, and D.I. Choi, Phys. Fluids **21**, 1366(1978).

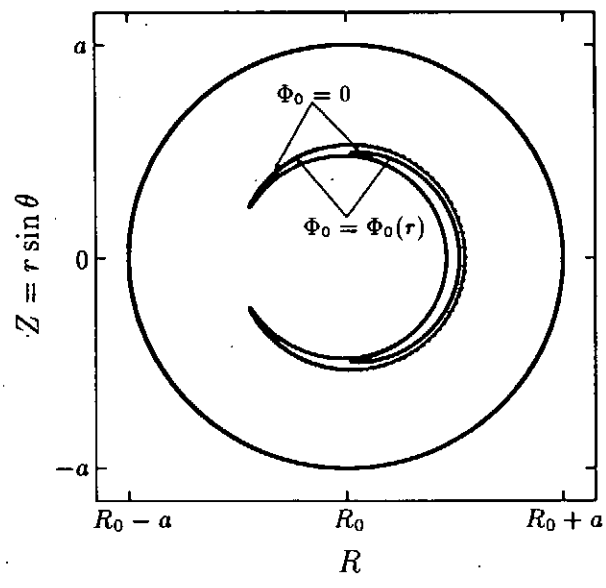

Fig.1

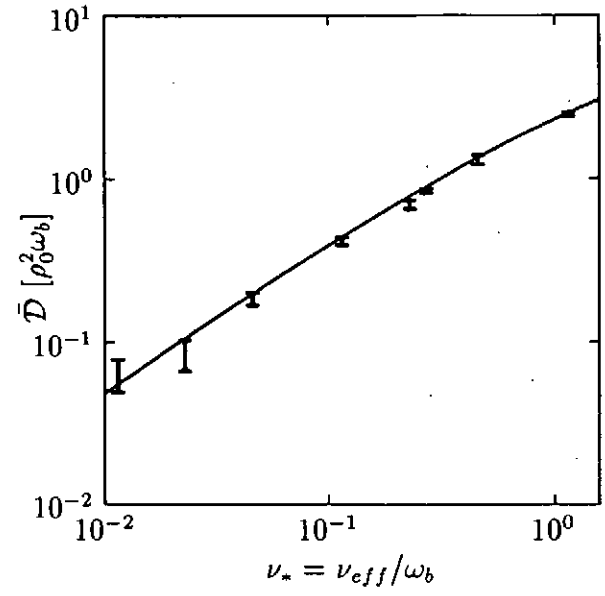

Fig.2

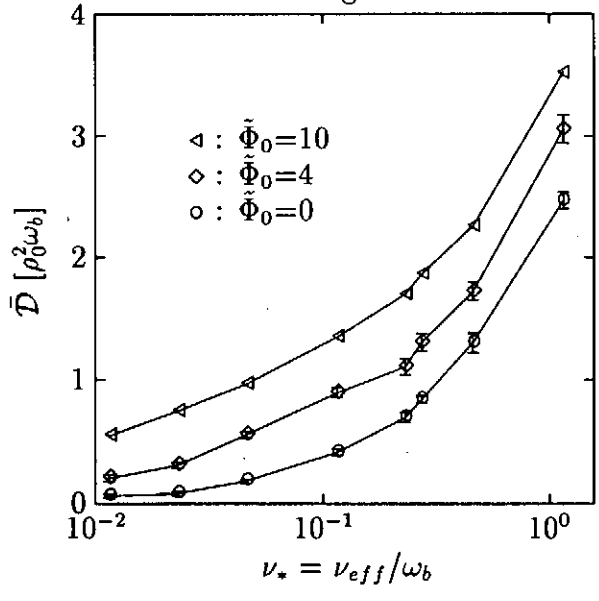

Fig.3

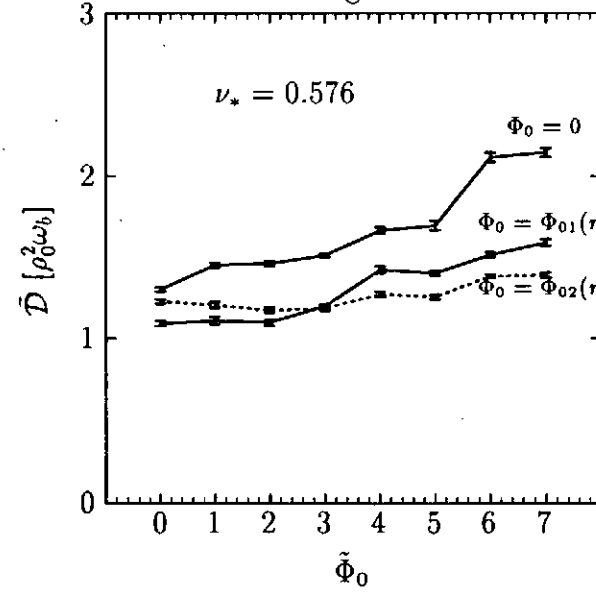

Fig.4

Fig.1 Orbit squeezing for D^+ ions with $\lambda = 0.88$ and 1.00.
Fig.2 Comparison of $\bar{\mathcal{D}}$ for $\Phi = 0$ with $\mathcal{D}_{nc}$.
Fig.3 Dependence of $\bar{\mathcal{D}}$ on ν_* for $\tilde{\Phi}_0 = 0$ ($\circ$), 4 ($\diamond$), and 10 ($\triangleleft$).
Fig.4 Dependence of $\bar{\mathcal{D}}$ on $\tilde{\Phi}_0$ for $\nu_* = 0.576$.

A Theoretical Impedance Calculation for the Solenoidal Inductively Coupled Plasma

K.-I. You, N. S. Yoon, S. M. Hwang, and D.-I. Choi*

Korea Basic Science Institute, Taejeon 305-333, Korea

** Also at Department of Physics, Korea Advanced Institute of Science and Technology, Taejeon 305-701, Korea*

A two-dimensional solution of the Maxwell Boltzmann equations in solenoidal inductively coupled plasma discharge including RF antenna source is obtained. Using this solution, we calculate the plasma impedance. The impedance is presented as a function of various parameters, such as plasma density and temperature, antenna position, collision frequency, excitation frequency, chamber geometry, and so on.

I. INTRODUCTION

Concerning the next generation semiconductor manufacture processing, many researchers have paid attention to the inductively coupled plasma (ICP) device because of the uniformity of this plasma, which is essential to the processing plasma. There are two types of ICP reactors, one is planar (TCP), the other is solenoidal, which are distinguished according to the position of coil in reactor. It is generally believed that the main heating mechanism is anomalous skin effects [1,2], where the wave energy goes to the particles through the resonant coupling. Although some theoretical studies for the anomalous skin effects in plasma have been reported [3–6], and recently the realistic theory for planar type [7,8] has been developed, the theory of collisionless heating for solenoidal type is not well estabilished.

In this work, we obtain an analytic solution of 2-dimensional wave equations with well known conductivity of homogeneous hot plasma and an external coil current. From this electromagnetic solution, plasma impedance can be calculated [9]. We study the effects of the various parameters, such as plasma density, plasma temperature, excitation frequency, chamber and coil geometry, coil shape, and so on, on the plasma impedance.

II. THEORY

Wave equation in plasma region

Let's introduce a schematic diagram for inductively coupled plasma (ICP) discharge device of which we calculate the electromagnetic field and impedance (Fig. 1).

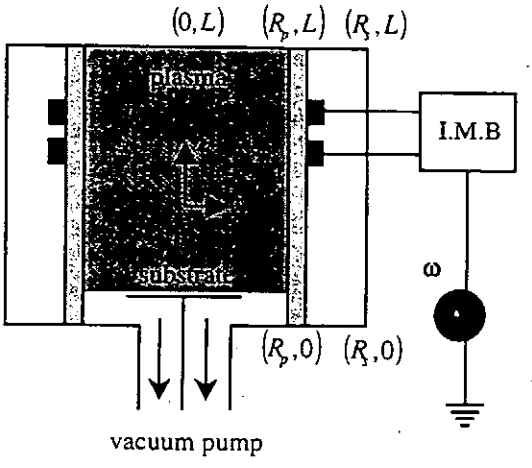

FIG. 1. Schematic diagram for ICP device

The ICP device is devided into two regions, namely, antenna and plasma regions. In plasma region we write 2-dimensional wave equation for azimuthal electric field E as follows

$$\left[\frac{\partial^2}{\partial r^2}+\frac{1}{r}\frac{\partial}{\partial r}-\frac{1}{r^2}+\frac{\partial^2}{\partial z^2}+\kappa^2\right]E = -i\kappa\frac{4\pi}{c}J_p, \qquad (1)$$

where κ is ω/c with radiofrequency (RF) wave angular speed ω, and speed of light c, and J_p is a plasma current density. In the above equation, electric field E is necessarily

$$E = 0 \qquad \text{at} \quad r = 0. \qquad (2)$$

Another boundary condition is related to the magnetic field in axial direction at plasma vacuum boundary as

$$B_z = B_p \qquad \text{at} \quad r = R_p. \qquad (3)$$

This boundary magnetic field can be expressed as a surface current form and inserted to wave equation resulting in

$$\left[\frac{\partial^2}{\partial r^2}+\frac{1}{r}\frac{\partial}{\partial r}-\frac{1}{r^2}+\frac{\partial^2}{\partial z^2}+\kappa^2\right]E = -i\kappa\frac{4\pi}{c}J_p - 2i\kappa B_p\delta(r-R_p). \qquad (4)$$

In Fourier-Dini Series, E and J_p are expanded as

$$E = \sum_{m,n} e_{mn} J_1(p_m r) sin(q_n z) \quad (5)$$

$$J_p = \sum_{m,n} e_{mn} \sigma_{pm} \sqrt{2\pi} J_1(p_m r) sin(q_n z), \quad (6)$$

where $p_m = \frac{\lambda_{0m}}{R_p}$, $q_n = \frac{n\pi}{L}$, with zeroth order Bessel function J_0's m-th root λ_{0m}, and plasma radius R_p, and length L, and σ_{pm} is m-th coefficient of plasma conductivity σ_p in Dini series. Expanding δ function in Dini series, e_{mn}'s are presented as

$$e_{mn} = \frac{2i\kappa b_{p,n}}{R_p J_1(p_m R_p) D_{mn}}, \quad (7)$$

with

$$D_{mn} = p_m^2 + q_n^2 - \kappa^2 - i\kappa \frac{4\pi}{c} \sqrt{2\pi} \sigma_{pm}. \quad (8)$$

In order to determine the e_{mn}, we have to know two unknowns $b_{p,n}$ and σ_{pm}. The $b_{p,n}$ is n-th coefficient of B_p in Fourier series

$$b_{p,n} = \frac{2}{L} \int_0^L B_p sin(q_n z) dz, \quad (9)$$

and this is obtained from the matching magnetic field with the one of antenna region at plasma vacuum boundary, and σ_{pm} is given from the solution of the Boltzmann equation.

Mode excitation method

At first we write a vector identity of

$$\nabla \cdot (\vec{E} \times \vec{B}_{no} - \vec{E}_{no} \times \vec{B}) = \frac{4\pi}{c} \vec{J}_c \cdot \vec{E}_{no}, \quad (10)$$

where J_c is source current density, and subscript no means electromagnetic fields satisfying the source-free wave equation,

$$\left[\frac{\partial^2}{\partial r^2} + \frac{1}{r} \frac{\partial}{\partial r} - \frac{1}{r^2} + \frac{\partial^2}{\partial z^2} + \kappa^2 \right] E_{no} = 0, \quad (11)$$

with $\vec{E}_{no} = E_{no} \hat{\theta}$. The boundary condition for E_{no} is

$$E_{no} = 0 \qquad \text{at} \quad r = R_s,$$

where R_s is chamber radius. The solution of this equation is written as

$$E_{no} = \sum_n C_n g_n(r) sin(q_n z), \quad (12)$$

where

$$g_n(r) = K_1(\beta_n R_s) I_1(\beta_n r) - I_1(\beta_n R_s) K_1(\beta_n r),$$

and I_1, K_1 are the 1st order modified Bessel functions, and $\beta_n^2 = q_n^2 - \kappa^2$. From the Maxwell equation, magnetic field $\vec{B}_{no}$ is obtained as

$$\vec{B}_{no} = \frac{1}{i\kappa} \sum_n C_n [-q_n cos(q_n z) g_n(r) \hat{r} + \beta_n sin(q_n z) h_n(r) \hat{z}], \quad (13)$$

where

$$h_n(r) = K_1(\beta_n R_s) I_0(\beta_n r) + I_1(\beta_n R_s) K_0(\beta_n r).$$

Volume integrating eq.(10) in antenna region, we get the relation of

$$\int_{r=R_p} (E_{no} B_z - B_{no,z} E) R_p dz = \frac{4\pi}{c} \int_{r,z} J_c E_{no} r dr dz \quad (14)$$

on the assumption of $E = 0$ at $r = R_s$, $z = 0$, and $z = L$, where $\int_{r,z} = \int_0^L \int_{R_p}^{R_s}$. After matching the E to inner region solution, expanding B_z at R_p as

$$B_z = \sum_n b_{p,n} sin(q_n z), \quad (15)$$

and some algebraic calculation, we can get the presentation of $b_{p,n}$ as

$$b_{p,n} = 2\beta_n \frac{4\pi}{c} I_c \int_{r,z} \left(\frac{J_c}{I_c} \right) f_n(r) sin(q_n z) \frac{r}{L} dr dz, \quad (16)$$

where I_c is a source current,

$$f_n(r) = \frac{g_n(r)}{\beta_n R_p A - 2S_1(n) B}, \quad (17)$$

$$S_1(n) = \sum_m \left(\frac{\beta_n^2}{D_{mn}} \right), \quad (18)$$

and

$$A = K_1(\beta_n R_s) I_1(\beta_n R_p) - I_1(\beta_n R_s) K_1(\beta_n R_p),$$
$$B = K_1(\beta_n R_s) I_0(\beta_n R_p) + I_1(\beta_n R_s) K_0(\beta_n R_p).$$

Plasma conductivity

The Boltzmann equation in dominant order is written as

$$\frac{\partial f_1}{\partial t} + v_r \frac{\partial f_1}{\partial r} - \frac{e}{m} E \frac{\partial f_0}{\partial v_\theta} = \left(\frac{\partial}{\partial t} \right)_{col} f, \quad (19)$$

where $f_0, f_1, v_r, v_\theta, e, m, \left(\frac{\partial}{\partial t}\right)_{col}$ are equilibrium and perturbed electron velocity distribution, velocity components in axial and azimuthal directions, electron charge, electron mass, and collision operator respectively. Using uniform Maxwellian distribution function for equilibrium and $L \gg \delta$, where L is plasma length along axis and δ is a skin depth along radial direction. And using a Krook's model for collision operator, we get

$$-i(\omega + i\nu)f_1 + v_r \frac{\partial f_1}{\partial r} + \frac{e}{T} E v_\theta f_0 = 0, \qquad (20)$$

where ν and T are collision frequency between electron and neutral gas particle and electron temperature respectively. Let's define two functions as

$$\begin{aligned} \psi^+ &= \frac{1}{2}\{f_1(v_r) + f_1(-v_r)\} \\ \psi^- &= \frac{1}{2}\{f_1(v_r) - f_1(-v_r)\}, \end{aligned} \qquad (21)$$

where the functions ψ^+ and ψ^- are even and odd for v_r respectively. The perturbed electron distribution can be calculated as

$$f_1 = \psi^+ + \psi^-. \qquad (22)$$

And at boundary R_p, ψ^- must be zero for perfect reflection of particles. Then we can devide Boltzmann equation into two equations with parity.

$$\begin{aligned} -i(\omega + i\nu)\psi^+ + v_r \frac{\partial \psi^-}{\partial r} &= -\frac{eE}{T} v_\theta f_0 \\ -i(\omega + i\nu)\psi^- + v_r \frac{1}{r}\frac{\partial}{\partial r}(r\psi^+) &= 0 \end{aligned} \qquad (23)$$

on the assumption of $R_p \gg \delta$, and two equations are also even and odd for v_r. Because the electric field E is proportional to Bessel J_1, we can let the function ψ^+ and ψ^- be proportional to J_1 and J_0 respectively. So, we can write

$$\begin{aligned} \psi^+ &= \sum_m \psi_m^+ J_1(p_m r) \\ \psi^- &= \sum_m \psi_m^- J_0(p_m r), \end{aligned} \qquad (24)$$

with $J_0(p_m R_p) = 0$. Now, we expand E in Dini series,

$$E = \sum_m E_m J_1(p_m r), \qquad (25)$$

then we get the coefficient ψ_m^+ as

$$\psi_m^+ = \frac{ieE_m}{2T} v_\theta f_0 \left[\frac{1}{\omega + i\nu + p_m v_r} + \frac{1}{\omega + i\nu - p_m v_r}\right]. \qquad (26)$$

With the above solution, the m-th coefficient of current density in azimuthal direction is presented as a 1st moment of f_1,

$$\begin{aligned} J_m &= \frac{ie^2 n}{T} E_m \int \frac{v_\theta^2 f_0}{\omega + i\nu + p_m v_r} d\vec{v} \\ &= \sqrt{2\pi}\sigma_{pm} E_m, \end{aligned} \qquad (27)$$

where n is plasma density. So, plasma conductivity σ_{pm} is expressed as

$$\sigma_{pm} = \frac{ie^2 n}{\sqrt{2\pi}T} \int \frac{v_\theta^2 f_0}{\omega + i\nu + p_m v_r} d\vec{v}. \qquad (28)$$

And f_0 is assumed as Maxwellian distribution, so plasma conductivity σ_{pm} is reduced to

$$\sigma_{pm} = -\frac{ie^2 n}{2\sqrt{2\pi}T p_m} Z_p\left(\frac{\omega + i\nu}{p_m v_r}\right), \qquad (29)$$

where Z_p is plasma dispersion function.

Plasma impedance

The impedance of plasma is defined using an absorbed power into plasma as follows

$$Z_{pl} \equiv \frac{1}{|I_c|^2} \int_{pl.vol.} \vec{J}_p^{\,*} \cdot \vec{E} d\vec{x}. \qquad (30)$$

All plasma absorbing power is flowed through the plasma vacuum boundary, so plasma impedance is presented as a surface integral,

$$Z_{pl} = -\frac{2}{|I_c|^2} \int_{pl.surf.} \vec{s} \cdot \hat{n} da, \qquad (31)$$

where $\vec{s} = \frac{c}{8\pi}\vec{E} \times \vec{B}^*$ is a Poynting vector, and $\hat{n}$ is an outward unit vector. After some algebra, plasma impedance can be presented as

$$Z_{pl} = -\frac{1}{|I_c|^2} \frac{i\omega L}{2} \sum_{m,n} \frac{|b_{p,n}|^2}{D_{mn}}. \qquad (32)$$

III. NUMERICAL RESULT AND DISCUSSION

The calculation of plasma impedance is presented in this section. In these calculation, we let the chamber radius be $20cm$, chamber length $20cm$, and plasma radius $10cm$. And the parameters are fixed, if each not to be used as a variable, the plasma density at $10^{13}cm^{-3}$, plasma temperature $5eV$, excitation frequency $13.56MHz$, and

antenna coil radius and height $11cm$ and $10cm$ respectively.

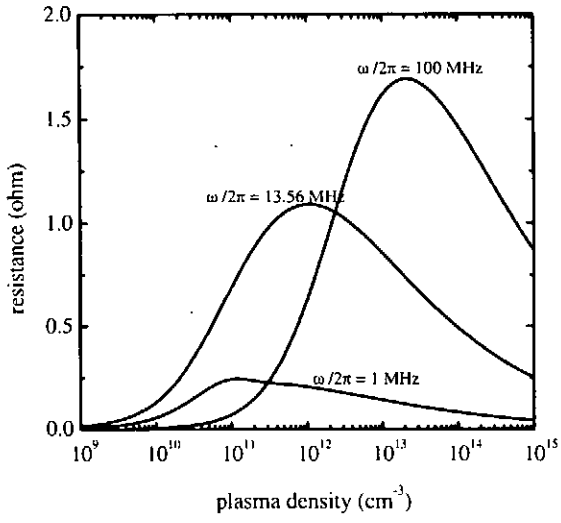

FIG. 2. Plasma resistance vs. plasma density n with various excitation frequencies

Figures 2 to 4 show the results with some system parameters, as plasma density, excitation frequency, and plasma temperature. At first, fig. 2 shows the dependance of plasma resistance on plasma density with varying excitation frequency. Along the same excitation frequency, the plasma resistance has a maximum at a certain plasma density. And these plasma density and maximum resistance go higher with excitation frequency.

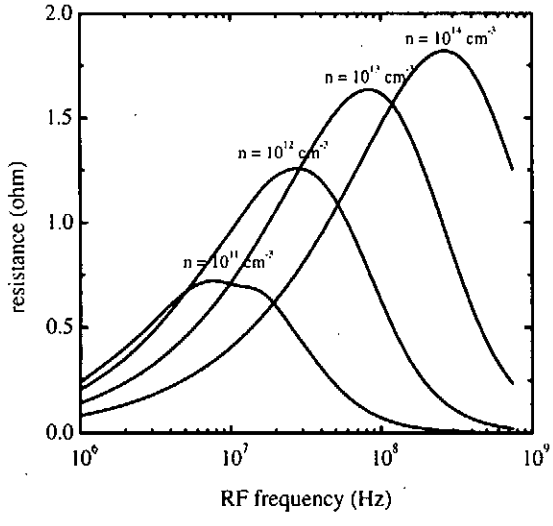

FIG. 3. Plasma resistance vs. excitation wave frequency with various plasma densities

Figure 3 shows plasma resistance as a function of excitation wave frequency with various plasma densities, which results in a similar situation with fig.2. These situations can be explained as, at low density (or low frequency), skin depth is the same with or larger than plasma size so that an absorbed power into plasma is proportional to plasma density (or RF wave frequency, when recall that inductive field is proportional to RF frequency), and at high density (or high frequency), skin depth is much smaller than plasma size so that absorbed power is merely proportional to skin depth but this skin depth is inversely proportional to plasma density (or RF frequency).

The fig. 4 shows dependence of plasma resistance on plasma temperature with varying RF frequency.

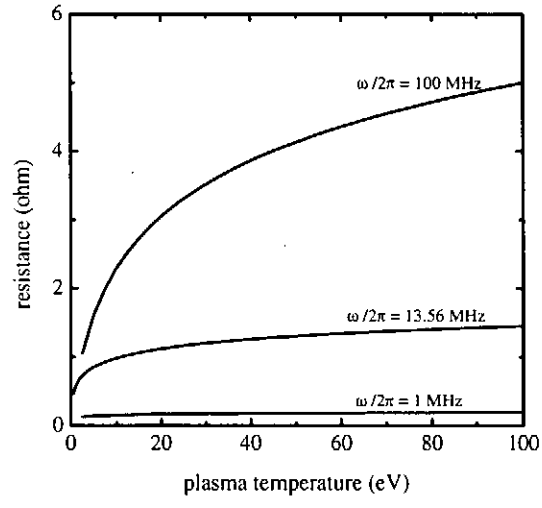

FIG. 4. Plasma resistance vs. plasma temperature T with various excitation frequencies

When plasma temperature goes higher, resistance increases because the particles resonating with RF frequency grow. And the resistance becomes higher with the frequency when plasma density is $10^{13}cm^{-3}$ (See fig.2).

Figure 5 shows the finite size effects of the coil antenna.

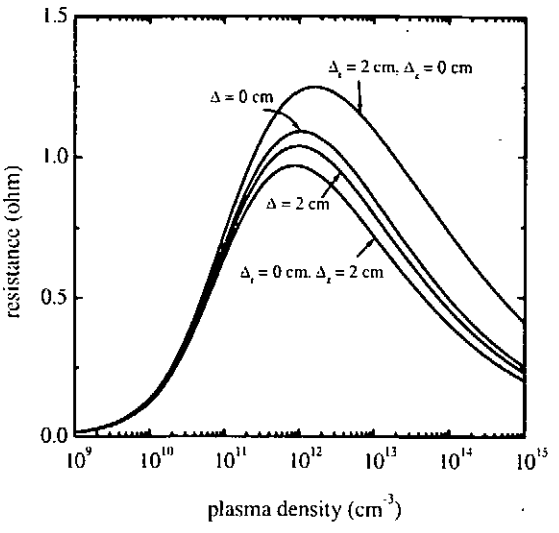

FIG. 5. Plasma resistance vs. plasma density n with various coil shape; Δ_r and Δ_z mean radial width and axial thickness, respectively, and Δ is used when width and thickness are the same.

When coil antenna has radial width, the plasma resistance is increasing, and when the coil antenna has axial thickness, the plasma resistance is decreasing. And coil has the same width and thickness, the plasma resistance is decreased slightly. This can be understood by seeing the fig.'s 6 and 7.

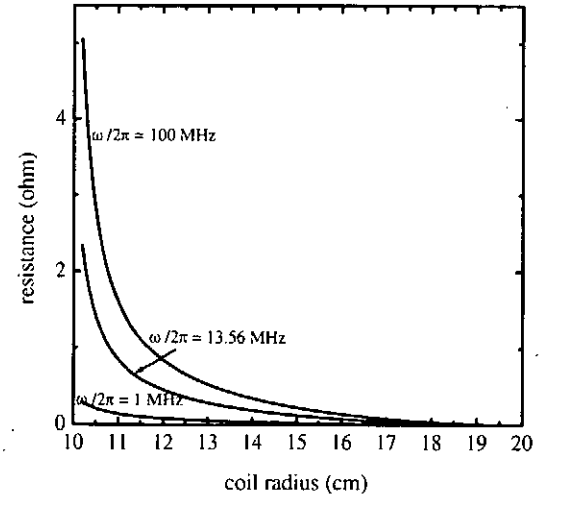

FIG. 6. Plasma resistance vs. coil radius with various excitation frequencies

Figures 6 and 7 are plots for the resistance as a function of antenna coil's position (radius and height).

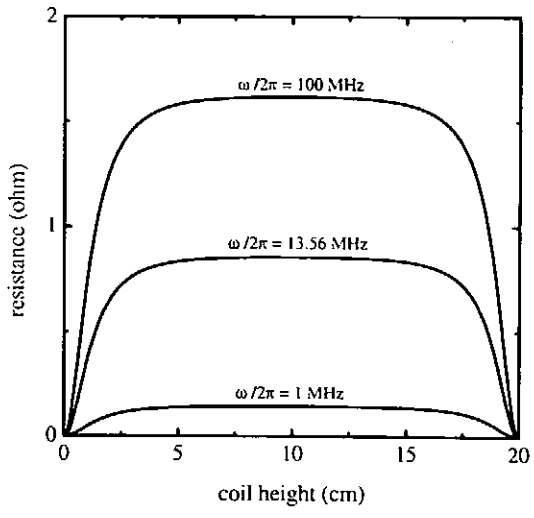

FIG. 7. Plasma resistance vs. coil height with various excitation frequencies

As coil is laid nearer the plasma, the resistance goes higher abruptly, and when the coil is laid at a half height of the plasma length, the resistance is maximum. So if coil has a radial width, inner part of the coil has positive effect and outer part has negative effect with a positive average. But if coil has an axial thickness, higher and lower part of the coil has negative effects together.

IV. CONCLUSION

For the theoretical impedance calculation of the solenoidal inductively coupled plasma, we solve the 2-dimensional Maxwell equations with the Boltzmann equation. From this solution, the plasma impedance is computed by a numerical method, in the wide variable parameter space. We can show the dependance of plasma impedance on the plasma density, excitation frequency, and plasma temperature. Through the calculation, we modeled the antenna coil as an infinitely thin and a finitely shaped wire. The effects of finite coil thickness and width are also investigated, and this is explained.

To know the total impedance of ICP device, we solve the wave equation in antenna region also. This subject is being studied now, and the results will be reported elsewhere.

For the self-consistent determination of plasma parameters, energy and particle tranport equations are solved, and this subject is also being investigated now.

[1] R. B. Piejak, V. A. Godyak and B. M. Alexandrovich, Plasma Sources Sci. Technol. **3** 169 (1994).
[2] M. M. Turner, Phys. Rev. Lett. **71**, 1844 (1993).
[3] E. S. Weibel, Phys. of Fluids, **10**, No. 4, 741 (1967).
[4] J. A. Reynolds, H. A. Blevin, and P. C. Thonemann, Phys. Rev. Lett. **22**, No. 15, 762 (1969).
[5] H. A. Blevin, J. A. Reynolds, and P. C. Thonemann, Phys. of Fluids, **13**, No. 5, 1259 (1970).
[6] Y. S. Sayasov, Helv. Phys. Acta, **52**, 288 (1979).
[7] N. S. Yoon, S. S. Kim, C. S. Chang, and D. I. Choi, Phys. Rev. E, **54**, No. 1, 757 (1996).
[8] N. S. Yoon, S. M. Hwang, and D. I. Choi, Phys. Rev. E, **55**, no. 6, 7536, (1997).
[9] J. D. Jackson, *Classical Electrodynamics*, (John Wiley & Sons, New York, 1975).

Theoretical study on helicon plasma discharge

B. H. Park, D. I. Choi and N. S. Yoon*
Department of Physics, Korea Advanced Institute of Science and Technology, Taejeon 305-701, Korea
** Korea Basic Science Institute, Taejeon 305-333, Korea*

We obtain the analytic solution of the wave equation with the cold plasma conductivity under realistic discharge conditions of helicon device which has a finite width antenna. Utilizing this solution, we calculate the plasma and antenna impedances as functions of various operational parameters such as width of antenna, plasma density, external magnetic field intensity, and so on.

I. INTRODUCTION

Many researchers are tried to give comprehension about the electromagnetic field in the helicon plasma device.[1]-[4] But they can't get the total impedance of antenna. In their studies, the antenna is considered as infinitly thin wire. It cause infinit antenna impedance. So, we consider the antenna with its width is finite. It gives the finite antenna impedance, we expect it is useful for circuit analysis.

II. WAVE EQUATION

The model of the helicon device used in our study is shown in Fig. 1. The plasma is filled in the region $0 \leq r \leq a$, and $-\frac{S}{2} \leq z \leq \frac{S}{2}$. Antenna is located at $r = b$, and has its length L, width W. The outer edge is assumed to be a perfectly conducting wall.

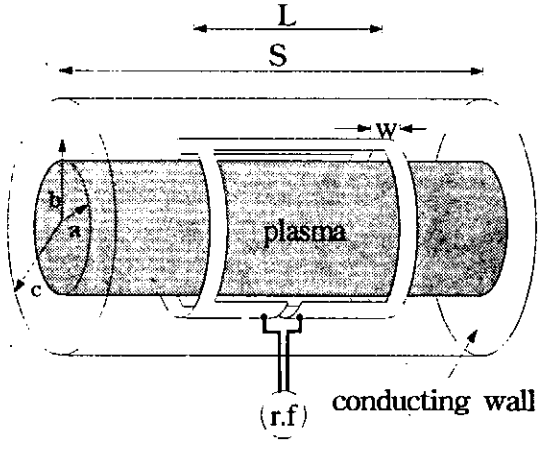

FIG. 1. Schematic diagram of helicon source

We assume that all the quantities we are interested in have dependence of $e^{-i(\omega t+im\vartheta)}sin(k_n z)$ or $e^{-i(\omega t+im\vartheta)}sin(k_n z)$. Therefore we only treat the radially dependent parts. Fig. 2 shows the region to be considered.

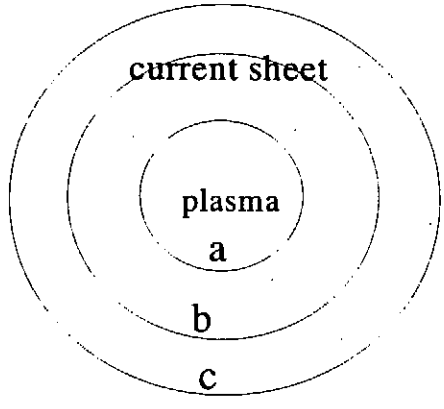

FIG. 2. Radial region to be solved

A. Governing equation

We start with Maxwell equation

$$\nabla \times \vec{E} = -\frac{1}{c}\frac{\partial \vec{B}}{\partial t} \tag{1}$$

$$\nabla \times \vec{B} = \frac{1}{c}\frac{\partial \vec{E}}{\partial t} + \frac{4\pi}{c}\vec{J}. \tag{2}$$

With the following assumption which satisfies the boundary conditions of the end plates,

$$\begin{aligned} &E_z \sim \cos k_z \\ &E_\vartheta, E_r \sim \sin k_z \\ &B_z \sim \sin k_z \\ &B_r, B_\vartheta \sim \cos k_z \end{aligned} \tag{3}$$

these vector equations are resolved into its components

$$\frac{im}{r}E_z - kE_\vartheta = \frac{i\omega}{c}B_r \tag{4}$$

$$kE_r - \frac{\partial E_z}{\partial r} = \frac{i\omega}{c}B_\vartheta \tag{5}$$

$$\frac{1}{r}\frac{\partial}{\partial r}(rE_\vartheta) - \frac{im}{r}E_r = \frac{i\omega}{c}B_z \tag{6}$$

$$\frac{im}{r}B_z + kB_\vartheta = -\frac{i\omega}{c}E_r + \frac{4\pi}{c}J_r \quad (7)$$

$$-kB_r - \frac{\partial B_z}{\partial r} = -\frac{i\omega}{c}E_\vartheta + \frac{4\pi}{c}J_\vartheta \quad (8)$$

$$\frac{1}{r}\frac{\partial}{\partial r}(rB_\vartheta) - \frac{im}{r}B_r = -\frac{i\omega}{c}E_z + \frac{4\pi}{c}J_z. \quad (9)$$

For convenience we define the following notations and normalize r with $\frac{c}{\omega}$.

$$F_\pm \equiv F_r \pm iF_\vartheta$$
$$\partial_\pm \equiv \left(\frac{\partial}{\partial r} \mp \frac{m}{r}\right)$$
$$J_\pm \equiv \sigma^\pm E_\pm$$
$$\epsilon^\pm \equiv 1 + \frac{4\pi i}{\omega}\sigma^\pm$$
$$k_n \equiv \frac{2\pi}{S}n, (n = 1, 2, 3, ...)$$
$$N \equiv \frac{ck_n}{\omega}.$$

Then Eq. (4)-(9) can be expressed as

$$kE^+ - \partial_+ E_z = B^+ \quad (10)$$

$$kE^- - \partial_- E_z = -B^- \quad (11)$$

$$\frac{1}{2r}\partial_-(rE^+) - \frac{1}{2r}\partial_+(rE^-) = -B_z \quad (12)$$

$$kB^+ + \partial_+ B_z = \epsilon^+ E^+ \quad (13)$$

$$kB^- + \partial_- B_z = -\epsilon^- E^- \quad (14)$$

$$\frac{1}{2r}\partial_-(rB^+) - \frac{1}{2r}\partial_+(rB^-) = \epsilon_z E_z \quad (15)$$

where $\sigma^\pm = \frac{i\omega_p^2}{4\pi(\omega \pm \Omega_e + i\nu)}$ and $\sigma^z = \frac{i\omega_p^2}{4\pi(\omega + i\nu)}$. Using Eq.(10)-(15), we can make equations containing only E_z and B_z.

$$\epsilon^z E^z = \frac{1}{2(\epsilon^+ - N^2)}\mathcal{L}_m\left(NB^z - \epsilon^+ E^z\right) - \frac{1}{2(\epsilon^- - N^2)}\mathcal{L}_m\left(NB^z + \epsilon^- E^z\right) \quad (16)$$

$$-B^z = \frac{1}{2(\epsilon^+ - N^2)}\mathcal{L}_m\left(-NE^z + B^z\right) + \frac{1}{2(\epsilon^- - N^2)}\mathcal{L}_m\left(NE^z + B^z\right). \quad (17)$$

The linear differential operator $\mathcal{L}_m$ is defined as

$$\mathcal{L}_m \equiv \frac{1}{r}\partial_\pm(r\partial_\mp)\Psi(r) = \left(\frac{\partial^2}{\partial r^2} + \frac{1}{r}\frac{\partial}{\partial r} - \frac{m^2}{r^2}\right)\Psi(r).$$

The linear differential operator $\mathcal{L}_m$ has eigenfunctions which are $J_m(\nu r)$ and $N_m(\nu r)$ with eigenvalue $-\nu^2$. Neumann function goes infinity at origin therefore only Bessel function can be the solution. If we set

$$\begin{pmatrix} E_z \\ B_z \end{pmatrix} \sim J_m(\nu r), \quad (18)$$

then Eq. (16)-(17) can be written as a system of linear equations

$$\begin{bmatrix} \epsilon^z - \nu^2 A & \nu^2 B \\ \nu^2 B & 1 - \nu^2 C \end{bmatrix}\begin{bmatrix} E_z \\ B_z \end{bmatrix} = 0 \quad (19)$$

where,

$$A = \frac{\epsilon^+}{2(\epsilon^+ - N^2)} + \frac{\epsilon^-}{2(\epsilon^- - N^2)}$$
$$B = \frac{N}{2(\epsilon^+ - N^2)} - \frac{N}{2(\epsilon^- - N^2)}$$
$$C = \frac{1}{2(\epsilon^+ - N^2)} + \frac{1}{2(\epsilon^- - N^2)}.$$

b becomes zero when external magnetic field or plasma density goes to zero. So, off-diagonal term of Eq. 19 is not zero in general. This fact prevents fields from being pure TE or TM mode. Therefore electromagnetic fields are nearly TE or nearly TM. Above linear algebraic equation has two solutions which are helicon(nearly TE) mode and T.G.(nearly TM) mode. When the determinant of matrix in Eq. 19 is zero, fields can alive. The determinant zero condition gives two radial eigenvalues, ν_1 and ν_2. Then z components of electric and magnetic fields can be written as

$$E_z^a(r) = \beta_1 B_z^a J_m(\nu_1 r) + E_z^a J_m(\nu_2 r) \quad (20)$$

$$B_z^a(r) = B_z^a J_m(\nu_1 r) + \beta_2 E_z^a J_m(\nu_2 r), \quad (21)$$

where superscript 'a' denotes 'the plasma region', $\beta_1 = -\frac{\nu_1^2 B}{\epsilon^z - \nu_1^2 A}$ and $\beta_2 = -\frac{\nu_2^2 B}{1 - \nu_2^2 C}$. But in the vacuume region 'b' or 'c', the Eq. 19 is separated into two independent equations

$$\mathcal{L}_m(E_z) + (1 - N^2)E_z = 0 \quad (22)$$

$$\mathcal{L}_m(B_z) + (1 - N^2)B_z = 0. \quad (23)$$

Its solution is modified bessel functions, therefore z components of electric and magnetic fields are

$$E_z^b = E_{z1}^b I_m(\delta r) + E_{z2}^b K_m(\delta r) \quad (24)$$

$$B_z^b = B_{z1}^b I_m(\delta r) + B_{z2}^b K_m(\delta r) \quad (25)$$

$$E_z^c = E_{z1}^c I_m(\delta r) + E_{z2}^c K_m(\delta r) \quad (26)$$

$$B_z^c = B_{z1}^c I_m(\delta r) + B_{z2}^c K_m(\delta r) \quad (27)$$

here superscripts 'b' and 'c' also denote vacuume regions shown in Fig. 2 and $\delta^2 = N^2 - 1$. All other components of electric and magnetic fields come from Eq. (10)-(15).

B. Antenna modeling

The antenna current is modeled based on Nagoya Type III antenna with width of W, and length of L. The Nagoya type III antenna is designed as the azimuthal current changes its direction on two points of antenna. The azimuthal antenna current density is firstly to be defined then the condition of $\nabla \cdot \vec{J} = 0$ gives axial antenna current density naturally. The azimuthal antenna current has to be designed carefully. If current changes abruptly like step function in azimuthal direction then $\nabla \cdot \vec{J} = 0$ condition gives filament axial current. This can not be a model of the finite width antenna. So, we smooth the azimuthal current a little. Final model current density is

$$
\begin{aligned}
J_\vartheta = & \sum_{m=-\infty}^{+\infty} \sum_{n=1}^{+\infty} I_a \delta(r-b) \frac{8}{\pi} sin(\frac{\pi}{2}m) cos(\frac{\Delta\vartheta}{2}m) \\
& \times \left(\frac{1}{m} + \frac{m}{\left(\frac{\pi}{\Delta\vartheta}\right)^2 - m^2} \right) sin(k_n \frac{L}{2}) \\
& \times sin(k_n \frac{W-\Delta z}{2}) sin(k_n \frac{\Delta z}{2}) \frac{1}{\Delta z k_n^2 S(w-\Delta z)} \\
& \times sin(k_n z) e^{im\vartheta} \\
J_z = & \sum_{m=-\infty}^{+\infty} \sum_{n=1}^{+\infty} I_a \delta(r-b) \frac{8}{\pi} sin(\frac{\pi}{2}m) cos(\frac{\Delta\vartheta}{2}m) \\
& \times \left(\frac{1}{m} + \frac{m}{\left(\frac{\pi}{\Delta\vartheta}\right)^2 - m^2} \right) sin(k_n \frac{L}{2}) \\
& \times \sin(k_n \frac{W-\Delta z}{2}) sin(k_n \frac{\Delta z}{2}) \\
& \times \frac{im}{\Delta z k_n^3 S b(w-\Delta z)} cos(k_n z) e^{im\vartheta}.
\end{aligned}
$$

In the above equations, Δz, $\Delta\vartheta$ are the smoothing factors and $n = 0$ component is not included. It will be treated in the next section.

C. $n = 0$ axial mode

When $n = 0$, fields are to be calculated by a different way. The solution in the plasma region

$$
E_z^a = \frac{b}{a} \frac{(J_m(b)N_m(c) - N_m(b)J_m(c)) \frac{4\pi}{c} I_a g_z^{m,0}}{Z_1 - Z_2} \quad (28)
$$

$$
E_\pm^a = 0,
$$

where

$$
\begin{aligned}
Z_1 &= J_m'(\nu a)(J_m(c)N_m(a) - N_m(c)J_m(a)) \\
Z_2 &= J_m(\nu a)(J_m(c)N_m'(a) - N_m(c)J_m'(a)). \\
g_z^{m,0} &= sin(\frac{\pi}{2}m) cos(\frac{\Delta\vartheta}{2}m)
\end{aligned}
$$

$$
\times \left(\frac{1}{m} + \frac{m}{\left(\frac{\pi}{\Delta\vartheta}\right)^2 - m^2} \right) \frac{i2mL}{\pi b S} \quad (29)
$$

III. ANTENNA AND PLASMA IMPEDANCE

Antenna impedance is defined as the total impedance across the antenna. It is

$$
Z_a = -\frac{1}{|I_a|^2} \int_{v_a} \vec{J}^* \cdot \vec{E} dv. \quad (30)
$$

IV. NUMERICAL RESULT AND DISCUSSION

With the radial boundary condition, we can solve all the field components. Fig.3 shows dispersion

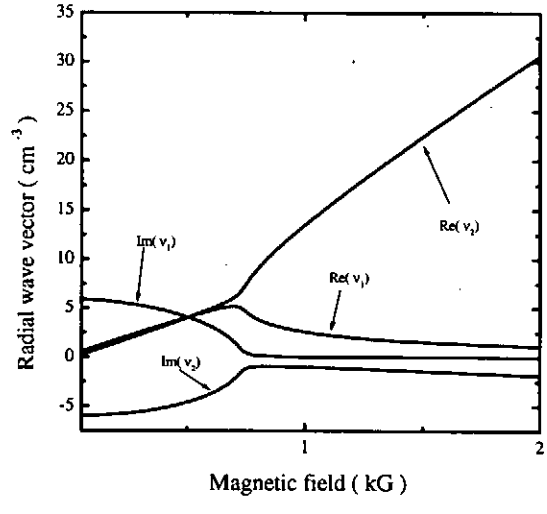

FIG. 3. Radial wave vector of helicon and T.G wave when $n = 10^{13} cm^{-3}$, $\nu_{collision}/\omega = 0.06$ and m=1,n=1.

Here, radial vector ν_1 and ν_2 correspond to helicon and T.G mode respectively. Imaginary part of ν_1 abruptly goes to zero when external magnetic field reaches some value. Therefore if external magnetic field is larger than some value then T.G. mode can not penetrate into plasma but helicon mode can. But Fig. 4 shows that the above comments are correct. Global feature resembles the helicon mode but, because of T.G mode, field is very rapidly oscillating in the vicinity of plasma vacuum boundary. It is the same structure shown in Ref.[5].

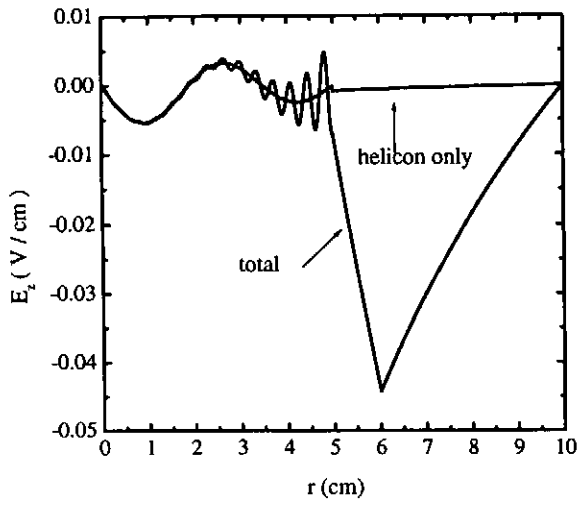

FIG. 4. Radial profile of E_z field when $n = 10^{13} cm^{-3}$, $B = 1.2kG$, $\nu_{collision}/\omega = 0.06$ and m=1,n=1.

Fig. 5 shows that antenna resistance is not so sensitive to antenna width but Fig. 6 shows that $Im(Z)$ is sensitive to antenna width. If we consider filament type antenna then $Im(Z)$ will be infinity. This the reason why we take finit width antenna into account. Fig. 7 is the contour plots of the helicon mode and T.G. for external magnetic field and plasma density. The right side is correspond to helicon mode and left side to T.G. mode. It shows that the helicon mode follows the well known helicon dispersion relation.

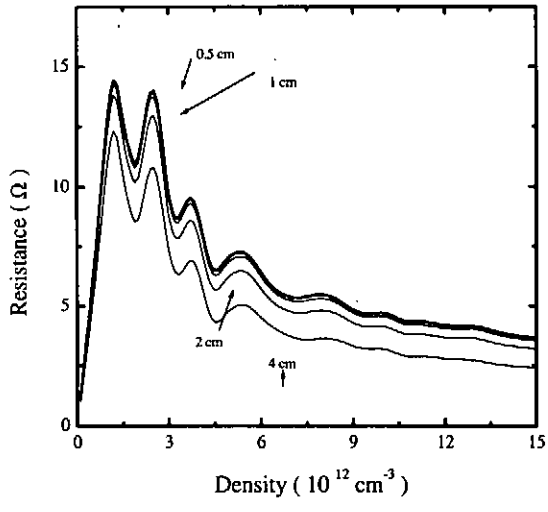

FIG. 5. Resistance of antenna vs. density with $B = 600G$, $\nu_{collision}/\omega = 0.2$ and m=1,n=1.

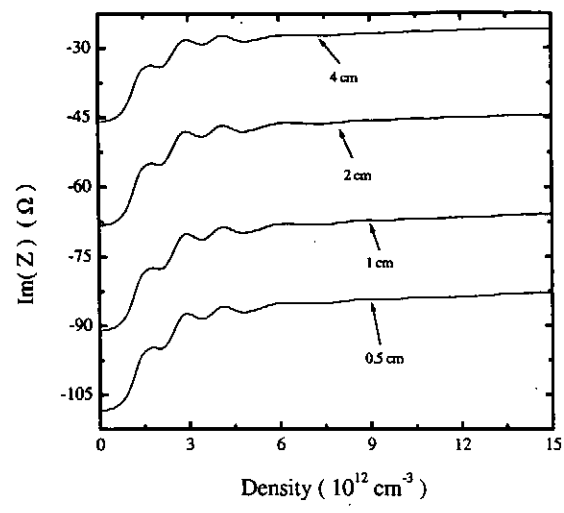

FIG. 6. $Im(Z)$ of antenna vs. density with $B = 600G$, $\nu_{collision}/\omega = 0.2$ and m=1,n=1.

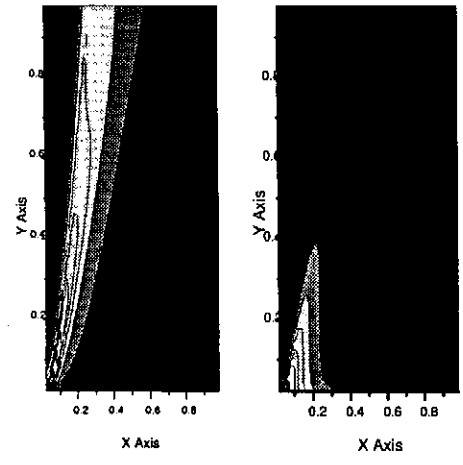

FIG. 7. Contour plot of helicon and T.G. mode when $\nu_{collision}/\omega = 0.2$ and m=1,n=1.

V. SUMMARY

We calculate the wave fields and the antenna impedances for the more realistic helicon device model. The helicon mode can penetrate into the plasma but T.G. mode can't. Antenna registance is not sensitive to antenna width but imaginary part of antenna impedance is goes to large value as antenna width goes to narrow size.

[1] K. P. Shamrai and V. B. Taranov, Plasma Phys.

Control. Fusion **36**,1719 (1994).
[2] K. P. Shamrai and V. B. Taranov, Physics Letter A **204**,139 (1995).
[3] S. W. Cho, Phys. Lett. A (1996).
[4] S. W. Cho, Phys. Plasmas. A (1996).
[5] F. F. Chen and Donald Arnush, *Generalized theory of helicon waves I: Normal modes*, UCLA Report PPG-1562(Revised) (1996).

Excitation and absorption of electromagnetic waves in helicon discharges by plasma immersed antennas

Suwon Cho
Kyonggi University, Suwon, Kyonggi-Do 442-760, Korea

Excitation and absorption of electromagnetic waves are numerically studied for helicon discharges driven by antennas immersed in the plasma. The Maxwell equations are reduced to a set of ordinary differential equations, which are solved for radially inhomogeneous plasmas by using the shooting method. Numerical results show that the plasma resistance is much larger and its peaks due to eigenmode resonance appear at higher densities for the immersed antenna case than for the case of the antenna located outside the plasma under otherwise same conditions. It is also found that the $m = -1$ mode can be excited in the nonuniform plasma with an inner antenna, while it can be hardly excited when the plasma is driven by an outer antenna. In addition, the fast wave approximation neglecting the electron inertia is discussed.

I. INTRODUCTION

Helicon plasmas have been of interest primarily because the high plasma density can be attained with a modest rf power [1–3]. It has been known that the density of a helicon plasma is linearly proportional to the magnetic field and there can be step-like increase in the density as the external parameters such as the input power, the rf frequency, and the magnetic field vary. Recently, the dependence of the plasma density on these parameters was explained in terms of the power balance [4–6].

There exist two kinds of wave in helicon plasmas; one is the fast electromagnetic wave called the helicon wave and the other is the Trivelpiece-Gould (TG) mode which is quasi-electrostatic. The rf frequency is quite smaller than the electron cyclotron frequency and the electron plasma frequency under the typical condition of helicon plasmas so that the electron inertia has been usually neglected, which is equivalent to assume that the wave electric field is transverse. This assumption utterly misses the existence of the TG mode and has been widely used in interpreting experimental results. But it has been recently found that eigenmode resonance is due to the TG mode which is heavily damped near the plasma boundary [7], the TG mode plays a major role in determining the plasma density [8], and, the fast wave approximation or the TE (transverse electric) approximation is not valid to describe the wave field in helicon plasmas [8].

However, these results are only applicable to the device where the antenna is located outside the plasma and there is a vacuum gap between the plasma and the conducting wall. When the antenna is inside the plasma, the helicon wave is the dominant mode for eigenmode resonance and it penetrates deeply into the plasma across the magnetic field. The plasma resistance is very large to be order of 10^1 Ω in the helicon discharge by an immersed antenna [9], while it is order of 10^0 Ω for the case of the outer antenna discharge [8]. Therefore, it is worthwhile to study in detail characteristics of helicon plasmas driven by immersed antennas along with the validity of the fast wave approximation and, consequently, to investigate the effect of the large plasma resistance on the plasma density.

In this work, the fast wave approximation is examined by comparing its results to those of the full wave analysis. The shooting method is used to obtain numerical solutions for the electromagnetic field and the power absorption in helicon plasmas with nonuniform density profiles. The plasma resistance is then obtained as a function of the density and its characteristics are compared for plasmas driven by inner and outer antennas.

II. MODEL EQUATIONS

The model of the helicon plasma device used in this study is depicted in Fig. 1. The plasma is confined in the region $0 \leq r \leq r_p$, and there is a single loop antenna at r_a, and the length of the antenna is a. Conducting plates are assumed to be located at $z = 0, L$. With the Fourier series

expansion for the current density and the electromagnetic fields [9], the Maxwell equations are combined to yield

$$E'_\phi = \left(\frac{m\epsilon_2}{\rho\epsilon_1} - \frac{1}{\rho}\right) E_\phi - \frac{Nm}{\epsilon_1\rho} B_\phi + \left(1 - \frac{m^2}{\epsilon_1\rho^2}\right) B_z, \tag{1}$$

$$E'_z = \delta E_\phi + \left(1 - \frac{N^2}{\epsilon_1}\right) B_\phi - \frac{Nm}{\epsilon_1\rho} B_z, \tag{2}$$

$$B'_\phi = \left(\frac{m^2}{\rho^2} - \epsilon_3\right) E_z - \frac{Nm}{\rho} E_\phi - \frac{B_\phi}{\rho}, \tag{3}$$

$$B'_z = -\alpha E_\phi - \frac{Nm}{\rho} E_z - \delta B_\phi - \frac{m\epsilon_2}{\rho\epsilon_1} B_z, \tag{4}$$

where $E_\phi = -iE_\theta$, $B_\phi = iB_\theta$, $\rho = r\omega/c$, $N = k_l c/\omega$, $k_l = l\pi/L$, $\alpha = \epsilon_1 - N^2 - \epsilon_2^2/\epsilon_1$, $\beta = \epsilon_3\left(1 - N^2/\epsilon_1\right)$, $\gamma = N\epsilon_2\epsilon_3/\epsilon_1$, $\delta = N\epsilon_2/\epsilon_1$, and ϵ's are elements of the cold plasma dielectric tensor.

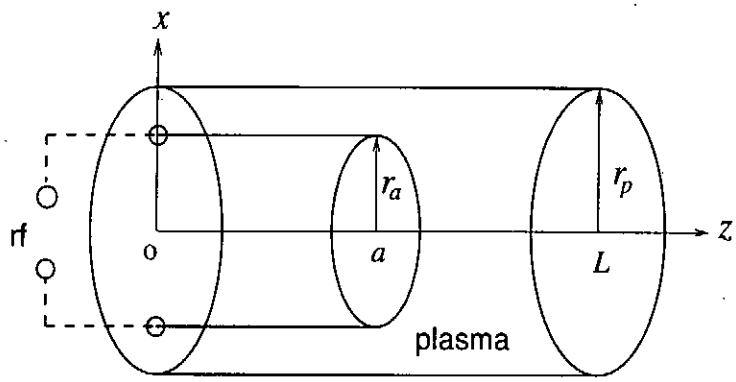

FIG. 1. The model of the helicon plasma device with an single loop antenna immersed in the plasma.

For a uniform plasma, Eqs. (1)-(4) can be reduced into [8]

$$B''_z + \frac{1}{\rho} B_z + \left(\alpha - \frac{m^2}{\rho^2}\right) B_z = \gamma E_z, \tag{5}$$

$$E''_z + \frac{1}{\rho} E_z + \left(\beta - \frac{m^2}{\rho^2}\right) E_z = \delta B_z. \tag{6}$$

If the electron inertia is ignored to take $E_z = 0$, then B_z is described by [8]

$$B''_z + \frac{1}{\rho} B'_z + \left(p^2 - \frac{m^2}{\rho^2}\right) B_z = 0 \tag{7}$$

where p satisfies the relation $p^2 = \epsilon_1^2 - N^2 - \epsilon_2^2/(\epsilon_1^2 - N^2)$.

The power absorbed by the plasma is given by

$$P_{\text{abs}} = \frac{\omega}{8\pi} \text{Im}\left[\mathbf{E} \cdot \epsilon^* \cdot \mathbf{E}^*\right] \tag{8}$$

where ϵ is the dielectric tensor, and it can be expressed as

$$P_{\text{abs}} = \frac{1}{2} R_{\text{p}} I_a^2 \tag{9}$$

where R_{p} is the plasma resistance and I_a is the antenna current.

III. COMPUTATIONAL METHOD

For a uniform plasma, the solution of the wave equation can be expressed in terms of Bessel functions and the expansion coefficients can be determined analytically from the jump condition at the antenna and the zero electric field condition at the chamber wall [9].

The electromagnetic field in a nonuniform plasma can be obtained numerically by using the shooting method [10]. The set of differential equations given by Eqs. (1)-(4) is integrated from the antenna at r_a to the wall at r_p with the jump condition and with zero fields for $0 < r < r_a$. Next, it is also integrated from the origin with trial boundary values, which are then to be corrected iteratively by the shooting method to satisfy the boundary condition at the wall. The linear combination of these solutions satisfy both conditions at the antenna and at the wall.

IV. RESULTS

The fast wave approximation is examined for a uniform plasma and its results are presented in Figs. 2 and 3, for which the following parameters are taken: $L = 50$ cm, $\omega/2\pi = 13.56$ MHz, $\nu_e/\omega = 0.2$, $r_p = 10$ cm, $r_a = 5$ cm, $a = L/2$, and $I_a = 1$ A. Figure 2 shows that there is difference between the results of the full analysis and the fast wave approximation in both values of the plasma resistance and the densities giving the peaks of the resistance. At $n_p = 3.69 \times 10^{11}$ cm^{-3} where the resistance is the same for both methods, the power deposition profiles are presented in Fig. 3 where the heavy and thin solid lines represent the result of the full wave analysis and the fast wave approximation, respectively. The approximation gives a profile which is quite different from that of the full analysis. The discontinuity near the antenna location ($r = 5$ cm) is due to the fact that the jump condition is not exactly satisfied with the approximation [8]. Comparing the absorption only by the fast wave component (in the full analysis) with the total absorption, it is seen that the oscillatory part comes from the contribution of the TG mode having a short wavelength. The TG contribution is not substantial so that the absorption only by the fast helicon wave can reasonably represent the total amount of absorption. For the case of nonuniform plasmas, the fast wave component is no longer separable with the shooting method, and the discrepancy between the results of the full wave analysis and the fast wave approximation is found to be larger from numerical studies.

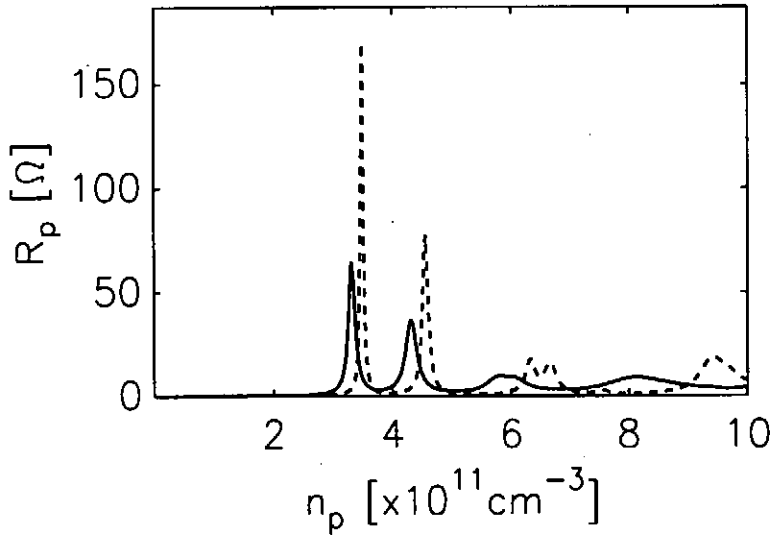

FIG. 2. The plasma resistance as a function of the plasma density at $B_0 = 300$ G for the uniform density profile. The dashed line represents the result of the fast wave approximation. The included modes are $m = \pm 1, \pm 3$ and $l = 1, 3$.

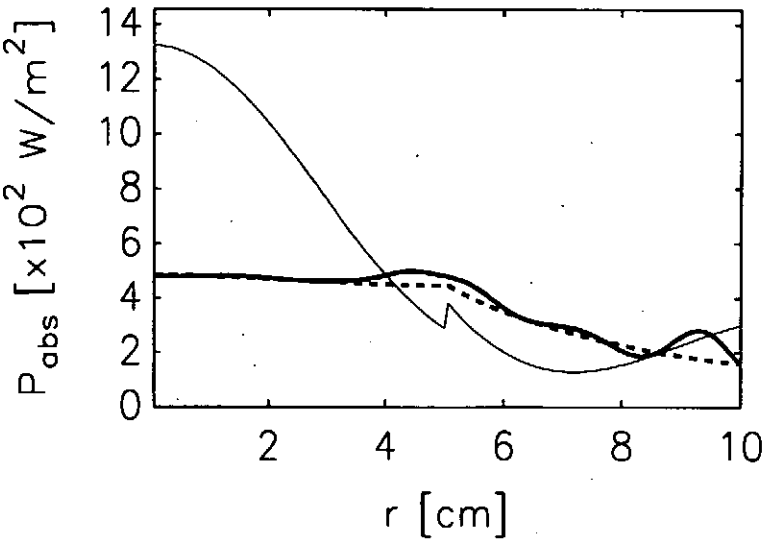

FIG. 3. The radial power absorption profile $\int_0^L \int_0^{2\pi} P_{\rm abs} d\theta dz$ is given for the unit antenna current at $n = 3.69 \times 10^{11}$ cm^{-3}, where the full analysis and the fast wave approximation yield the same amount of the total power absorption. The heavy and thin solid lines represent the result of the full wave analysis and the fast wave approximation, respectively, and the dashed line represents the absorption only by the fast wave component in the full wave analysis.

To investigate the effect of the antenna location, a numerical example for the plasma with an outer antenna is taken in such a way that the plasma volume is the same as that of the previous example for the immersed antenna. Then the power loss is identical for both plasmas under otherwise same conditions. The plasma is confined in the region $0 < r < r_p$ ($r_p = 10$ cm), an antenna and a conducting wall are assumed to be located at $r_a = 11$ cm and $r_b = 15$ cm, respectively. The density is assumed to have the profile of the zeroth order Bessel function in both models. In Fig. 4(a), the plasma resistance is presented as a function of the average density for both inner and outer antenna configurations. The first and second main peaks are due to the first radial eigenmodes with $m = 1$ and $l = 1$, and $m = 1$ and $l = 3$, respectively, for both cases.

As shown in Fig. 4(a), the resistance is generally larger and its peak values are much larger for the case of the immersed antenna. This can lead to the higher efficiency of the rf power absorption, which is defined as

$$P_{\rm net} = \frac{R_{\rm p}}{R_{\rm p} + R_{\rm c}} P_{\rm rf} \equiv \eta P_{\rm rf} \tag{10}$$

where $R_{\rm c}$ is the equivalent conduction resistance of the device, and $P_{\rm net}$ and $P_{\rm rf}$ are the net power absorbed by the plasma and the rf power from the power supply, respectively [11]. $R_{\rm c}$ consists of the resistance from components such as the antenna, the matching box,and the transmission line. $R_{\rm c}$ is assumed to be 0.5 Ω to obtain the power coupling efficiency η presented in Fig. 4(b) for the case of Fig. 4(a). The plasma density is determined from the intersection point of the resistance curve and the power loss line in the region of $\partial P_{\rm net}/\partial n < 0$ or $\partial \eta/\partial n < 0$ for a fixed rf power [4]. Fig. 4 indicates that the coupling efficiency and the density may be slightly higher for the case of the immersed antenna.

As seen from Fig. 5(a), the inhomogeneity of the plasma density results in strong suppression of the $m = -1$ mode when the antenna is outside the plasma. But, there is non-trivial contribution of the $m = -1$ mode to the resistance for the inhomogeneous plasma driven by the immersed antenna, and this contribution appear in the higher density region than that of the $m = 1$ mode. The different values of R_p between the two modes is not significant in the coupling efficiency, since R_c is much smaller than R_p. This implies that a high density discharge may be sustained by exciting the $m = -1$ mode in the plasma with an immersed antenna.

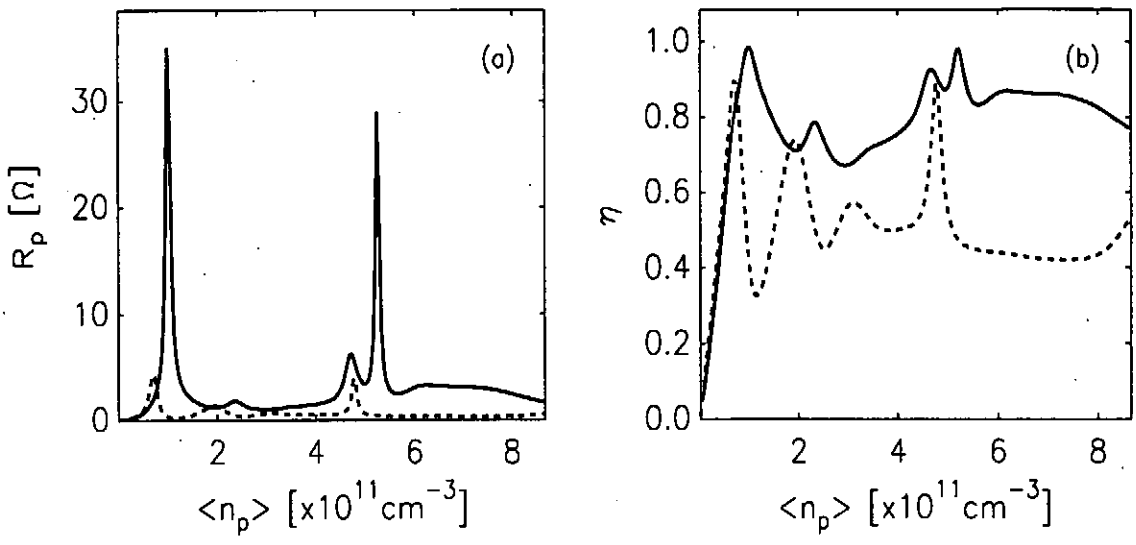

FIG. 4. The plasma resistance (a) and the power coupling efficiency (b) are given as a function of the average density at $B_0 = 300$ G for the inner (solid) and outer (dashed) antennas ($R_c = 0.5$ Ω). The included modes are $m = \pm 1, \pm 3$ and $l = 1, 3$.

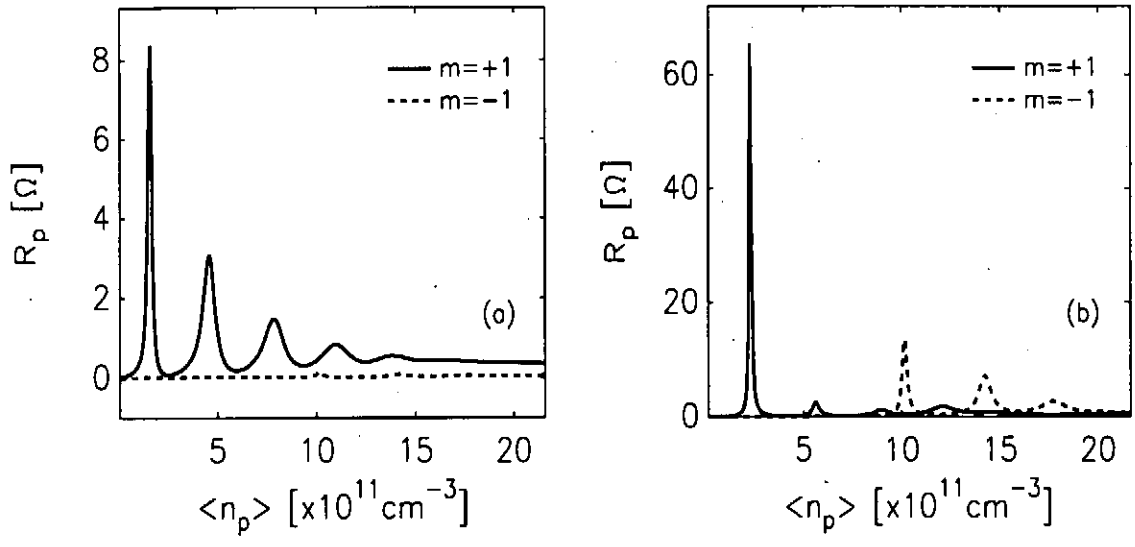

FIG. 5. The plasma resistance of the $l = 1$ mode as a function of the average density for (a) the outer and (b) inner antenna cases at $B_0 = 600$ G.

V. SUMMARY

When the antenna is immersed in the plasma, the contribution of the TG component to the power absorption is not substantial so that the absorption only by the helicon component can represent the total amount. However, it does not mean that the fast wave approximation is valid. In other words, if the existence of the TG mode is not taken into account from the beginning of the analysis, the result is not good in estimating neither the loading resistance nor the power deposition profile, although resonance is due to the fast helicon wave. It has been also found that the plasma resistance is much larger and its peaks appear in a higher density range for the case of an inner antenna than for the outer antenna case under otherwise same conditions. These results suggest that there is a

possibility to attain a higher density discharge operating at a higher coupling efficiency by using the inner antenna. The inhomogeneity of the plasma density influences the azimuthal structure of the electromagnetic field, and its effect depends on the antenna configuration. The $m = -1$ mode can be excited in the nonuniform plasma with an immersed antenna, while it can be hardly excited when the plasma is driven by an outer antenna.

ACKNOWLEDGEMENT

This work has been supported in part by Korea Basic Science Institute and the Korea Ministry of Education through Research Fund (BSRI-96-2458).

REFERENCES

[1] A. J. Perry, D. Vender, and R. W. Boswell, J. Vac. Sci. Technol. A **10**, 310 (1991).
[2] P. Zhu and R. W. Boswell, Phys. Rev. Lett. **63**, 2805 (1989).
[3] P. K. Loewenhardt, B. D. Blackwell and S. M. Hamberger, Plasma Phys. Controlled Fusion **37**, 229 (1995).
[4] S. Cho, Phys. Lett. A **216**, 137 (1996).
[5] K. P. Shamrai, V. P. Pavlenko, and V. B. Taranov, Plasma Phys. Controlled Fusion **39**, 505 (1997).
[6] J. G. Kwak, D. H. Choi, H. I. Bak, S. Cho, J. G. Bak, and S. K. Kim, Phys. Plasmas **4**, 1463 (1997).
[7] K. P. Shamrai and V. B. Taranov, Phys. Lett. A **204**, 139 (1995).
[8] S. Cho, Phys. Plasmas **3**, 4168 (1996).
[9] K. P. Shamrai and V. B. Taranov, Plasma Phys. Controlled Fusion **36**, 1717 (1994).
[10] D. N. Smith, P. L. Colestock, R. J. Kashuba, T. Kammash, Nucl. Fusion **27**, 1319 (1987).
[11] T. Shoji, Y. Sakawa, S. Nakazawa, and T. Sato, Plasma Sources Sci. Technol. **2**, 5 (1993).

Kinetic simulation on collisional bounded plasma

Shao-ping Zhu, Tetsuya Sato, Yukihiro Tomita and Tadatsugu Hatori
Theory and Computer Simulation Center, National Institute for Fusion Science,
Oroshi, Toki 509-52, Japan

Abstract

A self-consistent kinetic simulation model on collisional bounded plasma is presented. The electric field is given by solving Poisson equation and collisions among particles(including charged particles and neutral particle) are included. The excitation and ionization of neutral particle, and recombination are also contained in the present model. The formation of potential structure near a boundary for a discharge system was used as an application of this model.

1 Introduction

The study of plasma behavior near a boundary is important and has a long history[1]. This study, so far, is still active because of the application of it, such as, plasma processing, divertors of fusion device. Plasma behavior near a boundary is very complicated and difficult to deal with analytically. Much numerical simulation studies, including fluid simulation and kinetic simulation, were paid on this topic. In the strict sense, fluid approximation is invalid for plasma near a boundary because the particle distribution function is far from Maxwellian. The first kinetic simulation study on plasma behavior near a boundary was given by Chodura[2]. Chodura considered sheath formation of collisionless plasma. The kinetic simulation on plasma behavior near a boundary for a collisional plasma was proposed by T.Takizuka et al[3] as a model of divertor plasma. They solved particle motion by particle-in-cell method and included collision by Monte Carlo method. A more careful kinetic simulation on this topic was reported by Procassini et al[4]. But for all of these kinetic simulation neutral particle and secondary emission electron are not considered. It is widely believed that neutral particle plays a key role in the divertor plasma of fusion device. For example, plasma detachment is completely related with behavior of neutral particle. And secondary emission electron may play major role in formation of sheath potential and establishing equilibrium temperature. In the present report, a self-consistent kinetic simulation model on one dimensional collisional bounded plasma is presented. The electric field is given by solving Poisson equation and collisions among particles(including charged particles and neutral particle) are included by Monte Carlo method. The excitation and ionization of neutral particle, and recombination are also contained in the present model.

2 Basic equations and processes

The basic equations are as follows;

$$\frac{\partial^2 \phi}{\partial x^2} = -4\pi\rho, \tag{1}$$

$$\frac{dv_{x,j}}{dt} = -\frac{q_j}{m_j}\frac{\partial \phi}{\partial x} + \frac{dv_{x,j}}{dt}|_{col} + \frac{dv_{x,j}}{dt}|_{ex} + \frac{dv_{x,j}}{dt}|_{io} + \frac{dv_{x,j}}{dt}|_{re}, \tag{2}$$

$$\frac{dv_{y,j}}{dt} = \frac{dv_{y,j}}{dt}|_{col} + \frac{dv_{y,j}}{dt}|_{ex} + \frac{dv_{y,j}}{dt}|_{io} + \frac{dv_{y,j}}{dt}|_{re}, \tag{3}$$

$$\frac{dv_{z,j}}{dt} = \frac{dv_{z,j}}{dt}|_{col}\frac{dv_{z,j}}{dt}|_{ex} + \frac{dv_{z,j}}{dt}|_{io} + \frac{dv_{z,j}}{dt}|_{re}, \tag{4}$$

$$\frac{dx_j}{dt} = v_{x,j}, \qquad \rho = \sum_j^N q_j S(x - x_j(t)) \tag{5}$$

Where N is the total number of particles, and S(x) is the form function of particles. $\frac{dV_j}{dt}|_{col}$ represents collision among particles, $\frac{dV_j}{dt}|_{ex}$ and $\frac{dV_j}{dt}|_{io}$ represent excitation and ionization of neutral particle by electron impact, and $\frac{dV_j}{dt}|_{re}$ represents recombination process.

In the actual simulation, all the variables are normalized as follows:

$$t \rightarrow t\frac{t}{\omega_{pe}}, \quad x_j \rightarrow x_j\lambda_d, \quad v_j \rightarrow v_j v_{th}, \quad m_j \rightarrow m_j m_e, \quad q_j \rightarrow q_j e, \quad \phi \rightarrow \phi\frac{e}{kT_{be}},$$

where e is the charge of proton, m_{e0} is the static mass of electron, $\omega_{pe} = \frac{4\pi n_0 e^2}{m_e}$ is the plasma frequency of background plasma at initial state, $v_{th} = \sqrt{\frac{kT_{be}}{m_e}}$ is the electron thermal velocity background plasma at initial state, $\lambda_d = \sqrt{\frac{kT_{be}}{4\pi n_0 e^2}}$ is the Debye length of background plasma at initial state, n_0 and T_{be} are the electron density and temperature of background plasma at initial state respectively.

The simulation region is bounded by $x = 0$ and $x = L$. Source ion and electron are injected with equal and temporally constant number fluxes in the source region between $x = 0$ and $x = L_s$. Both source ion and electron satisfy Maxwellian distributions with the source temperature T_{se} and T_{si} respectively. The electrostatic potential is symmetric at $x = 0$, that is, the boundary conditions for the potential are given by

$$\frac{\partial\phi}{\partial x} = 0, \quad \phi = 0, \quad at\ x = 0. \tag{6}$$

We treat the boundary $x = 0$ as a reflecting wall for particles. Ions that cross the boundary $x = L$ are removed from system. Part of electrons that cross the boundary $x = L$ are removed from system, but another part of electrons that cross the boundary $x = L$ are replaced by the Secondary electrons. Secondary electrons are emitted at boundary $x = L$ with a half-Maxwellian distribution with temperature T_{ce}. Neutral particle is generated by ion-induced sputtering of the target plate and can also be injected temporally from source region of neutral particle. The simulation region of (0, L) is initially filled by the background ions end electrons that have Maxwellian distribution with temperature T_{bi} and T_{be}. The initial number density of electron is n_0.

The collision processes contained in the present simulation model are listed as follows;

$$e_1 + e_2 \rightarrow e_1^{'} + e_2^{'} \quad Coulomb\ collision \tag{7}$$

$$p_1 + p_2 \rightarrow p_1^{'} + p_2^{'} \quad Coulomb\ collision \tag{8}$$

$$e + p \rightarrow e^{'} + p^{'} \quad Coulomb\ collision \tag{9}$$

$$e + H(1s) \rightarrow e + H^{*}(2p) \quad excitation\ by\ electron\ impact \tag{10}$$

$$e + H(1s) \rightarrow e_1 + e_2 + p \quad ionization\ by\ electron\ impact \tag{11}$$

$$e + H \rightarrow e + H \quad elastic\ collision \tag{12}$$

$$H + p \rightarrow p + H \quad charge\ exchange \tag{13}$$

$$e + p \rightarrow h\nu + H(1s) \quad photorecombination \tag{14}$$

$$e_1 + e_2 + p \rightarrow e + H \quad three\ body\ recombination \tag{15}$$

where e represents electron, p represents proton and H means hydrogen atom.

3 Simulation method

For Coulomb collision between charged particles, small angle scattering is dominant. We employed Monte Carlo method proposed by Wang et al[5]. which is equivalent to Fokker-Planck approximation. We used a "probability decision" technique to handle other processes. We now explain what is "probability decision" method. Let us consider excitation of neutral hydrogen atom by electron impact

$$e + H(1s) \rightarrow e + H^{*}(2p) \tag{16}$$

Introducing probability $P_{ex} = 1 - e^{-<\sigma_{1s\to 2p}(v)v>n_H \Delta t}$ where $<\sigma_{1s\to 2p}(v)v>$ is excitation rate and n_H is density of neutral hydrogen atom, and R_{ex} which is a uniform random number between 0 and 1, we let excitation of neutral particle occur if $R_{ex} \leq P_{ex}$, so increment of $H^*(2p)$ is

$$\frac{\Delta n_H^*}{\Delta t} = <\sigma_{1s\to 2p}(v)v> n_H n_e \tag{17}$$

which is the rate equation for excitation of neutral particle by electron impact.

Once excitation occurs, we have to determine the particle velocity after excitation. We now find the velocity of electron and neutral particle after excitation. Considering energy and momentum conservation;

$$\frac{1}{2}m_e \mathbf{v}_{ei}^2 + \frac{1}{2}m_n \mathbf{v}_{ni}^2 = \frac{1}{2}m_e \mathbf{v}_{ef}^2 + \frac{1}{2}m_n \mathbf{v}_{nf}^2 + I \tag{18}$$

$$m_e \mathbf{v}_{ei} + m_n \mathbf{v}_{ni} = m_e \mathbf{v}_{ef} + m_n \mathbf{v}_{nf} \tag{19}$$

Introducing the relative velocity $\mathbf{u}$ and the velocity of the center of mass $\mathbf{V}$, defined respectively

$$\mathbf{u} = \mathbf{v}_e - \mathbf{v}_n, \qquad \mathbf{V} = \frac{m_e \mathbf{v}_e + m_n \mathbf{v}_n}{M}, \tag{20}$$

we obtain the energy and momentum conservation

$$\mathbf{u}_f^2 = \mathbf{u}_i^2 - \frac{2I}{m}, \qquad \mathbf{V}_f = \mathbf{V}_i, \tag{21}$$

where M is the total mass $M = m_e + m_n$, m is reduced mass $m = \frac{m_e m_n}{M}$. Let $\mathbf{u}_i$ be z-direction, the relative velocity after the collision $\mathbf{u}_f$ can be written in the form $\mathbf{u}_f = \sqrt{\mathbf{u}_i^2 - \frac{2I}{m}}[sin(\theta)cos(\phi), sin(\theta)sin(\phi), cos(\theta)]$, where θ is scattering angle and ϕ is azimuthal angle. Now let us find θ and ϕ. According to atomic collision theory, excitation is isotropic for angle ϕ, so we treat ϕ as a uniform random number. It is known that the first Born differential cross section for process (16) is[6]

$$(\frac{d\sigma}{d\Omega})_{1s\to 2p} = \frac{288 u_f}{u_i} \frac{1}{\Delta^2(\Delta^2 + \frac{9}{4})^6}, \tag{22}$$

where $\Delta^2 = u_i^2 + u_f^2 - 2\mathbf{u}_i \cdot \mathbf{u}_f$. The differential cross section exhibits a peak at small Δ. The total cross section is

$$\begin{aligned} \sigma_{1s\to 2p} &= 2\pi \int (\frac{d\sigma}{d\Omega})_{1s\to 2p} sin\theta d\theta \\ &= 2\pi \frac{288}{u_i^2} \int_{|u_i - u_f|}^{|u_i + u_f|} d\Delta \frac{1}{\Delta(\Delta^2 + \frac{9}{4})^6}, \end{aligned} \tag{23}$$

where $\Delta d\Delta = u_i u_f sin\theta d\theta$ are used. So we introduce a probability function $P(\Delta) = \frac{1}{ln\frac{|u_i+u_f|}{|u_i-u_f|}} \frac{1}{\Delta}$ and a cumulative distribution function $R = \int_{|u_i-u_f|}^{\Delta} P(\Delta')d\Delta'$. Using the definition of Δ, we get a relation for scattering angle θ,

$$cos\theta = -\frac{(|u_i - u_f|)^2[\frac{|u_i+u_{ef}|}{|u_i-u_f|}]^{2R} - u_i^2 - u_f^2}{2u_i u_f}. \tag{24}$$

It is should be noted that the θ and ϕ are measured in a coordinate in which z-direction is along $\mathbf{u}_i$, so it is necessary to transform $\mathbf{u}_f$ back into the laboratory coordinate. Then the final form of relative velocity after excitation reads;

$$\begin{bmatrix} u_{fx} \\ u_{fy} \\ u_{fz} \end{bmatrix} = \sqrt{\mathbf{u}_i^2 - \frac{2I}{m}} \begin{bmatrix} sin(\theta)cos(\phi)cos(\theta_0)cos(\phi_0) - sin(\theta)sin(\phi)sin(\phi_0) + cos(\theta)sin(\theta_0)cos(\phi_0) \\ sin(\theta)cos(\phi)cos(\theta_0)sin(\phi_0) + sin(\theta)sin(\phi)cos(\phi_0) + cos(\theta)sin(\theta_0)sin(\phi_0) \\ -sin(\theta)cos(\phi)sin(\theta_0) + cos(\theta)cos(\theta_0) \end{bmatrix}, \tag{25}$$

where $cos(\theta_0) = \frac{u_{ix}}{u_i}$, $cos(\phi_0) = \frac{u_{ix}}{u_i sin(\theta_0)}$, $sin(\phi_0) = \frac{u_{iy}}{u_i sin(\theta_0)}$. Finally, we have the velocities after excitation,

$$\mathbf{v}_{ef} = \mathbf{v}_{ei} + \frac{m_n}{M}(\mathbf{u}_f - \mathbf{u}_i) \tag{26}$$

$$\mathbf{v}_{nf} = \mathbf{v}_{ni} - \frac{m_e}{M}(\mathbf{u}_f - \mathbf{u}_i). \tag{27}$$

By above simulation method, we can get a correct rate equation, exact energy and momentum conservation and correct angle distribution of electrons after excitation. It should be noted that both collision rate $<\sigma v>$ and

differential scattering cross section, as we shaw, are needed in order to include collision processes by probability decision method. But no differential scattering cross section were available for some processes. In the following discussion, we use differential scattering cross section to determine scattering angle for processes where there exists differential scattering cross section. For the case of no differential scattering cross section, we assume the scattering is isotropic. For ionization process, we assumed that the emitted electron is cold, that is, the kinetic energy of emitted electron is zero. For photorecombination we assume that both energy and momentum of neutral particle is same as that of the ion. For three body recombination, we assume that the electron is captured into the state with level number $n = \infty$.

4 Collision rate $< \sigma v >$

In this section, we list the collision rate $< \sigma v >$ for all of processes contained in the present model. Collision rate for ionization of neutral particle by electron impact $< \sigma v >_{ionization}$ is[7];

$$< \sigma v >_{ionization} = \frac{10^{-5}\sqrt{\frac{T}{I}}}{I^{\frac{3}{2}}(6+\frac{T}{I})} e^{-\frac{I}{T}} \tag{28}$$

where T is temperature of plasma particle in unit of eV and $I = 13.6\ eV$ is ionization energy of hydrogen.

Collision rate for excitation of neutral particle by electron impact $< \sigma v >_{excitation}$ is[8];

$$< \sigma v >_{excitation} = 4.19 \times 10^{7} T^{\frac{1}{2}} e^{\sum_{n=0}^{8} a(n)(lnT)^n}. \tag{29}$$

where $a(n)$ is given in Ref.[8].

Collision rate for elastic collision between neutral particle and electron $< \sigma v >_{elastic}$ is[9];

$$< \sigma v >_{elastic} = 4.19 \times 10^{-8} T^{\frac{1}{2}} [2.275 - 0.757 ln(T)] \quad 0 < T < 10eV. \tag{30}$$

Collision rate for photorecombination $< \sigma v >_{photo-recom}$ is[7];

$$< \sigma v >_{photo-recom} = 5.2 \times 10^{-14} \sqrt{\frac{I}{T}} [0.43 + \frac{1}{2} ln(\frac{I}{T}) + 0.469 (\frac{I}{T})^{-\frac{1}{3}}]. \tag{31}$$

Collision rate for three-body recombination $< \sigma v >_{three-body}$ is[7];

$$< \sigma v >_{three-body} = 8.75 \times 10^{-27} n_e T^{-4.5}. \tag{32}$$

Collision rate for charge exchange process $< \sigma v >_{charge\ exchange}$ is[8];

$$< \sigma v >_{charge\ exchange} = e^{\sum_{i=0}^{8} \sum_{j=0}^{8} a(i,j)(lnE)^{i-1}(lnT)^{j-1}}. \tag{33}$$

where E is the kinetic energy of incident particle in unit of eV. And $a(i,j)$ is given in Ref.[8].

5 Neutral particles

Neutral particle, in the present model, is generated by ion-induced sputtering of the target plate and can also be injected from source of neutral particle. Ion-induced sputtering yield is given by empirical formula developed by Yamamura et al[10];

$$Y(E) = 0.42 \frac{\alpha^* Q K s_n(\epsilon)}{U_s [1 + 0.35 U_s s_e(\epsilon))]} [1 - \sqrt{\frac{E_{th}}{E}}]^{2.8}.] \tag{34}$$

where $Y(E)$ is the sputtering yield for incident ions of energy E; α^*, Q and E_{th} are empirical parameters; U_s is the sublimation energy in eV; $s_n(\epsilon)$ and $s_e(\epsilon)$ are Lindhard's elastic and inelastic reduced stopping cross sections, respectively. ϵ is reduced energy. The detail explanation on ion-induced sputtering can be found in Ref.[11].

Neutral particles, in the present model, can also be injected with temporally constant number fluxes in the neutral particle source region. Neutral particles injected in source region satisfies Maxwellian distributions with low temperature.

The trajectories of neutral particles are given by $x(t) = x(t_0) + v(t)(t - t_0)$, where t_0 is the time when neutral particle is generated. In realistic plasma discharge experiment, neutral particles are pumped out temporally. In order to simulate this process, we set a lifetime to every neutral particle. If the remaining time of neutral particle, that is $t - t_0$, is greater than the lifetime, the neutral particle is removed numerically from system.

6 Second emission electron

Electron emission from target plate under bombardment by energetic particle may play a major role in establishing the sheath potential. In the present model, the effect of electron emission from target(secondary emission electron) is considered. An empirical formula for secondary emission electron coefficient as a function of impact electron energy is used[12];

$$\delta = (2.72)^2 \delta_m \frac{E_p}{E_{p_m}} e^{-2(\frac{E_p}{E_{p_m}})^{0.5}}. \quad (35)$$

where E_p is the primary electron energy. δ_m is the maximum yield of secondary emission electron and E_{p_m} is the primary electron energy at which maximum yield δ_m occurs. The empirical values of δ_m and E_{p_m} can be found in Ref.[12]. For carbon, $\delta_m = 1$ and $E_{p_m} = 300\ eV$

7 Application

As an application of above kinetic model, we consider formation of electric potential near a boundary for a discharge system. For realistic plasma, the mean-free path of electrons λ is more than 10^6 times of Debye length. And the simulation system allowed by the present computer is about 10^3 Debye length. For this small simulation system it is impossible to include realistic collision. In the present simulation model, we enlarge the collisionality numerically by reducing the plasma parameter(particle numbers in Debye cubic) when we include collisions, that is, we use different time scales for plasma oscillation and particle collision.

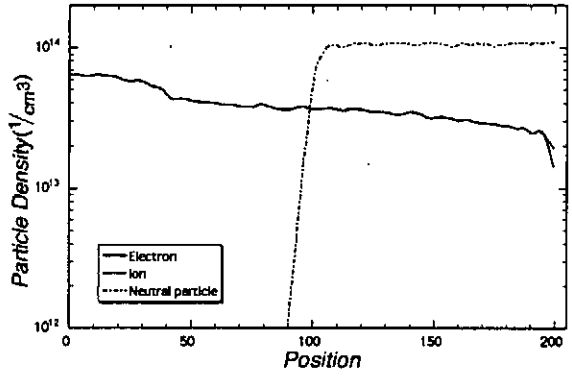

Figure 1: The profiles of density of electron, ion and neutral particle

The parameters for simulation run are presented here. The system length L is 200. The system is initially loaded with a uniform plasma where density of electron and ion is $1 \times 10^{13}\ 1/cm^3$, and electron temperature is 6 eV and ion temperature is 0.6 eV. Initial numerical numbers of electron and ion are 10000 respectively. The source region length L_s is equal to $0.2L$. And 2 numerical source electron and ion is injected into system every time step respectively. Source electron temperature is 18 eV and ion temperature is 3.6 eV. Mesh size Δx and time step Δt are 1 and 0.1 respectively. Twenty numerical neutral particle is injected into system every time step from the neutral particle source region located between $x = 0.5L$ and $x = L$. Neutral particle generated by ion-induced sputtering is ignored because the temperature is very low in the present simulation run. Also secondary emission electron is neglected due to the low electron temperature.

Figure 1 shows the profiles of density of electron, ion and neutral particle in the stationary state. The charge neutrality is satisfied well in the the most region of system. But ion is more abundant than electron in the region near the target plate. Accordingly, a sheath potential structure, which is shown in Fig. 2, is formed near the target plate. Figure 2 also shows that the total

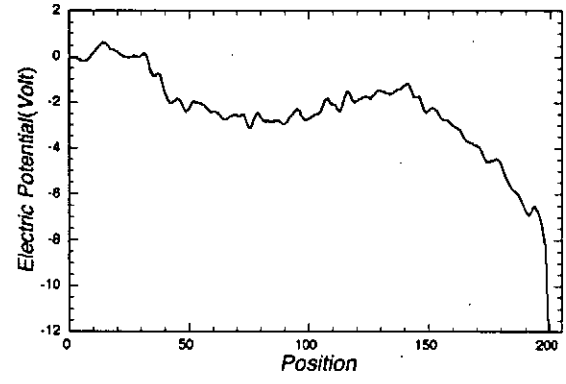

Figure 2: The profiles of potential

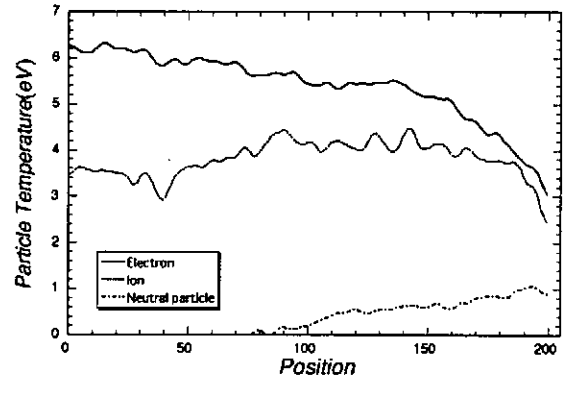

Figure 3: The profiles of temperature

potential drop consists of four parts, that is, charged particle source potential drop($0 < x < 40$), presheath potential drop($40 < x < 130$) which is very weak, neutral particle source potential drop ($130 < x < 195$) and sheath potential drop($195 < x < 200$). Figure 3 shows the profiles of electron, ion and neutral particle temperature. In the presheath region, electron temperature decreases as the position slowly. In the region where neutral particle is dominate, electron temperature de-

creases as position sharply. It can be explained easily. By the force balance relation of electron, we have $-e\mathbf{E} \sim \nabla n_e T_e$, that is, $e\phi \sim n_e T_e + constant$. The electron density is homogeneous except the sheath regi on, so potential is dependent of electron temperature directly.

8 Summary

We presented a self-consistent kinetic simulation model for studying plasma behavior near a boundary. The electric field is given by solving Poisson equation and collisions among particles(including charged particles and neutral particle) are included by Monte Carlo method. The excitation and ionization of neutral particle, and recombination are also contained in the present model. The formation of potential structure near a boundary for a discharge system was used as an application of this model.

Recently, several experimental measurements on a magnetized plasma column were reported[13, 14]. The comparisons of experimental measurements and the simulations given by the present model is now under consideration. And also a two dimensional model is constructed now.

References

[1] L. Tonks and I. Langmuir, Phys. Rev. **34**, 876(1929)

[2] R. Chodura, Phys.Fluids **25**, 1628(1982).

[3] T. Takizuka, K. Tani, M. Azumia, K. Shimizu, J.Nucl.Mater. **128 – 129**, 104(1984).

[4] R. J. Procassini and C. K. Birdsall, Phys.Fluids B **3**, 1876(1991).

[5] W. X. Wang et al, Nucl. Fusion **36**, 1633(1996).

[6] Charles J.Joachain, Quantum Collision Theory, North-Holland publishing company - Amsterdam, 1975.

[7] D. L. Book, NRL Plasma Formulary (1984).

[8] R. K. Janev, W. D. Langer, K. Evans, Jr., and D. E. Post, Elementary Processes in Hydrogen-Helium Plasmas(Springer-Verlag, New York, 1987).

[9] K. Takayanagi and H. Suzuki, Report IPPJ-DT-48, Institute of Plasma Physics, Nagoya University(1981).

[10] Y. Yamamura, N. Matsunami and N. Itoh, Radiat .Eff. **71**, 65(1983).

[11] N. Matsunami et al., Atomic Data and Data tables **31**, 2(1984).

[12] R. A. Langley et al., Nuclear fusion, special issue, 94(1984).

[13] G. S. Chiu and S. A. Cohen, Phys. Rev. Lett. **76**, 1248(1996).

[14] N. Ohno et al., Contrib. Plasma Phys. **36**, 339(1996).

Potential Structure Formed by Local Production of Negative Ions in a Magnetized Plasma

W. Oohara, S. Ishiguro, R. Hatakeyama, and N. Sato
Department of Electronic Engineering, Tohoku University, Sendai 980-77, Japan

Abstract

We have investigated the formation process of field-aligned structures due to local production of negative ions in a plasma by means of one-dimensional electrostatic particle simulation. The plasma becomes unstable for a large production rate, being accompanied by the intermittent generation of negative solitary waves. The solitary waves play a role in making negative ions ejected rapidly from the system.

1. Introduction

A growing attention has been paid to phenomena in dusty plasmas since charged fine particles are recognized to coexist with space, fusion-oriented, and materials-processing plasmas [1]. As these heavy particles are often negatively charged in such plasmas, it is of considerable interest to investigate effects of the negative ion production on microscopic and macroscopic plasma structures.

So far most of the investigations have been concerned with clarification of characteristics of low-frequency plasma waves and instabilities in plasmas including negative ions. They have mainly been carried out by using SF_6 (sulphurhexafluoride gas, mass number $\simeq$ 146) particles as a negative ion source [2]. In this work, C_{60} (fullerene, mass number $\simeq$ 720) particles, which are large cage-like molecules composed of 60 carbon atoms, are used as a negative ion source. C_{60} particles belonging to ultrafine particles are much smaller than usual fine particles, but are much larger than positive ions K^+ (potassium, mass number $\simeq$ 39) in our Q-machine plasma. The Q-machine plasma is fully-ionized and quiscent, which consists of thermal electrons and positive ions produced by contact ionization of alkaline metal on a hot tungsten plate. In the presence of C_{60} particles, negative ions C_{60}^- are produced in the plasma as a result of electron attachment [3]. C_{60} particle is not attached to by more than two electrons in our plasma.

Behaviors of a plasma in the presence of local production of negative ions have been investigated by a particle simulation and a Q-machine experiment [4]. This paper presents results of a particle simulation.

2. Simulation Model

A computer simulation is performed by means of a one-dimensional electrostatic particle simulation code. The simulation model is schematically shown in Figure 1. A grounded plasma emitter is placed at $z/\lambda_{Ds} = 0$, and a floated electrode is placed at $z/\lambda_{Ds} = 511$, where λ_{Ds} is the Debye length defined by using the plasma source parameters. All particles impinging on the electrodes are removed from the system. Positive ions and electrons

with half-Maxwellian distribution functions are continuously injected from the plasma emitter into the simulation system. The positive ion to electron mass ratio is fixed to be $m_+/m_e = 400$. The ratio of the emitted electron to positive ion flux is $\Gamma_{es}/\Gamma_{+s} = (m_+/m_e)^{1/2} = 20$. A sheath is formed in front of the electrode at $z/\lambda_{Ds} = 0$ to restrict electron flux since $\Gamma_{es}/\Gamma_{+s} > 1$. Positive ions are accelerated in the sheath and enter the plasma region. The ratio of the plasma to the plasma source density is 0.18, and the ratio of the electron plasma frequency is 0.43. All results are obtained with the time step $\omega_{ps}\Delta t = 0.2$. Here, ω_{ps} and Δt are the electron plasma frequency defined by using the plasma source parameters and the time step width, respectively.

In a localized region of the plasma ($80 < z/\lambda_{Ds} < 180$), some of electrons attach to C_{60} particles, and are replaced by negative ions in the way that a total momentum is conserved, $m_e v_e + m_{c60} v_{c60} = m_- v_-$, $m_- = m_e + m_{c60}$. Here, m_e, m_{c60}, m_-, v_e, v_{c60}, and v_- are masses and velocities of electrons, C_{60} particles, negative ions, respectively. The negative ion to electron mass ratio is fixed to be $m_-/m_e = 7360$ by taking the experimental value of $m_-/m_+ = 18.4$ into account. The spatial distribution of the C_{60} particles are assumed to be Gaussian, and the velocity distribution is Maxwellian with the C_{60} particle to electron temperature ratio $T_{c60}/T_e = 0.29$. The production rate of negative ions Γ_- depends on the electron number N_e in the negative ion production region ($80 < z/\lambda_{Ds} < 180$), and is defined $\Gamma_- = N_e/N_{e0} \cdot \alpha\Gamma_{+s}$. Here, N_{e0} is the electron number when negative ions are not present and α is the negative ion production rate. The production rate α is 0.01 or 0.3 in this paper.

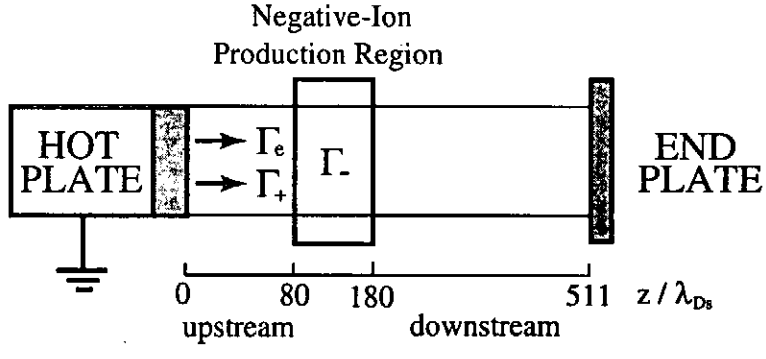

Fig. 1. Schematic diagram of simulation system, based on a Q-machine. Negative ions are produced in the localized region $80 < z/\lambda_{Ds} < 180$.

3. Simulation Results

When electrons and positive ions are emitted from the plasma emitter placed at $z/\lambda_{Ds} = 0$, they fill the system, providing a quasistationary state ($\omega_{ps}t = 0 \sim 14 \times 10^3$). After negative ions start to be produced ($\omega_{ps}t > 14 \times 10^3$), some of electrons are replaced by them every moment. The plasma is stable when the negative ion production rate is small ($\alpha = 0.01$). Figure 2 shows the potential profile (left hand side) which is averaged over twice of the electron plasma period defined at the plasma source and the phase space distribution of negative ions (right hand side) at $\omega_{ps}t = 314 \times 10^3$.

After negative ions start to be produced, a negative potential dip is formed at $z/\lambda_{Ds} \sim 130$, which is almost stationary in time. The depth of the negative dip is about $e\Delta\phi/T_e \sim 0.1$, which increases with an increase in the negative ion production rate α. The produced negative charge is not completely shielded by the positive ions. The produced negative ions are diffused to the upstream or downstream region. A sheath is formed in front of the floated electrode at $z/\lambda_{Ds} = 511$. An averaged positive charged flux is equal to an averaged negative charged flux toward the electrode because the electrode is kept at a floating potential. Most of the negative ions are reflected by the sheath and return to the negative ion production region. A part of them are reflected by the right side slope of the potential dip and return to the floated electrode again. Negative ions with low kinetic energies stay long in the downstream region. The other negative ions are slightly accelerated by the left side slope of the potential dip and form a weak beam. They are absorbed by the grounded electrode at $z/\lambda_{Ds} = 0$.

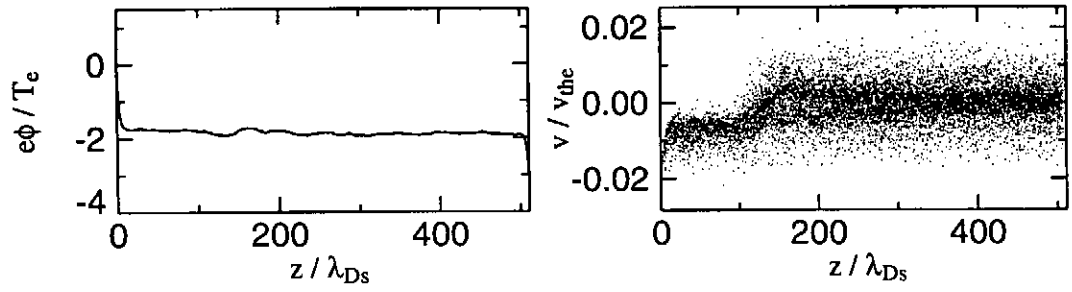

Fig. 2. Potential Profile (left hand side) and phase space distribution of negative ions (right hand side) in a stable state with $\alpha = 0.01$ at $\omega_{ps}t = 314 \times 10^3$.

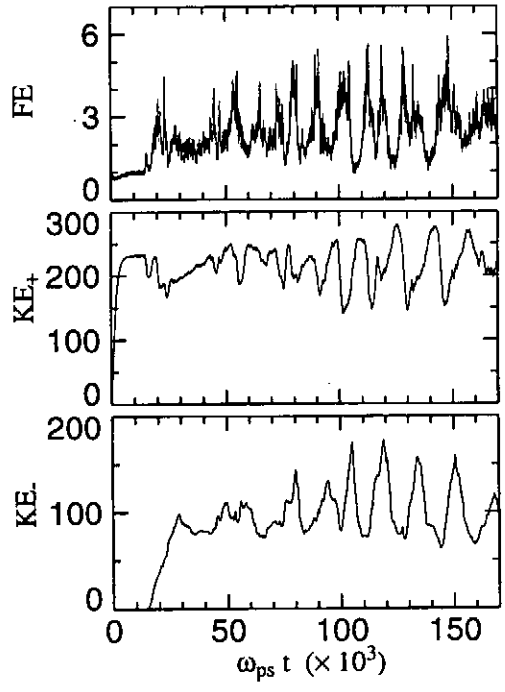

Fig. 3. Temporal evolutions of the electric field energy FE (top), the kinetic energies of positive ions KE_+ (middle), and negative ions KE_- (bottom) in the system with $\alpha = 0.3$.

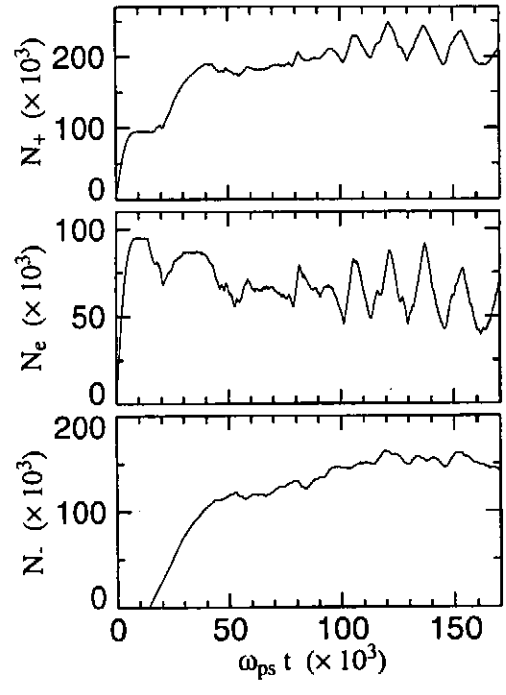

Fig. 4. Temporal evolutions of the numbers of positive ions N_+ (top), electrons N_e (middle), and negative ions N_- (bottom) in the system with $\alpha = 0.3$.

A large fluctuation appears for some plasma parameters in the case that the negative ion production rate is large ($\alpha = 0.3$). Figure 3 shows the temporal evolutions of the electric field energy FE (top), the kinetic energies of positive ion KE_+ (middle) and negative ion KE_- (bottom) in the system. The electric field energy are observed to increase intermittently after a while from the initiation of the negative ion production ($\omega_{ps}t > 80 \times 10^3$). This corresponds to the intermittent generation of large amplitude solitary waves, as shown in later. When the solitary waves are generated, the kinetic energy of positive ions decreases and the kinetic energies of negative ions and electrons increase. Thus, the energy is apparently transferred.

Figure 4 shows the temporal evolutions of the numbers of positive ions N_+ (top), electrons N_e (middle), and negative ions N_- (bottom) in the system. The numbers of positive ions and electrons in the system oscillate, but the number of negative ions does not oscillate so much. The positive ions and electrons respond sensitively to the solitary wave and are smoothly discharged from the system. The negative ions, however, do not respond sensitively since the mass is much larger than that of positive ions.

Figure 5 shows the space-time distribution of the potential during $\omega_{ps}t = 114 \sim 154 \times 10^3$ with $\alpha = 0.3$. It is observed that solitary waves are intermittently generated between the upstream region and the negative ion production region, and propagate toward downstream. The generation period of the waves is $\omega_{ps}T_1 \sim 16000$, the propagation speed is $v_{ph1}/v_{the} \sim 4.7 \times 10^{-2}$, and the amplitude of the potential is $e\Delta\phi_1/T_e \sim 3$. When the solitary wave is generated, the potential in the downstream region becomes high, yielding a double layer formation. The negative ion density is particularly high in the region where the solitary wave propagates.

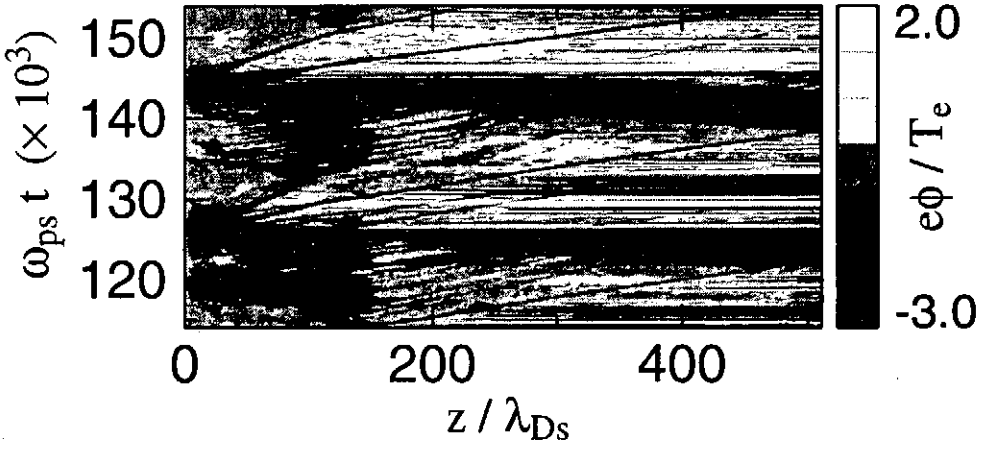

Fig. 5. Space-time distribution of the potential during $\omega_{ps}t = 114 \sim 154 \times 10^3$ with $\alpha = 0.3$.

Figure 6 shows the potential profiles at $\omega_{ps}t = 125.2$ (top), 125.4 (second), 125.6 (third), and 126.0 (bottom) $\times 10^3$, which demonstrate the generation process of the negative ion density pulses. The corresponding phase space distributions of negative ions are shown in Fig. 7. The generation process of the negative ion density pulses observed is summarized as follows :

A small amplitude density fluctuation of positive ions is generated in the upstream region ($z/\lambda_{Ds} < 50$); A double layer is formed in the negative ion production region when the

fluctuation arrives there; Negative ions are accelerated by the double layer, and a high density region is created by bunching.

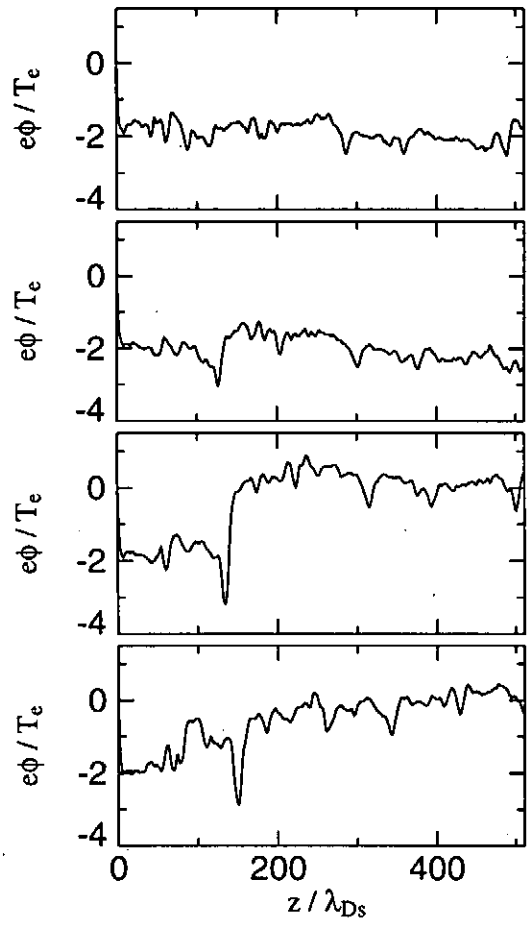

Fig. 6. Potential profiles at $\omega_{ps}t = 125.2$ (top), 125.4 (second), 125.6 (third), and 126.0 (bottom) $\times 10^3$ with $\alpha = 0.3$.

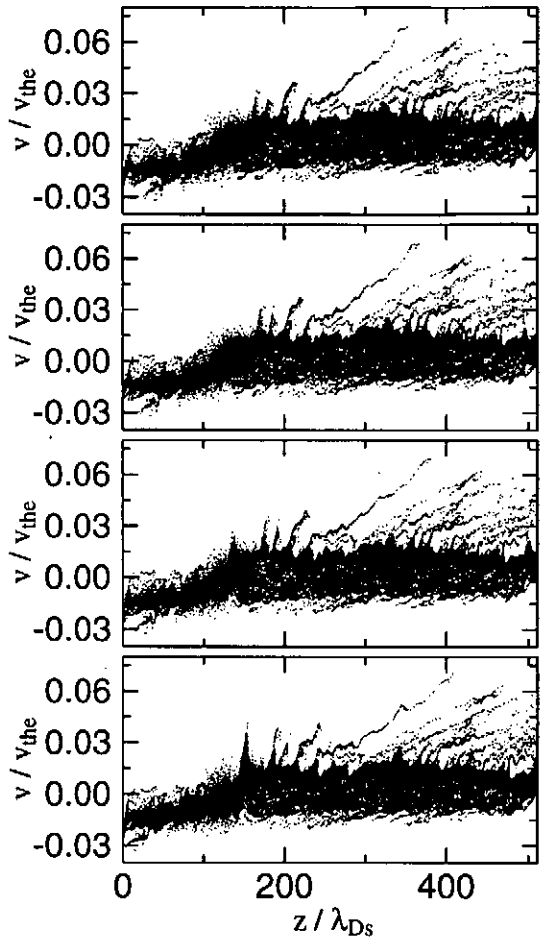

Fig. 7. Phase space distributions of negative ions at $\omega_{ps}t = 125.2$ (top), 125.4 (second), 125.6 (third), and 126.0 (bottom) $\times 10^3$ with $\alpha = 0.3$.

4. Discussion

Two different states on macroscopic plasma structure are realized in the open system that negative ions are produced in a localized region of a plasma and are ejected from the plasma. One is that the produced negative ions stay for a long time in the system and are calmly ejected. The other is that large density fluctuations of negative ions are generated and the negative ions are promptly ejected. Electrons behave as drowning out the electric field rapidly and providing a stable state, but the existence of negative ions disturbs the system. The increase of negative ions acts to bring a nonequilibrium state. If the number of negative ions exceeds a certain critical value, the stable state cannot be maintained any longer. As a result, the density fluctuation of negative ions is generated, negative ions are accelerated, and rapidly ejected from the system. The energy source of the fluctuation is the drift energy of positive ions. When the energy is continuously supplied from an external world, the system intermittently repeats an energy transfer and

does not reach an equilibrium state [5]. The balance of supplies and discharges of matter (particles) and energy affects the order of the system [6]. In view of these results, the present phenomenon may be considered as a kind of kinetic self-organization.

5. Summary

We have investigated the formation process of plasma structures due to localized negative-ion production by means of one-dimensional electrostatic particle simulation. The plasma state becomes unstable for the large rate of negative ion production, while the state is stable for the small rate. A double layer is formed and a negative solitary wave is intermittently generated. The solitary wave plays a role in ejecting negative ions rapidly from the system.

Acknowledgements

One of the authors (W.O.) would like to thank Prof. T. Kamimura and Mr. H. Takamaru for valuable suggestions. The computations were performed by NEC SX-3/44R at the computer center of Tohoku University and NEC SX-4B at the computer center of the National Institute for Fusion Science.

References

[1] C. K. Goertz, Rev. Geophys. **27**, 271 (1989); J. Winter *et al*, J. Nucl. Mater. **162-164**, 713 (1989); G. S. Selwyn *et al*, Appl. Phys. Lett. **57**, 1876 (1990).

[2] N. Sato, *A Variety of Plasmas*, edited by A. Sen and P. K. Kaw (Indian Academy of Sciences, Bangalore, 1989) p.79.

[3] N. Sato, T. Mieno, T. Hirata, Y. Yagi, R. Hatakeyama, and S. Iizuka, Phys. Plasmas **1**, 3480 (1994).

[4] W. Oohara, S. Ishiguro, R. Hatakeyama, and N. Sato : *Double Layers - Potential Formation and Related Nonlinear Phenomena in Plasmas*, edited by Sendai Plasma Forum (World Scientific, Singapore, 1997) p.149.

[5] T. Sato, H. Takamaru, and the Complexity Simulation Group, Phys. Plasmas **2**, 3609 (1995).

[6] H. Amo, T. Sato, A. Kageyama, and the Complexity Simulation Group, Phys. Rev. E **51**, 3838 (1995).

Plasma Turbulent Acceleration Mechanism of the Relativistic Jets in AGNs

Tong Yi Tian Lirong
(Department of Astronormy,Beijing Normal University,Beijing,China)

Abstract

In this paper we use the acceleration mechanism of plasma turbulence(Alfven) wave to explain completely two characters of jets in Active Galactic Nuclei(AGNs):first the jets are kept collimating for a long distance from pc scales to several Kpc scales; secondly the jets possess very high energy that the extreme relativistic speed reach to γ =20(γ is lorentz factor).Our theoretical value(γ =15) is near the observational maximum value.

key words: Active Galactic Nuclei, relativistic jet, plasma turbulence acceleration, Alfven wave

1. Introduction

Since jets were observed in strong radio galaxies,many astronomer are interested in it to research. As we have known the main characteristics of jets in AGNs are the high speed and collimation. The speeds of jets in AGNs cover a wide range from a few hundred kilometers per second to nearly the light speed. From the superluminal motion observed in some VLBI jets discovers that these collimated outflows may be relativistic moving, with a lorentz factor ranging from 2 to 20(Begelman, Blandford & Ree 1984). Here it is called relativistic jet.

First, about the collimation of the jet, for the AGNs the electromagnetically driven jet can be collimated by magnetic tension forces(Lovelance 1976; Blandford 1976) and it was shown explicitly in numerical calculation(Sakurai 1985; Camenzind 1989; Lovelace, Mobarry & Contopoulos 1989). But only the Heyraerts & Norman(1989) have shown analytically that hydromagnetically driven nonrelativistic jets always collimated. Chiueh, et al.(1991) get this result that a fully relativistic jet must became collimated by examining the possible asymptotic structure of flux surfaces.

Second, about the acceleration of the jet, the electromagnetic acceleration of matter surrounding a black hole or accretion disk may be a better mechanism for producing the jets(Blandfold & Znajek 1977; Blandford & Payne 1982; Phinney 1983).

The mechanism of jets in AGNs in the ideal MHD limit, has been investigated by many authors to explain the production of both nonrelativistic and relativistic jets(Phinney 1983; Camenzind 1986, 1987; Li 1992,1993).Due to the complex nature of the MHD equations we must make the necessary simplification to get the solution for the outflow. Therefore most workers have assumed that the jet has a radial geometry. The main acceleration force at large distances, when thermal pressure is negligible is almost exactly counterbalanced by the magnetic tension fore. So it leads in the relativistic case to

singularly weak acceleration of flow(Bogeyman & li 1993)

The other concrete acceleration mechanisms are posed such as acceleration by magnetic reconnection (Begelman ,Blandford Rees 1984; Asso & ol 1987; Lesch 1992); the diffusive acceleration by shock(Christiansen, Pachoczyk & cott 1976; Krimsky 1977; Blandford & Ostriker 1978; Eilek &Huges 1990) and the acceleration by MHD turbulent Alfven wave (Locombe 1977; Jabelice &Opher 1987), etc.

In this paper we consider that the core of AGNs possess very high energy which can result in the instability of the plasma around it . So the turbulent waves in plasma are excited easily.

It(here is Alfven wave) accelerates the charged particles which are spurted from the nozzle and jets are formed. Then under certain condition the velocity of jet increases fast up to relativistic jet last.This is a strong acceleration machanism which the wave pressure takes mainly effect that is different from the weak acceleration in MHD.

2.Plasma turbulent acceleration of relativistic jets

We suppose the construction of AGNs is a nucleus with accretion disk around it (Fig.1). The nucleus is composed of superdense matter with mass of $M=10^8 M_\odot$ (Netzer1989) in the range of the Schwarzschild radius $r_g = \frac{2GM}{c^2}$ .The"central engine" provides the energy and the turbulence wave can transfer its energy to the particles, so that the jets are accelerated and maintained for a long distance.

Considering optically thick disk around the black hole, we adopt the spherical coordinate and the radial lines are along the jets. In order to simplify the problems, we just consider 1-dimension case, in the radial direction, that is reasonable.

The basic equations are as follows:

(1). The conservation equation of the wave action density (Whitham 1965):

Let the coordinate system with fluid move, so the wave energy density satisfy:

$$\frac{\partial}{\partial t}\left[\frac{W}{\omega_0}\right] + \nabla \cdot \left[v_g \frac{W}{\omega_0}\right] = 0 \qquad (1)$$

Suppose the jets are symmetry and steady, i.e. $\frac{\partial}{\partial t} = 0$,we have

$$\frac{d}{dr}\left[r^2 v_g \frac{W}{\omega_0}\right] = 0 \qquad (2)$$

Because the jet speed is very high near the light speed, so considering the relativistic effect, the group velocity of turbulent wave is

$$v_g = \frac{v + v_{g0}}{1 + \frac{v \cdot v_{g0}}{c^2}} \qquad (3)$$

where v is plasma speed in jet, v_{g0} is the group velocity of wave in proper coordinate,ω_0

is wave frequency in proper coordinate.Let the Alfven wave take mainly action in process of accelerating the particles, so we can adopt its group velocity.

$$v_g = \frac{\omega}{k} = \frac{v_A}{(1+\frac{v_A^2}{c^2})^{1/2}} \qquad (4)$$

where $$v_A = \frac{B}{\sqrt{4\pi\rho}} \qquad (5)$$

is the Alfven velocity. Considering Doppler effect under the relativistic condition:

$$\omega_0 = \gamma(\omega - kv) = \gamma\omega\frac{v_g - v}{v_g} \qquad (6)$$

Where γ is Lorentz factor : $\gamma = \frac{1}{(1-\frac{v^2}{c^2})^{1/2}}$

The Eq.(2) becomes $$\frac{d}{dr}\left[r^2 v_g \frac{W}{\gamma\omega\frac{v_g - v}{v_g}}\right] = \frac{d}{dr}\left[r^2\frac{v_g^2}{\gamma(v_g - v)}\frac{W}{\omega}\right] = 0$$

Where ω is the wave frency, considering shot wave approximate, the ω ≈ constant.

the last eqution become: $$r^2\frac{v_g^2}{\gamma(v_g - v)}W = A_0 \qquad (7)$$

Where A_0 is decideded by initial condition: $A_0 = \frac{r_0^2 v_{g00}^2 W_0}{v_{g00} - v_0}\sqrt{1-\frac{v_0^2}{c^2}}$

Therefore Eq.(7) can be writen as

$$W = \frac{A_0\gamma(v_g - v)}{r^2 v_g^2} = \frac{A_0 v_{g0}\sqrt{1-\frac{v^2}{c^2}}(1+\frac{v}{c^2}v_{g0})}{\gamma^2(v_{g0}+v)^2}(1+\frac{v\cdot v_{g0}}{c^2}) \qquad (8)$$

By means of equations (3),(4),(5) ,we get

$$v_{g0} = \frac{v_g - v}{1-\frac{v}{c^2}v_{g0}} = \frac{cB - v\sqrt{4\pi\rho c^2 + B^2}}{\sqrt{4\pi\rho c^2 + B^2} - \frac{vB}{c}}$$

The initsal value $$v_{g00} = \frac{cB_0 - v_0\sqrt{4\pi\rho_0 c^2 + B_0^2}}{\sqrt{4\pi\rho_0 c^2 + B_0^2} - \frac{v_0}{c}B_0}$$

(2). The dynamic equation of ralativisic fluid:

According Landau's theory,we can derive out,

$$\frac{\rho v}{1-\frac{v^2}{c^2}}\nabla\cdot v+(v\cdot\nabla)\frac{\rho v}{1-\frac{v^2}{c^2}}+\nabla\rho+\nabla\cdot P=0$$

$$P=wk^0k^0-\frac{1}{2}wI=\frac{1}{2}wk^0k^0$$

Where P is the tension tensor .Substituting Eq.(10) into Eq. (9) and considering the action of gravitation of the core ,we have:

$$\frac{\rho v}{1-\frac{v^2}{c^2}}\frac{1}{r^2}\frac{d}{dr}(r^2v)+v\frac{d}{dr}(\frac{\rho v}{1-\frac{v^2}{c^2}})+\frac{d}{dr}(\frac{\rho k_BT}{m})+\frac{1}{2}\frac{d}{dr}W+\rho\frac{GM}{r^2}=0 \quad (12)$$

(3). The equation of state: $T=C_0\rho^{\sigma-1}$

here $C_0=T_0\rho_0^{1-\sigma}$ is decided by initsal condition.For the relativistic elections, we adopt $\sigma=1.5$.

(4) The continuity equation:

$$\frac{\partial\rho}{\partial t}+\nabla\cdot(\rho V)=0$$

Considering steady case and using sphere coorindation, then

$$r^2\rho v=d_0 \quad (13)$$

Here $d_0=r_0^2\rho_0v_0$ is also disided by initial condition.

(5)The conservation of equation of magnetic flux:

$$\nabla\cdot B=0 \qquad \text{i.e.} \qquad r^2B=f_0 \quad (14)$$

Where $f_0=r_0^2B_0$ is desided by initial condition.

From (8) (11) (12) (13) (14) , we get

$$\frac{dv}{dr}\left[\frac{d_0}{r_0}\frac{1+\frac{v^2}{c^2}}{1-\frac{v^2}{c^2}}-\frac{\sigma C_0k_B}{mv}(\frac{d_0}{r^2v})^\sigma+\frac{A_0\pi d_0v_{g0}^3(v+2v_{g0}\frac{v^2}{c^2}-v_{g0})\sqrt{1-\frac{v^2}{c^2}}}{(v_{g0}+v)^3f_0^2v^2}\right.$$

$$\left.+\frac{A_0v_{g0}}{2c^2r^2}\frac{(v^2-2c^2-2v.v_{g0}+v_{g0}^2-2\frac{v^2v_{g0}^2}{c^2})}{(v_{g0}+v)^3\sqrt{1-\frac{v^2}{c^2}}}\right]$$

$$=\frac{2\sigma C_0k_B}{rm}(\frac{d_0}{2c^2v})^\sigma+\frac{2\pi A_0d_0v_{g0}^2(v+2v_{g0}\frac{v^2}{c^2}-v_{g0})\sqrt{1-\frac{v^2}{c^2}}}{f_0^2rv(v_{g0}+v)^2}$$

$$+\frac{A_0v_{g0}(1+\frac{v\cdot v_{g0}}{c^2})}{r^3(v_{g0}+v)^2}\sqrt{1-\frac{v^2}{c^2}}-\frac{d_0GM}{r^4v} \quad (15)$$

3. Calculation and Conclusion :

It is very important to set the initial conditions. Abramowiz and Piran(1980) pointed out the jets are generated in pc scale, namely the particles start to be accelerated nearby10^3 — 10^4 r_g region. On the assumption of the construction of ANGs which we stated above, the nuclei possess not only the supermassive black hole M ~ $10^8 M_\odot$ but also the strong magnetic field B. So we can take initial position r_0 ~ 10^{16} — 10^{18}cm and the magnetic strength B_0 ~ 10---10^2 Guass at r_0 in the direction of pole(lesch 1992). On the basic of the recent observational data and theoretical studies (Cannizzo and Reiff 1992), we choose three sets of initial values:

(1). r_0 ~ 10^{16} cm, ρ_0 ~ 10^{-10}g/cm^3,v_0 ~ 2×10^7cm/s,B_0 ~ 200G,W_0 ~ 10erg/cm^3.

(2). r_0 ~ 10^{17}cm, ρ_0 ~ 10^{-11}g/cm^3, v_0 ~ 10^6cm/s, B_0 ~ 100G, W_0 ~ 50erg/cm^3.

(3).r_0 ~ 10^{18}cm, ρ_0 ~ 10^{-12}g/cm^3, v_0 ~ 10^5cm/s, B_0 ~ 10G, W_0 ~ 100erg/cm^3.

The three sets of values above are corresponding to the different condition of active galaxies.

It is interest to make the choice of the initial value for the energy of the wave.The energy exchange between waves and particles is the most effective only when the resonance of waves with particles takes place. So for each set of initial value only there is one choise which lead to the most effective acceleration, so that the particles reach maximum energy.

By means of equations above to calculation, we get three r — γ Figures (fig.2,3,4) and their Lorentz factors are γ =1,5,15 respectively.

Finally we can conclude that the pressure tensor of plasma turbulent waves (here the Alfven wave) are quite effective to accelerate particles along the magnetic fore lines that can make jets collimate permanently and extend far away, and then can make velocity of jets to reach the relativistic velocity.

Refrences:

1.Asseo,E.& Ol,H.,1987,Phys.148,301

2.Begelman,M.C.,Blandford R.D.,& Rees,M.J.,1984,Rev.Mod.Phys.,56 256

3.Begelman,M.C. & Li Z - Y,1993,Ap.J.

4.Blandford,R.D.,1976,MNRA,176,465.

5.Blandford,R.d.& Ostriker,J.P.,1978,Ap.J.Lett.221,L29.

6.Blandford,R.D.& Payne,D.G.,1982,MNRA,199,88.

7.Blandford,R.D.& Znajek,R.L.1977,MNRA,179,433.

8.Camenzind,M.,1986,A.& A,162,32.

9.Camenzind,M.,1987,A.& A,184,341.

10.Camenzind,M.,1989,in Accretion Disks and Magnetic Fields in Astrophysics,ed. G.Belvedere (Dordrecht:Kluvwer),129.

11.Chiueh,T.,Li,z.y.& Begelman,M.C.,1991,Ap.J.,377,462.

12.Christansen,W.A.,Pacholczyk,A.G.& Cott,J.,1976,Ap.J.,210,311.
13.Eilek,J.A.&Hughes,P.E.,1990, in Astrophysical Jets,ed.P.E. Hughes, P.428, Cambridge Univ.Press.
14.Heyvaerts,J,& Norman,C.A.1989,Ap.J.347,1055.
15.Jafelice,L.C.& Opher,R.1987,Astrophys.space sci.137,303.
16,Krimsky,G.F.,1977,Docl,Acad.Nauk R,234,1306.
17.Lesch,H.,1992,in Extragalactic Radio Sources From Beams to Jets,P.82,Cambrige Univ.Press.
18.Li Z - y.,1993,Ap.J.,415,118.
19.Li Z - y.,Chiueh,T.& Begelman,M.C.,1992,Ap.J.,394,459.
20.Locombe,C.1977,A.& A.,54,1.
21.Lovelace,R.v.E.,1976,Nature,262,649.
22.Lovelace,R.V.E.,Mobarry,C.M.& Contopoulos,J.,1989,in Accretion Disks and Magneticfilds in Astrophysics, Ed.G.Belvedere.
23.Netzer,H,1989,in Active Galactic Nuclei, eds. D.E.Osterbrock and J.Miller,p.69, Cambridge Univ.Press.
24.Phinney,E.,1983,Ph.D.Thesis,Cambrige Univ.
25.Sakuai,T.,1985,A.& A.,152,121.
26.Whitham G.B.,1965,J. Fluid Mech.22. 273.

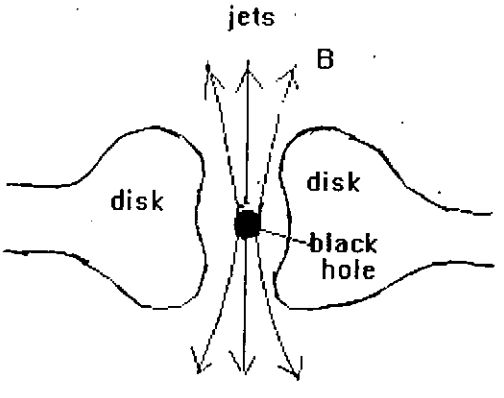

Fig.1 The Modle Of Jets and Accretion

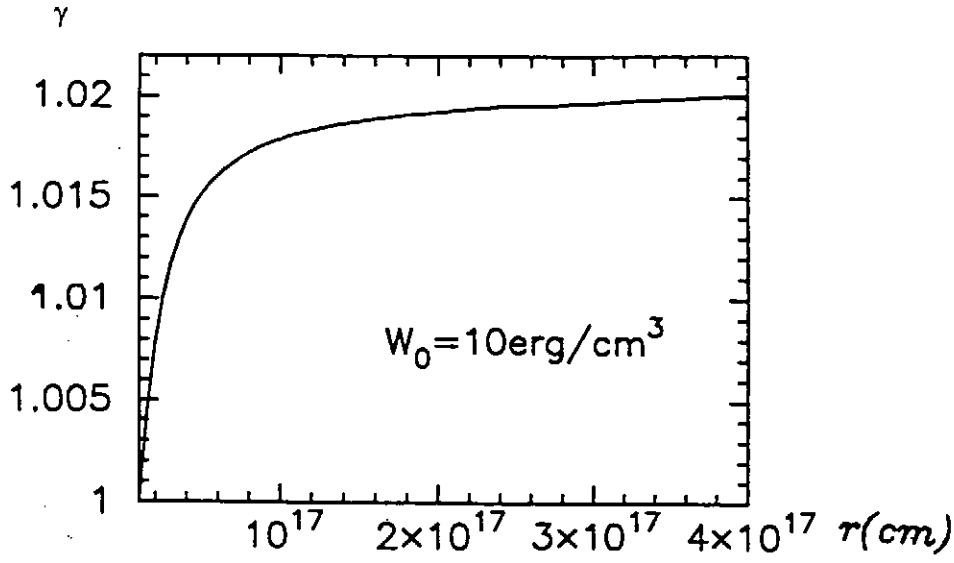

Fig.2 The Maximum Of Lorentz Factor is 1.02

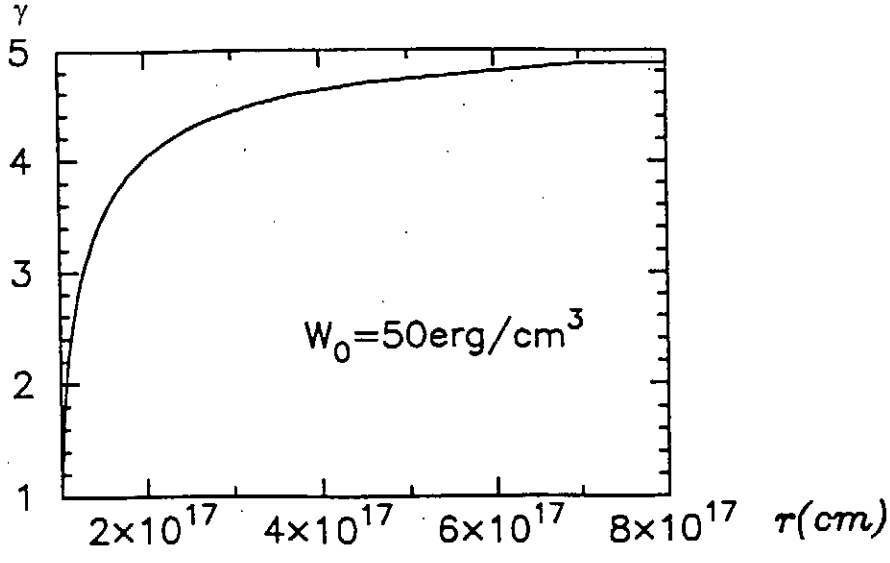

Fig.3 The Maximum Of Lorentz Factor is 4.84

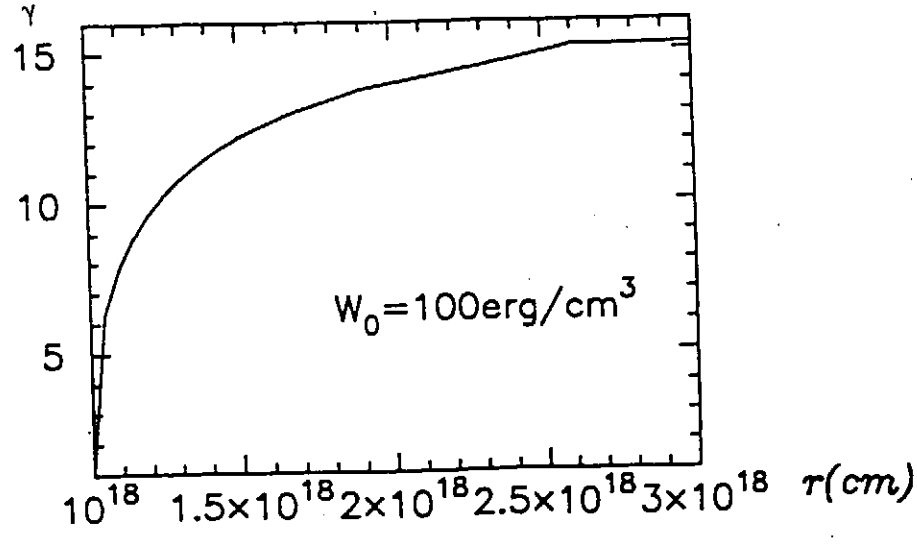

Fig.4 The Maximum Of Lorentz Factor is 15.18

X-RAY VARIABILITY AND MASS OUTFLOWS IN CLASS I PROTOSTAR

MITSURU HAYASHI
Japan Atomic Energy Research Institute(JAERI)
801-1 Mukouyama,Naka-machi,Naka-gun,
Ibaraki,311-01,Japan

KAZUNARI SHIBATA
National Astronomical Observatory
Mitaka, Tokyo 181, Japan

AND

RYOJI MATSUMOTO
Department of Physics, Faculty of Science, Chiba University
Inage-Ku, Chiba 263, Japan

Abstract.

Recent X-ray astronomical observations show that magnetohydrodynamic(MHD) view is of vital importance in understanding the dynamics of the X-ray emitting hot plasmas in the universe. Especially they show that magnetic reconnection plays a key role.

The Solar X-ray satellite, *Yohkoh*, showed various evidences of magnetic reconnection in solar corona. Here we extend the magnetic reconnection model of solar flares to hard X-ray flares observed in star forming regions. We carried out 2.5-dimensional magnetohydrodynamic (MHD) simulations of the disk-star interaction. The closed magnetic loops connecting the central star and the disk are twisted by the rotation of the disk. In the presence of resistivity, magnetic reconnection takes place in the current sheet formed inside the expanding loops. Hot, outgoing plasmoid and post flare loops are formed as a result of the reconnection. Numerical results are consistent with the observed plasma temperature ($10^7 - 10^8$K), the length of the flaring loop ($10^{11} - 10^{12}$cm), and the velocity of optical jets ($200 - 400$km/s). We showed by high-resolution numerical simulations using parallel computers that multiple magnetic islands are created in the current sheet due to the growth of the tearing mode instability. The magnetic islands are ejected

quasi-periodically. The intermittent flaring activity continues so long as the disk matter twists the post-flare loops.

1. Introduction

Observations by the Hubble Space Telescope (HST) and X-ray satellites revealed various energetic phenomena associated with star formation. One remarkable phenomena is the well collimated bipolar plasma outflows (optical jets). Although protostars are obscured in optical wavelength, hard X-rays can peer deep into the core of star forming regions. Observations by Japanese X-ray satellite ASCA showed that protostars are strong hard X-ray emitting sources. By using ASCA, Koyama et al. (1994,1996) carried out a systematic survey of hard X-ray sources in molecular clouds. A protostar (R1 in Coronet cluster) exhibited a powerful X-ray flare whose spectrum indicates significantly higher temperature ($T \sim 10^8$ K) than that in solar flares and X-ray flares in T Tauri stars which is usually $\sim (1-2) \times 10^7$ K (Koyama et al. 1996). Another hard X-ray flare from a protostar in YLW15 was reported by Tsuboi et al. (1997). Protostellar flares are also observed in lower energy band (0.1 - 2.4 KeV) by ROSAT in YLW15 (Grosso et al. 1997). The total energy released by the protostellar flare ($10^{35} - 10^{36}$ erg) is 10^5 times larger than solar flares. The size of the X-ray emitting region is several times larger than the protostar. The decay time of protostellar flare is comparable to that of the solar flare. It suggests that basic physics of protostellar flares is similar to that of solar flares. X-ray observations of the solar corona by the *Yohkoh* satellite (Tsuneta et al. 1991) gave us the evidences which support the model that magnetic reconnection is responsible for the energy release in solar flares (Tsuneta et al. 1992). We should explain why the loop size of X-ray emission and the released energy of protostellar flares are larger than those of solar flares.

The essential difference between the Sun and protostar is the existence of a rotating disk in protostar. In the innermost region of protostellar disk, the magnetic fields of the protostar may affect the dynamical evolution of the disk. Since the rotation of the disk continuously injects helicity into the closed magnetic fields connecting the central star and the disk, we expect magnetic nonequilibrium and resulting magnetic reconnection similar to those studied in the context of solar flares (e.g. Mikić & Linker 1994; Kusano, Suzuki & Nishikawa 1995). Recently, Hayashi et al.(1996) carried out nonlinear time-dependent MHD simulations of the interaction between the dipole magnetic field of the central star and the rotating disk threaded by the dipole field. In the following, we show that the outgoing hot rotat-

ing spheromak created by the magnetic reconnection can be the origin of optical jets and hard X-ray emission.

2. Numerical Models

We solve the resistive MHD equations in cylindrical coordinate (r, ϕ, z) by applying a modified Lax-Wendroff scheme with artificial viscosity. The initial state consists of the magnetized central star and a dense disk rotating in the spherical static halo. The disk is assumed to be in rotational equilibrium. The angular momentum distribution of the disk is nearly Keplerian ($L/L_0 = (r/r_0)^{0.494}$) where the reference radius r_0 is at the pressure maximum of the disk. The density ratio between the disk and the halo is taken to be $\rho_h/\rho_0 = 2 \times 10^{-5}$ where ρ_0 is the maximum density of the disk. The unit velocity is the Keplerian speed v_{K0} at $r = r_0$. The plasma β in the disk at the pressure maximum is $\beta_0 = 8\pi P_0/B_0^2 = 20$.

We use free boundary conditions at the outer boundaries. At the equatorial plane, we assume a symmetric boundary condition. The stellar surface is treated as a thin shell-like damping region where all quantities except magnetic fields are damped. The stellar surface is at $r = 0.528 r_0$. As for resistivity, we assume anomalous resistivity $\eta(r, z) = \eta_0[\max(v_d/v_c - 1.0, 0)]^2$ where v_c is the critical value above which the anomalous resistivity sets in and $v_d = |\mathbf{J}|/\rho$ (Sato & Hayashi 1979). Here, $\mathbf{J}$ is the current density. We adopt $v_c = 1000$ and $\eta_0 = 0.01$ in non-dimensional units.

3. Numerical Results

The results of the simulation of a typical model are shown in Figure 1. Solid curves, gray scale and arrows show the magnetic field lines , temperature, and velocity vectors, respectively. The magnetic field lines connecting the central star and the disk are twisted by the rotation of the disk. As the magnetic twist accumulates, the magnetic loops begin to inflate. They expand quasi-statically in the early stage but after half rotation they expand dynamically. Magnetic reconnection takes place in the current sheet formed inside the expanding loops. Hot plasmas created by the reconnection are confined in the outgoing magnetic island. Note that the magnetic island is a rotating spheromak. The speed of the outflowing hot plasma is the order of the local Alfvén speed $v_A \sim (2-5)v_{K0}$. Crest-shaped fast MHD shock waves are formed in front of the expanding magnetic loops.

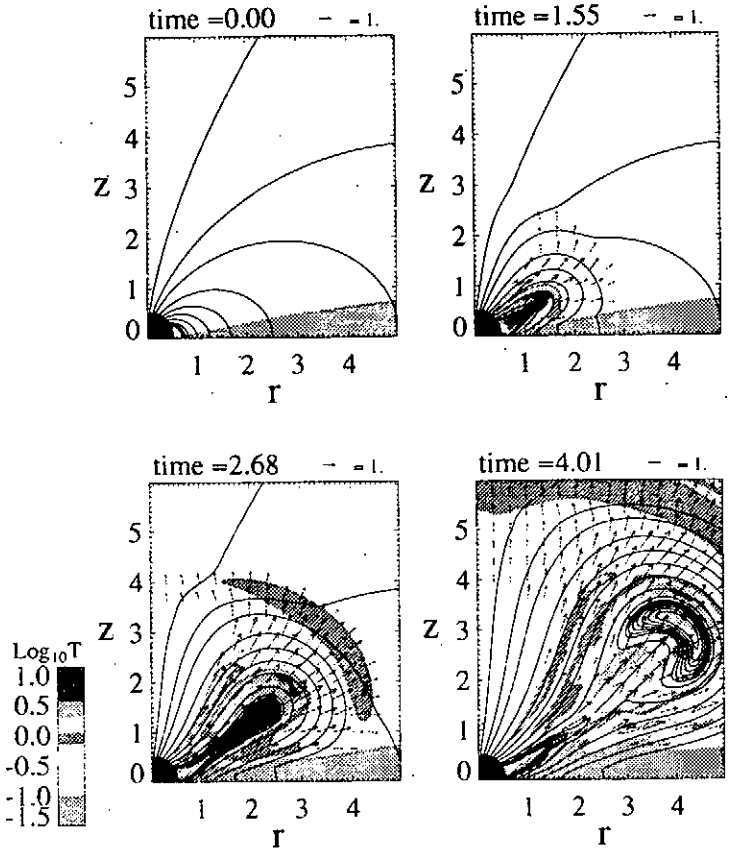

Figure1. The results of the simulation of a typical model

In the model we showed above, magnetic reconnection occurs only once because the dipole magnetic field of the central star is not strong enough to support the magnetically braked disk matter. Since the accreting matter drags the magnetic field lines anchored to the disk, it deforms the magnetosphere of the central star. The footpoints of post flare loops created after the magnetic recoonection event are advected to the stellar surface before the rotation of the disk injects suffient twist into the loop. We carried out another simulation by using magnetic field five times stronger than that in the above typial model and by truncating the disk at the innermost radius at $r=r_0$. Although in this model the surrounding disk is not exactly in dynamical equilibrium, the deviation from the equilibrium is small because its rotation is nearly Keplerian. The results are shown in Figure 2. Solid curves, gray scale and arrows show the magnetic field lines, density, and velocity vectors, respectively. Even after the first reconnection, the inner edge of the disk is detached from the stellar surface. Since the rotation of

the disk twists the post flare loops again, they begin to inflate. Magnetic reconnection and plasmoid ejections occur intermittently.

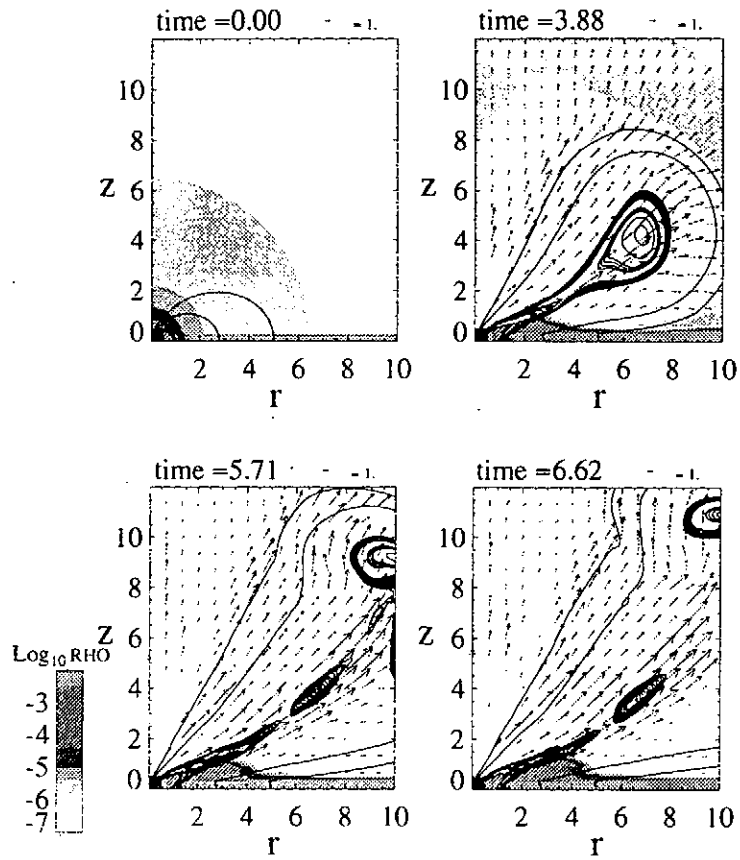

Figure2. Recursive flaring in protostars

4. Discussion

We demonstrated that if the dipole magnetic field of the central star is connected to the rotating disk, the dipole magnetic field loses equilibrium due to the twist injection and that magnetic reconnection takes place. We also showed that hot plasmoids are ejected in bipolar directions with velocity 2−5 times larger than the Keplerian rotation speed. The plasma temperature can rise up to the temperature determined by $v_s \sim v_A \sim 2-5v_K$. Since $v_K \sim 170$ km s^{-1} at $r = 0.03$ AU around 1 $M_\odot$ star, the temperature of the plasmoid and the post flare loop can be $10^7 - 10^8$ K. This temperature is consistent with the temperature obtained from the observation of an X-ray flare from a protostar (Koyama et al. 1996). Since magnetic reconnection

accelerates electrons, we expect synchrotron radiation from ejected plasmoids. Recently, Hughes (1997) reported that in the young star forming region Cepheus A, nonthermal sources are separating with a relative transverse velocity($\sim$ 370 km/s). In T-Tauri region, Ray et al. (1997) found two lobes which emit radio emission exhibiting strong circular polarization of opposite helicity. These observations are consistent with our reconnection model of hot plasmoid ejections.

Numerical results show that hot plasmas are created in gigantic loops several times larger than the stellar radius. It is consistent with the observational constraint that hard X-ray emitting region is larger than the size of the protostar. After the X-ray emitting gas is cooled down (cooling time $\sim$ 1 day), it will be observed as optical jets.

Next, let us discuss whether the magnetospheric flares can release the observed total energy of X-ray flares. In our simulation, initial magnetic energy is thermalized within one rotation period ($\sim 10^5$ sec at 0.03 AU). If the size of the flaring region is $d \sim 10^{11}$ cm and the mean strength of magnetic field in the flaring region is $B \sim 100 - 200$ G, the released energy $L \sim (B^2/8\pi)\, d^3 \sim 10^{36}$ erg is the order of the observed luminosity.

In conclusion, both hard X-ray flares and optical jets in protostars can be explained by magnetic reconnection driven by the helicity injection from the disk to the magnetosphere. Numerical results show recursive flares and intermittent mass ejections in magnetically linked disk-star system.

Recently, ASCA detected X-ray flaring variability which repeats three times recursively (Tsuboi et al. 1997). This can be the first observation which supports intermittent flaring variability in star forming region.

References

Grosso, N., Montmerle, T., Feigelson, E.D., André, P., Cassanova, S., & Gregorio-Hetem, J. 1997, *Nature*, **385**, 56
Hayashi, M.R., Shibata, K. & Matsumoto, R. 1996, *ApJ*, **468**, L37
Hughes, V. A., 1997, *ApJ*, **481**, 857
Koyama, K., Hamaguchi, K., Ueno, S., Kobayashi, N., & Feigelson, E. D. 1996, *PASJ*, **48**, L87
Koyama, K. et al. 1994, *PASJ*, **46**, L125
Kusano, K., Suzuki, Y., & Nishikawa, K. 1995, *ApJ*, **441**, 942
Mikić, Z., & Linker, J. A. 1994, *ApJ* , **430**, 898
Ray, T. P., Muxlow, T. W. B., Axon, D. J., Brown, A., Corcoran, D., Dyson, J., & Mundt, R. 1997, *Nature*, **385**, 415
Sato, T. & Hayashi, T. 1979, *Phys. Fluids*, **22**, 1189
Tsuboi, Y. et al. 1997 IAU Symposium No.188, "The Hot Universe"
Tsuneta, S. et al. 1991, *Sol. Phys* ,**136**,37
Tsuneta, S.,1992, IAU Colloquim No. 153,"Magnetohydrodynamic Phenomena in the Solar Atmosphere", ed. Kosugi & Uchida, Kluwer
Woltjer, L. 1958, *Proc. Natl. Acad. Sci. U.S.A.*, **44**, 489

Quantum Effects on the Motion of Charged Particles Near Neutral Surface of a Magnetic Field

Sergei BULANOV[1,2], Enzo LAZZARO[3], and Jun-ichi SAKAI[1]

[1]Laboratory for Plasma Astrophysics and Fusion Science,
Department of Electronics and Information, Faculty of Engineering,
Toyama University, Toyama 930, Japan
[2] General Physics Institute of Russian Academy of Sciences, Moscow, Russia
[3] Institute for Plasma Physics - CNR, Milan, Italy

Abstract

We present results of the classical and quantum descriptions of the charged particle motion near a neutral surface of the magnetic field, where the magnetic field vanishes. Far from the neutral surface the drift approximation is valid in the classical limit meanwhile the Landau description of the charged particle in the magnetic field can be used in the quantum case. In the vicinity of the neutral surface, at the distance in the classical regime less then the Larmor radius, the particle motion is described by the Schrödinger equation with the potential that corresponds to that of the harmonic oscillator with the frequency that depends on the particle momentum along the neutral surface.

1 Introduction

Quantum effects in the charged particle motion in the magnetic field come into play when the particle energy becomes comparable with the energy difference between the Landau levels, [1].

$$E \approx \hbar\omega_B, \tag{1}$$

where $\omega_B = eB/mc$. In the magnetic field with the strength of order of $10^{10}\,Gauss$ the quantum effects must be taken into account for the electrons with the energy less than $100\,eV$.

Multi terawatt and petawatt lasers with intensity is as high as $10^{19-21}W/cm^2$ [2] have proved to be a source of the strongest electromagnetic fields available in laboratories. The electromagnetic radiation with such the intensity excites in plasmas magnetic fields with a magnitude of the order of $10^{10}\,Gauss$ [3-5] meanwhile the temperature of order of $100\,eV$ corresponds to the temperature of the cold component of the laser plasma that is why the quantum effects must be incorporated into description of ultra high intensity laser pulse interaction with matter.

Due to the symmetry of the laser pulse, the magnetic field reverses its sign on the laser beam axis. We use 2D approximation when the magnetic field is supposed to depend on the y-coordinate and vanish on the neutral surface $y = 0$ where it can be approximated as

$$\mathbf{B} = -by\mathbf{e}_z. \tag{2}$$

We assume also that the electric field is uniform and is directed along the x-axis:

$$\mathbf{E} = -\mathcal{E}\mathbf{e}_x. \tag{3}$$

2 Classical Orbits near Neutral Surface

We modify the equation of particle motion to take into account its interaction with magnetic field due to the spin: the particle is supposed to possess an intrinsic magnetic moment μ. It reads

$$\ddot{x} = \frac{e\mathcal{E}}{m} + \frac{eb}{mc}\dot{y}y, \tag{4}$$

$$\ddot{y} = -\frac{eb}{mc}\dot{x}y - \frac{\mu\sigma}{ms}b. \tag{5}$$

These can be reduced to equations with a time dependent Hamiltonian

$$\mathcal{H}(p_y, y, t) = \frac{p_y^2}{2m} + W(y,t) = \frac{p_y^2}{2m} + \frac{eby^2\mathcal{P}(t)}{2m^2} + \frac{e^2b^2y^4}{8m^2c^2} + \frac{\mu by}{m}, \tag{6}$$

where

$$\mathcal{P}(t) = m\left(v_0 + \frac{e\mathcal{E}}{m}t - \frac{eb}{2mc}y_0^2\right). \tag{7}$$

When $\mathcal{P}$ is negative the effective potential $W(y)$ has two minima (see Fig.1). For negative value of the Hamiltonian, $\mathcal{H} = h$, the particle is trapped in the region far from the the surface $y = 0$. The trajectory is localized either near the surface $y = y_+$ or near $y = y_-$. If $\delta = \mu/\mu_c \ll 1$, where $\mu_c = (8e|\mathcal{P}|^3/27m^2c)^{1/2}$, we have for the coordinates $y_\pm$: $y_\pm(\mathcal{P}) \approx \pm(2|\mathcal{P}|c/eb)^{1/2} - \mu(m^2cb/8e|\mathcal{P}|^3)^{1/2}$. When $\mathcal{P} < 0$ and $h > 0$ the particle trajectory is meandering in the vicinity of the neutral surface (Fig.2).

For $\mathcal{P}$ positive the particle trajectory is in the inner region near the neutral surface. If $h < 2\mathcal{P}/m - \mu^2 b/2e\mathcal{P}$, the particle moves along the x-axis with the velocity $v_0 - eby_0^2/2mc$ and oscillates in the transverse direction. The frequency of oscillations is equal to $\Omega = (eb\mathcal{P}/m^2c)$.

When $\delta \gg 1$ the effective potential has only one minimum. In this case the separatrix in the phase plane disappears.

In the electric field the coordinate, $y_\pm$, and the giration frequency, $\omega_B(y_\pm)$, change with time. In Fig.3 the particle trajectory is shown for the parameter $\delta = 1$.

We find the dependence of the y-coordinate on time in the inner region as

$$y \approx y_0\left(\frac{1}{\Omega_V(t)T}\right)^{1/4}\sin\left(\int_0^t \Omega_V(t)\,dt + \frac{\pi}{4}\right), \tag{8}$$

with $\Omega_V(t) = (e^2\mathcal{E}btm^2c)^{1/2}$ being instantaneous frequency of oscillations. We can see there is an adiabatic invariant $J_{\text{in}} = E_{\perp\text{in}}(t)/\Omega_V(t)$, associated with the transverse motion. The adiabatic invariant associated with the particle motion along the y-coordinate far from the neutral surface is $J_{\text{out}} = E_{\perp\text{out}}(t)/\omega_B(t)$.

To match solutions in the outer and inner regions we assume the parameter $\varepsilon_c = (e\mathcal{E}^2 c/mbv^3)^{1/2}$ to be small. The boundary between the outer and inner regions corresponds to the separatrix in the phase plane (p_y, y). It divides the phase plane into three regions. In Fig.3c the particle trajectory in the phase plane $(\dot{y}, y)$ is shown. We see change of the particle motion during the separatrix crossing. The adiabatic invariant magnitude, it is the area of the surface enclosed by the trajectory, increases in two times. Accuracy of the adiabatic invariant conservation during the separatrix crossing is of order $\varepsilon_c \ln \varepsilon_c$ [6].

If $\delta \ll 1$, we obtain relationship between the values of the adiabatic invariants in the outer and inner regions. It is $J_{\rm in} = 2J_{\rm out} + o(\varepsilon_c \ln \varepsilon_c)$.

For $\delta > 1$ the effective potential has only one minimum. In this case we obtain that $J_{\rm in} = J_{\rm out} + o(\varepsilon_c^{5/6})$ [7]. In Fig.4 the particle trajectory in the phase plane $(\dot{y}, y)$ is shown for $\delta = -10$.

3 Quantum Motion near Neutral Surface

For stationary motion of the particle with the energy E in the magnetic field with the neutral surface the Schrödinger equation for a wavefunction ψ is

$$\hat{H}\psi = \left(\frac{1}{2m} \left(\hat{p}_x + \frac{eb}{2c} y^2 \right)^2 + \frac{\hat{p}_y^2 + \hat{p}_z^2}{2m} - e\mathcal{E}x + \frac{\mu \hat{s}}{s} by \right) \psi = E\psi. \tag{9}$$

At first we suppose the electric field to vanish, $\mathcal{E} = 0$, and introduce a function $\chi(y)$ which is related the ψ function as $\psi = \exp(i(p_x x + p_z z)/\hbar)\chi(y)$. From (9) we obtain the equation

$$\frac{d^2\chi}{dy^2} + \frac{2m}{\hbar^2} \left(E + \frac{\mu\sigma}{s} by - \frac{p_z^2}{2m} - \frac{1}{2m} \left(p_x + \frac{eb}{2c} y^2 \right)^2 \right) \chi = 0. \tag{10}$$

For large negative p_x and relatively small energy E the χ-function is localized in the vicinity of the minimums of the effective potential, $y = y_\pm \approx \pm(2p_x c/eb)^{1/2}$. Electron motion in the y-direction is described by the Landau theory with the magnetic field equal $by_\pm$. The energy is quantized being equal to

$$E_{out} = \hbar\omega_B(y_\pm) \left(n_{out} + \frac{1}{2} \right) + \frac{p_z^2}{2m} - \mu \frac{\sigma}{s} by_\pm. \tag{11}$$

For large enough positive x-component of the momentum, $p_x \gg (\hbar^2 eb/16c)^{1/3}$ the χ function is localized in the inner region near the surface $y = 0$. The χ function obeys equation

$$\frac{d^2\chi}{dy^2} + \frac{2m}{\hbar^2} \left(E - \frac{p_x^2 + p_z^2}{2m} + \frac{e\hbar^2 b\sigma^2}{8mc^2 p_x s^2} - \frac{ebp_x}{2mc} (y - \tilde{y})^2 \right) \chi = 0, \tag{12}$$

where $\tilde{y} = \mu\sigma mc/ep_x s$. This is the Schrödinger equation for the harmonic oscillator with the energy levels given by relationship

$$E_{in} = \hbar \left(\Omega \left(n_{in} + \frac{1}{2} \right) + \frac{e\hbar b}{8mc^2 p_x} \right) + \frac{p_x^2 + p_z^2}{2m}. \tag{13}$$

Here $\Omega = (ebp_x/m^2c)^{1/2}$ corresponds to the frequency of transverse oscillations of the classical particle with the x-component of momentum $p_x = \mathcal{P}$ in the inner region. The ψ-function of harmonic oscillator is expressed in terms of the Hermite polinomials [1], with the width of localization of the wave function equal $Y = (c\hbar^2/ebp_x)^{1/4}$.

The electric field modifies dependence of the ψ-function on the longitudinal component of the momentum. To study this effect we rewrite the stationary Schrödinger equation (9) for the wave function $a(p,\eta)$ in the momentum representation with respect to the ξ-coordinate. It reads

$$\left(i\partial_p - p^2 + \varepsilon_q^{1/2}\left(\partial_{\eta\eta} - \eta^2 p\right) + \varepsilon_q^{3/4}\frac{\sigma}{s}\eta - \varepsilon_q\frac{1}{4}\eta^4\right)a(p,\eta) = 0. \tag{14}$$

Here ξ and η are normalized x- and y-coordinates. The parameter $\varepsilon_q = (\hbar b/2\mathcal{E}mc)^{1/2}$ we assume to be small to look for solution of equation (14) in the form

$$a(p,\eta) = \frac{C(v,w)}{(2\pi)^{1/2}}\exp\left(i\left(\varepsilon_q^{1/2}\int^p E_\perp(p)dp - \frac{p^3}{3}\right)\right), \tag{15}$$

where new variables v and w depend on η and p as $v = \eta p^{1/4}$, $w = \varepsilon_q p$. The transverse energy, $E_\perp(p)$ depends on the momentum $p = w/\varepsilon_q$. This yields for the function $C(v,w)$ equation

$$\left(w^{1/2}\left(\partial_{vv} - v^2\right) + \varepsilon_q^{1/2}E_\perp\left(\frac{w}{\varepsilon_q}\right)\right.$$
$$\left.+\varepsilon_q\left(\partial_w - \frac{v}{4w}\partial_v + \frac{\sigma v}{sw^{1/4}}\right) - \varepsilon_q^{3/2}\frac{v^4}{w^{1/2}}\right)C = 0. \tag{16}$$

To leading order in the parameter ε_q we obtain that the function $C(v,w)$ depends only on the variable v as

$$C(v) = \left(\frac{1}{\pi}\right)^{1/4}\frac{1}{(2^n n!)^{1/2}}\exp\left(-\frac{v^2}{2}\right)H_n(v), \tag{17}$$

with the transverse energy equal $E_{\perp\,in}(p) = p^{1/2}(n_{in} + 1/2)$. In dimensional units expression for the transverse energy takes the form

$$E_{\perp\,in}(p) = \Omega_V(p)\left(n_{in} + \frac{1}{2}\right) \tag{18}$$

with $\Omega_V(p) = (ebp/m^2c)^{1/2}$.

This expression is valid for large enough momentum value of the particle, $p \gg 1$.

Above we have found asymptotic representations of solution valid in the limit $p \to -\infty$ in the outer region and in the limit $p \to +\infty$ in the inner region, respectively. To match the solutions when the value of the variable p varies from large in absolute value negative magnitudes to large positive magnitudes we invoke the fact that there is a well known correspondence between quantum numbers and the adiabatic invariants of the classic motion: under slow adiabatic perturbations the quantum numbers do not change. That is why for slow dependence on the variable p we use the connection between the adiabatic invariants in the outer and inner regions given by relation

$$J_{\text{in}} = 2J_{\text{out}} + o(\varepsilon_c \ln \varepsilon_c) \tag{19}$$

for relatively small μ. This gives

$$n_{in} = 2n_{out}. \tag{20}$$

If the value of μ is so large that the effective potential has only one minimum we obtain for the case when

$$J_{\text{in}} = J_{\text{out}} + o(\varepsilon_c^{5/6}) \tag{21}$$

a relationship

$$n_{in} = n_{out}. \tag{22}$$

Conclusions

Far from the neutral surface approximations based on the drift motion theory in the classical limit and the Landau theory in quantum case, respectively, can be used to describe the particle behavior. Near the neutral surface these approximations do not valid. In the inner region the trajectory has the meander form in the classical limit with the frequency of transverse oscillations that depends on the particle longitudinal momentum. In the quantum limit the particle transverse energy is quantized with the distance between energy levels that depends on the longitudinal component of the momentum. The matching of the solutions in outer and inner regions has been performed invoking the adiabatic invariant conservation. In the quantum limit this gives relationships between quantum numbers in outer and inner regions.

Acknowledgement

One of the authors (S.B.) appreciates the financial support from the Japan Society for Promotion of the Sciences (grant ID No. L96556).

References

[1] L. D. Landau, and L. M. Lifshits: *Quantum Mechanics.* (Pergamon Press, New York, 1959).

[2] M. D. Perry, and G. Mourou: *Science*, **264** (1994) 917.

[3] D. W. Forslund, et al.: *Phys. Rev. Lett.*, **54** (1985) 558.

[4] S. C. Wilks, et al.: *Phys. Rev. Lett.*, **69** (1992) 1383; M. Tabak, et al.: *Phys. Plasmas*, **1** (1994) 1626.

[5] G. A. Askar'yan, S. V. Bulanov, F. Pegoraro, and A. M. Pukhov: *JETP Lett.*, **60** (1994) 241; *Plasma Physics Reports*, **21** (1995) 985; *Comments on Plasma Physics and Controlled Fusion*, **17** (1995) 35; A. M. Pukhov, and J. Meyer-ter-Vehn: *Phys. Rev. Lett.*, **76** (1996) 3975; S. V. Bulanov, T. Zh. Esirkepov, M. Lontano, F. Pegoraro, and A. M. Pukhov: *Phys. Rev. Lett.*, **76** (1996) 3562.

[6] A. V. Timofeev: *Sov. Phys. JETP*, **75** (1978) 1303; A.I.Neishtadt: *Sov. J. Plasma. Phys.*, **12** (1986) 992; J. L. Tennyson, J. R. Cary, and D. F. Escande: *Phys. Rev. A*, **32** (1986) 4256.

[7] S. V. Bulanov, and S. G. Shasharina: *Nuclear Fusion*, **32** (1992) 1531; S. V. Bulanov, and N. M. Naumova: *Physica Scripta*, **T63** (1996) 190.

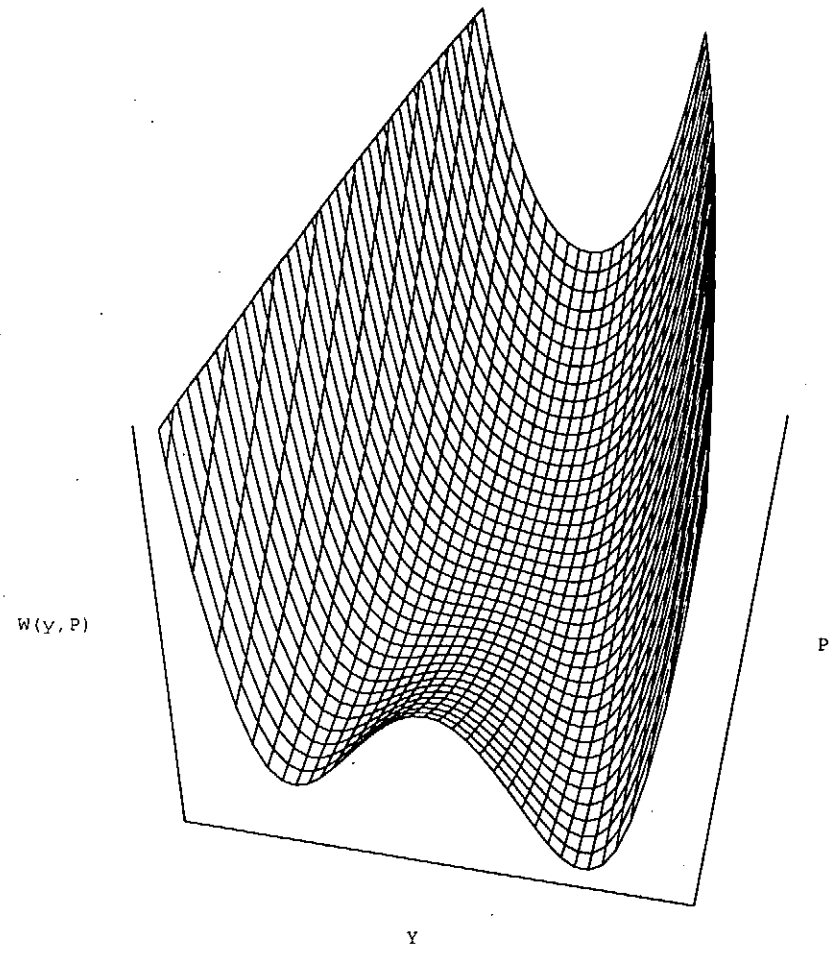

Fig. 1. Effective potential $W(y, \mathcal{P})$.

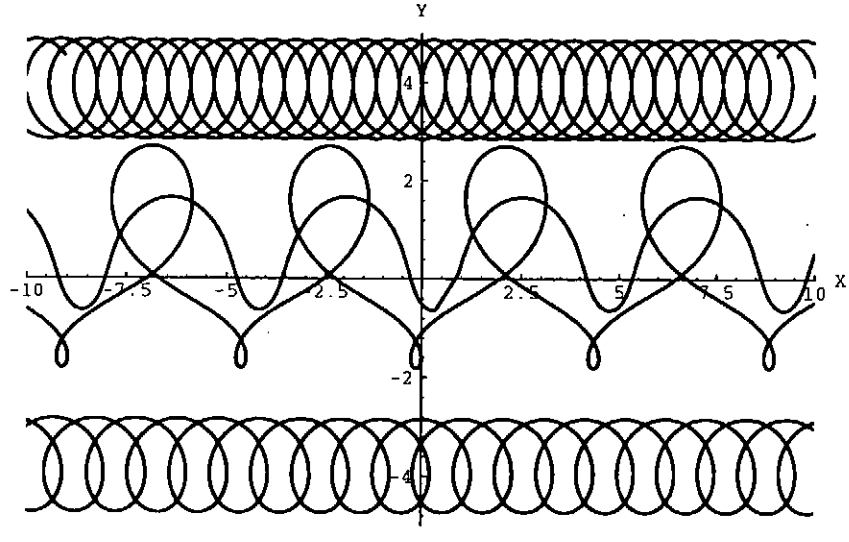

Fig. 2. Particle trajectories near the neutral surface of the magnetic field for $\dot{\mathcal{E}} = 0$.

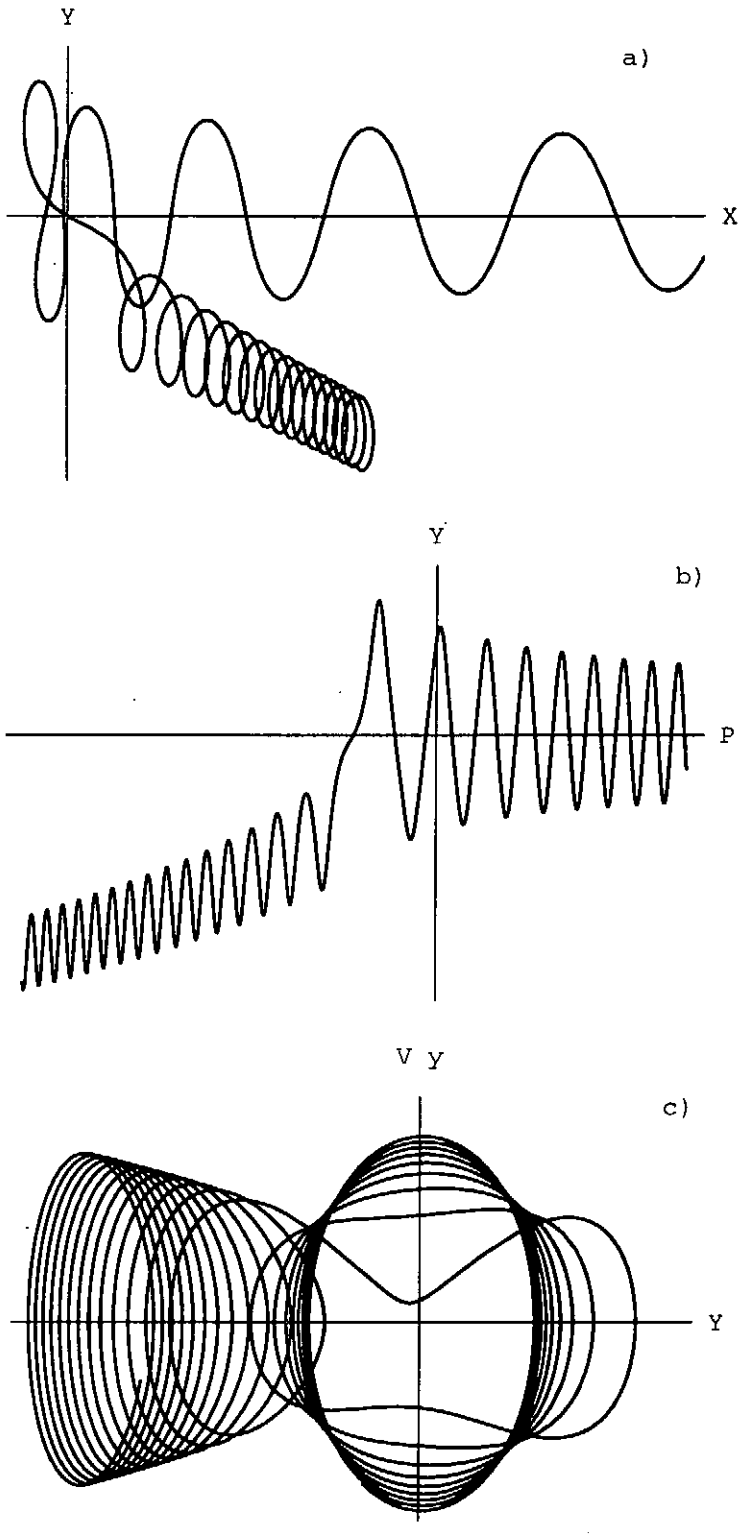

Fig. 3. Particle motion near the neutral surface of the magnetic field for $\mathcal{E} = 1$, $v_0 = -5$, $\dot{y}(0) = 1$, $x(0) = 0$, $y_0 = 0$, $\delta = 1$: a) trajectory in the (x, y) plane; b) a) trajectory in the (x, p_y) plane; c) rajectory in the phase plane $(\dot{y}, y)$.

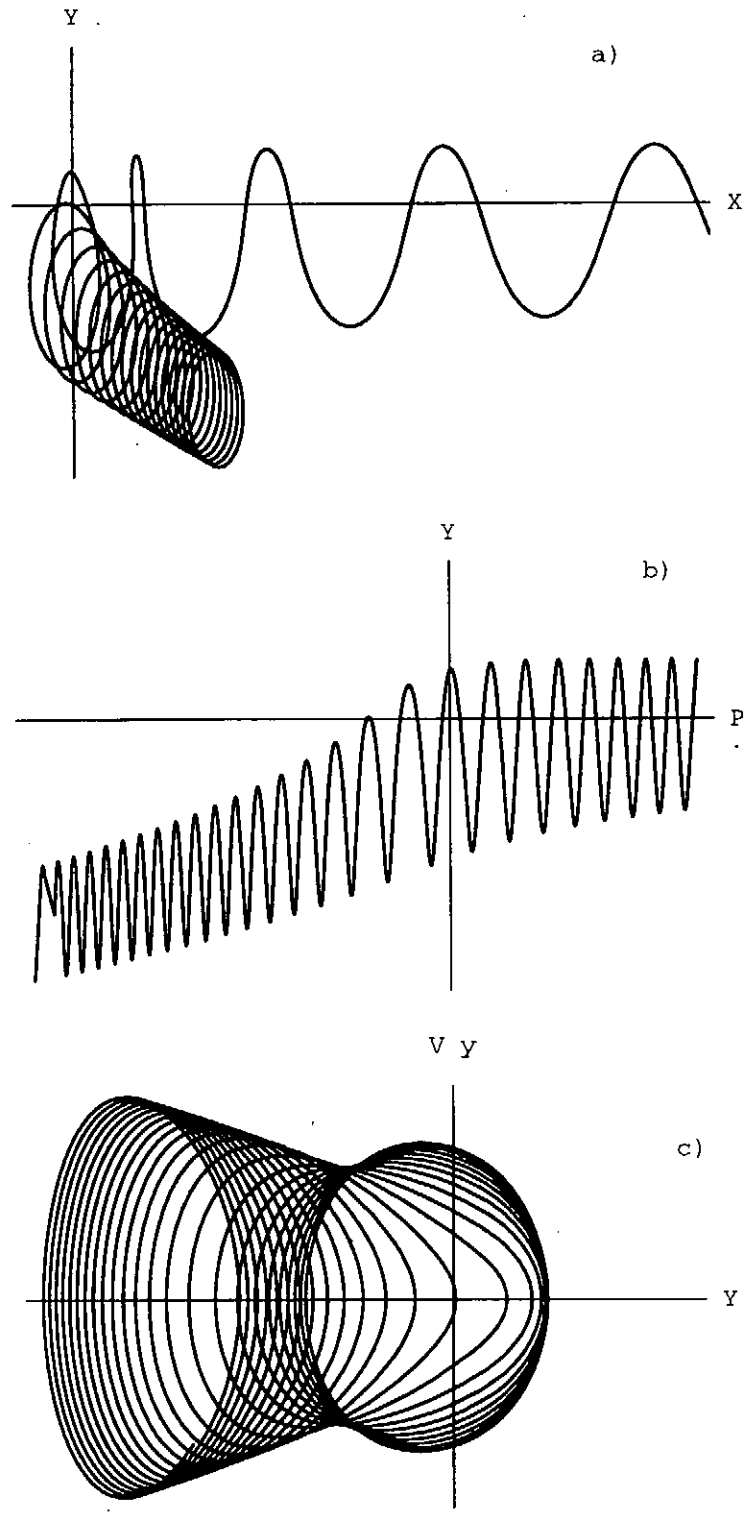

Fig. 4. Particle motion near the neutral surface of the magnetic field for $\mathcal{E} = 1$, $v_0 = -5$, $\dot{y}(0) = 1$, $x(0) = 0$, $y_0 = 0$, $\delta = -10$: a) trajectory in the (x, y) plane; b) trajectory in the (x, p_y) plane; c) trajectory in the phase plane $(\dot{y}, y)$.

Resonance with saddle virtual potential and transition to spatio-temporal chaos via crisis

He Kaifen
Inst. of Low Ener. Nucl. Phys., Beijing Normal Univ., 100875, Beijing, China

Chaotic motions with spatial coherence and incoherence are found to exhibit different spatial spectra. A crisis may induce a transition from the former to latter state. It is found that resonance of a realized solution with a 'virtual potential' is responsible for the onset of crisis. Another solution that can not be realized due to saddle instability plays the role of 'virtual potential'.

I. INTRODUCTION

One of the motivations of studying nonlinear dynamics is to answer a natural question: what is the mechanism for the transition from laminar to turbulence? Indeed, in recent years there has been great progress in understanding bifurcation behaviors in nonlinear systems. Different scenarios to chaos are found, e.g., period doubling, intermittency, Ruelle-Takens route. With these scenarios people successfully explained how the temporal behavior of a motion becomes chaotic. However, when discussing turbulence one should speak of space-time chaos (see Ref. [1], in the following, when mention turbulence we mean a chaotic motion with spatial incoherence), then a question can not be avoided: what causes the collapse of spatial coherence? Unfortunately the above mentioned bifurcation scenarios can not explain this problem. In fact, even as a phenomenon we know very little about turbulence. For example, are there also different routes leading to spatial irregularity? If this is true, do they have respective spatial features? In the present paper we can not answer all these questions, but we do find that in space-time-dependent system chaotic motions can display different spatial behaviors, either coherent or incoherent. And there is evidence to show that a crisis is responsible for the transition from the former to latter. In Sec.II we describe different spatial characters of the temporal chaos and spatio-temporal chaos. In Sec.III and IV we show that the transition is induced by a crisis which is essentially a spatio-temporal resonance with a saddle solution, the latter plays a role of a 'virtual potential' that causes instability. In Sec.V, the mechanism is further discussed, it is shown that the crisis is so called heteroclinic tangency [2].

II. DIFFERENT SPATIAL FEATURES OF CHAOTIC MOTIONS

For investigating turbulence one has to use space-time-dependent system as a model, for in such a system the motion has freedom to develop in space. In the present paper a nonlinear drift-wave equation driven by a sinusoidal wave [3] is used as our model,

$$\partial\phi/\partial t + a\partial^3\phi/\partial x^2\partial t + c\partial\phi/\partial x + f\phi\partial\phi/\partial x = -\gamma\phi - \epsilon sin(x - \Omega t). \quad (1)$$

Here c is drift velocity, $a < 0$ linear dispersion arising from the convection term, and the nonlinear term comes from temperature derivative. Pseudo-spectral method is used to simulate Eq.1 with 2π boundary condition.

In analyzing the solutions of Eq.1 a remarkable phenomenon attracted our attention. That is, the steady 'wave energy' E_0 as a function of driving strength ϵ displays as groups of hysteretic curves, and each group of hystereses is clearly connected with a regime where turbulent solutions can be observed [3]. In contrast in the regimes where there is no hysteresis we did not find such solutions. Here $E_0 \equiv E(\phi_0)$, with $E(t) = \frac{1}{4\pi}\int_0^{2\pi}[\phi^2(x,t) - a\phi_x^2(x,t)]dx$ and $\phi_0 \equiv \phi_0(x - \Omega t)$ is a steady wave solution of Eq.1. This phenomenon suggests that hysteresis might play very important role inthe onset of turbulence.

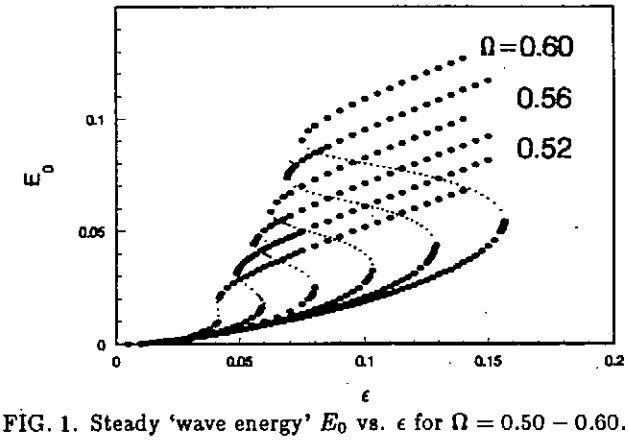

FIG. 1. Steady 'wave energy' E_0 vs. ϵ for $\Omega = 0.50 - 0.60$.

Fig.1 gives a group of hysteretic curves. Each S-shaped curve corresponds to a fixed driving phase speed Ω. To look for the curves one can set $\xi = x - \Omega t, \tau = t$, and expand $\phi_0(\xi) = \sum_k A_k \cos(k\xi + \theta_k)$, then solve the algebraic mode equations of the steady equation

$\partial\phi_0(\xi)/\partial\tau = 0$. If starting from a state that is unstable one can find periodic or chaotic $E(t)$. If $E(t)$ is chaotic, the temporal behavior of $\phi(x,t)$ is definitely chaotic, but its spatial behavior can be either coherent or incoherent. The latter case is a space-time chaos or turbulence. In the following analysis we realize that indeed the existence of hysteresis plays a key role for the onset of turbulence in our case. The reason is, in each hysteretic curve there is a negative tangent branch (middle branch of S-curve), on which the steady solution is a saddle-node [4]. It is this saddle wave solution that plays important role in the transition to turbulence. Before going to the details of the mechanism let's first discuss the different spatial features of the chaotic motions.

Since in the case of Fig.1 turbulent states appear in the regime near the middle or upper branch of a hysteresis, in the following investigations we focus on the solutions in such regime. For this purpose in simulating Eq.1 the initial distribution $\phi(x,t=0)$ must be chosen properly so as to avoid the solutions falling onto the vicinity of lower branch of the hysteresis. As mentioned above, in the simulations we find two different types of chaotic $\phi(x,t)$. One is chaotic in time but regular in space (TC), the other is chaotic both in time and in space (STC). Fig.2 is a spatio-temporal pattern of TC state for $\{\Omega,\epsilon\} = \{0.65, 0.19\}$. In the plot one can see that the temporal variation is chaotic, but its spatial structure is very smooth, i.e. the solution is spatially coherent.

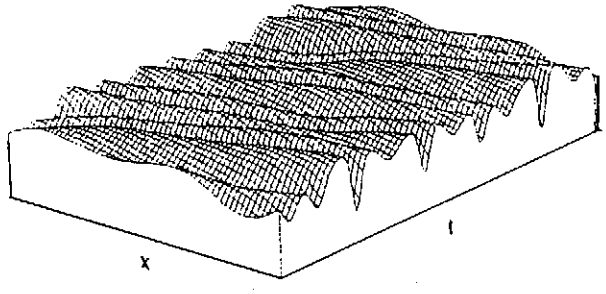

FIG. 2. Spatio-temporal pattern $\phi(x,t)$ in TC state for $\Omega = 0.65, \epsilon = 0.19$.

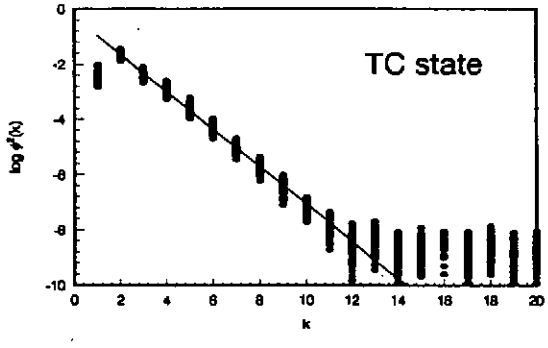

FIG. 3. Power spectra $\phi^2(k)$ for a TC state, $\Omega = 0.65, \epsilon = 0.19$.

Fig.3 gives its spatial spectrum, $\phi^2(k)$, at different times. The solid line is the fitting to the time-averaged value $\langle\phi^2(k)\rangle$ for $2 \le k < k_{\max}$, here $k_{\max}$ is determined by the roundoff error. One can see the spectrum decreases exponentially with k .

Figs.4(a)(b) give an example of transition from TC to STC state for $\{\Omega,\epsilon\} = \{0.65, 0.22\}$. In the early stage of this example the motion is chaotic in time but coherent in space (TC phase, omitted in Figs.4), which looks very similar to that in Fig.2. Then somehow due to a crisis, the spatial coherence is destroyed, and the motion becomes very turbulent(STC phase). In between TC and STC phases, the motion seems to experience a transition phase, in which the amplitude is excited to much higher level but the pattern is still smooth. Fig.4(a) starts from the motion in this transition phase followed by STC phase. In Fig.4(b) it keeps in STC state.

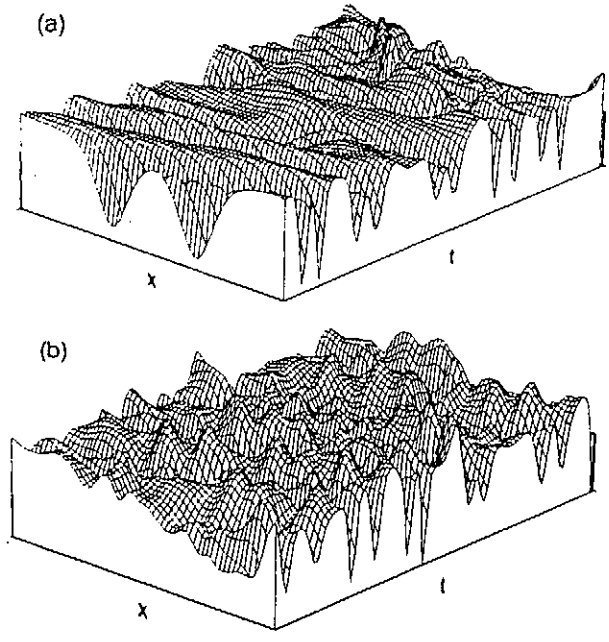

FIG. 4. Spatio-temporal patterns $\phi(x,t)$ for $\Omega = 0.65, \epsilon = 0.22$.

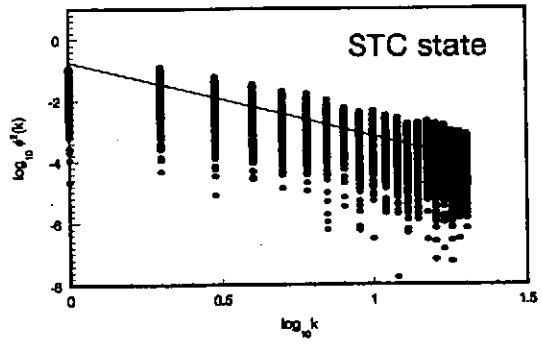

FIG. 5. Power spectra $\phi^2(k)$ for a STC state, $\Omega = 0.65, \epsilon = 0.22$.

Fig.5 is the spatial spectrum $\phi^2(k)$ corresponding to Fig.4(b), again the solid line gives the fitting to $\langle\phi^2(k)\rangle$. In this case, however, the spectrum follows a power law, $k^{-\alpha}$.

III. RESONANCE WITH AN UNREALIZED WAVE SOLUTION

The results shown in Figs.4 is a solution realized in simulation. However, with the same parameters $\{\Omega, \epsilon\}$ there is another solution that can not be realized. It would be heuristic if we draw them in the same plot. In Fig.6(a-f) solid line gives the spatial pattern of $\phi(x,t)$ obtained in numerical simulation of Eq.1 at different times. The dashed line gives another steady solution $\phi_0^{(m)}(x,t)$ corresponding to the same parameters $\{\Omega, \epsilon\} = \{0.65, 0.22\}$. However, $\phi(x,t)$ is a realized one in simulation of Eq.1, while $\phi_0^{(m)} = \phi_0^{(m)}(x - \Omega t)$ can not be realized, whose 'wave energy' locates at the middle branch of S-curve [denoted by superscript (m)].

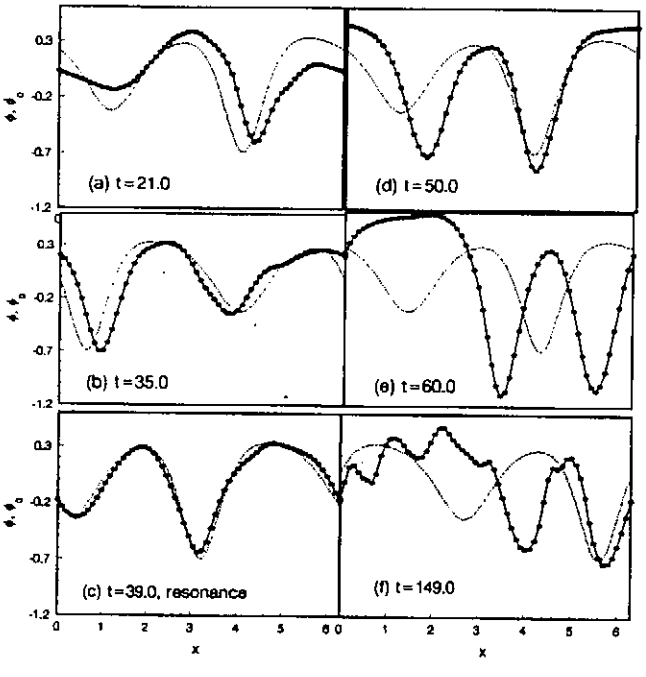

FIG. 6. Spatial patterns $\phi(x,t)$ and $\phi_0^{(m)}(x,t)$ in different times, $\Omega = 0.65, \epsilon = 0.22$.

One can see in Figs.6(a),(b) ($t = 21.0, 35.0$) $\phi(x,t)$ is in TC phase, its spatial pattern looks very smooth although it is variable with time. The crisis happens at about $t^* = 39.0$ [Fig.6(c)], at this critical moment the spatial form $\phi(x,t^*)$ is very close to that of unstable solution $\phi_0^{(m)}(x - \Omega t^*)$. Immediately after that, a remarkable phenomenon happens. The amplitude of $\phi(x,t)$ is excited to a level much higher than that of $\phi_0^{(m)}$, but its spatial pattern still smooth [Figs.6(d)(e), $t = 50.0, 60.0$]. This period corresponds to the transition phase in Fig.4(a). After this short transition phase, the motion transits to turbulence. Fig.6(f) ($t = 149.0$) gives such an example where the motion is in turbulent or STC phase. In this case $\phi(x)$ is no longer smooth for the high k modes are excited. These phenomena strongly suggests that a spatio-temporal resonance seemingly occurs at critical time t^* that induces the onset of turbulence.

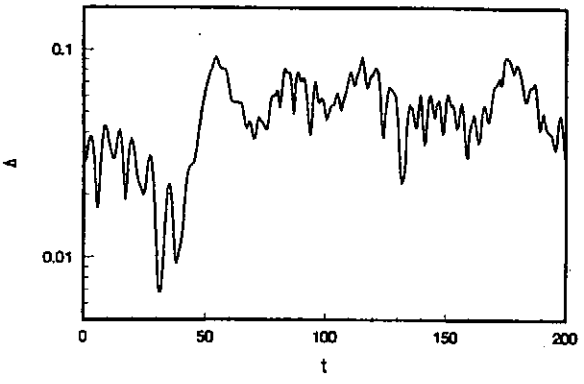

FIG. 7. Variation of the distance between $\phi(x)$ and $\phi_0^{(m)}$.

Fig.7 shows the temporal evolution of spatial distance between $\phi(x)$ and $\phi_0^{(m)}(x)$, $\Delta(t) \equiv \mid \phi(x,t) - \phi_0^{(m)}(x,t) \mid$. One can see that at $t^* = 30.0$ $\Delta(t)$ has a sharp spike to its minimum (resonance), then after a transition phase (an oscillation) it jumps up to a much higher level (STC phase). The initial values of $\phi(x, t = 0)$ in Fig.7 is a little different from that in Figs.6, so the critical time t^* is also different. But the resonance phenomena are much similar in these two examples. We have tried many examples with different parameters and initial conditions, the phenomena are qualitatively the same. Before the system transits to STC state, one can always find a resonance moment at which the spatial pattern of ϕ becomes very close to that of $\phi_0^{(m)}$ with $\Delta(t)$ going to a minimum. And after resonance occurs one can always find a transition phase as in Figs.6(d)(e) before finally arriving to STC state.

It is remarkable that although $\phi_0^{(m)}(\xi)$ is a solution that can never be realized, it plays so important role in the pattern realization of the system. In the following one can see that the role of $\phi_0^{(m)}(\xi)$ looks like a 'virtual potential', which causes saddle instability of the realized solution $\phi(x,t)$.

IV. SADDLE SOLUTION AND 'VIRTUAL POTENTIAL'

In this section we show that the instability of $\phi_0^{(m)}(\xi)$ is of a saddle type. For this purpose we take a steady

solution $\phi_0(\xi)$ as a carrier wave and set $\phi(\xi,\tau) = \phi_0(\xi) + \delta\phi(\xi,\tau)$. Then the following equation for $\delta\phi(\xi,\tau)$ results:

$$(\partial/\partial t - \Omega\partial/\partial\xi)[1 + a\partial^2/\partial\xi^2]\delta\phi + c\partial\delta\phi/\partial\xi + f\partial/\partial\xi[\phi_0(\xi)\delta\phi] + f\delta\phi\partial\delta\phi/\partial\xi = 0 \,. \quad (2)$$

To investigate the stability of $\phi_0(\xi)$, we neglect the last term in l.h.s. of Eq.2, i.e. the term nonlinear to $\delta\phi$. Eq.2 then becomes a linear one for $\delta\phi$. However, due to the system nonlinearity, $\delta\phi$ is coupled with ϕ_0 . Consequently for $\delta\phi$ the carrier wave $\phi_0(\xi)$ plays a role of a 'potential well'.

Now we fix $\phi_0(\xi)$ at the middle branch of a hysteretic curve, i.e., take $\phi_0^{(m)}(\xi)$ as the carrier wave. In this case from the linearized Eq.2 one can find numerically that $\delta\phi$ has stable and unstable directions. In Fig.8 we give the orbits $\delta E_{k=1}(\tau)$ vs. $\delta E_{k=2}(\tau)$, here $\delta E_k \equiv (1 - ak^2)[A_k b_k \cos(\theta_k - \alpha_k) + b_k^2/2]/2$ is the kth component of $\delta E(\tau) = E(\tau) - E_0$, in which the stable and unstable directions are denoted by bullets and hollow triangles respectively. Here $\delta\phi(\xi,\tau) = \sum_k b_k(\tau)cos[k\xi + \alpha_k(\tau)]$. Consequently $\delta\phi = 0$ at carrier wave $\phi_0^{(m)}$ is a saddle-node.

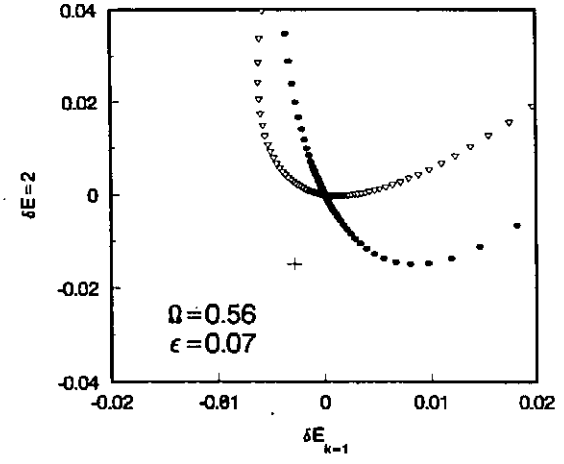

FIG. 8. Stable and unstable directions of $\delta\phi = 0$ at $\phi_0^{(m)}$, $\Omega = 0.56, \epsilon = 0.07$. The cross gives the position of $\delta\phi_g$.

Physically speaking, existance of steady wave $\phi_0(\xi)$ causes additional dispersions. If it locates at the middle branch of the hysteresis, i.e. $\phi_0^{(m)}(\xi)$, a mode of $\delta\phi(x,t)$ can experience a saddle instability due to nonlinear resonance with the applied sinusoidal wave $sin(x - \Omega t)$. For the details of the discussion one can refer to Ref. [5].

As mentioned in the last section, at the critical moment when the spatio-temporal resonance occurs, the spatial form of $\phi(x,t)$ is very close to that of $\phi_0^{(m)}(x - \Omega t)$. In this case their difference $\delta\phi(x)$ becomes extremely small. Neglecting the last nonlinear term of $\delta\phi$ in Eq.2 is valid. Then the above analysis tells us that the system would experience saddle instability, it is this instability which finally leads to turbulence. In this sense $\phi_0^{(m)}(\xi)$ plays a role of 'virtual potential' causing saddle instability.

V. GAP SOLITARY WAVE AND HETEROCLINIC TANGENCY

Further investigation shows that the above spatio-temporal resonance is a crisis of heteroclinic tangency [2]. As well known, heteroclinic tangency is a collision between two manifolds. In Sec.III we have already known that $\delta\phi = 0$ at 'virtual potential' $\phi_0^{(m)}(\xi)$ is a saddle-node. In the following we describe another manifold involved in the tangency. Since in previous work [6] we have given the details, here we only briefly mention the result.

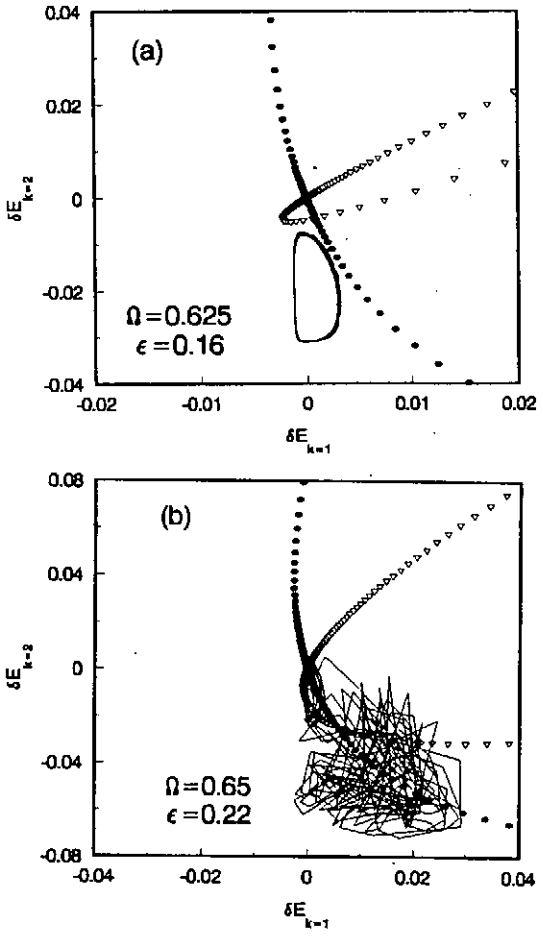

FIG. 9. Phase plot of 'wave energy', $\delta E_{k=1}$ vs. $\delta E_{k=2}$, spots and hollow triangles show stable and unstable directions of the saddle point $\delta\phi = 0$ at $\phi_0^{(m)}$, solid line gives attractor of nontrivial solution $\delta\phi_g$ with (a). $\Omega = 0.625, \epsilon = 0.16$, limit cycle, (b). $\Omega = 0.65, \epsilon = 0.22$, after a transient time crisis occurs, the orbit jumps to a created large attractor.

In the last section we neglect the nonlinear term re-

spect to $\delta\phi$ in Eq.2. If this nonlinear term is taken into account, then when $\delta\phi$ is large enough this term is comparable with the term containing $\phi_0^{(m)}$. Due to balance between the nonlinearity and dispersions (including the contribution from $\phi_0^{(m)}$), $\delta\phi$ can be prevented from going to infinity. To show this one can solve mode evolutions of Eq.2 with expansion $\delta\phi(\xi,\tau) = \sum_k b_k(\tau)\cos[k\xi + \alpha_k(\tau)]$.

Asymptotically soliton-like structure $\delta\phi(\xi, \tau \to \infty) = \delta\phi_g$ can be obtained in certain parameter regime, as an example the cross in Fig.8 gives the position of $\delta\phi_g$ in $E_{k=1}$ vs. $E_{k=2}$ space for $\Omega = 0.56, \epsilon = 0.07$. The structure $\delta\phi_g(\xi)$ combined with the 'virtual potential' $\phi_0^{(m)}(\xi)$ forms a new steady wave solution, $\phi_g(\xi) \equiv \phi_0^{(m)}(\xi) + \delta\phi_g(\xi)$. The 'wave energies' of such new solutions occupy the room that unstable $\phi_0^{(m)}(\xi)$'s leave. In this sense $\phi_g(\xi)$ can be called as a gap state [7].

When $\{\Omega, \epsilon\}$ are varied $\delta\phi_g(\xi)$ may bifurcate to limit cycle, then to chaotic attractor. With chaotic $\delta\phi(\xi,\tau)$ the motion of $\phi(x,t)$ is still in TC state. However if the chaotic attractor of $\delta\phi(\xi,\tau)$ collides with the unstable saddle orbit of $\phi_0^{(m)}(\xi)$, heteroclinic tangency or crisis occurs, the old small chaotic attractor is destroyed, and a large new attractor is created. This tangency process is demonstrated in Fig.8 and Figs.9, in which $\delta E_{k=1}$ vs. $\delta E_{k=2}$ are shown. In Fig.8 ($\Omega = 0.56, \epsilon = 0.07$) $\delta\phi_g$ is stable denoted by a cross. In Fig.9(a) ($\Omega = 0.625, \epsilon = 0.16$) it bifurcates to limit cycle. The limit cycle can further become chaotic. Finally in Fig.9(b) ($\Omega = 0.65, \epsilon = 0.22$) the chaotic orbit of $\delta\phi(\xi,\tau)$ collides with the unstable saddle orbit. In the plot one can find a chaotic attractor before crisis and a large attractor created after the crisis. The motion in this new attractor is in STC state.

What analyzed in this section does not contradict to the mechanism of resonance with 'virtual potential' given in Sec.IV, they are from different view angles but agree with each other. Most significant result in this paper is that a saddle solution like $\phi_0^{(m)}(\xi)$, although can not be realized, as a 'virtual potential' it can play so significant role in our real world.2

Acknowledgement This work is supported by the National Natural Foundation of China, Project of Basic Research of China "Nonlinear Science", and the Foundation for Doctorial Training of National Education Committee.

[1] R.Z.Sagdeev, D.A.Usikov, G.M.Zaslavsky, *Nonlinear Physics* , Harwood Academic Publishers, Switzerland (1988), pp460.

[2] C.Grebogi, E.Ott and J.A.Jorke, Phys. Rev. Lett., 48 , 1507(1982). C.Grebogi, E.Ott and F.Romerias, Phys. Rev. A, 36, 5365(1987).

[3] Kaifen He, A.Salat, Plasma Phys. and Contr. Fusion, 31, 123(1989).

[4] J.Guckenheimer, P.Holmes, *Nonlinear Oscillations, Dynamical Systems, and Bifurcations of Vector FieldsPhysics* , Springer-Verlag, New York (1983), pp73.

[5] Kaifen He, Gang Hu, Phys. Lett., A169, 341(1992). Kaifen He, Phys.Lett. A202, 369(1995).

[6] Kaifen He, submitted(1997).

[7] Kaifen He, Zhou Luqun, Phys. Lett. A231, 65(1997).

Anomalous Diffusion and Multiple-periodic Accelerator Modes in the Standard Map

*Yoshi H. Ichikawa †Kei Hirose and ‡T. Kamimura

*College of Engineering, Chubu University, Kasugai, 487, Japan
†Graduate University for Advanced Studies, Toki, 509-52, Japan
‡National Institute for Fusion Science, Toki, 509-52, Japan

ABSTRACT

Analysis of the structure of magnetic fields, and of long time behavior of plasma particles in toroidal magnetic devices is the central problem for magnetic control fusion. Extensive research has been developed on these problems in terms of nonlinear dynamical approach. Thus the mapping analysis attracts active interests in co-operation with full advantage of computational methods. Since almost of all nonlinear dynamical mappings are reduced to the standard map in local approximation, the standard map have been the central focus in the field of nonlinear dynamics of the Hamiltonian system. In spite of the extensive studies of the systems continuing over three decades, there remains still unsolved critical problems. Here, we examine interplay of the anomalous stochastic diffusion phenomena and multiple-periodic accelerator modes in the standard map. Detailed analysis has been carried out to identify the observed anomalous enhancement of stochastic diffusion in the small nonlinear parameter region as due to contribution of the period-2, period-3 and period-5 accelerator modes.

1 Introduction

In order to achieve confinement of high temperature plasma in toroidal magnetic devices, it is crucial to have good knowledge of magnetic surface. It is the central issues of controlled fusion research to understand the long time behavior of plasma particles confined in the magnetic vessels[1]. Since the configuration of magnetic field lines is described in terms of the Hamiltonian canonical equations, many studies of the magnetic surface have been carried out by adopting the methods of nonlinear

dynamic theory [2] and [3]. In particular, the Poincare's mapping approach is useful to deal with the conserved Hamiltonian system of a few degrees of freedom.

The magnetic surface of toroidal configuration such as those of tokamaks, steralators and other helical devices has been analyzed by full use of the two dimensional area preserving maps. Almost all of two dimensional area preserving maps are reduced to the standard map by local linear approximation,

$$\begin{aligned} q_{n+1} &= q_n + p_{n+1} \\ p_{n+1} &= p_n + F(q_n) \equiv p_n + A\sin(2\pi q_n) \pmod 1 \end{aligned} \tag{1.1}$$

When the nonlinear parameter A is sufficiently small, orbits described by (1.1) encircles the fixed point $(q_0 = 0, p_0 = 0)$ with closed curves representing regular motion. Greene [4] has determined the critical value of A at which the last invariant surface called KAM surface is destroyed, and the system undergoes transition to the state of global chaos.

The stochastic properties of the system in the global chaos is best characterized by the stochastic diffusion of the orbits in the phase space. Numerical observation of the mean square fluctuation of the momentum variables can define the diffusion coefficient. As for the standard map (1.1), the characteristic function gives rise to asymptotic expression of the diffusion coefficient [5],

$$D = \frac{A^2}{4}\frac{1 - 2J_1^2(2\pi A) - J_2^2(2\pi A) + 2J_3^2(2\pi A)}{(1 + J_2(2\pi A))^2} \tag{1.2}$$

where $J(x)$ is the n-th order Bessel function. Although [2] has been derived under the asymptotic condition of $2\pi A \gg 1$, the numerically observed diffusion processes are consistent with this theoretical prediction, except in the region of

$$|l| < A < \left(1 + \left(\frac{2}{\pi l}\right)^2\right)^{\frac{1}{2}} |l| \tag{1.3}$$

where the fundamental accelerator modes

$$q_0 = \frac{1}{2\pi}\sin^{-1}\left(\frac{l}{A}\right) \qquad p_0 = 0 \tag{1.4}$$

are stable. Here, l is an integer measuring the size of acceleration in momentum direction. Surrounding this fundamental accelerator mode, there occur the Poincare-Birkhoff bifurcation to generate higher order periodic accelerator modes.

In numerical observation of the stochastic diffusion [6], we have found that even in small values of the nonlinear parameter A, there appear many sharp peaks of anomalous enhancement of diffusion, where the fundamental accelerator mode can not exist. These peaks of anomalous diffusion are attributed to multiple-periodic accelerator mode which can exist even if the nonlinear parameter A is smaller than 1. The purpose of the present paper is to develop quantitative analysis of the structure, and the stability of the period-3 and the period-5 accelerator modes, and to give quantitative account of the numerically observed diffusion coefficient.

2 Analysis of the Period-3 Accelerator Modes

The period-3 accelerator mode is determined from the triple iterated map of the standard map [1] by substituting the conditions

$$p_3 = p_0 + l \qquad q_3 = q_0 + m \tag{2.1}$$

with arbitrary integers l and m. Here, it should be noticed that the integer l stands for the accelerating step size. Our numerical observation suggests that the initial momentum variable is $p_0 = 0$. With this choice, the coordinate q_0 is determined from the following equation,

$$\Phi^{(3)}(A, q_0) \equiv 2F(q_0) + F(q_0 + F(q_0)) = m - l \equiv M \tag{2.2}$$

where $M = m - l$ is an integer. Fig.1 illustrate the relationship of (2.2), where the intersection of the curves with the horizontal lines of $M = 1, 2$ and 3 determine the coordinates of the period-3 step-1 orbits. It is straightforward to determine the critical values of A where the peak T_1 and T_2 contact with the line $M = 1$ as

$$A = 0.5589, q_0 = 0.0733 \qquad A = 0.6578, q_0 = 0.2762 \tag{2.3}$$

respectively. As for the line of $M = 2$, only the peak T_2 can have intersections. The critical value of A is determined as

$$A = 0.8144 \quad q_0 = 0.2720 \tag{2.4}$$

Following the temporal evolution of the momentum variables of the orbits starting at the positions of (2.3) and (2.4), we can identify that at the critical values of (2.3) the period-3 step-1 accelerator mode is set in, while the period-3 step-2 mode appears at the critical value of (2.4). Upon increasing the parameter A, these intersections split into a pair of $(c_1; c_2)$ from the peak T_1 , and a pair of $(c_3; c_4)$ from the peak T_2 , where c_1, c_2, c_3 and c_4 are named from the left to the right on the M line.

Constructing the tangential map for the third iterated map, we can evaluate the residue R. In the region of $0 < R < 1$, the system is stable. In the present case, the points c_1 of the peak T_1 ,and c_3 of the peak T_2 are unstable at the intersection with the line of $M = 1$, while the point c_3 of the peak T_2 is unstable at the intersection with the line of $M = 2$.

Summarizing the analysis, we find the period-3 step-1 accelerator modes exist in the domains of

$$0.5589 < A < 0.5595 \tag{2.5}$$

$$0.6578 < A < 0.6605 \tag{2.6}$$

$$0.7421 < A < 0.7674 \tag{2.7}$$

Here, it is worth to notice that the orbit at the intersection c_4 becomes once unstable above the value of $A = 0.6605$, then it becomes stable again in the second region of A above 0.7421. In the same way, we find that the period-3 step-2 mode is stable in the domains of

$$0.8144 < A < 0.8158 \tag{2.8}$$

$$0.8734 < A < 0.8919 \tag{2.9}$$

3 The Period-5 Accelerator Modes

Extending the similar analysis of the section 2 to the fifth iterated map, we obtain the condition to determine the coordinate of the period-5 accelerator mode as

$$\Phi^{(5)}(A,q) \equiv 4F(q) + 3F(q+F(q)) + 2F(q+2F(q)+F(q+F(q))) \\ +F(q+3F(q)+2F(q+F(q))+F(q+2F(q)+F(q+F(q)))) \qquad (3.1)$$

Fig.2 illustrates the relationship of (3.1) for the values of $A = 0.4200$ and $A = 0.6064$. Unlike the case of the period-3 mode, now we get many intersections with the line of $M = 1, 2, 3$ and 4. We pay special attention to the flat tops of the curves at $A = 0.4200$ and $A = 0.6064$, respectively. Avoiding laborious estimatation of the residues of many intersections, we carry out direct observation of temporal evolution of the orbits near the flat tops which contact with the lines of $M = 2$ and $M = 4$. Then, at $A = 0.4200$, the orbits nearby $(p_0 = 0, q_0 = 0.105)$ behave as the period-5 step-1 accelerator mode, while the orbits around $(p_0 = 0, q_0 = 0.070)$ are the period-5 step-2 accelerator mode.

4 Stochastic Diffusion in the Region of A<1

We have carried out numerical observation of the stochastic diffusion in the momentum direction for the initial uniform distribution of 1000 orbits in the region of $-0.5 < q < +0.5$ with $p_0 = 0$. Time duration is taken as 10^5. Fig.3 shows the diffusion coefficient observed in the range of $0.5 < A < 1.0$.

Referring to the analysis of the previous sections, we can identify the anomalous peak at $A = 0.55$ as due to the period-3 step-1 mode of (2.5), the broad peaks at $A = 0.65$ is due to the period-3 step-1 mode of (2.6), the broad peaks at $A = 0.75$ is due to the period-3 step-1 mode of (2.7), the peaks at $A = 0.82$ is due to the period-3 step-2 mode of (2.8) and finally the broad peaks at $A = 0.88$ is the period-3 step-2 mode of (2.9).

Now, as for the sharp peak at $A = 0.6$ it is attributed to contribution of the period-5 step-2 accelerator mode. We may refer to our early observation to identify that the peak at $A = 0.42$ is due to the period-5 step-1 mode determined in the analysis of the section 3.

Lastly, let us examine the effect of the period-2 step-1 accelerator mode determined by Hirose et.al.[7]. It exists in the region of

$$0.64037 < A < 0.65130 \qquad (4.1)$$

Since the position of the mode is determined as $(p_0 = -0.2, q_0 = 0.11)$ the numerical observation with the initial distribution for $p_0 = 0$ will not exhibits the evidence of the anomalous enhancement of the stochastic diffusion. Fig.4 confirms that indeed the anomalous contribution of the period- 2 step-1 mode is observed for the initial distribution of orbits with $p_0 = -0.2$ and $-0.5 < q < +0.5$.

5 Conclusions

In the present studies of the multi-periodic accelerator mode of the standard map, we have determined quantitatively the regions of the anomalous enhancement of diffusion with the contribution of the accelerator modes. It is very interesting to notice that the accelerator modes of large periodicity manifest their contribution at smaller nonlinear parameter A. In the present analysis, we have some indication of observing the contribution of the period-7 accelerator mode at the value of $A = 0.5$. It is reserved for future studies to account quantitatively the stickiness around the regular orbits, and to explore the scaling law of the transport property in the system described by the standard map.

References

[1] *Hamiltonian Dynamical Systems,* compiled by R.S.MacKay and J.D.Meiss Adam Hilger, **1987**

[2] M.N.Rosenbluth, R.Z.Sagdeev, J.B.Taylor and G. M. Zaslafsky *Nuclear Fusion* **6** (1966) 297

[3] N.N.Filonenko, R.Z.Sagdeev and G.M.Zasalavsky *Nuclear Fusion* **7** (1967) 253

[4] J.M.Greene *J.Math.Phys* **9** (1968) 760

[5] J.D.Meis, J.R.Cary, C.Grebogi, J.D.Crawford and H.D.I.Abarbanel *Physica* **6D** (1983)

[6] Y.H.Ichikawa,T.Kamimura and T.Hatori *Physica* **29D** (1987) 247

[7] Kei Hirose, S.Saitô and Y.H.Ichikawa *Plasma Phys. Report* **22** (1996) 842

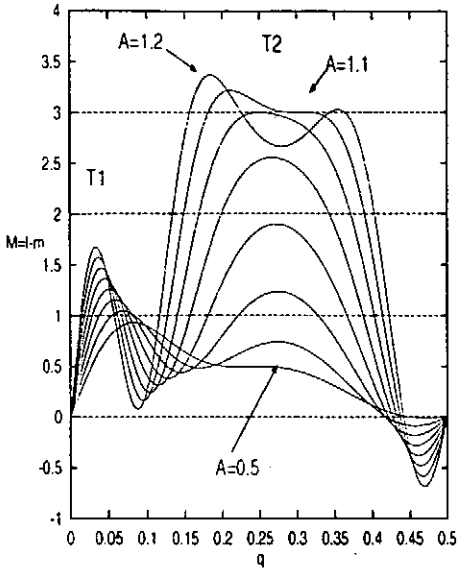

Figure 1: Existence condition for the period-3 accelerator modes

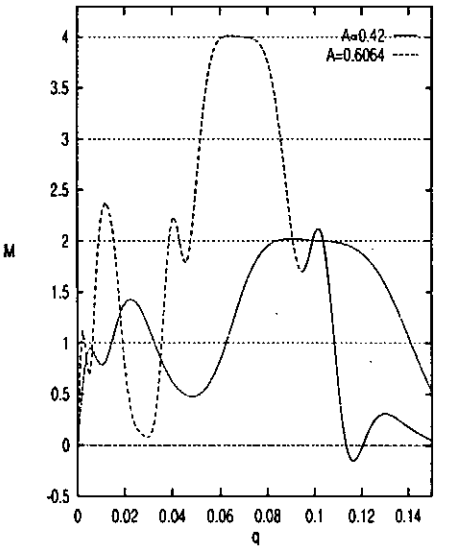

Figure 2: Existence condition for the period-5 accelerator modes

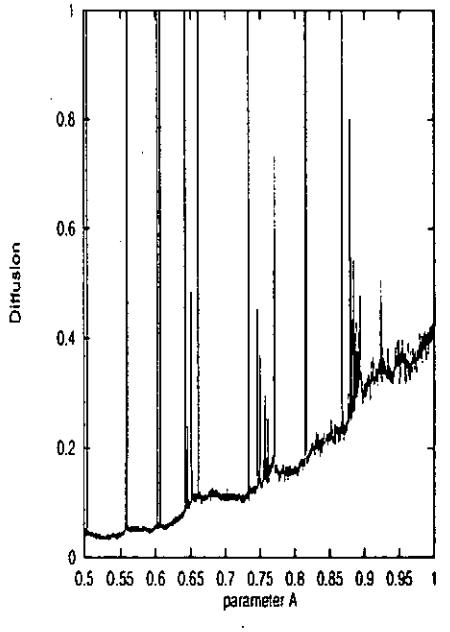

Figure 3: Diffusion observed for the initial distribution at ($p_0 = 0, -0.5 < q_0 < +0.5$)

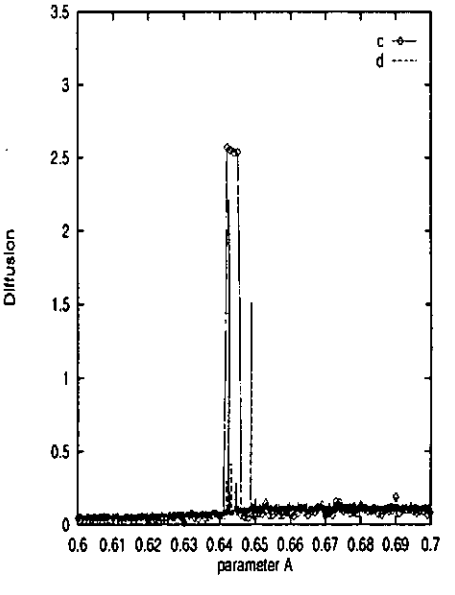

Figure 4: Numerically observed diffusion for the initial distribution at ($p_0 = -0.2, -0.5 < q_0 < +0.5$).

Vortex Lattice Formation in 2D Magnetized Plasmas

M. Kono
Faculty of Policy Studies, Chuo University,
Hachioji, Tokyo 192-03, Japan

September 10, 1997

1 Introduction

Formation and self-organization of coherent structures have been a topic in plasmas and fluids. Such structures are supposed to play a crucial role on the macroscopic properties of the system, especially on long distance transport of particles and energy. The emergence of self-organized motions has been observed experimentally in a magnetically confined pure electron columns by K. S. Fine, A. C. Case, W. G. Flynn and C. F. Driscoll[(1)] and numerically in decaying and force-driven drift wave turbulence by N. Kurkhakin, S. A. Orszag and V. Yakhot[(2)]. Both observations are commonly concerning long-lived ordered motions (cryatallization) of well defined vortices, suggesting that the relaxation to the ordered states may be described by introducing point vortices with which partial differential equations designed to describe vortical motions are converted to a set of ordinary differential equations.

An unperturbed non-uniform density yields a potential which drives a $\mathbf{E} \times \mathbf{B}$ drift in an azimuthal direction. Then the fluctuations resonate with the $\mathbf{E} \times \mathbf{B}$ rotation to give a localized structure of the fluctuations, that is, a descretization of the density fluctuations, which provides a basis of introducing point vortices to describe the nonlinear development of the self-organizing processes. Although point vortex systems are known to be a Hamilton system which exhibits a chaotic behavior of vortices whose number is more than three[(3)-(4)], the resonance phenomenon is eventually supplemented by dissipation incorporated into the vortex system, leading to structures similar to a dissipative structure.

Equations describing the motion of 2D electron fluid are given as follows:

$$\frac{\partial n}{\partial t} + \mathbf{v}_\perp \cdot \nabla n = 0, \tag{1}$$

$$\mathbf{v}_\perp = \frac{c}{B_0} \mathbf{z} \times \nabla (\phi - \frac{T}{e} \ln n), \tag{2}$$

$$\nabla^2 \phi = 4\pi e n. \tag{3}$$

These equations are combined to give

$$\frac{\partial}{\partial t} \nabla^2 \phi + [\phi, \nabla^2 \phi] = 0, \tag{4}$$

where space and time are normalized by the Debye length and ω_p^2/Ω ($\omega_p^2 = 4\pi N_0 e^2/m, \Omega = eB/mc$), respectively. An electric potential ϕ is normalized by e/T and $[\ ,\ ]$ denotes a Poisson braket.

Equation for low frequency electrostatic fluctuations is given by replacing eq.(3 with

$$\nabla^2 \phi = 4\pi e (n_0 e^{e\phi/T} - n), \tag{5}$$

which is to give

$$\frac{\partial}{\partial t} (\phi - \nabla^2 \phi) - [\phi, \nabla^2 \phi] = 0, \tag{6}$$

The linear stability of the two dimensional crossed-field electron column has been studied by Briggs, Daugherty and Levy[(5)] who showed that there occurs no instability when the density profile is monotonically decreasing. This result is confirmed by several authors[(6)-(7)] for specified density profiles. It is nicely illustrated by Gould [(8)] that linear eigen-functions are localized with positive growth rates for hollow density profiles[(9)-(10)], leading to density descretization in a nonlinear stage.

In the next section, the point vortex description is formulated and some comments are made on the dynamical properties of point vortices. In Section 3, equilibrium configurations of point vortices are obtained and in Section 4 the vortex lattice formation is demonstrated. Discussions are given in the last section.

2 Point vortex description

The linear eigen-functions indicate that the fluctuations can be large only at the discrete points where the linear resonance occurs. This gives a basis of introducing point vortices to analyze the nonlinear evolution of both fluctuations in the electron column and low frequency electrostatic fluctuations. In the following, we consider

$$\frac{\partial}{\partial t}(\kappa^2\phi - \nabla^2\phi) - [\phi, \nabla^2\phi] = 0, \tag{7}$$

which includes both eqs.(4) and (6) for $\kappa = 0$ and $\kappa = 1$, respectively. Here κ denotes a screening effect.

Point vortices can be introduced through

$$(\kappa^2 - \nabla^2)\phi(\mathrm{r}, t) = \sum_\alpha \gamma_\alpha \delta(\mathrm{r} - \mathrm{r}_\alpha), \tag{8}$$

which gives the potential as

$$\phi(\mathrm{r}, t) = \sum_\alpha \frac{\gamma_\alpha}{2\pi} K_0(\kappa|\mathrm{r} - \mathrm{r}_\alpha(t)|), \tag{9}$$

where K is a modified Bessel function of the second kind. In the limit of $\kappa \to 0$, eq.(9) reduces to

$$\phi(\mathrm{r}, t) = \sum_\alpha \frac{\gamma_\alpha}{2\pi} \ln(|\mathrm{r} - \mathrm{r}_\alpha(t)|), \tag{10}$$

which is a solution of Eq.(8) for $\kappa = 0$. Therefore κ is a parameter controlling the range of the interaction between vortices. Then the equations for the vortices are given by

$$\frac{d}{dt}\mathrm{r}_\alpha = \mathrm{z} \times \nabla\phi(\mathrm{r}_\alpha, t) = \frac{\kappa}{2\pi} \sum_\beta \gamma_\beta \frac{\mathrm{z} \times (\mathrm{r}_\alpha - \mathrm{r}_\beta)}{|\mathrm{r}_\alpha - \mathrm{r}_\beta|} K_1(\kappa|\mathrm{r}_\alpha - \mathrm{r}_\beta|). \tag{11}$$

The short range nature of the interaction between the vortices is stemed from the screening effect. This implies that when the distance between the vortices is short enough for the shielding to be neglected, the dynamical behavior of the vortices is described by the following equation

$$\frac{d}{dt}\mathrm{r}_\alpha = \frac{1}{2\pi} \sum_\beta \gamma_\beta \frac{\mathrm{z} \times (\mathrm{r}_\alpha - \mathrm{r}_\beta)}{|\mathrm{r}_\alpha - \mathrm{r}_\beta|^2}, \tag{12}$$

which is given from eq.(11) in the limit of $\kappa \to 0$ or from eq.(10) directly.

Many works have been reported on eq.(12)[11]-[12] among which remarkable works are concerned with the vortex collapse for which three vortices self-similarly converge or diverge, depending on the sign of vorticities $\{\kappa_\alpha,\ \alpha = 1, 2\ and\ 3\}$ [13]. For the collapse to occur, suitable initial conditions have to be satisfied in addition to the condition that $\kappa_1\kappa_2 + \kappa_2\kappa_3 + \kappa_3\kappa_1 = 0$. The significance of the vortex collapse is thought to provide a key to understanding of fundamental processes of strong turbulence. However the vortex collapse is algebraically unstable: a small deviation from the condition no longer leads to the collapse. In those cases three vortices first converge to some extent and then turn to diverge. Once they start to diverge, they keep diverging as long as they follow eq.(12). This is not the case for eq.(11). When they diverge, because of the short range nature of the interaction, two of them are to form a pair to travel together and the third one is almost left behind. However since the vorticities of two vortices travelling together are opposite in sign and different in magnitude, the two vortices return to the place where third one remains. At the time they come to the position where the two sides of the triagle become equal, the pair is renewed by changing the partner. The new pair travels in a similar way as before until it comes back to the place and again, exchanges its partner. This Boomerang interaction is shown in Fig.4(a) as well as the vortex collapse in (b).

Equation (11) has the following constants of motion:

$$\mathrm{G} = \sum_\alpha \gamma_\alpha \mathrm{r}_\alpha, \tag{13}$$

$$L = \sum_\alpha \gamma_\alpha |\mathrm{r}_\alpha|^2, \tag{14}$$

$$E = \sum_{\alpha \neq \beta} \gamma_\alpha \gamma_\beta K_0(\kappa|\mathrm{r}_\alpha - \mathrm{r}_\beta|), \tag{15}$$

which are related to the symmetry properties of eq.(11). Because of these conserved quantities, systems with three vortices or less than three vortices are integrable, while dynamical behavior of systems with more than three vortices can become chaotic. Therefore at the first glance it seems impossible to describe vortex lattice formation in terms of point vortices. However some of the equilibrium configurations such that vortices are equally distributed on a circle are shown stable by Morikawa and Swenson[14]. Furthermore the linear resonance eventually introduces dissipation which is an averaged effect of fluctuations through the fluctuation-dissipation theorem.

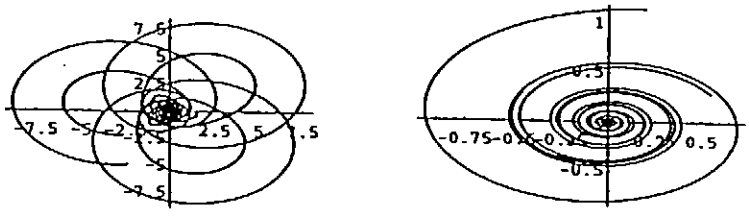

Figure 1: (a) The Boomerang interaction of three vortices, and (b) the vortex collapse

3 Equilibrium configurations of point vortices

Equilibrium configurations of point vortices have been discussed by Morikawa and Swenson for the case that N vortices are equally distributed on a circle with and without a center vortex. They found that the configuration is stable for $2 \leq N \leq 6$ in the case of $\kappa \leq 1.289$ with a center vortex and for $4 \leq N \leq 8$ in the case of $\kappa \leq 1$ without a center vortex.

We show other equilibrium configuraltions. Starting from the vortex equation eq.(11) and introducing the distribution function

$$f(\mathrm{r},t) = \sum_{\alpha} \gamma_{\alpha} \delta(\mathrm{r} - \mathrm{r}_{\alpha}(t)), \tag{16}$$

eq.(11) is rewritten as

$$\frac{\partial}{\partial t} f(\mathrm{r},t) = -\frac{\kappa}{2\pi} \int d\mathrm{r}' \frac{K_1(\kappa|\mathrm{r}-\mathrm{r}'|)}{|\mathrm{r}-\mathrm{r}'|} \mathrm{z} \times (\mathrm{r}-\mathrm{r}') \cdot \nabla f(\mathrm{r}',t) f(\mathrm{r},t). \tag{17}$$

Changing from cartesian variables $(x,\ y)$ to cylindrical coordinates $(r,\ \theta)$ and noting

$$\mathrm{z} \times (\mathrm{r}-\mathrm{r}') \cdot \nabla = -r' \sin(\theta - \theta') \frac{\partial}{\partial r} + [1 - \frac{r'}{r} \cos(\theta - \theta')] \frac{\partial}{\partial \theta},$$

we have

$$\frac{\partial}{\partial t} f(r,\theta,t) + \Omega(r,\theta,t) \frac{\partial}{\partial \theta} f(r,\theta,t) + V(r,\theta,t) \frac{\partial}{\partial r} f(r,\theta,t) = 0, \tag{18}$$

where

$$\Omega(r,\theta,t) = \frac{\kappa}{2\pi} \int dr' \frac{K_1(\kappa|\mathrm{r}-\mathrm{r}'|)}{|\mathrm{r}-\mathrm{r}'|} [1 - \frac{r'}{r} \cos(\theta - \theta')] f(r',\theta',t), \tag{19}$$

$$V(r,\theta,t) = -\frac{\kappa}{2\pi} \int dr' r' \frac{K_1(\kappa|\mathrm{r}-\mathrm{r}'|)}{|\mathrm{r}-\mathrm{r}'|} \sin(\theta - \theta') f(r',\theta',t). \tag{20}$$

From the above equation, equilibrium configurations are obtained by conditions that $V(r,\theta,t)$ are identically zero and $\Omega(r,\theta,t) = \Omega_0 = constant$, for which the vortex system is rigidly rotating around origin without any displacement in the radial direction. These equilibrium configurations consist of the fixed points of the dynamical system given by eq.(11).

In the following we look for the concentric structure of M rings on each of which $N_m (m = 1, \cdots, M)$ vortices are equally distributed, assuming that all the vortices are the same, i.e., $\gamma_{\alpha} = \gamma$, with/without a center vortex γ_0 ($\gamma_0 = \gamma$ or $\gamma_0 = 0$):

$$f(r,\theta,t) = \sum_{m,n} \frac{\gamma}{a_m} \delta(r - a_m) \delta(\theta - \theta_{m,n}) + \frac{\gamma_0}{r} \delta(r) \delta(\theta), \tag{21}$$

for which following two relations hold in the equilibrium

$$V(m_0,n_0) = -\frac{\kappa^2}{2\pi} \gamma \sum_{m,n} \frac{a_m}{\sigma_{m,n}} K_1(\sigma_{m,n}) \sin(\theta_{m_0,n_0} - \theta_{m,n}) = 0, \tag{22}$$

and

$$\Omega(m_0,n_0) = \frac{\kappa^2}{2\pi} \gamma \sum_{m,n} \frac{1}{\sigma_{m,n}} K_1(\sigma_{m,n}) [1 - \frac{a_m}{a_{m_0}} \cos(\theta_{m_0,n_0} - \theta_{m,n})] + \frac{\kappa}{2\pi} \gamma_0 \frac{K_1(\kappa a_{m_0})}{a_{m_0}} = const, \tag{23}$$

where

$$\sigma_{m,n} = \kappa\sqrt{a_{m_0}^2 + a_m^2 - 2a_{m_0}a_m\cos(\theta_{m_0,n_0} - \theta_{m,n})},$$

and (m,n) refers to the n-th vortex on the m-th circle. The (m_0,n_0) is an arbitrarily chosen reference vortex.

For the case that vortices on each circle is distributed in a way that the separation distance between neighbouring vortices is the same, that is, $\theta_{m,n} = 2\pi n/N_m$ where N_m is the number of vortices on m th circle, $V(m_0,n_0)$ is always equal to zero and $\Omega(m_0,n_0)$ does not depend on n_0 because of the symmetry. There are many combinations of the number of rings and the number of vortices on each ring to make $\Omega(M_0,n_0)$ constant.

Although the above equilibrium configurations are certainly not all, some of these configurations are found to be long-lived even without introducing any damping, indicating that they may be considered as candidates of coherent structures which may be realized as a vortex lattice.

4 Vortex lattice formation

We start with a Langevin equation, that is, the point vortex equation with fluctuation and dissipation

$$\frac{d}{dt}\mathrm{r}_\alpha = \frac{\kappa}{2\pi}\sum_\beta \gamma_\beta \frac{\mathrm{z}\times(\mathrm{r}_\alpha - \mathrm{r}_\beta)}{|\mathrm{r}_\alpha - \mathrm{r}_\beta|}K_1(\kappa|\mathrm{r}_\alpha - \mathrm{r}_\beta|) - \nu\mathrm{r}_\alpha + \tilde{\mathrm{f}}_\alpha(t), \tag{24}$$

where the fluctuating force is assumed to obey the following statistics:

$$< \tilde{\mathrm{f}}_\alpha(t) >= 0, \quad < \tilde{\mathrm{f}}_\alpha(t)\cdot\tilde{\mathrm{f}}_\beta(t') >= C\delta_{\alpha\beta}\delta(t-t'). \tag{25}$$

Here we split the coordinates into an average part and a fluctuating part

$$\mathrm{r}_\alpha = \mathbf{R}_\alpha + \tilde{\mathrm{r}}_\alpha. \tag{26}$$

Substituting it into eq.(24) and taking average with respect to the fluctuations, we have for the average part

$$\frac{d}{dt}\mathbf{R}_\alpha = < \frac{\kappa}{2\pi}\sum_\beta \gamma_\beta \frac{\mathrm{z}\times(\mathbf{R}_\alpha - \mathbf{R}_\beta + \tilde{\mathrm{r}}_\alpha - \tilde{\mathrm{r}}_\beta)}{|\mathbf{R}_\alpha - \mathbf{R}_\beta + \tilde{\mathrm{r}}_\alpha - \tilde{\mathrm{r}}_\beta|}K_1(\kappa|\mathbf{R}_\alpha - \mathbf{R}_\beta + \tilde{\mathrm{r}}_\alpha - \tilde{\mathrm{r}}_\beta|) > -\nu\mathbf{R}_\alpha, \tag{27}$$

Subtracting the averaged part of the equation from eq.(24), we obtain for the fluctuationg part

$$\begin{aligned}\frac{d}{dt}\tilde{\mathrm{r}}_\alpha &= \frac{\kappa}{2\pi}\sum_\beta \gamma_\beta\{\frac{\mathrm{z}\times(\tilde{\mathrm{r}}_\alpha - \tilde{\mathrm{r}}_\beta)}{|\mathbf{R}_\alpha - \mathbf{R}_\beta|}K_1(\kappa|\mathbf{R}_\alpha - \mathbf{R}_\beta|) \\ &- \frac{\mathrm{z}\times(\mathbf{R}_\alpha - \mathbf{R}_\beta)}{|\mathbf{R}_\alpha - \mathbf{R}_\beta|}\frac{(\mathbf{R}_\alpha - \mathbf{R}_\beta)\cdot(\tilde{\mathrm{r}}_\alpha - \tilde{\mathrm{r}}_\beta)}{|\mathbf{R}_\alpha - \mathbf{R}_\beta|^2}[2K_1(\kappa|\mathbf{R}_\alpha - \mathbf{R}_\beta|) \\ &+ \kappa|\mathbf{R}_\alpha - \mathbf{R}_\beta|K_0(\kappa|\mathbf{R}_\alpha - \mathbf{R}_\beta|)]\} - \nu\tilde{\mathrm{r}}_\alpha + \tilde{\mathrm{f}}_\alpha(t),\end{aligned} \tag{28}$$

where we have remained only linear terms. As a formal solution of eq.(28), we have

$$\tilde{\mathrm{r}}_\alpha = \sum_\beta \int G_{\alpha\beta}(t|t')\tilde{\mathrm{f}}_\beta(t')dt', \tag{29}$$

where $G_{\alpha\beta}(t|t')$ is a Green function of eq.(28) which may be approximated by

$$G_{\alpha\beta}(t|t') \simeq \delta_{\alpha,\beta}e^{-2\nu(t-t')}, \tag{30}$$

From the assumed statistics for the fluctuating force, we can estimate the right hand side of eq.(27) under the quasi-linear approximation

$$\begin{aligned}\frac{d}{dt}\mathbf{R}_\alpha &= \frac{\kappa}{2\pi}\sum_\beta \gamma_\beta \frac{\mathrm{z}\times(\mathbf{R}_\alpha - \mathbf{R}_\beta)}{|\mathbf{R}_\alpha - \mathbf{R}_\beta|}\{1 + \frac{1}{2}\frac{D_{\alpha\beta}(t)}{|\mathbf{R}_\alpha - \mathbf{R}_\beta|^2}[1 + \kappa|\mathbf{R}_\alpha - \mathbf{R}_\beta|\frac{K_0(\kappa|\mathbf{R}_\alpha - \mathbf{R}_\beta|)}{K_1(\kappa|\mathbf{R}_\alpha - \mathbf{R}_\beta|)}] \\ &+ \frac{1}{2}\kappa^2 D_{\alpha\beta}(t)\}K_1(\kappa|\mathbf{R}_\alpha - \mathbf{R}_\beta|) - \nu\mathbf{R}_\alpha,\end{aligned} \tag{31}$$

where

$$D_{\alpha\beta}(t) = \frac{1}{2} < (\mathrm{r}_\alpha - \mathrm{r}_\beta)^2 >\simeq C\frac{1 - e^{-2\nu t}}{2\nu}(1 - \delta_{\alpha\beta}). \tag{32}$$

Equation (31) shows that the effect of the fluctuations can be renormalized into the vorticity γ.

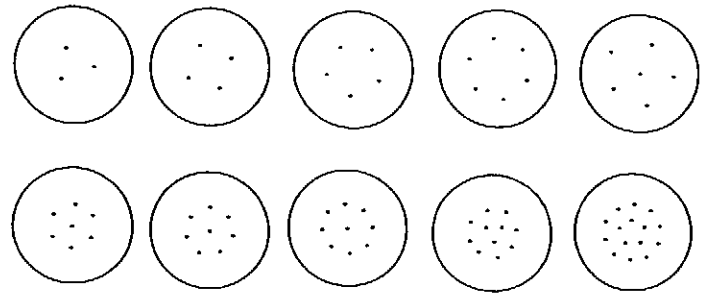

Figure 2: Vortex lattice structures obtained from eq.(40)

Table 1: Vortex distribution in the lattice formation

No. of vortices	2	3	4	5	6	6	7	8	9	10
Center	-	-	-	-	-	1	1	1	1	-
1st Ring	2	3	4	5	6	5	6	7	8	2
2nd Ring	-	-	-	-	-	-	-	-	-	8
No. of vortices	11	12	13	14	15	16	17	18	19	20
Center	-	-	-	-	-	-	1	1	1	1
1st Ring	3	3	4	4	5	5	5	6	6	7
2nd Ring	8	9	9	10	10	11	11	11	12	12
No. of vortices	21	22	23	24	25	26	27	28	29	30
Center	1	1	1	-	-	-	-	-	-	-
1st Ring	7	8	8	2	3	3	3	4	4	5
2nd Ring	13	13	14	8	8	9	9	9	10	10
3rd Ring	-	-	-	14	14	14	15	15	15	15

We have solved eq.(31) numerically with initial vortices distributed randomly. Without the damping the energy and momentum are conserved in the acuracy of 10 digits. The results are checked by both the forth order Runge-Kutta method and error control Runge-Kutta-Fehlberg method. Without damping the motion of vortices is chaotic and there occationally appears an ordered structure which is certainly trangent. However damping organizes the vortices in such a way that vortices are equally separated in distance and rotate in accord. Some of the ordered structures are given in Fig.2 for $\kappa = 0$ where vortices on a ring with/without a center vortex are equilibrium configurations examined by Morikawa and Swenson, while the others are those found in the previous section. Table 1 shows how vortices are distributed in the lattice formation starting from arbitrary chosen initial configurations which are produced by a random number generator. The structures with 6 vortices depend on the choice of initial configurations. It should be noted that Table 1 does not give all possible configurations since initial conditions are determined randomly and it is impossible to check all the cases. However there seems to be a selection rule for stable lattice configurations. The equiriblium configurations for eq.(31) are obtained similarly in the previous section though we have not examined those stability yet.

The vortex lattices in Fig.2 are compared with the experimental results in ref.(1). The same structures have been obtained for $\kappa = 1$. The magnitude of damping just affects the time until the lattice is formed. The level of the fluctuations is not crucial to the result as long as it is kept sufficiently small compared with the vorticity γ. One of the course of the relaxation to the ordered states is shown in Fig.3. In a long run, the ordered structures eventually shrink to the origin because of the dissipation.

5 Discussion

In this article we have shown the vortex lattice formation based on the point vortex equation with fluctuations and dissipation, whose basis is confirmed by solving eigen-value problems associated with the linear resonance both in a magnetically confined electron column and in a low frequency fluctuation which revieled the density descretization. Some of equilibrium configurations have been also obtained and shown realized in the numerical simulations.

The structure of vortex lattice which is intimately related to the profile of the linear eigen-function may be controlled by the unperturbed density profile. In experiments the density profile is rather sensitive to the plasma production and the relation between the unperturbed density profiles and the vortex lattice structures are not studied yet. We

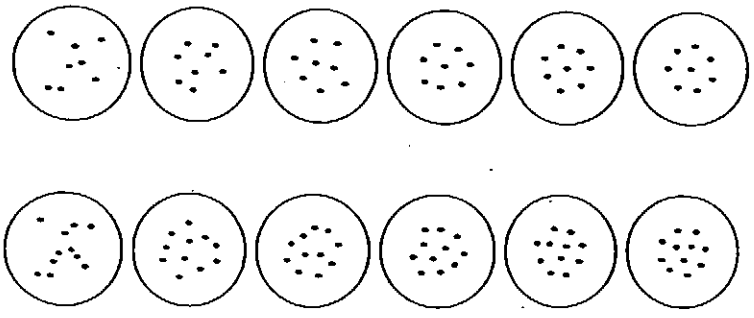

Figure 3: The time evolution of spatial configuration of vortices initially distributed randomly

have used a random number generator in producing initial configurations of vortices by which the final structures are chosen among the equilibrium configurations. However the number of equilibrium configurations is large for the large number of vortices. We have not examined whether all the equilibrium configurations can be realized though we anticipate they are because dissipation plays an essential role for the structure formation.

References

1. K. S. Fine, A. C. Case, W. G. Flynn and C. F. Driscoll, Phys. Rev. Lett. **75**, 3277 (1995)
2. N. Kukharkin, S. A. Orszag and V. Yakhot, Phys Rev. Lett. **75**, 2486 (1995)
3. H. Aref, Phys. Fluids **22**, 393 (1979)
4. E. A. Novikov and Yu B. Sedov, Sov. Phys. JETP **48**, 440 (1978)
5. R. J. Briggs, J. D. Daugherty and R. H. Levy, Physs. Fluids **13**, 421 (1970)
6. N. R. Comgold, Phys. Plasma **2**, 620 (1995)
7. R. L. Spencer and S. N. Rasband, Phys. Plasma **4**, 53 (1997)
8. R. W. Gould, Phys. Plasma **2**, 2151 (1995)
9. T. M. Mitchell and C. F. Driscoll, Phys. Rev. Lett. **73**, 2196 (1994)
10. C. F. Driscoll and K. S. Fine, Phys. Fluids **B2**, 1359 (1990)
11. L. Onsager, Nuovo Cimento **6**, 279 (1949)
12. E. A. Novikov, Sov. Phys. JETP **41**, 937 (1976)
13. E. A. Novikov and Yu B. Sedov, Sov. Phys. JETP **50**, 297 (1979)
14. G. K. Morikawa and E. V. Swenson, Phys Fluids **14**, 1058 (1971)

Collisionless Damping of Perpendicular Magnetosonic Pulses in a Two-Ion-Species Plasma

Daiju Dogen, Mieko Toida, and Yukiharu Ohsawa
Department of Physics, Nagoya University, Nagoya 464-01, Japan

Abstract

One dimensional electromagnetic simulation code based on a three-fluid model is used to study evolution of perpendicular magnetosonic pulses in a two-ion-species plasma. A magnetosonic pulse accelerates heavy ions in the direction parallel to the wave front, which results in the excitation of a long-wavelength perturbation behind the original pulse. Thus the original pulse is damped even if the plasma is collisionless and the pulse amplitude is small. The damping rate of a solitary pulse is theoretically obtained. It decreases with increasing amplitude. The theory is in good agreement with the simulation result. Also, it is confirmed that small-amplitude periodic waves are not damped.

1. INTRODUCTION

Recently, it has been found that in a plasma containing multiple ion species magnetosonic waves behave quite differently from those in a single-ion-species plasma [1]-[5]. First of all, the magnetosonic wave is split into two modes in a two-ion species plasma; the low- and high-frequency modes. The low-frequency mode has the ion-ion hybrid resonance frequency ω_{-r}, while the high-frequency mode has the lower hybrid resonance frequency ω_{+r}. Even though the high-frquency mode has a cutoff frequency of the order of ion cyclotron frequency, Korteweg-de Vries (KdV) equations were derived for both of the modes [1]. The solitary wave of the low frequency mode has a soliton width about the ion skin depth. The KdV equation for this mode is valid when the wave amplitudes are quite small. On the other hand, the solitay wave of the high-frequency mode has a soliton width about the electron skin depth. The KdV equation for this mode is valid when the amplitude ϵ is not too small. It is because this mode has a finite cutoff frequency ω_{+0} and the frequency is nearly constant in the long-wavelength region, $k < k_c$; k_c is defined as ω_{-r}/v_A with v_A the Alfven speed.

Furthermore, in a multi-ion-species plasma, a magnetosonic pulse (high frequency mode) can accelerate heavy ions to high-energies as well as some of the hydrogens [2],[5]; here, as in a space plasma, hydrogens are assumed to be the dominant component. As in a single-ion-species plasma, some fraction of hydrogens are reflected (accelerated) by the longitudinal electric field. The reflection does not take place when the amplitude is small. On the other hand, heavy ions are accelerated by the transverse electric field. If the pulse has a large-amplitude shock-like profile, all the particles of all the heavy species are accelerated to nearly the same speed. This result was applied to the solar physics [5] to account for the observations that the elemental compositions of solar energetic particles are similar to that of the background plasma, i.e., the solar corona. When the pulse has a small-amplitude soliton-like profile, all the heavy ions are also accelerated. In this case, however, the maximum speed is lower and depends on ion species.

Because of the heavy ion acceleration, magnetosonic pulses are damped, even when they propagate perpendicular to a magnetic field with small amplitudes. In this paper, using a one-dimensional electromagnetic simulation code based on a three-fluid model, we study the collisionless damping of perpendicular magnetosonic waves (high-frequency mode) in a two-ion-species plasma.

2. WAVE DAMPING

In a two-ion-species plasma, the heavy ion acceleration occurs in either large-amplitude or small-amplitude magnetosonic pulses [2]. A small-amplitude soliton-like pulse can accelelate heavy ions to the speed

$$v_{bym} = g_{vB} B_{\rm n}^{1/2}, \tag{1}$$

where $B_{\rm n}$ is the amplitude of the perturbed magnetic field normalized to the external field, B_0, and the coefficient g_{vB} is defined as

$$g_{vB} = \frac{4\alpha'^{1/2}}{\eta^3} \frac{\Omega_b \omega_{\rm pa}^2}{|\Omega_e| \omega_{\rm pe}^2} \left(1 - \frac{\Omega_b}{\Omega_a}\right) v_{\rm h}. \tag{2}$$

Here, $\omega_{{\rm p}j}$ and Ω_j are the plasma and the cyclotron frequencies of particle species j, respectively. The subscript a refers to the lighter ion species and the subscript b refers to the heavier ion species. The coefficient α' is an order-unity quantity, η is of the order of m_e/m_a, and the speed $v_{\rm h}$ is slightly higher than the Alfvén speed $v_{\rm A}$; for their precise expressions, see ref. 3.

The heavy ion acceleration causes the damping of the original pulse. The physical process of energy transfer is summarized as follows. In the pulse region, heavy ions are accelerated in the direction parallel to the wave front up to the speed (1). This heavy-ion motion across the magnetic field produces a long-wavelength perturbation behind the original pulse (see Fig. 4 in the next section). Simulations show that the wave number of such a perturbation is $k \sim k_{\rm c}$ and thus the frequency is $\omega \sim \omega_{+0}$. The energy of the original pulse is thereby gradually transferred to the long-wavelength perturbation through the acceleration of the heavy ion.

The wave-enegy density of the long wave length perturbations can be written as $w(\omega) v_{bym}^2$, where $w(\omega)$ is given by

$$w(\omega) = \frac{1}{2} \frac{m_b n_{b0}}{m_a n_{a0}} (m_a n_{a0} + m_b n_{b0}) \left(\frac{\omega_{-{\rm r}}^2}{\omega^2} + \frac{(\omega^2 - \omega_{-{\rm r}}^2)^2}{\omega^2 (\omega_{+0}^2 - \omega_{-{\rm r}}^2)} \right). \tag{3}$$

The amount of energy that the perturbation gains per unit time is $w(\omega) v_{bym}^2 M v_{\rm h}$, where $M v_{\rm h}$ is the propagation speed of the original pulse (M is the Mach number). This is equal to the time rate of change in the totla wave energy $E_{\rm w}$ of the original pulse

$$\frac{{\rm d}E_{\rm w}}{{\rm d}t} = -w(\omega) v_{bym}^2 M v_{\rm h}. \tag{4}$$

The total energy of the original pulse can be given by

$$E_{\rm w} = \int \left(\frac{(B - B_0)^2 + E^2}{8\pi} + \sum_j \frac{m_j n_j v_j^2}{2} \right) {\rm d}x. \tag{5}$$

Substituting the soliton solution into this equation, we can obtain the specific form for $E_{\rm w}$ of the original pulse as a function of the normalized amplitude $B_{\rm n}$. The wave energy $E_{\rm w}$ is proportional to $B_{\rm n}^{3/2}$, because the wave-energy density is proportional to $B_{\rm n}^2$ and the soliton width is proportional $B_{\rm n}^{-1/2}$.

The Mach number M is related to $B_{\rm n}$ through $B_{\rm n} = 2(M-1)$. We therefore obtain a differential equation for the amplitude of the magnetic field

$${\rm d}B_{\rm n}^{3/2}/{\rm d}t = -(3/2)\gamma B_{\rm n}(1 + B_{\rm n}/2), \tag{6}$$

where γ is

$$\gamma = \frac{\omega_{\rm pe} v_{\rm h}}{8(\alpha')^{1/2} c} \left(\frac{w(\omega) g_{vB}^2}{B_0^2/(8\pi)} \right). \tag{7}$$

If we neglect the second term on the right-hand side of eq. (6), we have

$$B_{\rm n}(t) = B_{\rm n}(0)[1 - \gamma B_{\rm n}(0)^{-1/2} t/2]^2. \tag{8}$$

When the second term in the square bracket on the right-hand side of eq. (8) is smaller than unity, this equation can be approximated as

$$B_{\rm n}(t) = B_{\rm n}(0)[1 - \gamma B_{\rm n}(0)^{-1/2} t]. \tag{9}$$

The damping rate, $\gamma_{\rm d}$, is thus given by

$$\gamma_{\rm d} = \gamma B_{\rm n}^{-1/2}(0). \tag{10}$$

Note that it decreases with increasing initial amplitude $B_{\rm n}(0)$ (The soliton theory for this mode is valid for amplitudes $(m_{\rm e}/m_{\rm i})^{1/2} \ll B_{\rm n} \ll 1$.). If we retain the second term on the right-hand side of eq. (6), we have

$$B_{\rm n}(t) = 2\tan^2[C - \gamma t/(2\sqrt{2})], \tag{11}$$

where C is given by $C = \arctan\,[B_{\rm n}(0)/2]^{1/2}$. When t and $B_{\rm n}$ are small, eq. (11) reduces to eq. (8).

3. Simulation Results

We consider waves propagating in the x direction ($\partial/\partial y = \partial/\partial z = 0$) in a magnetic field $\boldsymbol{B}$ that points in the z direction. To study the space-time evolution of finite amplitude waves, we carry out numerical simulations of the three-fluid model, employing the pseudo spectral method.

We simulate a hydrogen-helium plasma. Thus we have chosen the mass and charge ratios between heavy and light ions as $m_b/m_a = 4$ and $q_b/q_a = 2$, respectively. The

density ratio is $n_b/n_a = 0.1$, as in space plasmas. The mass and charge ratios between light ions and electrons are $m_a/m_e = 1000$ and $q_a/q_e = -1$. The magnetic field strength is $|\Omega_e|/\omega_{pe} = 0.5$, so that $c/v_A = 68.3$ and $v_A/v_h = 0.967$.

First, let us confirm that a small-amplitude periodic (sine) wave is not damped.As the initial wave profile, we use a sine wave with the amplitude, $B_n = 0.001$. Figure 1 shows the amplitude as a function of time. Even though $B_n(t)$ oscillate with very small amplitude, it is constant on average; the damping is not observed for periodic waves.

Let us also confirm that a solitary wave is not damped in a single-ion-species plasma. We impose a solitary wave solution for a single-ion-species plasma. Figure 2 represents the time variation of the amplitude, $B_n(t)$. In the early stage, the pulse propagation is not stationary, because of the initial disturbance. However, after the self-consistent solitary wave is established, i.e., $\Omega_H t \gtrsim 10$, it propagates steadily, and its amplitude becomes nearly constant in time.

Now, we study the damping of solitary pulses in a two-ion-species plasma. As initial wave profiles, we set solitary wave solutions obtained from the KdV equation for the high-frequency mode. In Fig. 3 we show profiles of the magnetic field at various times for a solitary wave with the initial amplitude $B_n(0)$ =0.1. Figure 4 shows the profiles of v_{by}, the y component of the velocity of the heavy ions. Although the magnetic field nearly keeps its initial profile, the heavy-ion velocity v_{by}, which is quite small at $t = 0$, increases with time in the pulse region; in this case it reaches its steady state value, $v_{by} \simeq 0.01 v_h$, at about $\omega_{pe} t = 1500$. That is, even in the fluid model, the heavy ions are accelerated in the direction parallel to the wave front. The heavy-ion motion across the magnetic field produces a long-wavelength perturbation behind the pulse region. This is the high-frequency mode, with the wavelength $\lambda \sim 2\pi/k_c$: more precisely, $\lambda = 1.2(2\pi/k_c)$ (and hence $\omega = 1.053\omega_{+0}$) for this case.

Because the energy is transfered to the long-wavelength perturbation, original pulse is gradually damped. Plotted in Fig. 5 is the time variation of the amplitude of the original pulse. The dots show simulation results, while the straight line represent the theory, eq.(10). When the solitary wave solution is imposed at $t = 0$ in the simulation, small-amplitude fluctuations (such as backward waves) as well as solitary wave are generated. Thus, the magnetic amplitudes in the simulation also have small fluctuations. We observe that the solitary wave is damped and that the theoretical damping rate agrees well with the simulation result.

We have carried out simulations with different initial amplitude, keeping the other parameters unchanged. Figure 6 shows the dependence of the maximum value of v_{by} on the amplitude $B_n(0)$. Here, the solid line was obtained from the theory, eq.(1). In the region $B_n \gtrsim \eta$, the agreement between the theory and simulation is especially nice. We show in Fig. 7 the damping rate as a function of the amplitude of the original pulse. The theoretical line represents eq.(10). Again, in the region $B_n \gtrsim \eta$, the theory agrees well with the simulation results.

References

[1] M. Toida and Y. Ohsawa, J. Phys. Soc. Jpn. **63**, 573 (1994).

[2] M. Toida and Y. Ohsawa: J. Phys. Soc. Jpn. **64**, 2036 (1995).

[3] M. Toida, Y. Ohsawa, and T. Jyounouchi: Phys. Plasmas **2**, 3329 (1995).

[4] D. Dogen, M. Toida, and Y. Ohsawa, J. Phys. Soc. Jpn. **65**, 3686 (1996).

[5] M. Toida and Y. Ohsawa, Solar Physics **171**, 161 (1997).

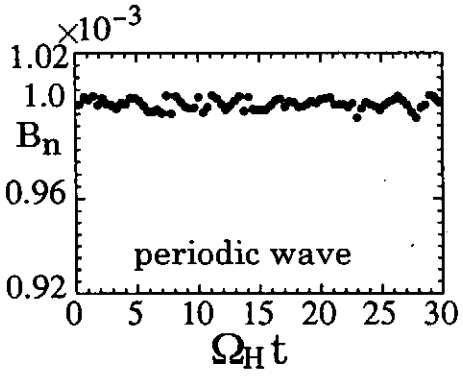

Figure 1: Time variation of the amplitude of a periodic wave.

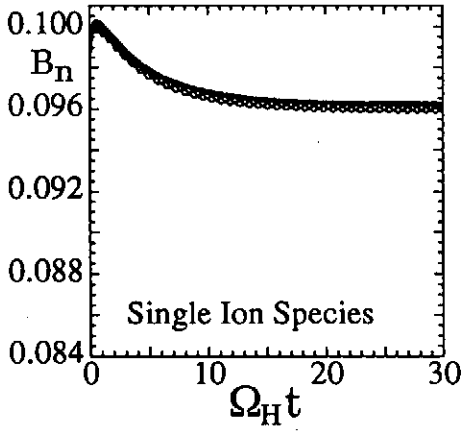

Figure 2: Time variation of the amplitude of solitary wave in a single-ion-species plasma.

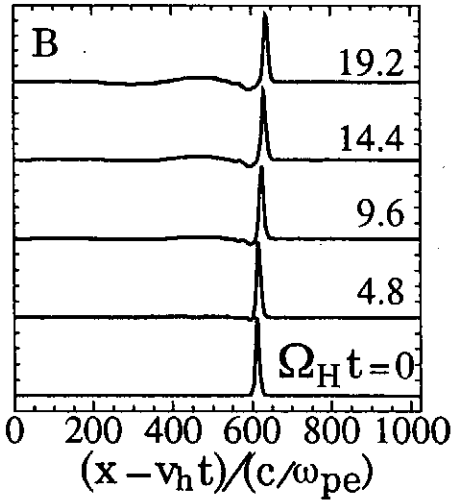

Figure 3: Magnetic field profiles of a solitary wave in a two-ion-species plasma at various times. The initial amplitude is $B_n(0) = 0.1$

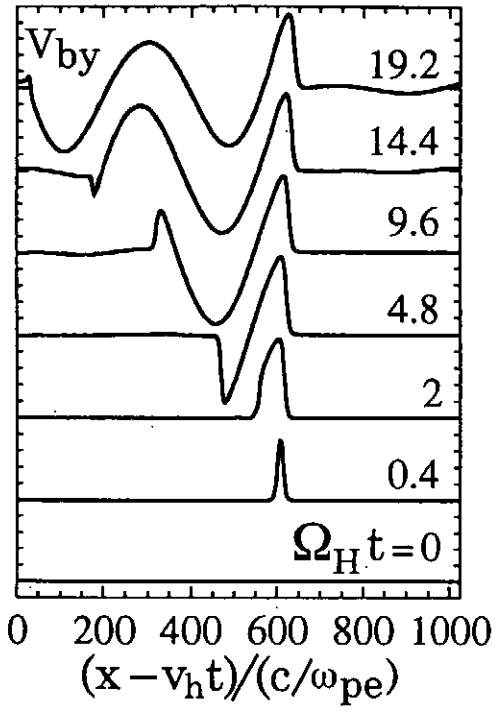

Figure 4: Profiles of the heavy ion velocity parallel to the wave front, v_{by}, at various times.

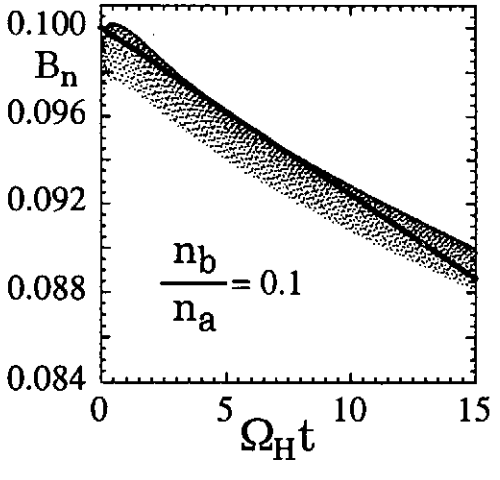

Figure 5: Time variation of the amplitude of a solitary wave in a two-ion-species plasma. The solid line and the dots show theory and simulation results, respectively.

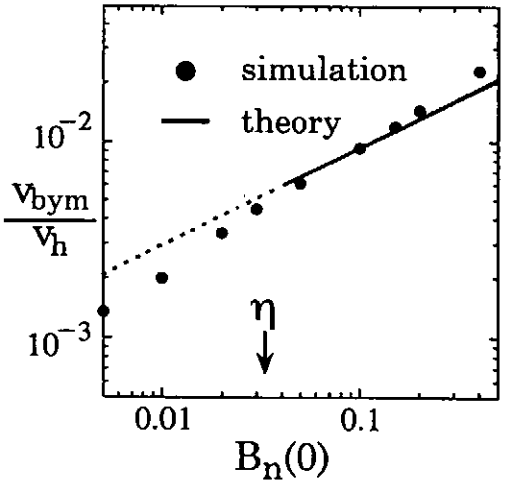

Figure 6: Maximum value v_{bym} as a function of the normalized amplitude $B_n(0)$. The theoretical curve (-) is compared with the simulation results (•).

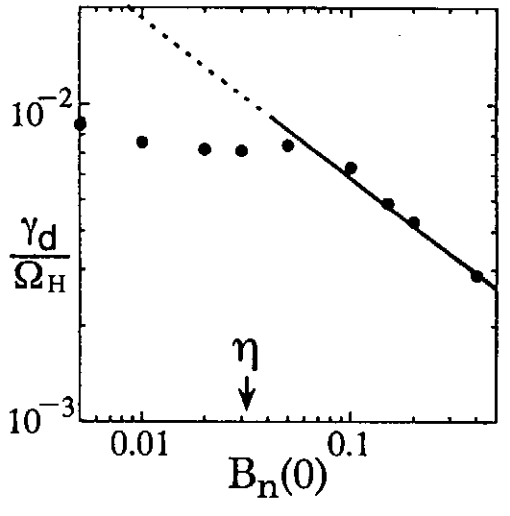

Figure 7: Damping rate γ_d as a function of the normalized amplitude $B_n(0)$. The theoretical curve (-) is compared with the simulation results (•). The theory is valid for $B_n(0) \gtrsim \eta$.

Production of High-Energy Electrons by Oblique Magnetosonic Shocks

Naoki BESSHO and Yukiharu OHSAWA
Department of Physics, Nagoya University, Nagoya 464-01, Japan

Abstract Electron motions in magnetosonic shock waves propagating obliquely to a magnetic field are studied by means of a one-dimensional (one spatial coordinate and three velocity components), fully relativistic particle simulation code with full ion and electron dynamics. It is found that highly relativistic electrons can be produced by oblique shock waves. This occurs when non-stationary electric fields in oblique shocks reflect some fraction of electrons. These electrons then oscillate in the shock region; the observed maximum energies of these particles were $\gamma \sim 100$, where γ is the Lorentz factor. This takes place when the propagation angle is $\sim 45°$ and when the magnetic field is rather strong, $\omega_{ce} \gtrsim \omega_{pe}$, where ω_{ce} and ω_{pe} are the cyclotron and plasma frequencies, respectively, in the upstream region.

1. Introduction

The ion acceleration by shock waves has been discussed by many authors [1]-[3]. The large electric potential formed in a shock wave can reflect some of the ions and accelerate them to high energies. A shock wave has a positive electric potential; thus some of the ions can be reflected. (For the heavy ion acceleration by the transverse electric field, see Refs. [4]-[6].)

Recently, however, it has been found by particle simulations that in some cases electrons can be reflected in a shock wave and have great kinetic energies. The strong electron acceleration can take place in an oblique shock wave when the external magnetic field is rather strong, i.e., $\omega_{ce} \gtrsim \omega_{pe}$. This is most appreciable when the angle between the wave normal and the external magnetic field is around $\pi/4$. The maximum electron energies observed in the simulations were $\gamma \sim 100$, where γ is the Lorentz factor. This paper briefly describes this phenomenon.

2. Simulation Results

We consider shock waves propagating in the x direction ($\partial/\partial y = \partial/\partial z = 0$) in an external magnetic field $\boldsymbol{B}_0$; in the upstream region it is in the (x, z) plane (see Fig. 1). To study space-time evolution of shock waves, we carried out simulations using a one-dimensional (one spatial coordinate and three velocity components), fully electromagnetic, relativistic particle code with full ion and electron dynamics

(for the details of the simulation method, see Ref. [4]). The simulation parameters are as follows: The number of simulation particles are $N_\mathrm{i} = N_\mathrm{e} = 131072$. The ion-to-electron mass ratio is $m_\mathrm{i}/m_\mathrm{e} = 100$, and the light speed is $c = 4$. The electron and ion thermal velocities are $v_\mathrm{Te} = 1.51$ and $v_\mathrm{Ti} = 0.04$. The electron skin depth is $c/\omega_\mathrm{pe} = 4$. The strength of the external magnetic field was chosen so that $\omega_\mathrm{ce}/\omega_\mathrm{pe} = 3.0$. For these parameters, the beta value, which is defined as the ratio of the plasma pressure to the magnetic energy, is $\beta = 0.01$, and the Alfvén speed is $v_A = 1.2$. The ion gyro-radius is $\rho_\mathrm{i} = 0.77$. The angle between the wave normal and the external magnetic field is $\theta = \pi/4$.

We show in Fig. 2 phase-space plots of electrons, $(x,\ p_x)$, $(x,\ p_y)$, $(x,\ p_z)$, and $(x,\ \gamma)$: the momenta and lengths are normalized to the electron mass and grid spacing, respectively. We see that in the shock region the maximum values of p_x and p_z are larger than that of p_y. The maximum electron energy (shown by the Lorentz factor γ) is $\gamma \sim 40$ in this case.

Figure 3 shows time variations of $(x - v_\mathrm{sh}t)$, y, and γ of electrons, where v_sh denotes the shock propagation speed; the thin lines show trajectories of an electron that was not accelerated while the thick lines show the ones of an electron that was accelerated. For the bulk of the electrons the quantity $(x - v_\mathrm{sh}t)$ just decreases with time, as shown by the thin line, and their energies do not increase much. On the other hand, the quantities $(x - v_\mathrm{sh}t)$ and y of an accelerated electron oscillate in the shock region; it is trapped. The energy also oscillates and has a large value. It has its maximum value when y is maximum; at that moment $(x - v_\mathrm{sh}t)$ is increasing and the potential energy $-e\varphi$ is minimum.

We show in Fig. 4 profiles of the electric field parallel to the magnetic field, $E_\parallel$, and of $-eF$; F is defined by $E_\parallel = -\mathrm{d}F/\mathrm{d}s$ where $\mathrm{d}s$ is the length along the magnetic field (Because $E_\parallel$ contains both the longitudinal and transverse electric fields, F is not the potential). Comparing the profiles at $\omega_\mathrm{pe}t = 212$ and 216, we see that either $E_\parallel$ or F is not stationary. We note that, at $\omega_\mathrm{pe}t = 216$, the quantity $-eF$ has its maximum value behind the deepest dip, i.e., at $x = 730 \sim 740$.

In summary, even though the potential is positive, some electrons can be reflected and are trapped in the shock region. They have great kinetic energies. The reflection can occur because the shock profile is not stationary; some of the electrons feel positive $-eF$ at some x positions. After the reflection, the kinetic energy of an electron increases.

References

[1] D. Biskamp, and H. Welter: Nuclear Fusion **12**, 663 (1972).

[2] R. L. Tokar, S. P. Gary and K. B. Quest, Phys. Fluids **30**, 2569 (1987).

[3] Y. Ohsawa: J. Phys. Soc. Jpn. **59** (1990) 2782.

[4] M. Toida and Y. Ohsawa: J. Phys. Soc. Jpn. **64**, 2036 (1995).

[5] D. Dogen, M. Toida, and Y. Ohsawa, J. Phys. Soc. Jpn. **65**, 3686 (1996).

[6] M. Toida and Y. Ohsawa, Solar Physics **171**, 161 (1997).

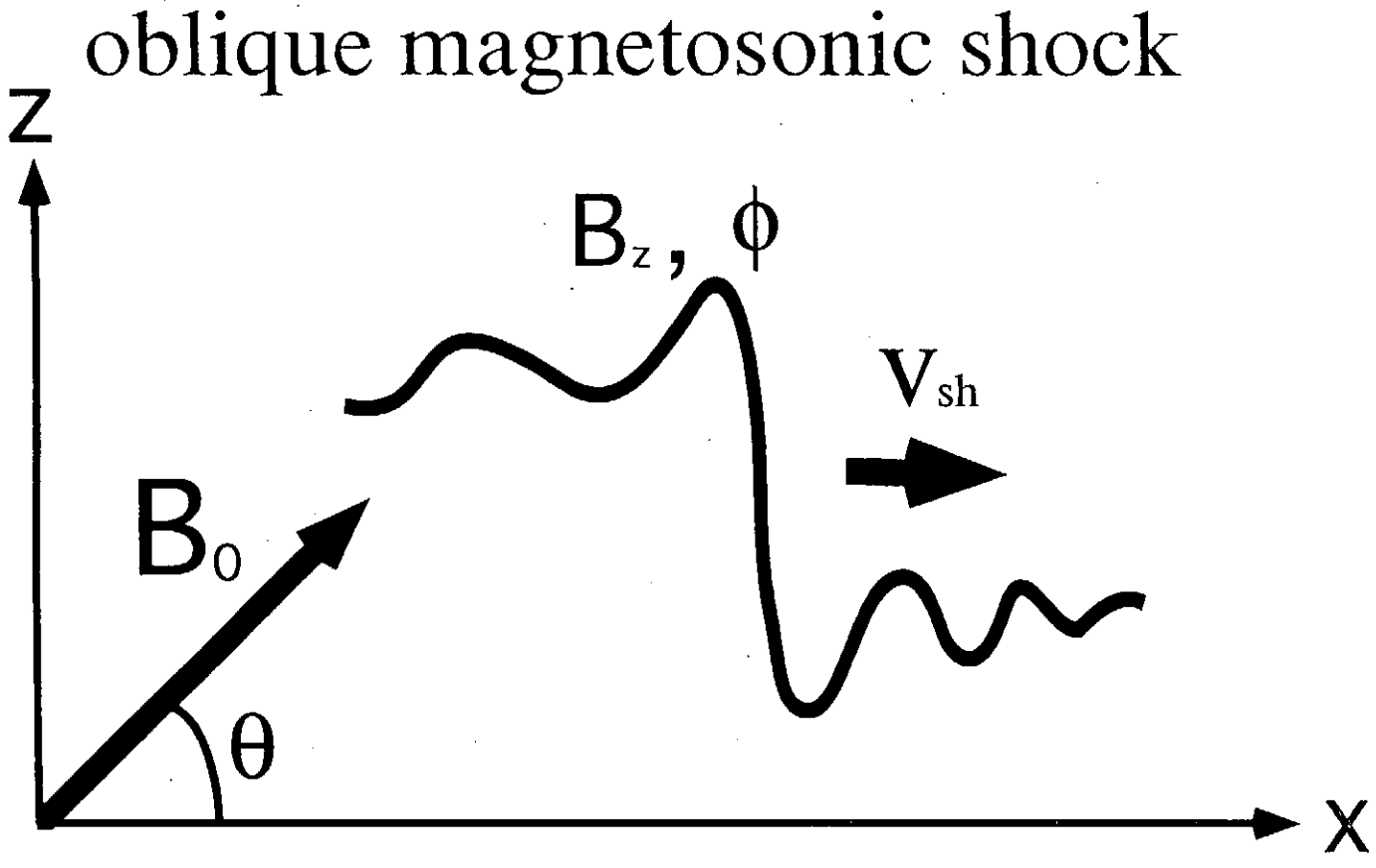

Fig. 1. Schematic diagram of shock propagation.

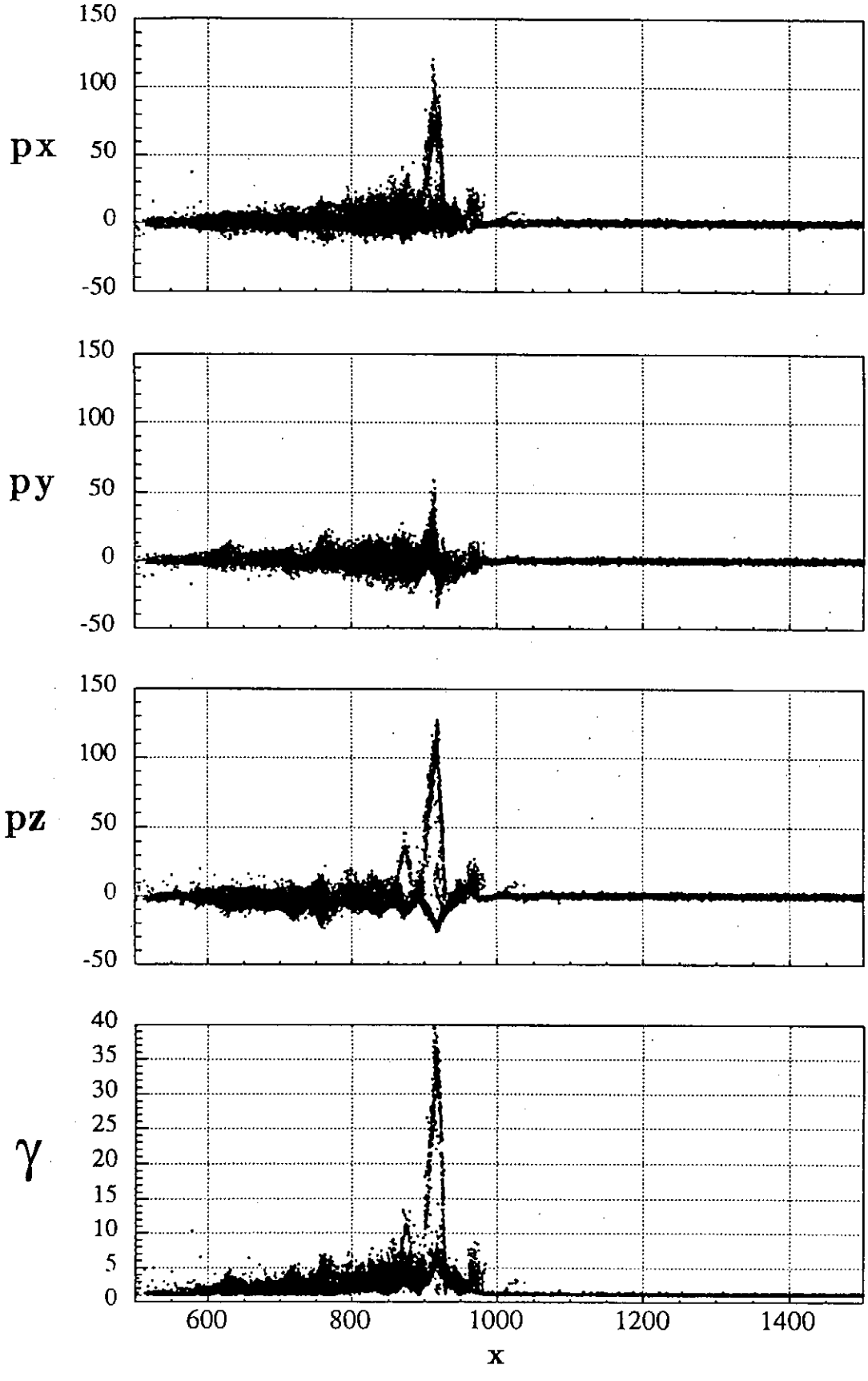

Fig. 2. Phase space plots of electrons in an oblique shock.

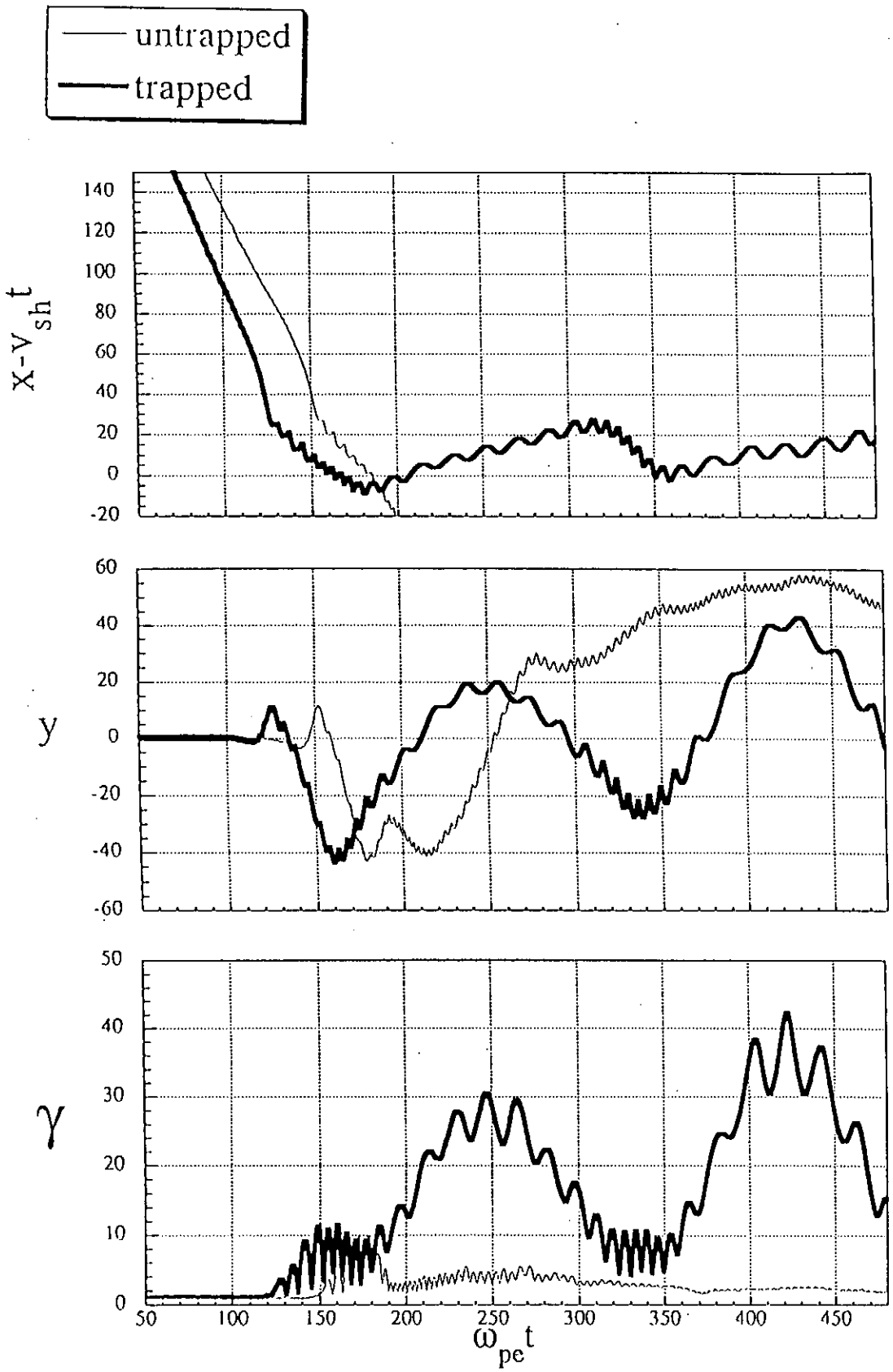

Fig. 3. Time variations of $(x - v_{sh}t)$, y, and γ of electrons.

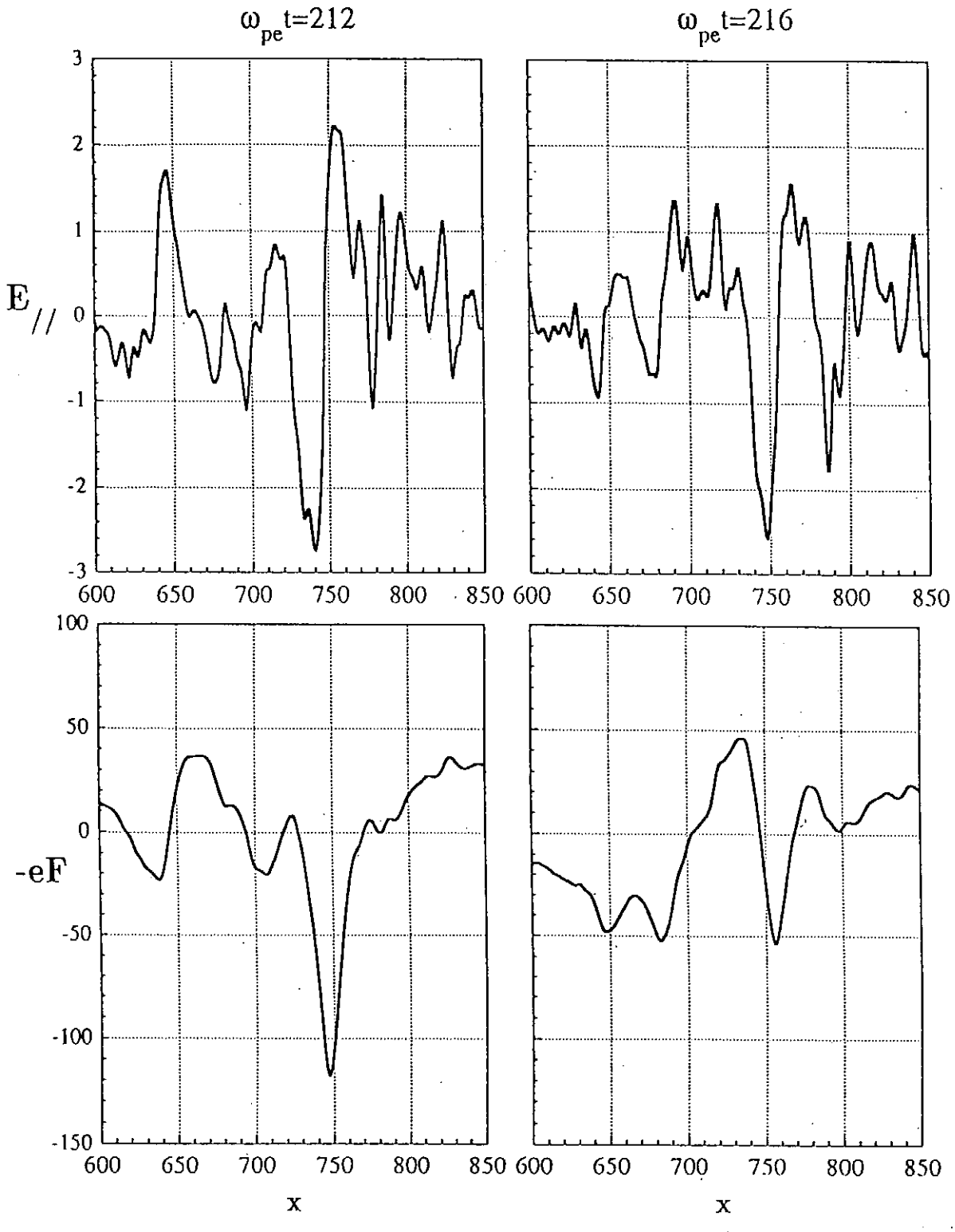

Fig. 4. Profiles of parallel electric field $E_{parallel}$ and of $-eF$.

Acceleration of Energetic Ions by Magnetosonic Shocks

Kentaro MARUYAMA and Yukiharu OHSAWA
Department of Physics, Nagoya University, Nagoya 464-01, Japan

Abstract Wave-particle interactions in nonlinear magnetosonic waves are studied with a one-dimensional (one spatial coordinate and three velocity components), fully relativistic particle simulation code with full ion and electron dynamics. Particular attention is given to the acceleration of energetic ions whose initial speeds are comparable to or greater than the Alfvén speed. Simulations show that some of the energetic ions can be accelerated by the transverse electric field in a magnetosonic wave. The change in energy increases with increasing initial particle energy. The present results suggest that, if particles encounter with magnetosonic pulses many times, then high-energy ions with speeds much greater than the Alfvén speed could be produced.

1. Introduction

Some ions can be reflected by a magnetosonic pulse and have speeds comparable to or greater than the Alfvén speed $v_{\rm A}$ [1]-[3]. It is expected that in a plasma with strong disturbance a number of magnetosonic pulses as well as other kinds of waves are propagating. Hence the energetic ions with $v \gtrsim v_{\rm A}$ that were produced by one pulse would encounter with many other pulses. In this paper, using a particle simulation code, we will study how these energetic ions interact with magnetosonic pulses (or shocks).

It is found that some energetic ions can be further accelerated by the transverse electric field. The change in the kinetic energy increases with the magnitude of the initial momentum; ions with higher energies can gain greater energies. Indeed, assuming that the gyration speed of an ion is much greater than the shock speed $v_{\rm sh}$ and that the distance d between the shock front and the guiding center is close to the gyroradius ρ (Figure 1 shows the particle orbit under consideration), we can obtain the increase in p^2 of energetic ions as

$$\delta(p^2/2) = \left[\frac{2}{\omega_{\rm ci}}\left(\frac{2(\rho-d)}{\rho}\right)^{1/2} + 2\frac{v_{\rm sh}}{\rho\omega_{\rm ci}^2}\right] qE_y p_0, \qquad (1)$$

where p_0 is the magnitude of initial momentum. Substituting the expression for the transverse electric field E_y known from the nonlinear wave theory [4]-[6], we

find δp^2 as

$$\delta(p^2/2) = \left[\frac{2}{\omega_{ci}}\left(\frac{2(\rho-d)}{\rho}\right)^{1/2} + 2\frac{v_{sh}}{\rho\omega_{ci}^2}\right] qB_0\frac{2v_{sh}}{c}(M-1)p_0. \qquad (2)$$

2. Simulation Results

To further study, we have carried out simulations for perpendicular shock waves propagating in the x direction ($\partial/\partial y = \partial/\partial z = 0$) in a magnetic field $\boldsymbol{B}$ that points in the z direction, using a one-dimensional, fully electromagnetic, relativistic particle code with full ion and electron dynamics. Initially we have bulk ions (and electrons) with Maxwellian velocity distribution. Also, we have a small number (5 %) of energetic ions whose initial momenta are $p = p_0$.

Figure 2 shows profiles of the transverse electric field E_y in a shock wave and energies (Lorentz factor γ) of energetic ions at $\omega_{pe}t = 450$ and at 1200. In this case the initial energy of energetic ions was $\gamma = 5.1$. We see in the upper panel that in front of the shock there are many ions with energies higher than the initial values, $\gamma = 5.1$. As illustrated in Fig. 1, they had once entered the shock region and then went back to the upstream region. When they were in the shock region, they gained some energies from the transverse electric field E_y. Because the ions are gyrating around the magnetic field lines and the shock keeps propagating, ions are eventually left behind the shock. The lower panel shows that a number of accelerated energetic ions keep high energies behind the shock (some of them lose energies when they move to the downstream region).

The upper panel in Fig. 3 shows x positions of an ion (shown by the curve similar to sine wave) and of the leading edge of the shock (shown by the straight line) as a function of time. The area under the straight line is the shock or downstream region. The lower panel shows time variation of the energy (Lorentz factor) of an accelerated energetic ion. These two pictures clearly indicates that the particle is accelerated by the mechanism shown by Fig. 1.

We show in Fig. 4 the increase in p^2 as a function of the magnitude of initial momentum p_0. (Here heavy ions as well as protons are shown; in the simulations a small number of heavy ions were included.) Both theory (eq.(2)) and simulation show that δp^2 increases with increasing p_0.

References

[1] D. Biskamp, and H. Welter: Nuclear Fusion **12**, 663 (1972).

[2] R. L. Tokar, S. P. Gary and K. B. Quest, Phys. Fluids **30**, 2569 (1987).

[3] Y. Ohsawa: J. Phys. Soc. Jpn. **59** (1990) 2782.

[4] J. H. Adlam and J. E. Allen, Philos. Mag. **3**, 448 (1958).

[5] L. Davis, R. Lüst and A. Schlüter, Z. Naturforsch. Teil **A13**, 916 (1958).

[6] Y. Ohsawa: Phys. Fluids **29**, 2474 (1986).

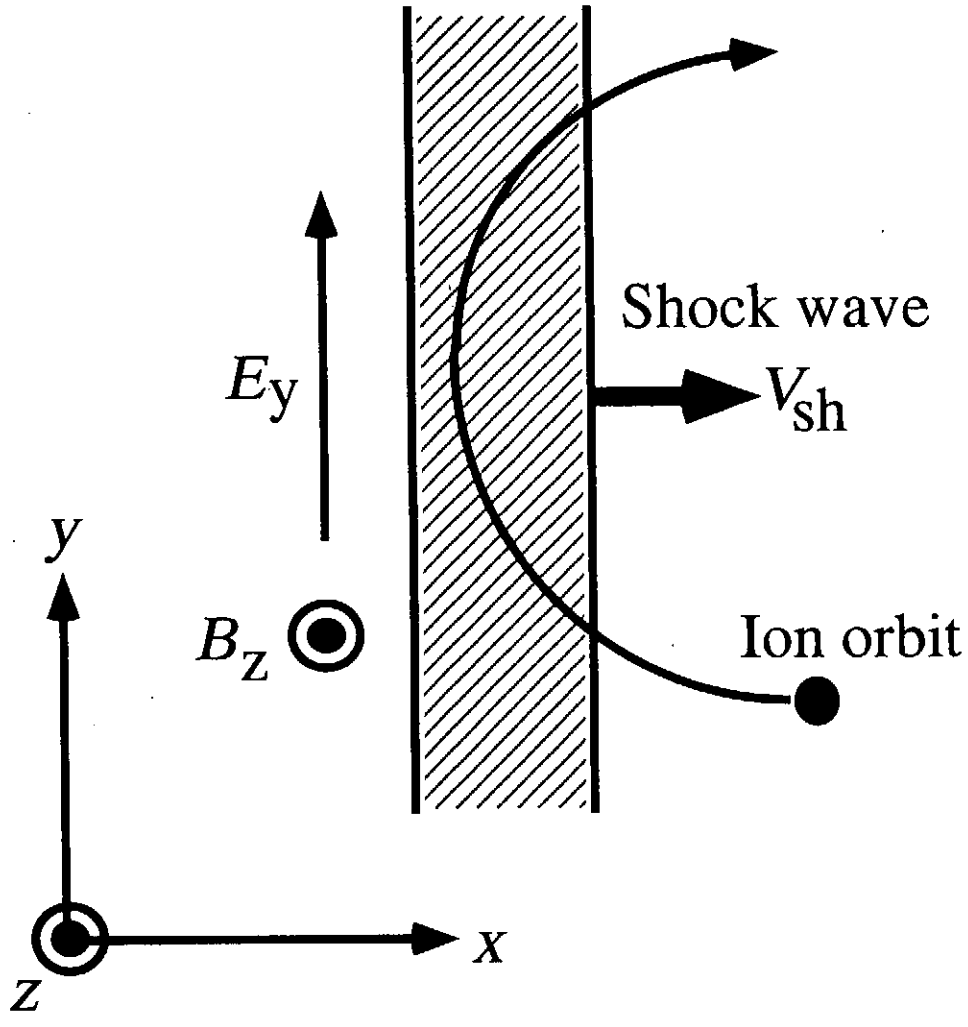

Fig.1. Schematic diagram of shock wave and orbit of an energetic ion.

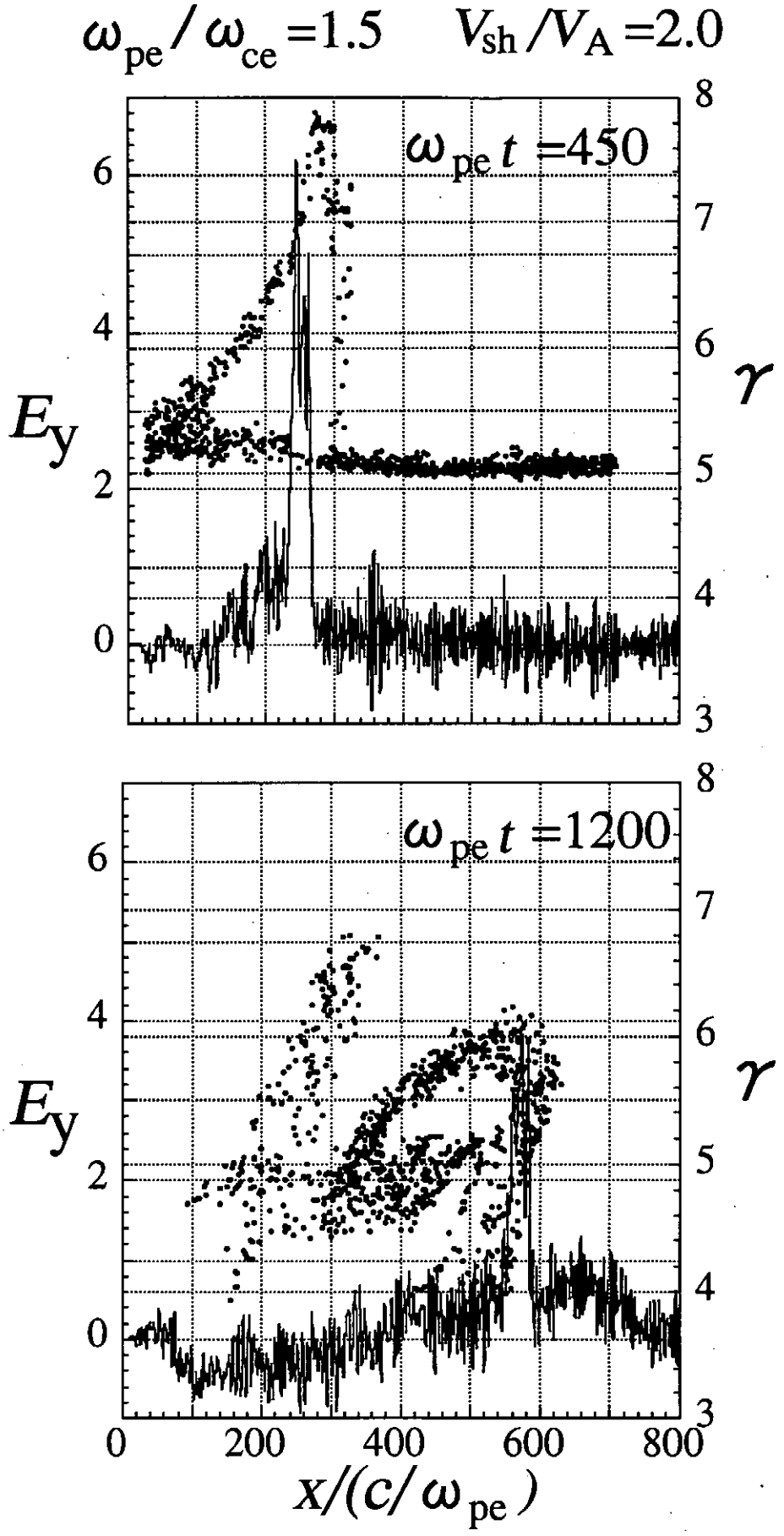

Fig.2. Profiles of transverse electric field Ey and phase space plots (x, γ) of energetic ions.

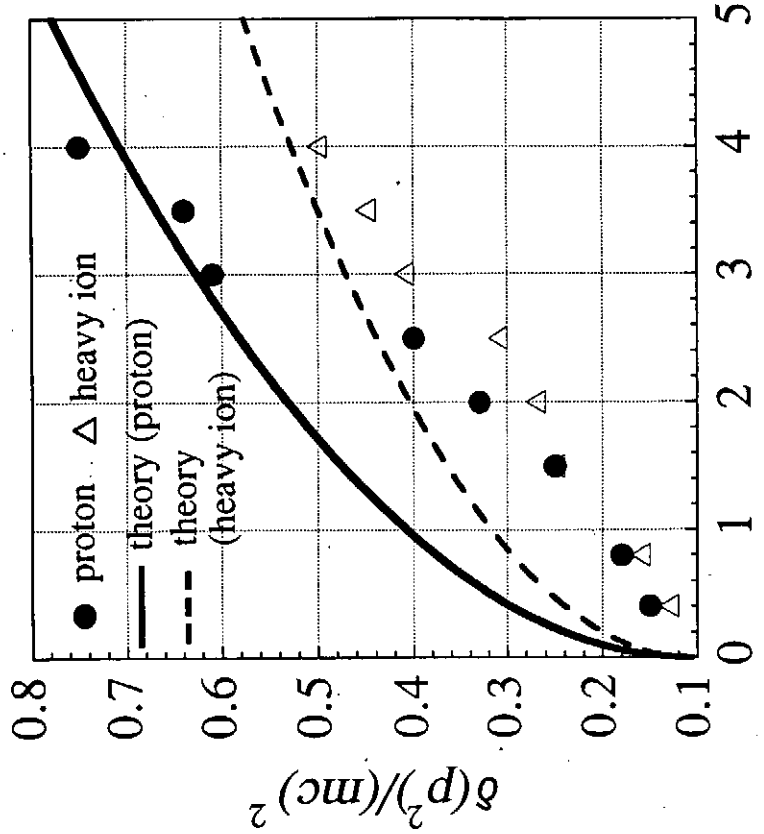

Fig.4. Increase in p^2 versus initial momentum p_0.

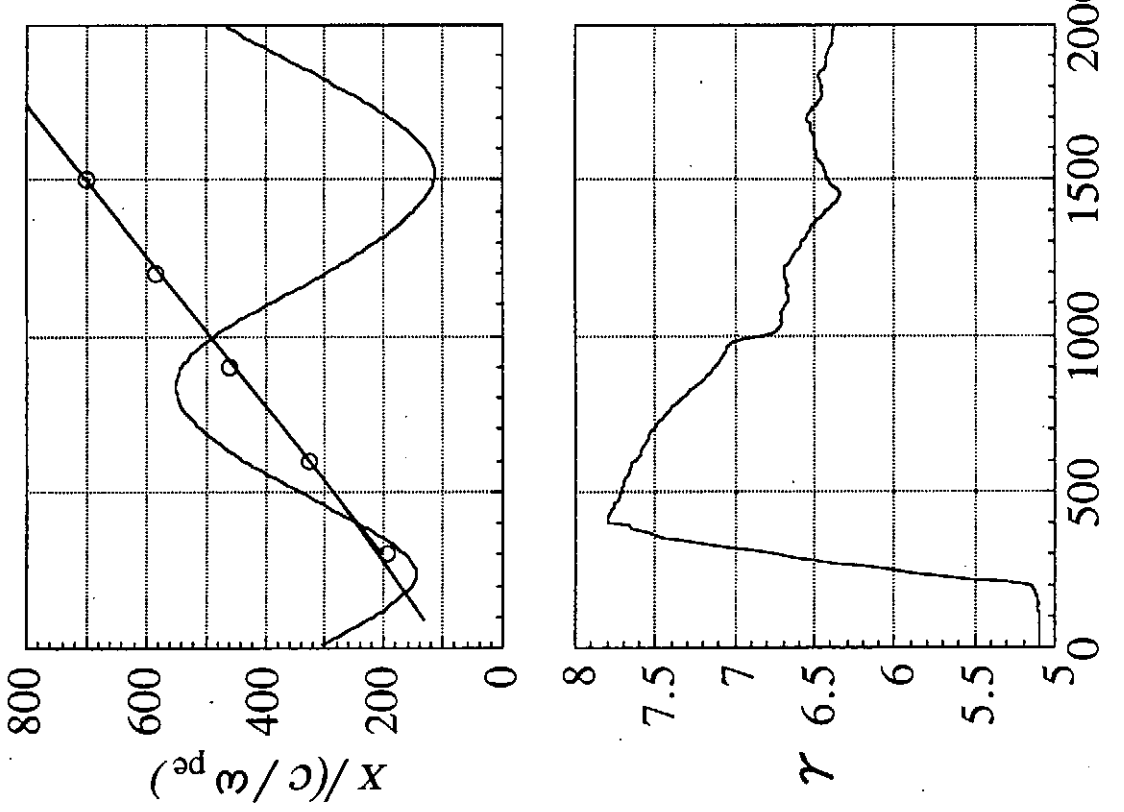

Fig.3. Positions of the shock and an energetic ion as functions of time.

Simulation Study of Radial Electric Field Enhancement by ECRH in Heliotrons

S. Murakami, N. Nakajima, U. Gasparino[†], M. Okamoto

National Institute for Fusion Science,
Oroshi, Toki 509-52, Japan

[†]*Max-Planck-Institut für Plasmaphysik, EURATOM Ass.,*
D-85748 Garching, Germany

Abstract

The effect of ECRH generated suprathermal electrons on the radial electric field is studied in relation to the transition phenomena of the radial electric field observed in CHS. A new Monte Carlo simulation code in 5D phase space is used to evaluate the suprathermal electron distribution and the enhanced electron flux by ECRH. It is found that in low density discharges ($n_e \leq 1 \times 10^{19}\mathrm{m}^{-3}$, $T_e \geq 400\mathrm{eV}$) the positive radial electric field can be enhanced by applying off-axis ECRH with significant heating power ($\geq$ 150kW). The simulated profile of the radial electric field is found to be in good agreement with the experimental one.

1. Introduction

Strong radial electric fields, E_r, can reduce the orbit deviation of ripple trapped particles from the magnetic surface and improve the confinement properties. Operation with strongly positive E_r (electron root) is expected to improve the neoclassical transport in heliotrons at low collisionality regime and at the same time to prevent impurity accumulation. It is, therefore, important to clarify the physics determining E_r in heliotrons.

Due to the lack of the axisymmetry the intrinsic ambipolarity condition is violated in non-axisymmetric configurations and the electron and ion neoclassical diffusion coefficients depend on E_r. Therefore E_r can be determined by imposing the ambipolarity condition of the neoclassical particle fluxes. The observed E_r have shown agreements with neoclassical estimations even in cases where radial losses are predominantly anomalous[1].

However, recent experiments[2] at the Compact Helical System[3] (CHS:l = 2 and m = 8 heliotron) have shown a transition of E_r which can not be explained simply by

neoclassical theory. E_r was observed to change from negative to positive when ECR waves was applied to low density NBI heated CHS plasma. The heating point of ECR heating was set at the region $r/a = 0.5$ and the larger change of E_r was observed near the region $r/a = 0.8$ to 0.9 with the ECRH power larger than about 100kW.

Ripple trapped suprathermal electrons are expected to be created during ECRH. Their fast drift motions across the magnetic surfaces could enhance the electron flux, affecting the condition of ambipolarity and could therefore be responsible for this E_r transition phenomena. The radial diffusion of suprathermal electrons could also be responsible for the broadening of ECRH deposition observed in W7-AS experiments[4]. In order to solve this problem we must consider electron behaviours in both velocity and real space.

In this paper the effect of ECRH on E_r is studied on the base of the ambipolarity of neoclassical and ECRH driven fluxes. The ECRH driven electron flux is evaluated using a New Monte Carlo simulation code (in 5D phase space) [5,6] based on a technique similar to the adjoint equation for dynamic linearized problems.

2. Simulation Model

We have developed a new Monte Carlo simulation code based on a technique similar to the adjoint equation for dynamic linearized problems[7]. The linearized drift kinetic equation for the deviation from the Maxwellian background $f_1(\underline{x}, \underline{v})$,

$$\vec{v} \cdot \nabla f_1 + \vec{a} \cdot \nabla_v f_1 = C(f_1) + S^0_{ql}, \tag{1}$$

is evaluated as,

$$f_1(\underline{x}, \underline{v}) = \int_0^\infty dt \int d\underline{x}' \int d\underline{v}' S^0_{ql}(\underline{x}', \underline{v}') g(\underline{x}, \underline{v}, t|\underline{x}', \underline{v}'), \tag{2}$$

where $C(f_1)$ is the linear Coulomb collision operator and S^0_{ql} is the wave induced flux in velocity space (quasi-linear diffusion term) which is assumed to be a given function (evaluated, e.g. by ray-tracing). The time dependent Green function $g(\underline{x}, \underline{v}, t|\underline{x}', \underline{v}')$ is the solution of the drift kinetic equation

$$\frac{\partial g}{\partial t} + \vec{v} \cdot \nabla g + \vec{a} \cdot \nabla_v g = C(g), \tag{3}$$

with initial condition $g(\underline{x}, \underline{v}, t = 0|\underline{x}', \underline{v}') = \delta(\underline{x} - \underline{x}')\delta(\underline{v} - \underline{v}')$. The solution of Eq. (3) is obtained using the Monte Carlo simulation in which the complex magnetic field configuration, the finite-β effect, and the radial electric field can be included[8]. Using this code we investigate the kinetic effect of suprathermal electrons and evaluate the ECRH driven flux.

In addition to the ECRH driven flux we have also taken into account the effect of enhanced radial flux by NBI beam particles[6]. We first calculate the birth profile of

NBI particles and evaluate the contribution to the particle flux due to particle losses by prompt orbit loss.

We assume that E_r is determined by the ambipolarity condition of neoclassical particle fluxes and those related to energetic particles,

$$\Gamma_e^{NC}(E_r) + \Gamma_e^{fast} = \Gamma_i^{NC}(E_r) + \Gamma_i^{fast}, \tag{4}$$

where Γ_s^{NC} and Γ_s^{fast} are, respectively, the neoclassical and the energetic particles contribution to the s-species (electron and ion).

3. Simulation Results

At first were investigated the characteristic of the (collisional) orbits of suprathermal electrons in the magnetic configuration of CHS. Test suprathermal electrons were started at the radial position $r/a = 0.5$. As time passes the energy of the suprathermal electron is slowed down by Coulomb collisions with the background plasma and the orbit affected by pitch-angle scattering. It is found that fast radial motion can be seen if the electron becomes helically trapped during the change of pitch angle. This shows that the radial drift motion of ripple trapped electron is the main mechanism for the radial transport of suprathermal electrons.

Next the enhanced radial flux by ECRH was evaluated using the approach of section 2 for the case where we assume $n_0 = 1.0 \times 10^{19}\mathrm{m}^{-3}$, $T_{e0} = 400\mathrm{eV}$, and the ECRH power of 200kW. The heating scenario is the "bottom heating case" at $r/a = 0.5$ of the CHS experiments[2].

The quasi-linear diffusion term S_{ql}^0 is estimated through an analytical model of E-CR heating. Figure 1 shows the comparison of the ECRH driven flux with background electron flux. An outward flux is observed in the region $r/a > 0.5$ and an inward one for $r/a < 0.5$. The magnitude of the obtained ECRH radial flux is less than 1/3 of the neoclassical flux of the background electron .

The effect on E_r of this ECRH driven flux was studied. Figure 2 shows the radial profiles of E_r obtained by solving the ambipolarity condition eq. (4). We changed the ECRH power from 0 to 200kW. It is found that E_r becomes positive at the region where the ECRH driven flux is directed outwardly. The strongest positive E_r is observed at $r/a \simeq 0.8$ for ECHR power larger than 150kW, while the maximum outwardly driven flux corresponds to $r/a \simeq 0.6$ (See Fig. 1).

This discrepancy can be understood by analyzing the background neoclassical fluxes and the ECRH driven one. The ion flux reaches its maximum vale near $E_r = 0$. In the case of $r/a = 0.6$ the background electron flux is smaller than the value of the maximum point of the ion flux and by adding the ECRH driven flux only a relatively small change in E_r is observed. On the other side in case of $r/a = 0.8$ the background

electron flux is close to the value of the maximum point of ion flux. Therefore a large change in E_r occurs by adding the relatively small contribution of the ECRH driven flux.

4. Conclusions

We have studied the effects of ECRH generated suprathermal electrons on the radial electric field by means of a new Monte Carlo simulation code in 5D phase space. The radial transport of suprathermal electrons is mainly due to the radial drift motions of particles trapped in the helical ripples. We have simulated the situation of the CHS experiment in which a transition of the radial electric field was observed in low density discharges ($n_e \leq 1 \times 10^{19}\mathrm{m}^{-3}$, $T_{e0} \geq 400\mathrm{eV}$). Significant ECRH driven flux (but smaller than the neoclassical one) is observed due to the radial transport of suprathermal electrons in the magnetic field configuration of CHS. Assuming the ambipolarity condition of the electron and ion fluxes E_r is estimated taking into account the neoclassical and the high energetic particle driven fluxes. A strong positive E_r is observed $r/a \sim 0.8$ if significant heating power ($\geq$ 150kW) is applied. This agrees with experimental observations. Therefore the important role of ECRH driven flux has been shown in the interpretation of E_r transition phenomena observed in CHS.

REFERENCES

[1] G. Kühner, et al., in Plasma Physics and Controlled Nuclear Fusion Research 1994 (Proc. 15th Int. Conf. Sevilla, 1994), Vol. 1, IAEA, Vienna (1995) 145.

[2] H. Idei, H., et al., Phys. Plasmas **1** (1994) 3400.

[3] K. Nishimura, et al, Fusion Technol. **17** (1990) 86.

[4] M. Romé, et al., Plasma Phys. Control. Fusion, **39** (1997) 117.

[5] S. Murakami, et al., in Proc. Int. Conf. Plasma Phys. 1996 Nagoya, Vol. 1 (1997) 1014.

[6] S. Murakami, et al., Plasma Physics and Controlled Nuclear Fusion Research, 1996 (Proc. 16th Int. Conf. Montreal, 1996) (in press), IAEA/CP-6.

[7] N. J. Fisch, Phys. Fluids **29** (1986) 172.

[8] S. Murakami, et al., Nucl. Fusion **34** (1994) 913.

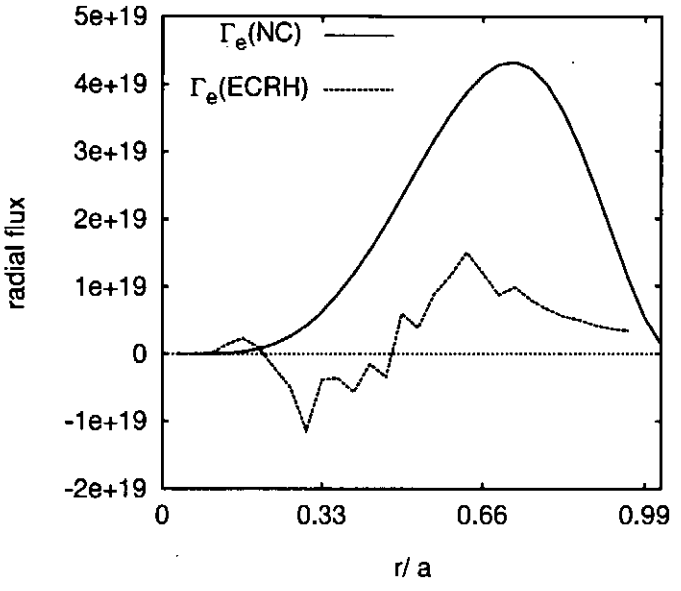

Fig. 1 : Comparison of the ECRH driven flux with the background neoclassical flux in CHS [P_{ECRH} = 200kW, $n_0 = 1.0 \times 10^{19}\mathrm{m}^{-3}$ and T_0 = 400eV].

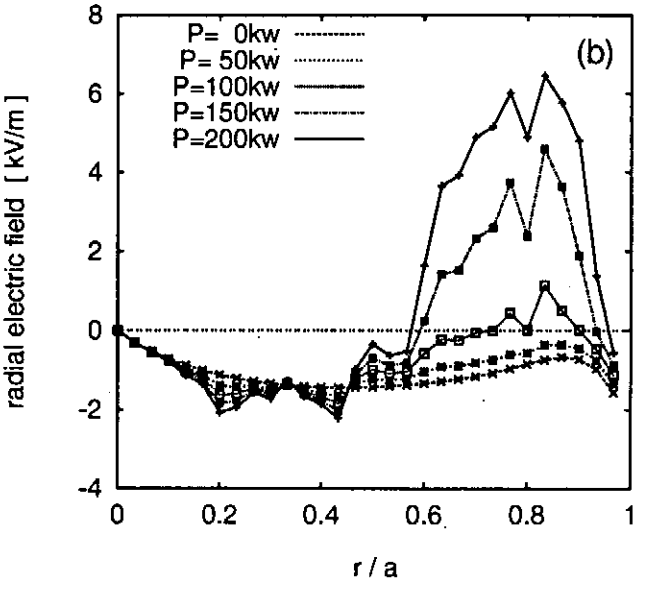

Fig. 2 : Change of the radial electric field due to the ECRH driven flux in CHS [$n_0 = 1.0 \times 10^{19}\mathrm{m}^{-3}$ and T_0 = 400eV].

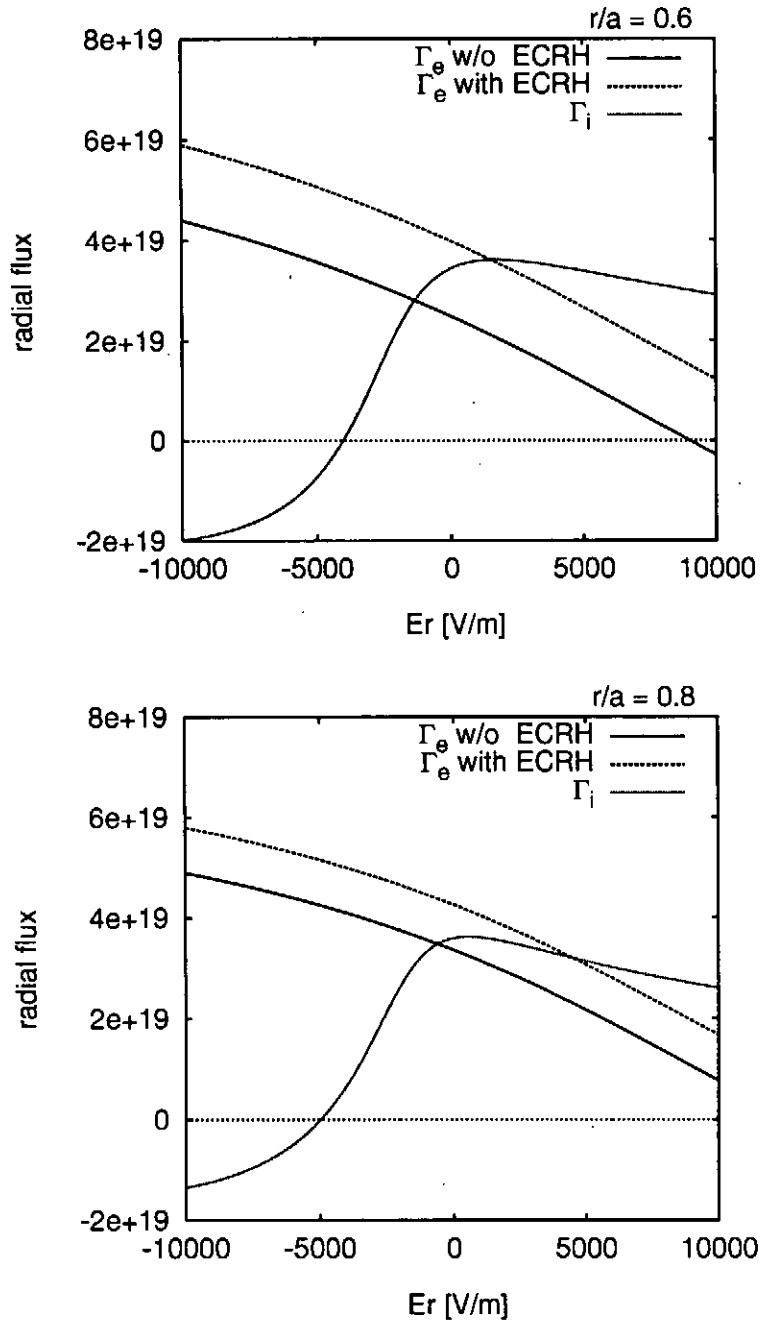

Fig. 3 : Comparison of the ion and electron fluxes with and without ECRH driven flux for different radial points; (a) $r/a = 0.6$ and (b) $r/a = 0.8$.

Averaged RMHD Equations

Katsuji ICHIGUCHI

National Institute for Fusion Science
Oroshi-cho 322-6, Toki 509-52, JAPAN

Abstract

A new reduced set of resistive MHD equations is derived by averaging the full MHD equations on specified flux coordinates, which is consistent with 3D equilibria. It is confirmed that the total energy is conserved and the linearized equations for ideal modes are self-adjoint.

Key Words: reduced MHD equation, averaging method, three-dimensional equilibrium

1 Introduction

Recently, several codes have been developed for the magnetohydrodynamic (MHD) linear stability analysis of the three-dimensional (3D) equilibria calculated by the VMEC code[1]. A comparison study of the codes is summarized in [2]. The codes are classified into two categories. One is the 3D approach, which has an advantage that the stability of the exact 3D equilibrium can be calculated without any approximation. However, these codes can only examine ideal modes because they are based on the energy principle, and it is difficult to provide sufficient perturbation space to search for the largest growth rate.

The other is the 2D approach. Some of them employ reduced MHD equations, which can treat not only ideal modes but also resistive ones. The nonlinear growth of the unstable modes can also be studied as an initial value problem. However, understanding the approximation which is used in reducing the 3D equilibrium properties to 2D expressions is essential in these approach. Recently, Todoroki[3] derived a Grad-Shafranov type equation by averaging the 3D equilibrium equation on specified coordinates without any ordering. This means that any 3D equilibrium solution satisfies the equation. In this paper, the averaging method is applied to the derivation of a reduced set of MHD equations, in order to study the stability of the 3D equilibria against the resistive modes as well as the ideal ones. Since the coordinates introduced by Todoroki are not easy to treat in the stability analysis, the use of flux coordinates is considered. In this case,

every flux coordinates system cannot give the Grad-Shafranov type equation in the averaging method, because the equation has to be expressed with only metric and surface quantities.

In Section 2, the averaged equilibrium equation in flux coordinates is discussed. The reduced MHD equations based on the averaging method are derived and the basic properties of them are examined in Section 3. In Section 4, numerical results are presented. Conclusions are given in Section 5.

2 Averaged equilibrium equation

In arbitrary flux coordinates (ρ, θ, ζ), where ρ is the label of the magnetic flux and θ and ζ are the poloidal and the toroidal angles, respectively, the magnetic field, $\boldsymbol{B}$, and the current density, $\boldsymbol{J}$, are expressed by

$$\boldsymbol{B} = \nabla\rho \times \nabla\left(\frac{d\chi}{d\rho}\theta - \frac{d\Psi}{d\rho}\zeta + \tilde{\mu}(\rho,\theta,\zeta)\right) \tag{1}$$

and

$$\boldsymbol{J} = \nabla\rho \times \nabla\left(\frac{dI}{d\rho}\theta + \frac{dF}{d\rho}\zeta - \tilde{\nu}(\rho,\theta,\zeta)\right), \tag{2}$$

respectively. Here $\chi(\rho)$ and $\Psi(\rho)$ denote the toroidal and the poloidal magnetic fluxes inside the flux surfaces, respectively, and $I(\rho)$ and $F(\rho)$ are the total toroidal current inside the flux surface and the total poloidal current outside the flux surface, respectively. $\tilde{\mu}$ and $\tilde{\nu}$ are periodic functions with respect to both θ and ζ. By substituting the contravariant components of $\boldsymbol{B}$ and $\boldsymbol{J}$ into the force balance equation, $\nabla P = \boldsymbol{J} \times \boldsymbol{B}$, and averaging the equation in the ζ direction, we can obtain

$$\langle\sqrt{g}\rangle_\zeta \frac{dP}{d\rho} = -\frac{dF}{d\rho}\langle\sqrt{g}B^\zeta\rangle_\zeta - \frac{d\Psi}{d\rho}\langle\sqrt{g}J^\zeta\rangle_\zeta + \langle\frac{\partial\tilde{\nu}}{\partial\zeta}\frac{\partial\tilde{\mu}}{\partial\theta}\rangle_\zeta - \langle\frac{\partial\tilde{\nu}}{\partial\theta}\frac{\partial\tilde{\mu}}{\partial\zeta}\rangle_\zeta, \tag{3}$$

where $\langle f\rangle_\zeta = \oint f d\zeta / \oint d\zeta$ is used. The periodic functions of $\tilde{\mu}$ and $\tilde{\nu}$ must not enter this equation for the averaged equilibrium equation to be expressed with only metric and surface quantities. Therefore, a constraint must be imposed on the flux coordinates to elimination the last two terms,

$$\tilde{\mu} = \tilde{\mu}(\rho,\theta) \quad or \quad \tilde{\nu} = \tilde{\nu}(\rho,\theta). \tag{4}$$

It can easily be shown that the former condition corresponds to that used in Todoroki's approach[3]. Therefore, this condition is used here. In this case, $\langle\sqrt{g}B^\zeta\rangle_\zeta$ and $\langle\sqrt{g}J^\zeta\rangle_\zeta$ can be obtained with the relations of $B_i = g_{ij}B^j$. Then, we obtain a Grad-Shafranov type equation in flux coordinates with $\tilde{\mu} = \tilde{\mu}(\rho,\theta)$, which can be written as

$$\frac{d\Psi}{d\rho}\left[\frac{\partial}{\partial\rho}\left(G_\perp^{\theta\theta}\frac{d\Psi}{d\rho}\right) - \frac{\partial}{\partial\theta}\left(G_\perp^{\rho\theta}\frac{d\Psi}{d\rho}\right) + \frac{\partial(Fh_\theta)}{\partial\rho} - \frac{\partial(Fh_\rho)}{\partial\theta}\right]$$
$$= -\langle\sqrt{g}\rangle_\zeta\frac{dP}{d\rho} - T\frac{dF}{d\rho}, \tag{5}$$

where $G^{\perp}_{ij} = G_{ij} - G_{i\zeta}G_{j\zeta}/G_{\zeta\zeta}$, $h_i = G_{i\zeta}/G_{\zeta\zeta}$, $T = F/G_{\zeta\zeta} - h_\theta d\Psi/d\rho$ and $G_{ij} \equiv \langle g_{ij}/\sqrt{g}\rangle_\zeta$. It is noted that no ordering or approximation is used in the derivation; therefore, any 3D equilibrium solution satisfies this equation. Thus, if a reduced set of MHD equation is derived in flux coordinates with (4), it must be consistent with a 3D equilibrium. An equation similar to (5) is derived by Pustovitov[4], however, he used an ordering with respect to the magnetic field. More recently, he has obtained a similar equation without making any approximation[5] If we take $\tilde{\mu} = 0$ as the special case of the constraints of (4), which corresponds to the condition that the magnetic field line is expressed as a straight line in the flux coordinates, the averaged equilibrium equation is simplified to

$$\frac{d\Psi}{d\rho}\left[\frac{\partial}{\partial\rho}\left(G_{\theta\theta}\frac{d\Psi}{d\rho} + G_{\theta\zeta}\frac{d\chi}{d\rho}\right) - \frac{\partial}{\partial\theta}\left(G_{\rho\theta}\frac{d\Psi}{d\rho} + G_{\rho\zeta}\frac{d\chi}{d\rho}\right)\right] = -\langle\sqrt{g}\rangle_\zeta\frac{dP}{d\rho} - \frac{dF}{d\rho}\frac{d\chi}{d\rho}, \tag{6}$$

because $\sqrt{g}B^\zeta = d\chi/d\rho$.

3 Reduced MHD equations consistent with 3D equilibrium

A reduced set of MHD equations including resistivity is derived by reducing and averaging the full MHD equations in the flux coordinates which give the Grad-Shafranov type equation. In order to express the magnetic differential operator in an algebraic form, the condition of $\tilde{\mu} = 0$ is employed here. The procedure is similar to the one developed by Strauss[6], however, only the following assumptions are used here: First, the magnetic field is expressed as

$$\boldsymbol{B} = \nabla\chi \times \nabla\theta + \nabla\zeta \times \nabla\Psi \tag{7}$$

with the condition that $\chi_0, \Psi \gg \chi_1$, where the subscripts, 0 and 1 denote the equilibrium and the perturbed parts, respectively, and the variable (except for the metrics) without either of the subscripts includes both of them. Plasma incompressibility and the condition of $v^\zeta \ll v^\rho, v^\theta$ are also assumed to eliminate the compressional modes. Furthermore, the assumption that the pitch number of the equilibrium quantities is much larger than the toroidal mode number of the perturbation is used.

Then, the reduced equations for the poloidal flux, Ψ, the stream function Φ and the plasma pressure P are obtained. These consist of the Ohm's law including resistivity η,

$$\frac{\partial\Psi}{\partial t} = -\langle\frac{\sqrt{g}}{\chi_0'}\boldsymbol{B}\cdot\nabla\rangle_\zeta\Phi + \eta\langle J_\zeta\rangle_\zeta, \tag{8}$$

the vorticity equation

$$-\frac{\langle\rho_m\sqrt{g}\rangle_\zeta}{\chi_0'}\frac{d}{dt}\frac{\langle\sqrt{g}U^\zeta\rangle_\zeta}{\chi_0'} = -\langle\frac{\sqrt{g}}{\chi_0'}\boldsymbol{B}\cdot\nabla\rangle_\zeta\frac{\langle\sqrt{g}J^\zeta\rangle_\zeta}{\chi_0'} + [\langle\Omega\rangle_\zeta, P], \tag{9}$$

and the equation of state

$$\frac{dP}{dt} = 0. \tag{10}$$

Here the vorticity is given by

$$\langle \sqrt{g} U^{\zeta} \rangle_{\zeta} = \frac{\partial \langle v_{\theta} \rangle_{\zeta}}{\partial \rho} - \frac{\partial \langle v_{\rho} \rangle_{\zeta}}{\partial \theta} \tag{11}$$

with the relations $\langle v^{\rho} \rangle_{\zeta} = (1/\chi_0')\partial\Phi/\partial\theta$, $\langle v^{\theta} \rangle_{\zeta} = -(1/\chi_0')\partial\Phi/\partial\rho$ and $\langle v_i \rangle_{\zeta} = \langle g_{ij} \rangle_{\zeta} \langle v^j \rangle_{\zeta}$, and the current density components are given by

$$\langle \sqrt{g} J^{\zeta} \rangle_{\zeta} = \frac{\partial \langle B_{\theta} \rangle_{\zeta}}{\partial \rho} - \frac{\partial \langle B_{\rho} \rangle_{\zeta}}{\partial \theta} \quad \text{and} \quad \langle J_{\zeta} \rangle_{\zeta} = G_{\zeta j} \langle \sqrt{g} J^j \rangle_{\zeta} \tag{12}$$

with the relations $\langle \sqrt{g} B^{\rho} \rangle_{\zeta} = -(1/\chi_0')\partial\Psi/\partial\theta$, $\langle \sqrt{g} B^{\theta} \rangle_{\zeta} = (1/\chi_0')\partial\Psi/\partial\rho$ and $\langle B_i \rangle_{\zeta} = G_{ij} \langle \sqrt{g} B^j \rangle_{\zeta}$. The convective and the magnetic derivatives are expressed as

$$\frac{df}{dt} = \frac{\partial f}{\partial t} - [\Phi, f] \quad \text{and} \quad \langle \frac{\sqrt{g}}{\chi_0'} \boldsymbol{B} \cdot \nabla \rangle_{\zeta} f = \frac{\partial f}{\partial \zeta} + [\Psi, f], \tag{13}$$

respectively, with the Poisson bracket defined by

$$[f, g] = \frac{1}{\chi_0'} \left(\frac{\partial f}{\partial \rho} \frac{\partial g}{\partial \theta} - \frac{\partial f}{\partial \theta} \frac{\partial g}{\partial \rho} \right). \tag{14}$$

The averaged curvature of a field line is given by

$$\langle \Omega \rangle_{\zeta} = \frac{\langle \sqrt{g} \rangle_{\zeta}}{\chi_0'}. \tag{15}$$

In this derivation, the large aspect ratio approximation is not used, therefore, these reduced MHD equations can be applied to a configuration with a small aspect ratio.

As the above assumptions are used in the derivation, the basic properties have to be examined. First, by taking $\partial/\partial t = \Phi = 0$, the equation that

$$\frac{\partial}{\partial \theta} \left(\frac{d\Psi}{d\rho} \frac{\langle \sqrt{g} J^{\zeta} \rangle_{\zeta}}{\chi_0'} + \frac{dP}{d\rho} \frac{\langle \sqrt{g} \rangle_{\zeta}}{\chi_0'} \right) = 0 \tag{16}$$

is obtained. (6) is obtained by setting the constant of integration equal to $-dF/d\rho$. This means that the reduced equations are consistent with 3D equilibrium.

Next, when we defined the volume element, the internal energy, the kinetic energy, and the magnetic energy as

$$d\tau \equiv \langle \sqrt{g} \rangle_{\zeta} d\rho d\theta d\zeta, \tag{17}$$

$$\mathsf{U} \equiv - \int P d\tau, \tag{18}$$

$$\mathsf{K} \equiv \frac{1}{2} \int \langle \rho_m \rangle_{\zeta} \langle v^i \rangle_{\zeta} \langle v_i \rangle_{\zeta} d\tau, \tag{19}$$

$$\mathsf{M} \equiv \frac{1}{2} \int \langle B^i \rangle_{\zeta} \langle B_i \rangle_{\zeta} d\tau, \tag{20}$$

respectively, the energy conservation law is given by

$$\frac{\partial}{\partial t}(\mathsf{K}+\mathsf{M}+\mathsf{U})=-\eta\int\langle\sqrt{g}J^{\zeta}\rangle_{\zeta}\frac{\langle J_{\zeta}\rangle_{\zeta}}{\langle\sqrt{g}\rangle_{\zeta}}d\tau. \tag{21}$$

Finally, the normalized and linearized equations are given by

$$\frac{\partial\Psi}{\partial t}=-\left(\frac{\partial}{\partial\zeta}+\iota\frac{\partial}{\partial\theta}\right)\Phi+\frac{1}{S}\langle J_{\zeta}\rangle_{\zeta}, \tag{22}$$

$$-\frac{\partial}{\partial t}\langle\sqrt{g}U^{\zeta}\rangle_{\zeta}=-\left(\frac{\partial}{\partial\zeta}+\iota\frac{\partial}{\partial\theta}\right)\langle\sqrt{g}J^{\zeta}\rangle_{\zeta}$$
$$-\chi_0[\Psi,\frac{\langle\sqrt{g}J_0^{\zeta}\rangle_{\zeta}}{\chi_0'}]+\frac{\beta_0}{2}\chi_0\left[\langle\Omega\rangle_{\zeta},P\right], \tag{23}$$

and

$$\frac{\partial P}{\partial t}=-\frac{1}{\chi_0'}\frac{dP_0}{d\rho}\frac{\partial\Phi}{\partial\theta}. \tag{24}$$

Here S and β_0 denote the magnetic Reynolds number and the beta value at the magnetic axis. The linearized equation for ideal modes with a time dependence of $\exp(i\omega t)$ can be written in the following form;

$$\begin{aligned}
&-\omega^2\int\frac{1}{\chi_0'}\left\{\langle g_{\theta\theta}\rangle_{\zeta}\left|\frac{\partial\Phi}{\partial\rho}\right|^2-\langle g_{\theta\theta}\rangle_{\zeta}\left(\frac{\partial\Phi^*}{\partial\rho}\frac{\partial\Phi}{\partial\theta}+\frac{\partial\Phi}{\partial\rho}\frac{\partial\Phi^*}{\partial\theta}\right)+\langle g_{\rho\rho}\rangle_{\zeta}\left|\frac{\partial\Phi}{\partial\theta}\right|^2\right\}d\tau\\
&=\int\left\{G_{\theta\theta}\left|\frac{\partial\Psi}{\partial\rho}\right|^2-G_{\rho\theta}\left(\frac{\partial\Psi^*}{\partial\rho}\frac{\partial\Psi}{\partial\theta}+\frac{\partial\Psi}{\partial\rho}\frac{\partial\Psi^*}{\partial\theta}\right)+G_{\rho\rho}\left|\frac{\partial\Psi}{\partial\theta}\right|^2\right.\\
&+\frac{\langle\sqrt{g}J_0^{\zeta}\rangle_{\zeta}}{\chi_0'}\left(\frac{\partial\Phi}{\partial\rho}\frac{\partial^2\Phi^*}{\partial\theta\partial\zeta}+\frac{\partial\Phi^*}{\partial\rho}\frac{\partial^2\Phi}{\partial\theta\partial\zeta}\right)+\iota\left|\frac{\partial\Phi}{\partial\theta}\right|^2\frac{\partial}{\partial\rho}\left(\frac{\langle\sqrt{g}J_0^{\zeta}\rangle_{\zeta}}{\chi_0'}\right)\\
&\left.+\frac{\beta_0}{2}\frac{P_0'}{\chi_0'}\frac{\partial\langle\Omega\rangle_{\zeta}}{\partial\rho}\left|\frac{\partial\Phi}{\partial\theta}\right|^2\right\}d\tau
\end{aligned} \tag{25}$$

The self-adjointness of this equation can easily be confirmed.

4 Numerical Calculation

The ARMS code has been developed to solve (22) $\sim$ (24) by applying the RESORM code[7] to these equations employing the geometrical toroidal angle as ζ. Figure 1 shows the linear growth rates and one of the flow patterns of the resistive and the ideal interchange modes in the equilibria used in [2]. The growth rates of the ideal mode with $m=3/n=2$ given by the ARMS code are compared with those by the CHAFAR code[8]. Good agreement between them is obtained. The resistive modes are also calculated and it is shown that they are unstable below the ideal beta limit.

(a) (b)

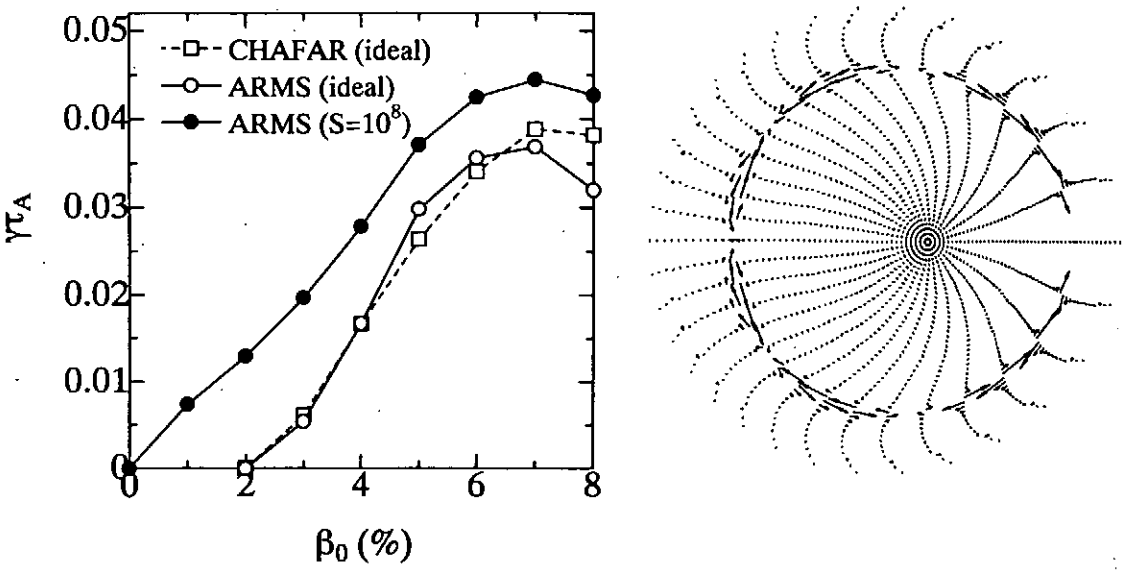

Fig.1 (a) Linear growth rates of ideal and resistive interchange modes normalized by the poloidal Alfven time and (b) the flow pattern at $\beta_0 = 4\%$ and $S = 10^8$.

5 Conclusion

A set of nonlinear reduced MHD equations for resistive modes is derived based on the averaging method without an assumption of large aspect ratio. This set of the equations is consistent with 3D equilibria if the flux coordinates satisfying $\partial\tilde{\mu}/\partial\zeta = 0$ or $\partial\tilde{\nu}/\partial\zeta = 0$ are employed.

It is confirmed that the energy conservation law can be derived and that are self-adjoint the linearized equations for ideal modes. The growth rate of the ideal interchange mode agrees well with the results of the CHAFAR code.

References

[1] S.P.Hirshman, et al., Comp. Phys. Comm. **43**, 143 (1986).

[2] Y.Nakamura et al., J. Comp. Phys. **128**, 43 (1996).

[3] J.Todoroki, J. Phys. Soc. Jpn. **58**, 3979 (1989).

[4] V.D.Pustovitov, Nucl. Fusion **23**, 1079 (1983).

[5] V.D.Pustovitov, Asia Pacific Plasma Theory Conference 1997, 4A-6 (unpublished).

[6] H.R.Strauss, Plasma Phys. **22**, 733 (1980).

[7] K.Ichiguchi et al., Nucl. Fusion **31**, 2073 (1991).

[8] L.Garcia el al., Phys. Fluids **B2**, 2162 (1990).

Nonlinear Electromagnetic Gyrokinetic Equation for Magnetically Confined Plasmas with Large Flow Velocities

Hideo Sugama* and Wendell Horton†

*National Institute for Fusion Science, Toki 509-52, Japan
†Institute for Fusion Studies, The University of Texas at Austin, Austin, Texas 78712, USA

Abstract

A new nonlinear electromagnetic gyrokinetic equation is derived for plasmas with large flow velocities on the order of the ion thermal speed. The gyrokinetic equation derived here is given in the form which is valid for general magnetic geometries including the slab, cylindrical and toroidal configurations.

1. Introduction

A basic kinetic equation for a turbulent plasma is written as

$$\left[\frac{\partial}{\partial t}+\mathbf{v}\cdot\nabla+\frac{e_a}{m_a}\left\{\left(\mathbf{E}+\hat{\mathbf{E}}\right)+\frac{1}{c}\mathbf{v}\times\left(\mathbf{B}+\hat{\mathbf{B}}\right)\right\}\cdot\frac{\partial}{\partial\mathbf{v}}\right](f_a+\hat{f}_a)=C_a(f_a+\hat{f}_a) \quad (1)$$

where $C_a\equiv\sum_b C_{ab}$ denotes a collision term and the distribution function for species a (the electromagnetic fields) is divided into the ensemble average part f_a ($\mathbf{E}=-\nabla\Phi-c^{-1}\partial\mathbf{A}/\partial t, \mathbf{B}=\nabla\times\mathbf{A}$) and the fluctuating part $\hat{f}_a$ ($\hat{\mathbf{E}}=-\nabla\hat{\phi}-c^{-1}\partial\hat{\mathbf{A}}/\partial t, \hat{\mathbf{B}}=\nabla\times\hat{\mathbf{A}}$). Taking an ensemble average $\langle\cdot\rangle_{\rm ens}$ of Eq. (1) gives the kinetic equation for f_a as [1]

$$\left[\frac{\partial}{\partial t}+\mathbf{v}\cdot\nabla+\frac{e_a}{m_a}\left(\mathbf{E}+\frac{1}{c}\mathbf{v}\times\mathbf{B}\right)\cdot\frac{\partial}{\partial\mathbf{v}}\right]f_a=\langle C_a\rangle_{\rm ens}+\mathcal{D}_a \quad (2)$$

where the right-hand side consists of the collision term and the fluctuation-particle interaction term $\mathcal{D}_a$ defined by $\mathcal{D}_a=-(e_a/m_a)\langle(\hat{\mathbf{E}}+\mathbf{v}\times\hat{\mathbf{B}}/c)(\partial\hat{f}_a/\partial\mathbf{v})\rangle_{\rm ens}$. Subtracting Eq. (2) from Eq. (1) gives the equation for the $\hat{f}_a$ as

$$\left[\frac{\partial}{\partial t}+\mathbf{v}\cdot\nabla+\frac{e_a}{m_a}\left(\mathbf{E}+\frac{1}{c}\mathbf{v}\times\mathbf{B}\right)\cdot\frac{\partial}{\partial\mathbf{v}}\right]\hat{f}_a=-\frac{e_a}{m_a}\left(\hat{\mathbf{E}}+\frac{1}{c}\mathbf{v}\times\hat{\mathbf{B}}\right)\cdot\frac{\partial(f_a+\hat{f}_a)}{\partial\mathbf{v}}+C_a-\langle C_a\rangle_{\rm ens}-\mathcal{D}_a. \quad (3)$$

We employ the drift ordering parameter $\delta\equiv\rho_a/L$ [$\rho_a\equiv v_{Ta}/\Omega_a$: the thermal gyroradius, $v_{Ta}\equiv(2T_a/m_a)^{1/2}$: the thermal velocity, $\Omega_a\equiv e_aB/(m_ac)$: the gyrofrequency, L: the equilibrium scale length] to expand the distribution functions and the electromagnetic fields as $f_a=f_{a0}+f_{a1}+f_{a2}+\cdots$, $\hat{f}_a=\hat{f}_{a1}+\hat{f}_{a2}+\cdots$, $\mathbf{E}=\mathbf{E}_0+\mathbf{E}_1+\mathbf{E}_2+\cdots$, $\hat{\mathbf{E}}=\hat{\mathbf{E}}_1+\hat{\mathbf{E}}_2+\cdots$, $\mathbf{B}=\mathbf{B}_0$, and $\hat{\mathbf{B}}=\hat{\mathbf{B}}_1+\hat{\mathbf{B}}_2+\cdots$ where the fluctuating quantities are assumed to be $\mathcal{O}(\delta)$ of the ensemble-averaged values. Note that we can put $\mathbf{B}_1=\mathbf{B}_2=\cdots=0$ since $\mathbf{B}$ is used as the basis for defining the expansion parameter δ.

Here we allow the large mean flow on the order of the thermal velocity v_{Ta} to exist and the lowest-order flow velocity is denoted by $\mathbf{V}_0[=\mathcal{O}(\delta^0)]$. We introduce the phase variables $(\mathbf{x},w,\mu,\xi)$ in which the particle position $\mathbf{x}$ is observed from the laboratory frame while the particle kinetic energy w, the magnetic moment μ, and the gyrophase ξ are defined in terms of the velocity $\mathbf{v}'\equiv\mathbf{v}-\mathbf{V}_0$ in the moving frame as $w=m_a(v')^2/2$, $\mu=m_a(v'_\perp)^2/2B$, and $\mathbf{v}'_\perp/v'_\perp=\mathbf{e}_1\cos\xi+\mathbf{e}_2\sin\xi$ where $(\mathbf{e}_1,\mathbf{e}_2,\mathbf{b}\equiv\mathbf{B}/B)$ are unit vectors which forms a right-handed orthogonal system at each point, and $\mathbf{v}'=v'_\parallel\mathbf{b}+\mathbf{v}'_\perp$ with $v'_\parallel=\mathbf{v}'\cdot\mathbf{b}$.

From the lowest order [$= \mathcal{O}(\delta^{-1})$] of Eq. (2) [or of Eq. (1)], we obtain

$$\mathbf{E}_0 + \mathbf{V}_0 \times \mathbf{B}/c = 0 \tag{4}$$

and $\partial f_{a0}/\partial\xi = 0$. Thus, the lowest-order distribution function f_{a0} is independent of the gyrophase ξ. We also assume that the temporal variation of the ensemble-averaged quantities is so slow that the transport ordering $\partial/\partial t = \mathcal{O}(\delta^2)$ is applicable for them. Then, the ensemble-averaged inductive field $\mathbf{E}^{(A)} \equiv -c\partial\mathbf{A}/\partial t$ is of $\mathcal{O}(\delta^2)$ while the $\mathcal{O}(\delta^0)$ and $\mathcal{O}(\delta)$ electric fields are electrostatic: $\mathbf{E}_0 = -\nabla\Phi_0$, $\mathbf{E}_1 = -\nabla\Phi_1$.

From the next order [$= \mathcal{O}(\delta^0)$] of Eq. (2), we have $[\mathbf{v}\cdot\nabla + (e_a/m_a)\mathbf{E}_1\cdot\partial/\partial\mathbf{v}]f_{a0} - \Omega_a\partial f_{a1}/\partial\xi = C_a(f_{a0})$. Taking a gyrophase average $\overline{\cdots} \equiv \oint\cdots d\xi/2\pi$ of it, we have

$$\overline{\mathcal{L}}_0 f_{a0} \equiv \left[(\mathbf{V}_0 + v_\parallel'\mathbf{b})\cdot\nabla + \overline{\left(\frac{dw}{dt}\right)}_0\frac{\partial}{\partial w} + \overline{\left(\frac{d\mu}{dt}\right)}_0\frac{\partial}{\partial\mu}\right] f_{a0} = C_a(f_{a0}) \tag{5}$$

where the time derivatives $\overline{(dw/dt)}_0$ and $\overline{(d\mu/dt)}_0$ along the lowest-order guiding center orbit are given by $\overline{(dw/dt)}_0 = -m_a\mathbf{V}_0\cdot\nabla\mathbf{V}_0\cdot\mathbf{b}v_\parallel' + e_a\mathbf{E}_1\cdot\mathbf{b}v_\parallel' - m_a(v_\parallel')^2\mathbf{b}\cdot\nabla\mathbf{V}_0\cdot\mathbf{b} - \frac{1}{2}m_a(v_\perp')^2(\nabla\cdot\mathbf{V}_0 - \mathbf{b}\cdot\nabla\mathbf{V}_0\cdot\mathbf{b})$ and $\overline{(d\mu/dt)}_0 = -\mu\mathbf{V}_0\cdot\nabla\ln B - \mu(\nabla\cdot\mathbf{V}_0 - \mathbf{b}\cdot\nabla\mathbf{V}_0\cdot\mathbf{b})$, respectively.

2. Nonlinear electromagnetic gyrokinetic equation for general geometry

In the present work, we follow the ballooning representation for the system with large sheared flows [2] and assume that any fluctuating field $\hat{F}$ is written as a superposition of components in the WKB (or eikonal) form:

$$\hat{F}(t,\mathbf{x},w,\mu,\xi) = \sum_{\mathbf{k}_\perp}\hat{F}(t,\mathbf{x},w,\mu,\xi;\mathbf{k}_\perp)\exp[iS_{\mathbf{k}_\perp}(\mathbf{x},t)] \tag{6}$$

where the eikonal $S_{\mathbf{k}_\perp}(\mathbf{x},t)$ represents the rapid variation in the directions perpendicular to the magnetic field lines. The wavenumber vector is given by $\mathbf{k}_\perp = \nabla S_{\mathbf{k}_\perp}$. The eikonal $S_{\mathbf{k}_\perp}(\mathbf{x},t)$ also contains the rapid Doppler shift frequency due to the large flow, which is given by $-\partial S_{\mathbf{k}_\perp}/\partial t = \mathbf{k}_\perp\cdot\mathbf{V}_0$. The gyrokinetic ordering employed here for the turbulent fluctuations is written in terms of δ as $\hat{f}_a/f_a \sim e_a\hat{\phi}/T_a \sim e_a v_{Ta}|\hat{\mathbf{A}}|/(cT_a) \sim k_\parallel/k_\perp \sim (\omega - \mathbf{k}\cdot\mathbf{V}_0)/\Omega_a \sim \delta$ where $(\omega - \mathbf{k}\cdot\mathbf{V}_0)$ denotes the characteristic frequency observed in the moving frame. The characteristic parallel and perpendicular wavenumbers are given by $k_\parallel \sim L^{-1}$ and $k_\perp \sim \rho_a^{-1}$, respectively.

The lowest-order part of Eq.(3) in δ is written for the fluctuations in the WKB form of Eq.(6) as

$$\begin{aligned}\left(i\mathbf{k}_\perp\cdot\mathbf{v}' - \Omega_a\frac{\partial}{\partial\xi}\right)\hat{f}_{a1}(\mathbf{k}_\perp) &\equiv -\Omega_a e^{-i\mathbf{k}_\perp\cdot\boldsymbol{\rho}_a}\frac{\partial}{\partial\xi}\left[e^{i\mathbf{k}_\perp\cdot\boldsymbol{\rho}_a}\hat{f}_{a1}(\mathbf{k}_\perp)\right] \\ = \; -ie_a(\mathbf{k}_\perp\cdot\mathbf{v}_\perp')&\left[\left(\hat{\phi}(\mathbf{k}_\perp) - \frac{1}{c}\mathbf{V}_0\cdot\hat{\mathbf{A}}(\mathbf{k}_\perp)\right)\left(\frac{\partial}{\partial w} + \frac{\partial}{B\partial\mu}\right) - \frac{v_\parallel'}{c}\hat{A}_\parallel(\mathbf{k}_\perp)\frac{\partial}{B\partial\mu}\right] f_{a0}\end{aligned} \tag{7}$$

where $\boldsymbol{\rho}_a \equiv (\mathbf{b}\times\mathbf{v}')/\Omega_a$ represents the gyroradius. Integrating Eq. (7) in ξ, we have

$$\hat{f}_{a1}(\mathbf{k}_\perp) = e_a\left[\left(\hat{\phi}(\mathbf{k}_\perp) - \frac{1}{c}\mathbf{V}_0\cdot\hat{\mathbf{A}}(\mathbf{k}_\perp)\right)\left(\frac{\partial}{\partial w} + \frac{\partial}{B\partial\mu}\right) - \frac{v_\parallel'}{c}\hat{A}_\parallel(\mathbf{k}_\perp)\frac{\partial}{B\partial\mu}\right] f_{a0} + \hat{g}_a(\mathbf{k}_\perp)e^{-i\mathbf{k}_\perp\cdot\boldsymbol{\rho}_a} \tag{8}$$

where $\hat{g}_a(\mathbf{k}_\perp)$ is independent of ξ.

From the $\mathcal{O}(\delta)$ part of Eq.(3), we have the equation for the second-order fluctuating function $\hat{f}_{a2}$ as

$$
\begin{aligned}
& -\Omega_a e^{-i\mathbf{k}_\perp\cdot\boldsymbol{\rho}_a}\frac{\partial}{\partial\xi}\left[e^{i\mathbf{k}_\perp\cdot\boldsymbol{\rho}_a}\hat{f}_{a2}(\mathbf{k}_\perp)\right] \\
= & -\left(\frac{\partial}{\partial t}+\mathbf{v}\cdot\nabla+\frac{e_a}{m_a}\mathbf{E}_1\cdot\frac{\partial}{\partial\mathbf{v}}\right)\hat{f}_{a1}(\mathbf{k}_\perp) \\
& -\frac{e_a}{m_a}\left(\hat{\mathbf{E}}_1(\mathbf{k}_\perp)+\frac{1}{c}\mathbf{v}\times\hat{\mathbf{B}}_1(\mathbf{k}_\perp)\right)\frac{\partial f_{a1}}{\partial\mathbf{v}}-\frac{e_a}{m_a}\left(\hat{\mathbf{E}}_2(\mathbf{k}_\perp)+\frac{1}{c}\mathbf{v}\times\hat{\mathbf{B}}_2(\mathbf{k}_\perp)\right)\frac{\partial f_{a0}}{\partial\mathbf{v}} \\
& -\frac{e_a}{m_a}\sum_{\mathbf{k}'_\perp+\mathbf{k}''_\perp=\mathbf{k}_\perp}\left(\hat{\mathbf{E}}_1(\mathbf{k}'_\perp)+\frac{1}{c}\mathbf{v}\times\hat{\mathbf{B}}_1(\mathbf{k}'_\perp)\right)\frac{\partial\hat{f}_{a1}(\mathbf{k}''_\perp)}{\partial\mathbf{v}}+C_a^L[\hat{f}_{a1}(\mathbf{k}_\perp)] \qquad (9)
\end{aligned}
$$

where $\hat{\mathbf{E}}_1(\mathbf{k}_\perp)=-i\mathbf{k}_\perp\hat{\phi}(\mathbf{k}_\perp)$, $\hat{\mathbf{B}}_1(\mathbf{k}_\perp)=i\mathbf{k}_\perp\times\hat{\mathbf{A}}(\mathbf{k}_\perp)$, $\hat{\mathbf{E}}_2(\mathbf{k}_\perp)=-\nabla\hat{\phi}(\mathbf{k}_\perp)-c^{-1}\partial\hat{\mathbf{A}}(\mathbf{k}_\perp)/\partial t$, and $\hat{\mathbf{B}}_2(\mathbf{k}_\perp)=\nabla\times\hat{\mathbf{A}}(\mathbf{k}_\perp)$. From the solvability condition of Eq. (9) given by $\oint d\xi\ \exp(i\mathbf{k}_\perp\cdot\boldsymbol{\rho}_a)$ [RHS of Eq. (9)] $=0$ with Eqs. (5) and (8), we obtain the nonlinear electromagnetic gyrokinetic equation after lengthy calculation as

$$
\begin{aligned}
& \left(\frac{\partial}{\partial t}+\overline{\mathcal{L}}_0+i\mathbf{k}_\perp\cdot\mathbf{v}_{da}\right)\hat{h}_a(\mathbf{k}_\perp)-\oint\frac{d\xi}{2\pi}e^{i\mathbf{k}_\perp\cdot\boldsymbol{\rho}_a}C_a^L\left[\hat{f}_a(\mathbf{k}_\perp)\right] \\
= & \ e_a\hat{\psi}_a(\mathbf{k}_\perp)\frac{i(\mathbf{b}\times\mathbf{k}_\perp)}{m_a\Omega_a}\cdot\left[-\nabla+\left\{m_a\mathbf{V}_0\cdot\nabla\mathbf{V}_0+m_a v'_\parallel[\mathbf{b}\cdot(\nabla\mathbf{V}_0)+(\nabla\mathbf{V}_0)\cdot\mathbf{b}]+e_a\nabla\Phi_1\right\}\frac{\partial}{\partial w}\right]f_{a0} \\
& -\left[\left\{\frac{\partial}{\partial t}+\overline{\mathcal{L}}_0-v'_\parallel\mathbf{b}\cdot\nabla\right\}(e_a\hat{\psi}_a(\mathbf{k}_\perp))\right]\frac{\partial f_{a0}}{\partial w}-\frac{\partial(e_a\hat{\psi}_a(\mathbf{k}_\perp))}{\partial w}v'_\parallel\mathbf{b}\cdot\nabla f_{a0} \\
& -e_a\gamma_a\frac{\partial\hat{\psi}_a(\mathbf{k}_\perp)}{\partial\gamma_a}\left(\nabla\cdot\mathbf{V}_0-\mathbf{b}\cdot\nabla\mathbf{V}_0\cdot\mathbf{b}+\frac{\mathbf{V}_0\cdot\nabla B}{B}\right)\left(\frac{\partial}{\partial w}+\frac{\partial}{B\partial\mu}\right)f_{a0} \\
& -e_a\hat{\psi}_a(\mathbf{k}_\perp)\overline{\mathcal{L}}_0\frac{\partial f_{a0}}{\partial w}-J_0(\gamma_a)\frac{e_a}{c}v'_\parallel\hat{A}_\parallel(\mathbf{k}_\perp)\frac{\partial}{\partial w}\overline{\mathcal{L}}_0 f_{a0} \\
& -J_1(\gamma_a)e_a\frac{v'_\perp}{c}\frac{\hat{B}_\parallel(\mathbf{k}_\perp)}{k_\perp}\left(\frac{\partial}{\partial w}+\frac{\partial}{B\partial\mu}\right)\overline{\mathcal{L}}_0 f_{a0}+\frac{c}{B}\sum_{\mathbf{k}'_\perp+\mathbf{k}''_\perp=\mathbf{k}_\perp}[\mathbf{b}\cdot(\mathbf{k}'_\perp\times\mathbf{k}''_\perp)]\,\hat{\psi}_a(\mathbf{k}'_\perp)\hat{h}_a(\mathbf{k}''_\perp) \qquad (10)
\end{aligned}
$$

where $\hat{h}_a(\mathbf{k}_\perp)$ is independent of ξ and is related to $\hat{f}_a(\mathbf{k}_\perp)$ by

$$
\begin{aligned}
& \hat{f}_a(\mathbf{k}_\perp)=e_a\left(\hat{\phi}(\mathbf{k}_\perp)-\frac{1}{c}\mathbf{V}_0\cdot\hat{\mathbf{A}}(\mathbf{k}_\perp)\right)\frac{\partial f_{a0}}{\partial w} \\
& +e_a\left[\left(\hat{\phi}(\mathbf{k}_\perp)-\frac{1}{c}\mathbf{V}_0\cdot\hat{\mathbf{A}}(\mathbf{k}_\perp)-\frac{1}{c}v'_\parallel\hat{A}_\parallel(\mathbf{k}_\perp)\right)-e^{-i\mathbf{k}_\perp\cdot\boldsymbol{\rho}_a}\hat{\psi}_a(\mathbf{k}_\perp)\right]\frac{\partial f_{a0}}{B\partial\mu}+\hat{h}_a(\mathbf{k}_\perp)e^{-i\mathbf{k}_\perp\cdot\boldsymbol{\rho}_a}. \qquad (11)
\end{aligned}
$$

In Eqs. (10) and (11), $\hat{\psi}_a(\mathbf{k}_\perp)$ is defined by

$$
\begin{aligned}
\hat{\psi}_a(\mathbf{k}_\perp) &= \overline{e^{i\mathbf{k}_\perp\cdot\boldsymbol{\rho}_a}\left[\hat{\phi}(\mathbf{k}_\perp)-\frac{1}{c}(\mathbf{V}_0+\mathbf{v}')\cdot\hat{\mathbf{A}}(\mathbf{k}_\perp)\right]} \\
&= J_0(\gamma_a)\left(\hat{\phi}(\mathbf{k}_\perp)-\frac{\mathbf{V}_0}{c}\cdot\hat{\mathbf{A}}(\mathbf{k}_\perp)-\frac{v'_\parallel}{c}\hat{A}_\parallel(\mathbf{k}_\perp)\right)+J_1(\gamma_a)\frac{v'_\perp}{c}\frac{\hat{B}_\parallel(\mathbf{k}_\perp)}{k_\perp} \qquad (12)
\end{aligned}
$$

where $\hat{A}_\parallel(\mathbf{k}_\perp)\equiv\mathbf{b}\cdot\hat{\mathbf{A}}(\mathbf{k}_\perp)$ and $\hat{B}_\parallel(\mathbf{k}_\perp)\equiv i\mathbf{b}\cdot\mathbf{k}_\perp\times\hat{\mathbf{A}}(\mathbf{k}_\perp)$. Here J_0 and J_1 are the zero-th and first-order Bessel functions of $\gamma_a\equiv k_\perp v'_\perp/\Omega_a$. In Eq. (10), the first-order guiding center drift velocity is defined by $\mathbf{v}_{da}\equiv(c\mu/e_aB)(\nabla\times\mathbf{B})\cdot\mathbf{bb}+(c/e_aB)\mathbf{b}\times[\mu\nabla B+m_a(v'_\parallel)^2\mathbf{b}\cdot\nabla\mathbf{b}+e_a\nabla\Phi_1+m_a\mathbf{V}_0\cdot\nabla\mathbf{V}_0+m_a v'_\parallel\mathbf{b}\cdot\nabla\mathbf{V}_0+m_a v'_\parallel\mathbf{V}_0\cdot\nabla\mathbf{b}]$.

Representation of the gyrokinetic equation in the real x-space is useful. Following Eq. (6), multiplying Eq. (11) by $\exp[iS_{\mathbf{k}_\perp}(\mathbf{x},t)]$ and summing up with respect to $\mathbf{k}_\perp$, we have

$$\begin{aligned}\hat{f}_a(\mathbf{x}) &= e_a\left(\hat{\phi}(\mathbf{x})-\frac{1}{c}\mathbf{V}_0\cdot\hat{\mathbf{A}}(\mathbf{x})\right)\frac{\partial f_{a0}}{\partial w}\\ &\quad+e_a\left[\left\{\hat{\phi}(\mathbf{x})-\frac{1}{c}(\mathbf{V}_0+v_\parallel'\mathbf{b})\cdot\hat{\mathbf{A}}(\mathbf{x})\right\}-\hat{\psi}_a(\mathbf{X})\right]\frac{\partial f_{a0}}{B\partial\mu}+\hat{h}_a(\mathbf{X})\end{aligned}\tag{13}$$

where $\mathbf{X}\equiv\mathbf{x}-\boldsymbol{\rho}_a$ denotes the position of the guiding center. In deriving Eq. (13), we have used $S_{\mathbf{k}_\perp}(\mathbf{x},t)\simeq S_{\mathbf{k}_\perp}(\mathbf{X},t)+i\mathbf{k}_\perp\cdot\boldsymbol{\rho}_a$, $\hat{h}_a(\mathbf{X})=\sum_{\mathbf{k}_\perp}\hat{h}_a(\mathbf{k}_\perp)\exp[iS_{\mathbf{k}_\perp}(\mathbf{X})]$, and $\hat{\psi}_a(\mathbf{X})=\sum_{\mathbf{k}_\perp}\hat{\psi}_a(\mathbf{k}_\perp)\exp[iS_{\mathbf{k}_\perp}(\mathbf{X})]=\langle\hat{\phi}(\mathbf{X}+\boldsymbol{\rho}_a)-\frac{1}{c}(\mathbf{V}_0+\mathbf{v}')\cdot\hat{\mathbf{A}}(\mathbf{X}+\boldsymbol{\rho}_a)\rangle_{\mathbf{X}}$ where $\langle\cdot\rangle_{\mathbf{X}}$ represents the gyrophase average with $\mathbf{X}$ fixed. Multiplying the gyrokinetic equation (10) in the $\mathbf{k}_\perp$-space by $\exp[iS_{\mathbf{k}_\perp}(\mathbf{X})]$ and summing up with respect to $\mathbf{k}_\perp$ gives the gyrokinetic equation for the nonadiabatic fluctuating distribution function $\hat{h}_a(\mathbf{X},w,\mu)$ as

$$\begin{aligned}&\left[\frac{\partial}{\partial t}+\overline{\mathcal{L}}_0+\left(\mathbf{v}_{da}-\frac{c}{B}\nabla\hat{\psi}_a(\mathbf{X})\times\mathbf{b}\right)\cdot\nabla\right]\hat{h}_a(\mathbf{X})-\left\langle C_a^L\left[\hat{f}_a(\mathbf{X}+\boldsymbol{\rho}_a)\right]\right\rangle_{\mathbf{X}}\\ &=\frac{c}{B}\nabla\hat{\psi}_a(\mathbf{X})\times\mathbf{b}\cdot\left[\nabla-\left\{m_a\mathbf{V}_0\cdot\nabla\mathbf{V}_0+m_av_\parallel'[\mathbf{b}\cdot(\nabla\mathbf{V}_0)+(\nabla\mathbf{V}_0)\cdot\mathbf{b}]+e_a\nabla\Phi_1\right\}\frac{\partial}{\partial w}\right]f_{a0}\\ &\quad-e_a\left[\left(\frac{\partial}{\partial t}+\overline{\mathcal{L}}_0-v_\parallel'\mathbf{b}\cdot\nabla\right)\hat{\psi}_a(\mathbf{X})\right]\frac{\partial f_{a0}}{\partial w}-e_a\frac{\partial\hat{\psi}_a(\mathbf{X})}{\partial w}v_\parallel'\mathbf{b}\cdot\nabla f_{a0}\\ &\quad-2\mu\frac{\partial\hat{\psi}_a(\mathbf{X})}{\partial\mu}\left(\nabla\cdot\mathbf{V}_0-\mathbf{b}\cdot\nabla\mathbf{V}_0\cdot\mathbf{b}+\frac{\mathbf{V}_0\cdot\nabla B}{B}\right)\left(\frac{\partial}{\partial w}+\frac{\partial}{B\partial\mu}\right)f_{a0}\\ &\quad-e_a\hat{\psi}_a(\mathbf{X})\overline{\mathcal{L}}_0\frac{\partial f_{a0}}{\partial w}-\frac{e_a}{c}v_\parallel'\left\langle\hat{A}_\parallel(\mathbf{X}+\boldsymbol{\rho}_a)\right\rangle_{\mathbf{X}}\frac{\partial}{\partial w}\overline{\mathcal{L}}_0f_{a0}\\ &\quad-\frac{e_a}{c}\left\langle\mathbf{v}_\perp'\cdot\hat{\mathbf{A}}(\mathbf{X}+\boldsymbol{\rho}_a)\right\rangle_{\mathbf{X}}\left(\frac{\partial}{\partial w}+\frac{\partial}{B\partial\mu}\right)\overline{\mathcal{L}}_0f_{a0}\end{aligned}\tag{14}$$

where the spatial gradient is taken with respect to $\mathbf{X}$ as $\nabla=\partial/\partial\mathbf{X}$. We should note in Eq. (14) that differences of equilibrium quantities' values at the particle's position $\mathbf{x}$ from those at the guiding center's position $\mathbf{X}$ are neglected as $\mathcal{O}(\delta)$ smaller [$\mathbf{B}(\mathbf{x})\simeq\mathbf{B}(\mathbf{X})$, $\mathbf{V}_0(\mathbf{x})\simeq\mathbf{V}_0(\mathbf{X})$, and $f_{a0}(\mathbf{x})\simeq f_{a0}(\mathbf{X})$] although that is not the case for the fluctuating quantities $\hat{\phi}$, $\hat{\mathbf{A}}$, and $\hat{h}_a$ because of small perpendicular wavelengths of $\mathcal{O}(\rho_a)$.

2. Cylindrical and slab configurations

Let us consider a cylindrical configuration in which the magnetic field and the mean flow velocity are given by $\mathbf{B}=B_\theta(r)\hat{\boldsymbol{\theta}}+B_z(r)\hat{\mathbf{z}}$ and $\mathbf{V}_0=V_\theta(r)\hat{\boldsymbol{\theta}}+V_z(r)\hat{\mathbf{z}}$, respectively, where the cylindrical coordinates (r,θ,z) are used and the unit vectors in the r, θ, and z directions are denoted by $\hat{\mathbf{r}}$, $\hat{\boldsymbol{\theta}}$, and $\hat{\mathbf{z}}$, respectively. Surfaces defined by $r=$ const are regarded as magnetic flux surfaces. Here, $B_\theta(r)$, $B_z(r)$, $V_\theta(r)$, and $V_z(r)$ are flux surface functions independent of θ and z. The lowest-order electric field is given from Eq. (4) as $\mathbf{E}_0=-[d\Phi_0(r)/dr]\hat{\mathbf{r}}=c^{-1}[V_\theta(r)B_z(r)-V_z(r)B_\theta(r)]\hat{\mathbf{r}}$. The first-order electrostatic potential is also assumed to be a surface function as $\Phi_1=\Phi_1(r)$. We easily find that $\mathbf{V}_0\cdot\nabla B=\nabla\cdot\mathbf{V}_0=\mathbf{b}\cdot\nabla\mathbf{V}_0\cdot\mathbf{b}=\mathbf{V}_0\cdot\nabla\mathbf{V}_0\cdot\mathbf{b}=0$ from which we have $\overline{(dw/dt)}_0=\overline{(d\mu/dt)}_0=0$ and $\overline{\mathcal{L}}_0=(\mathbf{V}_0+v_\parallel'\mathbf{b})\cdot\nabla$. Assuming the lowest-order distribution function to be homogeneous in the θ and z directions and using Eq. (5), we obtain $\mathbf{V}_0\cdot\nabla f_{a0}=\mathbf{b}\cdot\nabla f_{a0}=C_a(f_{a0})=0$ which requires f_{a0} to be the Maxwellian distribution function $f_{a0}=n_a(m_a/2\pi T_a)^{3/2}\exp(-w/T_a)$ with the density $n_a=n_a(r)$ and the temperature $T_a=T_a(r)$. Thus we have $\partial f_{a0}/\partial\mu=0$.

For the cylindrical configuration, the gyrokinetic equation (14) is simplified as

$$\left[\frac{\partial}{\partial t}+\left(\mathbf{V}_0+v_{\parallel}'\mathbf{b}+\mathbf{v}_{da}-\frac{c}{B}\nabla\hat{\psi}(\mathbf{X})\times\mathbf{b}\right)\cdot\nabla\right]\hat{h}_a(\mathbf{X})-\left\langle C_a^L\left[\hat{f}_a(\mathbf{X}+\boldsymbol{\rho}_a)\right]\right\rangle_{\mathbf{X}}$$
$$=\frac{c}{B}\nabla\hat{\psi}_a(\mathbf{X})\times\mathbf{b}\cdot\left[\nabla+\frac{e_a}{T_a}\nabla\Phi_1+\frac{m_a}{T_a}\mathbf{V}_0\cdot\nabla\mathbf{V}_0+\frac{m_a v_{\parallel}'}{T_a}\{\mathbf{b}\cdot(\nabla\mathbf{V}_0)+(\nabla\mathbf{V}_0)\cdot\mathbf{b}\}\right]f_{a0}$$
$$+\frac{e_a}{T_a}\left[\left(\frac{\partial}{\partial t}+\mathbf{V}_0\cdot\nabla\right)\hat{\psi}_a(\mathbf{X})\right]f_{a0} \tag{15}$$

where $\hat{h}_a(\mathbf{X})$ is related to $\hat{f}_a(\mathbf{x}=\mathbf{X}+\boldsymbol{\rho}_a)$ by $\hat{f}_a(\mathbf{x})=-(e_a/T_a)[\hat{\phi}(\mathbf{x})-\mathbf{V}_0\cdot\hat{\mathbf{A}}(\mathbf{x})/c]f_{a0}+\hat{h}_a(\mathbf{X})$.

In the similar way to the case of the cylindrical configuration, we can consider a slab configuration in which the magnetic field and the mean flow velocity are given by $\mathbf{B}=B_y(x)\hat{\mathbf{y}}+B_z(x)\hat{\mathbf{z}}$ and $\mathbf{V}_0=V_y(x)\hat{\mathbf{y}}+V_z(x)\hat{\mathbf{z}}$, respectively, where the Cartesian coordinates (x,y,z) are used and the unit vectors in the x, y, and z directions are denoted by $\hat{\mathbf{x}}$, $\hat{\mathbf{y}}$, and $\hat{\mathbf{z}}$, respectively. Planes defined by $x=$ const are regarded as magnetic flux surfaces. Here, $B_y(x)$, $B_z(x)$,$V_y(x)$, and $V_z(x)$ are flux surface functions independent of y and z. The lowest-order electric field is given from Eqs. (4) as $\mathbf{E}_0=-[d\Phi_0(x)/dx]\hat{\mathbf{x}}=c^{-1}[V_y(x)B_z(x)-V_z(x)B_y(x)]\hat{\mathbf{x}}$. The first-order electrostatic potential is also assumed to be a surface function as $\Phi_1=\Phi_1(x)$. Then, for the slab configuration, $\mathbf{V}_0\cdot\nabla f_{a0}=\mathbf{b}\cdot\nabla f_{a0}=C_a(f_{a0})=0$ is still valid and f_{a0} is the Maxwellian distribution function $f_{a0}=n_a(m_a/2\pi T_a)^{3/2}\exp(-w/T_a)$ with the density $n_a=n_a(x)$ and the temperature $T_a=T_a(x)$. Thus, we find that the gyrokinetic equation for the slab configuration is also given by Eq. (15) with $\mathbf{V}_0\cdot\nabla\mathbf{V}_0=\mathbf{b}\cdot\nabla\mathbf{V}_0=0$.

3. Axisymmetric toroidal configuration

In this section, we consider an axisymmetric system, for which the magnetic field is given by $\mathbf{B}=I(\Psi)\nabla\zeta+\nabla\zeta\times\nabla\Psi$ where ζ is the toroidal angle, Ψ represents the poloidal flux, and $I(\Psi)=RB_T$ denotes the covariant toroidal component of the magnetic field. Hinton and Wong [3] showed that, in the axisymmetric systems, the poloidal flow decays in a few transit or collision times and that the lowest-order flow velocity $\mathbf{V}_0$ is in the toroidal direction and is derived from $\mathbf{E}_0+\mathbf{V}_0\times\mathbf{B}/c=0$ as $\mathbf{V}_0=V_0\hat{\boldsymbol{\zeta}}$ with $V_0=RV^{\zeta}=-Rc\partial\Phi_0(\Psi)/\partial\Psi$ where the lowest-order electrostatic potential $\Phi_0(\Psi)$ is a flux surface function and $\mathbf{E}_0\equiv-\nabla\Phi_0\equiv-(\partial\Phi_0/\partial\Psi)\nabla\Psi$. We should note that the toroidal angular velocity $V^{\zeta}=-c\partial\Phi_0/\partial\Psi$ is directly given by the radial electric field and is also a flux-surface quantity. Then, we easily find that $\mathbf{V}_0\cdot\nabla B=\nabla\cdot\mathbf{V}_0=\mathbf{b}\cdot\nabla\mathbf{V}_0\cdot\mathbf{b}=0$ and $\mathbf{V}_0\cdot\nabla\mathbf{b}=\mathbf{b}\cdot\nabla\mathbf{V}_0$. Here it is convenient to use independent phase space variables $(\mathbf{x},\varepsilon,\mu,\xi)$ instead of $(\mathbf{x},w,\mu,\xi)$ where the new energy variable ε is defined by $\varepsilon=\frac{1}{2}m_a(v')^2+\Xi_a$, $\quad\Xi_a\equiv e_a\tilde{\Phi}_1-\frac{1}{2}m_aV_0^2$. Here, $\tilde{\Phi}_1\equiv\Phi_1-\langle\Phi_1\rangle[=\mathcal{O}(\delta)]$ is the poloidal-angle-dependent part of the electrostatic potential and $-\frac{1}{2}m_aV_0^2$ represents the potential for the centrifugal force due to the toroidal rotation. The magnetic flux surface average is denoted by $\overline{\langle\cdot\rangle}$. It is shown that ε and μ are conserved along the lowest-order guiding center orbit: $\overline{(d\varepsilon/dt)}_0=\overline{(d\mu/dt)}_0=0$. Thus we have $\overline{\mathcal{L}}_0=(\mathbf{V}_0+v_{\parallel}\mathbf{b})\cdot\nabla$ with the independent variables $(\mathbf{x},\varepsilon,\mu,\xi)$. The lowest-order distribution function f_{a0} is written in the Maxwellian form $f_{a0}=n_a(m_a/2\pi T_a)^{3/2}\exp[-m_a(v')^2/2T_a]=N_a(m_a/2\pi T_a)^{3/2}\exp(-\varepsilon/T_a)$ which satisfies $\overline{\mathcal{L}}_0f_{a0}=C_a(f_{a0})=0$. Here the temperature $T_a=T_a(\Psi)$ and $N_a=N_a(\Psi)$ are flux-surface functions although generally the density n_a depends on the poloidal angle θ through Ξ_a and is given by $n_a=N_a\exp(-\Xi_a/T_a)$. The charge neutrality $\sum_a e_an_a=0$ imposes the constraints on $\tilde{\Phi}_1$ and N_a.

Using the independent phase-space variables $(\mathbf{x}, \varepsilon, \mu, \xi)$, we find that, for the axisymmetric configuration, the gyrokinetic equation (14) simplifies to

$$\begin{aligned}
&\left[\frac{\partial}{\partial t} + \left(\mathbf{V}_0 + v_\parallel' \mathbf{b} + \mathbf{v}_{da} - \frac{c}{B}\nabla\hat{\psi}(\mathbf{X}) \times \mathbf{b}\right) \cdot \nabla\right] \hat{h}_a(\mathbf{X}) - \left\langle C_a^L \left[\hat{f}_a(\mathbf{X} + \boldsymbol{\rho}_a)\right]\right\rangle_{\mathbf{X}} \\
= \;& \frac{c}{B}\nabla\hat{\psi}_a(\mathbf{X}) \times \mathbf{b} \cdot \left[\nabla + \left\{\frac{e_a}{T_a}\frac{\partial\langle\Phi_1\rangle}{\partial\Psi} + \frac{m_a}{T_a}\left(R^2 V^\zeta + \frac{I}{B}v_\parallel'\right)\frac{\partial V^\zeta}{\partial\Psi}\right\}\nabla\Psi\right] f_{a0} \\
& + \frac{e_a}{T_a}\left[\left(\frac{\partial}{\partial t} + \mathbf{V}_0 \cdot \nabla\right)\hat{\psi}_a(\mathbf{X})\right] f_{a0} \\
= \;& f_{a0}\left[\hat{w}_{a1}(\mathbf{X}) X_{a1}^A + \hat{w}_{a2}(\mathbf{X}) X_{a2}^A + \hat{w}_{aV}(\mathbf{X}) X_{aV}^A + \hat{w}_{aT}(\mathbf{X}) X_{aT}^A\right]. \qquad (16)
\end{aligned}$$

where the nonadiabatic part of the fluctuation distribution function $\hat{h}_a(\mathbf{X})$ is related to $\hat{f}_{a1}(\mathbf{x})$ by $\hat{f}_a(\mathbf{x}) = -(e_a/T_a)[\hat{\phi}(\mathbf{x}) - \mathbf{V}_0 \cdot \hat{\mathbf{A}}(\mathbf{x})/c] f_{a0} + \hat{h}_a(\mathbf{X})$. In the right-hand side of (16), we have defined the thermodynamic forces $(X_{a1}^A, X_{a2}^A, X_{aV}^A, X_{aT}^A)$ as $X_{a1}^A \equiv -\partial \ln(N_a T_a)/\partial\Psi - (e_a/T_a)\partial\langle\Phi_1\rangle/\partial\Psi$, $X_{a2}^A \equiv -\partial \ln T_a/\partial\Psi$, $X_V^A \equiv -T_a^{-1}\partial V^\zeta/\partial\Psi = (c/T_a)\partial^2\Phi_0/\partial\Psi^2$, $X_{aT}^A \equiv 1/T_a$ and the fluctuating functions $(\hat{w}_{a1}, \hat{w}_{a2}, \hat{w}_{aV}, \hat{w}_{aT})$ as

$$\begin{aligned}
\hat{w}_{a1}(\mathbf{X}) &\equiv -\frac{c}{B}\nabla\hat{\psi}_a(\mathbf{X}) \times \mathbf{b} \cdot \nabla\Psi, \qquad \hat{w}_{a2}(\mathbf{X}) \equiv \left(\frac{\varepsilon}{T_a} - \frac{5}{2}\right)\hat{w}_{a1}(\mathbf{X}) \\
\hat{w}_{aV}(\mathbf{X}) &\equiv \left\langle -\frac{c}{B}\nabla\left(\hat{\phi}(\mathbf{x}) - \frac{1}{c}(\mathbf{V}_0 + \mathbf{v}') \cdot \hat{\mathbf{A}}(\mathbf{x})\right) \times \mathbf{b} \cdot \nabla\Psi \, m_a(\mathbf{V}_0 + \mathbf{v}') \cdot (R\hat{\boldsymbol{\zeta}})\right\rangle_{\mathbf{X}} \\
\hat{w}_{aT}(\mathbf{X}) &\equiv e_a\left\langle\left(\frac{\partial}{\partial t} + \mathbf{V}_0(\mathbf{x}) \cdot \frac{\partial}{\partial \mathbf{x}}\right)\left(\hat{\phi}(\mathbf{x}) - \frac{1}{c}(\mathbf{V}_0 + \mathbf{v}') \cdot \hat{\mathbf{A}}(\mathbf{x})\right)\right\rangle_{\mathbf{X}}. \qquad (17)
\end{aligned}$$

4. Conclusions

In this work, we have presented the nonlinear electromagnetic gyrokinetic equation for plasmas with general magnetic geometries and large flow velocities on the order of the ion thermal speed. In the derivation, we have used the recursive formulation to give the relation of the perturbed distribution function to the equilibrium distribution and the electromagnetic fluctuations. The reduced forms of the gyrokinetic equation for the slab, cylindrical, and toroidal configurations were obtained from the general one [see Eqs. (10), (14), (15), and (16)].

Acknowledgments

The author (HS) thanks Professor M. Okamoto for his encouragement of this work.

References

[1] H. Sugama and W. Horton, Phys. Plasmas **4**, 405 (1997).
[2] W. A. Cooper, Plasma Phys. Controlled Fusion **30**, 1805 (1988).
[3] F. L. Hinton and S. K. Wong, Phys. Fluids **28**, 3082 (1985).

Effects of net current on the HINT computation

R. KANNO, N. NAKAJIMA, T. HAYASHI, M. OKAMOTO

National Institute for Fusion Science,

Oroshi-cho, Toki

Japan

The HINT computation is developed to study three-dimensional MHD equilibria in toroidal helical systems. This calculation is based on the time-dependent relaxation technique using small values of resistivity and viscosity, which was developed by Park *et al.* [1]. The original HINT code was proposed in Ref.[2]. First targets of the computational study were finite beta stellarator equilibria with **no** net current. It was founded on fact that stellarators have the possibility of net current-free steady operation.

One of important advantages of the HINT computation is that it does not need to assume existence of nested flux surfaces in equilibria. Using this computational method, we can study the breaking of magnetic surfaces and properties of magnetic islands without a restriction of existence of nested surfaces. Thus, the HINT code enabled us to investigate quantitatively 1) the deterioration of magnetic surfaces, 2) the formation and self-healing of magnetic islands in finite beta plasma (Refs.[3, 4]).

Unfortunately, in the original HINT code we assume that no net current exists, and we cannot study effects of net current on stellarator equilibria. The net current can change drastically the rotational transform, and maybe it affects phenomena which are the magnetic surface breaking and formation/self-healing of magnetic islands. Thus, next target should be investigation of effects of net current; the Ohmic current, the bootstrap current, and the Ohkawa current. The HINT computation has a potential to overcome this trial. To apply the HINT computational method to obtaining equilibria with net current, we need to revise this computation.

Before we discuss modification of the HINT code, we introduce relaxation equations which are solved by the HINT code. We find MHD equilibria starting from an arbitrary nonequilibrium initial plasma and field configuration by means of a time-dependent relaxation method with small values of resistivity η and viscosity ν. We consider that the relaxation progresses physically through excitation of MHD waves. Calculations are performed in the following two steps. The A-step is the relaxation process of pressure along field lines under a fixed magnetic field. The relaxation of pressure is expected to be so slow as compared to other relaxation processes. To speed up the relaxation, we solve the artificial sound wave equation until $\boldsymbol{B} \cdot \nabla p = 0$ is satisfied.

A-step

$$\frac{\partial p}{\partial t} = \boldsymbol{B} \cdot \nabla v_s, \tag{1}$$

$$\frac{\partial v_s}{\partial t} = \boldsymbol{B} \cdot \nabla p, \qquad (B \text{ fixed}) \tag{2}$$

where v_s is the artificial sound wave velocity. The B-step is the relaxation process of magnetic field under a fixed pressure profile.

B-step

$$\rho_m \frac{\partial \boldsymbol{v}}{\partial t} = -\nabla p + \boldsymbol{j} \times \boldsymbol{B} + \nu \nabla^2 \boldsymbol{v}, \tag{3}$$

$$\frac{\partial \boldsymbol{B}}{\partial t} = -\nabla \times \boldsymbol{E} = \nabla \times (\boldsymbol{v} \times \boldsymbol{B} - \eta \boldsymbol{j}), \tag{4}$$

$$\mu_0 \boldsymbol{j} = \nabla \times \boldsymbol{B} \qquad (p \text{ fixed}). \tag{5}$$

The equation (3) gives the equilibrium condition $\boldsymbol{j} \times \boldsymbol{B} = \nabla p$, when both the time variation of momentum (the left-hand-side) and the viscosity term are zero. In the steady state, Eq.(4) is reduced to the Ohm's law;

$$\boldsymbol{v} \times \boldsymbol{B} - \eta \boldsymbol{j} = -\boldsymbol{E} = \nabla \phi, \tag{6}$$

where ϕ is a scalar potential. If there is no loop voltage, we have the following result from Eq.(6).

$$\text{Eq.(6)} \quad \Longrightarrow \quad \langle \boldsymbol{E} \cdot \boldsymbol{B} \rangle = -\langle \nabla \phi \cdot \boldsymbol{B} \rangle = 0 = \eta \langle \boldsymbol{j} \cdot \boldsymbol{B} \rangle, \tag{7}$$

where $\langle\ \rangle$ means the flux surface average. Thus, we obtain stellarator equilibria **without** net current.

Next, we consider stellarator equilibria with a loop voltage, $V_L = \text{const}$. The scalar potential ϕ is a multi-valued function, and we have

$$\eta \langle \boldsymbol{j} \cdot \boldsymbol{B} \rangle = - \langle \nabla \phi \cdot \boldsymbol{B} \rangle = \langle \boldsymbol{B} \cdot \nabla \zeta \rangle \frac{V_L}{2\pi} \neq 0. \tag{8}$$

Thus, the Ohmic current in the steady state is given as

$$\langle \boldsymbol{j} \cdot \boldsymbol{B} \rangle_{\text{Ohmic}} = \frac{1}{\eta} \langle \boldsymbol{B} \cdot \nabla \zeta \rangle \frac{V_L}{2\pi}. \tag{9}$$

To satisfy Eq.(7); $\langle \boldsymbol{E} \cdot \boldsymbol{B} \rangle = 0$, we should revise Eq.(4) as follows.

$$\frac{\partial \boldsymbol{B}}{\partial t} = -\nabla \times \boldsymbol{E} = \nabla \times \left(\boldsymbol{v} \times \boldsymbol{B} - \eta \left\{ \boldsymbol{j} - \boldsymbol{B} \frac{\langle \boldsymbol{j} \cdot \boldsymbol{B} \rangle_{\text{Ohmic}}}{B^2} \right\} \right). \tag{10}$$

This equation means any net current except the Ohmic current is decreased by resistivity. Thus, in the steady state, we can obtain stellarator equilibria **with** net current;

$$\langle \boldsymbol{E} \cdot \boldsymbol{B} \rangle = 0 = \eta \left\{ \langle \boldsymbol{j} \cdot \boldsymbol{B} \rangle - \langle \boldsymbol{j} \cdot \boldsymbol{B} \rangle_{\text{Ohmic}} \right\}. \tag{11}$$

Here, after sufficient time we can see that $\langle \boldsymbol{j} \cdot \boldsymbol{B} \rangle$ becomes $\langle \boldsymbol{j} \cdot \boldsymbol{B} \rangle_{\text{Ohmic}}$

When there are also the bootstrap current and/or the Ohkawa current, we can set as follows.

$$\frac{\partial \boldsymbol{B}}{\partial t} = -\nabla \times \boldsymbol{E} = \nabla \times \left(\boldsymbol{v} \times \boldsymbol{B} - \eta \left\{ \boldsymbol{j} - \boldsymbol{B} \frac{\langle \boldsymbol{j} \cdot \boldsymbol{B} \rangle_{\text{net}}}{B^2} \right\} \right), \tag{12}$$

where

$$\langle \boldsymbol{j} \cdot \boldsymbol{B} \rangle_{\text{net}} = \langle \boldsymbol{j} \cdot \boldsymbol{B} \rangle_{\text{Ohmic}} + \langle \boldsymbol{j} \cdot \boldsymbol{B} \rangle_{\text{bootstrap}} + \langle \boldsymbol{j} \cdot \boldsymbol{B} \rangle_{\text{Ohkawa}}. \tag{13}$$

We apply our new scheme to LHD equilibria and try to solve the modified relaxation equations which we proposed above. To check the new scheme, we use the following artificial ohmic current. We assume that a net current is proportional to the pressure profile.

$$\langle \boldsymbol{j} \cdot \boldsymbol{B} \rangle_{\text{Ohmic}} = f(\Psi_{\text{T}}) \ \propto \ \left(1 - \Psi_{\text{T}} / \Psi_{\text{T}}^{\text{edge}} \right)^2 \ \sim p/p_0. \tag{14}$$

And we choose values of the total net current $J_{\rm net}$ as follows.

$$J_{\rm net} = \int \mathrm{d}\boldsymbol{S}_{\rm T} \cdot \boldsymbol{j}_{\rm Ohmic} = \pm 50[\mathrm{kA}]. \tag{15}$$

Directions of the toroidal and poloidal magnetic field are shown in Fig.1, where B_T is the toroidal field and B_P is the poloidal field. If we add -50 [kA] of net current into equilibria, the poloidal magnetic field is increased by the net current. It means that the rotational transform ι is increased. While, if we add $+50$ [kA] of net current, ι is decreased. In Fig.2, we have results of the modified HINT computation. These are equilibria of LHD obtained by using the modified code. We can see that ι is changed by adding a net current. Error of force balance R_f in calculations is less than 10^{-5}, thus new computational method is correctly working, where R_f is defined as

$$R_f = \frac{\int \mathrm{d}\tau \left(\nabla p - \boldsymbol{j} \times \boldsymbol{B}\right)^2}{\int \mathrm{d}\tau \left\{(\nabla p)^2 + (\boldsymbol{j} \times \boldsymbol{B})^2\right\}}. \tag{16}$$

We are planing to calculate equilibria with the bootstrap current and the Ohkawa current.

References

[1] PARK,W., et al., Phys. Fluids **29** (1986) 1171.

[2] HARAFUJI,K., et al., J. Comput. Phys. **81** (1989) 169.

[3] HAYASHI,T., et al., Phys. Fluids B **2** (1990) 329.

[4] HAYASHI,T., et al., Phys. Plasmas **1** (1994) 3262.

Fig.1. Directions of the toroidal and poloidal magnetic field

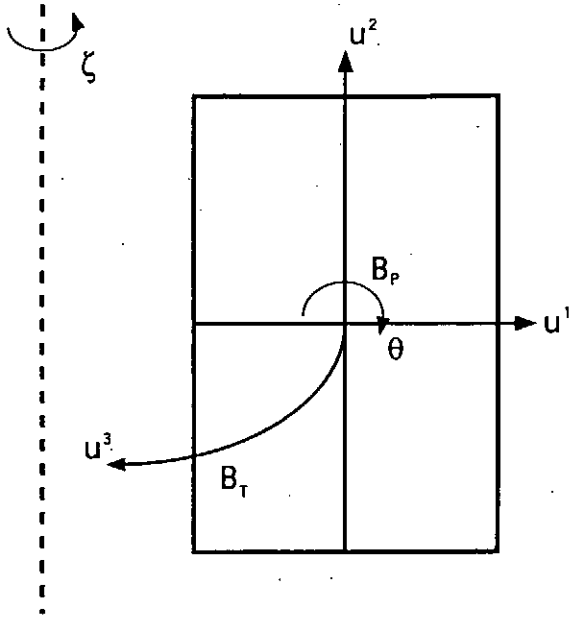

Fig.2-a. Equilibrium of LHD ($\beta_0 = 1.4\%$, currentless)

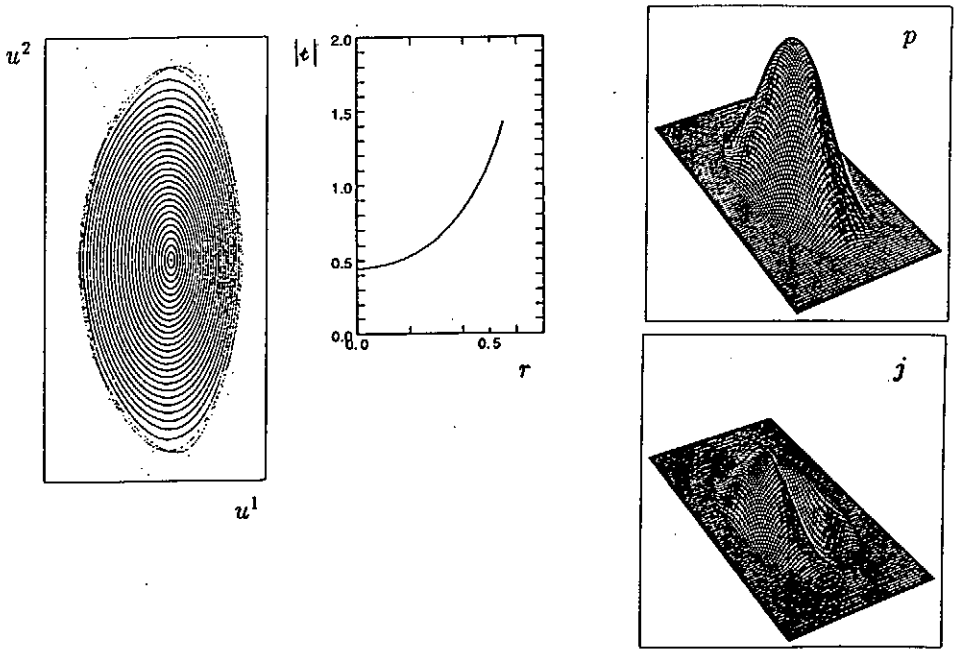

Fig.2-b. Equilibrium of LHD with net current ($\beta_0 = 1.4\%$, $J_{\rm net} = -50$[kA])

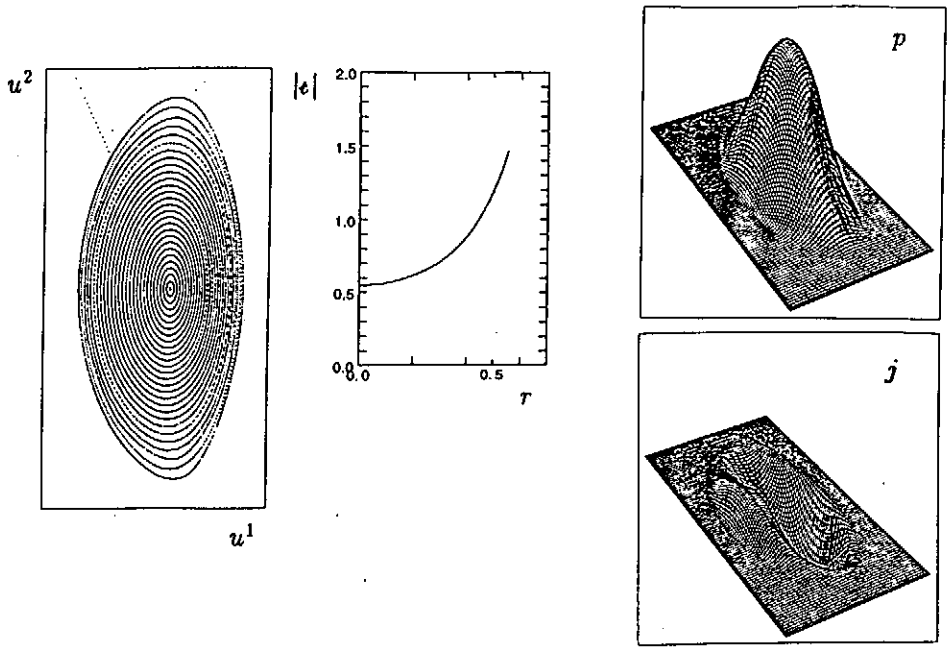

Fig.2-c. Equilibrium of LHD with net current ($\beta_0 = 1.4\%$, $J_{\rm net} = +50$[kA])

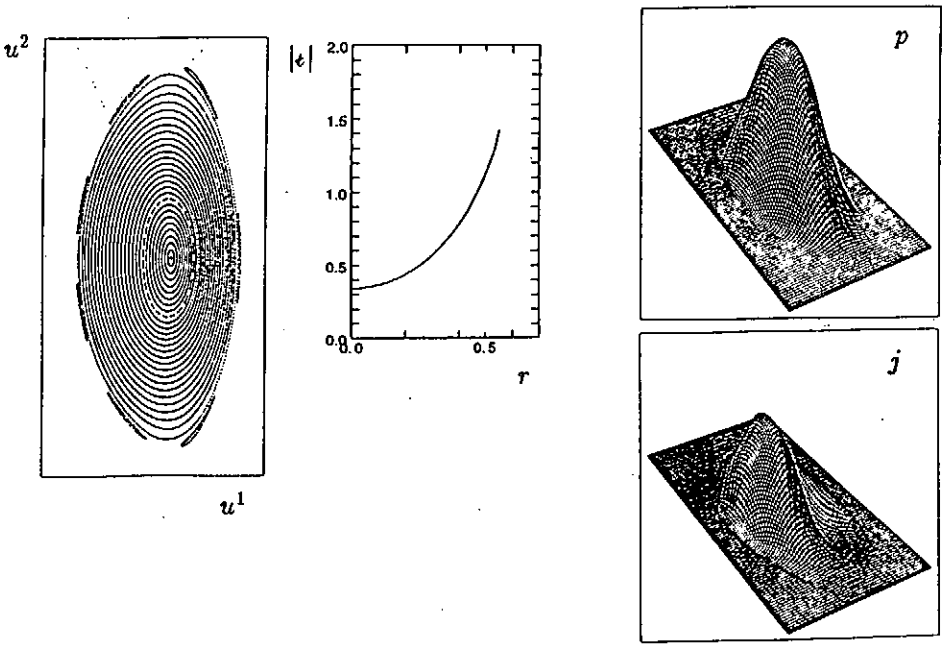

The Recipe for Handling Magnetic Field Properties for Desirable Stellarator Configurations

YOKOYAMA Masayuki, NAKAJIMA Noriyoshi and OKAMOTO Masao

National Institute for Fusion Science, Toki, 509-52, Japan

Abstract

Basic roles of several essential plasma boundary modulations on magnetic field properties are investigated. The appropriate combination of principle helical modulations to eliminate bumpy field is explained to realize quasi-axisymmetric (QAS) and quasi-helically symmetric (QHS) configurations. The triangular modulation is effectively utilized to form the magnetic well. The bumpy modulations of plasma boundary is essential to reduce the toroidicity in the magnetic field, which can lead to QHS configurations. Based on these roles of plasma boundary modulations, the classification of QAS and QHS configurations is considered. The possibility of quasi-bumpy symmetric (QBS) configuration is also mentioned.

1 Introduction

Stellarator configurations have a large flexibility to optimize confinement properties utilizing their three dimensionality. Magnetic configurations can be controlled by the plasma boundary modulations because MHD equilibria can be specified by boundary value problem. Several concepts to improve confinement properties in stellarators have been proposed based on this approach. In quasi-helically symmetric (QHS) configurations, the essential point to improve reflected particle confinement is to eliminate the toroidicity in the magnetic field in the Boozer coordinates [1]. However, the bootstrap current is expected to flow even in the QHS configurations [2]. It is particularly dangerous in low shear stellarators, where the rotational transform has to be carefully adjusted to avoid low order rational surfaces. For the reduction of bootstrap current, the appropriate combination of helical, toroidal and bumpy field components is employed in the W7-X [3]. Another concept is the quasi-axisymmetric (QAS) configuration [4]. It has a similar magnetic field structure as in tokamaks in the Boozer coordinates.

The plasma boundary shape are different between QAS, QHS and W7-X based on different desired physical criteria. It is essential to grasp basic roles of plasma boundary modulations to understand approaches to these configurations and to consider more desirable stellarator configurations.

Basic roles of several plasma boundary modulations on magnetic field properties are described in Section 2. Summary will be given in Section 3. The classification of symmetric stellarator configurations is also mentioned as an application of this study.

2 Magnetic Field Control with Plasma Boundary Modulations

In order to clarify basic roles of plasma boundary modulations, several effects on magnetic field properties have been studied by the fixed boundary version of VMEC [5]. The plasma boundary can be Fourier decomposed in the cylindrical coordinates (R, ϕ, Z) as

$$\begin{aligned} R(s, \theta_V, \zeta_V) &= \sum_{mn} R_{mn}(s) \cos(m\theta_V - nM\zeta_V), \\ Z(s, \theta_V, \zeta_V) &= \sum_{mn} Z_{mn}(s) \sin(m\theta_V - nM\zeta_V), \end{aligned}$$

where s is the magnetic surface label and θ_V (ζ_V) is the poloidal (toroidal) angle and m (n) is the poloidal (toroidal) mode number in the VMEC coordinates. Here, M is the field period number. The left hand side description for boundary harmonics are employed.

We choose the exact axisymmetric configuration described by $R_{00} = 2.0$ m, $R_{10} = 0.4$ m, $Z_{00} = 0.0$ m and $Z_{10} = 0.6$ m as the basic configuration for this study. The ratio of the magnetic axis (R_{axis}) to the center of mass of magnetic surface cross section in the major radius direction ($R_{C.M.}$) at four poloidal cross sections with the interval of 1/4 toroidal period is also considered as the measure of magnetic well. In this configuration, the magnetic well is evaluated to be about 5%. The magnetic well is defined by $(V'(0) - V'(\psi_T))/V'(0)$, where V is the volume enclosed by the magnetic surface corresponding to the toroidal flux function ψ_T and the prime denotes the derivative with respect to ψ_T.

It is noted that magnetohydrodynamic (MHD) equilibrium properties can also be varied by changing geometrical aspect ratio and the field period number. In other words, MHD equilibrium properties are different in the configurations with the same plasma boundary shape with different geometrical aspect ratio and/or field period number [6]. In the rest of this section, $M = 2$ cases are considered to investigate roles of plasma boundary modulations. It is noted that the following descriptions are well valid for $M = 2$ case, and should be carefully considered to apply to different M cases.

2.1 Principle Helical Modulations: $R_{11}, Z_{11}, R_{1,-1}$ and $Z_{1,-1}$

Principle helical modulations are firstly considered. Especially, R_{11} and Z_{11} appear in several magnetic configurations.

When R_{11} and Z_{11} are applied on the basic configuration independently, the bumpy field component, B_{01}, is significantly enhanced due to the magnetic flux conservation, which enhances the magnetic field strength where the area of magnetic surface cross section becomes small. The area is the smallest at $\phi = 0$ for the negative R_{11} case, on the other hand, it is the case at $\phi = (1/2)(2\pi/M)$ for the positive Z_{11} case. Therefore, the sign of B_{01} is opposite each other between these cases.

The variation of area of magnetic surface cross sections along the toroidal direction greatly governs the amplitude of bumpy field as long as the magnetic axis excursion is not remarkable. Therefore, it is important to make the area of magnetic surface cross section at $\phi = 0$ and $\phi = (1/2)(2\pi/M)$ almost the same to eliminate B_{01} for QAS and QHS configurations. The condition to realize this requirement in the presence of principle helical modulations leads to the relation,

$$E_{RZ} \times (R_{11} + R_{1,-1}) \sim -(Z_{11} + Z_{1,-1}), \tag{1}$$

where E_{RZ} is defined by Z_{10}/R_{10}. The magnetic configuration with $R_{11}/R_{10} = -0.5$, $Z_{11}/R_{10} = 0.75$ and $E_{RZ} = 1.5$ ("Conf. 1") almost satisfies eq. (1), which has relatively small B_{01} compared to the cases with R_{11} and Z_{11} independently.

2.2 Triangular Modulations: R_{21} and Z_{21}

When $R_{21}/R_{10} = 0.25$ is applied on the basic configuration, magnetic surface cross sections are changed to triangular ones. The $R_{axis}/R_{C.M.}$ is significantly enhanced around $\phi \sim 0$, where the magnetic surface cross section is deformed to the outward pointing triangular cross section. The inward pointing triangular one appears around $\phi \sim (1/2)(2\pi/M)$, and $R_{axis}/R_{C.M.}$ is below 1 there. However, the average $R_{axis}/R_{C.M.}$ is still above 1, which implies the deep magnetic well about 6.3%. The triangular modulation Z_{21} has almost the same effects as in R_{21} case when $Z_{21}/R_{10} = 0.25$ is applied on the basic configuration. However, in this case, the outward pointing triangular cross section appears around $\phi \sim (1/2)(2\pi/M)$, which is relatively effective to increase $R_{axis}/R_{C.M.}$ to enhance magnetic well.

The magnetic configuration with both $R_{21}/R_{10} = 0.25$ and $Z_{21}/R_{10} = 0.25$ simultaneously on the "Conf. 1" is mentioned ("Conf. 2"). In this case, the magnetic surface cross section is indented at $\phi = 0$ due to R_{21} and becomes outward pointing triangular cross section around $\phi \sim (1/2)(2\pi/M)$ due to Z_{21}. This variation of magnetic surface cross sections is familiar in the W7-X, QAS and QHS configurations.

2.3 Principle Bumpy Modulations: R_{01} and Z_{01}

When $R_{01}/R_{10} = 0.5$ is applied on the basic configuration, magnetic axis shifts more outward around $\phi \sim (1/2)(2\pi/M)$, and also the average $R_{axis}/R_{C.M.}$ is greatly enhanced. This average value is significantly larger than that in the basic configuration and the magnetic well becomes deeper to about 8.5%. The $B_{10}/(a/R_{maj})$ is reduced to 0.89.

When both radial and vertical bumpy modulations R_{01} and Z_{01} are applied on the "Conf. 2" with $R_{01}/R_{10} = 0.5$ and $Z_{01}/R_{10} = -0.25$, the magnetic axis excursion becomes remarkable. It is noted that $B_{10}/(a/R_{maj})$ is reduced to 0.61 in this configuration. In other words, the decoupling of magnetic field structure from the real torus geometry is successfully realized. If much larger bumpy modulations of plasma boundary are applied, magnetic configurations without B_{10} would be possible. This role can be utilized to reduce B_{10} to realize QHS and QBS configurations.

3 Summary

The effects of plasma boundary modulations on magnetic field properties have been described.

The principle helical modulations give the variation of area of magnetic surface cross sections between at the beginning of the field period ($\phi = 0$) and at the middle of the field period ($\phi = (1/2)(2\pi/M)$). Here M is the field period number. This variation causes the relatively large bumpy field component (B_{01}) due to the magnetic flux conservation. This is not appropriate to realize quasi-axisymmetric (QAS) or quasi-helically symmetric (QHS) configurations. The appropriate combination of principle helical modulations to suppress B_{01} is presented, eq. (1), by considering the area of magnetic surface cross sections.

The triangular modulations can be utilized to form or deepen magnetic well by shifting the magnetic axis outward compared to the center of mass of magnetic surface cross section. The favorable radial triangular modulation gives the indentation on the magnetic surface cross section around $\phi \sim 0$ and the favorable vertical one leads to the outward pointing triangular cross section around $\phi \sim (1/2)(2\pi/M)$, which are frequently seen in the W7-X, QAS and QHS configurations.

The bumpy modulations of plasma boundary shape is also investigated. The significant feature is that the toroidicity in the magnetic field (B_{10}) is effectively reduced as the magnetic axis excursion is enhanced. The necessary magnetic axis excursion to reduce B_{10} sufficiently depends on M [6]: the larger excursion is required as M is decreased because B_{10} becomes relatively larger compared to helical fields.

Based on these roles of plasma boundary modulations, the classification of QAS and QHS configurations is summarized in Fig.1, where the magnetic surface cross sections at $\phi = 0$, $\phi = (1/4)(2\pi/M)$ and $\phi = (1/2)(2\pi/M)$ are shown in one figure in each case for simplicity.

The essential point to realize a QAS configuration is that the fine suppression of B_{01} with keeping helical fields sufficiently small. For the formation of vacuum magnetic well, efforts are made to realize the outward pointing triangular cross section around $\phi \sim (1/2)(2\pi/M)$ and tear-drop shaped cross section around $\phi \sim (1/4)\ (2\pi/M)$. It is also intuitively recognized that the configurations with smaller M and/or with smaller aspect ratio A_p are suitable to realize QAS configurations due to the relatively larger toroidicity compared to helical fields.

On the other hand, the reduction of B_{10} is indispensable factor to realize QHS configurations. This role is effectively played by the bumpy modulations of plasma boundary shape. The large magnetic axis excursion is applied to reduce the toroidicity in the magnetic field to about 1% in $M = 4$ systems. The requirements to form the magnetic well and to realize a pure magnetic field structure lead to the appropriate combination of triangular modulations. This application causes the indented cross section around $\phi \sim 0$

and the outward pointing triangular cross section around $\phi \sim (1/2)(2\pi/M)$. The relatively larger helical field contributions in larger M cases allow to reduce the magnetic axis excursion to suppress B_{10}. The configurations with larger A_p are also suitable to realize QHS configurations due to the relatively smaller toroidicity.

The possibility of a quasi-bumpy (or poloidally) symmetric (QBS) configuration is also mentioned. The breaking of eq. (1) gives the large B_{01} with either sign depending on the variation of area of magnetic surface cross sections. By utilizing this, the magnetic field with B_{01} dominantly is possible. It is noted that this configuration has a finite ι, and therefore, it is distinguishable from the so-called bumpy torus. The detailed confinement properties of QBS configurations are now in investigations.

Acknowledgements

The authors gratefully acknowledge productive and fruitful discussions with Prof. J. Nührenberg and Prof. M. Wakatani.

References

[1] BOOZER, A. H., Phys. Fluids **23**(1980)904.

[2] SHAING, K. C., et al., Phys. Fluids **B1**(1989)148.

[3] MAASSBERG, H., et al., Phys. Fluids **B5**(1993)3728.

[4] NÜHRENBERG, J., in Theory of Fusion Plasmas (Proc. Workshop Varenna, 1994) Editrice Compositori, Bologna (1994)3.

[5] HIRSHMAN, S. P., et al., Comput. Phys. Commun. **43**(1986)143.

[6] YOKOYAMA, M., NAKAJIMA, N., OKAMOTO, M., submitted to Nucl. Fusion.

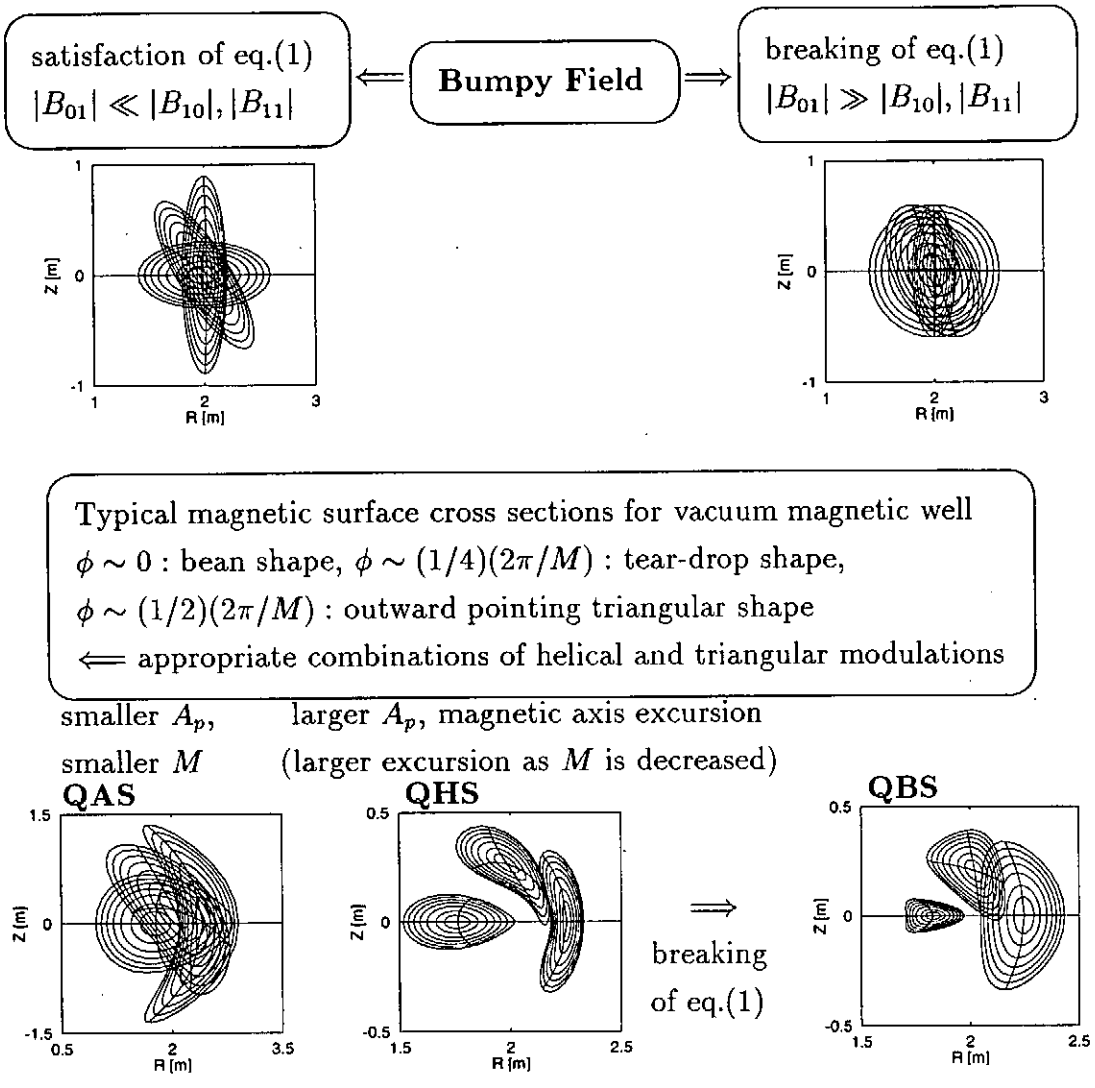

Fig. 1: The classification of QAS, QHS and QBS configurations are shown based on the bumpy field control by considering eq. (1), field period number (M), geometrical aspect ratio (A_p) and magnetic axis excursion.

Simulation Study of the Structural Formation in Systems with Short-Range Interaction

Susumu FUJIWARA and Tetsuya SATO

Theory and Computer Simulation Center, National Institute for Fusion Science, 322-6, Oroshi-cho, Toki 509-52, Japan

Abstract

By carrying out the molecular dynamics simulations of 100 short polymer chains, each of which consists of 20 CH_2 groups, we show that the orientationally ordered structure at low temperature is formed from a random structure at high temperature by a sudden cooling. The essentially extended chains form a monolayer structure. The ratio of the lattice constants a/b takes the hexagonal value $\sqrt{3}$ at 400 K and decreases as the temperature decreases. From detailed analysis of the local orientational order, it is found that the growth of the local ordered clusters proceeds *in a stepwise fashion*. From the analysis of the molecular mobility, we find that the longitudinal chain motion increases dramatically with increasing temperature while the transverse chain motion is not so dependent on the temperature variation.

I. INTRODUCTION

Recently much attention has been given to the structural formation in plasma physics and condensed matter physics. In plasma physics, the structural formation in systems with the long-range interaction such as the Coulomb interaction has so far been discussed. By contrast, in dusty plasmas and molecular systems, it is important to understand the mechanism of the structural formation based on the short-range interaction. As the system with the short-range interaction, we choose a polymer system.

The purpose of this paper is to understand the mechanism of the structural formation in a polymer system *at the molecular level*. To this end, we carry out the molecular dynamics (MD) simulations of 100 short polymer chains, each of which consists of 20 CH_2 groups, and analyze the formation process of the orientationally ordered structure and the molecular motion. We believe that our simulation results can provide an essential clue to understand the molecular motion in the metastable hexagonal phase whose importance in crystal growth has been recently pointed out [1].

Some work has been done in relation to the structural formation of short polymer chains. Esselink *et al.* carried out MD simulations of nucleation and melting of bulk *n*-alkane systems in order to determine the crystallization and melting temperatures [2]. They introduced a new method to identify crystalline regions and computed the crystallization rate of a nucleus. Structures and molecular motions in the rotator phases of *n*-alkanes have been studied by Monte Carlo (MC) simulations [3–5] and MD simulations [6–8].

II. MODEL AND METHOD

The present computational model is the same as that used in the previous work on the structural formation of a single long polymer chain [9]. The model polymer chain consists of a sequence of CH_2 groups, which are treated as united atoms. The united

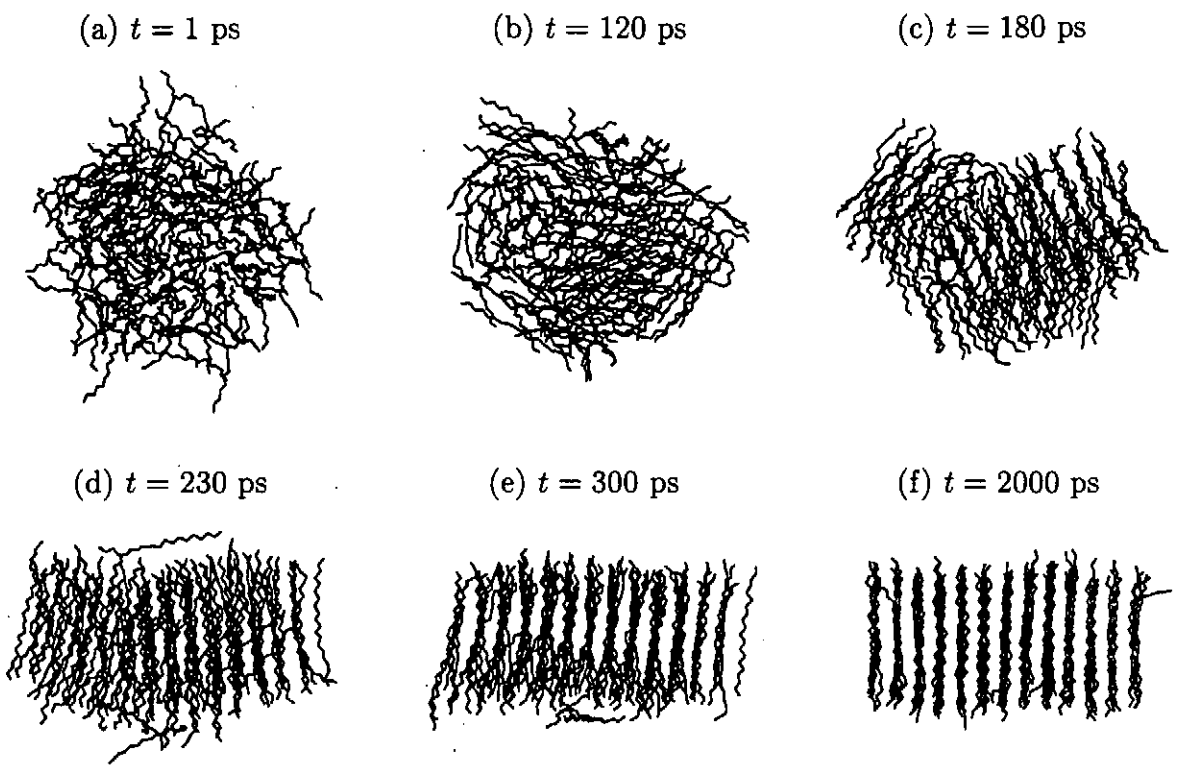

Figure 1: The chain configurations of 100 short polymer chains for $T = 400$ K viewed along the b-axis. (a) $t = 1$ ps, (b) $t = 120$ ps, (c) $t = 180$ ps, (d) $t = 230$ ps, (e) $t = 300$ ps and (f) $t = 2000$ ps.

atoms interact via the bonded potentials (bond-stretching, bond-bending and torsional potentials) and the non-bonded potential (12-6 Lennard-Jones potential). The atomic force field used here is the DREIDING potential [10]. The numerical integrations of the equations of motion are performed using the velocity version of the Verlet algorithm [11]. We apply the Nosé-Hoover method in order to keep the temperature of the system constant [12–14]. The integration time step and the relaxation constant for the heat bath variable are 0.001 ps and 0.1 ps, respectively. The cutoff distance for the Lennard-Jones potential is 10.5 Å. The polymer chains are exposed to vacuum and there is no box to confine them. The total momentum and the total angular momentum are taken to be zero in order to cancel overall translation and rotation of chains. The MD simulations are carried out by the following procedure. At first, we provide a randomly distributed configuration of 100 short polymer chains at high temperature ($T = 700$ K). It is then quenched to $T = 400$ K and subsequently it is cooled stepwise to $T = 100$ K with the rate of 100 K/2000 ps.

III. SIMULATION RESULTS

We show, in Fig. 1, the chain configurations viewed along the b-axis at various times ($t = 1$, 120, 180, 230, 300 and 2000 ps) obtained by our MD simulations at $T = 400$ K. The a, b and c axes respectively correspond to the crystalline a, b and c axes in the orthorhombic system. From Fig. 1, we find the following features: (i) In the early time ($t = 1$ ps), the configuration of the polymer chains is *random*. (ii) With the elapse of time, the local orientationally-ordered regions (clusters) grow in several positions ($t = 120$, 180

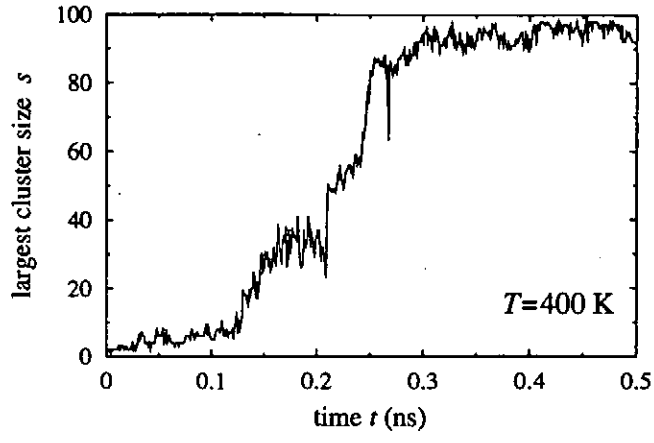

Figure 2: The size of the largest cluster s versus time t at $T = 400$ K.

and 230 ps) and at last they coalesce into a large cluster ($t = 300$ ps). (iii) At $t = 2000$ ps, a highly ordered structure is formed.

In order to investigate the growth process of the local orientational order, we introduce the concept of "*cluster*" according to Ref. [2]. The definition of "cluster" is as follows. Two polymer chains belong to the same cluster if the following two conditions are satisfied: (i) $|\mathbf{r}_c^i - \mathbf{r}_c^j| < r_0$ and (ii) $\alpha_{ij} < \alpha_0$, where $\mathbf{r}_c^i$ is the position vector of the center of mass of the i-th chain, α_{ij} is the angle between the principal axis with the smallest moment of inertia of the i-th chain and that of the j-th chain and satisfies $0 < \alpha_{ij} < \pi/2$. In our calculations, we set $r_0 = 1.5\sigma$ ($\sigma = 0.36239$ nm) and $\alpha_0 = 10°$. We show, in Fig. 2, the largest cluster size s at $T = 400$ K as a function of time. It can be seen from this figure that the growth of the clusters proceeds *stepwise*. The stepwise behavior is also found in the global bond-orientational order parameter.

Next, we investigate the orientationally ordered structure. At $T = 400$ K, since the ratio a/b is equal to $1.733 \approx \sqrt{3}$, polymer chains are found to be packed hexagonally (Fig. 3). The lattice constants a and b, and the ratio a/b are plotted in Fig. 4 at various temperatures. Figure 4(a) indicates that the parameter a decreases as the temperature decreases while the parameter b stays almost constant in this temperature region. The temperature dependence of the parameters a and b in our isolated short polymer system is in qualitative agreement with the experimental results for odd-numbered n-alkanes [15] and the MD calculations for the infinite chain model of the bulk odd-numbered n-alkanes [6]. From Fig. 4(b), it is found that the ratio a/b takes the hexagonal value $\sqrt{3}$ at $T = 400$ K and decreases as the temperature decreases.

Then, we study the distribution of *gauche* defects. We define the *gauche* state by $|\phi| > \pi/3$, where ϕ is the dihedral angle. We plot the fraction of *gauche* states P_{gauche} versus bond number in Fig. 5 at various temperatures. This figure tells us that almost all the bonds are in the *trans* state at low temperatures ($T = 100$ and 200 K) while *gauche* states are excited predominantly in the chain ends at $T = 300$ and 400 K. This feature is in qualitative accord with the experimental results for n-$C_{21}H_{44}$ [16] and the MD results [6]. It should be noted that *gauche* states are excited even in the chain interiors at $T = 400$ K.

Finally, we investigate the molecular motion at various temperatures. In order to measure the extent of the molecular motion of polymer chains, we define the average

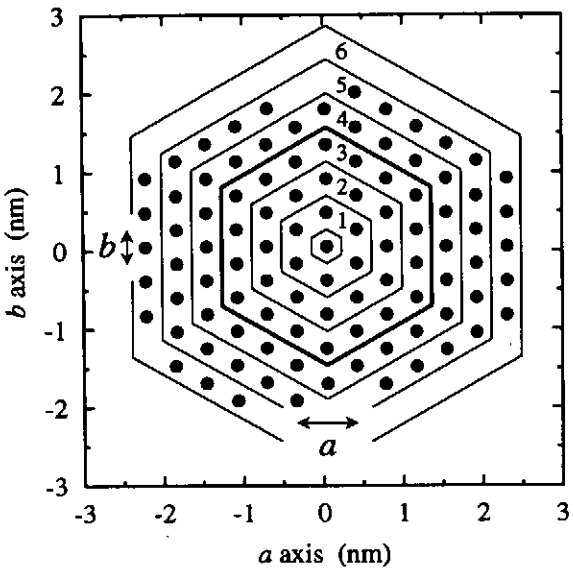

Figure 3: The center-of-mass positions of individual polymer chains for $T = 400$ K viewed along the c-axis. Hexagons are depicted in order to show a hexagonal packing of the polymer chains. A figure in each layer denotes a layer number.

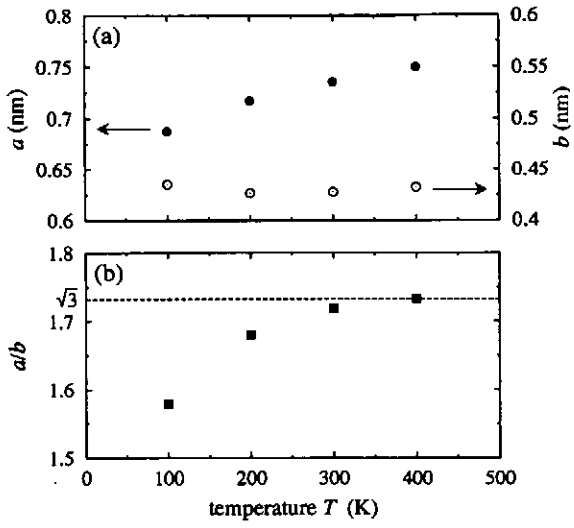

Figure 4: (a) Lattice constants a and b, and (b) the ratio a/b versus temperature T. A dashed line indicates the hexagonal value $\sqrt{3}$.

fluctuation along individual axes in each layer l as

$$\Delta a(l) = \sqrt{\sum_{m\in l\text{-th layer}} \frac{1}{n_l} \left\langle (a_c^m - \langle a_c^m \rangle)^2 \right\rangle}, \quad (1)$$

$$\Delta b(l) = \sqrt{\sum_{m\in l\text{-th layer}} \frac{1}{n_l} \left\langle (b_c^m - \langle b_c^m \rangle)^2 \right\rangle}, \quad (2)$$

$$\Delta c(l) = \sqrt{\sum_{m\in l\text{-th layer}} \frac{1}{n_l} \left\langle (c_c^m - \langle c_c^m \rangle)^2 \right\rangle}, \quad (3)$$

where $\mathbf{r}_c^m = (a_c^m, b_c^m, c_c^m)$ is the position vector of the center of mass of the m-th polymer chain, n_l denotes the number of polymer chains involved in the l-th layer, $\langle \cdots \rangle$ represents the time average between 1500 and 2000 ps and the zeroth layer corresponds to the central polymer chain. In Fig. 6, we show the average fluctuation Δa and Δc as a function of the layer number l at various temperatures. From Fig. 6(a), we find that the transverse chain motion is not so sensitive to the temperature variation. By contrast, it is found from Fig. 6(b) that the longitudinal chain motion increases dramatically as the temperature increases. It is also found that the transverse chain motion as well as the longitudinal chain motion increases remarkably in the outer three layers ($l = 4$, 5 and 6). This finding is in good agreement with the results of MC simulations on n-alkanes by Yamamoto *et al.* [4,5].

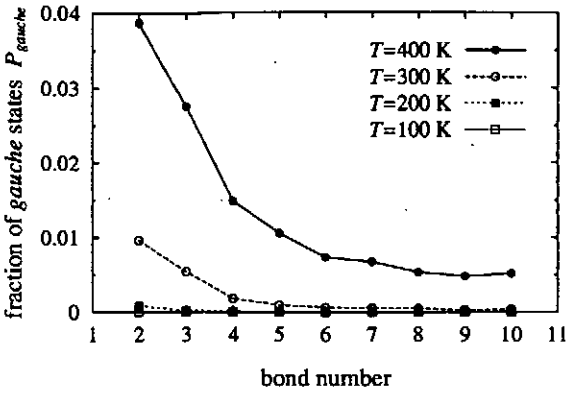

Figure 5: The fraction of the *gauche* states P_{gauche} versus bond number at various temperatures.

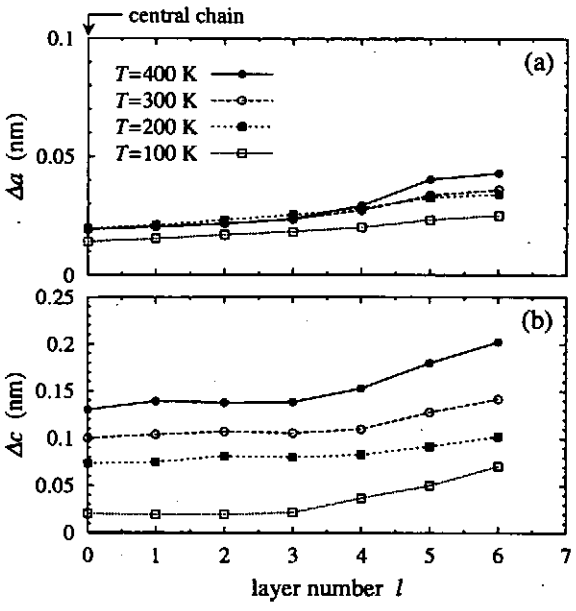

Figure 6: Average fluctuation (a) along the a-axis Δa and (b) along the c-axis Δc versus layer number at various temperatures.

IV. SUMMARY AND DISCUSSION

By carrying out MD simulations of 100 short polymer chains and analyzing the growth process of clusters and the molecular motion, we have obtained the following results:

(1) The orientationally ordered structure at low temperature is formed from a random structure at high temperature by cooling.

(2) The ratio of the lattice constants a/b decreases from the hexagonal value $\sqrt{3}$ at 400 K as the temperature decreases.

(3) The local orientationally-ordered clusters grow in a *stepwise* fashion.

(4) The *gauche* defects are located predominantly in the chain ends.

(5) The longitudinal chain motion increases dramatically as the temperature increases.

(6) The chain motion increases remarkably in the outer three layers.

The stepwise behavior in the growth process of clusters have also been confirmed by the MD simulations at different temperatures (T = 300, 320, 340, ..., 460 K).

For the future work, we will carry out MD simulations of long polymer chains in order to investigate the effect of the entanglement on the structural formation.

References

[1] M. Hikosaka, S. Rastogi, A. Keller and H. Kawabata, J. Macromol. Sci. Phys. **B31**, 87 (1992).

[2] K. Esselink, P.A.J. Hilbers and B.W.H. van Beest, J. Chem. Phys. **101**, 9033 (1990).
[3] T. Yamamoto, J. Chem. Phys. **82**, 3790 (1985); **89**, 2356 (1988).
[4] T. Yamamoto, M. Hikosaka and N. Takahashi, Macromolecules **27**, 1466 (1994).
[5] T. Yamamoto, J. Chem. Soc. Faraday Trans. **91**, 2559 (1995).
[6] J.P. Ryckaert and M.L. Klein, J. Chem. Phys. **85**, 1613 (1986).
[7] J.P. Ryckaert, M.L. Klein and I.R. McDonald, Phys. Rev. Lett. **58**, 698 (1987).
[8] J.P. Ryckaert, I.R. McDonald and M.L. Klein, Molecular Physics **67**, 957 (1989).
[9] S. Fujiwara and T. Sato, J. Chem. Phys. **107**, 613 (1997).
[10] S.L. Mayo, B.D. Olafson and W.A. Goddard III, J. Phys. Chem. **94**, 8897 (1990).
[11] L. Verlet, Phys. Rev. **159**, 98 (1967).
[12] S. Nosé, Mol. Phys. **52**, 255 (1984).
[13] S. Nosé, J. Chem. Phys. **81**, 511 (1984).
[14] W.G. Hoover, Phys. Rev. A **31**, 1695 (1985).
[15] G. Ungar, J. Phys. Chem. **87**, 689 (1983).
[16] M. Maroncelli, H.L. Strauss, and R.G. Snyder, J. Chem. Phys. **82**, 2811 (1985).

Dust Acoustic Instabilities in a Plasma with a Background of Neutrals

P. Kaw, R. Singh and A. Sen

Institute For Plasma Research, Bhat, Gandhinagar, 382428, India

Abstract

Instabilities of dust acoustic waves in a plasma with a significant background pressure of neutrals has been investigated. A long wavelength mode, relevant at relatively high pressure, is found to be unstable due to recombination of electrons and ions on the surface of dust particles and ion-neutral collisional momentum transfer. At short wavelengths, a dissipative instability driven by relative drift between ions and the dust particles, is found to be important. Additional features of the instabilities associated with electron and ion temperature fluctuations, strong correlation in the dust fluid and dynamics of charge fluctuations on the dust particles have also been discussed. Nonlinear features of the instabilities have been investigated and are briefly commented upon.

I. INTRODUCTION

Dusty plasmas have acquired considerable importance because of applications to astrophysics and planetary physics, problems of plasma processing and the physics of strongly coupled Coulomb systems[1-4]. Experimentally, an important area of investigation is the study of low frequency collective modes[5-8]. The most characteristic low frequency mode is the dust acoustic mode[9], a typical compressional mode in which the dust particles provide the inertia and electrons and ions bring in the pressure effects through their shielding clouds ($kv_{the,i} \gg \omega \gg kv_{thd}$).

Interpretations of dust acoustic wave excitation in experiments have typically relied on collisionless inverse Landau damping mechanism[10,11]. However, a closer examination of experimental conditions reveals that waves are often excited when there is a significant background pressure of neutrals *e.g.,* in many situations the collisional mean free path λ_f is smaller than the wavelength λ. It is therefore necessary to extend the wave excitation theories into the collisional regime. The objectives of this paper are :

1. to look for excitation mechanisms for dust acoustic waves in a plasma where collisions of various charged species with neutrals are important [12];
2. to consider any special effects due to strongly correlated nature of the dust fluid [13];
3. to explore nonlinear features of the excited waves [12].

II. LOW FREQUENCY DISPERSION RELATION IN A DUSTY PLASMA:

When small dust particles are introduced in a plasma, they get charged up to the floating potential because of unbalanced electron and ion fluxes striking their surfaces. A typical micron size dust particle thus acquires a negative charge $-Z_d e$ where Z_d may be a high as

10^4. Plasma charge neutrality then takes the form

$$n_{e0} + Z_d n_{d0} = n_{i0}$$

Electrostatic perturbations may be described by the Poisson equation :

$$\nabla^2 \phi = 4\pi e \left[\delta n_e + Z_d \delta n_d - \delta n_i\right] \tag{1}$$

Introducing susceptibility functions χ_α :

$$\delta n_\alpha = -\frac{\chi_\alpha}{4\pi e Z_\alpha} k^2 \phi \tag{2}$$

where $Z_\alpha = -1,\ -Z_d,\ +1$ for electrons, dust particles and ions respectively, we get the dispersion relation

$$1 + \sum_\alpha \chi_\alpha = 0 \tag{3}$$

For very low frequency modes ($\omega \ll k v_{the,i}$), electrons and ions typically acquire the Boltzmann distribution

$$\frac{n_\alpha}{n_0} = \exp\left[-\frac{Z_\alpha e \phi}{T_\alpha}\right] \qquad \alpha = e, i$$

This assumes that $\tilde{T}_\alpha = 0$ and comes by balancing the electric field forces with isothermal pressure gradient forces; linearizing, we get

$$\frac{\delta n_\alpha}{n_{\alpha 0}} = -\frac{Z_\alpha e \phi}{T_\alpha}$$

which leads to the electron/ion susceptibility

$$\chi_\alpha = \frac{1}{k^2 \lambda_\alpha^2} \qquad \alpha = e, i \tag{4}$$

where $\lambda_\alpha = (T_\alpha / 4\pi e^2 n_{\alpha 0})^{1/2}$ is the relevant Debyelength.

The dust fluid susceptibility χ_d for the cold fluid limit ($\omega \gg k v_{thd}$) may be obtained from the hydrodynamic equations :

$$\frac{\partial}{\partial t} \delta n_d + n_{d0} \vec{\nabla} \cdot \vec{v}_d = 0$$

$$\frac{\partial}{\partial t} \delta v_d = \frac{Z_d}{M_d} e \nabla \phi$$

Fourier analyzing and expressing δn_d in terms of ϕ, we get

$$\chi_d = -\frac{\omega_{pd}^2}{\omega^2} \tag{5}$$

where $\omega_{pd} = (4\pi Z_d^2 e^2 n_{d0}/M_d)^{1/2}$ is the dust plasma frequency.

The basic dust acoustic wave dispersion relation is thus given by

$$1 + \frac{1}{k^2\lambda_e^2} + \frac{1}{k^2\lambda_i^2} - \frac{\omega_{pd}^2}{\omega^2} = 0 \tag{6}$$

For $k\lambda_{e,i} \ll 1$, we get the non-dispersive dust acoustic wave:

$$\omega^2 = \frac{k^2 C_{d*}^2}{1+\tau^*} \tag{7}$$

where $C_{d*}^2 = (Z_d n_{d0}/n_{e0})(Z_d T_e/M_d)$ and $\tau^* = (T_{e0} n_{i0}/T_{i0} n_{e0})$. In this acoustic wave, the dust particles provide the inertia for compressions and rarefactions and electrons and ions do the shielding bringing in finite pressure effects through self-consistent electrostatic fields.

We now move on to describe the effect of background neutrals. χ_d is modified because dust exchanges momentum with the background neutral fluid. Introducing a momentum loss term $-\nu_{dn} M_d v_d$ on the right side of equation of motion for the dust fluid, and proceeding as before, we get the modified susceptibility :

$$\chi_d = -\frac{\omega_{pd}^2}{\omega\left(\omega + i\nu_{dn}\right)} \tag{8}$$

Electron response is unaltered as long as $k^2 v_{the}^2/\nu_{en}\omega \gg 1$. However, if $k^2 v_{the}^2/\nu_{en}\omega \sim 1$, the ion response is modified and has to be recalculated. We shall do so but will also include effects due to a relative drift between the ion and dust fluids and additional effects due to electron–ion recombination on dust particles. The basic equations are :

$$\left(\frac{\partial}{\partial t} + \vec{v}_0 \cdot \vec{\nabla}\right)\frac{\delta n_i}{n_{i0}} + \vec{\nabla}\cdot\vec{v}_i = -\nu_R \frac{\delta n_d}{n_{d0}} \tag{9}$$

$$v_i = -\frac{v_{thi}^2}{\nu_{in}} \nabla\left(\frac{e\phi}{T_{i0}} + \frac{\delta n_i}{n_{i0}}\right) \tag{10}$$

where $\nu_R = \beta n_{d0} \pi r_d^2 c_s$ is the recombination frequency of electrons and ions on the surface of dust particles (β is an electrostatic focusing factor arising because the dust is negatively

charged and pulls the positive ions towards itself). In equilibrium, the recombination term is balanced by a source term S (such as that due to ionization) so that on perturbation we have on right side $\delta(S - \nu_R n_i) = \delta S - \nu_R \delta n_i - \delta\nu_R n_{i0}$; in writing eqn. (9) we have assumed that the first two terms balance each other. Eqn. (10) shows that ion velocity is driven by a mobility term and a diffusion term, a reasonable assumption when $\omega \ll \nu_{in}$. Fourier analyzing eqs. (9) and (10) and proceeding as usual we get the modified ion susceptibility.

$$\chi_i = \left(k^2\lambda_i^2\right)^{-1}\left[1 - \frac{c_d^2}{v_{thi}^2}\frac{\nu_R\nu_{in}}{\omega\left(\omega + i\nu_{dn}\right)}\frac{T_{i0}}{T_{e0}}\right] \Big/ \left[1 - i\frac{\nu_{in}}{k^2 v_{thi}^2}\left(\omega - kv_0\right)\right] \tag{11}$$

Combining the susceptibility functions to get a new dispersion relation and solving for the real and imaginary parts of the frequency, ω_R and γ, we get

$$\omega_R^2 = \frac{k^2 C_{d*}^2 + \alpha\nu_{in}\nu_R}{1 + \tau^*} \tag{12a}$$

$$\gamma = -\frac{\nu_{dn}}{2} + \frac{\nu_{in}}{2\left(1+\tau^*\right)^2}\left[\alpha\frac{\nu_{in}\nu_R}{k^2 v_{thi}^2} - \tau^*\frac{C_{d*}^2}{v_{thi}^2}\right]\left(1 - \frac{kv_0}{\omega_R}\right) \tag{12b}$$

Eqn.(12a) shows that for $k \to 0$, the dust acoustic wave frequency approaches a constant determined by recombination physics ; this leads to a novel form of dispersion for these waves. Eqn. (12b) shows that the dust acoustic waves are damped by dust neutral collisions. For $v_0 = 0$, there is a recombination induced growth which leads to an instability, if it overpowers the dust–neutral collisional damping and the diffusive damping due to ion–neutral collisions. For $v_0 \neq 0$ and $> \omega_R/k$, the dust acoustic wave is a negative energy wave in the ion frame; it is then driven unstable by dissipative effects due to diffusion.

We now give a physical description of these instabilities. Starting from the basic equations one may derive the following expression :

$$\frac{\partial}{\partial t}\int\left[\mid v_d \mid^2 + C_{d*}^2 \mid \delta n_d \mid^2\right] d^3r = -\nu_{dn}\int \mid v_d \mid^2 d^3r + C_d^2\frac{n_{i0}}{n_{e0}}\int\frac{\delta n_i}{n_{i0}}\left(\vec{\nabla}\cdot\vec{v}_d^*\right) d^3r$$

The left side may be interpreted as the rate of change of the wave energy. The first term on the right hand side is the loss of wave energy due to the momentum sink to neutrals. The last term represents a possible source and may be rewritten as,

$$\left(C_d^2\frac{n_{i0}}{n_{e0}}\right)\int d^3k \mid \phi_k \mid^2 \left(\nu_{in}\nu_R - \omega_R^2\frac{v_{thi}^2}{C_d^2}\tau\right)\left(\frac{k^2C_d^2}{\omega_R^2}\right)^2 \frac{\left[\nu_{in}\omega_R\left(\omega_R - \vec{k}\cdot\vec{v}_0\right)\right]}{\left[\nu_{in}^2\left(\omega_R - \vec{k}\cdot\vec{v}_0\right)^2 + k^4 v_{thi}^4\right]}$$

Again for $v_0 = 0$, we get a recombination instability if the ν_R term dominates in the first bracket. A streaming induced instability is obtained if $v_0 > \omega_R/k$ and the negative energy waves are driven by diffusive dissipation. Both instabilities may be traced to a modified $\delta n_i - \phi$ phase relationship :

$$\frac{\delta n_i}{n_0} = -\frac{e\phi}{T_e}\left(\tau - \frac{k^2 C_d^2}{\omega^2}\frac{\nu_{in}\nu_R}{k^2 v_{thi}^2}\right) / \left[1 - i\frac{\nu_{in}\left(\omega - \vec{k}\cdot\vec{v}_0\right)}{k^2 v_{thi}^2}\right]$$

which permits a positive feedback between the dust acoustic wave and the ion fluid. For $v_0 \neq 0$, the short wavelength waves extract free energy from ion streaming; the long wavelength recombination instability arises (for $v_0 = 0$) because the introduction of dust wants to extinguish the plasma discharge by surface recombination effects. The homogeneous steady state is thus prone to localized quenching at dust compressions when $\omega \sim \nu_R$.

We now investigate the influence of other physical effects on the above instabilities. Let us first consider the effect of dust charge fluctuations. This means that the mean dust charge Z_d is not treated as a constant but is treated as a dynamical variable responding to electron and ion currents driven by self-consistent fields [14,15]. We write the charging equation for dust particles ($Q_d = -eZ_d$)

$$\frac{dQ_d}{dt} = I_e + I_i$$

where

$$I_e = -\pi a^2 e \left(8kT_e/\pi m_e\right)^{1/2} n_e \exp\left[\frac{e}{kT_e}\left(\phi_f - V\right)\right]$$

$$I_i = \pi a^2 e \left(8kT_i/\pi m_i\right)^{1/2} n_i \left[1 - \frac{e}{kT_i}\left(\phi_f - V\right)\right]$$

and ϕ is the floating potential of the particle, V is the plasma space potential. ϕ_{f0} is determined by the condition that in equilibrium $I_{e0} + I_{i0} = 0$. Perturbing the above equation, we find

$$\frac{\partial}{\partial t}\tilde{Z}_d + \eta\tilde{Z}_d = \mid I_{e0}/e \mid \left(\frac{\delta n_e}{n_{e0}} - \frac{\delta n_{i0}}{n_{i0}}\right)$$

where the charge relaxation rate η is given by $\eta = [e \mid I_{e0} \mid /c](T_e^{-1} + T_i^{-1})$. Retaining the $\tilde{Z}_d$ effects in the Poisson equation, we get a new dispersion relation

$$1 + \chi_e\left(1 + \frac{i\beta}{\omega + i\eta}\right) + \chi_i\left(1 + \frac{i\beta}{\omega + i\eta}\frac{n_{e0}}{n_{i0}}\right) + \chi_d = 0$$

where $\beta = \mid I_{e0}/e(\mid n_{0d}/n_{0e})$. Typically $\mid \omega \mid < \eta$ and we get reactive corrections of order $\beta/\eta \simeq (n_{d0}/n_{e0})(Ta/e^2) \ll 1$ to χ_e, χ_i. This effect is negligible. In the special case when $\mid \omega \mid > \eta \simeq 10^{-2}\omega_p(n_{e0}a/n_{i0}\lambda_D)$, we get an additional damping of dust acoustic waves

$$\gamma = -\frac{\nu_{dn}}{2} + \frac{\nu_{in}}{2\left(1+\tau^*\right)^2}\left[\alpha\frac{\nu_{in}\nu_R}{k^2v_{thi}^2} - \tau^*\frac{C_{d*}^2}{v_{thi}^2}\right]\left(1 - \frac{kv_0}{\omega_R}\right) - \frac{1}{2}\frac{n_{d0}}{n_{e0}} \mid \frac{I_0}{e} \mid \frac{\omega_{d*}^2}{(\omega_{d*}^2 + \alpha\nu_{in}\nu_R)} \quad (13)$$

We may next investigate the effect of electron and ion temperature fluctuations on these instabilities. For simplicity we consider only the streaming instabilities with $\nu_R = 0$. When the waves satisfy the inequalities

$$(m_iT_e/m_eT_i)^{1/2}(k^2v_{the}^2/\nu_{en}^2) \gg 1 \sim (k^2v_{thi}^2/\nu_{in}^2) > (kv_0 - \omega)/\nu_{in}$$

the electron temperature fluctuations are washed out by thermal conduction effects but ion temperature fluctuations are finite. In this limit the growth term due to streaming effects is the same as before with ν_{in} replaced by ν_{in}^{eff}:

$$\nu_{in}^{eff}/\nu_{in} = 1 + 1/\left(\hat{K}_i + \frac{3}{2}\frac{m_i}{m_n}\frac{\nu_{in}^2}{k^2v_{thi}^2}\right)$$

The second term arises due to ion–thermal conduction and ion–neutral energy exchange and contributes to the growth as before; this growth has similarities to ion–acoustic instabilities driven by electron streaming in a collisional plasma[16,17]. For very long wavelengths $k^2v_{the}^2/\nu_{en}^2 \sim m_e/m_i \ll 1$, we have a situation with $\delta T_i, \delta n_i \to 0$ and $\delta\tilde{T}_e \neq 0$; we then get similar effects as above due to electron thermal conduction and electron–neutral energy exchange.

We now consider the effect of strong correlations in the dust fluid[13]. It is widely known that the dust fluid often satisfies the condition of a strongly coupled coulomb plasma, $\Gamma = (Z_de)^2/a_gT_d > 1$ where $a_g \sim n_d^{-1/3}$ is the intergrain distance. This is especially true with a significant background pressure of neutrals because neutrals cool the dust. When $\Gamma \sim 10^3$, Coulomb crystals of the dust fluid form and have been seen in laboratory experiments. For $1 < \Gamma < 10^3$, the crystal melts and we have a molten dust fluid with strong correlations. It is possible to treat collective modes in such fluids with a generalized hydrodynamic model[13].

This model contains some viscoelastic transport coefficients in the equations for the dust fluid, which for weak correlations act like dissipative viscosity whereas for stronger correlations, take the form of dispersive elasticity. The generalized hydrodynamic eqn. of motion is written in the form

$$\left(1+\tau_m\frac{\partial}{\partial t}\right)\left[\frac{\partial}{\partial t}\vec{v}_d-\frac{eZ_d}{M_d}\vec{\nabla}\phi+\frac{\vec{\nabla}p_d}{n_{d0}M_d}\right]=\eta\vec{\nabla}\cdot\nabla\vec{v}_d+\left(\zeta+\frac{\eta}{3}\right)\nabla\left(\nabla\cdot\vec{v}_d\right) \tag{14}$$

In one dimension as $\omega\tau_m\to 0$, we recover the Navier-Stokes fluid equations with $(\zeta+(4/3)\eta)$ taking the role of a viscosity coefficient. For $\omega\tau_m\to\infty$, η/τ_m and ζ/τ_m act as shear and bulk modulii of elasticity, respectively and support elastic waves. For times of order τ_m, the strongly correlated fluid acts as an amorphous solid with aspects of rigidity, elasticity etc. For longer times, the 'solid' changes to new amorphous configurations and acquires fluidity as a highly viscous fluid. Molecular dynamics simulations and various approximation schemes from statistical mechanics of strongly correlated systems are used to derive expressions for the various phenomenological coefficients used in generalized hydrodynamics. Thus the viscoelastic relaxation time τ_m is given by

$$\tau_m=\left[\left(\frac{4}{3}\eta+\zeta\right)/\left(T_{d0}/M_d\right)\right]\left[1-\gamma_d\mu_d+\frac{4}{15}\frac{E_c}{n_{d0}T_d}\right]^{-1}$$

where γ_d is the adiabatic index and the compressibility μ_d is given by

$$\mu_d=T_d^{-1}\left(\partial P/\partial n\right)_T=1+E_c/n_{d0}T_d$$

and the correlation energy E_c is given by :

a) weakly coupled plasmas[16] ($\Gamma<1$)

$$u\left(\Gamma\right)=\frac{E_c}{n_{d0}T_d}\simeq-\frac{\sqrt{3}}{15}\Gamma^{3/2}$$

b) strongly coupled plasmas[19] ($1<\Gamma<200$).

$$u\left(\Gamma\right)=-0.89\Gamma+0.95\Gamma^{1/4}+0.19\Gamma^{-1/4}-0.81$$

and the dependence of η, ζ on Γ is quite complex and is usually given in the form of tabulated results and/or curves obtained from molecular dynamics simulations.

Using the generalized hydrodynamics model we may now derive a new expression for χ_d and get the dispersion relation :

$$0 = 1 + \frac{1}{k^2\lambda_e^2} + \frac{1}{k^2\lambda_i^2} - \omega_{pd}^2 / \left[\omega^2 - \gamma_d \mu_d k^2 v_{thd}^2 + i\omega k^2 \left(\frac{4}{3}\eta + \zeta\right) / \left(1 - i\omega\tau_m\right)\right]$$

For $\omega\tau_m \ll 1$, the dispersion relation may be solved to give

$$\omega_R^2 = \omega_{pd}^2 \left[\gamma_d \mu_d k^2 \lambda_d^2 + k^2\lambda_p^2 / \left(1 + k^2\lambda_p^2\right)\right]$$

$$\frac{\gamma}{\omega_R} = -\left(\frac{4}{3}\eta + \zeta\right) k^2 / 2\omega_R \;\; ; \;\; \lambda_p^{-2} = \lambda_e^{-2} + \lambda_i^{-2}$$

For $\Gamma < 1$, this gives standard damping due to viscous effects. As Γ increases, the viscosity goes through a minimum from 1 to 10 and then rises rapidly as Γ exceeds 10^2. The real part shows that $\omega_R \to \omega_{pd}$ for $k\lambda_p \gg 1$ and $\Gamma < 1$; however, as Γ crosses $10 - 10^2$, ω_R drops at high k due to μ_d terms which change sign. Thus the phase velocity at high k is reduced and the growth characteristics of streaming instabilities discussed above will be modified. Similarly, for $\omega\tau_m > 1$, the viscous damping contributions disappear but the 'elastic' terms give modifications to the phase velocity

$$\omega_R / k v_{thd} = \left[1 + \frac{4}{15} u\left(\Gamma\right) + \left(\lambda_p^2/\lambda_d^2\right) / \left(1 + k^2\lambda_d^2\right)\right]^{1/2}$$

Note that $u(\Gamma) < 0$ and typically reduces the phase velocity.

Finally, we make some comparison with experimental results and make a few remarks about nonlinear aspects of these instabilities. In the experiments of Prabhakara and Tanna[5], ion drift effects seem to dominate since the neutral pressure is low and the dust particles are held by sheath electric fields against gravity ; in this region $n_n \simeq 2.10^{13}$ cm^{-3}, $n_d \simeq 10^3$ cm^{-3}, $n_i \simeq 10^8$ cm^{-3} , $m_i/m_d \simeq 10^{-11}$, $Z_d \simeq 10^4$, $V_0/c_s \simeq 1$, $\lambda \simeq 1$ cm, and we find $\omega_R \sim \gamma \sim 10$ sec^{-1}. The experiments of Prabhuram and Goree[6] are in the range of high neutral pressures and we expect recombination effects to play a role. Thus, taking $n_n \simeq 2.10^{16}$ cm^{-3}, $n_i \simeq 5.10^{10}$ cm^{-3}, $m_i/m_d \simeq 5.10^{-8}$, $Z_d \simeq 2.10^2$, $n_d \simeq 10^8$ cm^{-3}, $V_0 \sim 0$, we find that for $\lambda \sim 2$ cm $\gg \lambda_f \sim .005$ cm, $\omega_R \sim 5$ sec^{-1} and $\gamma \sim 1$ sec^{-1}. The growth here is due to recombination instability.

We have also examined the nonlinear aspects of the streaming and recombination instabilities[12]. For short wavelengths with $\nu_R = 0$, we find that the nonlinear equation is a Korteweg de Vries equation with ion streaming source terms on the right side. Solving this equation perturbatively we find that the instability leads to the growth of k–dv solitons of dust acoustic waves which finally saturate at an amplitude where the propagation speed matches the ion drift speed. For the long wavelengths driven by recombination effects (with $V_0 = 0$) the nonlinear equation turns out to be a nonlinear Schrodinger equation with appropriate sources. In one dimension, this predicts envelope soliton solutions at saturation. However, in more than one dimension,this equation predicts a 'collapse' of waves with localized regions of high intensity pushing the dust out and creating 'voids' and 'cavities' in the dust density[6].

To sum up, we have investigated collisional instabilities in a dusty plasma with a background of neutrals. We find,

1. A short wavelength instability driven by ion drift effects. In the ion frame it is a negative energy wave driven by ion dissipation. Nonlinearly it breaks up into a collection of k-dv solitons.

2. A long wave instability driven by recombination on dust particles physically related to localized quenching of the discharge at dust compressions. Nonlinearly it generates envelope solitons in 1-d and collapsing cavities in 2 and 3 dimensions.

3. Important modifications of wave dispersion in the strongly correlated regime $\Gamma > 1$ as seen by a Generalized Hydrodynamics model for the dust fluid with characteristic viscoelastic transport coefficients. Further work on physics of transverse shear waves and nonlinear equations in such generalized fluids with 'memory' is in progress.

References

1. Physics of Dusty Plasma, Proc. of VI Workshop in Dusty Plasma, La Jolla, Calif., USA, 22-25 March (1995)., Eds. P.K. Shukla, D.A. Mendis and V. Chew [World Scientific, Singapore]
2. C.K. Goertz, Rev. Geophys.27, 271 (1989)
3. D.B. Graves, IEEE Trans. on Plasma Science 22,31 (1994)
4. H. Ikezi, Phys. Fluids 29, 1764 (1986)
5. H.R. Prabhakara and V.L. Tanna, Phys. Plasmas 3,3176 (1996)
6. G. Prabhuram and J. Goree, Phys. Plasmas 3, 1212 (1996)
7. A. Barkan, R.L. Merlino and N.D'Angelo, Phys. Plasmas 2, 3563 (1995)
8. J.H. Chu and I. Lin, Phys. Rev. Letters 72, 4009 (1994)
9. N.N. Rao, P.K. Shukla and M.Y. Yu, Planet Space Sci. 38, 4 (1990)
10. M. Rosenberg, Planet. Space Sci. 41, 229(1993)
11. N.D'Angelo, J. Phys. D (Appl.Phys.) 28, 1009 (1995)
12. P. Kaw and R. Singh, Phys. Rev. Letters 79, 423 (1997)
13. P. Kaw and A. Sen, to be published
14. F. Melanso, Physica Scripta 45, 515 (1992)
15. M.R. Jana, A. Sen and P.K. Kaw, Phys. Rev. E 48, 3930 (1993)
16. B. Coppi and E. Mazzucato Phys. Fluids 14, 134 (1971)
17. T.D. Rognlien and S.A. Self, Phys. Rev. Letters 27, 792 (1971)
18. S. Ichimaru, H. Iyatomi and S. Tanaka, Phys. Reports 149, 91(1987)
19. W.L. Slattery, G.D. Doolen and H.E. DeWitt, Phys. Rev. A 21, 2087 (1980)

Dynamical behaviors of strongly coupled dusty plasmas: from crystal to chaos

Lin I, Wen-Tau Juan, and Jeng-Mei Liu
Department of Physics, National Central University, Chungli, Taiwan 32054, Republic of China

A dusty plasma system consits of many fine dust particles immersed in a gaseous plasma background. In this strongly coupled system, the presence of dust particles with large charges and masses adds new degrees of freedom with slow time scale, modifies the dielectric properties, and generates many interesting ordered to disordered behaviors which can be directly monitored through an optical microscopes. In this paper, our recent studies on the dynamcial behaviors of different states from crystal, melting, liquid, dust density sliton, waves, etc. of a strongly coupled dusty plasma with micrometer size SiO_2 suspensions in a low pressure rf argon discharge are reviewed. Our new first finding of the stable few body structures are also presented.

The dusty plasma is a plasma system consisting of massive dust particles suspended in a gaseous background of electrons and ions. It widely exists in various places from astroplasma to laboratory plasma systems [1,2]. Typically, with a few ev electron temperature, a micrometer dust particle can be charged up to a few or a few tens of thounsands electrons. It turns the systems into a strongly coupled Coulomb system. By properly increasing the coupling constant which is defined as the ratio of the pair Coulomb interaction energy to the random thermal energy, the system is expected to condense from the disorded plasma phase to the ordered solid phase [3]. Comparing to the typical atomic-scale solid or liquid systems in nature, the dusty plasma has the advantage of directly observing the particle dynamical behavior through optical imaging technique due to the large dust particle size and proper time scale. Recently, after the theoretical prediction of dusty plasma crystals by Ikezi [4], the formation in dusty plasma systems of crystals, liquids and density waves have been demonstrated in our and other laboratories [5-8]

The dusty plasma provides a bridge connecting the condense matter physics and plasma physics. From the condense matter side, in addition to the structures, the subjects such as the microscopic motions of particles in the crystals, liquids, phase transitions, defect dynamics, etc. are open and interesting issues. From the plasma physics side, the addition of dust particles adds new degrees of freedom. They are strongly coupled to the background plasma. It not only changes the dielectric property of the plasma, which in turn modifies the existing high frequency waves, but also directly respond to the low frequency electric field fluctuations. It generates new type of macroscopic collective excitations, induces stochastic heating and affects particle trapping and transport. In addition, the typical rf laboratory dusty plasma is a nonlinear open dissipative system which generates many interesting self-organized nonlinear behaviors. In this paper, in addition to the brief review of the typical motions from the crystal, melting, and states, we further concentrate on the dynamical behaviors of the collective motions and anomalous diffusions in the melting state, the self-organized low-frequency dust density waves and solitions, and the induced dust particle motions. Our recent finding of the stable few body structure is also presented.

The experiment is conducted in an annular radio-frequency (rf) dusty plasma trap described elsewhere [5]. SiO_2 particles with about 10 micrometer diameter are generated through gas-phase reaction and aggregation by introduing oxygen and silane gases into the lower pressure rf argon discharge and are confined in an annular plasma trap. Increasing the rf power can increase background plasma fluctuation which increases the effective temperature. Particle motion is monitored with a digital video recording system through an optical microscope. The optical axis is along the vertical axis of the system. For the density wave study, the plasma trap is modified to make particles only confined in a closed torus between two concentric electrodes. The plasma emission, the scattered light from a point measurement, and the microscopic particle motions are simultaneously monitored.

In the dusty plasma, the dust particles are Debye-shielded by the background electrons and ions. Basically, particles are interacting through Yukawa type interaction. However, the ion focusing behind the particle due to the ion flow or due to the overscreening by the wake flow can generate dipole-interaction in addition to the mono-pole interaction [9,10]. At low rf power, dust particles can be condensed into highly ordered crystal state. Besides the observation of the bcc, fcc, hcp, structures usually observed for other systems with mono-pole interactions, the observation of the hexagonal cylinder structure with c-axis aligned with the ion flow is the unique feature of the dusty plasma system when the particle dimeter is large enough [5]. Namely, in the vertical plane, particles form oscillating polymer chains. In the horizontal plane, particles are self-organized in a hexgonal lattice oscillating around their equilibrium positions (Figure 1)

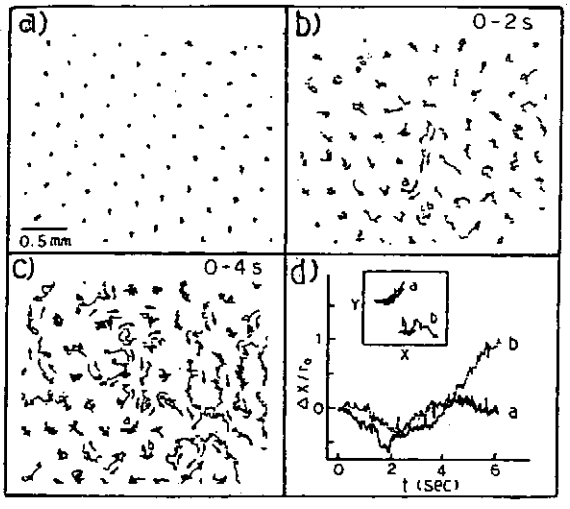

Fig. 1. (a) Trajectories of the hexagonal state (5-s exposure time and 15 Hz sampling rate). (b) and (c) Evolution of a typical liquid state with 15 Hz CCD frame rate. The arrows indicate the direction of motion. (d) Partially corelated particle displacement normalized by the mean particle distance (r_o) of a pair of adjacent particles (particle a and b in Fig.1 (c))

As rf power increases, the systems can be turned into the liquid state. Figure 1(b) and (c) show that particles no longer oscillate around their equilibrium lattice sites [11,12]. They loose their long range translation and orientation orders. However, the nearby particles still show quite similar displacements (Figure 1(d)) [11]. Namely, in the liquid state, the adjacent particles are still strongly correlated and the system is still quite imcompressible. The thermally induced collective rotational motion can be observed from Figure 1(c) with longer exposure time.

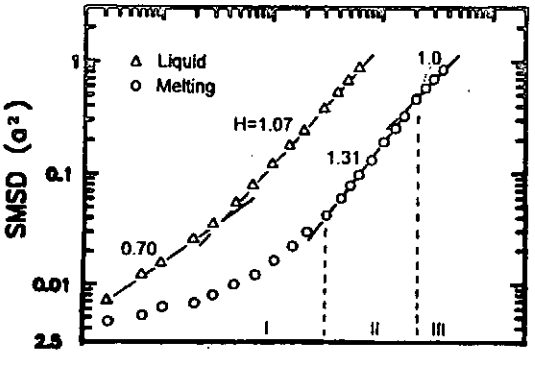

Fig. 2. The SMSD versus time for the melting and liquid state.

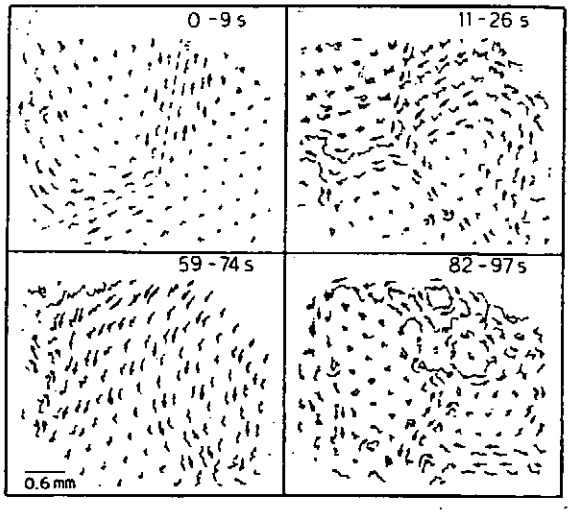

Fig. 3. The evolution of the melting state under a fixed control condition.

The state around melting is a state where the long range correlation due to Coulomb interaction starts to be deteriorated by thermal excitation. Figure 2 shows the single particle

mean square displacement (SMSD) of the system in the melting and liquid states. The double logrithmic plot shows regimes with different slopes (i.e. the power law has different scaling exponent H). In the melting state, H < 1 for the small spatial and temporal scale. H then becomes 1.31 when the root mean square displacement RMSD > 0.2 a (a is the mean lattice constant). H returns back to 1 when RMSD > 0.7 a. For the liquid state, H directly switches from the antipersistent regime with H = 0.7 to the almost normal regime with H = 1.07 when RMSD > 0.2 a [13].

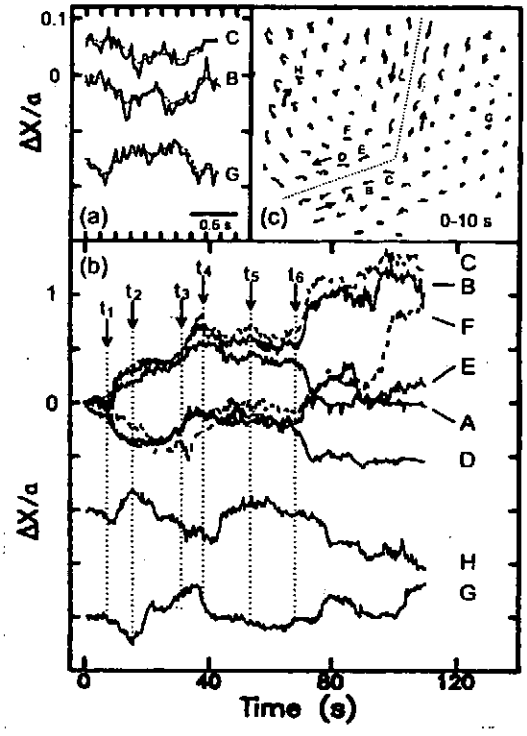

Fig. 4. (a) and (b) The typical short and long time particle displacements along the x axis in the melting state with 0.3 and 1/30 s frame rates respectively. Their corresponding positions can be found in (c) which shows the 2-D trajectories over 10 s.

Figure 3 shows a serious sequential pictures of the melting state at fixed control parameters. Basically, the systems runs through different micro-states with many self-excited rotational domains. Although the Coulomb coupling is weaken, it is still strong enough to hold collective motion in a finite domain. The domain is usually quite hard and supports strong shears around the domain boundaries. The time evolutions of the displacement of the adjacent particles in the system show strong correlation (Figure 4). They usually remain similar untill the onset of the sudden jump. Namely, the excitation and relaxation of the collective rotational motion follows a "stick-slip" rule similar to the case of earth quake [13]. As time evolves, rotational domains are excited, relaxed and reorganized. The sudden jump and the following small amplitude oscillation corespond to the slipping and sticking period respectively. Figure 3(a) shows the uncorrelated small amplitude high frequency oscillation of the neighboring particles. However, when the time scale reaches 0.5 sec, particle motion becomes correlated spatially. Namely, each particle is caged by its surrounding neighbors. The initial anti-persistent diffusion with H < 1 is due to the caged effect. For the motion with lower frequency (longer time scale), the collective rotation or vibration dominate. The strain-energy graudally builds up in the sticking period as SMSD gradually increases. The strain energy is suddenly converted to the kinetic energy and sudden slip occurs. The system reneters the sticking period once the relative particle displament for the particle crossing the domain boundary reaches about one lattice constant and the lattice can be realigned. The temporal correlation in the sticking and sliping period makes H > 1. For scale larger than 1 a the rotational motion is random phased due to the relaxation and reexitation processes, H returns to the value of the normal diffusion. For the liquid phase, the sytem is not so brittle due to the weaker coupling constant. This almost imcompressible system still supports rotation motion but it is no longer stick-slip type. Domains are continuously excited and relaxed

without a typical time scale as long as RMSD > 0.2 a which is the Linderman criteria. H therefore directly switches from smaller than 1 to almost equal to 1.

The domain motion around the melting distorts the lattice and generates topological defects. The defects are mainly free-dislocations with bonded 5-7 pairs and move along the directions of their Burgers vectors. The systems can be treated as a strongly coupled defect gas interacting with each other through the four basic processes, defect generating, annhilation, dissociation and recombination. The details are described elsewhere [12].

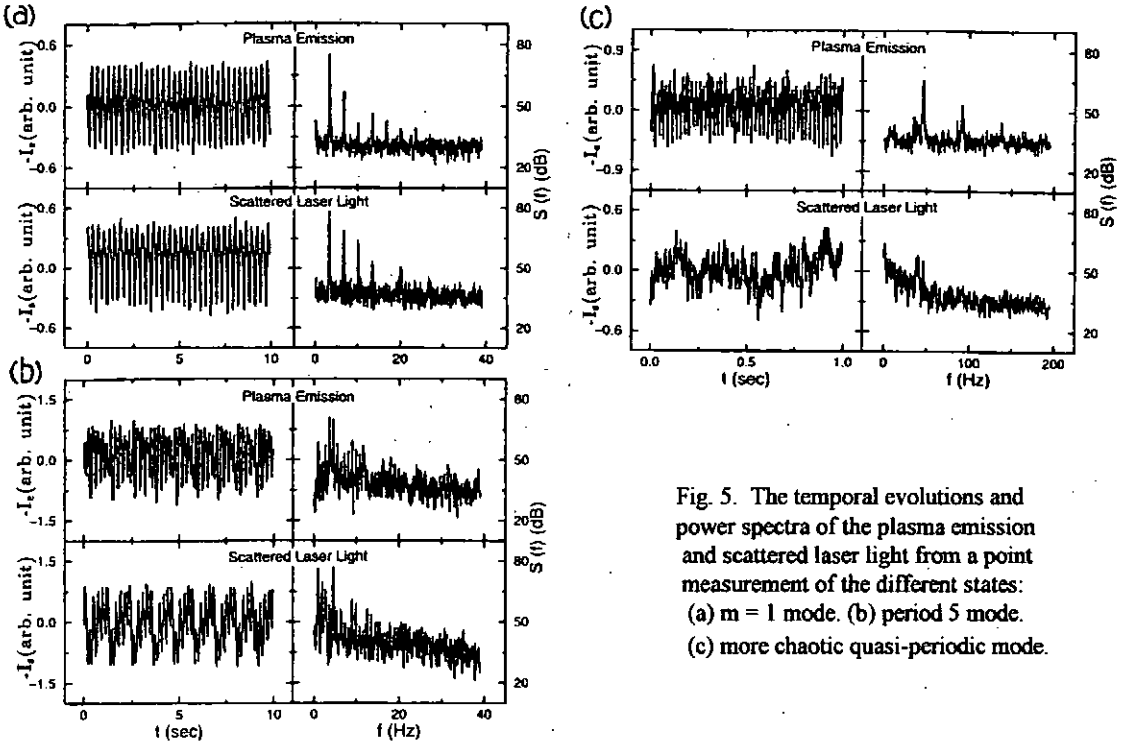

Fig. 5. The temporal evolutions and power spectra of the plasma emission and scattered laser light from a point measurement of the different states: (a) m = 1 mode. (b) period 5 mode. (c) more chaotic quasi-periodic mode.

The rf discharge is an open nonlinear system. Even in the absence of particles, the stationary rf discharge alone exhibits self-organized order to spatio-temporal disorder behavior in the macroscopic scale as rf power increases [14]. The presence of particles in the higher power state not only alters the nature of the existing plasma waves but also introduces low frequency dust density waves which is directly associated with the motions of dust particles.

Figure 5(a) shows the time evolutions and the power spectra of the plasma emission intensity and the intensity of the scattered laser light from the dust particles for a self organized 5 Hz dust density wave with m =1 in a toroidal discharge cell at 10 W rf power, 30 mTorr Ar pressure and 65 G magnetic field. The discharge is driven radially in the torus between the two concentric electrodes. The intensity of the scattered laser light is proportional to the local dust density. Increasing the rf power can drive the dust density wave to the chaotic state through the period-n tupling process. Figure 5(b) and (c) shows the corresponding information of the plasma emission intensity and the scattered laser light intensity for a period-5 state at 11.1 W and 65 G, and a more chaotic quasi-periodic mode at 35 W and 54G respectively.

In the dust density wave, the particle motions are also modulated by the associated fluctuating electric field. Through our microscope, we observe that dust particles are in the liquid state for the m = 1 mode. They move cyclically not only in the vertical plane normal to the azimuthal direction but also with an azimthal component as the wave passes by. The energy of particle can be as high as a few Mev which indicates that the particles are pushed by the strong oscillating space charge field which can reach a few tens of v. The regions with different ionization degrees have different dark space thickness and field intensity. The electric field also has an azimuthal component. For the chaotic mode with high frequency component, the power spectrum of the intensity of the scattered light has a large low-frequency floor (Fig.

5(c)). It indicates that the particles can not fully respond to the high frequency field and there are some nonlinear low frequency conversion processes which causes the low frequency floor.

Basically, this system is an open dissipative system driven by the strong radial inhomogeneity. The low frequency wave is a consquence of the interplay between the ionization instability and the elastic oscillation of the liquid state dust particle system [14]. The unfrozen electron impact ionization process, which has been usually neglected in the low frequency dusty wave studies, plays a source role similar to the reaction process in a chemical reaction system. Its rate is controlled by the local electron density and energy gained from the dark space field, which provides a positive feedback. The ambiplor diffusion and field induced drifts provide spatial coupling. The strong varying dark space field drives the dust particle motion which in turn modifies the spatial plasma density and electric field distribution through the electric field generated by their large charges and through the direct dust charging and electron releasing processes. The large dust inertia slows down the frequency to a few or a few tens of Hz. From the nonlinear dynamics point of view, the generation of self-organized standing waves are through the spontaneous breaking of the rotational symmetry. The observation of the period-n and quasi-periodic states manifest that, for such a complicated system, the universal dynamical behaviors are still followed as in many other differnet extended systems.

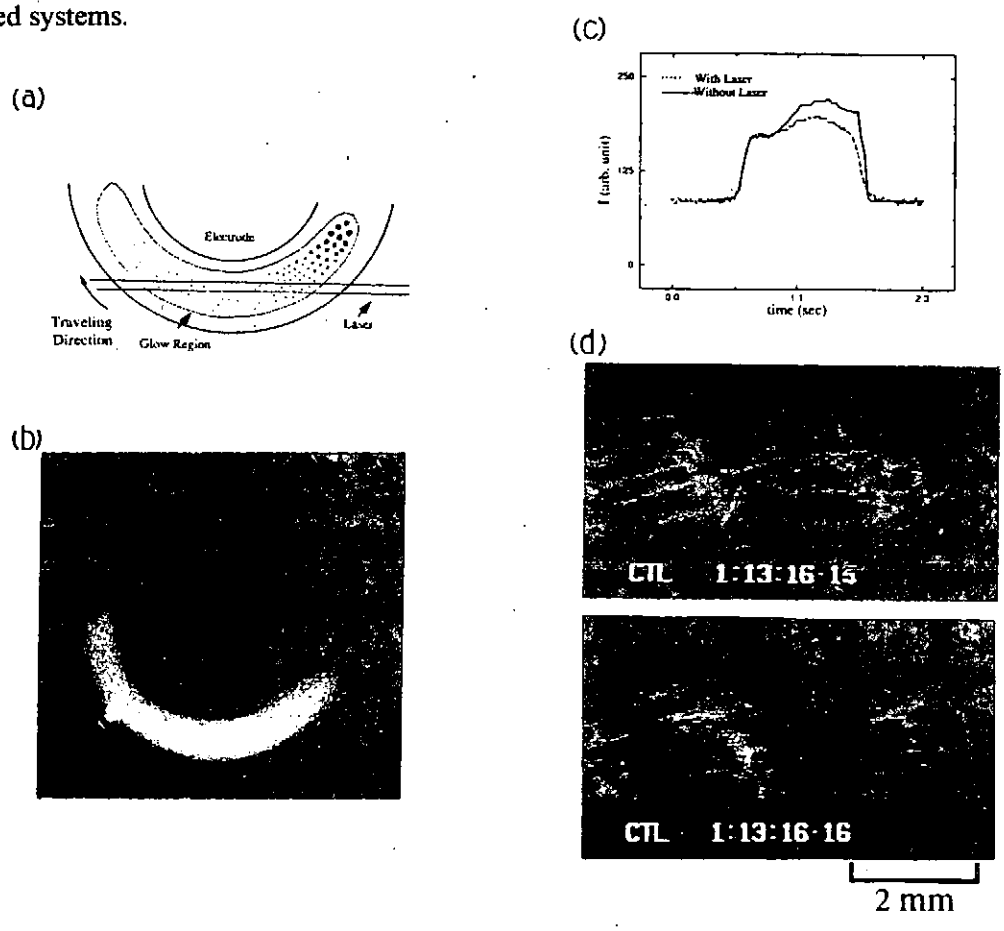

Fig. 6 (a) The sketch of the dust distribution in a solitary wave. (b) The corresponding image of the plasma emission. The bright horizontal line is the scattered laser light. (c) The time evolution of the intensity of the light from a point on the laser path under the traveling soliton.. Broken line: the plasma emission with laser off. Solid line: the total intensity with laser on. (d) Two sequential microscopic snap shots with 15 msec exposure time showing the dust density wave in the rear part of the soliton.

In addition to the m = 1 mode and the chaotic mode, the system can also be switched to a highly localized mode at very low power before the whole discharge turns off [15]. Figure 6(a) and (b) show the sketch and plasma emission image of the localized structure. Figure 6(c) shows the evolution of the point emission intensity with laser light on and off as the solition

travels through that point. The difference (i.e. the scatter laser light intensity) indicates that the larger dust particles are trapped in the rear part and move along with the localized structure. In the moving frame with the structure, a travelling wave with strong moduations on density and velocity on the trapped particle are found. Figure 6(d) shows the typical image of the particle trajectory with 15 msec exposure time. Namely, unlike the cyclic local modulation by the traveling wave, the strongly localized clump provides strong electric field to force the dust particles move with it. Particles with larger diameters suffers from larger ion drag and neutral flow. They are pushed to the rear part of the trap and the density waves are thereby self-excited in the trap. Note that in the dust-free discharge, localized ionization soliton also exists. However, they have a few times narrows spatial distribution.

In our recent study, by properly designing a new trap, we also found some interesting few body structures in addition to the many body systems mentioned above. Figure 7 shows the typical dimond shape and pentagon structures of the 4 and 6 body systems respectively. We were able to generates 1 to 3 D systems with a few to a few hundred dust particles. The details will be presented shortly.

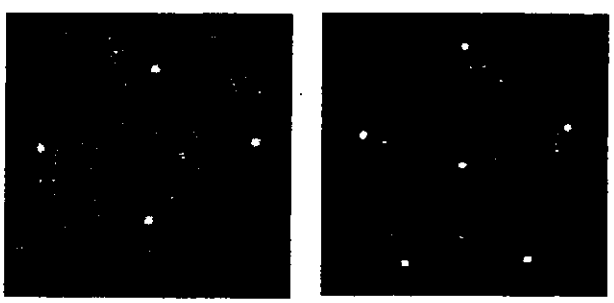

Fig. 7. The typical 4 and 6 body structures.

References

[1] C.K. Goertz, Rev. Geophys. 27, 271 (1989).
[2] D.A. Mendis and M. Rosenberg, Annu. Rev. Astron. Astrophys, 32, 419 (1994)
[3] S. Ichimaru, Rev. Mod. Phys. 54, 1017 (1982).
[4] H. Ikezi, Phys. Fluids 29, 1764 (1986).
[5] J.H. Chu and Lin I, J. Phys. D, 27, 296 (1994); J.H. Chu and Lin I, Phys. Rev. Lett, 72, 4009 (1994).
[6] Lin I, C.S. Chern, J.H. Chu, J.M. Liu and J.B. Du, Physica A 205, 443 (1994).
[7] Y. Hayashi and K. Tachibana, Jpn. J. Appl. Phys. 33, 804 (1994).
[8] H. Thomas, G.E. Morfill, V. Demmel, J. Goree, B. Feuerbacher, and Mohmann, Phys. Rev. Lett, 73, 652 (1994).
[9] S. Vladimirov and M. Nambu, Phys. Rev. E. 52, R2172 (1995).
[10] F. Melandso and J. Goree, Phys. Rev. E. 52, 5312 (1995).
[11] Lin I, W.T. Juan, C.H. Chiang, and J.H. Chu, Science, 272, 1626 (1996).
[12] C.H. Chiang and Lin I, Phys. Rev. Lett, 77, 647 (1996).
[13] W.T. Juan and Lin I, to be published.
[14] e.g. J.H. Chu and Lin I, Phys. Rev. A. 39, 233 (1989); Lin I and J.M. Liu, Phys. Rev. Lett, 74 3161 (1995).
[15] J.M. Liu and Lin I, to be published.

Simulation Study of Magnetic Reconnection

Ritoku Horiuchi
Theory and Computer Simulation Center,
National Institute for Fusion Science,
Toki 509-52, Japan

Abstract

Dynamical process of collisionless driven reconnection is investigated by means of a two-and-one-half-dimensional particle simulation. Magnetic reconnection develops in two steps in accordance with the formation of ion and electron current layers. The dominant triggering mechanism for electron phase changes from electron meandering motion effect to electron inertia effect as a longitudinal magnetic field increases. It is also found that the energy conversion takes place from electrons to ions through the action of an electrostatic field excited in the downstream and thus the average ion temperature becomes about 1.5 of the average electron temperature.

1. Introduction

Magnetic reconnection[1] can lead to fast energy conversion from the field energy to the particle energy as well as a topological change of magnetic field. If a current-carrying particle is lost from a current layer, an electric field is induced so as to accelerate a particle along the equilibrium current and compensate it for the momentum loss. This electric field also plays a role in changing the topology of magnetic field, i.e., magnetic field reconnection. Magnetic reconnection, however, can not take place in an ideal magnetohydrodynamic (MHD) plasma because magnetic field is frozen in a plasma. This means that non-ideal effect, which breaks the frozen-in condition and leads to the generation of electric field, is needed for the excitation of magnetic reconnection.

In two-dimensional system there exist two types of microscale particle kinetic effect which are responsible for the decoupling of magnetic field from the particle motion in a collisionless plasma. One is the particle inertia effect which becomes significant in a spatial scale comparable to collisionless skin depth.[2,3,4] The other is the particle orbit effect which becomes effective in an excursion scale of particle thermal motion which is called a

meandering motion.[5,6,7] In this paper we will discuss the physical process of collisionless reconnection for the case where the system is subjected to an external driving flow, i.e., " collisionless driven reconnection ".

2. Simulation Model

Let us consider two-dimensional open system where physical quantities are translationally symmetric in the z-direction ($\partial/\partial z = 0$). Two types of particle simulation codes are used for this analysis. One is the standard explicit electromagnetic (EM) code,[8,9] and the other is the semi-implicit EM code.[6,7] As an initial condition we adopt a one-dimensional equilibrium with a sheared magnetic field as

$$\mathbf{B}(y) = [B_0 \tanh(y/L), 0, B_{z0}], \tag{1}$$

where B_0 and B_{z0} are constants and L is the scale height along the y-axis.

In order to drive magnetic reconnection at the center of the simulation domain we adopt an input boundary condition[6,8] at the boundary of the y-axis ($y = \pm y_b$) and a periodic boundary condition at the boundary of the x-axis ($x = \pm x_b$). At the input boundary the plasma is smoothly supplied with the $\mathbf{E} \times \mathbf{B}$ drift velocity into the simulation domain. The driving electric field is determined so as to be always normal to both the magnetic field and the input flow velocity. The amplitude of driving electric field $E_{d0}(x,t)$ is taken to be zero at $t = 0$ and gradually increases for an initial some period After this period, $E_{d0}(x,t)$ is described by a symmetric constant profile with a maximum input rate of magnetic flux E_0 at the center of the input boundary.

3. Two-step evolution of collisionless driven reconnection

Generation of electric field along the equilibrium current is needed for driving magnetic reconnection. Figures 1 and 2 show (1) the temporal evolution of reconnection electric field $E_z^{(1)}$, and (2) those of four spatial scales for the case of $B_{z0} = 0$ where d_h, d_{jz}, l_{mi}, and l_{me} are the half-width of the mass density profile, that of the current density profile, an excursion distance of ion meandering motion, and that of electron meandering motion, respectively. The electric field begins to grow slowly as soon as both d_h and d_{jz} start decreasing as a result of the compression by the convergent plasma flow in the slow

reconnection phase ($0.6t_A < t < 1.3t_A$). The width of the current layer is almost the same or a little larger than the ion thermal scale l_{mi} in this phase (" ion current layer "). Because most of the ions are unmagnetized in the ion current layer while the electrons are magnetized, the input flow (Poynting flux) no longer works on thinning the ion current layer, but it continues to compress the electron profile. Thus, electron current layer is created inside the ion current layer due to a finite ion Larmor radius effect. When the fast reconnection phase ($1.3t_A < t < 1.8t_A$) sets in, the inclination of the growth curve steepens suddenly and the half-width of electron current layer approaches the electron thermal scale l_{me}. These results lead us to the conclusion that the slow reconnection is triggered by the ion meandering motion effect while the fast reconnection is triggered by the electron meandering motion effect.

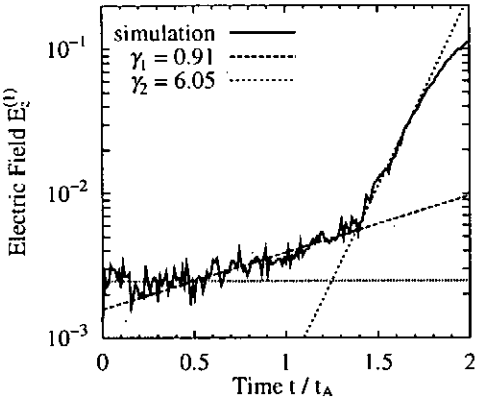

Figure 1: Temporal evolution of reconnection electric field.

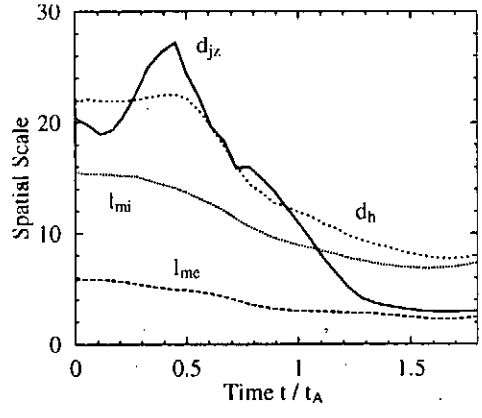

Figure 2: Temporal evolution of four spatial scales.

4. Reconnection mechanism

There exist two mechanisms associated with particle kinetic effect which lead to magnetic reconnection in a collisionless plasma. One is a particle inertia effect which becomes significant in a spatial scale comparable to collisionless skin depth c/ω_p. The other is a particle orbit effect which becomes effective in an excursion distance of particle meandering motion. Figure 3 illustrates the dependence of four spatial scales on the field ratio B_{z0}/B_0 when the current layer becomes thinnest in the fast reconnection phase. The width is nearly equal to the excursion distance of meandering electrons l_{me} and is two times as large as the electron skin depth c/ω_{pe} for the case of $B_{z0} = 0$. The excursion

distance l_{me} decreases as the longitudinal field increases. On the other hand, the electron skin depth increases is almost independent of B_{z0}/B_0. Thus, the relation $l_{me} < c/\omega_{pe}$ holds for the strong longitudinal field of $B_{z0} > 1.5B_0$. In other words, the electron inertia scale is longer than the electron thermal scale for $B_{z0} > 1.5B_0$. It is clearly seen in Fig. 3 that the width of current layer decreases with the electron thermal scale l_{me} until l_{me} reaches c/ω_{pe}. Once $l_{me} < c/\omega_{pe}$, the width ceases to decease and exhibits the same behavior with the electron skin depth. Namely, collisionless driven reconnection in the fast reconnection phase proceeds keeping the width of current layer nearly equal to the electron skin depth for the strong longitudinal field of $B_{z0} > 1.5B_0$. Thus, the triggering mechanism for collisionless driven reconnection in the fast reconnection phase changes from the electron thermal effect to the electron inertia effect in accordance with the increase of longitudinal magnetic field.

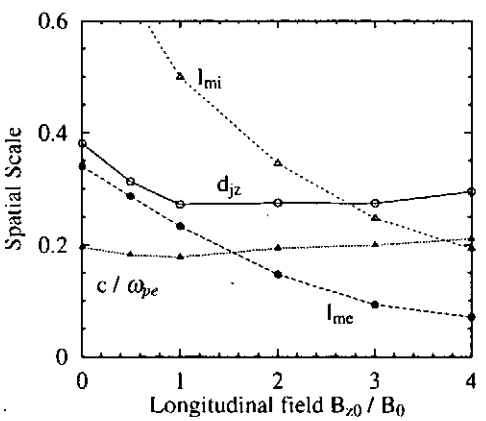

Figure 3: Dependence of four spatial scales on a logitudinal field.

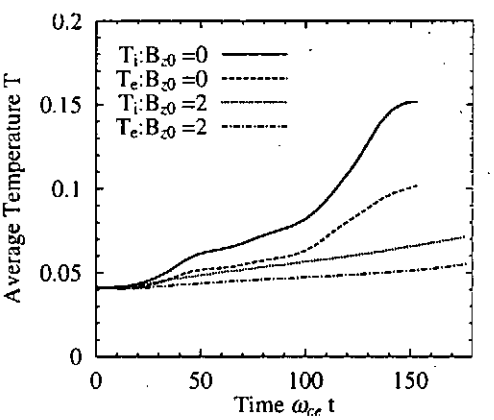

Figure 4: Temporal evolution of ion and electron temperature.

5. Energy conversion by electric field

The reconnection electric field leads to not only the topological change of magnetic field lines but also the energy conversion from the field energy to the particle energy through the acceleration and heating processes. Figure 4 shows the temporal evolutions of the average ion temperature T_i and the average electron temperature T_e for the cases of $B_{z0} = 0$ and $B_{z0} = 2B_0$. For the case of $B_{z0} = 0$, both the ion temperature and the electron temperature increase rapidly after the reconnection electric field becomes maximum ($t = 100\omega_{ce}^{-1}$). The saturation value of the ion temperature becomes about 1.5

of the electron temperature. The energy conversion occurs more actively in the plasma without any longitudinal magnetic field. These differences come from the nature of the energy conversion mechanism in the presence of the electric field, as will be discussed in the followings.

Let us decompose the electric field into the electrostatic component $\mathbf{E}_{st}$ and the electromagnetic component $\mathbf{E}_{mg}$, and the electric current into the ion current $\mathbf{j}_i$ and the electron current $\mathbf{j}_e$. The detailed examination of energy coversion rate $\mathbf{E} \cdot \mathbf{j}$ reveals that there are two spatial regions in which the energy conversion occurs actively, i.e., the vicinity of the reconnection point and the shock-like region in the downstream. The electromagnetic component $\mathbf{E}_{mg}$, which is dominated by the reconnection field E_z, acts on the particles in the vicinity of the reconnection point and leads mainly to the increase of the electron energy. On the other hand, the electrostatic field $\mathbf{E}_{st}$, which has only the x- and y-components, becomes significant at the shock-like region in the downstream, and leads to the rapid increase of the ion energy and the decrease of the electron energy.

The mechanism is as follows. Both the transverse component of magnetic field B_y and the strong electron current j_z are generated as a result of magnetic reconnection. When an electron moves outside the narrow reconnection area, it becomes magnetized to be accelerated along the x axis by the resultant $\mathbf{j} \times \mathbf{B}$ force. The electron acceleration becomes so strong that the average electron velocity in the downstream is much larger than the average ion velocity and the net electric current along the x axis appears in the downstream. The mass density profile is dynamically compressed by the magnetic flux which is carried by the divergent plasma flow. The electrostatic field is strongly generated in the region with steep density gradient due to the finite Larmor radius effect. This electrostatic field, in turn, works on decelerating the electron flow and accelerating the ion flow in the downstream, that is to say, the ambipolar interaction by the electrostatic field leads to the fast energy conversion from the electron energy to the ion energy in the downstream. These facts explain why the average ion temperature increases about 1.5 of the average electron temperature.

6. Summary

We have investigated the nonlinear development of collisionless driven reconnection

and the consequent energy conversion between particles and an electromagnetic field in a sheared magnetic field by making use of a two-and-one-half dimensional particle simulation. Collisionless reconnection develops in two steps in accordance with the formation of two current layers, i.e., ion current layer for the early ion phase and electron current layer for the late electron phase. The dominant triggering mechanism for the electron phase changes from electron thermal effect to electron inertia effect as the longitudinal magnetic field increases. Because the energy conversion takes place from electrons to ions through the action of an electrostatic field excited in the downstream, the average ion temperature becomes about 1.5 of the average electron temperature.

References

1. T. Sato and T. Hayashi, Phys. Fluids **22**, 1189(1979); T. Sato, T. Hayashi, K. Watanabe, R. Horiuchi, M. Tanaka, N. Sawairi and K. Kusano, Phys. Fluids B **4**, 450(1992).

2. D. W. Hewett, G. E. Frances and C. E. Max, Phys. Rev. Lett. **61**, 893(1988).

3. M. Ottaviani and F. Forcelli, Phys. Rev. Lett. **71**, 3802(1993).

4. D. Biskamp, E. Schwarz, and J. F. Drake, Phys. Rev. Lett. **75**, 3850(1995);B. Rogers and L. Zakharov, Phys. Plasmas **3**, 2411 (1996).

5. A. A. Galeev, *Basic Plasma Physics II* (North-Holland Physics Publishing, New York, 1984), p.305.

6. R. Horiuchi and T. Sato, Phys. Plasmas **1**, 3587(1994).

7. R. Horiuchi and T. Sato, Phys. Fluids B **2**, 2652(1990).

8. R. Horiuchi and T. Sato, Phys. Plasmas **4**, 277(1997).

9. C. K. Birdsall and A. B. Langdon, *Plasma Physics via Computer Simulation* (McGraw-Hill, New York, 1985).

STRUCTURE OF ALFVEN WAVES OF SMALL TRANSVERSE SCALE AND RELATION TO AURORAL PROCESSES

G.J. Morales, J.E. Maggs and J.R. Peñano

Department of Physics and Astronomy
University of California, Los Angeles
Los Angeles, CA 90095 USA

Abstract

A comprehensive theoretical and experimental study has identified key properties of shear Alfvén waves of small transverse scale that shed new insight into spacecraft observations and models of the auroral ionosphere.

Overview

Two outstanding problems related to the auroral ionosphere are:1) the acceleration mechanism responsible for the formation of energetic auroral beams (of energy 1 keV and larger), 2) the generation of a small population of ions with large perpendicular energy in the neighborhood of density striations. Although numerous scenarios have been proposed to solve these problems, no satisfactory answer has been found[1]. However, in recent years observations made by spacecraft[2] have stimulated great interest[3,4] in the role that shear Alfvén waves of small transverse scale length play in these auroral processes. By small it is understood that the transverse dimension is comparable to the electron skin-depth (in regions where the electron plasma beta, β_e, is smaller than the electron to ion mass ratio, i.e., $\beta_e<<m/M$) or comparable to the ion sound gyroradius ρ_s (in regions where $\beta_e>>m/M$). The reasons why these situations are of interest are that shear waves in this environment can develop substantial electric fields along the geomagnetic field (e.g., waves with relative magnetic fluctuations on the order of $\delta B/B\sim10^{-3}$, as are frequently observed, can give energy gains of 1 keV within one Alfvén wavelength) and the auroral ionosphere naturally sweeps a large range of β_e values. In addition, shear waves are susceptible to trapping and amplification within density striations having steep density gradients.

Our group at UCLA is presently engaged in a comprehensive theoretical and experimental effort that aims to illustrate key features of these waves and to establish a connection between controlled laboratory studies[5] and spacecraft observations. This presentation reports on some highlights of these studies. The theoretical problems investigated include : the intrinsic pattern of shear Alfvén waves radiated by small sources in the two extreme limits--inertial[6] and deeply kinetic; the stability of drift-Alfvén eigenmodes trapped[7] in narrow density and temperature striations; PIC simulations of narrow electron streams and the process of transverse ion acceleration resulting in the formation of density channels. The experimental studies have explored the properties of the spontaneous Alfvénic fluctuations generated within a controlled density striation[8,9], and have mapped the spatial pattern of Alfvén waves excited by small axial current modulators[10].

Excitation by Localized Axial Current Modulators

A useful model that illustrates the non-trivial spatial structure of shear Alfvén waves excited by narrow sources (a situation easily realized in the laboratory and encountered naturally in various space environments) consists of an azimuthally symmetric disk of radius, a, positioned perpendicular to the confining magnetic field and to which an oscillatory voltage is applied that induces axial current modulations at frequency ω. Using a cylindrical coordinate system (r,θ,z)

centered on the disk and with z along the ambient field, the complex amplitude of the wave magnetic field is calculated to be

$$\tilde{B}_\theta(r,z,w) = \frac{4\pi a j_0}{c}\int_0^\infty dk \frac{J_1(ka)}{k} J_1(kr) e^{ik_\parallel(k)z} \quad ,$$

where $k_{\parallel} = (\omega/v_A)[1+(k_\perp\delta)^2]^{1/2}$ for the inertial regime (Alfvén speed v_A larger than the electron thermal velocity v_e), and $k_{\parallel} = (\omega/v_A)[1+(k_\perp\rho_s)^2]^{-1/2}$ in the kinetic regime ($v_A << v_e$). j_0 is the current density delivered by the disk.

The fundamental quantity that determines the propagation path from a localized source is the ratio of the perpendicular group velocity, $v_{g_\perp}$, to the parallel group velocity, $v_{g_\parallel}$. In the inertial regime

$$\frac{v_{g_\perp}}{v_{g_\parallel}} = -\frac{\omega\delta}{v_A}\frac{k_\perp\delta}{\left[1+(k_\perp\delta)^2\right]^{1/2}}$$

which exhibits an asymptotic cone-like behavior (for $k_\perp\delta >> 1$) that maps the sharp features of the source along a cone angle given by $\tan\theta_c = (\omega/\Omega_i)(m/M)^{1/2}$, with Ω_i the ion cyclotron frequency. The physical significance of this angle is that it bounds the collisionless radial spread of current channels in plasmas having a low value of β_e. In the deeply kinetic regime

$$\frac{v_{g_\perp}}{v_{g_\parallel}} = \frac{\omega\rho_s}{v_A}\frac{k_\perp\rho_s}{\left[1+(k_\perp\rho_s)^2\right]^{3/2}}$$

This expression indicates that there is a maximum angle of energy propagation given by $\tan\theta_{MAX} = (\omega/\Omega_i)(\beta_e)^{1/2}/(2.6)$ for wave number $k_\perp\rho_s = (2)^{-1/2}$, and that for smaller angles two different wave numbers propagate simultaneously.

The characteristic radial pattern of the inertial regime is shown in Fig. 1. It consists of an inner part that increases with radius (current channel spreading) up to a position determined by the cone angle. The sharp corners of the disk exciter follow the cone trajectory (in r-z space) and at large r merge abruptly onto the asymptotic pattern that drops as 1/r (no axial current is induced beyond the cone boundary).

Figure 2 displays the radial structure in the kinetic regime. It consists of 4 regions: a Bessel function behavior for r<a, a near null at r≅a, and a driven Airy pattern for r>>a which merges onto the 1/r asymptotic region. For a fixed axial position z the location of the Airy maximum is determined by the maximum angle θ_{MAX}. An unusual feature of the kinetic regime is that the axial wavelength (and hence the parallel phase velocity) changes significantly with radius, as shown in Fig. 3. At large values of r the phase velocity is close to the Alfvén speed.

Alfvén Waves in Field-Aligned Striations

A controlled field-aligned striation whose scaled properties closely resemble those observed[2] in the auroral ionosphere has been formed[9] in the Large Plasma Device (LAPD) at UCLA. A schematic of the device and the striation is shown in Fig. 4. It is found that the steep gradients in plasma density and temperature at the edge of the striation trigger the spontaneous growth of drift-Alfvén eigenmodes that are trapped within the striation. Figure 5 shows excellent agreement between the theoretically calculated radial eigenfunction of the fastest growing mode (solid curve) and the experimental observation (open symbols). The theory solves exact

coupled equations for the (E_z, B_z) wave fields (i.e., not the approximate ϕ, A_z description) with the electron response calculated from a drift-kinetic equation with a Lorentz collision operator.

The perspective that emerges from these studies is that field-aligned striarions of width ~c/ω_{pe} are intrinsic generators of shear Alfvén waves that achieve $\delta B_\perp/B_0 \geq 10^{-3}$, as is observed in FREJA flights through narrow auroral arcs. The striations are robust, i.e., they support large oscillations and Alfvénic turbulence but are not destroyed by them, hence they provide a natural environment for parallel electron acceleration. The key question that needs an urgent answer is: How are field-aligned striations formed in magnetized plasmas?

Summary

Alfvén waves of small transverse scale exhibit intrinsic features that can result in strong energization of electrons and ions in magnetized plasmas. Their importance in auroral processes is presently a subject of great interest and suggests that related features may may worth considering in describing energy transport in magnetized plasmas.

Acknowledgement

This work is sponsored by the Office of Naval Research. The LAPD facility has been developed[11] at UCLA by Prof. W. Gekelman.

References

1. J.E. Borovsky, J. Geophys. Res. 98,6101 (1993)
2. K. Stasiewicz et al., J. Geophys. Res. 102, 2565 (1997)
3. A. Strelsov and W. Lotko, J. Geophys. Res. 100, 19,457 (1995)
4. E.V. Mishin and M. Förster, Geophys. Res. Lett. 22, 1745 (1995)
5. J.E. Maggs, G.J. Morales and W. Gekelman, Phys. Plasmas 4, 1881 (1997)
6. G.J. Morales, R.S. Loritsch and J.E. Maggs, Phys. Plasmas 1, 3765 (1994)
7. J.R. Peñano, G.J. Morales and J.E. Maggs. Phys. Plasmas 4, 555 (1997)
8. J.E. Maggs and G.J. Morales, Geophys. Res. Lett. 23, 633 (1996)
9. J.E. Maggs and G.J. Morales, Phys. Plasmas 4, 290 (1997)
10. W. Gekelman et al., Phys. Plasmas 1, 3775 (1994)
11. W. Gekelman et al., Rev. Sci. Instrum. 62, 2875 (1991)

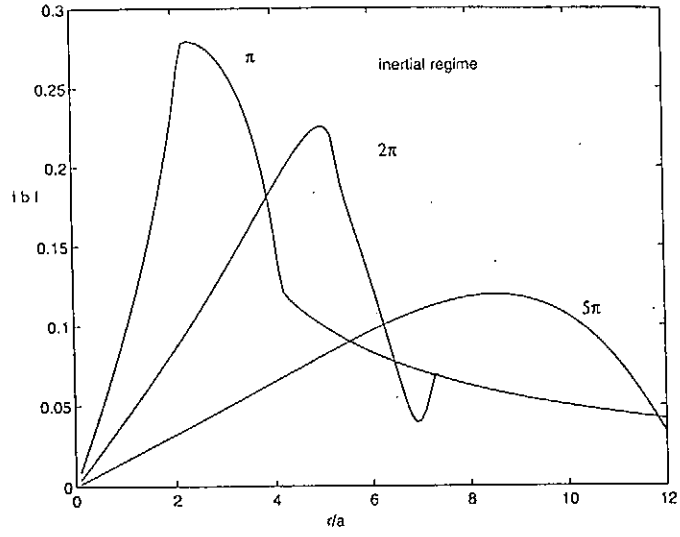

Fig. 1 Radial dependence of magnitude of scaled azimuthal magnetic field of an inertial Alfvén wave at three different scaled axial positions $k_A z=(\pi, 2\pi, 5\pi)$ launched by a disk exciter whose radius equals c/ω_{pe}

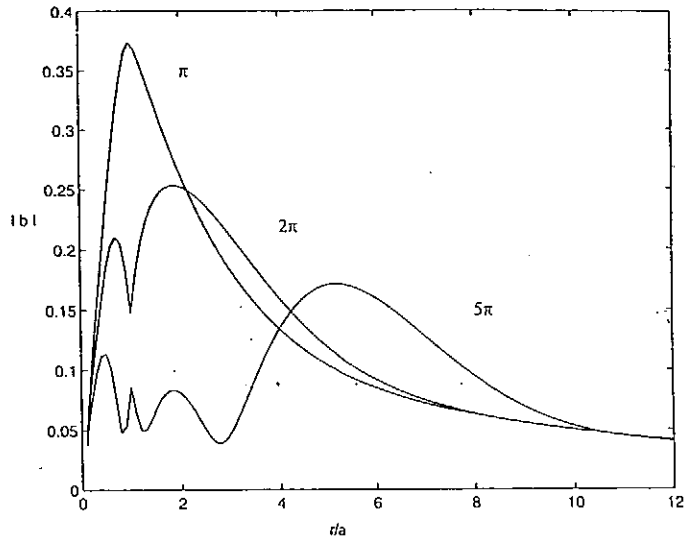

Fig. 2 Radial dependence of magnitude of scaled azimuthal magnetic field of a kinetic Alfvén wave at three different scaled axial positions $k_A z=(\pi, 2\pi, 5\pi)$ launched by a disk exciter whose radius equals c_s/Ω_i

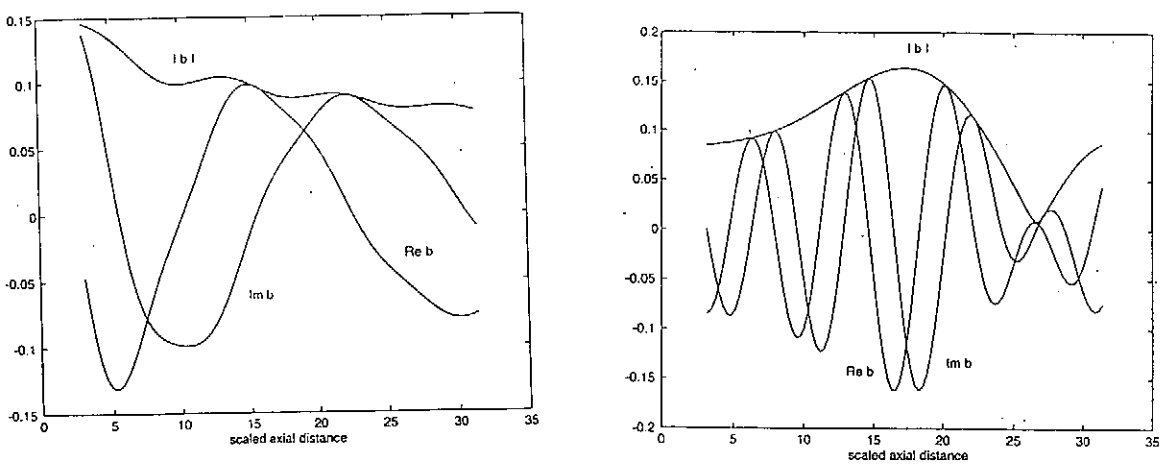

Fig. 3 Axial dependence of scaled azimuthal magnetic field of a kinetic Alfvén wave excited by a disk whose radius is c_s/Ω_i . Left panel is at a radial position close to the axis (r/a=.3) and shows a wavelength larger than $2\pi/k_A$. Right panel displays the behavior far from the axis (r/a=6) where the wavelength is close to $2\pi/k_A$.

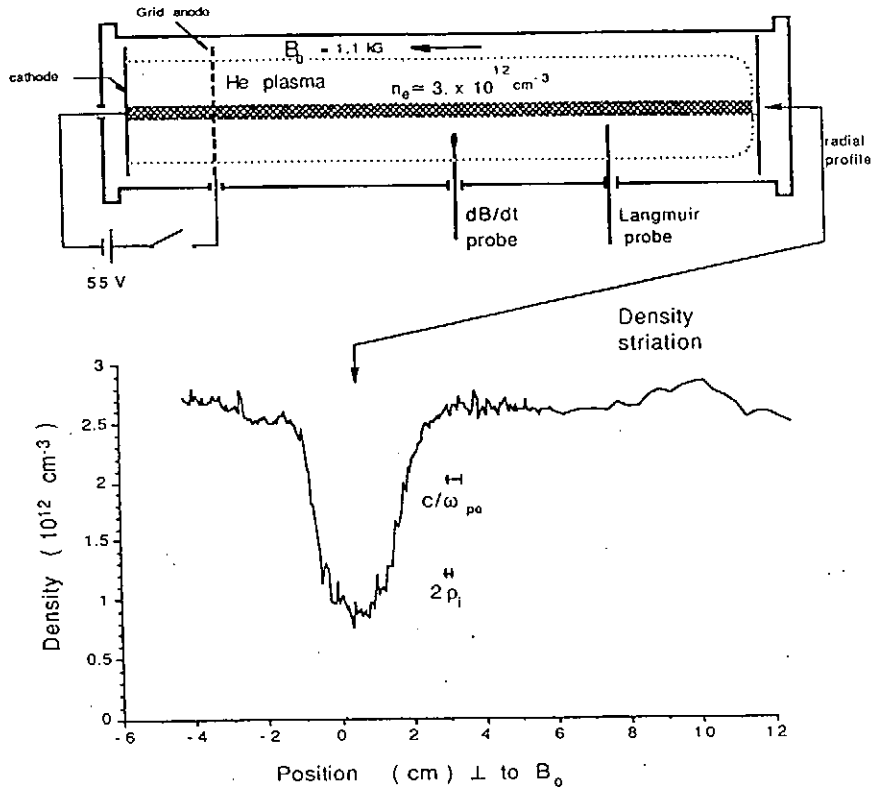

Fig. 4 Schematic of experimental arrangement used in the Large Plasma Device (LAPD at UCLA) to study spontaneously generated Alfvén waves in a narrow field-aligned density striation embedded in a large uniform plasma

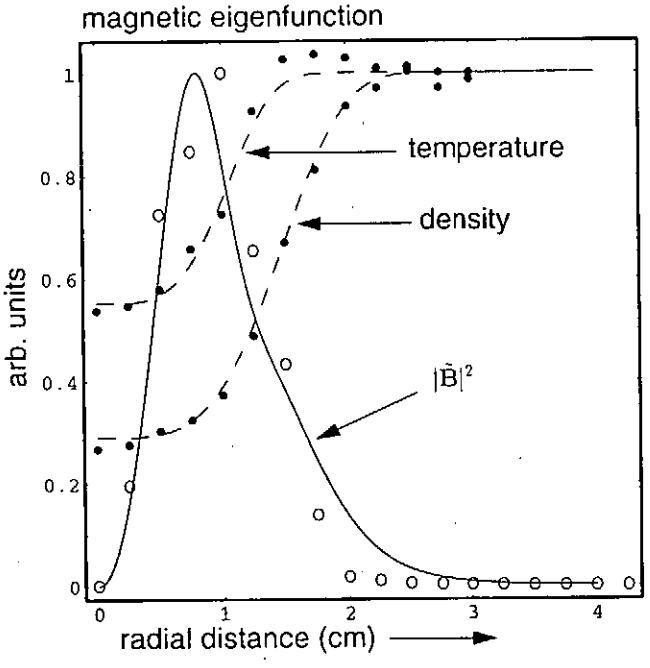

Fig. 5 Comparison of theoretical prediction (solid curve) of the radial structure of unstable drift-Alfvén waves to experimental observations (open circles) made in the LAPD facility. The predicted eigenfrequency also agrees with the measured value within experimental accuracy.

Generation of Mirror Waves, Slow-Mode Waves and Ion Cyclotron Waves in the Earth's Magnetosheath

L. C. Lee and B. H. Wu

Department of Physics, National Cheng Kung University, Tainan, Taiwan
E-mail address: loulee@sparc1.cc.ncku.edu.tw

As the supersonic solar wind impinges on the earth's magnetosphere, a bow shock is formed in front of the magnetosphere. The region between the bow shock and magnetosphere is called the magnetosheath. Low-frequency fluctuations in the plasma density and magnetic fields are often observed in the magnetosheath. These fluctuations can be identified as mirror waves, ion cyclotron waves and slow-mode waves. In addition, sunward plasma flows are also observed in the region near the bow shock. These fluctuations can be generated by the ion temperature anisotropy associated with bow shock or by the interaction of interplanetary discontinuities with the bow shock. Observations, theoretical models and simulations of these wave phenomena will be discussed in this paper.

1. Introduction

The interaction of the solar wind with the earth's magnetosphere leads to the formation of the bow shock, magnetosheath, magnetopause, and boundary layer, as shown in Figure 1. Mirror waves, ion cyclotron waves, and slow-mode waves are found to be present in the magnetosheath [*Kaufmann et al.*, 1970; *Tsurutani*, 1982; *Lee et al.*, 1988; *Hubert et al.*, 1989; *Anderson and Fuselier*, 1993; *Song et al.*, 1994; *Yan*, 1995]. In addition, events of anomalous plasma flows are often observed in the region near bow shock [*Paschmann et al.*, 1988; *Schwartz et al.*, 1988]. In these events, plasma flows are highly deflected from the stationary flow direction.

2. Mirror Waves in the Magnetosheath

Figure 2 shows an example of low-frequency (period ~ 10 - 100 s) waves observed by AMPTE/IRM on September 1, 1984 [*Song et al.*, 1994; *Denton et al.*, 1995; *Lin et al.*, 1997]. From top to bottom are the plasma number density, total magnetic field magnitude, three components of magnetic field and three components of velocity. It can be easily seen that the perturbed plasma density and magnetic field strength have an anti-phase relationship, which is a property shared by slow-mode waves and mirror waves. Song et al. [1994] identified this wave event as slow-mode waves. However, recent correlation studies of the observed waves [*Lin et al.*, 1997] show that (a) the plasma density and field strength have a phase delay of 180°, and (b) the magnetic field and velocity have a phase delay of 90°. The property in (b) can be used to firmly identify the observed waves as mirror waves.

Theoretical and observational studies have expanded our knowledge of the structure of quasi-perpendicular shocks. Hybrid simulations show that a large ion temperature anisotropy ($T_{i\perp} / T_{i//} \approx 2$ - 3) is produced downstream of a quasi-perpendicular shock [e.g., *Lee et al.*, 1987]. Magnetosheath mirror waves may be excited by the ion temperature anisotropy with $T_{i\perp} > T_{i//}$. Hybrid simulations show that large amplitude mirror waves are produced downstream of quasi-perpendicular shocks with an Alfven Mach number $M_A \geq 3$ [*Lee et al.*, 1988; *Hubert et al.*, 1989].

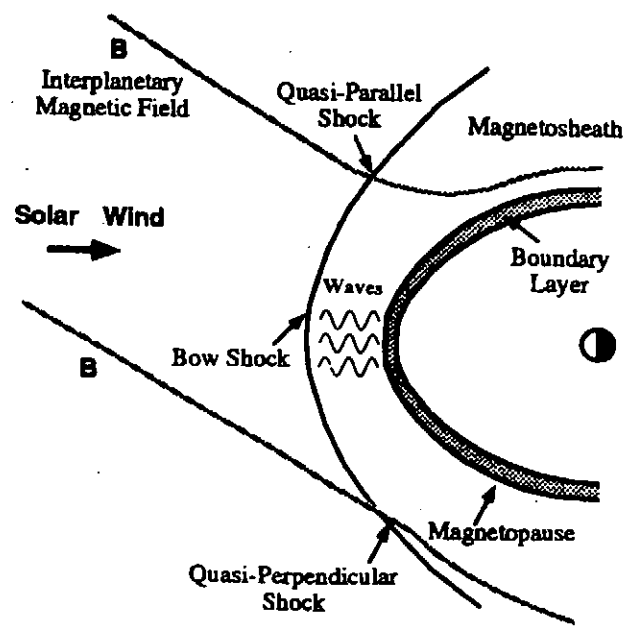

Figure 1. The interaction of solar wind with the earth's magnetosphere leads to the formation of bow shock, magnetosheath, and magnetopause

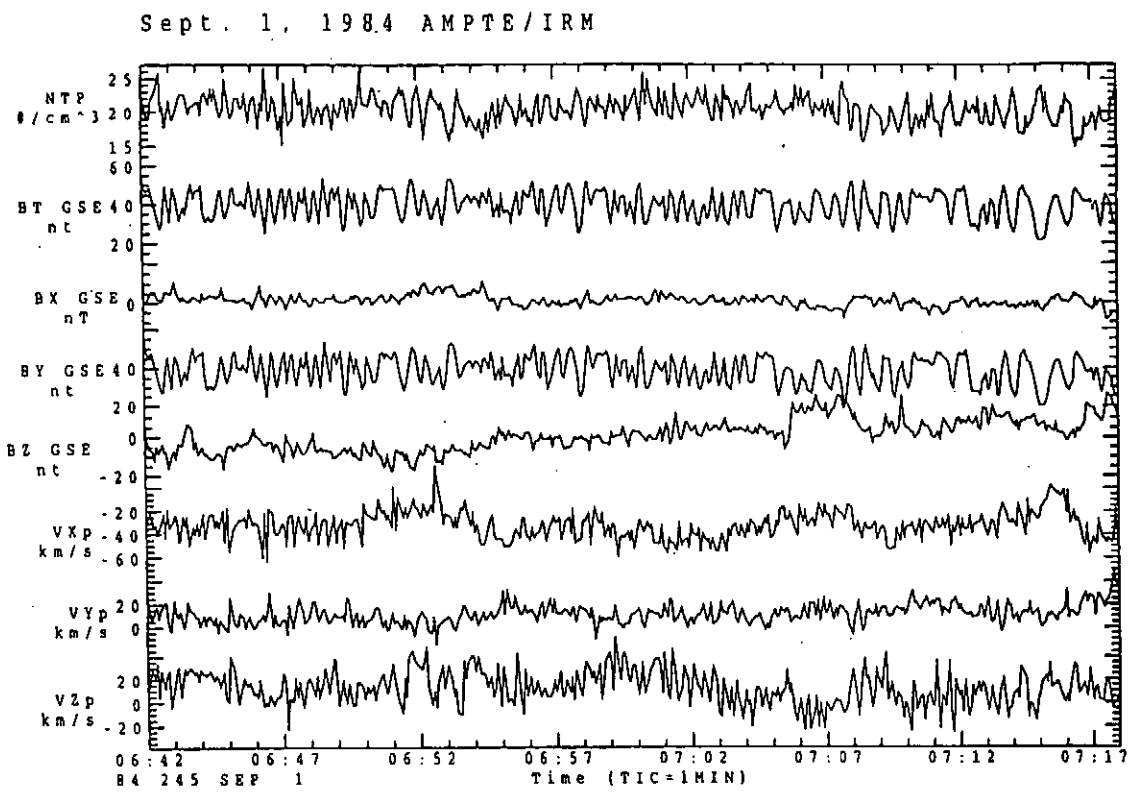

Figure 2. An example of mirror waves observed by AMPTE/IRM satellite.

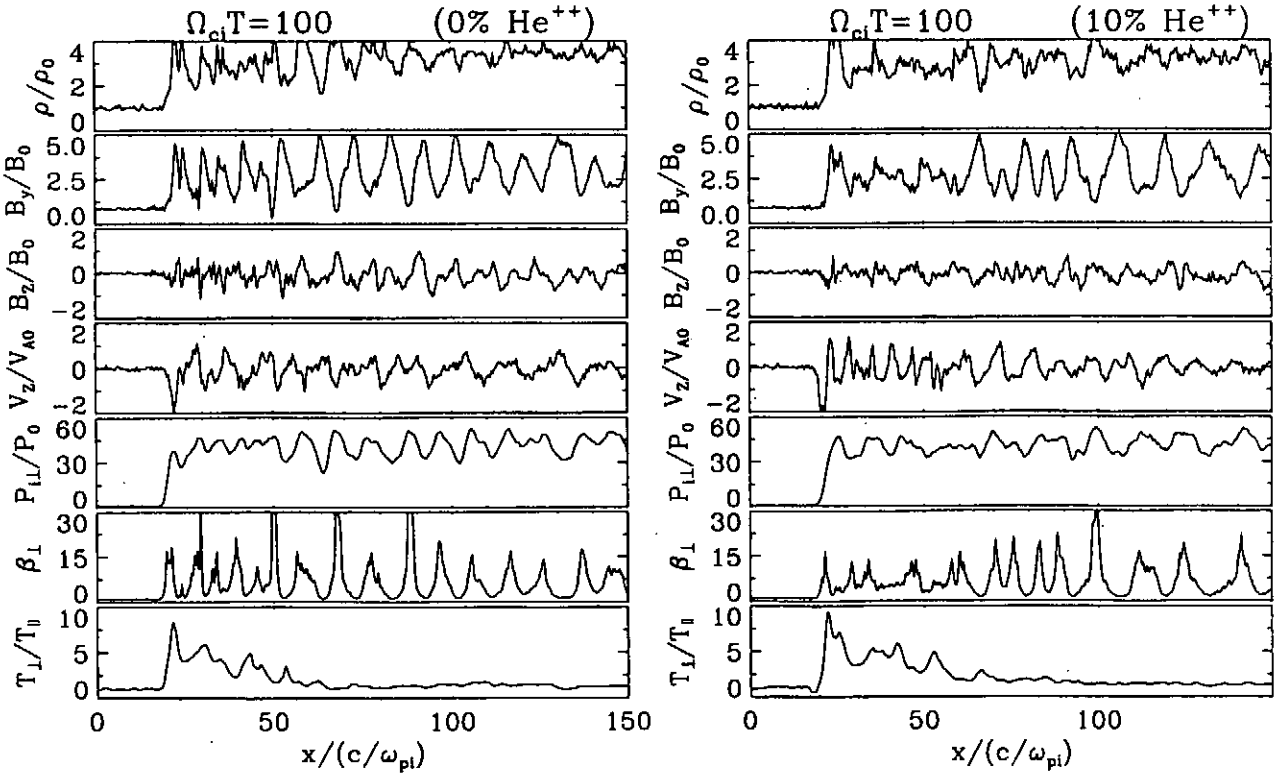

Figure 3. Formation of mirror waves downstream of a quasi-perpendicular shock. The presence of 10% He^{++} (right side) increase the wave length of mirror waves.

Figure 3 shows the results of our recent hybrid simulations of quasi-perpendicular shocks and the associated downstream mirror waves. The presence of a 10% He^{++} in the upstream solar wind (left side of Figure 3) tends to increase the temperature anisotropy ($T_\perp / T_{//}$) immediately downstream of the bow shock and increase the wavelength of downstream mirror waves.

In Figure 3, the upstream magnetic field **B** lies on the x-y plane and the shock normal **n** is in the x direction. The upstream plasma beta $\beta = 1$, the angle between **B** and **n** is 60°, and the Alfven Mach number $M_A = 6$. Also shown in Figure 3 are B_z and v_z, which can be considered as the "transverse" perturbations of **B** and velocity **v**. A correlation study between B_y and v_z shows a strong correlation and a phase delay of 90°.

3. Slow-mode Waves in the Magnetosteath

The convection of solar wind past the magnetosphere causes magnetic flux to pile up at the dayside magnetopause. *Lees* [1964] and *Zwan and Wolf* [1976] predicted that the pile-up of magnetic flux at the magnetopause would create a plasma depletion layer in front of the dayside magnetopause as the flux tubes are compressed and plasma is squeezed out of the ends. The existence of depletion layer was subsequently confirmed by observations [*Paschmann et al.*, 1978; *Crooker et al.*, 1979]. The squeezing of plasma along field lines can produce a temperature anisotropy in the ions with $T_{i\perp} / T_{i//} > 1$ since particles with a high parallel velocity will leave the region faster. This temperature anisotropy favors the generation of ion cyclotron waves since the plasma β is not very high in this region.

The analysis of ISEE spacecraft data revealed that large scale structures with an anti-correlation between plasma density and magnetic field strength are often present in the inner magnetosheath [*Yan*, 1995].

Figure 4 shows ISEE 2 data obtained during an outbound magnetosheath crossing on September 12, 1988. The top panels show the three components and the magnitude of the magnetic field. The lower panels show the ion density, ion temperature, and bulk flow velocity. As indicated by the shadings in the B_T (total field strength) and density profiles, variations in B_T and density are anti-correlated. The time scales of these variations are much longer than those for the mirror waves in Figure 2.

Figure 4 also shows ISEE 3 observations of the magnetic field and ion density (dashed lines) with a time shift of 56 minutes to account for the traveling time of solar wind from ISEE 3 to ISEE 2. Corresponding to the plasma density enhancement events observed in the magnetosheath (ISEE 2), there are similar signatures in the solar wind (ISEE 3). However, the signatures observed in the magnetosheath deviate from the signatures observed in the solar wind because of the modification by bow shock.

Based on the study of 51 magnetosheath passes, *Yan* [1995] found the following features. (i) Fluctuations with time scales over 5 minutes frequently appear in the magnetosheath. A majority of large scale fluctuations are associated with an anti-correlated plasma density and magnetic field, indicating that they are slow-mode structures. These slow-mode fluctuations are more frequently observed in the inner magnetosheath close to the magnetopause. (ii) Some of the slow-mode fluctuations observed in the magnetosheath have their sources in the solar wind. (iii) Some of the slow-mode fluctuations are caused by interplanetary Alfven waves in which the plasma density and magnetic field magnitude do not vary, but the field direction changes significantly.

Two-dimensional MHD simulations show that the interaction of interplanetary MHD waves with bow shock may lead to observed slow-mode waves in the inner region of dayside magnetosheath [*Yan and Lee*, 1994]. The transmission of MHD waves throuth the bow shock generally produces fast, Alfven, and slow-mode waves within the magnetosheath [see Figure 5]. Both the flow speed and the slow-mode phase speed normal to the magnetopause decrease to zero at the magnetopause, which allows the slow-mode waves to stay in front of the magnetopause for a long time (over 15 minutes) before the wave energy is convected tailward. Since MHD waves are common in the solar wind, this mechanism may lead to the frequent appearance of slow-mode structures in front of the magnetopause. As shown in Figure 6, these waves will have the observed anti-correlated variations in plasma pressure P and magnetic field B along the sun-earth line. It is interesting to note that the interaction of Alfven waves (no density variations) with the bow shock also leads to the generation of slow-mode waves with density variations in the downstream magnetosheath. Recently, *Yan and Lee* [1996], *Lin et al.* [1996a, 1996b] used MHD and hybrid simulations to further study the generation of slow-mode structures by the interaction of interplanetary discontinuities with bow shock. These studies all indicated that slow-mode structures and dynamic pressure pulses can indeed be generated by the interaction of bow shock with

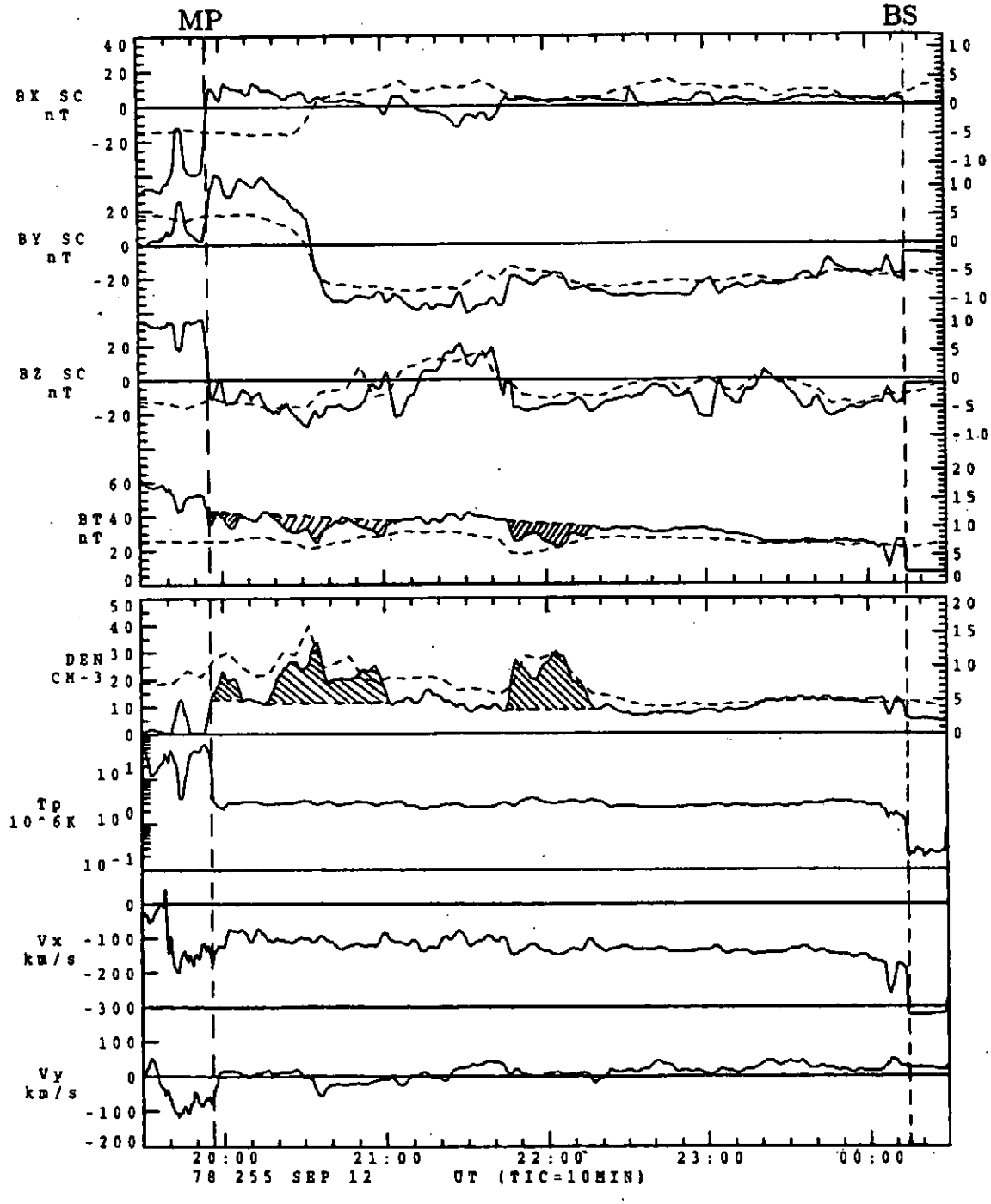

Figure 4. Slow-mode structure in the magnetosheath : an outbound magnetosheath crossing by ISEE 2 (solid lines) and corresponding solar wind conditions observed by ISEE 3 (dashed lines).

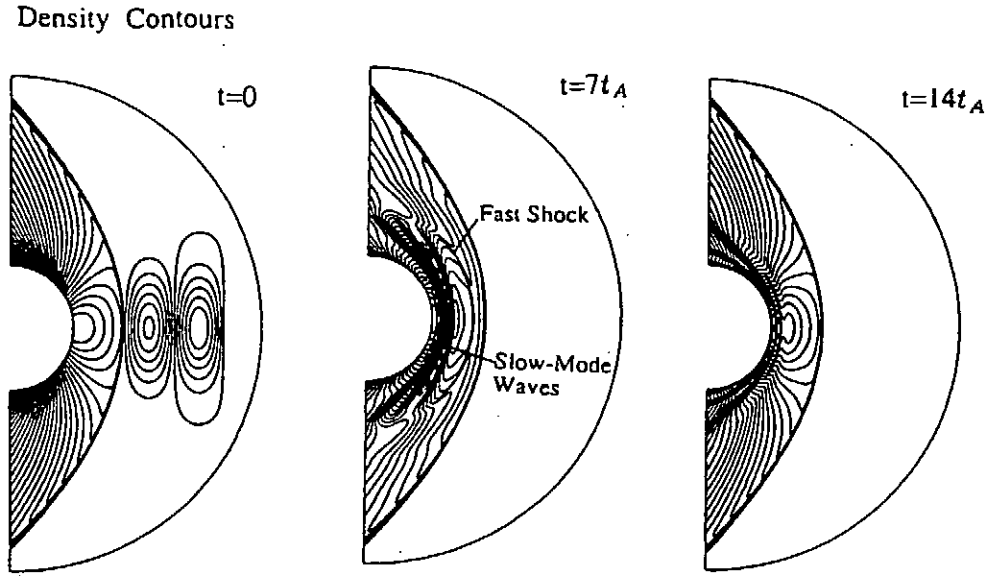

Figure 5. The evolution of plasma density contours between the bow shock and magnetopause shows that MHD waves in the solar wind will generate fast and slow waves in the magnetosheath.

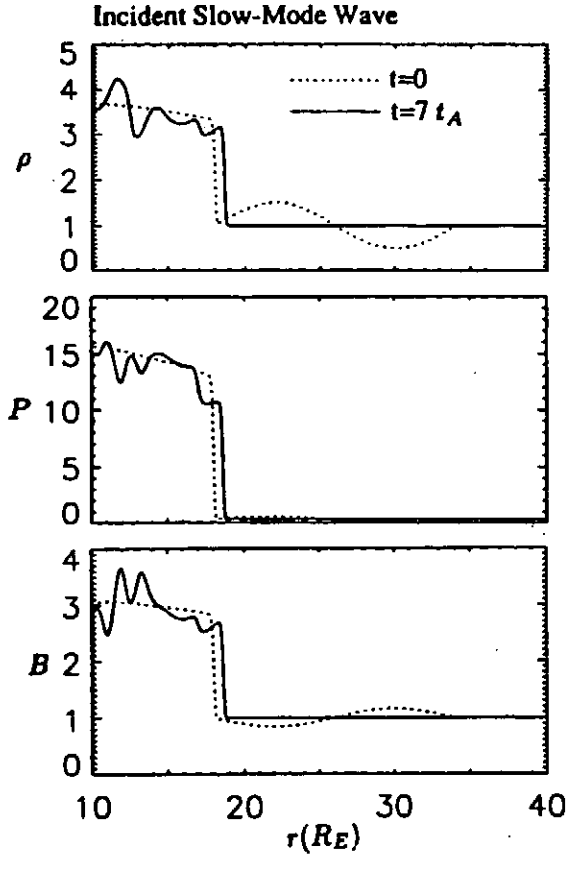

Figure 6. Profiles of plasma pressure P, and magnetic field B along the sun-earth line at t = 0 (dashed line) and t = $7t_A$ (solid lines) for contours shown in Figure 5.

fast waves, Alfven waves or slow-mode waves in the solar wind.

4. Summary

The sources and generation mechanisms of mirror waves, slow-mode waves, ion cyclotron waves and anomalous plasma flows observed in the magnetosheath can be summarized as follows.

(i) The temperature anisotropy downstream of quasi-perpendicular shocks leads to the generation of mirror waves (period ~ 10 – 100s) in the magnetosheath. These waves can be identified by (a) the phase delay of 180° between B_T and density, and (b) the phase delay of 90° between **B** and velocity **v**.

(ii) The large-scale slow-mode fluctuations (period > 100s) can be generated by the interaction of bow shock with fast, Alfven or slow-mode waves/shocks in the solar wind.

(iii) The depletion layer near the magnetopause, which has a low plasma beta ($\beta < 1$) and a temperature anisotropy ($T_\perp / T_{//} > 1$), favors the generation of ion cyclotron waves.

(iv) The anomalous plasma flows (not reviewed here) can be generated by the interaction of tangential discontinuity and bow shock.

Acknowledgements. This work was supported by the National Science Council grant NSC 87-2119-M-006-001-AP8 to National Cheng Kung University

References

Anderson, B. J., and S. A. Fuselier, Magnetic pulsasions from 0.1 to 0.4 Hz and associated plasma properties in the Earth's subsolar magnetosheath and plasma depletion layer, *J. Geophys. Res., 98*, 1461, 1993.

Crooker, N. U., T. E. Eastman, and G. S. Stiles, Observation of plasma depletion in the magnetosheath at the dayside magnetopause, *J. Geophys. Res., 84*, 869, 1979.

Denton, R. E., S. P. Gary, X. Li, B. J. Anderson, J. W. Labelle, and M. Lessard, Low-frequency fluctuations in the magnetosheath near the magnetopause, *J. Geophys. Res., 100*, 5665, 1995.

Hubert, D., C. Perche, C. C. Harvery, C. Lacombe, and C. T. Russell, Observation of mirror waves downstream of a quasi-perpendicular shock, *Geophys. Res. Lett., 16*, 159, 1989.

Kaufmann, R. L., J.-T. Horng, and A. Wolfe, Large amplitude hydro-magnetic waves in the inner magnetosheath, *J. Geophys. Res., 75*, 4666, 1970.

Lee, L. C., M. E. Mandt, and C. S. Wu, Increase of ion kinetic temperature across a collisionless shock: II. A simulation study, *J. Geophys. Res., 92*, 13438, 1987.

Lee, L. C., C. P. Price, C. S. Wu, and M. E. Mandt, a study of mirror waves generated downstream of a quasi-perpendicular shock, *J. Geophys. Res., 93*, 247, 1988.

Lees, L., Interaction between the solar wind and the geomagnetic cavity, *AIAA J.*, 2, 1576, 1964.

Lin, Y., L. C. Lee, and M. Yan, Generation of dynamic pressure pulses downstream of the bow shock by the variation of IMF orientation, *J. Geophys. Res., 101*, 479, 1996.

Lin, Y., D. W. Swift, and L. C. Lee, Simulation of pressure pulses in the bow shock and magnetosheath driven by variations in interplanetary magnetic field direction, *J. Geophys. Res., 101*, 27251, 1996.

Lin, C. H., J. K. Chao, L. C. Lee, and B. H. Wu, Identification of mirror waves in the magnetosheath: a new method, to appear in *J. Geophys. Res.*, 1997.

Paschmann, G., N. Sckopke, G. Haerendel et al., ISEE plasma observations near subsolar magnetopause, *Space Sci. Rev., 22.*, 717, 1978.

Paschmann, G., G. Haerendel, N. Sckopke, and E. Mobius, Three-dimensional plasma structures with anomalous flow directions near the Earth's bow shock, *J. Geophys. Res., 93*, 11279, 1988.

Schwartz, S. J., R. L. Kessel, C. C. Brown, L. J. C. Woolliscroft, M. W. Dunlop, C. J. Farrugia, and D. S. Hall, Active current sheets near the Earth's bow shock, *J. Geophys. Res., 93*, 11295, 1988.

Song, P., C. T. Russell, and S. P. Gary, Identification of low-frequency fluctuations in the terrestrial magnetosheath, *J. Geophys. Res., 99*, 6011, 1994.

Tsurutani, B. T., E. J. Smith, R. R. Anderson, K. W. Ogilvie, J. D. Scudder, D. N. Baker, and S. J. Bame, Lion roars and nonoscillatory drift mirror waves in the magnetosheath, *J. Geophys. Res., 87*, 6060, 1982.

Yan, M, Observations and generation mechanisms of slow-mode waves in the magnetosheath, Ph.D. thesis, University of Alaska, Fairbanks, 1995.

Yan, M., and L. C. Lee, Interaction of interplanetary shocks and rotational discontinuities with the Earth's bow shock, *J. Geophys. Res., 101*, 4835, 1996.

Zwan, B. J., and R. A. Wolf, Depletion of solar wind plasma near a planetary boundary, *J. Geophys. Res., 81*, 1636, 1976.

Nonlinear Magnetohydrodynamics of Weakly Ionized Plasmas

Sergei BULANOV[1,2], Francesco PEGORARO[3], and Jun-ichi SAKAI[1]

[1]Laboratory for Plasma Astrophysics and Fusion Science,
Department of Electronics and Information, Faculty of Engineering,
Toyama University, Toyama 930, Japan

[2] General Physics Institute of Russian Academy of Sciences, Moscow, Russia

[3] Physics Department of the University of Pisa and INFM, Pisa, Italy

Abstract

We present the results of our studies of the magnetic field line reconnection and of the Rayleigh-Taylor instability in weakly ionized plasmas. We investigate the propagation of small-amplitude MHD waves near the critical lines of the magnetic field and show the occurrence of accumulation of the electric current. This magnetic collapse is described by the self-similar solutions which show the formation of singular structures in the vicinity of the separatrix surfaces of the magnetic field. We obtain the growth rate of the tearing mode instability of the current sheet and present a solution of the Taylor problem corresponding to forced magnetic reconnection in a slab of weakly ionized plasma. In the case of the Rayleigh-Taylor instability of a thin shell of weakly ionized plasmas we present an analytical solution of the Cauchy problem for the evolution of nonlinear perturbations in the slab in terms of analytical functions of complex variable, and discuss the generic type of singularities formed in the nonlinear stage of the instability.

1 Introduction

Recently the MHD behaviour of weakly ionized plasmas has been the subject of theoretical studies in space physics [1]. The dynamics of weakly ionized plasmas plays an important role in space plasmas since they occur in molecular clouds [2] where stars form, and near the photosphere of the Sun. Molecular clouds have ionization fractions around $\varepsilon = \rho/\rho^{(n)} \approx 10^{-7}$, while at the Sun photosphere $\varepsilon \approx 10^{-3}$. Under typical conditions for space plasmas the magnetic field is as important as gravity in molecular clouds [3] while, in the solar photosphere, magnetic reconnection is invoked in order to explain bright point formation [4].

An important factor in weakly ionized plasmas, besides Ohmic and viscous dissipation, is the momentum and energy exchange between the ionized and the neutral components.

2 Magnetic field line reconnection in weakly ionized plasmas

2.1 Ambipolar diffusion

The equations of weakly ionized plasmas were considered in Ref. [5]. In our case we use these equations in order to describe a gas that includes hydrogen atoms, hydrogen ions and electrons. Due to the fast energy exchange between ions and neutrals provided by charge exchange, their temperatures are equal, $T^{(i)} = T^{(n)} = T$. The plasma is assumed to be quasineutral i.e., ions and electrons have equal concentrations, $n^{(e)} = n^{(i)} = n$, and hydrodynamic velocities $v_i^{(e)} = v_i^{(i)} = v_i$. Here the superscripts e, i and n denote electron, ion and neutral components, respectively. The equations used below are presented in our paper [6]. Here we only discuss the "ambipolar diffusion" term which appears due to ion-neutral collisions.

In the strong coupling approximation, when the Lorentz force is balanced by the pressure gradient and by the ion-neutral friction, the MHD equations lead to the following expression for the ion velocity:

$$\mathbf{v} = \mathbf{v}^{(n)} - \frac{M}{(\varpi^{(in)})\rho^{(n)}} \left(\frac{\nabla(\rho T)}{\rho} - \frac{(\nabla \times \mathbf{B}) \times \mathbf{B}}{4\pi\rho} \right). \quad (1)$$

Here $\varpi^{(in)} n n^{(n)} = \nu^{(in)} n$, i.e., $\varpi^{(in)} = \bar{v}\sigma^{(in)}$ with $\sigma^{(in)}$ the cross section of ion-neutral collisions. Substituting v_i into the induction equation for the magnetic field we introduce an additional nonlinear term:

$$\partial_t \mathbf{B} = \nabla \times (\mathbf{v}^{(n)} \times \mathbf{B}) - \nabla \times \left(\frac{M}{(\varpi^{(in)})\rho^{(n)}} \left(\nabla(\rho T) - \frac{(\nabla \times \mathbf{B}) \times \mathbf{B}}{4\pi} \right) \times \mathbf{B} \right) + \nu_m \Delta \mathbf{B}, \quad (2)$$

where the magnetic diffusivity is $\nu_m = c^2/4\pi\sigma$.

According to Eq.(2) the magnetic field is not frozen in the motion of the neutral component even for $\nu_m = 0$ due to the second term in its right hand side. Nevertheless the magnetic field topology remains unchanged when $\nu_m = 0$ since it is frozen in the ionized component. We can say that the ambipolar diffusion leads to isotopological damping of the magnetic perturbations.

2.2 MHD waves near critical points

Reconnection of the magnetic field lines occurs near the critical points of the magnetic field and in particular where the magnetic field vanishes (near the null lines). As the distance from the critical point increases, the value of the magnetic field increases. This means that the ratio of the magnetic field associated with the perturbations to the background magnetic field decreases and we can use a linear approximation to describe the plasma dynamics.

As is known, in a cold dissipationless plasma embedded in a uniform magnetic field, the perturbation eigenmodes correspond to magnetosonic and to Alfvén waves. The relationship between the frequency ω and the wavevector $\mathbf{k}$ is given by the dispersion equation $\omega_m = |\mathbf{k}|v_a$ for the magnetosonic wave and by $\omega_a = (\mathbf{k} \cdot \mathbf{v}_a) \equiv k_\parallel v_a$ for the Alfvén wave. Here $\mathbf{v}_a = \mathbf{B}/(4\pi\rho_0)^{1/2}$, and $k_\parallel = (\mathbf{k} \cdot \mathbf{B})/|\mathbf{B}|$ are the Alfvén velocity and the component of the wave vector parallel to the magnetic field. If the MHD waves are excited with given frequency ω, their amplitude grows near the resonance region where $\omega = \omega_m$ or $\omega = \omega_a$. In the vicinity of points, lines or surfaces where the value of ω_m or ω_a vanishes, i.e. where $(\mathbf{k} \cdot \mathbf{B}) = 0$ or $\mathbf{B} = 0$, this resonance occurs formally at zero frequency. This means that arbitrarily

slow perturbations result in a nonadiabatic response and cause the electric current density associated with either the magnetosonic or with the Alfvén wave to tend to infinity [7,8].

We assume that the plasma is initially at rest ($\mathbf{v}$, $\mathbf{v}^{(n)} = 0$) in a potential magnetic field ($\nabla \times \mathbf{B}_0 = 0$), which has only x and y components. All values depend on the coordinates x and y and on time t. We linearize the MHD equations around the equilibrium solution $\mathbf{v}_0 = 0$, $\mathbf{v}_0^{(n)} = 0$, $\rho^{(n)} = \rho_0^{(n)}$, $\rho = \rho_0$, and $A = A_0(x, y)$ and obtain

$$(\varepsilon A_D \partial_{tt} + (1+\varepsilon)\partial_t)\partial_t a - (A_D \partial_t + 1)\frac{\varepsilon}{4\pi\rho_0}|\nabla A_0|^2 \Delta a = 0, \tag{3}$$

for the magnetosonic wave, and

$$(\varepsilon A_D \partial_{tt} + (1+\varepsilon)\partial_t)\partial_t b_\parallel - (A_D \partial_t + 1)\frac{\varepsilon}{4\pi\rho_0}(\mathbf{B}_{0\perp}\cdot\nabla)^2 b_\parallel = 0, \tag{4}$$

for the Alfvén wave. Here $a(x, y, t)$ is the perturbation of the z-component of the vector potential, $b_\parallel(x, y, t)$ is the perturbation of the z-component of the magnetic field and $A_D = 1/\varpi^{(in)} n_0$. In the approximation used above the magnetosonic and the Alfvén waves are decoupled.

We see that the main difficulty in obtaining analytical solutions arises from the dependence of the Alfvén speed on the coordinates, caused by the nonuniformity of the background magnetic field. To solve these equations we shall use an approach developed in Ref.[8]. Following this approach we describe the magnetic field with the complex variable $\zeta = x + iy$, as

$$\mathbf{B}_{0\perp} = B_{0x} - iB_{0y} = -df_0/d\zeta. \tag{5}$$

Here $f_0(\zeta) = F_0 - iA_0$ is a complex potential with F_0 and A_0 the scalar and the vector potential of the magnetic field, respectively. We rewrite the linearized MHD equations as

$$(\varepsilon A_D \partial_{tt} + (1+\varepsilon)\partial_t)\partial_t a - (A_D \partial_t + 1)\frac{\varepsilon}{4\pi\rho_0}|f_0'|^2 \Delta a = 0, \tag{6}$$

and

$$(\varepsilon A_D \partial_{tt} + (1+\varepsilon)\partial_t)\partial_t b_\parallel - (A_D \partial_t + 1)\frac{\varepsilon}{4\pi\rho_0}\left(|f_0'|^2_{A_0=\text{const}}\partial_{F_0}\right)^2 \partial_t b_\parallel = 0. \tag{7}$$

A prime denotes differentiation with respect to the variable ζ: $f_0' = df_0/d\zeta$.

The solutions of Eq.(7) for Alfvén waves depend on time t and on the coordinate $l = \int d\,F_0/|f_0'|^2_{A_0=\text{const}}$, where the dependence of $|f_0'|$ on the coordinates is expressed via F_0 and A_0, with A_0 constant. Thus we have

$$(\varepsilon A_D \partial_t + (1+\varepsilon))\partial_{tt} b_\parallel - (A_D \partial_t + 1)\frac{\varepsilon}{4\pi\rho_0}\partial_{ll} b_\parallel = 0. \tag{8}$$

Assuming that the Alfvén wave varies as $\exp(i(kl - \omega t))$, we obtain the dispersion equation

$$\frac{\varepsilon}{4\pi\rho_0}N(\omega) \equiv \frac{\varepsilon}{4\pi\rho_0}\left(N_R(\omega) + iN_I(\omega)\right) \equiv \frac{\varepsilon}{4\pi\rho_0}\left(\frac{k^2}{\omega^2}\right) = \left(\varepsilon + \frac{1 + iA_D\omega}{1 + A_D^2\omega^2}\right). \tag{9}$$

We see that the effects of ambipolar diffusion lead to both damping of the wave and to dispersion due to the dependence of the wave propagation velocity on the wave frequency.

As is known, under the conformal mapping $w(\zeta) = u + iv$, the Laplacian changes into $\Delta_\zeta = |w'|^2 \Delta_w$, where $\Delta_\zeta = \partial_{xx} + \partial_{yy}$, $\Delta_w = \partial_{uu} + \partial_{vv}$ and $|w'| \equiv |\,dw/d\zeta|$ is the Jacobian of the transformation. If we choose $w(\zeta)$ equal to

$$w(\zeta) = \exp(iC)\int_{\zeta_0}^{\zeta} \frac{d\zeta}{f_0'} \tag{10}$$

with C and ζ_0 arbitrary constants, the coefficients, $|f_0'|^2$, in front of the Laplacians become equal to one. Under the conformal mapping, Eq. (6) for magnetosonic waves is transformed into

$$(\varepsilon A_D \partial_t + (1+\varepsilon))\partial_{tt} a - (A_D \partial_t + 1)\frac{\varepsilon}{4\pi\rho_0}\Delta_w a = 0. \tag{11}$$

We have thus reduced the problem under consideration to the problem of the magnetosonic wave propagation in a uniform magnetic field with the effects of ambipolar diffusion taken into account. This equation has special solutions when the wave depends on one Cartesian coordinate, for example u, and on time t, or it can be solved in the cylindrical coordinates $s = (u^2+v^2)^{1/2}$, $\phi = \arctan(u/v)$. Each of these solutions corresponds to a particular pattern of the magnetosonic wave propagation in the x, y plane.

Assuming that the magnetosonic wave varies as $\exp(i(k_u u + k_v v - \omega t))$, we reobtain Eq. (9) with $k^2 = k_u^2 + k_v^2$. In the high-frequency limit, when $A_D\omega \gg 1/\varepsilon$, the effects of ion-neutral collisions are negligible. The ionized component of the plasma is decoupled from the neutral component. The MHD waves propagate with the local value of the velocity $B/(4\pi\rho_0)^{1/2}$. Instead, in the opposite limit when $A_D\omega \ll 1$, the velocity of propagation is equal to $B/(4\pi(\rho_0+\rho^{(n)})^{1/2}$. In both these cases the wave damping is weak. In the intermediate regime, when $1 \ll A_D\omega \ll 1/\varepsilon$, the ion-neutral collisions lead to damping of the MHD perturbations, and to diffusion of the magnetic field perturbations instead of propagation in the form of waves. In this intermediate regime the imaginary part of the function $N(\omega)$ is larger than the real part, $N_R(\omega)$.

In the vicinity of an X-line of the magnetic field, the magnetic field is described by the complex potential $f_0(\zeta) = -h\zeta^2/2 = -h(x^2-y^2-i2xy)/2$ with h the magnitude of the field gradient. The conformal mapping is given by the function $w(\zeta) = ih^{-1}\ln\zeta$ with $u = h^{-1}\varphi$ and $v = h^{-1}\ln r$. If we assume that the magnetosonic wave has a harmonic time dependence and that it depends on the $v = \ln r$ coordinate only, we find a cylindrical wave where the perturbation of the vector potential is given by

$$a(r,t) = a_0 r^{\frac{\omega}{\Omega^{(n)}}K_I(\omega)} \exp\left(i\frac{\omega}{\Omega^{(n)}}\left(K_R(\omega)\ln r - \Omega^{(n)}t\right)\right). \tag{12}$$

The constant a_0 is determined by the boundary conditions, $\Omega^{(n)} = \varepsilon^{1/2}h/(4\pi\rho_0)^{1/2}$, and $K_R(\omega)+iK_I(\omega) \equiv \sqrt{N(\omega)} = ((N_R^2+N_I^2)^{1/2}+N_R)^{1/2}/\sqrt{2}+i((N_R^2+N_I^2)^{1/2}-N_R)^{1/2}/\sqrt{2}$. We see that, as the magnetosonic wave propagates toward the null line, $r \to 0$, the amplitude of the perturbation of the vector potential tends to zero. However, the azimuthal magnetic field $b_\varphi = \partial a/\partial r$ is equal to

$$b_\varphi(r,t) = \frac{\omega}{\Omega^{(n)}}(K_R(\omega)+iK_I(\omega))a_0 r^{\left(\frac{\omega}{\Omega^{(n)}}K_I(\omega)-1\right)} \exp\left(i\frac{\omega}{\Omega^{(n)}}\left(K_R(\omega)\ln r - \Omega^{(n)}t\right)\right), \tag{13}$$

and its amplitude of the magnetic field tends to infinity when $r \to 0$ if $\omega K_I(\omega) < \Omega^{(n)}$.

Now we analyze the role of the ambipolar diffusion on the Alfvén mode propagation. The background magnetic field expressed in terms of F_0 and A_0 can be written as $|\mathbf{B}_0| \equiv |f_0'| = (F_0^2+A_0^2)^{1/4}$. The Alfvén wave depends on $l = \operatorname{arcsinh}(F_0/A_0) = \operatorname{arcsinh}(\operatorname{tg}2\varphi)$ at $A_0 = hr^2\sin(2\varphi) = \text{const}$. Similarly to what has been found for the magnetoacoustic wave, we can show that the amplitude of the magnetic field associated with the Alfvén wave tends to zero when $t \to \infty$. However, the value of the electric current density in the wave tends to infinity along the separatrix surfaces of the magnetic field when $\omega K_I(\omega) < \Omega^{(n)}$.

We see that the ambipolar diffusion does not avoid the formation of singular regimes for low-frequency MHD perturbations.

2.3 Self-similar motion of weakly ionized plasma near null points

When the nonlinear effects become dominant we can use self-similar solutions of the MHD equations in order to describe the motion of the plasma-neutral-components near the critical points of the magnetic configurations. In these solutions the Euler coordinates x_i, t and the Lagrange coordinates of the ion component, x_i^0, t, and of the neutral component, $x_i^{0(n)}, t$, are related by $x_i = M_{ij}(t)x_i^0$, $x_i^{(n)} = M_{ij}^{(n)}(t)x_i^{0(n)}$. The velocities are $v_i(\mathbf{x},t) = w_{ij}(t)x_j = \dot{M}_{ij}(t)M_{ij}^{-1}(t)x_j$, $v_i^{(n)}(\mathbf{x},t) = w_{ij}^{(n)}x_j = \dot{M}_{ij}^{(n)}(t)\left(M_{ij}^{(n)}(t)\right)^{-1}x_j$. Here M_{ij}^{-1} and $\left(M_{ij}^{(n)}\right)^{-1}$ are the inverse matrices of deformation of the ion and of the neutral components, respectively.

Assuming both ionized and neutral component densities, ρ and $\rho^{(n)}$, to depend only on time, and the magnetic field to be given by the relationship $B_i = A_{ij}(t)x_j$, we find that, in the Lagrange coordinates, the solutions of the continuity and Faraday equations are of the form

$$\rho = \rho_0/D, \qquad \rho^{(n)} = \rho_0^{(n)}/D^{(n)}, \qquad A_{ij} = M_{ik}A_{kl}^0M_{lj}^{-1}/D, \tag{14}$$

where subscripts and superscripts "0" denote initial values, and $D = \det(M_{ij})$, and $D^{(n)} = \det(M_{ij}^{(n)})$ are the determinants of the deformation matrices M_{ij} and $M_{ij}^{(n)}$. Similar solutions were obtained in the case of standard MHD [9] and for the electron magnetohydrodynamics (EMHD) [10]. Self-similar solutions of this type were considered in Refs. [11] in application to the 2D dynamics of a plasma near the X-lines of the magnetic field.

Substituting the above expressions into the MHD equations we find, in the strong coupling regime, the following equations for the matrices M_{ij} and $M_{ij}^{(n)}$

$$\dot{M}_{ij} - \dot{M}_{ik}^{(n)}\left(M_{kl}^{(n)}\right)^{-1}M_{lj} = -A_D\frac{\left(D^{(n)}\right)^2\left(M_{ik}A_{kl}^0A_{lj}^0 - M_{sk}A_{kl}^0M_{li}^{-1}M_{st}A_{tj}^0\right)}{4\pi\rho_0^{(n)}D}, \tag{15}$$

and

$$\ddot{M}_{ij}^{(n)} + \frac{s}{D^{(n)}}\dot{M}_{ij}^{(n)} + \frac{1}{A_DD}(\dot{M}_{ij}^{(n)} - \dot{M}_{ik}M_{kl}^{-1}M_{lj}^{(n)}) = 0. \tag{16}$$

Now we suppose that the neutrals are at rest, which corresponds to the case when the effects of ambipolar diffusion are dominant, and obtain

$$\dot{M}_{ij} = -\frac{R}{D}\left(M_{ik}A_{kl}^0A_{lj}^0 - M_{sk}A_{kl}^0M_{li}^{-1}M_{st}A_{tj}^0\right). \tag{17}$$

Here the same time units are adopted as in the case of linear MHD perturbations and $R \equiv A_D/4\pi\rho_0^{(n)}$. In the simplest 3D magnetic configuration with a null point, the magnetic field $B_i = A_{ij}(t)x_j$ is current-free and is given at the initial time by the diagonal matrix $A_{ij}^0 = \mathrm{diag}\,\{a, b, -(a+b)\}$. For these initial conditions we have

$$\begin{pmatrix} \dot{M}_{11} & \dot{M}_{12} & 0 \\ \dot{M}_{21} & \dot{M}_{22} & 0 \\ 0 & 0 & \dot{M}_{33} \end{pmatrix} = \frac{R(b-a)(M_{11}M_{12}+M_{22}M_{21})}{M_{33}(M_{11}M_{22}-M_{12}M_{21})^2}\begin{pmatrix} -aM_{21} & -bM_{22} & 0 \\ aM_{11} & -bM_{12} & 0 \\ 0 & 0 & 0 \end{pmatrix}. \tag{18}$$

The solutions of these equations describe the formation of current sheets. These current sheets can be oriented at an arbitrary angle with respect to the separatrix surface, however the most probable configuration corresponds to a current sheet on the separatrix surface directed along the minimum gradient of the magnetic field. The equations for self-similar motion have solutions for which the components M_{11} and M_{12} tend to zero when $\tau = (t_0 - t) \to 0$ as $M_{11} \approx \tau^{1/3}$ and $M_{12} \approx \tau^{1/3}$. The magnetic field gradients, $A_{12} \approx \tau^{-2/3}$, as well as the velocity field gradients, $w_{11} \approx \tau^{-1}$, and the plasma density, $\rho \approx \tau^{-1/3}$, tend to

infinity. If both a and b have the same sign, the current sheet is orthogonal to the separatrix surface, while if a and b have opposite signs the current sheet is parallel to the separatrix surface.

In the generic case, by expanding the solution near the singularity we find

$$w_{ij} \approx \begin{pmatrix} -1/3\tau & \tilde{w}_{12} & \tilde{w}_{13} \\ \tilde{w}_{21}/\tau^{1/3} & \tilde{w}_{22} & \tilde{w}_{23} \\ \tilde{w}_{31}/\tau^{1/3} & \tilde{w}_{32} & \tilde{w}_{33} \end{pmatrix}, \quad A_{ij} \approx \begin{pmatrix} \tilde{A}_{11}/\tau^{1/3} & \tilde{A}_{12} & \tilde{A}_{13} \\ \tilde{A}_{21}/\tau^{2/3} & \tilde{A}_{22}/\tau^{1/3} & \tilde{A}_{23}/\tau^{1/3} \\ \tilde{A}_{31}/\tau^{2/3} & \tilde{A}_{32}/\tau^{1/3} & \tilde{A}_{33}/\tau^{1/3} \end{pmatrix}. \tag{19}$$

Here $\tilde{w}_{ij}$ and $\tilde{A}_{ij}$ are constants. As the result of the development of the singular solution, a quasi-one-dimensional regime is reached during which the plasma is compressed toward the separatrix surface of the magnetic field and shear motion appears. This implies that the magnetic collapse is accompanied by a vortex collapse.

2.4 Tearing mode instability in weakly ionized plasmas

Now we consider spontaneous reconnection in a current sheet with $\Phi_0 = 0$, $\Phi_0^{(n)} = 0$, $A_0 = B_0 L \ln(\cosh(y/L))$. Assuming a dependence of perturbations on time and coordinates of the form $\sim f(y)\exp(\gamma t + ikx)$, and reintroducing the effect of magnetic diffusivity neglected in the previous sections, we find for the perturbations of the vector potential

$$\gamma a = ikB_0 \tanh(y/L)\,\phi + \nu_m\left(a'' - k^2 a\right), \tag{20}$$

of the stream function of the plasma motion

$$\left(\gamma + \frac{1}{\varepsilon A_D}\right)\left(\phi'' - k^2\phi\right) - \frac{1}{\varepsilon A_D}\left(\phi^{(n)\prime\prime} - k^2\phi^{(n)}\right) \tag{21}$$

$$= ik\frac{B_0}{4\pi\rho_0}\tanh(y/L)\left(a'' - \left(k^2 - \frac{2}{\cosh^2(y/L)}\right)a\right), \tag{22}$$

and of the stream function of the neutral motion

$$\left(\gamma + \frac{1}{A_D}\right)\left(\phi^{(n)\prime\prime} - k^2\phi^{(n)}\right) - \frac{1}{A_D}\left(\phi'' - k^2\phi\right) = 0. \tag{23}$$

Following Ref.[12] we divide the current sheet into two regions: the external and the nonadiabatic regions. The width of the nonadiabatic region can be estimated as $\delta_\sigma \approx L(\kappa(A_D\gamma)\tau_a^2/\varepsilon A_D k^2 L^2\tau_\sigma)^{1/4}$, where $\kappa(A_D\gamma) = A_D\gamma(\varepsilon A_D\gamma + 1 + \varepsilon)/(A_D\gamma + 1)$. Matching the solutions in these two regions we find that the current sheet is unstable against tearing modes with sufficiently long wavelength such that $kL < 1$. The dispersion equation for the growth rate γ as a function of the wavenumber k has the form

$$\Delta'(\gamma) = \frac{1 - k^2L^2}{kL} = 2\pi\gamma\left(\frac{\kappa(A_D\gamma)\tau_a^2\tau_\sigma^3}{\varepsilon A_D k^2 L^2}\right)^{1/4}\frac{\Gamma(3/4)}{\Gamma(1/4)}, \tag{24}$$

with $\Delta'(\gamma)$ the jump in the logarithmic derivative of a through the nonadiabatic region and the resistive time $\tau_\sigma = 4\pi\sigma L^2/c^2$.

When $A_D = 0$ we obtain the standard expression[12] for the growth rate of the tearing mode with the renormalized Alfvèn time $\tau_a^{(n)} = \tau_a(\varepsilon)^{-1/2}$. In the limit $\varepsilon A_D\gamma \gg 1 \gg \varepsilon$ we recover the known result [12]. In the strong coupling approximation when $1 \gg \varepsilon A_D\gamma \gg \varepsilon$ we have $\kappa(A_D\gamma) \approx 1$. Then the growth rate is equal to

$$\gamma = \frac{(1 - k^2L^2)\,\Gamma(1/4)}{2\pi\,(kL)^{1/2}\,\Gamma(3/4)}\left(\frac{\varepsilon A_D}{\tau_\sigma^3\tau_a^2}\right)^{1/4}. \tag{25}$$

We see that the effects of ambipolar diffusion do not stabilize the tearing modes. However they change the typical time scale of the magnetic field line reconnection. In the limit $A_D\gamma \gg 1 \gg \varepsilon$ the growth rate of the tearing mode is of the order $\gamma \approx \tau_\sigma^{-1}\left(\tau_a/\tau_\sigma\right)^{2/5}$ [12], while in the strong coupling approximation we have $\gamma \approx \tau_\sigma^{-1}\left(\varepsilon A_D \tau_\sigma/\tau_a^2\right)^{1/4}$.

2.5 The Taylor problem in weakly ionized plasmas

In this subsection we solve the so called "Taylor problem" in the framework of the MHD model taking into account the effects of ambipolar diffusion. In this problem a simple slab equilibrium is perturbed from the boundary, leading to the formation of magnetic islands at the center of the slab. This problem was solved in the framework of the MHD description [13]. In the long time limit the growth of the magnetic island width is algebraic.

Following the standard formulation of Taylor's problem of forced reconnection, we consider a slab configuration in the region $-L < y < L$, with a neutral plane of the magnetic field at $y = 0$. The unperturbed magnetic field is taken to be a linear function of y, i.e., $A_0 = -y^2/2$, which gives $\mathbf{B}_0 = B_0\mathbf{e}_x = y\mathbf{e}_x$.

The boundaries of the configuration are perturbed as follows: $y = \pm L(1 - \delta\cos kx/L)$, where δ is the perturbation amplitude, and k is the wavenumber. We assume the ratio δ/L to be small.

Linearization of the MHD equations for $A = A_0 + a$, $\Phi = \Phi_0 + \phi$, and $\Phi^{(n)} = \Phi_0^{(n)} + \phi^{(n)}$ gives

$$sa = ik\frac{B_0 y\phi}{L} + \nu_m\left(a'' - k^2 a\right), \tag{26}$$

$$\left(s + \frac{1}{\varepsilon A_D}\right)\left(\phi'' - k^2\phi\right) - \frac{1}{\varepsilon A_D}\left(\phi^{(n)\prime\prime} - k^2\phi^{(n)}\right) = ik\frac{B_0 y}{4\pi\rho_0 L}\left(a'' - k^2 a\right), \tag{27}$$

$$\left(s + \frac{1}{A_D}\right)\left(\phi^{(n)\prime\prime} - k^2\phi^{(n)}\right) - \frac{1}{A_D}\left(\phi'' - k^2\phi\right) = 0. \tag{28}$$

Here we have performed the Laplace transform with respect to time. We assume that the unperturbed vector potential is $A_0 = -y^2/2$ and that the perturbations are of the form $a = a(y)\cos kx$, $\phi = \phi(y)\sin kx$ and $\phi^{(n)} = \phi^{(n)}(y)\sin kx$.

Following the usual approach adopted for tearing modes, we divide the slab into two subregions: the external region where the adiabatic approximation is valid, i.e. where we can set $\partial_t = 0$, and the internal region where we must take into account dissipation effects. The size of the internal region has been determined above.

The equations that give the dependence of $a(0)$ on time in the a =const (ψ = const) approximation are given in Ref. [13] (see Eqs.(34) etc.). These equations porovide the relationship between $a(0, s)$, the amplitude of the perturbation δ and the function $\Delta'(s)$:

$$a(s,0) = \frac{B_0 2\delta k}{s\left(2k\cosh kL + \Delta'(s)\sinh kL\right)}, \tag{29}$$

where Δ' must be expressed via the dispersion equation of the tearing mode (24).

Renormalizing variables we can write

$$a(t,0) = \frac{1}{2\pi i}\oint\frac{\exp(pt)dp}{p(1+p)} = (1 - \exp(-t)). \tag{30}$$

We see that $a(t,0)$ tends to $a(0) = B_0\delta/\cosh kL$ when $t \to \infty$ exponentially with a typical time $\tau = \pi\left(\tau_\sigma^3\tau_a^2/\varepsilon A_D\right)^{1/4}\left(\Gamma(3/4)/\Gamma(1/4)\right)\tanh kL$, i.e., with the time scale of the tearing mode given by Eq. (25).

2.6 Collision of two current loops

The problems considered above shed light on the local properties of magnetic reconnection in weakly ionized plasmas in the vicinity of critical points of magnetic configurations or in the neighborhood of a current sheet. In order to elucidate the global properties of magnetic reconnection in weakly ionized plasmas, in Ref.[6] we have simulated the coalescence of two current loops. The collision of two current-loops was proposed as a solar flare model by Gold and Hoyle [14]. It provides a way of understanding many of the characteristic properties of solar flares, such as plasma heating, high-energy particle acceleration and oscillations in the amplitude of the electromagnetic emission [15]. Observations made with the *Yohkoh* satellite show two-loop coalescence in small solar flares [16].

We start from the one fluid MHD equations in which the ion-neutral drift is taken into account in the form of the ambipolar diffusion. Assuming that the density of the ionized component is relatively small, $\varepsilon \ll 1$, we neglect effects that may change the energy and the momentum of the neutral component due to ion-neutral collisions. In our simulations we choose the following parameter values: $\mathrm{R_m} = \tau_\sigma/\tau_a = 10^2$, $\beta = 1$, and A_D in the range 0-0.5. The plasma density, the magnetic field and the velocity are normalized to ρ_0, B_0, and to the Alfvén velocity $v_a = B_0/(4\pi\rho_0)^{1/2}$. Space is normalized to L and time to the Alfvén transit time $\tau_a = L/v_a$. The system dimensions are $0 \le x \le 6\pi L$, and $0 \le y \le 6\pi L$.

Each of two current loops is initially an equilibrium. The magnetic field in two loops is given by $B_\theta = B_m(r/a)/(1+(r/a)^2)$, $B_z = \pm B_0/(1+(r/a)^2)$: the radius of each loop is $a = 3L$, the z-component of the magnetic field is $\pm B_0$, and the maximum value of azimuthal component is $B_m/2 = 1$. The z-component of the magnetic field has opposite signs in the two loops. This corresponds to the case of counter-helicity of the magnetic configuration and leads to complete reconnection during the interaction of the two loops. When $B_m = B_0$ the two current loops become a force-free configuration. Initially the centers of two loops are on the lines $(x, y) = (3\pi L, 4.5\pi L)$ and $(x, y) = (3\pi L, 1.5\pi L)$, respectively.

We investigated the case without ambipolar diffusion, when $A_D = 0$, and the case when $A_D = 0.5$. In both cases a thin current sheet is formed between the two current loops where the magnetic field lines reconnect. Ambipolar diffusion leads to faster reconnection and makes the electric current distribution smoother than in the case without ambipolar diffusion. The analysis of the time evolution of the magnetic and of the kinetic energy inside the computation region shows that the effects of the ambipolar diffusion result in faster dissipation of the magnetic energy.

3 Interchange (Rayleigh-Taylor) instability of a thin plasma slab

We shall use the thin shell approximation [17]. We assume that initially the shell (infinite in the y- and z-directions) is located in the $x = 0$ plane. It moves under the action of the magnetic field and of a friction force on a neutral ion background. We take its thickness $l \to 0$ at constant surface mass $\sigma = \rho l$. We assume all variables to depend on two coordinates x and y and on time t.

We introduce the Lagrange variables, x_0, and y_0, related to the Euler coordinates by $x = x_0 + \xi_x(x_0, y_0, t)$ and $y = y_0 + \xi_y(x_0, y_0, t)$. Here $\xi_x(x_0, y_0, t)$ and $\xi_y(x_0, y_0, t)$ are the components of the shell displacement vector. We consider two points on the shell initially separated by the distance $ds_0 = |d\mathbf{r_0}| = ((dx_0)^2 + (dy_0)^2)^{1/2}$. Later, they are separated by the distance $ds = |d\mathbf{r}| = ((dx)^2 + (dy)^2)^{1/2}$. In the Lagrange variables we obtain for the surface mass $\sigma_0(s_0)\, ds_0 = \sigma(x_0, y_0, t) ds$. Next, we introduce the surface mass Lagrange variable m,

which is given by $m = \int^{s_0} \sigma_0(s_0)\, ds_0$.

The magnetic field pressure acts on an element of the shell of length $ds = |d\mathbf{r}|$ with the force $d\mathbf{f} = B^2(d\mathbf{r} \times \mathbf{e}_z)/8\pi$, where $d\mathbf{r}$ is a vector directed along the shell. Setting this force equal to $d\mathbf{f} = \nu^{(in)} dm \partial_t \mathbf{r}$ we obtain the equation of motion $\nu^{(in)} \sigma ds \dot{\mathbf{r}} = (B^2/8\pi)(d\mathbf{r} \times \mathbf{e}_z)$, where $\nu^{(in)}$ is the ion-neutral collision frequency.

Calculating $d\mathbf{r} = (d\mathbf{r}/ds_0)ds_0 = (d\mathbf{r}/dm)dm$, we write the equations of the shell motion in terms of the surface mass Lagrange variable and of the normalized time τ as

$$\partial_\tau x = \partial_m y, \qquad \text{and} \qquad \partial_\tau y = -\partial_m x. \tag{31}$$

Stationary motion of the plasma slab with constant velocity along the x-axis corresponds to the solution $x = \tau$, $y = m$. This solution is unstable against perturbations of the form $(x - \tau, y - m) \propto \exp(iqm)$, where q is the wavenumber of the perturbations in Lagrange variables. The growth rate of the instability is $\gamma = q$, while the growth rate of the Rayleigh-Taylor instability of a thin slab, where no friction is considered, is $\gamma_{RT} = q^{1/2}$.

The solution with initial conditions $x(0) = \xi_{x0} \sin(qm)$, and $y(0) = m + \xi_{y0} \cos(qm)$ describes the superposition of a uniform motion along the x-axis with constant velocity $V = 1$ and of exponentially growing perturbations with wavelength $2\pi/q$. In the nonlinear stage of the instability the shell is folded and cusps and bubbles are formed with a periodic chain of maxima and minima along the y-axis. The density of the plasma in the shell at the top of the bubbles decreases exponentially in time: $\sigma \sim \exp(-\gamma\tau)$ for $\tau \to \infty$. On the contrary, in the cusp region the density increases and a singularity appears in a finite time.

3.1 Conformal mapping to describe the R-T instability

In order to find the generic solution of the Cauchy problem we observe that Eqs.(31) are the Cauchy-Riemann conditions for the real and imaginary parts of an analytical function $W(\zeta)$ of complex variable $\zeta = m + i\tau$ (see also [18], where the nonlinear stage of the tearing mode was investigated). The real part of $W(\zeta)$ is equal to the x-coordinate of the shell, while the y-coordinate is the imaginary part. Thus we write $x + iy = W(\zeta)$. This expression is the conformal mapping from the complex plane $\zeta = m + i\tau$ to the plane $z = x + iy$. We notice that the analytical function $W(\zeta)$ is defined by its behavior on the real axis $t = 0$, i.e., by the initial conditions $\xi_x(y_0, 0)$ and $\xi_y(y_0, 0)$. This gives the solution of the Cauchy problem for the elliptical system of Eqs.(31).

The surface mass of the shell is equal to $\sigma = \sigma_0(m)/|W'(\zeta)|$, where a prime denotes differentiation with respect to the complex variable ζ. The function $|W'(\zeta)|$ is the Jacobian of the transformation that gives the time evolution of the position of the shell through the mapping of the curve $x + iy = W(m)$ into the curve $x + iy = W(m + i\tau)$.

A typical behavior of the solution corresponds to the initial conditions $x(m, 0) = \kappa_R/(1 + m^2)$, $y(m, 0) = -m + \kappa_I/(1 + m^2)$. The corresponding analytical function is

$$W(\zeta) = -i\zeta + \kappa/(1 + \zeta^2). \tag{32}$$

Here $\kappa = \kappa_R + i\kappa_I$ is a complex constant and its absolute value is the amplitude of the perturbation. These expressions describe perturbations that grow faster than exponential. It is easy to see that in the finite time $\tau = 1$, the Jacobian of the transformation $|W'|$ becomes infinite at $m = 0$. This corresponds to the rarefaction wave break which occurs with the formation of a hole in the plasma. For small amplitudes of the initial perturbation, $|\kappa| \ll 1$, we obtain

$$W(\zeta) \approx -i\zeta + \kappa/(2(\zeta - i)), \text{ and } W'(\zeta) \approx -i - \kappa/(2(\zeta - i)^2). \tag{33}$$

The typical singularity corresponds to the case when both the real and the imaginary parts of κ do not vanish. Then, first the compression wave break occurs at $t = 1 - (\kappa_I/2)^{1/2}$ at the point $m = -(\kappa_I/2)^{1/2}$ where the plasma density grows. Then, at the time $t = 1$, the plasma density vanishes at $m = 0$.

Conclusions

We conclude that the ambipolar diffusion in a weakly ionized plasma does not prevent reconnection of magnetic field lines. On the other hand, in itself it does not lead to reconnection because the magnetic field remains frozen in the ion component of the plasma and the magnetic field topology is unchanged. Ambipolar diffusion changes the time and space scales of reconnection, leading to a slowing-down of the process compared to that in the case where the neutral density vanishes, but it makes reconnection faster compared to the case without ion-neutral drift.

The solution of the Cauchy problem for the thin shell which describes the Rayleigh-Taylor instability in weakly ionized plasmas has been expressed in terms of analytical functions of complex variables. The singularities are of two types. The first type corresponds to the shell folding with compression wave breaking. The second one corresponds to the shell tearing with the formation of a density hole which occurs in a finite time.

References

[1] Kulsrud, R.M., Anderson, S.W., *Astrophys. J.*, **396**, 606 (1992); Suzuki, M., Sakai, J.I., *Astrophys. J.*, **465**, 393 (1996); Zweibel, E.G., Brandenburg, A., *Astrophys. J.*, **478**, 563 (1997).

[2] Shu, F.H., Adams, F.C., Lizano, S., *ARA & A*, **22**, 23 (1987).

[3] Heiles, C., in *Interstellar Processes* edited by D.J. Hollenbach, H.A. Thronson, Jr. (Dordrecht: Reidel. 1987); Mayers, P.C., Goodman, A., *Astrophys. J.*, **326**, L27 (1988).

[4] Sakai, J.-I., *Solar Physics*, **169**, 367 (1996).

[5] Vikhrev, V.V., Braginskii, S.I. *Rev. Plasma Phys.*, **10**, 243 (1980).

[6] Bulanov, S.V., Sakai, J.-I., *submitted to Astrophys. J.*.

[7] Syrovatskii, S.I., *Sov. Phys. JETP*, **50**, 1133 (1966); Bulanov, S.V., Syrovatskii, S.I., *Sov. J. Plasma Phys.*, bf 6, 1205 (1980).

[8] Bulanov, S.V., Pegoraro, F., *Phys. Lett. A*, **180**, 275 (1993), *Plasma Physics Reports*, **19**, 1120 (1993).

[9] Bulanov, S.V., Ol'shanetskij, M.A., *Phys. Lett.* A, **100**, 136 (1984); *Sov. J. Plasma Phys.*, **11**, 727 (1985); Bulanov, S.V., Sakai, J.-I., *J. Phys. Soc. Japan.* **67**, 1201 (1997).

[10] Bulanov, S.V., Pegoraro, F., Sakharov, A.S., *Phys. Fluids*, B, **4**, 2499 (1992).

[11] Dungey, J.W., *Phil. Mag.*, Ser. 7, **44**, 725 (1953); Imshennik, V.S., Syrovatskii, S.I.,*Sov. Phys. JETP*, **52**, 900 (1967); Tajima, T., Sakai, J.-I., *Sov. J. Plasma Physics*, 9, 606 (1989).

[12] Furth, H., Killen, H., Rosenbluth, M.N., *Phys. Fluids*, **6**, 459 (1963).

[13] Hahm, T.S., Kulsrud, R.M., *Phys. Fluids*, **28**, 2412 (1985).

[14] Gold, T., Hoyle, F., *MNRAS*, **120**, 89 (1960).

[15] Sakai, J.I., De Jager, C.,*Space Sci. Rev.*, **77**, 1 (1996).

[16] De Jager, C., Inda-Koide, M., Koide, S.J., Sakai, J.I., *Solar Physics*, **158**, 391 (1995); Inda-Koide, M., Sakai, J.I., et al., *Publ. Astron. Soc. Japan*, **47**, 323 (1995).

[17] Ott,E., *Phys. Rev. Lett.*, **29**, 1429 (1972).

[18] Bulanov, S.V., Sasorov, P.V., *Sov. J. Plasma Phys.*, **4**, 746 (1978).

Numerical Modeling on Thermal Plasma Characteristics and Plasma-Particle Interaction in Plasma Spray Process

Sang Hee Hong, Kyoung Doo Kang, and Byoung Lyong Choi

(Department of Nuclear Engineering, Seoul National University, Seoul, Korea)

ABSTRACT

A numerical analysis of thermal plasma produced by a nontransferred plasma torch is carried out both in an interior arc-gas interacting region and an exterior thermal plasma jet region. In addition, a numerical model is proposed to simulate the behavior of particles injected into the thermal plasma jet in atmospheric plasma spraying. The arc thermal plasma is described by a 2-D MHD model with the assumption of axisymmetric, LTE, and optically-thin plasma. A control volume method and a SIMPLER algorithm are used to solve conservation equations for mass, charge, momentum, and energy, along with standard k-ϵ equations for flow turbulence. Calculated images of arc thermal plasma jets are obtained from temperature and velocity distributions. Mixing effects of Ar-H_2 on plasma characteristics are found, and the role of shroud gas injection around the plasma flame is also examined. The plasma-particle interaction model includes the particle dense loading effect and the particle internal heat transfer. The influence of local dense loading of particles on the plasma flow is considered as the sources in the fluid conservation equations for semi 3-D calculations by PSI-cell method. The calculated particle velocities are compared with the measured ones by laser interferometry. The present models are applicable to prediction of thermal plasma characteristics and sprayed particle behavior as well as optimization of plasma spray process.

INTRODUCTION

Thermal plasma technologies are presently focused on two major thrust areas; materials processing and hazardous waste treatment. Typical materials processing includes plasma spraying, plasma synthesis, thermal plasma CVD, extractive metallurgy, etc.[1] Especially plasma spraying provides high-performance protective coatings, which enhance the service life of critical components exposed to aggresive environment.[2]

Plasma spraying uses a thermal plasma jet produced by arc discharge between cathode and anode nozzle in a dc plasma torch. An arc gas mixture supplied into the torch is ionized to form a plasma by the arc. Then the plasma expands through the nozzle as thermal plasma jet outside the torch. The coating powders injected into the high-temperature, high-velocity plasma jet are accelerated and heated to a molten state by momentum and heat transfers during their flight in the flame. Finally these high-speed molten particles impact on the substrate, and form lamella structured coatings by rapid solidification.

A conventional plasma spraying is carried out at an atmospheric pressure. Then the plasma jet is exposed to ambient air and mixed up with it. Therefore the coating structures are somewhat porous, and some coating properties are often unsatisfactory. In order to overcome these drawbacks of conventional spraying, a shroud gas injection device has been introduced. The torch operation with shroud gas injection is simple and economical compared with the low pressure plasma spraying with complicated and expensive vacuum facilities. The shroud gas forms a gas shielding shell around the plasma jet preventing ambient air from entering plasma flame.

Development of plasma spraying has been largely empirical and there is still lack of solid scientific and technological bases. Therefore, better understanding of complex phenomena and better control and optimization of spraying through process modeling are needed. Also, because of complexity of the process and the intrinsic versatile properties of thermal plasma,[3] there are still insufficient experimental database and poor understanding of physics of arc thermal plasma generation and plasma-particle interactions. Then process prediction by mathematical modeling approach is required for plasma spraying.

According to these reseach needs, the present work has carried out numerical modelings on arc thermal plasma jet and plasma-particle interaction in realistic situation of plasma spraying. Based on MHD approach, the thermal plasma characteristics of nontransferred torch for atmospheric plasma spraying is analyzed, and the Ar-H_2 mixing effect on the plasma jet characteristics is found by comparison of temperature, velocity, and enthalpy fields between Ar-H_2 and Ar plasmas. And the shroud gas injection effect on the air entrainment into the jet flame is investigated by calculating the distribution of air mole fractions mixed in thermal plasma jet. In the plasma-particle interaction modeling, a 3-D numerical code is developed to simulate the behavior of particles injected into the thermal plasma jet. The effects of dense loading and local injection of powder on the thermal plasma characteristics are found, and finally more

realistic information on optimal process conditions are obtained by observing trajectories and temperature histories of sprayed particles.

ARC THERMAL PLASMA JET MODELING

Theoretical Formulation

In the present work, the arc thermal plasmas are assumed to be in a stationary mode as commonly observed in the experiments. Since the system is axisymmetric, a 2-D cylindrical modeling gives a reasonable description of thermal plasmas. Most of regions of thermal plasma are considered to be in an LTE (local thermodynamic equilibrium) at the atmospheric condition. The plasma is optically thin, which means that reabsorption of radiation is negligible compared with total radiation losses over all wavelengths.

A set of nonlinear partial differential equations governing the arc thermal plasma system consists of conservation equations of mass, charge, momentum and energy of plasma flow. Mass fraction equation is taken into account to handle mixing of plasma with ambient air. The turbulent effects are included in the standard k- ε equations. For the convenience of deriving difference equations in numerical scheme, the governing equations can be expressed in a single conservation form as follows:[4]

$$\frac{\partial}{\partial z}\left(\rho u - \Gamma\frac{\partial}{\partial z}\right)\phi + \frac{1}{r}\frac{\partial}{\partial r}\left(r\left[\rho v - \Gamma\frac{\partial}{\partial r}\right]\right)\phi = S$$

	ϕ	Γ	S
Mass Continuity	1	0	0
Electric potential	Φ	σ	0
Axial momentum	u	μ	$j_r B_\theta - \frac{\partial P}{\partial z} + \frac{\partial}{\partial z}(\mu_e \frac{\partial u}{\partial z}) + \frac{1}{r}\frac{\partial}{\partial r}(r\mu_e \frac{\partial v}{\partial z})$
Radial momentum	v	μ	$-j_z B_\theta - \frac{\partial P}{\partial r} + \frac{\partial}{\partial z}(\mu_e \frac{\partial v}{\partial r}) + \frac{1}{r}\frac{\partial}{\partial r}(r\mu_e \frac{\partial v}{\partial r}) - \frac{2\mu_e v}{r^2}$
Azimuthal momentum	v_θ	μ	$-\frac{\rho v_r v_\theta}{r} - \frac{v_\theta}{r}\frac{\partial \mu}{\partial r} - \frac{\mu v_\theta}{r^2}$
Energy	T	μ/C_T	$\frac{1}{C_p}\left[v_r\frac{\partial P}{\partial r} + v_z\frac{\partial P}{\partial z} - S_R + \frac{j_z^2 + j_r^2}{\sigma} + \frac{5k_B}{2e}\left(j_z\frac{\partial T}{\partial z} + j_r\frac{\partial T}{\partial r}\right)\right]$
Mass fraction	m_f	μ/C_m	0
Turbulent K.E.	K	μ/C_K	$G - \rho\varepsilon$
Dissipation of T.K.E	ε	μ/C_ε	$C_1 G\frac{\varepsilon}{k} - C_2\rho\frac{\varepsilon^2}{k}$

ϕ represents the plasma variables to be solved, Γ is the effective transport coefficient, and S is the source term corresponding to ϕ. Compressible effect of fluids are also included in momentum equations. The interior arc-flow modeling includes electromagnetic body forces, joule heating generated by the arc, and electron enthalpy flux. But these terms are not involved in the outside plasma jet modeling. The appropriate boundary conditions are needed for finding unique solutions of these 2-D elliptic partial differential equations.[4]

Numerical Methods

Fig. 1 shows a computational domain of a nontransferred dc plasma torch with a shroud gas injection and realistic electrode geometry used in this numerical modeling. The domain is divided into two regions; an interior arc-gas interacting region and an exterior thermal plasma jet region. A numerical analysis of the arc-gas interaction inside the torch is first performed and then the resultant calculated values are used as boundary conditions at the torch exit for the outside modeling for plasma jet.

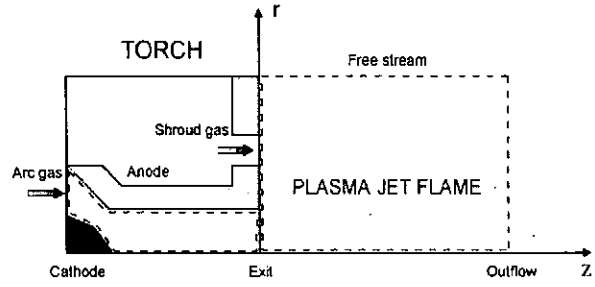

Fig. 1. Computational domain of numerical model for a nontransferred plasma torch with shroud gas injection.

In numerical calculations, two different grid generation methods are taken for inside and outside regions, respectively, because of large differences in spacial sizes between two domains and different flow phenomena between arc plasma generation and plasma jet expansion. Since the physical domain is not a rectangular inside the realistic torch, while it is a rectangular outside the torch, 2-D elliptic and algebraic grid generators are used respectively.

The control volume method is used for differencing the governing equations. The SIMPLER (semi-implicit method for pressure linked equation revised) algorithm[5] is employed for the iterative calculations. The finite difference equations are solved by MSI (modified strongly implicit) procedure which is an efficient method for solving the penta-diagonal matrices. For suppressing numerical instability during the iteration, an under-relaxation scheme is adopted.

Calculated Results

The effect of Ar-H_2 mixing on plasma properties is analyzed by using typical values of plasma torch parameters as listed in Table 1.

Table 1. Parameter values used in a typical operating condition of plasma torch.

Arc gas	Ar/(0-30)%H_2
Flow rate of arc gas	40 LPM
Input current	500 A
Nozzle diameter	7 mm
Inlet swirl number	0.5

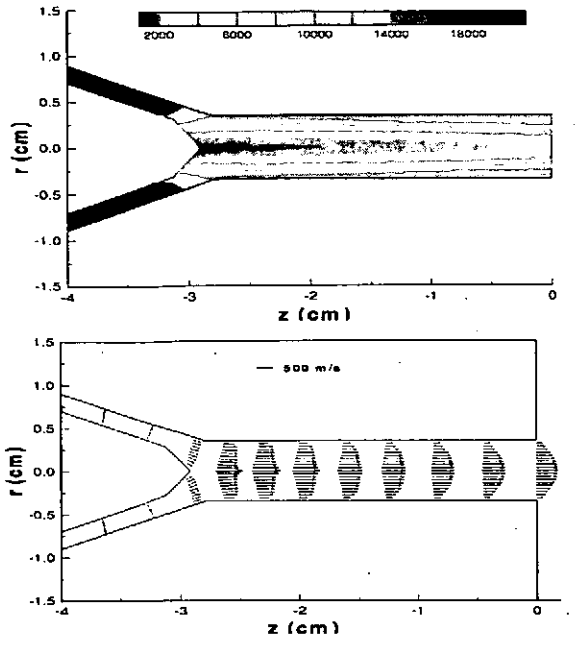

Fig. 2. Temperature distribution and velocity vectors of Ar arc plasma inside the torch.

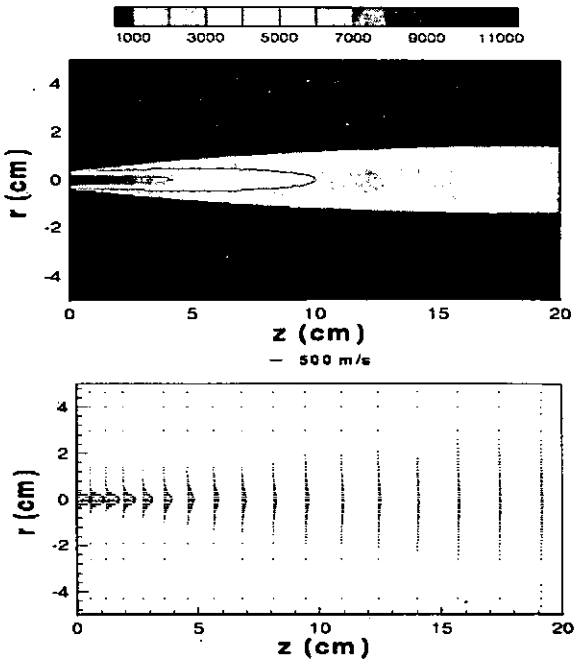

Fig. 3. Temperature distribution and velocity vectors of Ar thermal plasma jet outside the torch.

Plasma temperature and velocity vectors inside the torch between cathode and anode are plotted in Fig. 2.[6] The cathode jet overhelming the anode one has a maximum temperature of 22300 K near the cathode spot and a maximum axial velocity of 940 m/s in front of the cathode. The jets develop into parabolic profiles of temperature and axial velocity at the torch exit, which will be used as boundary conditions for the outside modeling.

Fig. 3 shows temperature distribution and velocity vectors of plasma jet flame ejected from the torch exit into the outside region.[6] The steep radial and axial gradients are seen in the turbulent-free upstream region of the flame. But the gradients are gradually reduced by turbulent effects caused by mixing of plasma jet with surrounding cold air in the downstream region.

The curves in Fig. 4 indicate the effects of addition of a secondary H_2 gas into a primary Ar gas on plasma temperature, velocity, and enthalpy at the torch exit. As the H_2 mixing mole fraction increases, the plasma temperature decreases due to high heat capacity of hydrogen molecular gas. On the other hand, the axial velocity is increased with mole fraction in consequence of low mass density of H_2. Ar-H_2 mixture plasma has a relatively broad radial profile of higher enthalpy than pure Ar plasma at the torch exit. The difference in enthalpy between pure and mixture plasma jets is more clearly observed in the enthalpy distributions not presented here.[4] Ar-H_2 plasma has larger heat content than pure Ar jet within a spray distance. Then the powder injected near the torch exit is expected to be fully melted during their flight in the high enthalpy jet region. Therefore, Ar-H_2 mixure plasma is preferable to

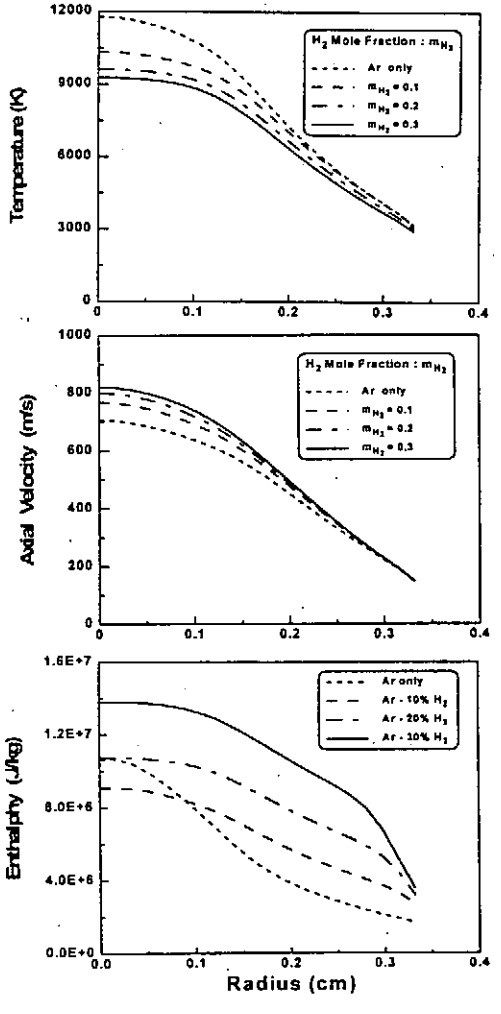

Fig. 4. Radial dependency of Ar-H_2 plasma fields at the torch exit on H_2 mole fraction mixed with Ar.

pure Ar plasma for plasma spray coating.

In the following, numerical results are discussed for a torch with Ar shroud gas injection operated with typcal values in Table 2.

Table 2. Operation parameters of the plasma torch with shroud gas injection.

Arc gas	Ar/20%H_2
Flow rate of arc gas	40 LPM
Input current	500 A
Nozzle diameter	7 mm
Shroud gas :	Ar
Flow rate	150 LPM
Swirl number	0.5
Radial injection position	1.85 cm
Annular channel width	2 mm

Fig. 5 shows the distributions of air mole fraction mixed up in the Ar-H_2 plasma jet without and with shroud gas. When no shroud gas injection is used, surrounding air has invaded a wide range of plasma flame. In the operation with shroud gas, the shroud gas forms a gas shielding shell around the jet flame which prevents ambient air from entering the jet. Then the plasma is almost in an air-free state within the spray distance.

The general feature of temperature configurations looks almost similar without and with shroud gas injection.[4] When Ar shroud gas is introduced, the axial velocities are a bit slowed down.[4] Then it is summarized from the calculated results for shroud gas that the shroud system has a great advantage of blocking air entrainment in the plasma jet without significant changes of plasma temperatures and velocities.

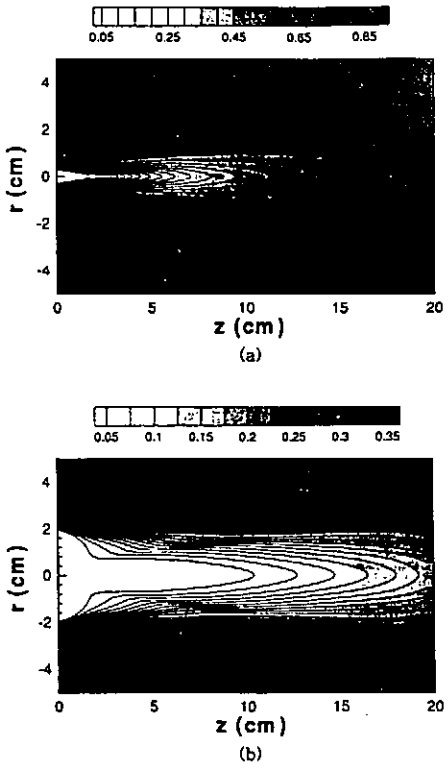

Fig. 5. Comparison of distributions of air mole fraction invaded in the plasma jet flame (a) without and (b) with Ar shroud gas.

PLASMA-PARTICLE INTERACTION MODELING

Theoretical Formulation and Numerical Methods

A numerical analysis of plasma-particle interaction is carried out to find the trajectories and temperature histories of sprayed particles in the plasma jet flame. The computational domain of interaction modeling is practically the same as that of the plasma jet modeling discussed so far. Only difference from the previous one is that a lot of particles with different sizes are injected locally from a powder feeding port just in front of the torch exit. These dense loading and local radial injection of powder make the plasma flow nonaxisymmetric. Then the previous 2-D jet code is no longer valid and needs to be extended to a 3-D code depending on the θ coordinate.

Under the influence of dense loading local injection of particles, the 3-D plasma jet fields can be described as the sum of axisymmetric unperturbed field and nonaxisymmetric perturbed one which is expressed by Fourier series expansions about θ:

$$f(r,\theta,z) = f_0(r,z) + \sum_{m=-\infty}^{\infty} f_{1m}(r,z)\, e^{im\theta}$$

A particle source generated by powder injection is also considered in the form of Fourier series expansion. Substituting these expressions into the conservation equations of mass, momentum and energy, a 3-D governing equations are derived for plasma jet fields perturbed by sprayed particles[7,8].

Compared with the previous 2-D case, some additional terms in the bracket and the source terms resulted from local particle injection appear. If the additional terms are treated as sources of

	Governing Equations for Thermal Plasma Jet Fields Perturbed by Sprayed Particles
Mass	$\frac{1}{r}\frac{\partial}{\partial r}r(\rho_0 v_1) + \frac{\partial}{\partial z}(\rho_0 u_1) = -\left\{\frac{1}{r}\frac{\partial}{\partial r}r(\rho_1 v_0) + \frac{\partial}{\partial z}(\rho_1 u_0)\right\} + S_p^{m,c}$
Momentum	$\frac{1}{r}\frac{\partial}{\partial r}r(2\rho_0 v_0 v_1 - \mu_e\frac{\partial v_1}{\partial r}) + \frac{\partial}{\partial z}(\rho_0 u_0 v_1 - \mu_e\frac{\partial v_1}{\partial z})$ $= -\frac{\partial P_1}{\partial r} + \frac{1}{r}\frac{\partial}{\partial r}(r\mu_e\frac{\partial v_1}{\partial r}) + \frac{\partial}{\partial z}(\mu_e\frac{\partial u_1}{\partial r}) - \frac{2\mu_e v_1}{r^2} - \left\{\frac{1}{r}\frac{\partial}{\partial r}r(\rho_1 v_0^2) + \frac{m^2\mu_e v_1}{r^2} + \frac{\partial}{\partial z}(\rho_0 v_0 u_1 + \rho_1 v_0 u_0)\right\} + S_p^{m,M_r}$
	$\frac{1}{r}\frac{\partial}{\partial r}r(\rho_0 v_0 u_1 - \mu_e\frac{\partial u_1}{\partial r}) + \frac{\partial}{\partial z}(2\rho_0 u_0 u_1 - \mu_e\frac{\partial u_1}{\partial z})$ $= -\frac{\partial P_1}{\partial z} + \frac{1}{r}\frac{\partial}{\partial r}(r\mu_e\frac{\partial v_1}{\partial z}) + \frac{\partial}{\partial z}(\mu_e\frac{\partial u_1}{\partial z}) - \left\{\frac{1}{r}\frac{\partial}{\partial r}r(\rho_0 v_1 u_0 + \rho_1 v_0 u_0) + \frac{m^2\mu_e u_1}{r^2} + \frac{\partial}{\partial z}(\rho_1 u_0^2)\right\} + S_p^{m,M_z}$
Energy	$\frac{1}{r}\frac{\partial}{\partial r}r(\rho_0 v_0 T_1 - \frac{\mu_e}{\sigma_T}\frac{\partial T_1}{\partial r}) + \frac{\partial}{\partial z}(\rho_0 u_0 T_1 - \frac{\mu_e}{\sigma_T}\frac{\partial T_1}{\partial z})$ $= -\frac{U_1}{c_p} - \left\{\frac{1}{r}\frac{\partial}{\partial r}r(\rho_0 v_1 T_0 + \rho_1 v_0 T_0) + \frac{m^2\mu_e T_1}{r^2\sigma_T} + \frac{\partial}{\partial z}(\rho_0 u_1 T_0 + \rho_1 u_0 T_0)\right\} + S_p^{m,E}$

the 2-D plasma jet modeling, the 3-D perturbed equations can be solved by using the existing 2-D jet code without considerable modification in its numerical scheme.

The loading effects of particles on plasma jet are calculated by PSI-C (particle source in-cell) method. This method is based on the idea of treating particles as sources of mass, momentum and energy produced by momentum and heat transfers in the cells crossed by particle trajectories.[7] The individual particle trajectory is found from a single particle equation motion:

$$\frac{du_p}{dt} = -\frac{3}{4} C_D (u_p - u) u_R \left(\frac{\rho}{\rho_p d_p}\right) + g$$

$$\frac{dv_p}{dt} = -\frac{3}{4} C_D (v_p - v) u_R \left(\frac{\rho}{\rho_p d_p}\right)$$

where C_D is the drag coefficient and $u_R = \sqrt{(u_p - u)^2 + (v_p - v)^2}$ is the relative speed between the particle and the plasma jet.

The internal heat transfer and phase transition are described by a heat conduction equation,

$$\rho(T_p) C_p(T_p) \frac{\partial T_p}{\partial t} = \frac{1}{r^2} \frac{\partial}{\partial r}\left[r^2 \lambda(T_p) \frac{\partial T_p}{\partial r}\right]$$

subject to the boundary conditions at the different phase state of particles. The movement of the phase change in the particle is calculated at moving grids with different spacings.[7] In general, the particle trajectory in plasma jet undergoes the phase states of solid, melting, evaporation and resolidification subsequently on its way of flight in the plasma jet flame.

Calculated Results

The effect of particle injection on jet plasma temperature calculated by the plasma-particle modeling is shown in Fig. 6. By direct comparison between two figures before and after powder injection, the isotherms are seen displaced in the tail of the flame and shortened a bit in the axial direction by particle injection. However, no appreciable changes are observed

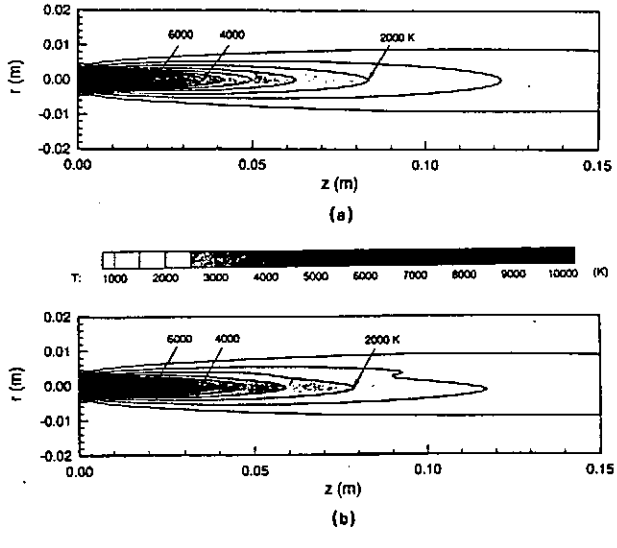

Fig. 6. Comparison of temperature contours of plasma jet (a) before and (b) after particle injection.

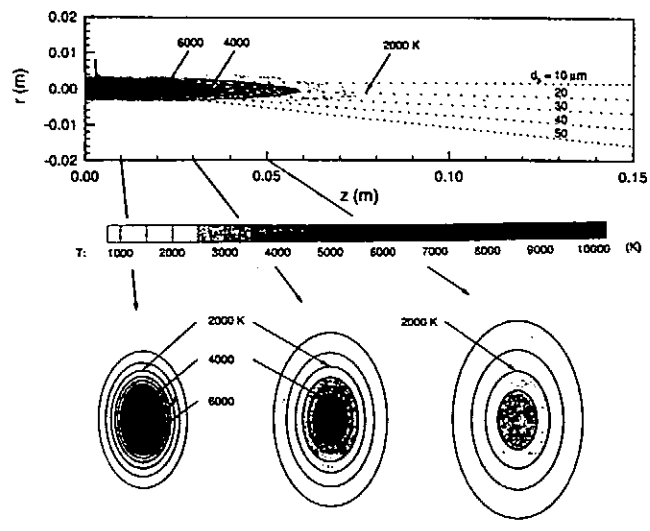

Fig. 7. Trajectories of sprayed particles with different diameters in the disturbed plasma flame and several cross-sectional views of temperature distribution at different axial positions.

between two velocity contours before and after particle injection.[7,8] This means that energy transfer from particle to jet plasma is rather serious than momentum transfer in the jet flame.

Figure 7 shows the trajectories of sprayed particles in the perturbed plasma flame. The motions of particles with different diameters d_p are indicated by dots with a time interval of 20 μs. The 20- μm particle is traveling along the axis of the flame where temperature and velocity are higher than other regions. Then this particle is expected to be in a high-speed molten state when it arrives at the substrate. Several cross-sectional views of particle temperature distribution at different axial positions are also displayed here from the present 3-D modeling. Steep temperature gradients along radial and axial directions are clearly seen, but their azimuthal changes are hardly appreciable in these figures.

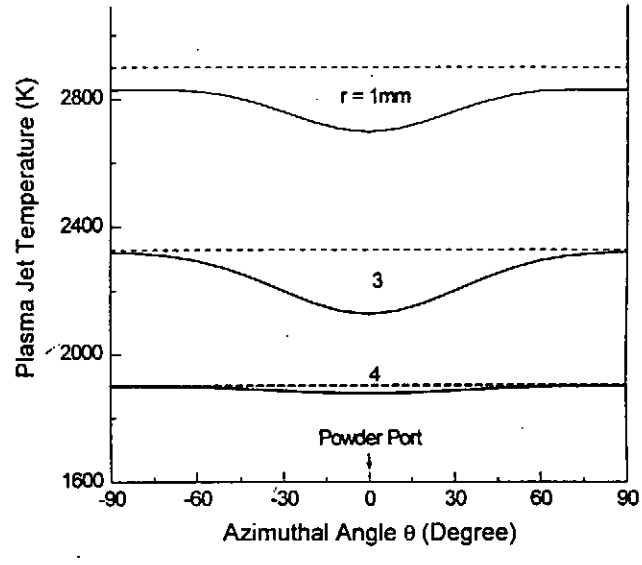

Fig. 8. Azimuthal profiles of plasma temperature calculated for different radial positions at a fixed axial position of 5 cm before (-----) and after (——) powder injection.

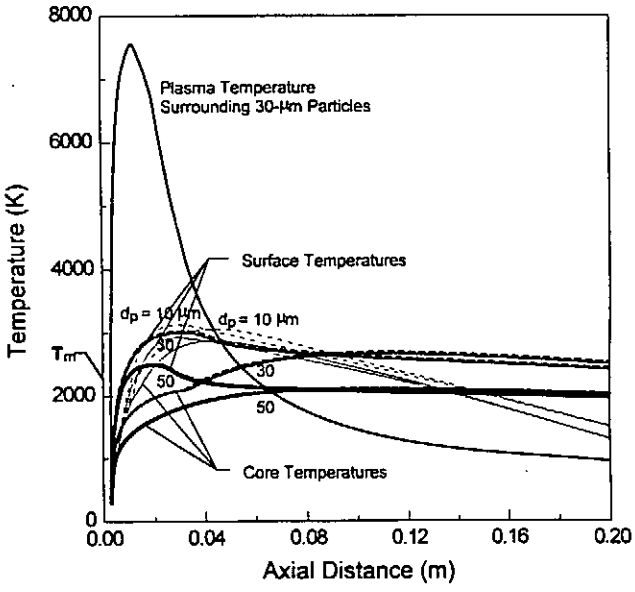

Fig. 9. Changes of surface and core temperatures of sprayed particle of different sizes traveling in the plasma jet flame before (----) and after (——) powder injection.

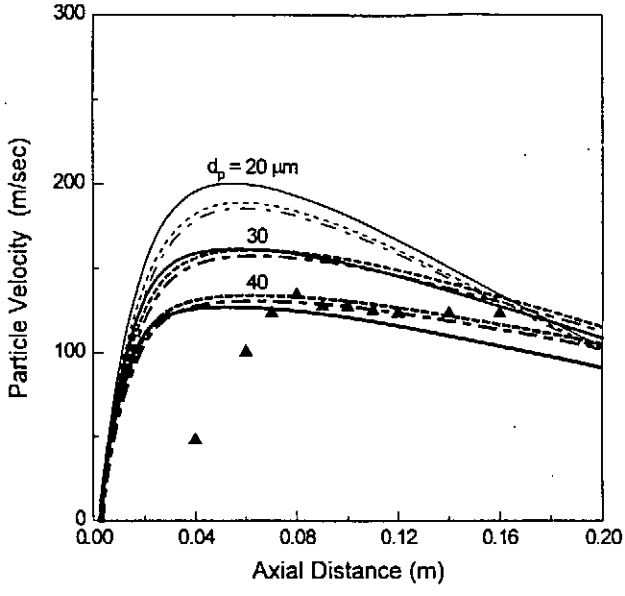

Fig. 10. Comparison of calculated particle velocities (curves) of different sizes with experimental ones (△ △△) measured by laser interferometry.

The θ-dependancy of plasma temperature on particle injection is recognized in the curves in Fig. 8 drawn at different radial positions. The temperature difference caused by particle injection is more significant in the core region than the peripheral region of the plasma flame.

Fig. 9 illustrates the changes of surface and core temperatures of several particle groups of different sizes when they are moving along plasma jet. This figure indicates that most of particle groups of different sizes are expected to be fully melted at the spray distance where a substrate is usually placed for spray coating.

The present numerical results of parcicle velocities for different sizes are compared with experimental ones measured by laser interferometry[9] as shown in Fig. 10. Although calculated velocities are higher than measured ones in the plasma upstream region, the trend and values of computed velocities are in good agreement with those of measured ones in the downstream region where the plasma spray process is mostly performed. Therfore the present analysis of plasma-particle interaction modeling is applicable to predict and evaluate operating conditions for plasma spray process.

CONCLUSION

In the arc thermal plasma jet modeling of a nontransferred plasma torch at atmospheric condition, numerical calculations show that cathode jet prevails in the interior arc-gas interacting region, and that turbulent effects appear in temperature and velocity distributions in the exterior plasma jet region. High enthalpy thermal plasma can be achieved by addition of hydrogen to primary argon to get a dense adhesive spray coating. The entrainment of ambient air is almost shielded by shroud gas injection without significant changes of thermal plasma properties to produce a high quality spray coating with no unwanted composites in it.

In the plasma-particle interaction modeling of plasma spray process, a three-dimensional numerical code has been developed to simulate the behavior of sprayed particles under dense loading and local injection conditions. Energy transfer from thermal plasma to sprayed particle turns out to be significant while momentum transfer between them is comparatively negligible. The present numerical modelings for arc thermal plasma jet and plasma-particle interaction are useful not only for prediction of thermal plasma characteristics and sprayed particle behavior but for optimization of plasma spray process.

REFERENCES

1. O. P. Solonenko and M. F. Zhukov, *Thermal Plasma and Material Technology* (Interscience, Cambridge, 1994).
2. R. Suryanarayanan, *Plamsa Spraying* (World Scientific, Singapore, 1993).
3. M. I. Boulous, P. Fauchais, and E. Pfender, *Thermal Plasma, Vol.1 Fundamentals and Applications* (Plenum, New York, 1994).
4. K. D. Kang, Ph.D. Dissertation, Seoul National University, Seoul Korea, 1996.
5. K. C. Karki, Ph. D. Dissertation, University of Minnesota, Minneapolis, 1986.
6. K. D. Kang and S. H. Hong, IEEE Trans. Plasma Sci., **24**, 89 (1996).
7. B. L. Choi, Ph.D. Dissertation, Seoul National University, Seoul, Korea, 1996.
8. B. L. Choi and S. H. Hong, Mat. Manuf. Process, **12**, 309 (1997).
9. B. L. Choi, S. I. Lee, Y. H. Kim, and S. H. Hong, Proc. 14th Int. Thermal Spraying Conf., p.445, Kobe, Japan, 22-26 May 1995.

THE ION SPHERE MODEL OF A DUSTY PLASMA

Yan-Ping Chen
Institute of Physics & Center for Condensed Matter Physics
Chinese Academy of Sciences, Beijing 100080, P.R.China

ABSTRACT

An ion sphere model is extended to the strongly coupled dusty plasma. The single and complex ion sphere models are introduced for dust grain and the surrounding plasma.Their electronstatic potential are evaluated. Various characteristics, e.g. interaction between dusts, coagulation of dusts, polarization of dusty plasma, molecule-like state, are discussed with this model.

I.INTRODUCTION

Dusts are widely distributed in the universe, interstellar as well as labora-tory devices of plasma. They may be charged by their surrounding plasma up to high value, e.g, $10^3e - 10^4e$, where e is the elementary charge of an electron. According to Debye-Hückel theory, the potential of a charge in a plasma is screened in a length of λ, where

$$\lambda = (\lambda_e^{-2} + \lambda_i^{-2} + \lambda_d^{-2})^{-1/2}$$

$\lambda_e, \lambda_i, \lambda_d$, are Debye shielding length by electrons , ions and dusts respec-tively. In most cases for the experiments with low temperature plasma devices, $\lambda_d << \lambda_e$, λ_i, $\lambda \simeq \lambda_d$ and also $\lambda < a = (\frac{4\pi n_d}{3})^{1/3}$, mean distance between dusts. With a Debye sphere of radius λ_d, the number of dusts, $N_d = \frac{4\pi n_d \lambda_d^3}{3} \simeq \Gamma_d^{-1/2}$, decreases

with the coulomb coupling constant $\Gamma_d = \frac{(z_d e)^2}{T_d}$, where T_d is the dust temperature. With high z_d, Γ_d may be much larger than one, which means N_d less than one, i.e, no other dust can enter into the Debye sphere. How could the potential of a dust be shielded by other dust in sphere with radius λ_d? It is clearly uncoincident with the definition of the Debye sphere. Because Debye sphere model is a linear shielding theory, in the case of $\frac{e\phi}{T} \geq 1$, linear expansion is no longer applicable. In one component plasma, an ion sphere model is introduced[1]. Here we will extend this model to the dusty plasma and discuss some issues.

II. THE ION SPHERE MODEL

One component plasma consists of ions with charge Ze and uniform neutralizing background . An ion sphere is considered as a sphere with an ion Ze and its surrounding neutralizing charge sphere with density n_e , whose total electric charge is just enough to cancel the ion charge Ze. This sphere thus represents the territorial domain of influence for the charge Ze, hence is called ion sphere .Its radius is equal to $(\frac{3z}{4\pi n_e})^{1/3}$.

Dusty plasma consists of electrons, ions and dusts . Dusts are highly negatively charged by electrons usually and are much heavier than ions . Therefore ions and electrons may closely move together with dusts. So we may construct an ion sphere for a dust with a neutralizing background of electrons and ions . The radius of dust ion sphere is

$$a = \left[\frac{3z_d}{4\pi(n_i z_i - n_e)}\right]^{1/3}, \tag{1}$$

where $-z_d e$, $z_i e$ are the electric charge of a dust and an ion, n_i, n_e are the density of ions and electrons . There are following kinds of potential energy in the dust ion sphere:

$$\varphi_{id} = \int \frac{-z_d e}{r_{id}} z_i e n_i d\tau_i = -2\pi a^2 \left(1 - \frac{r^2}{3a^2}\right) n_i z_i z_d e^2, \tag{2}$$

$$\varphi_{ed} = \int \frac{-z_d e}{r_{ed}}(-en_e)d\tau_e = 2\pi a^2\left(1-\frac{r^2}{3a^2}\right)n_e z_d e^2, \tag{3}$$

$$\varphi_{ii} = \frac{1}{2}\int \frac{{z_i}^2 e^2}{r_{ii}} n_{i1} n_{i2} d\tau_{i1} d\tau_{i2} = \frac{16}{15}\pi^2 a^5 {n_i}^2 {z_i}^2 e^2, \tag{4}$$

$$\varphi_{ee} = \frac{1}{2}\int \frac{e^2}{r_{ee}} n_{e1} n_{e2} d\tau_{e1} d\tau_{e2} = \frac{16}{15}\pi^2 a^5 {n_e}^2 e^2 \tag{5}$$

$$\varphi_{ei} = -\frac{1}{2}\int \frac{z_i e^2}{r_{ei}} n_e n_i d\tau_e d\tau_i = -\frac{16}{15}\pi^2 a^5 n_e n_i z_i e^2, \tag{6}$$

where φ_{jk} is the interaction potential between species j and k , r_{jk} is the distance between particles j and k, $d\tau_{ei}$ is differential volume occupied by electrons and ions and the dust is assumed to be located at r from the center of the ion sphere . Summing up all above terms we obtain the total electrostatic energy associated with the ion sphere:

$$\begin{aligned}\varphi &= \varphi_{id} + \varphi_{ed} + \varphi_{ii} + \varphi_{ee} + \varphi_{ei} \\ &= \frac{-3{z_d}^2 e^2}{2a}\left(1-\frac{r^2}{3a^2}\right) + \frac{3{z_d}^2 e^2}{5a} c_d,\end{aligned} \tag{7}$$

where

$$c_d = \frac{{n_i}^2 {z_i}^2 + {n_e}^2 - n_e n_i z_i}{(n_i z_i - n_e)^2}.$$

With the neutral condition $n_i z_i = n_e + n_d z_d$, c_d may be written as:

$$c_d = 1 + \frac{n_e}{n_d z_d} + \frac{{n_e}^2}{{n_d}^2 {z_d}^2}. \tag{8}$$

If a dust is located at the center ,$r = 0$, the electric field outside the sphere is totally screened. The polarization of the ion sphere ($r \neq 0$) causes the nonzero electric field outside.When two dusts close each other, complex ion sphere could be constructed with radius of $a_2 = 2^{1/3}a$ by the charge balance: $\frac{4}{3}\pi {a_2}^3(n_i z_i - n_e) = 2z_d$. Similarly we can obtain the total electrostatic energy:

$$\Phi = \varphi_{dd} + 2(\varphi_{id} + \varphi_{ed}) + \varphi_{ii} + \varphi_{ei} + \varphi_{ee}$$

$$= \frac{z_d{}^2 e^2}{r} - 3 \cdot 2^{2/3} \frac{z_d{}^2 e^2}{a}(1 - \frac{r^2}{3 \cdot 2^{8/3} a^2}) + \frac{6 \cdot 2^{2/3}}{5} \frac{z_d{}^2 e^2}{a} c_d \qquad [9]$$

where r is the distance between two dusts.

III . CHARGING EFFECT OF DUST ON THE ION SPHERE POTENTIAL .

Dusts are charged by surrounding plasma particles. It's charge number is determined by the charging current of ions and electrons. The floating potential of a dust is $\phi_f = -z_{d\infty} e / r_g$, where r_g is the radius of a dust if the plasma effect is neglected. When two dusts close to each other by a distance r , the potential at the surface of dust 1 is caused by two dusts:

$$\varphi_{f1} = -\frac{z_{d1} e}{r_g} - \frac{z_{d2} e}{r}, \qquad (10)$$

here $r_g \ll r$ is assumed.By charging up to the same potential as φ_f , the charge z_d of dust 1 may be reduced from $z_{d\infty}$ in isolated case to z_{d1}:

$$z_{d1} = \frac{r}{r + r_g} z_{d\infty}. \qquad (11)$$

Let $z_d = z_{d1}$, the total electrostatic energy of the complex ion sphere in Eq.(9) becomes:

$$\Phi = \frac{(z_{d\infty} e)^2}{a} \left(\frac{r}{r + r_g} \right)^2 \left[\frac{a}{r} - 3 \cdot 2^{2/3} (1 - \frac{r^2}{3 \cdot 2^{8/3} a^2}) + \frac{3 \cdot 2^{5/3}}{5} c_d \right]. \qquad (12)$$

IV ANALYZATION OF THE CHARACTERISTICS OF THE ION SPHERE POTENTIAL

1. E-field outside the sphere

It is obvious that no electric field is induced outside the ion sphere when a dust is located at the center of the ion sphere, i.e, the electric potential is totally shielded by the neutralizing background charge in the ion sphere. In fact dusts are of finite temperature. They always move or oscillate in space. They are generally off the center due to inertia and cause the polarization of the ion sphere . Then the electric field outside the sphere is not zero and not isotropic. The potential of any point A at a distance R from the ion sphere center is

$$\Phi = \frac{z_d e}{R} - \frac{z_d e}{(R^2 + r^2 - 2rRcos\theta)^{1/2}}, \tag{13}$$

where the first term is from the background and second term from the dust. Then the electric fields E_R and E_θ in the R and θ direction are as follows:

$$E_R = \frac{z_d e}{R^2} - \frac{z_d e(R - rcos\theta)}{(R^2 + r^2 - 2rRcos\theta)^{3/2}}, \tag{14}$$

$$E_\theta = \frac{-z_d e r sin\theta}{(R^2 + r^2 - 2rRcos\theta)^{3/2}}. \tag{15}$$

From Eq.(14) we know that there is a critical angle

$$\theta_c \simeq cos^{-1}\frac{3r}{4R}, \tag{16}$$

where $r/R \ll 1$ is assumed. In region I of $-\theta_c \ll \theta \ll \theta_c$, E_R is negative, outside this region , denoted by region II, E_R is positive . When other negatively charged dusts enter region I , they will be repelled . When other dusts enter region II , they will be attracted. If $r/R \ll 1$, the E field of Eq.(14) is reduced to $\frac{-2z_d e}{R^3} r cos\theta$, it is a dipole field .

2 .The coagulation of dusts

Normalizing Φ by $(z_{d\infty} e)^2/a$, r and r_g by a , we obtain the dimensionless potential of the complex ion sphere from Eq.(12):

$$\Phi = \left(\frac{r}{r+r_g}\right)^2 \left[\frac{1}{r} - 3\cdot 2^{2/3}(1 - \frac{r^2}{3\cdot 2^{8/3}}) + \frac{3\cdot 2^{5/3}}{5}c_d\right]. \qquad (12')$$

Differentiating it with respect to r we have

$$\frac{\partial\Phi}{\partial r} = \frac{2r_g}{(r+r_g)^3}\left[r\left(\frac{3\cdot 2^{5/3}}{5}c_d - 3\cdot 2^{2/3} - \frac{1}{2r_g}\right) + \frac{1}{2} + \frac{3r^3}{4} + \frac{r^3}{2r_g}\right]. \qquad (17)$$

If the coefficient of r in square brackets of Eq.(17) , denoted by

$$c_1 \equiv \frac{3\cdot 2^{5/3}c_d}{5} - 3\cdot 2^{2/3} - 0.5r_g,$$

is positive, Φ is monotonic. Only for negative c_1, i.e :

$$\frac{n_e}{n_d z_d} < c_+ \equiv \frac{1}{2}\left[\left(7 + \frac{5}{3\cdot 2^{2/3}r_g}\right)^{1/2} - 1\right], \qquad (18)$$

Φ may have extremums: a maximum at small r and a minimum at larger r. The potential Φ vs. r with different values of $n_e/n_d z_d$ is shown in Fig.1, where r_g/a is taken to be 0.1 and the corresponding c_+ is 1.59. The curves 1-5 correspond to five values of $\frac{n_e}{n_d z_d}$: 2.0 , 1.59 , 1.0 , 0.5 , 0 . For curves 1 and 2, $\frac{n_e}{n_d z_d} \geq c_+$, Φ is monotonicly increasing with r. For small dusts charged with small z_d , the condition $\frac{n_e}{n_d z_d} \geq c_+$ is easily satisfied. Hence when two small dusts close ,they are attracted each other. Finally they are coagulated being a larger one to reach the minimum potential. By growing up the charge number of dust increases, then $\frac{n_e}{n_d z_d} < c_+$ is satisfied, which leads to a peak of the potential, e.g curves 3-5 in Fig.1. Only those dusts with enough kinetic energy can climb over the potential peak to be coagulated. By raising radio frequency heating power dusts may grow up larger. From $\frac{n_e}{n_d z_d} = c_+$ we obtain the critical value of r_g:

$$\frac{r_g}{a} \simeq \frac{5}{3\cdot 2^{8/3}}\left(\frac{n_d z_d}{n_e}\right)^2, \qquad (19)$$

where we have assumed $a/r_g > 7$. The experiment of Y.Hayashi and K.Tachibana[2] is in good agreement with Eq.(19). In this experiment $r_g \sim 1100nm$,

$n_d \sim 6 \times 10^5 cm^{-3}$, $n_i \sim 10^9 cm^{-3}$, $T_d \sim 0.03ev$, $\Gamma \sim 200$. From these z_d may be estimated as ~ 500 and both sides of Eq.(19) are about 0.02.

3. Molecule-like state .

When dusts grow up to a size larger than r_g , the potential peak between dusts prevents them further coagulation and may be in a molecule-like state. There is a potential well at $r = r_{min}$, determined by the following equation :

$$\frac{r}{a}\left(-3 \cdot 2^{2/3} + \frac{6 \cdot 2^{2/3}}{5} c_d - \frac{a}{2r_g}\right) + \frac{1}{2} + \frac{r^3}{2a^3} + \frac{r^4}{4a^3 r_g} = 0. \tag{20}$$

By letting $r = a + \delta$ with $\delta/a \ll 1$, keeping up to $o(\frac{\delta}{a})^2$ we obtain from Eq.(20) :

$$\frac{\delta}{a} \simeq \frac{(B^2 - 4AC)^{1/2} - B}{2A}, \tag{21}$$

where $A = \frac{3}{2}(\frac{a}{r_g} + 1)$, $B = \frac{a}{2r_g} + \frac{3}{2} - 3 \cdot 2^{2/3} + \frac{6 \cdot 2^{2/3}}{5} c_d$, $C = B - \frac{1}{2} - \frac{3a}{4r_g}$. If $a >> r_g$, the expression(21) may be reduced, then we have :

$$\frac{r_{min}}{a} \simeq \frac{5}{6} + \frac{1}{3}\left(\frac{7}{4} - 6 \cdot 2^{2/3} \frac{r_g}{a} c_d\right)^{1/2}. \tag{22}$$

When two dust grains close to each other, they may form a complex ion sphere. If the electrostatic energy Φ of complex ion sphere is less than the sum of that of the previous two single ion spheres, i.e. 2φ for totally same grains, the complex ion sphere can be maintained for a long time as a molecule-like state. The necessary condition for the existence of a molecule-like state is

$$\Delta \equiv \Phi(r_{min}) - 2\varphi < 0, \tag{23}$$

By using the results of Eqs.(7) and (12) the above condition is reduced to the following:

$$0.7 c_d + \frac{a}{r_{min}} < 1.76 \tag{24}$$

By combining it with Eq.(12) we obtain the necessary condition:

$$c_d < 1.49, \quad i.e. \quad \frac{n_e}{n_d z_d} < 0.36, \qquad [25]$$

which means that the dust-molecule may appear only in the case of dust grains with high enough density and charge. The potential well Δ, i.e. the binding energy of a dust molecule depends on c_d, from zero to $\Delta_{max} = -0.35\frac{(z_d e)^2}{a}$ corresponding to c_d from 1.49 to 1.

V CONCLUSION

The ion sphere model has been extended to a dusty plasma. Although this model is rather simple and rough, it can describe various characteristics of strongly coupled dusty plasma, e.g, interaction between dusts, coagulation of dusts, polarization of dusty plasma, molecule-like state, which is the first stage of the plasma crystal. I believe that more properties of the dusty plasma can be described.

ACKNOWLEDGEMENTS

This work was supported by the National Nature Science Foundation of China and the AAAPT exchange program. The author wishes to acknowledge the Association for Plasma Studies of China.

REFERENCES

1. S.Ichimaru, *Statistical Plasma Physics, Vol.I. Basic Principle P.17*, Addison-Wesley Publishing Company, 1992.

2. Y.Hayashi and K.Tachibana, J.Vac.Sci.Technol. *A14 (1996)506.*

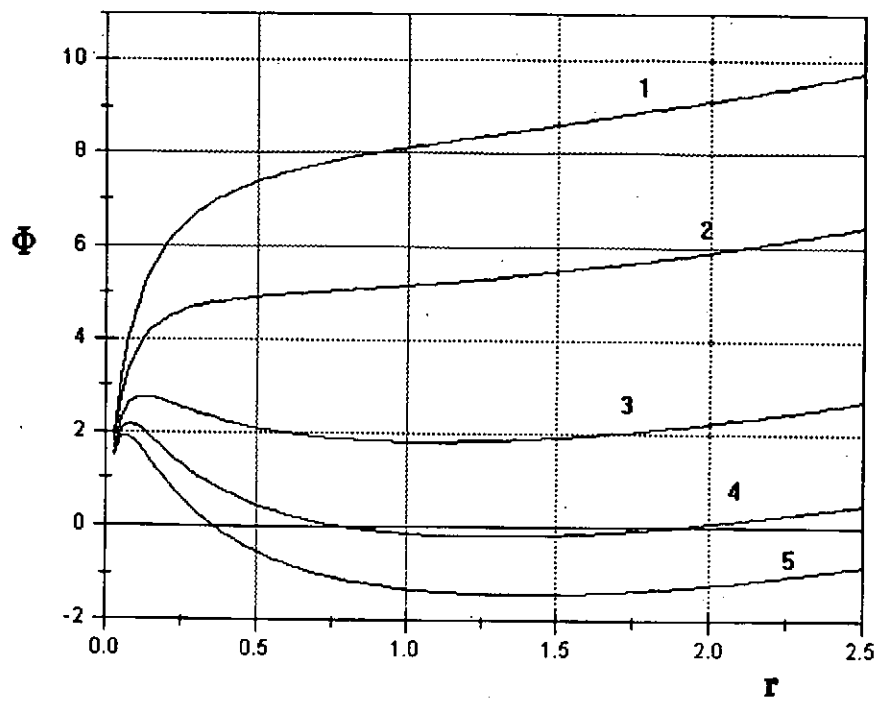

Fig.1 $r_g/a = 0.1$, curves 1-5 correspond to five values of $n_e/n_d z_d$: 2.0, 1.59, 1.0, 0.5, 0

THE NEIGHBOUR EFFECT ON DUST GRAIN CHARGING IN A PLASMA

Yan-Ping Chen
Institute of Physics & Center for Condensed Matter Physics
Chinese Academy of Sciences, Beijing 100080, P.R.China

ABSTRACT

A current balance equation of a grain is established by considering the momentum variation due to other grains. The effect of the nearest neighbouring grains on grain charging is phenomenologically evaluated, which shows the surface potential of a grain descreasing with grain density and in the structure of simple cubic and body center cubic the surface potential will decrease about 30% – 40% with the isothermal electrons and ions.

I.INTRODUCTION

Dusts are widely distributied in the universe, interstellar as well as laboratory devices, especially of low temperature plasmas to process the solid materials. The originally neutral dust grains could be charged up to high value , e.g, $10^3 - 10^4$ electron charge by the surrounding plasma, which in turn changes the characteristics of the plasma and leads to a lot of new phenomena, e.g, a new material state: plasma crystal. Hence the recent interest in dusty plasma has been driven. The charging process of dust grains is a basic problem. In low temperature laboratory plasmas , the collection of ions and electrons is the dominant charging process. In the case of an isolated dust grain in the plasma the charge on the spherical

dust is easily calculated. From the balance of ion and electron currents the surface potential of the grain, then its charge is determined. In the case of the densely packed grains, e.g. in plasma crystal, where the spacing between grains is comparable to the Debye length, the average charge on a dust grain is smaller than that of an isolated grain due to the effect of other grains, which is proved experimentally[1]. Goertz[2] analyzed this effect for one dimensional situation of a plasma with a series of equally spaced infinite plane dust sheets by numerically solving the Poisson equation and current balance equation .Young et al[3] analyzed this effect in the case of a two dimentional array of infinitely long dust rods in a plasma by partical-in-cell simulation. In this paper we will establish a current balance equation in consideration of the effect on the ion and electron current due to the nearly spacing of dust grains analytically and then the effect of the neighbouring grains on grain charging is phenomenologically evaluated.

II. THE CURRENT BALANCE EQUATION

A plasma system consists of dust grains, electrons and ions. Grain 1 is placed at the origin of the coordinate system. Now we will establish a current balance equation for grain 1. Electrons and ions moving toward grain 1 would have a contribution to charging current. In devices of low temperature plasmas the mean free paths of electrons, ions and neutrals are usually much larger than the mean distance between grains. So the energy and momentum must be conserved when electrons and ions more toward grain 1 along their trajectories from space point A far away from grain 1 to space point B on the surface of the grain 1, hence we have

$$\frac{1}{2}mv^2 + ze\sum_{i=1}^{N}\phi(r_i) = \frac{1}{2}mv_B^2 + ze\left[\phi(r_g) + \sum_{i=2}^{N}\phi(a_{i1})\right], \qquad [1]$$

$$\frac{d}{dt}\mathbf{r}_1 \times m\mathbf{v} = \mathbf{r}_1 \times \sum_{i=2}^{N}\mathbf{F}_i, \qquad [2]$$

where $\mathbf{r_i}$ is the distance vector from grain i to electron(ion), a_{i1} is the distance between 1st and ith grains, r_g is the radius of grain 1, $r_g << a_{i1}$ is assumed, v_B is the velocity of electron(ion) reaching the surface of grain 1 , $\phi(r_i)$ and $\mathbf{F_i}$ are the electrostatic potential and force acting on the electron(ion) due to grain i. For an isolated grain, the right hand side of Eq.(2) is zero. When the effect of other dust grains is taken into consideration , the nonzero $\mathbf{r} \times \sum_{i=2}^{N} \mathbf{F_i}$ will change the electron(ion) momentum. This is the main term of densely packed dust grains on the charging. The left hand side of Eq.(2) can be easily integrated leading to:

$$mvh - mv_B r_g = \int_{t_B}^{t_A} dt \left(\mathbf{r_1} \times \sum_{i=2}^{N} \mathbf{F_i} \right)_{r_1 \times v} , \qquad [3]$$

where h is the impact parameter and $(\mathbf{r_1} \times \sum_{i=2}^{N} \mathbf{F_i})_{r_1 \times v}$ is a component parallel to $\mathbf{r_1} \times \mathbf{v}$. From Eq.(1) we have

$$\frac{v_B^2}{v^2} = 1 + \frac{2ze(\Phi - \Phi_B)}{mv^2}, \qquad [4]$$

where

$$\Phi = \sum_{i=1}^{N} \phi(r_i),$$

$$\Phi_B = \phi(r_g) + \sum_{i=2}^{N} \phi(a_{i1}).$$

By combining Eqs.(3) and (4) we have

$$h = r_g \left\{ \left[1 + \frac{2ze(\Phi - \Phi_B)}{mv^2} \right]^{\frac{1}{2}} + \frac{1}{mvr_g} \int_{t_B}^{t_A} dt (\mathbf{r_1} \times \sum_{i=2}^{N} \mathbf{F_i})_{r_1 \times v} \right\}. \qquad [5]$$

The differential charging current is:

$$dI = ze\pi^2 h^2 v dn. \qquad [6]$$

If electrons and ions are in thermal equilibrium, they should have the Maxwellian distribution. Then the charging current has the following form:

$$I = 4ze\pi^2 r_g^2 n_o \int_{v_c}^{\infty} dv v^3 exp\left(-\frac{v^2}{v_t^2}\right) \left\{ \left[1 + \frac{2ze(\Phi - \Phi_B)}{mv^2}\right]^{\frac{1}{2}} + \frac{1}{mvr_g} \int_{t_B}^{t_A} dt (\mathbf{r_1} \times \sum_{i=2}^{N} \mathbf{F_i})_{r_1 \times v} \right\}^2 , \quad [7]$$

where v_t is the thermal velocity.For electrons(z=-1) and negatively charged grains, $ze(\Phi - \Phi_B) < 0$, only electrons with $v > v_c$ can reach to grains, where

$$v_c = \left[\frac{2}{m_e} e(\Phi - \Phi_B)\right]^{\frac{1}{2}} . \quad [8]$$

For ions the lower limit of velocity integration is zero. By performing the integration over velocity we obtain the electron and ion current as follows:

$$I_e = -2e\pi^{-\frac{1}{2}} r_g^2 n_{oe} v_{te} exp\left[-\frac{e(\Phi - \Phi_B)}{kT_e}\right] \left(1 + \frac{\pi^{\frac{1}{2}} \Sigma_e}{m_e v_{te} r_g} + \frac{\Sigma_e^2}{m_e^2 v_{te}^2 r_g^2}\right) , \quad [9]$$

$$I_i = 2z_i e\pi^{-\frac{1}{2}} r_g^2 n_{oi} v_{ti} \left\{ 1 + \Delta + \frac{2\Sigma_i}{m_i v_{ti} r_g} \left[\frac{\pi^{\frac{1}{2}}}{2} e^{\Delta} (1 - erf(\sqrt{\Delta}) + \Delta^{\frac{1}{2}}\right] + \frac{\Sigma_i^2}{m_i^2 v_{ti}^2 r_g^2} \right\} , \quad [10]$$

where

$$\Sigma_{e,i} = \int_{t_B}^{t_A} dt (\mathbf{r_1} \times \sum_{i=2}^{N} \mathbf{F_i})_{r_1 \times v} , \quad [11]$$

$$\Delta = \frac{2z_i e(\Phi - \Phi_B)}{mv_{ti}^2} , \quad [12]$$

and erf is the error function. In equilibrium $I_i + I_e = 0$, from which $\Phi - \Phi_B$ may be determined. By letting $\Sigma_{e,i} = 0$, the result of an isolated grain is recovered.

III. ESTIMATION OF THE EFFECT OF THE NEAREST NEIGHBOURING DUST GRAINS ON CHARGING

In general the neighbouring dust grain effect term Σ in Eq.(11) is difficult to be evaluated. The trajectory of an electron (ion) under the action of these dusts is complicated.It is obvious that the nearest neighbouring dust grains have the greatest contribution.An isolated grain would be charged by electrons and ions from all of the sides isotropically. When a grain is neighbored by N grains,located at X_i (i=1,2,...N), the trajectories of electrons and ions coming from $X_i \pm \delta$ would be seriously effected by grain i.The moment of momentum is exerted on an electron (ion) by grain i may be estimated phenomenologically:

$$\int (\mathbf{r_1} \times \mathbf{F_i})_{r_1 \times v} dt \sim \frac{z z_d e^2 r^2}{\delta^2 v_t}, \qquad [13]$$

where δ is the impact parameter of an electron (ion) to the grain i. The fraction of the solid angle the surface of radius δ is seen from grain 1 is:

$$\frac{\int_0^{\delta/r} sin(\theta) d\theta}{\int_0^{\pi} sin(\theta) d\theta} \sim \frac{\delta^2}{4r^2}, \qquad [14]$$

for $\delta/r << 1$. So the effective moment of momentum exerted by grain i should be $z z_d e^2 r^2/(v_t \delta^2)$ multiplied by $\delta^2/(4r^2)$ i.e. $z z_d e^2/(4v_t)$. If all grains are the same spheres, the term Σ may be estimated as :

$$\Sigma \simeq N \frac{z z_d e^2}{4 v_t}, \qquad [15]$$

then

$$\frac{\Sigma}{m v_t v_g} = \frac{N z z_d e^2}{8 T r_g} = -\frac{N z e \Phi_B}{8T}. \qquad [16]$$

By using Eq.(16) the current balance equation becomes as follows:

$$\frac{n_i}{n_e} \left(\frac{m_e T_i}{m_i T_e}\right)^{\frac{1}{2}} \left\{ 1 + a_i + \frac{N}{4} a_i \left[\frac{\pi^{\frac{1}{2}}}{2} e^{a_i} (1 - \phi(a_i^{\frac{1}{2}})) + a_i^{\frac{1}{2}} \right] + \frac{N^2}{64} a_i^2 \right\}$$

$$= e^{-a_e}\left(1 - \frac{N\pi^{\frac{1}{2}}a_e}{8} + \frac{N^2 a_e^2}{64}\right), \qquad [17]$$

where

$$a_i = -\frac{e\Phi_B}{T_i}, \qquad a_e = a_i\frac{T_i}{T_e} \qquad [18]$$

and $z_i = -z = 1$, $\Phi - \Phi_B \approx -\Phi_B(|\ \Phi/\Phi_B\ | \sim r_g n_d^{-\frac{1}{3}} << 1)$ are taken.Now the neighbouring grain effect on the surface potential of a grain

$$\frac{e\Phi(r_g)}{T_e} = -\frac{a_e}{(1 + N\frac{r_g}{a})}, \qquad [19]$$

can be solved numerically from Eq.(18). In Eq.[19] $a_{i1} = a$ is assumed, i.e, all grains are equally spaced. For hydrogen plasma the numerical results are shown in table 1. For N=0, the value of a_e is the same as one in isolated case.By increasing the neighbouring grains, the value of a_e ,the normalized surface potential of a grain, hence its charge decreases.For example ,a_e decrease to about 40% or 30% of ones in isolated case for N=6(corresponding to simple cubic crystal) or N=8(body center cubic) when $T_i = T_e$ and reduce more when $T_i < T_e$.

Table 1 Effect of neighbouring grain number N on surface potential a_e

N	$\frac{n_i}{n_e}$	$\frac{T_i}{T_e}$	a_e	$\frac{n_i}{n_e}$	$\frac{T_i}{T_e}$	a_e	$\frac{n_i}{n_e}$	$\frac{T_i}{T_e}$	a_e	$\frac{n_i}{n_e}$	$\frac{T_i}{T_e}$	a_e
0	1	1	2.5	2	1	2.0	1	0.1	1.9	2	0.1	1.5
1			2.0			1.5			1.3			0.98
2			1.6			1.3			0.97			0.74
3			1.3			1.1			0.78			0.60
4			1.2			0.92			0.66			0.51
5			1.0			0.81			0.57			0.44
6			0.92			0.73			0.50			0.39
7			0.85			0.66			0.45			0.35
8			0.78			0.60			0.41			0.31

IV. Conclusion

The electron and ion current balance equation including the variation of the angular momentum due to the neighbouring grains has been established. The nearest neighbouring grain effect has been analyzed phenomenologically in the case of $r_g << n_d^{-1/3}$ and the surface potential of grain was evaluated. Although it is a rough estimation, it has presented a tendency of surface potential of grains decreasing with grain density, which has been proved experimentally. In the structure of simple cubic and bcc crystal the surface potential of grain will decrease to below 30% or 40% with the isothermal electrons and ions.

ACKNOWLEDGEMENTS

This work was supported by the National Nature Science Foundation of China and the AAAPT exchange program. The author wishes to acknowledge the Association for Plasma Studies of China.

REFERENCES

1 A.Barkan, N.D'Angelo and R.L.Merlino, Phys Rev.Lett. 73(1994)3093.

2 C.K.Goertz, Rev.Geophys. 27(1989)271

3 B.Young,T.E.Cravens, T.P.Armstrong and R.J.Friauf, J.Geophys. 99 (1994)2255

Non-local Heating Theory of Inductively Coupled Plasma Discharge

N. S. Yoon, K.-I. You, Duk-In Choi*, and S. M. Hwang
Korea Basic Science Institute, Taejeon 305-333, Korea
* *Also at Department of Physics, Korea Advanced Institute of Science and Technology, Taejeon 305-701, Korea*

Recently developed one- and two-dimensional non-local heating theories of planar type inductively coupled plasma discharge are reviewed and some extensions of the results are presented. The important results of the one- and two-dimensional theories are integrated into the representative concepts of surface impedance and impedance of plasma respectively. Relevant physics are discussed and the works in progress are presented.

I. INTRODUCTION

The interaction of a transverse electromagnetic (EM)-wave with plasma electrons is a traditional problem in plasma physics. If the collision frequency of the electron is high enough for the plasma conductivity to become local, the problem is called *normal*. In certain conditions, however, there is non-negligible thermal motion of the electron in which case the response of the plasma should be explained by a non-local conductivity and we call this case *anomalous skin effect*. Moreover, if the plasma is enclosed by walls and the transit time of electron is comparable to the wave period, a modulation effect by the walls becomes important. Weibel [1] has studied the anomalous skin effect in semi-infinite plasma and Blevin *et al.* [2–4] and Sayasov [5] have introduced the bounded plasma effect on the assumption of a symmetric source configuration.

Recently, the anomalous skin effect is reconsidered by Godyak *et al.* [6] and Turner [7] being concerned with the problem of collisionless heating mechanism in inductively coupled plasma (ICP) discharge which is an important plasma source of semi-conductor fabrication devices.

There are two types of ICP reactors, classified according to the shape and the position of the coil. One has a planar coil on top of the cylindrical chamber (planar-type) and the other has a solenoidal coil wound on the side of the chamber (solenoidal type). They both have many attractive features such as workability without electrode and having low and controllable ion energies. Moreover, an ICP reactor can be easily scaled up to accommodate a larger wafer size compared to the other reactors (Helicon, ECR, etc.) because the system is substantially simpler. Accordingly, semi-conductor industries now pay attention to ICP reactors as a large-area plasma source of the new generation. In this work, we consider only the planar-type but the solenoidal-type can be done in the same manner, which is now in progress.

Even though the anomalous skin effect has been widely accepted to be the primary mechanism in sustaining low-pressure inductive radio frequency discharges, the quantitative description of the phenomenon has not been well established [8] until Yoon *et al.* [9,10] has developed the one- and two-dimensional theories. In the one-dimensional theory [9], the wave equation is solved on the assumption of a source at one side and a conductor at the other side of boundaries. The source is described with an effective surface current and the solution of the wave equation yields the *surface impedance* of plasma. In the two-dimensional theory [10], the anomalous skin effect modes in plasma are obtained by solving the two-dimensional wave equation with an effective surface current density on the interface of plasma-antenna regions, and, then, the excitation of the modes by the antenna source current is determined by utilizing the Maxwell equations. However, in Ref. [10], the finite size of antenna coil was not considered, but, it is well known that the electric field at infinitely thin wire is not finite. Moreover, many other factors should be still included to make a more useful theory of the collisionless heating of ICP-discharges.

In this paper, the one- and two-dimensional heating theories of planar type ICP discharge are reviewed discussing the relevant physics and basic concept, and some results of the two-dimensional theories including the finite size effect of the antenna coils are presented. Finally, the works in progress are explained and summarized.

II. HEATING THEORIES OF PLANAR TYPE ICP DISCHARGE

A. Basic concepts

Figure 1 shows the schematic diagram of the planar type ICP reactor. The radio frequency (RF) power generator is connected through a matching box to an antenna which is placed on top of a dielectric plate. The time-varying magnetic field flux

induces an electric field (or equivalently, an electromotive force) and the electrons, which gain energy from the induced electric field, ionize the neutral atoms. For convenience, whole chamber space is divided into two parts: antenna region, which is surrounded by the shielding cap, and plasma region.

According to the Helmholz's theorem for a vector, the electric and magnetic fields can be resolved into irrotational (longitudinal or capacitive) and solenoidal (transverse or inductive) parts. Since $\nabla \cdot \mathbf{B} = 0$, the magnetic field $\mathbf{B}$ is always inductive, on the other hand the electric field has the inductive ($\mathbf{E}_{in}$) and capacitive ($\mathbf{E}_{cp}$) components. There are two important roles of the capacitive field: One is an active participation in the electron heating mechanism of plasma at low power and the other is formation of displacement current and making a difference between the conduction and input currents. Therefore a self-consistent treatment on the iteration scheme such as done in Ref. [13] is necessary to include the capacitive field effect. However, under the practical ICP discharge condition, the inductive part of the electric field, as an electron heating source, dominates the capacitive part and the capacitive field is usually Faraday-shielded. Therefore only the inductive field is considered in this work.

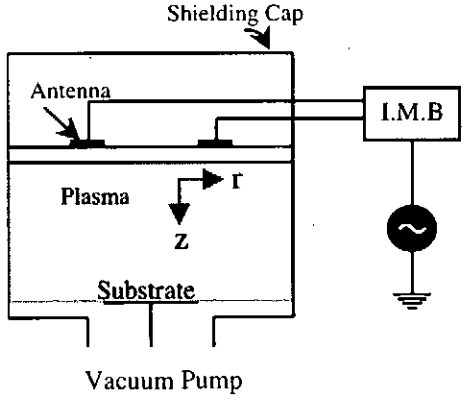

FIG. 1. Schematic diagram of planar type ICP reactor

Assuming all physical quantities have θ-symmetry, thus $\mathbf{E}_{in}$ with only a θ-component, the two-dimensional wave equation describing the inductive electric field component becomes

$$\nabla^2(E_\theta\hat{\theta}) + \kappa^2 E_\theta\hat{\theta} = -iZ_0\kappa(J_c + J_p)\hat{\theta}, \qquad (1)$$

where the impedance of free space, $Z_0 = 4\pi/c$, $\kappa = \omega/c$, ω is the angular frequency, and J_c, J_p are the coil and plasma currents.

With the time varying factor $\exp(-i\omega t)$, the plasma current density can be expressed by a non-local conductivity of plasma Σ, in general, as

$$J_p(r,z) = \int_{V_p} \Sigma(r,z,r',z')E_\theta(r',z')dr'dz'. \qquad (2)$$

The conductivity of plasma can be calculated from the linearized Boltzmann equation as

$$-i\omega f_1 + v_r\frac{\partial f_1}{\partial r} + v_z\frac{\partial f_1}{\partial z} + \frac{eE_\theta}{T_e}v_\theta f_0 = -\nu f_1, \qquad (3)$$

where the distribution function $f = f_0 + f_1$, f_0 is the Maxwellian velocity distribution function, f_1 is its perturbed part, T_e is the electron temperature, ν is the collision frequency of electron with neutral atoms, and v_r, v_z and v_θ are r-, z-, and θ- components of electron velocity, respectively. Since ω is much larger than the ion plasma frequency, the ion motion is neglected. Recently, Tuszewski [11] pointed out that the effect of the wave magnetic field on the skin effect can be strong when the excitation frequency is sufficiently low so that it is comparable to the cyclotron frequency related to the wave magnetic field. In this case, the plasma becomes a non-linear medium and the conductivity can not be calculated from the Eq. (3). This induced magnetic field effect is an open problem and it can be studied by a particle simulation [12] or a new analytic method. Moreover, since the collision frequency between the charge particles is not negligible in the low density, the diffusion in the velocity space should be considered.

In the typical ICP discharge condition, the term, $v_r\partial f_1/\partial r$, is much smaller than $v_z\partial f_1/\partial z$, and it can be neglected [10] in Eq. 3. This means that the non-local nature of conductivity can be treated as a one-dimensional problem regardless of the dimensionality of the whole heating problem. As in the case of the Landau damping, the non-local heating effect becomes notable when the phase velocity of wave, v_ϕ, is comparable to the electron thermal velocity: $v_\phi \sim \omega/(2\pi/\delta_s) \sim v_{th}$, where δ_s is skin depth and v_{th} is the thermal velocity of electrons. Moreover, if the transit time of electrons and the wave period are comparable to each other, the modulation effect by walls becomes dominant. When the bounded plasma effect is important, the boundary condition of the particle reflection on the walls should be assigned. Since there is a sheath and the sheath potential is much larger than the electron temperature, the perfect reflection is a good approximation. Therefore, as shown in Fig. 4, two types of resonances are possible: The first type occurs when the electrons traverse the plasma length L_p in a time equal to a multiple of the wave half period.

$$\frac{L_p/v_{th}}{\tau/2} = 1, 2, 3, \ldots \quad (4)$$

The second type resonance occurs when the electrons traverse a skin depth in a time equal to an odd multiple of the wave half period.

$$\frac{\delta_s/v_{th}}{\tau/2} = 1, 3, 5, .. \quad (5)$$

However, in usual process plasma discharges, electron energy distribution is not often a Maxwellian and there are non-negligible high energy electrons which can overcome the sheath potential. Therefore the effect of the non-Maxwellian electron energy distribution is another future work to be done.

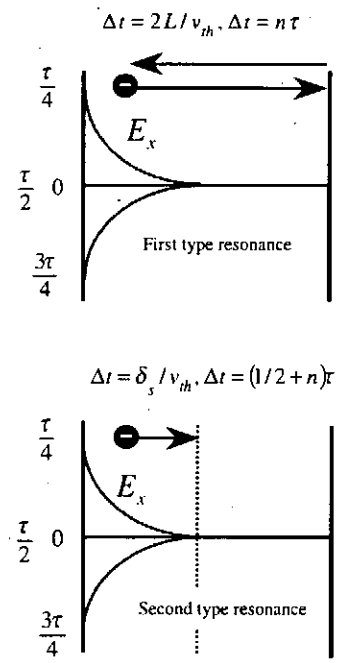

FIG. 2. Two types of resonances

B. One-dimensional Theory and Surface Impedance

If one tries with a one-dimensional model, it is a problem how the source current is to be described. However, as shown in Ref. [10], uniqueness theorem holds for the solution of Maxwell equation with the boundary field components transversing to the boundary walls. Therefore we can try with an effective surface current which replaces the real antenna current in the source direction.

Figure 3 is the schematic diagram of the one-dimensional model.

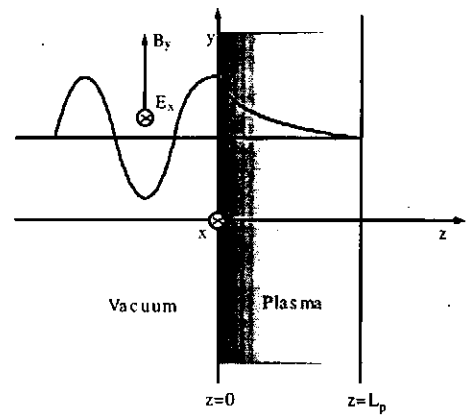

FIG. 3. Schematic diagram of the one-dimensional model

The region $0 \leq z \leq L_p$ is occupied by the plasma and a linearly polarized plane electromagnetic wave enters the plasma from the vacuum region. For the electromagnetic field boundary conditions we take $B_y(0) = B_0$ and $E_x(L_p) = 0$. In Ref. [9], the perfect reflection boundary condition is utilized to convert the original bounded problem to an equivalently periodic problem and the solution is obtained as

$$E_x(z) = \frac{e_0}{2} + \sum_{n=1}^{\infty} e_n \cos(q_n z) \quad (6)$$

with

$$e_n = -i\frac{2\kappa}{L_p} B_0[1 - (-1)^n \Sigma_2/\Sigma_1]/D_n, \quad (7)$$

where

$$D_n \equiv q_n^2 - iZ_0\kappa\sqrt{2\pi}\sigma_n. \quad (8)$$

Here σ_n is the Fourier component of the conductivity of the homogeneous plasma,

$$\Sigma_1 \equiv \frac{1}{2D_0} + \sum_{n=1}^{\infty} \frac{1}{D_n},$$
$$\Sigma_2 \equiv \frac{1}{2D_0} + \sum_{n=1}^{\infty} \frac{(-1)^n}{D_n}, \quad (9)$$

and $q_n \equiv \pi/L_p$,

The surface impedance,

$$Z_s \equiv Z_0 \frac{E_y(0)}{B_z(0)} = -i2\kappa \frac{Z_0}{L_p} \Sigma_1 \left[1 - \left(\frac{\Sigma_2}{\Sigma_1}\right)^2\right], \quad (10)$$

and the skin depth,

$$\delta_a \equiv -\frac{2dz}{d\ln|E_x|^2} = -\frac{1}{Z_0\kappa}\frac{|Z_s|^2}{\mathrm{Im}[Z_s]}. \quad (11)$$

When the plasma density is sufficiently high and the plasma length is much greater than the skin depth we have [1,5,9]

$$Z_a = \frac{8\pi^{5/6}}{3}\left(\frac{1}{\sqrt{3}} - i\right)\left(\frac{\omega^2 v_{th}}{c^4\omega_p^2}\right)^{1/3} - \frac{32\pi^{1/6}}{9}\left(\frac{1}{\sqrt{3}} + i\right)(\omega + i\nu)\left(\frac{\omega}{c^2\omega_p^4 v_{th}}\right)^{1/3} \quad (12)$$

and the skin depth,

$$\delta_a = -\frac{1}{Z_0\kappa}\frac{|Z_a|^2}{\mathrm{Im}[Z_a]} \quad (13)$$

On the other hand, the collisional skin depth with local conductivity is [1]

$$\delta_{col} = \frac{c}{\omega_p}\frac{(1+\nu^2/\omega_p^2)^{1/4}}{\cos(\epsilon/2)}, \quad \epsilon \equiv \tan^{-1}(\nu/\omega). \quad (14)$$

Figure 4 shows the three kinds of the skin depths as functions of density. We can see that δ_a is a good approximation of the exact skin depth δ_s even though $\nu/\omega \approx 5$.

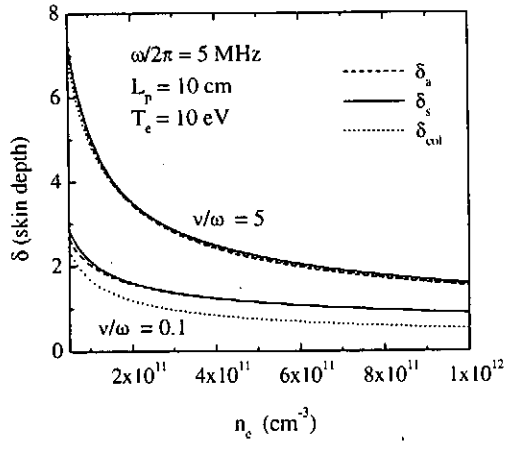

FIG. 4. Skin depths as functions of n_e

We notice here that since

$$J_p \simeq J_0 \exp(-z/\delta) \quad (15)$$

as long as

$$E_x \simeq E_0 \exp(-z/\delta) \quad (16)$$

although the conductivity is non-local as proved in Ref. [10], the local power absorption can be written as

$$P(z) \simeq P_0 \exp(-z/2\delta). \quad (17)$$

C. Two-dimensional Theory and Impedance of Discharge Reactor

In the two-dimensional theory, the source current should be included. In Ref. [10], a tentative surface current on the interface between the antenna and plasma regions is introduced and it is determined by an extended Poynting formula which is obtained by utilizing the Maxwell equations.

Figure 5 is the schematic diagram of the two-dimensional model.

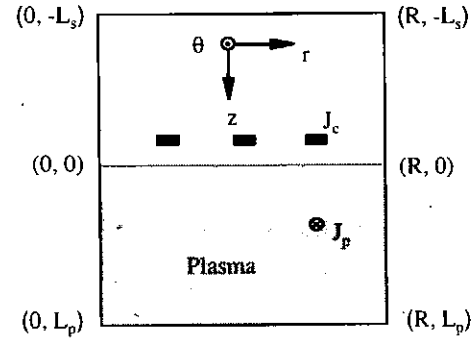

FIG. 5. Schematic diagram of the two-dimensional model

The solution in plasma region obtained in Ref. [10] is

$$E_\theta(r,z) = \sum_{m=1}^{\infty} J_1(p_m r)\left[\frac{e_{m0}}{2} + \sum_{n=1}^{\infty} e_{mn}\cos(q_n z)\right] \quad (18)$$

with

$$e_{mn} = \frac{2i\kappa}{L_p}\frac{b_{0,m}}{D_{mn}}\left[1 - (-1)^n\frac{S_m^{(2)}}{S_m^{(1)}}\right], \quad (19)$$

where

$$D_{mn} = \beta_m^2 + q_n^2 - i\sqrt{2\pi}Z_0\kappa\sigma_n, \quad (20)$$

and where $\beta_m^2 = p_m^2 - \kappa^2$, $p_m = \alpha_m/R$, and α_m is the mth zeros of the first order Bessel function, J_1. Here

$$S_m^{(1)} = \sum_{n=0}^{\infty}\frac{1}{D_{mn}}, \quad S_m^{(2)} = \sum_{n=0}^{\infty}\frac{(-1)^n}{D_{mn}}, \quad (21)$$

and $b_{0,m}$ is given by

$$b_{0,m} = \frac{2\pi L_s}{c}\sinh(\beta_m L_s) j_{c,m}^{(sh,L_s)}\hat{b}_m,$$
$$\hat{b}_m = (1 + (2\beta_m/L_p)\coth(\beta_m L_s)S_m)^{-1}, \quad (22)$$

where

$$S_m = \frac{\left(S_m^{(1)}\right)^2 - \left(S_m^{(1)}\right)^2}{S}_m, \qquad (23)$$

where the coil form factor,

$$j_{c,m}^{(sh,L_s)} \equiv \frac{2}{L_s R^2 J_2^2(\alpha_{1,m})} \int_{-L_s}^{0} \int_0^R J_c(r,z) J_1(p_m r) \times \sinh\left[\beta_m(z+L_s)\right] r dr dz. \qquad (24)$$

From these obtained electromagnetic fields, the impedance of plasma can be determined:

$$Z_p = -\frac{2}{|I|^2}\left(-\int_{S_p} \mathbf{S}\cdot\hat{n}da\right) = -i\frac{\omega R^2}{4L_p}\sum_{m=1}^{\infty} J_2^2(\alpha_m)\left|\frac{b_{0m}}{I}\right|^2 S_m \qquad (25)$$

where S_p denotes the interface between the plasma and antenna region and I is the input current. In Ref. [10], although the results of Eq. (25) include general cases, the numerical results are given when the antenna size is negligible so that the source current is described by the Dirac delta functions. However, it is well known that the electric field at an infinitely thin wire is infinite, and, thus it is necessary to include the finite size of antenna.

If we assume that the antenna size is finite and surface current flows on the antenna surface, after some calculation, we can show that

$$Z_p = 2i\pi\kappa\frac{Z_0}{L_p}\sum_{m=1}\frac{1}{J_2^2(\alpha_m)\alpha_m^2} \sum_{i,j}^{\#\text{ of coils}} \frac{I_i^* I_j}{|I|^2} T_{mi} T_{mj} a_{mi} a_{mj} |\hat{b}_m|^2 S_m, \qquad (26)$$

where

$$T_{mi} = \frac{\sinh\left(\beta_m(z_{c,i}+L_s)\right)\sinh\left(\beta_m \Delta r_{c,i}/2\right)}{\sinh\left(\beta_m L_s\right)}$$

$$a_{mi} = A_{mi} + B_{mi}\tanh\left(\beta_m \Delta z_{c,i}/2\right)$$

$$A_{mj} \equiv \frac{\beta_m}{\Delta r_{c,j}} \int_{r_{c,j}+\Delta r_{c,j}/2}^{r_{c,j}+\Delta r_{c,j}/2} J_1(p_m r) r dr$$

$$B_{mj} \equiv \frac{r_{c,j}}{\Delta z_{c,j}}\left[J_1\left(p_m(r_{c,j}+\Delta r_{c,j})\right) + J_1\left(p_m(r_{c,j}-\Delta r_{c,j})\right),\right] \qquad (27)$$

where I_i, $\Delta r_{c,i}$, and $\Delta z_{c,i}$ are the current, width, and thickness respectively. Figures 6 and 7 show the plasma resistance and reactance as functions of electron density with various coil sizes Δ.

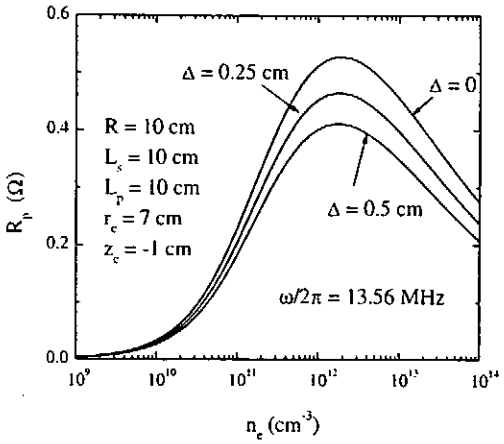

FIG. 6. Dependence of the plasma resistance on the electron density with various coil sizes

We can see that the impedances decrease as the coil size increases. Although the difference between the surface current and the delta function results is not negligible, it is checked that the surface current results go to the delta-function results with decreasing coil size, and thus, the non-physical assumption of the infinitely thin antenna does not yield a non-physical plasma impedance.

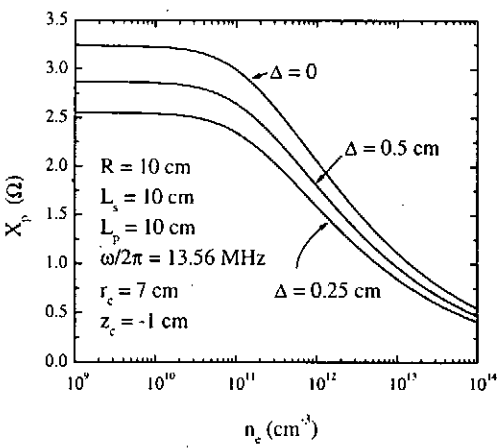

FIG. 7. Dependence of the plasma reactance on the electron density with various coil sizes

The plasma density in parameter space is shown in Fig. 8. The mountain in high-density regime is the collisionless heating and the small hill in the low-density regime indicates the collisional heating. As the collision frequency increases, the collisional hill rises and it overwhelming the collisionless mountain. Actually, the high density regime greater than 10^{13} cm^{-3} is not feasible in practical ICP-reactor, and thus we can think that the

collisionless heating is meaningful when the wave frequency is in the RF-regime.

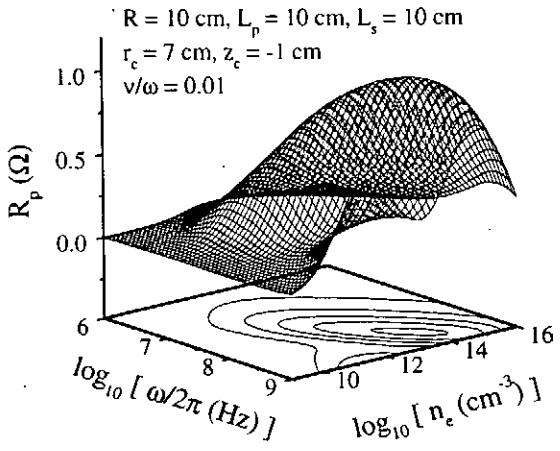

FIG. 8. Plasma density in parameter space

In the previous works for two-dimensional model, the fields are calculated only in the plasma region and the source current is used only for determining the anomalous skin effect mode excitation in the plasma region. However, the electrical characteristics of the whole discharge chamber can not be fully understood without the antenna region field, especially, on the surface of the antenna coil because the electromagnetic energy flow starts on this surface. Moreover, since the real power source is the power supply, and the source current is related to it through a matching network, it is necessary to consider the impedance matching network to make a self-consistent heating model. Besides, the capacitive field can strongly affect the conduction source current through a form of the displacement current. As long as a self-consistent heating model is completed, it should be combined with a transport model to become a full discharge model.

We further notice that the all previous techniques can be applied to develop non-local heating models of the other similar discharges such as solenoidal type ICP, magnetically enhanced ICP(MICP), and helicon discharges.

III. SUMMARY AND FUTURE WORKS

One- and two-dimensional non-local heating theories of planar type inductively coupled plasma discharge are reviewed and further results available from the theories are presented. Main results of the present study show that the delta-function source current, which is not physical, yields only a quantitative difference.

The future works in the one-dimensional model in progress are Coulomb collision effect, two-temperature effect, induced magnetic field effect, and so on. The future extensions in two-dimensional model are calculation of the reactor impedance, inclusions of the capacitive field and impedance matching network, matching with a transport model, and so on.

Furthermore, developments of collisionless heating theories of solenoidal type ICP, MICP, and helicon discharge are in progress and will be reported elsewhere.

[1] E. S. Weibel, Phys. of Fluids, **10**, No. 4, 741 (1967).
[2] J. A. Reynolds, H. A. Blevin, and P. C. Thonemann, Phys. Rev. Lett. **22**, No. 15, 762 (1969).
[3] H. A. Blevin, J. A. Reynolds, and P. C. Thonemann, Phys. of Fluids, **13**, No. 5, 1259 (1970).
[4] H. A. Blevin, J. A. Reynolds, and P. C. Thonemann, Phys. of Fluids, **16**, No. 1, 82 (1973).
[5] Y. S. Sayasov, Helv. Phys. Acta, **52**, 288 (1979).
[6] R. B. Piejak, V. A. Godyak and B. M. Alexandrovich, Plasma Sources Sci. Technol. **3** 169 (1994).
[7] M. M. Turner, Phys. Rev. Lett. **71**, 1844 (1993).
[8] M. A. Lieberman and A. J. Lichtenberg, *Principles of Plasma Discharges and Materials Processing*, (John Wiley & Sons, New York, 1994).
[9] N. S. Yoon, S. S. Kim, C. S. Chang, and D. I. Choi, Phys. Rev. E, **54**, No. 1, 757 (1996).
[10] N. S. Yoon, S. M. Hwang, and D. I. Choi, Phys. Rev. E, **55**, no. 6, 7536, (1997).
[11] M. Tuszewski, Phys. Rev. Lett. **77**, 1286 (1996).
[12] V. I. Kolobov, D. P. Lymberopoulos, and D. J. Economou, Phys. Rev. E **55**, 3408 (1997).
[13] E. F. Jaeger, L. A. Berry, J. S. Tolliver, and D. B. Batchelor, Phys. Plasmas **2** (6), 2597, (1995).
[14] B. D. Fried and S. D. Conte, *The Plasma Dispersion Function*, (Acad. Press, New York and London, 1961).

Large Diameter Plasma Production by Surface Waves in Bounded Plasmas

I. Ghanashev, M. Nagatsu and H. Sugai

Department of Electrical Engineering, Nagoya University
Furo-cho, Chikusa-ku, Nagoya 464-01, Japan

1 Introduction

Surface-wave sustained microwave discharges have been exhaustively investigated, both theoretically and experimentally, in the case of a long cylindrical plasma column contained in a dielectric tube [1]–[4]. In this case the plasma is sustained by a surface wave travelling along the interface between the plasma and the dielectric tube. Such discharges are easily reproducible, clean, stable and quiescent. Since no external DC magnetic field is needed, plasma sources applying surface-wave sustained plasmas are compact and easy to operate. Still they are capable of producing high-density ($n_e \sim 10^{11} - 10^{12}$ cm^{-3}) cold (typical electron temperatures are a few eV) plasma in a wide pressure range (from atmospheric pressure down to a few mTorr), both in inert and reactive gases. However, long thin plasma columns, whose operation is fairly well understood, cannot be applied for plasma processing of large-area flat surfaces, in particular large diameter wafers in the microelectronic industries. Processing of such objects can be achieved in large-area surface-wave sustained sources, in which the surface wave propagates along the plane interface between a large-area flat overdense plasma and a dielectric plate of approximately the same area [5]–[12]. This makes such plasmas applicable for plasma processing, as demonstrated already in some commercially available installations [5]. We recently proposed a new large-area surface-wave plasma source applying a two-slot-antenna for coupling of the microwave to the plasma [13]. An eigen-mode analysis assuming plasma homogeneity results in a closed form dispersion equation [14] which was successfully applied to identify the modes observed experimentally. A more sophisticated analysis [15] applying step-approximation of the actual axial plasma density profile was found to be not always applicable to the case when the overdense bulk plasma is surrounded by an underdense sheet due to singularities when the plasma density approaches the critical density in the transition layer. Since this case is most interesting for understanding the discharge properties, in the present contribution we present an eigen-mode analysis taking into account a continuous plasma density profile in the discharge chamber. The eigen-mode resonance frequencies were found to be only slightly different from those obtained assuming homogeneous plasma (this justifying the homogeneous plasma approximation if only resonance frequencies are needed), but the electromagnetic field distributions changed significantly, giving deeper insight into the discharge physics.

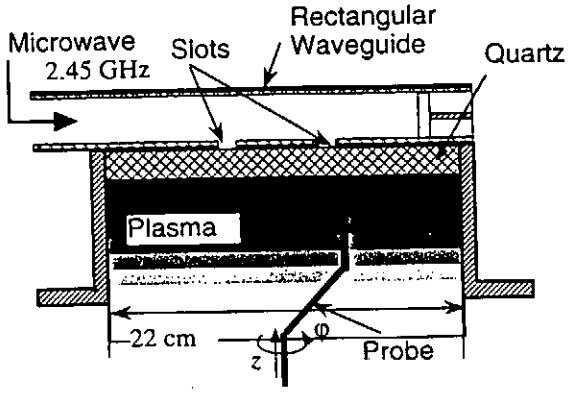

Figure 1. Schematic drawings of the upper part of the slot-antenna surface-wave planar plasma source.

2 Experimental set-up

A sketch of the slot-excited planar circular SWP source is presented in figure 1 [13]. The plasma is maintained at pressures 3 mTorr–1.1 Torr in a metal chamber coupled via two small slot antennas to a feeding rectangular waveguide. There is a quartz plate along the chamber wall containing the slots and the plasma is produced below this plate. The plate thickness is $d = 17$ mm and its permittivity is $\varepsilon_d = 4$. The plasma radius is $R = 11$ cm. The slots are cut in the broad wall of the feeding rectangular waveguide. A microwave power of 0.2–1.5 kW at $f = 2.45$ GHz is fed to the chamber. The generator is isolated from the chamber by a high power ferrite circulator with a high power matched load connected to its third port. An impedance transformer with remote control matches the chamber impedance to the feeding waveguide. At its other end the waveguide is short-circuited by a movable plunger. Thus a standing wave (measured standing wave ratio about 20dB) is maintained between this plunger and the impedance transformer. The plunger is used to optimize the chamber coupling by adjusting the standing wave configuration to the slot antenna positions.

3 Experimental results

Such a structure can support pure transverse magnetic (TM_{mn}) and transverse electric (TE_{mn}) modes with $H_z = 0$ and $E_z = 0$, respectively. We experimentally found that the axial electric field component was of the same order of magnitude as the radial and azimuthal components, which excludes the case of pure TE modes, thus hereafter we consider only the TM modes. However TE modes might occur at other experimental conditions. Some details can be found in [14].

When changing the gas pressure p and/or the net absorbed microwave power P, the azimuthal and radial mode indices (m and n, respectively) of the surface wave eigen-modes sustaining the plasma change. At higher pressures the light emission pattern corresponds to the microwave field intensity distribution, thus one can obtain the values of m and n directly by visual observation. The primary reason for the mode change was identified to be the change of the electron density n_e in the chamber (which can be caused itself by changes of the gas pressure p, P, the gas composition, or any combination thereof). At a given electron density distribution a discrete set of eigenmodes can be exited at some discrete resonance frequencies. In experiments usually the frequency is fixed ($\omega/2\pi = 2.45$ GHz in our case), which means that there will be a discrete set of plasma density profiles corresponding to the various eigenmodes.

The electron density was measured by means of a movable Langmuir probe. In figure 2 we show the axial plasma density distributions obtained in argon at $P = 0.4$ kW for $p = 1.1$ and 0.3 Torr. Figure 3 shows that these profiles coincide, if properly normalized. The plasma density measured close to the window ($z = 0$) is about 40% of the density in the bulk plasma. The normalized plasma density can be approxi-

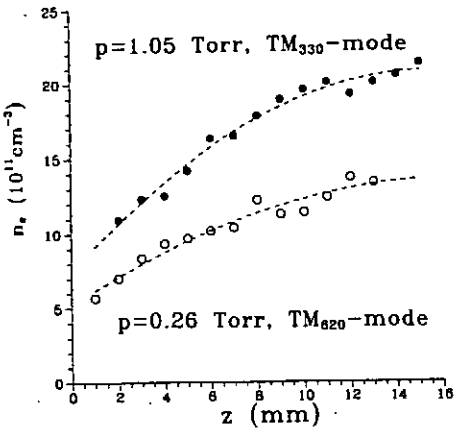

Figure 2. Measured axial electron density profiles for $P = 0.4$ kW at $p = 0.26$ Torr (o o o, TM_{620} mode) and 1.05 Pa (• • •, TM_330 mode) at a distance $r = 5$ cm from the chamber axis. z is the distance from the dielectric-plasma interface.

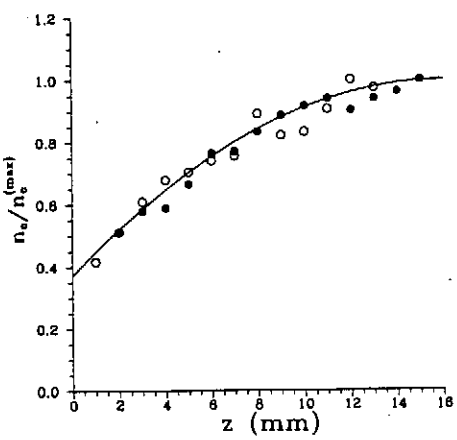

Figure 3. Normalized measured axial electron density profiles and the analytical approximation (1). Parameters as in figure 2.

mated by a parabola

$$\frac{n_e}{n_\infty} = \begin{cases} 1 - \left(1 - \frac{z}{L}\right)^2 \left(1 - \frac{n_0}{n_\infty}\right), & z < L \\ 1, & z \geq L \end{cases} \quad (1)$$

with $L = 16$ mm, $n_0/n_\infty = 0.372$ for both modes, $n_\infty = 2.1 \times 10^{12}$ cm^{-3} for the TM_{33} mode and 1.4×10^{12} cm^{-3} for the TM_{62} mode.

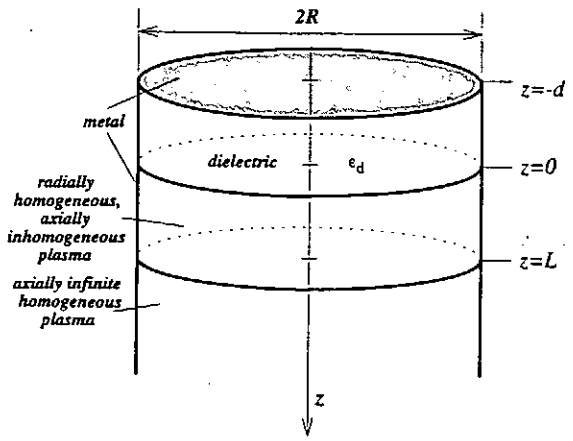

Figure 4. Model structure.

4 Theoretical dispersion analysis

We simplify the chamber geometry to the model structure presented in figure 4, assuming radial plasma homogeneity. For $z > L$ we assume infinite homogeneous plasma. The actual plasma density profile decreases at $z \gg L$, but this region is of no importance for the surface wave propagation due to its short penetration length $\delta \ll L$.

The transverse wave number κ depends only on the chamber geometry and the mode indices and for the TM_{mn} mode it is

$$\kappa = U_{mn}/R, \quad (2)$$

where U_{mn} is the n-th root of the m-th Bessel function J_m, i.e. $J_m(U_{mn}) = 0$. The axial propagation constant γ depends on the axial position z via the permittivity dependence $\varepsilon(z)$:

$$\gamma(z) = -\left[\kappa^2 - \varepsilon(z)\omega^2/c^2\right]^{1/2} \quad (3)$$

and may be both real and imaginary (or complex if ε is not real). Note that $\mathrm{Re}\,\gamma < 0$.

For any TM mode in a *transversely homogeneous* structure the two functions $y_1(z)$ and $y_2(z)$ defined as

$$y_1(z) = \frac{1}{\varepsilon}\frac{\mathrm{d}E_z}{\mathrm{d}z}, \; y_2(z) = \varepsilon E_z \quad (4)$$

are continuous (including at the dielectric-plasma interface), because

$$y_1 \propto \mathrm{E}_\perp,\ y_2 \propto \mathrm{H}_\perp. \qquad (5)$$

They satisfy the ordinary differential equations

$$\frac{\mathrm{d}y_1}{\mathrm{d}z} = \varepsilon y_2,\ \frac{\mathrm{d}y_2}{\mathrm{d}z} = \frac{\gamma^2}{\varepsilon} y_1. \qquad (6)$$

This equations have a singularity at $\varepsilon = 0$, which may happen in the plasma at a location where $\omega_\mathrm{p} = \omega$ if one neglects the collision frequency ν in the complex plasma permittivity

$$\varepsilon(z) = 1 - \frac{\omega_\mathrm{p}^2(z)}{\omega(\omega + \mathrm{i}\nu)}. \qquad (7)$$

The solution for $-d < z < 0$, where $\varepsilon = \varepsilon_\mathrm{d}$ =const., satisfying the boundary condition $y_2(-d) = 0$ (equivalent to $\mathrm{E}_\perp = 0$) is

$$\begin{aligned} y_1(z) &= \varepsilon_d \cosh \gamma_d (z + d), \\ y_2(z) &= \gamma_d \sinh \gamma_d (z + d), \end{aligned} \qquad (8)$$

which gives the starting values for a numerical solution with Runge-Kuta method of (6) in the region $0 < z < L$.

$$\begin{aligned} y_1(0) &= \varepsilon_d \cosh \gamma_d d, \\ y_2(0) &= \gamma_d \sinh \gamma_d d. \end{aligned} \qquad (9)$$

The numerical solution yields the values $y_1(L)$ and $y_2(L)$ in the beginning of the infinite homogeneous plasma region $z > L$. In this region the permittivity ε and the axial propagation constant γ are again constant: $\varepsilon = \varepsilon(L)$, $\gamma = \gamma(L)$. Thus (6) have a simple analytical solution

$$y_1(z) = \varepsilon(L) \left[A\mathrm{e}^{\gamma(L)(z-L)} + B\mathrm{e}^{-\gamma(L)(z-L)} \right],$$

$$y_2(z) = \gamma(L) \left[A\mathrm{e}^{\gamma(L)(z-L)} - B\mathrm{e}^{-\gamma(L)(z-L)} \right].$$

The coefficients A and B are easily written down in terms of the already computed values of y_1 and y_2 at $z = L$:

$$A = \frac{1}{2} \left[\frac{y_1(L)}{\varepsilon(L)} + \frac{y_2(L)}{\gamma(L)} \right], \qquad (10)$$

$$B = \frac{1}{2} \left[\frac{y_1(L)}{\varepsilon(L)} - \frac{y_2(L)}{\gamma(L)} \right]. \qquad (11)$$

At this point we notice that the values of A and B depend on the wave frequency ω. In order the wave to be evanescent for $z > L$ along z the coefficient $B(\omega)$ must vanish. This gives the dispersion equation of the eigen-modes in the form

$$D(\omega) \equiv B(\omega)/A(\omega) = 0. \qquad (12)$$

5 Numerical results

Following this procedure we computed the wave frequency at which the TM_{33} and TM_{62} modes should appear, taking the plasma density profile to be the one defined in (1) with $n_\infty = 2.1$ and 1.4×10^{12} cm^{-3}, respectively, and found $\omega/2\pi = 2.29$ and 2.22 GHz, respectively, which is quite close to the experimental frequency 2.45 GHz.

It is known that very close to a wall the plasma density decreases practically to zero and there should be a very thin underdense sheet along the dielectric window. Unfortunately Lamgmuir measurements very close to the window ($z \sim 1$ mm) are not possible. Even at $z \sim 5$ mm the measurements are not reliable due to the strong microwave fields. Thus we decided to consider a density profile of the kind (1) with $n_0/n_\infty = 0$ (such a profile goes to zero at $z = 0$), $L = 1, 2, 3$ mm and $n_\infty = 2.1 \times 10^{12}$ cm^{-3}, the latter value corresponding to the bulk plasma density at which the TM_{33} mode was observed. Here again the computed eigen mode frequencies for the TM_{33} mode ($\omega/2\pi = 2.40$, 2.35 and 2.30 GHz for $L = 1, 2$ and 3 mm, respectively) were found to be very close to the experimental frequency 2.45 GHz, but we found, as expected, a high peak in the E_z field component just at the dielectric-plasma interface (figure 5). This peak occurs at the position where the plasma density is equal to the cut-off density ($\omega_\mathrm{p} = \omega$). In order to avoid the sin-

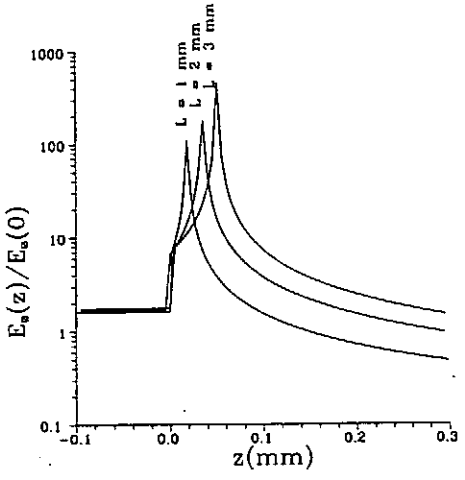

Figure 5. Axial electric field distribution near the dielectric-plasma interface for the TM_{33} mode. The electron density distribution was taken in the form (1) with $n_0/n_\infty = 0$, $n_\infty = 2.1 \times 10^{12}$ cm^{-3} and $L = 1, 2, 3$ mm.

gularity in (6) at $\varepsilon = 0$ we included a non-zero collision frequency $\nu = 1.5 \times 10^9$ s^{-1} (this corresponds to argon at ~1 Torr) in the plasma permittivity (7).

6 Conclusion

We developed a semi-analytical model giving the eigenmode spectrum in finite-area surface-wave plasmas and found a very good coincidence between the computed and measured eigen frequencies of the experimentally identified modes. Using the model we demonstrated the existence of a very thin high-field layer along the dielectric-plasma interface. The intensive ionisation in this area is most significant for sustaining the discharge.

Acknowledgments

This paper was supported by the Manufacturing Research Center of Toshiba Corp. and by Nisshin Electronic MFG Co., Ltd.

References

[1] Ferreira C M and Moisan M (eds.) 1993 *Microwave Discharges: Fundamentals and Applications (NATO ASI series* **B302***)* (New York, Plenum)

[2] Moisan M, Shivarova A and Trivelpiece A W 1982 *Plasma Phys.* **24** 1331

[3] Ferreira C M and Moisan M 1985 *Surface Waves in Plasmas and Solids*, ed. S. Vukovic (Singapore: World Scientific) p. 113

[4] Moisan M, Ferreira C M, Hubert J, Margot J and Zakrzewski Z 1995 *Phenomena in Ionized Gases*, eds. K. H. Becker and W. E. Carr (Woodbury: AIP Press) p. 25

[5] Komachi K and Kobayashi S 1989 *J. Microwave Power & Electromagn. Energy* **24** 140

[6] Komachi K 1993 *J. Vac. Sci. Technol. A* **11** 164

[7] Akimoto T, Ikawa E, Sango T, Komachi K, Katayama K and Ebata T 1994 *Jpn. J. Appl. Phys.* **33** 7037

[8] Fujimura S, Shinagawa K, Suzuki M and Nakamura M 1991 *J. Vac. Sci. Technol. B* **9** 357

[9] Tamura H, Otsubo T, Sasaki I, Ohara K, Yamaguchi Y and Kato S 1994 *41st Nat. Symp. of the Am. Vac. Soc.* p. 191

[10] Ikushima T, Tochitani G and Fujita H 1995 *J. Phys. D: Appl. Phys.* **28** 1851

[11] Yoshida Y, Miyazawa T, Kazawa A 1996 *Rev. Sci. Instrum.* **68** 79

[12] Odrobina I, Kudela J and Kando M 1997 *10th Symp. Plasma Sci. for Materials Abstr.*, p. 47 (Tokyo: Jpn. Soc. Prom. Sci.)

[13] Nagatsu M, Xu G, Yamage M, Kanoh M and Sugai H 1996 *Jpn. J. Appl. Phys.* **35** L341

[14] Ghanashev I, Nagatsu M and Sugai H 1997 *Jpn. J. Appl. Phys.* **36** 337

[15] Ghanashev I, Xu G, Nagatsu M and Sugai H 1997 *Trans. Inst. Electr. Eng. Jpn.* **EP-97**, p. 45

List of Participants

Sergey V.Bazdenkov	National Institute for Fusion Science, Toki sergey@sriran.nifs.ac.jp	
Naoaki Bessho	Department of Physics, Nagoya University, Nagoya bessho@npmi.phys.nagoya-u.ac.jp	248
Sergei V.Bulanov	General Physics Institute of Russian Academy of Sciences, Moscow sbul@plasma.gpi.msk.su	217,329
Liu Chen	Dept. of Physics and Astronomy, University of California, Irvine liuchen@uci.edu	15
Yan-Ping Chen	Institute of Physics, Academia Sinica, Beijing, Beijing user105@aphy01.iphy.ac.cn	345,354
Chio Z. Cheng	Princeton Plasma Physics Laboratory, Princeton University, Princeton fcheng@pppl.gov	
Suwon Cho	Dept. of Physics, Kyonggi University, Suwon swcho@kuic.kyonggi.ac.kr	186
Duk-In Choi	Korea Basic Science Institute, Taejeon dichoi@comp.kbsi.re.kr	10,169,175,181,361
Sami Cuperman	School of Physics and Astronomy, Tel-Aviv University, Tel-Aviv samcup@ccsg.tau.ac.il	157
Sean A. Dettrick	Theoretical Physics Department, Australian National University, Canberra sean@dettric@anu.edu.au	163
Robert L.Dewar	Department of Theoretical Physics, Australian National University, Canberra robert.dewar@anu.edu.au	74,163
Daiju Dogen	Department of Physics, Nagoya University, Nagoya dougen@np1422a.nifs.ac.jp	242
Susumu Fujiwara	National Institute for Fusion Science, Toki fujiwara@toki.theory.nifs.ac.jp	289
Henry J. Gardner	Department of Computer Science,Australian National University, Canberra henry.gardner@anu.edu.au	163
Ivan P. Ghanashev	Dept. of Electrical Engineering, Nagoya University, Nagoya g44228a@nucc.cc.nagoya-u.ac.jp	367
Susumu Goto	National Institute for Fusion Science, Toki goto@toki.theory.nifs.ac.jp	
Tadatsugu Hatori	National Institute for Fusion Science, Toki hatori@srhatori.nifs.ac.jp	192

Mitsuru Hayashi	Naka Fusion Res. Establishment, Japan Atomic Energy Research Institute, Naka hayashim@fusion.naka.jaeri.jo.jp	211
Takaya Hayashi	National Institute for Fusion Science, Toki hayashi@nifs.ac.jp	128
Kaifen He	Inst. of Low Energy Nuclear Physics, Beijing Normal University, Beijing kfhe@bnu.edu.cn	225
Xian-Tu He	Inst. of Applied Physics and Comp. Math. (IAPCM), Beijing xthe@sun.ihep.ac.jp	
Keiichi Hirose	National Institute for Fusion Science,Toki hirose@nifs.ac.jp	230
Steven P. Hirshman	Fusion Energy Division, Oak Ridge National Laboratory, Oak Ridge hirshman@ornl.gov	
Hitoshi Hojo	Plasma Research Center, University of Tsukuba, Tsukuba hojo@prc.tsukuba.ac.jp	
Sang-Hee Hong	Dept. of Nuclear Engineering, Seoul National University, Seoul hongsh@plaza.snu.ac.kr	339
Ritoku Horiuchi	National Institute for Fusion Science, Toki hori@toki.theory.nifs.ac.jp	312
Stuart R. Hudson	Naka Fusion Res. Establishment, Japan Atomic Energy Research Institute, Naka stuart@ptl01.naka.jaeri.go.jp	145
Lin I	National Central University, Chungli lini@phyast.phy.ncu.edu.tw	306
Katsuji Ichiguchi	National Institute for Fusion Science, Toki ichiguch@nifs.ac.jp	265
Yoshi-Hiko Ichikawa	College of Engineering, Chubu University, Kasugai ichikawa@isc.chubu.ac.jp	230
Atsuo Iiyoshi	National Institute for Fusion Science, Toki iiyoshi@nifs.ac.jp	
Akio Ishida	Dept. of Environmental Science, Niigata University, Niigata ishida@artemis.sc.niigata-u.ac.jp	
Seiji Ishiguro	Dept. of Electronic Engineering, Tohoku University, Sendai ishiguro@ecei.tohoku.ac.jp	198
Norio Ishihara	National Institute for Fusion Science, Toki ishihara@toki.theory.nifs.ac.jp	
Yasutomo Ishii	Naka Fusion Res. Establishment, Japan Atomic Energy Research Institute, Naka ishiiy@fusion.naka.jaeri.go.jp	

Takuya Iwasaki	Interdisciplinary Graduate School of Engineering Sciences, Kyushu University, Kasuga takuya@post.riam.kyusyu-u.ac.jp	139
John L. Johnson	Princeton Plasma Physics Laboratory, Princeton University, Princeton jlj@pppl.gov	
Akira Kageyama	National Institute for Fusion Science, Toki kage@toki.theory.nifs.ac.jp	
Tetsuo Kamimura	National Institute for Fusion Science, Toki kamimura@nifs.ac.jp	230
Ryutaro Kanno	National Institute for Fusion Science, Toki ryu@tadws08.nifs.ac.jp	277
Isao Katanuma	Plasma Research Center, University of Tsukuba, Tsukuba katanuma@prc.tsukuba.ac.jp	52
Predhiman K.Kaw	Institute for Plasma Research, Bhat kaw@plasma.ernet.in	295
Shigeo Kida	National Institute for Fusion Science, Toki kida@toki.theory.nifs.ac.jp	
Yasuaki Kishimoto	Naka Fusion Res. Establishment, Japan Atomic Energy Reseach Institute, Naka kishi@expert1.naka.jaeri.go.jp	
Hideaki Kitauchi	National Institute for Fusion Science,Toki kitauchi@toki.theory.nifs.ac.jp	
Mituo Kono	Faculty of Policy Studies, Chuo University, Hachiouji kono@fps.chuo-u.ac.jp	236
Lev M. Kovrizhnykh	Dept. of Plasma Physics, General Physics Institute, Russian Academy of Sciences, Moscow lmkov@fp2.gpi.msk.su	
Kanya Kusano	Faculty of Science, Hiroshima University, Higashi-Hiroshima kusano@sci.hiroshima-u.ac.jp	
Jae-Koo Lee	Pohang University of Science and Technology, Pohang jkl@vision.postech.ac.kr	69
Lou-Chuang Lee	College of Science, National Cheng Kung University, Tainan loulee@plasma.et.ncku.edu.tw	323
Ding Li	Institute of Plasma Physics, Academia Sinica, Hefei dingli@ipncl.hfcas.ac.cn	27
S.S.Lloyd	Faculty of Engineering and Information Technology, Australian National University, Canberra henry.gardner@anu.edu.au	
Richard V.Lovelace	Graduate School for Astronomy, Cornell University, Ithaca rvl1@cornell.edu	86

Quankang Lu	Department of Physics, Fudan University, Shanghai fax: +86-21-65493232	33
Kentaro Maruyama	Department of Physics, Nagoya University, Nagoya maruyama@npmi.phys.nagoya-u.ac.jp	254
Donald B.Melrose	Research Centre for Theoretical Astrophysics, University of Sydney, Sydney melrose@physics.usyd.edu.au	96
Kunioki Mima	Institute of Laser Engineering, Osaka University, Osaka mima@ile.osaka-u.ac.jp	
Hideaki Miura	National Institute for Fusion Science, Toki miura@toki.theory.nifs.ac.jp	
Osamu Miwa	National Institute for Fusion Science, Toki miwa@tnifs.ac.jp	
Naoki Mizuguchi	National Institute for Fusion Science, Toki mizu@toki.theory.nifs.ac.jp	
George J.Morales	Dept. of Physics and Astronomy, University of California, Los Angeles morales@physics.ucla.edu	318
Sadayoshi Murakami	National Institute for Fusion Science, Toki murakami@nifs.ac.jp	259
Hideo Nagatomo	Institute of Laser Engineering, Osaka University, Osaka naga@ile.osaka-u.ac.jp	
Hiroshi Naitou	Dept. of Electrical and Electronic Engineering, Yamaguchi University, Ube naitou@plasma.eee.yamaguchi-u.ac.jp	151
Noriyoshi Nakajima	National Institute for Fusion Science, Toki nori@tadws04.nifs.ac.jp	259,277,283
Yuji Nakamura	Graduate School of Energy Science, Kyoto University, Uji nakamura@energy.kyoto-u.ac.jp	
Shinji Nakazawa	Department of Physics, Nagoya University, Nagoya nakazawa@rddfuji.nifs.ac.jp	
Kyoji Nishikawa	Research Inst. of Industrial Technology, Kinki University, Higashi-Hiroshima nisikawa@hiro.kindai.ac.jp	
Kazumi Nishimura	National Institute for Fusion Science, Toki nisimura@toki.theory.nifs.ac.jp	
Marcia Midori Ochi	National Institute for Fusion Science, Toki midori@toki.theory.nifs.ac.jp	
Naofumi Ohnishi	Institute of Laser Engineering, Osaka University, Osaka ohnishi@ile.osaka-u.ac.jp	

Yukiharu Ohsawa	Department of Physics, Nagoya University, Nagoya ohsawa@npmi.nifs.ac.jp	242,248,254
Masao Okamoto	National Institute for Fusion Science, Toki okamoto@nifs.ac.jp	1,259,277,283
Wataru Oohara	Dept. of Electronic Engineering, Tohoku University, Sendai saton15@ec.ecei.tohoku.ac.jp	198
Byoung-Ho Park	Korea Advanced Institute of Science and Technology, Taejeon bhpark@yebbi.kaist.ac.kr	181
Xiao-Dong Peng	Southwestern Institute of Physics, Chengdu yegaoy@publi.bta.net.cn	48
Vladimir D.Pustovitov	Institute of Nuclear Fusion, Russian Research Center, "Kurchatov Institute", Moscow pustovit@qq.nfi.kiae.su	63
Xiao-Ming Qiu	Southwestern Institute of Physics, Chengdu yegaoy@public.bta.net.cn	
Hamid Saleem	Pakistan Institute of Nuclear Science and Technology, Islamabad / National Institute for Fusion Science, Toki pinstech@paknet1.ptc.pk / saleem@tadws27.nifs.ac.jp	
Heiji Sanuki	National Institute for Fusion Science, Toki sanuki@nifs.ac.jp	
Tetsuya Sato	National Institute for Fusion Science, Toki sato@toki.theory.nifs.ac.jp	43,128,192,289
Sudip Sen	Max-Planck-Institut fuer Plasmaphysik, Garching s.sen@kfa-juelich.du	122
Vitalij D.Shafranov	Institute of Nuclear Fusion, Russian Research Center, "Kurchatov Institute", Moscow shafran@qq.nfi.kiae.su	
Milos M.Skoric	Vinca Institute of Nuclear Sciences, Belgrade / National Institute for Fusion Science, Toki mskoric@rt270.vin.bg.ac.yu / skoric@nifs.ac.jp	
Robin G.Storer	Department of Physics, Flinders University, Adelaide robin.storer@flinders.edu.au	21
Hideo Sugama	National Institute for Fusion Science, Toki sugama@tadws03.nifs.ac.jp	271
Linda E.Sugiyama	Massachusetts Institute of Technology, Massachusetts sugiyama@psfc.mit.edu	80
Atsushi Sunahara	Institute of Laser Engineering, Osaka University, Osaka suna@ile.osaka-u.ac.jp	
Yoshio Suzuki	National Institute for Fusion Science, Toki suzuki@toki.theory.nifs.ac.jp	

Hideaki Takabe	Institute of Laser Engineering, Osaka University, Osaka takabe@ile.osaka-u.ac.jp	
Takeshi Takaishi	Faculty of Engineering, Hiroshima Denki Institute of Technology, Hiroshima ttks@g.hiroshima-dit.ac.jp	
Hisanori Takamaru	National Institute for Fusion Science, Toki taka@toki.theory.nifs.ac.jp	
Arimichi Takayama	National Institute for Fusion Science, Toki takayama@nifs.ac.jp	
Gonta Tateishi	Interdisciplinary Graduate School of Engineering Sciences, Kyushu University, Kasuga tateishi@post.riam.kyusyu-u.ac.jp	133
Yasushi Todo	National Institute for Fusion Science, Toki todo@nifs.ac.jp	43
Mieko Toida	Department of Physics, Nagoya University, Nagoya toida@np1422a.nifs.ac.jp	242
Shinji Tokuda	Naka Fusion Res. Establishment, Japan Atomic Energy Research Institute, Naka tokudas@fusion.naka.jaeri.go.jp	145,151
Yukihiro Tomita	National Institute for Fusion Science, Toki tomita@nifs.ac.jp	192
Yi Tong	Department of Astronomy, Beijing Normal University, Beijing yitong@bnu.edu.cn	204
Levan N.Tsintsadze	Institute of Laser Engineering, Osaka University, Osaka levan@ile.osaka-u.ac.jp	
Yutaka Uchida	Faculty of Science, Science University of Tokyo, Tokyo uchida@astro1.yy.kagu.sut.ac.jp	104
James W.Van Dam	Institute for Fusion Studies, University of Texas at Austin, Austin vandam@hagar.ph.utexas.edu	
De-Yu Wang	Purple Mountain Observatory, Academia Sinica, Nanjing wangdy@njnet.nj.ac.cn	110
Kuni-Hiko Watanabe	National Institute for Fusion Science, Toki kuni@toki.theory.nifs.ac.jp	
Tomo-Hiko Watanabe	National Institute for Fusion Science, Toki tomo@nifs.ac.jp	
Masatoshi Yagi	Research Institute for Applied Mechanics, Kyushu University, Kasuga yagi@riam.kyusyu-u.ac.jp	57,133,139
Masayuki Yokoyama	National Institute for Fusion Science, Toki yokoyama@nifs.ac.jp	283

Nam-Sik Yoon	Korea Basic Science Institute, Taejeon nsyoon@comp.kbsi.re.kr	175,181,361
Zensho Yoshida	Faculty of Engineering, University of Tokyo, Tokyo yoshida@plasma.gen.u-tokyo.ac.jp	116
Kwnag-Il You	Korea Basic Science Institute, Taejeon kiyou@comp.kbsi.re.kr	175,361
Shao-Ping Zhu	Inst. of Applied Physics and Comp. Math. (IAPCM), Beijing js2s@mail.iapcm.ac.cn	192
Fulvio Zonca	Associazione Euratom-Enea Sulla Fusione, Rome zonca@frascati.enea.it	15

Publication List of NIFS-PROC Series

NIFS-PROC-1 "*U.S.-Japan on Comparison of Theoretical and Experimental Transport in Toroidal Systems Oct. 23-27, 1989*", Mar. 1990

NIFS-PROC-2 "*Structures in Confined Plasmas –Proceedings of Workshop of US-Japan Joint Institute for Fusion Theory Program–* "; Mar. 1990

NIFS-PROC-3 "*Proceedings of the First International Toki Conference on Plasma Physics and Controlled Nuclear Fusion –Next Generation Experiments in Helical Systems– Dec. 4-7, 1989*" Mar. 1990

NIFS-PROC-4 "*Plasma Spectroscopy and Atomic Processes –Proceedings of the Workshop at Data & Planning Center in NIFS–*"; Sep. 1990

NIFS-PROC-5 "*Symposium on Development of Intensed Pulsed Particle Beams and Its Applications February 20 1990*"; Oct. 1990

NIFS-PROC-6 "*Proceedings of the Second International TOKI Conference on Plasma Physics and Controlled Nuclear Fusion , Nonlinear Phenomena in Fusion Plasmas -Theory and Computer Simulation-*"; Apr. 1991

NIFS-PROC-7 "*Proceedings of Workshop on Emissions from Heavy Current Carrying High Density Plasma and Diagnostics*"; May 1991

NIFS-PROC-8 "*Symposium on Development and Applications of Intense Pulsed Particle Beams, December 6 - 7, 1990*"; June 1991

NIFS-PROC-9 "*X-ray Radiation from Hot Dense Plasmas and Atomic Processes*"; Oct. 1991

NIFS-PROC-10 "*U.S.-Japan Workshop on "RF Heating and Current Drive in Confinement Systems Tokamaks" Nov. 18-21, 1991*, Jan. 1992

NIFS-PROC-11 "*Plasma-Based and Novel Accelerators (Proceedings of Workshop on Plasma-Based and Novel Accelerators) Nagoya, Japan, Dec. 1991*"; May 1992

NIFS-PROC-12 "*Proceedings of Japan-U.S. Workshop P-196 on High Heat Flux Components and Plasma Surface Interactions for Next Devices*"; Mar. 1993

NIFS-PROC-13 「NIFS シンポジウム
「核燃焼プラズマの研究を考える－現状と今後の取り組み方」
1992 年 7 月 15 日、核融合科学研究所」1993 年 7 月
NIFS Symposium "Toward the Research of Fusion Burning Plasmas -Present Status and Future strategy-", 1992 July 15, National Institute for Fusion Science"; July 1993 (in Japanese)

NIFS-PROC-14 "*Physics and Application of High Density Z-pinches*", July 1993

NIFS-PROC-15 岡本正雄、講義「プラズマ物理の基礎」
平成 5 年度 総合大学院大学1994 年 2 月
M. Okamoto,
"Lecture Note on the Bases of Plasma Pysics"Graduate University for Advanced Studies Feb. 1994
(in Japanese)

NIFS-PROC-16 代表者 河合良信
平成 5 年度 核融合科学研究所共同研究
研究会報告書「プラズマ中のカオス現象」
*"Interdisciplinary Graduate School of Engineering Sciences" Report of the meeting on Chaotic Phenomena in Plasma*Apr. 1994 (in Japanese)

NIFS-PROC-17 平成 5 年度 NIFS シンオジウム報告書
「核融合炉開発研究のアセスメント」平成 5 年 11 月 29 日-30 日 於 核融合科学研究所
"Assessment of Fusion Reactor Development" Proceedings of NIFS Symposium held on November 29-30, 1993 at National Insitute for Fusion Science" Apr. 1994(in Japanese)

NIFS-PROC-18 "*Physics of High Energy Density Plasmas Produced by Pulsed Power*" June 1994

NIFS-PROC-19 K. Morita, N. Noda (Ed.),

"*Proceedings of 2nd International Workshop on Tritium Effects in Plasma Facing Components at Nagoya University, Symposion Hall, May 19-20, 1994*", Aug. 1994

NIFS-PROC-20 研究代表者 阿部 勝憲 (東北大学・工学部)
所内世話人 野田信明
平成6年度 核融合科学研究所共同研究〔研究会〕「金属系高熱流束材料の開発と評価」成果報告書

K. Abe and N. Noda (Eds.),
"Research and Development of Metallic Materials for Plasma Facing and High Heat Flux Components" Nov. 1994(in Japanese)

NIFS-PROC-21 世話人:森田 健治(名大工学部)、金子 敏明(岡山理科大学理学部)
「境界プラズマと炉壁との相互作用に関する基礎過程の研究」研究会報告
K. Morita (Nagoya Univ.), T. Kaneko (Okayama Univ. Science)(Eds.)
"*NIFS Joint Meeting "Plasma-Divertor Interactions" and "Fundamentals of Boundary Plasma-Wall Interactions" January 6-7, 1995 National Institute for Fusion Science*" Mar. 1995 (in Japanese)

NIFS-PROC-22 代表者 河合 良信
プラズマ中のカオス現象
Y. Kawai,
"*Report of the Meeting on Chaotic Phenomena in Plasma,* 1994" Apr. 1995 (in Japanese)

NIFS-PROC-23 K. Yatsui (Ed.),
"*New Applications of Pulsed, High-Energy Density Plasmas*"; June 1995

NIFS-PROC-24 T. Kuroda and M. Sasao (Eds.),
"*Proceedings of the Symposium on Negative Ion Sources and Their Applications, NIFS, Dec. 26-27, 1994*", Aug. 1995

NIFS-PROC-25 岡本 正雄
新古典輸送概論(講義録)
M. Okamoto,
"*An Introduction to the Neoclassical Transport Theory" (Lecture note),* Nov. 1995 (in Japanese)

NIFS-PROC-26 Shozo Ishii (Ed.),
"*Physics, Diagnostics, and Application of Pulsed High Energy Density Plasma as an Extreme State*";
May 1996

NIFS-PROC-27 代表者 河合 良信
プラズマ中のカオスとその周辺非線形現象
Y. Kawai ,
"*Report of the Meeting on Chaotic Phenomena in Plasmas and Beyond, 1995*", Sep. 1996 (in Japanese)

NIFS-PROC-28 T. Mito (Ed.),
"*Proceedings of the Symposium on Cryogenic Systems for Large Scale Superconducting Applications*", Sep. 1996

NIFS-PROC-29 岡本 正雄
講義「核融合プラズマ物理の基礎 - I」
平成8年度 総合研究大学院大学 数物科学研究科 核融合科学専攻 1996年10月
M. Okamoto
"*Lecture Note on the Fundamentals of Fusion Plasma Physics - I" Graduate University for Advanced Studies;* Oct. 1996 (in Japanese)

NIFS-PROC-30 研究代表者 栗下 裕明(東北大学金属材料研究所)
所内世話人 加藤 雄大
平成8年度核融合科学研究所共同研究「被損傷材料の微小体積強度評価法の高度化」研究会 1996年10月 9日 於:核融合科学研究所

H. Kurishita and Y. Katoh (Eds.)
NIFS Workshop on Application of Micro-Indentation Technique to Evaluation of Mechanical Properties of Fusion Materials, Oct. 9, 1996, NIFS ; Nov. 1996 (in Japanese)

NIFS-PROC-31 岡本 正雄
講義「核融合プラズマ物理の基礎 - II」
平成8年度 総合研究大学院大学 数物科学研究科 核融合科学専攻 1997年4月
M. Okamoto
"*Lecture Note on the Fundamentals of Fusion Plasma Physics - II" Graduate University for Advanced*

Studies; Apr. 1997 (in Japanese)

NIFS-PROC-32 代表者 河合 良信
平成8年度 核融合科学研究所共同研究 研究会報告「プラズマ中のカオスとその周辺非線形現象」

Y. Kawai (Ed)
Report of the Meeting on Chaotic Phenomena in Plasmas and Beyond, 1996; Apr. 1997 (mainly in Japanese)

NIFS-PROC-33 H. Sanuki,
Studies on Wave Analysis and Electric Field in Plasmas; July 1997

NIFS-PROC-34 プラズマ対向機器・PSI・熱・粒子制御合同研究会報告
平成9年6月27日（金）9:00～16:20 核融合科学研究所・管理棟4F第1会議室
1997年 10月
T. Yamashina (Hokkaido University)
Plasma Facing Components, PSI and Heat/Particle Control June 27, 1997, National Institute for Fusion Science T. Yamashina (Hokkaido University) ; Oct. 1997 (in Japanese)

NIFS-PROC-35 T. Watari,
Plasma Heating and Current Drive; Oct. 1997

NIFS-PROC-36 T. Miyamoto and K. Takasugi (Eds.)
Production and Physics of High Energy Density Plasma; Production and Physics of High Energy Density Plasma; Oct. 1997

NIFS-PROC-37 (Eds.)T. Fujimoto, P. Beiersdorfer,
Proceedings of the Japan-US Workshop on Plasma Polarization Spectroscopy and The International Seminar on Plasma Polarization Spectroscopy January 26-28, 1998, Kyoto; June 1998

NIFS-PROC-38 (Eds.) Y. Tomita, Y. Nakamura and T. Hayashi,
Proceedings of the Second Asian Pacific Plasma Theory Conference APPTC '97; Aug. 1998